frontiers | Research Topics

Advanced protection for the smart grid

Edited by
Mahamad Nabab Alam, Tahir Khurshaid, Meng Yen Shih,
Almoataz Abdelaziz and Srete Nikolovski

Published in
Frontiers in Energy Research

ISSN 1664-8714
ISBN 978-2-8325-4113-5
DOI 10.3389/978-2-8325-4113-5

About Frontiers

Frontiers is more than just an open access publisher of scholarly articles: it is a pioneering approach to the world of academia, radically improving the way scholarly research is managed. The grand vision of Frontiers is a world where all people have an equal opportunity to seek, share and generate knowledge. Frontiers provides immediate and permanent online open access to all its publications, but this alone is not enough to realize our grand goals.

Frontiers journal series

The Frontiers journal series is a multi-tier and interdisciplinary set of open-access, online journals, promising a paradigm shift from the current review, selection and dissemination processes in academic publishing. All Frontiers journals are driven by researchers for researchers; therefore, they constitute a service to the scholarly community. At the same time, the *Frontiers journal series* operates on a revolutionary invention, the tiered publishing system, initially addressing specific communities of scholars, and gradually climbing up to broader public understanding, thus serving the interests of the lay society, too.

Dedication to quality

Each Frontiers article is a landmark of the highest quality, thanks to genuinely collaborative interactions between authors and review editors, who include some of the world's best academicians. Research must be certified by peers before entering a stream of knowledge that may eventually reach the public - and shape society; therefore, Frontiers only applies the most rigorous and unbiased reviews. Frontiers revolutionizes research publishing by freely delivering the most outstanding research, evaluated with no bias from both the academic and social point of view. By applying the most advanced information technologies, Frontiers is catapulting scholarly publishing into a new generation.

What are Frontiers Research Topics?

Frontiers Research Topics are very popular trademarks of the *Frontiers journals series*: they are collections of at least ten articles, all centered on a particular subject. With their unique mix of varied contributions from Original Research to Review Articles, Frontiers Research Topics unify the most influential researchers, the latest key findings and historical advances in a hot research area.

Find out more on how to host your own Frontiers Research Topic or contribute to one as an author by contacting the Frontiers editorial office: frontiersin.org/about/contact

Advanced protection for the smart grid

Topic editors

Mahamad Nabab Alam — National Institute of Technology Warangal, India
Tahir Khurshaid — Yeungnam University, Republic of Korea
Meng Yen Shih — Autonomous University of Campeche, Mexico
Almoataz Abdelaziz — Ain Shams University, Egypt
Srete Nikolovski — Josip Juraj Strossmayer University of Osijek, Croatia

Citation

Alam, M. N., Khurshaid, T., Shih, M. Y., Abdelaziz, A., Nikolovski, S., eds. (2023). *Advanced protection for the smart grid*. Lausanne: Frontiers Media SA.
doi: 10.3389/978-2-8325-4113-5

Table of contents

frontiers | Frontiers in Energy Research

TYPE Editorial
PUBLISHED 29 November 2023
DOI 10.3389/fenrg.2023.1298557

OPEN ACCESS

EDITED AND REVIEWED BY
ZhaoYang Dong,
Nanyang Technological University,
Singapore

*CORRESPONDENCE
Mahamad Nabab Alam,
itsmnalam@gmail.com
Tahir Khurshaid,
tahir@ynu.ac.kr

RECEIVED 21 September 2023
ACCEPTED 20 November 2023
PUBLISHED 29 November 2023

CITATION
Alam MN, Abdelaziz A, Khurshaid T, Nikolovski S and Shih MY (2023), Editorial: Advanced protection for the smart grid.
Front. Energy Res. 11:1298557.
doi: 10.3389/fenrg.2023.1298557

Editorial: Advanced protection for the smart grid

Mahamad Nabab Alam[1]*, Almoataz Abdelaziz[2], Tahir Khurshaid[3]*, Srete Nikolovski[4] and Meng Yen Shih[5]

[1]Department of Electrical Engineering, National Institute of Technology Warangal, Warangal, India, [2]Faculty of Engineering and Technology, Future University in Egypt, Cairo, Egypt, [3]Department of Electrical Engineering, Yeungnam University, Gyeongsan, Republic of Korea, [4]Faculty of Electrical Engineering, Josip Juraj Strossmayer University of Osijek, Osijek, Croatia, [5]Faculty of Engineering, Autonomous University of Campeche, Campeche, Mexico

KEYWORDS

protection coordination, transmission line protection, active distribution networks, microgrids, overcurrent proctection, distance protection

Editorial on the Research Topic
Advanced protection for the smart grid

1 Introduction

Recently, a growing trend in clean renewable power integration to electric grids has been observed around the globe. This trend aims to reduce carbon emissions by reducing dependence on fossil fuel-based electricity generation. As per the International Renewable Energy Agency 2023 (IRENA, 2023) report, 27.8% of electricity generation is shared by renewable sources, including hydroelectric, wind, solar, bioenergy, and geothermal energy (IRENA, 2023). The renewable total electricity generation counts for 7,858 T Wh in 2021. The two most promising sources are wind and solar energy, which account for 23% and 13%, respectively. Further, wind-based and solar-based energy generations, 15.7% and 22.7%, respective annual growth, were observed in 2021 compared to 2020. Trends indicate further development in these sources to meet future electricity needs. The electricity generation from solar power plants and wind farms is mainly distributed in nature and spread over broad geographical areas. These sources are also called distributed energy resources (DERs). These renewable sources are integrated into the grid through various static power converters. As a result, system electrical inertia reduces compared to the same done through rotating machine-based conventional sources. This makes the electric network protection task very challenging (Bakkar et al., 2023). Modern technologies such as power electronics-based flexible AC transmission systems (FACTS) devices to control and smooth power flow over the networks also add protection issues (Albasri et al., 2007).

2 Protection issues with renewable power integration

Proper electrical protection is necessary to run power networks with the highest reliability. Increased penetration of converter-interfaced distributed generations (CIDGs) and the deployment of smart grid technologies are changing fault current levels and

flow direction, challenging the existing protection schemes (Hooshyar and Iravani, 2017). Reduction in system inertia is one of the main reasons for modern protection challenges at the transmission and distribution levels. At the transmission level, conventional protection schemes using distance protection philosophy are affected by reduced fault current as the percentage of low energy power contribution from DERs increases. The correct fault direction and location are also challenging because of the heavy integration of renewable-based electricity generation into the grid. Removing the faulted section must be faster to prevent system instability at the transmission level where the zone-1 setting of the distance relay is responsible for this task. In the conventional system, distance relays work appropriately. However, in the modern renewable-rich transmission system, fault currents are lower which causes zone-1 to remain silent and zone-2 usually clears the fault of the distance relay which acts slower. On the one hand, the renewable-rich system has reduced inertia; on the other hand, fault clearing will take longer, which may result in stability issues. This may result in a widespread blackout. Therefore, there is a need for advanced protection schemes for the modern grid, called smart grid.

Power distribution networks face protection issues from the transmission systems because of massive renewable integration at the distribution level. Traditional distribution networks are radial, and power flow is unidirectional from an electric substation to the loads through electric feeders. However, the integration of renewables at distribution feeders disturbs the unidirectional flow of current during the faults (Hong et al., 2021). Not only the fault current magnitude but also the direction of the flow of fault current is also affected by the integration of renewables to the distribution level. Such distribution networks are termed active distribution networks (ADNs). The protection of renewable-rich ADNs is under scrutiny because the change in fault currents and network reconfiguration creates protection coordination issues (Zarei and Khankalantary, 2021). Extensive research activities are going on to provide simple and reliable solutions to the protection challenges of ADNs.

Additionally, the formation of microgrids (AC, DC and hybrid AC-DC) and their grid-connected and islanded mode operation provide several benefits by improving reliability and resiliency. Furthermore, networked microgrid systems are emerging and more reliable and resilient electricity infrastructure that can withstand harsh environmental conditions by isolating one another and powering by their internal sources (Alam et al., 2022). However, providing proper protection to such systems is more challenging. Existing protection schemes are prone to such changes. High impedance faults are going unnoticed and leading to damage to the system. Advanced protection schemes developed considering such issues can mitigate these impacts and maintain proper protection coordination. Adaptive protection, islanding detection, communication-assisted protection, and synchronized wide-area measurement-based protection schemes are emerging as potential solutions to the protection issues of the modern smart grid. Artificial intelligence (AI) based protection schemes may help to provide adequate answers to the smart grid's protection challenges because of renewable integration and new technological adaptations.

The adaptive protection scheme is one of the advanced protection schemes which can provide reliable protection to the smart grid. Figure 1 shows one of the adaptive protection schemes (Alam et al., 2019). The system's topology and operating states are dynamically tracked in such schemes. If any significant changes in the network, such as loss of a line, generator, transformer, or large load changes (addition/removal), are observed, then relay settings are updated. In directional overcurrent-based protection schemes, the fault current calculations are performed under those operating conditions. The protection coordination status is checked with the obtained fault current values at various relay locations. In case of any miscoordination, relay settings are calculated using the updated fault information and older settings are replaced with newer settings (Alam, 2019). Similarly, in the distance protection scheme, zone settings and differential protection schemes, slop settings are updated following a major change in the system operating condition (George et al., 2023).

3 Identified areas of research on advanced protection to the smart grid

This Research Topic aimed to provide field deployable solutions to smart grid protection issues. High penetration of DERs, FACTS devices, dynamically changing network topology, and grid decentralization pose several protection challenges, although they provide flexible, reliable and resilient network operation. Indeed, the existing protection practices do not appropriately handle many issues caused by such changes. The ADNs and the formation of microgrids and networked microgrids add more protection challenges at the distribution level. The key research areas identified in this special call of papers on the Advanced Protection of the Smart Grid are the following.

- Development of adaptive protection scheme for smart grid
- High impedance fault detection and location scheme
- Protection of active distribution networks
- Protection of AC and DC microgrids
- Communication-assisted and Wide-area measurement system-based protection
- Application of artificial intelligence and soft computing techniques for power system protection

In addition to these key topics, a few more topics are very relevant in smart grid protections, such as the impact assessment of different types of DERs on fault current calculation, anti-islanding protection and fault direction identification in renewable rich networks.

4 Contributions to advanced protection to the smart grid

In this Research Topic, 24 papers were submitted, of which only 13 were accepted for publication. The key contributions of the accepted papers are briefed here.

Prabhu et al. propose an intelligent distance relaying scheme that utilizes only current measurements for a series-compensated line integrated with a wind farm system. In this scheme, the fault detection task is performed using the signs of the half-cycle magnitude differences of the line end positive-sequence currents,

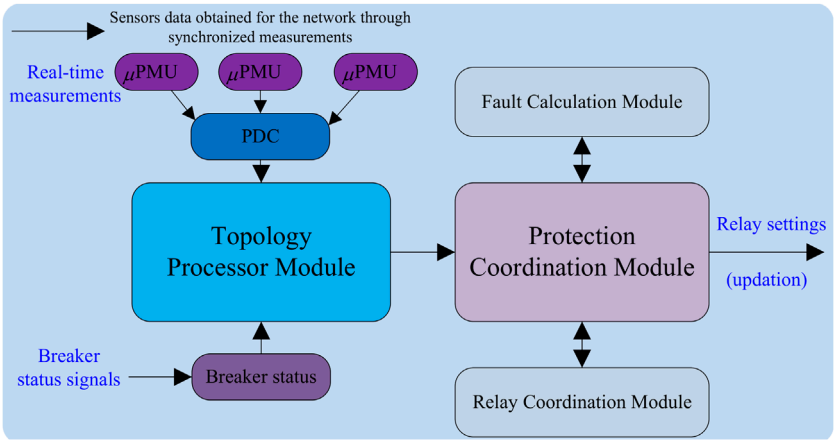

FIGURE 1
Adaptive protection scheme.

and the fault classification task is performed using only the local current measurements processed through the Fourier–Bessel series expansion bagging ensemble classifier.

Nobakhti and Ketabi propose a protection scheme based on impedance that can detect high-impedance faults in both islanded and grid-connected modes of low-voltage and median-voltage microgrids. Additionally, it can handle load and generation uncertainty and network reconfigurations.

Liang et al. propose a novel approach for fault location in transmission lines using power line communication (PLC) equipment. In this approach, the channel frequency response obtained from the PLC receiver is used to estimate the high-frequency input impedance to monitor and locate the ground fault of the power grid in real-time.

Li et al. propose a direct current circuit breaker (DCCB) failure protection method and a secondary accelerated fault isolation scheme of voltage source converter-based high-voltage direct current (VSC-HVDC) grids. The scheme achieves the accelerated isolation of DC faults after the failure of the DCCB and avoids the trip of the AC circuit breaker effectively which is verified through PSCAD simulation.

Esmail et al. propose simultaneous series and shunt earth fault detection and classification using the Clarke transform for power transmission systems under different fault scenarios. The fault detection time of the proposed schemes is reported to be as low as 20 ms. The behaviour of the proposed schemes is tested and validated by considering different fault scenarios with varying locations of fault, inception angles, fault resistance, and noise.

Kant et al. introduce an advanced short-circuit protection scheme for a bipolar DC microgrid. It is based on the multi-resolution analysis of travelling waves using discrete wavelet transform. The proposed approach is tested on a 500 V ring-type bipolar DC microgrid test model in the MATLAB/Simulink environment and validated with the real-time OPAL-RT simulator.

There are some miscellaneous contributions in this Research Topic.

Zeng et al. propose an interline hybrid DC circuit breaker by combining SCR string and a small number of H-bridge modules (SCR-IHCB). The proposed SCR-IHCB can block the DC fault of two adjacent lines by sharing only one main breaker branch (MB) mainly composed of low-cost SCR string and H-bridge module instead of IGBT-in-series string. He et al. propose multi-port hybrid DC circuit breakers (M-HCBs) with fewer devices for fault blocking in multi-terminal VSC-HVDC systems.

Zhang et al. discuss arc fault detection using ResNet and gamma transform regularization. Xiong et al. analyze overheating fault alarming for compact insulated busways in buildings by gas sensing. Vishnuram et al. present a comprehensive review of EV power converter topologies charger types infrastructure and communication techniques. Zhou et al. introduce the gas production law of free gas in oil-immersed power transformers under discharge faults of different severity. Finally, load frequency control of the power system based on an improved AFSA-PSO event-triggering scheme is presented by Huang and Lv.

5 Future scope of study

Further scope of this Research Topic is on providing solutions to high-impedance fault detection and location, developing wide-are measurement-based advanced backup protection schemes and artificial intelligence-based protection schemes for the smart grid.

Author contributions

MA: Writing–review and editing, Conceptualization, Investigation. AA: Writing–review and editing, Investigation. TK: Writing–review and editing, Investigation. SN: Investigation, Writing–review and editing. MS: Writing–review and editing, Investigation.

Acknowledgments

The guest editorial board would like to thank the authors for contributing to this topic, the reviewers for doing an excellent task

in helping the editorial board to select quality contributions and additional editors for their contributions to this topic.

Conflict of interest

The authors declare that the research was conducted in the absence of any commercial or financial relationships that could be construed as a potential conflict of interest.

Publisher's note

References

Alam, M. N. (2019). Adaptive protection coordination scheme using numerical directional overcurrent relays. *IEEE Trans. Industrial Inf.* 15, 64–73. doi:10.1109/TII.2018.2834474

Alam, M. N., Chakrabarti, S., and Pradhan, A. K. (2022). Protection of networked microgrids using relays with multiple setting groups. *IEEE Trans. Industrial Inf.* 18, 3713–3723. doi:10.1109/TII.2021.3120151

Alam, M. N., Chakrabarti, S., Sharma, A., and Srivastava, S. C. (2019). "An adaptive protection scheme for ac microgrids using pmu based topology processor," in 2019 IEEE International Conference on Environment and Electrical Engineering and 2019 IEEE Industrial and Commercial Power Systems Europe (EEEIC/ ICPS Europe), Genova, Italy, June, 2019, 1–6. doi:10.1109/EEEIC.2019.8783396

Albasri, F. A., Sidhu, T. S., and Varma, R. K. (2007). Performance comparison of distance protection schemes for shunt-facts compensated transmission lines. *IEEE Trans. Power Deliv.* 22, 2116–2125. doi:10.1109/TPWRD.2007.900283

Bakkar, M., Bogarra, S., Córcoles, F., Iglesias, J., and Hanaineh, W. A. (2023). Multi-layer smart fault protection for secure smart grids. *IEEE Trans. Smart Grid* 14, 3125–3135. doi:10.1109/TSG.2022.3229848

George, N., Naidu, O. D., and Pradhan, A. K. (2023). Distance protection for lines connecting converter interfaced renewable power plants: adaptive to grid-end structural changes. *IEEE Trans. Power Deliv.* 38, 2011–2021. doi:10.1109/TPWRD.2022.3231403

Hong, L., Rizwan, M., Wasif, M., Ahmad, S., Zaindin, M., and Firdausi, M. (2021). User-defined dual setting directional overcurrent relays with hybrid time current-voltage characteristics-based protection coordination for active distribution network. *IEEE Access* 9, 62752–62769. doi:10.1109/ACCESS.2021.3074426

Hooshyar, A., and Iravani, R. (2017). Microgrid protection. *Proc. IEEE* 105, 1332–1353. doi:10.1109/JPROC.2017.2669342

Irena, (2023). Renewable-energy-statistics-2023. https://www.irena.org/Publications/2023/Mar/Renewable-capacity-statistics-2023.

Zarei, S. F., and Khankalantary, S. (2021). Protection of active distribution networks with conventional and inverter-based distributed generators. *Int. J. Electr. Power & Energy Syst.* 129, 106746. doi:10.1016/j.ijepes.2020.106746

frontiers | Frontiers in Energy Research

TYPE Original Research
PUBLISHED 17 January 2023
DOI 10.3389/fenrg.2023.1103298

OPEN ACCESS

EDITED BY
Srete Nikolovski,
Josip Juraj Strossmayer University of Osijek, Croatia

REVIEWED BY
Ravi Samikannu,
Botswana International University of Science and Technology, Botswana
Dubravko Sabolić,
University of Zagreb, Croatia

*CORRESPONDENCE
Dong Liang,
liangdong@xaut.edu.cn

SPECIALTY SECTION
This article was submitted to Smart Grids, a section of the journal Frontiers in Energy Research

RECEIVED 20 November 2022
ACCEPTED 02 January 2023
PUBLISHED 17 January 2023

CITATION
Liang D, Zhang K, Ge S, Wang Y and Wang D (2023), A novel fault monitoring method based on impedance estimation of power line communication equipment. *Front. Energy Res.* 11:1103298. doi: 10.3389/fenrg.2023.1103298

A novel fault monitoring method based on impedance estimation of power line communication equipment

Dong Liang*, Kaiwen Zhang, Song Ge, Yang Wang and Deyi Wang

Xi'an Key Laboratory of Intelligent Energy, Xi'an University of Technology, Xi'an, China

Due to the close relationship between power grid fault and impedance, there is a significant defect in the use of power line communication (PLC) equipment to monitor and locate power grid faults, which is the lack of real-time impedance information. Therefore, this study proposes a new fault monitoring method based on impedance estimation of power line communication equipment. The channel frequency response (CFR) obtained from the PLC receiver is used to estimate the high-frequency input impedance to monitor and locate the ground fault of the power grid in real time. Firstly, based on the multi-conductor transmission line theory, bottom-up channel modeling method and impedance estimation technology, the basic principles of fault monitoring and location methods are clarified. Then, modeling and analysis of cables in different situations are carried out, and the characteristics of the factors affecting the impedance in CFR are extracted by variational modal decomposition (VMD), and the estimation results of impedance are obtained by inversion analysis. Based on this, the impedance change and machine learning algorithm are used to track and identify the abnormal state of the power line to achieve high-sensitivity positioning of the cable fault. The simulation results show that the method has a good identification effect on high and low impedance cable fault, and has a better effect on low resistance fault monitoring. The fault location error is less than 2.13%, and has a good positioning accuracy.

KEYWORDS

channel modeling, impedance estimation, power line communication, fault detection, fault location

Introduction

As the power electronic power system continues to promote, the control of the power electronic converter changes the fault characteristics of the power grid. For example, the fault current is reduced by power electronic control. The Alternating Current (AC) sequence component is isolated, making almost all current protection principles based on AC work frequency quantities fail (current, voltage, distance, zero sequence, negative sequence, *etc.*), even differential protection due to short circuit current controlled by power electronic reduction also fail. These situations present new challenges for the monitoring of grid faults (Aucoin et al., 1982; Lee et al., 1985; Balser et al., 1986; Wang et al., 2018; Bhandia et al., 2020; Guillen et al., 2022).

Reusing power line communication (PLC) devices that spread throughout the grid to monitor faults has become a hot research topic (Lai et al., 2005; Sedighi et al., 2005; Costa

et al., 2015; Chul-Hwan et al., 2002; Liang et al., 2022). This method is not affected by fault currents and is thus suitable for power electronic grid fault monitoring. Moreover, research has proven that this method is also effective for high impedance fault (HIF) that are difficult to monitor (Chul-Hwan et al., 2002; Lai et al., 2005). However, one drawback of such methods is that they do not use the broadband impedance information closely associated with the fault for real-time monitoring. This paper takes this as a breakthrough to start the research of new fault monitoring methods.

Considerable research has been conducted on fault monitoring and localization, and have achieved specific research results. These methods include voltage-, current-(Aucoin et al., 1982; Lee et al., 1985; Balser et al., 1986; Wang et al., 2018; Bhandia et al., 2020), and PLC-based methods (Sedighi et al., 2005; Costa et al., 2015; Chul-Hwan et al., 2002; Lai et al., 2005; Michalik et al., 2007; Michalik et al., 2008). Conventional methods based on voltage and current: Aucoin et al. (1982) proposed using current waveforms in the 2–10-kHz band as fault features and features of high-frequency information for high-impedance fault monitoring. Lee et al. (1985) used a microcomputer to obtain information on three-phase currents, zero-sequence currents, and network locations to monitor faults. Balser et al. (1986) observed substation fundamental and third and fifth harmonic unbalance of feeder currents and set the unbalance threshold to monitor faults. Wang et al. (2018) proposed a novel high-impedance fault detection method based on non-linear voltage and current characteristics. Bhandia et al. (2020) used voltage and current waveform distortion detection of the distribution system to distinguish and detect HIF. Sedighi et al. (2005) proposed a novel method for high-impedance fault detection based on a pattern recognition system in which wavelet transform was used for signal decomposition and feature extraction. Costa et al. (2015) used boundary distortion and wavelet transform for real-time monitoring of HIFs. Furthermore, discrete wavelet transform was used to monitor HIF (Chul-Hwan et al., 2002; Lai et al., 2005; Michalik et al., 2007). Artificial intelligence (Michalik et al., 2008; García et al., 2014; Routray et al., 2015; Lu et al., 2022) is commonly used to perform high-impedance fault detection. PLC-based methods: Stefanidis et al. (2019) studied the applicability of high impedance fault (HIF) detection and location method based on high frequency signal injection into overhead transmission lines (TLs). Use the power line communication (PLC) infrastructure to transmit and receive high-frequency signals. Huo et al. (2018) studied the use of power line communication (PLC) to monitor the state of the power grid, and the principle that the PLC channel will change when the network fails, so as to monitor the power grid failure. This method does not combine fault and impedance. Cao et al. (2016) describes the fault location principle of zero sequence current phase, and closes the node to isolate the fault through power line communication. This method only uses the communication function of PLC, and has not integrated the power line communication with the physical state of power grid. Milioudis et al. (2015); Milioudis et al. (2012a); Milioudis et al. (2012b) proposed using PLC devices to monitor faults by calculating the difference in the unit impulse response. High-impedance faults that can be easily missed by overcurrent protection can be detected using this method. Furthermore, dynamic monitoring can be realized using less equipment. In this method, initial information-physical fusion can be realized. However, such a solution through phenomena is yet to be investigated comprehensively. Passerini et al. (2019) and subsequent studies implemented dynamic monitoring of complex distribution network faults based on the impedance characteristics of the PLC band, allowing real-time tracking of fault progress. However, initial studies required specialized equipment for impedance monitoring.

Most traditional fault voltage and current based methods applied to future highly power electronic grids will degrade monitoring performance as power electronic control reduces fault currents and isolates the AC sequence component (Aucoin et al., 1982; Lee et al., 1985; Balser et al., 1986; Wang et al., 2018; Bhandia et al., 2020; Jia et al., 2018). Most of the existing monitoring methods use low-frequency monitoring quantity, thus may ignore the fault information in the high frequency band; and in locating the fault often need to install additional equipment for signal injection or monitoring, which increases the cost to some extent (Teng et al., 2014; Niu et al., 2021). In existing PLC-based intelligent sensing methods, channel frequency-domain response (or channel transmission function) is generally considered for fault sensing, whereas the real-time impedance characteristics that are closely related to faults have not been studied extensively.

The main contribution of this study is in introducing real-time impedance estimation techniques into PLC-based fault monitoring, thus increasing sensitivity and accuracy. Moreover, combines channel frequency response (CFR) and grid impedance using machine learning techniques (Prasad et al., 2019; Huo et al., 2021; Huo et al., 2020) that are frequently used in cable monitoring, and predicts grid impedance directly from CFR data using impedance estimation techniques. The expected input impedance is then used for fault detection and location. The CFR data can be obtained easily from PLC equipment and can be used to respond to faults quickly. Because PLC technology is already applied to lay power lines, additional equipment is not required in the proposed method, which reduces costs. The high-frequency range of PLC technology allows access to information in the high-frequency band.

Theoretical analysis

First, CFR can be obtained in real time by PLC equipment. According to the relationship between CFR and impedance spectrum, the characteristics of CFR are extracted by variational modal decomposition (VMD), and the key factors affecting impedance are obtained. Through back analysis, the machine learning algorithm model of decision tree is established, and the impedance estimation model is obtained. Using the input impedance predicted by CFR and impedance estimation technology obtained by power line communication equipment, the fault monitoring matrix is constructed to detect the fault from the perspective of channel frequency response (CFR) and input impedance. Impedance data contains some location information. The fault location is determined by impedance data and wave velocity, and the distance function is obtained. The overall scheme diagram is shown in Figure 1.

Power line channel modeling

This section uses a bottom-up approach to model the PLC channel to obtain the CFR of the system (Niu et al., 2021), where

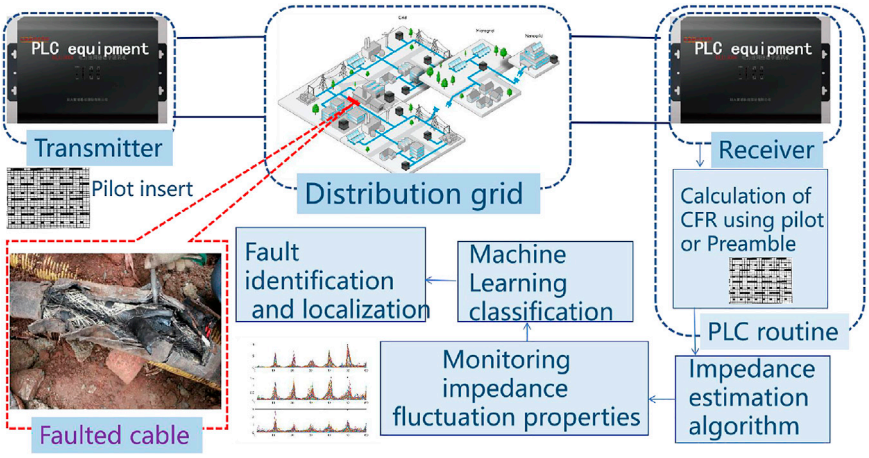

FIGURE 1
Overall scheme diagram.

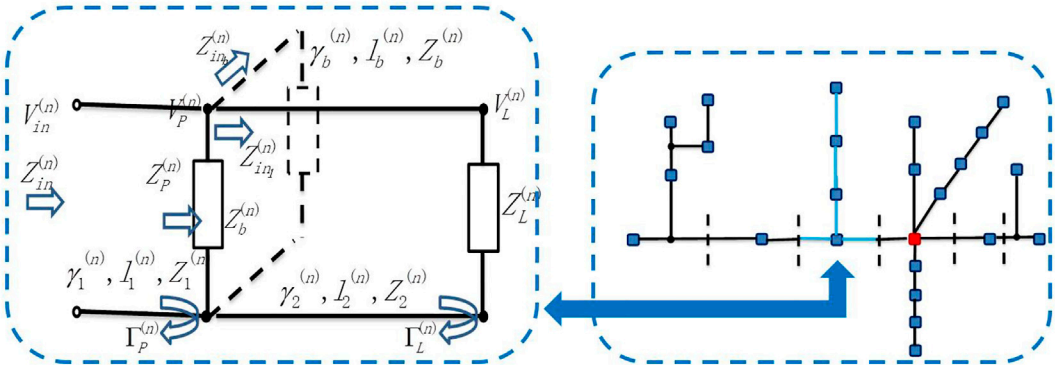

FIGURE 2
Typical network topology diagram.

CFR is the voltage ratio between two nodes (transmitter and receiver). According to the transmission line theory, the characteristics of the transmission line are mainly expressed by the characteristic impedance and transmission constant, Z; γ can be obtained from equations (1); (2), which are calculated according to the resistance, inductance, conductivity and capacitance (R, L, G and C) per unit length (Meng et al., 2004; Papaleonidopoulos et al., 2003; Paul et al., 1994).

$$Z_0 = \sqrt{\frac{R + j2\pi fL}{G + j2\pi fC}} \tag{1}$$

$$\gamma = \alpha + j\beta = \sqrt{(R + j2\pi fL)(G + j2\pi fC)} \tag{2}$$

The bottom-up channel modeling method needs to consider the network topology and simplify the network topology; As shown in Figure 2, the path between two nodes (Tx and Rx) in a typical network topology is called the trunk path (Tonello et al., 2009; Versolatto et al., 2010). All nodes on the trunk path are divided into n basic units according to the trunk path, and each basic unit has a unique trunk part and branch part; Further, the branch portion may have no branches, branches, or multiple branches. To simplify the calculation, the equivalent branch impedance of nodes with different branch levels is transmitted back to the trunk part (Paul et al., 2008). According to the bottom-up approach, each unit is divided into three parts, namely the first part, the second part and the branch part. Calculate the CFR of each basic unit. The detailed topology of each basic unit is shown in Figure 2.

As illustrated in Figure 2, the input impedance of the first part of the receiver can be obtained from the following equation:

$$Z_{in}^{(n)} = Z_1^{(n)} \frac{Z_p^{(n)} + Z_1^{(n)} tanh\left(\gamma_1^{(n)} l_1^{(n)}\right)}{Z_1^{(n)} + Z_p^{(n)} tanh\left(\gamma_1^{(n)} l_1^{(n)}\right)} \tag{3}$$

where Z_1 is the characteristic impedance, γ is the transmission constant, l is the line length, and Z_p can be obtained from the following equation:

$$Z_P^{(n)} = \frac{Z_L^{(n)} Z_{inb}^{(n)}}{Z_L^{(n)} + Z_{inb}^{(n)}} \tag{4}$$

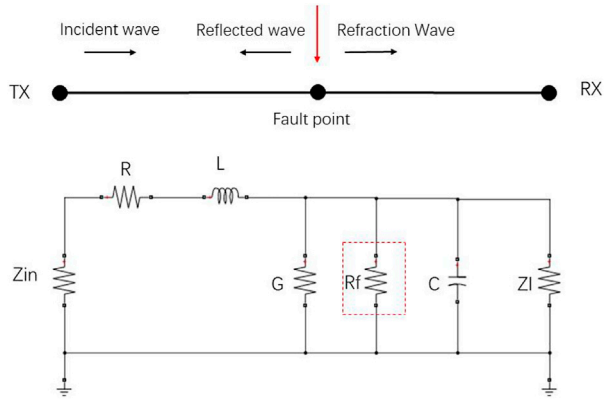

FIGURE 3
Fault cable equivalence diagram.

Here, Z_L is the impedance on the load side of the network, and Z_{inb} is the impedance on the branch side of the network. The CFR of the nth basic unit can be obtained by the voltage ratio of the receiving side to the transmitting side, expressed by the following equation:

$$H^{(n)}(f) = \frac{V_l^{(n)}}{V_{in}^{(n)}} = \frac{V_l^{(n)}}{V_p^{(n)}} \frac{V_p^{(n)}}{V_{in}^{(n)}} \tag{5}$$

$$\frac{V_l^{(n)}}{V_p^{(n)}} = \frac{1 + \Gamma_L^{(n)}}{e^{\gamma_2^{(n)} l_2^{(n)}} + \Gamma_L^{(n)} e^{-\gamma_2^{(n)} l_2^{(n)}}} \tag{6}$$

$$\frac{V_p^{(n)}}{V_{in}^{(n)}} = \frac{1 + \Gamma_p^{(n)}}{e^{\gamma_1^{(n)} l_1^{(n)}} + \Gamma_p^{(n)} e^{-\gamma_1^{(n)} l_1^{(n)}}} \tag{7}$$

$$\Gamma_L^{(n)} = \frac{Z_L^{(n)} - Z_2^{(n)}}{Z_L^{(n)} + Z_2^{(n)}} \tag{8}$$

$$\Gamma_P^{(n)} = \frac{Z_P^{(n)} - Z_1^{(n)}}{Z_p^{(n)} + Z_1^{(n)}} \tag{9}$$

Where Z_2 is the characteristic impedance of the line of the basic unit part 2, γ_2 is the transmission constant of the line of the basic unit part 2, l_2 is the line length of the line of the basic unit part 2, Γ_P is the reflection coefficient of the basic unit part 1, Γ_L is the reflection coefficient of the basic unit part 2.

Using these equation, we can obtain the CFR of the nth basic unit. Therefore, iterating from the back to front, the CFR of each basic unit can be determined. The total channel frequency response can be obtained using the following equation:

$$H(f) = \prod_{n=1}^{N} H^{(n)}(f) \tag{10}$$

Similarly, the CFR between any two points can be determined by simply cascading the CFR of all the essential cells between the two points.

Faulty cable model

First, when a ground fault is generated, it will cause a transient change in the topology, and this change will cause a more drastic change in the CFR and impedance spectrum.

Since the ground fault is mainly manifested in one fault point, the fault is simulated by the resistance R_f, the cable in case of fault is equated into a distributed parameter model, as displayed in Figure 3, to describe the transmission characteristics of the signal in the cable (Xie et al., 2017). The CFR in case of a cable fault is obtained through previously proposed channel modeling.

The resistance R, inductance L, capacitance C, and conductance G at each unit length of the cable can be approximated by the following equation (van der Wielen et al., 2008):

$$R \approx \frac{1}{2\pi}\sqrt{\frac{\mu_0 \omega}{2}}\left(\frac{1}{r_c}\sqrt{\rho_c} + \frac{1}{r_s}\sqrt{\rho_s}\right) \tag{11}$$

$$L \approx \frac{\mu_0}{2\pi} ln\frac{r_s}{r_c} + \frac{1}{4\pi}\sqrt{\frac{2\mu_0}{\omega}}\left(\frac{1}{r_c}\sqrt{\rho_c} + \frac{1}{r_s}\sqrt{\rho_s}\right) \tag{12}$$

$$C = \frac{2\pi\varepsilon}{ln\ (r_s/r_c)} \tag{13}$$

$$G = \frac{2\pi\delta}{ln\ (r_s/r_c)} \tag{14}$$

where the angular frequency $\omega = 2\pi f$, r_c, and r_s are the cable core version diameter and shield inner radius, respectively, ρ_c and ρ_s are the cable core resistivity and shield resistivity, respectively, μ_0 is the vacuum permeability, ε is the dielectric constant of the dielectric, and δ is the dielectric conductivity. Knowing the distribution parameters of the cable, the channel can be modeled by the bottom-up presented approach above for the normal and fault cases. Its transmission characteristics change when a fault occurs, as displayed in Figure 3. When the value of R_f is greater than 10 Z_0, it is a high impedance fault, for R_f less than 10 Z_0, it is a low impedance fault, and Z_0 is the characteristic impedance of the cable (Lu et al., 2004). The high and low resistance fault sizes in this paper's simulation section are set to 10 Z_0 and Z_0, or 500 and 50 Ω, respectively.

Fault detection theory

Eq. 3 indicates that when a ground fault occurs, the branch and backbone structure of the network changes. Changes in structure will affect the topology and reflection coefficient of the network; changes in structure will also affect the impedance of each part. Under the influence of both, the input impedance will also change (Passerini et al., 2017). Therefore, whether a fault occurs from the perspective of input impedance can be determined, and the following equation is defined from the perspective of fault detection.

$$\Delta(IN) = \frac{Z_{NF} - Z_{fault}}{Z_{NF}} \times 100(\%) \tag{15}$$

Here, Z_{NF} is the input impedance under normal conditions, and Z_{fault} is under fault conditions.

However, no direct correlation was observed between CFR and input impedance in the aforementioned derivation, even though a certain mathematical relationship exists. In (Papaleonidopoulos et al., 2003), the input impedance was postulated to depend on the ratio between two functions (current transfer function and voltage transfer function) (Piante et al., 2019) as follows:

$$H_V = \frac{Z_l}{Z_{in}} H_I = Z_l Y_{in} H_I \tag{16}$$

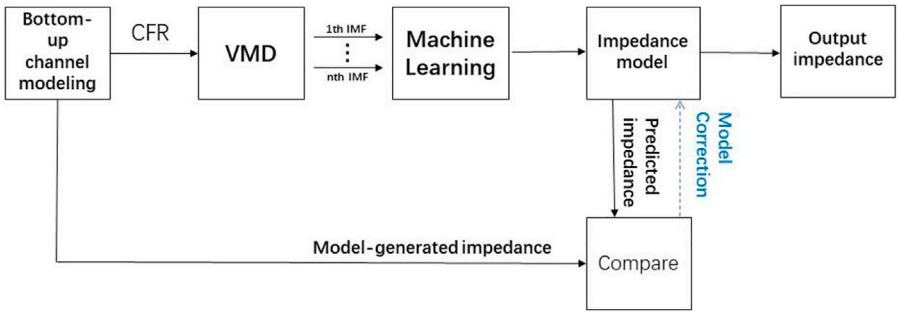

FIGURE 4
Flow chart of impedance estimation technique.

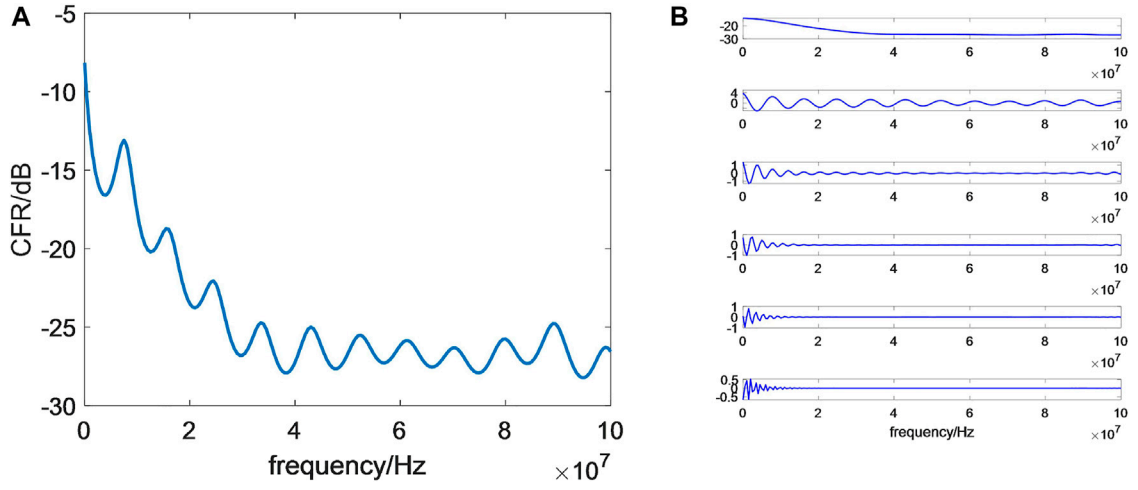

FIGURE 5
A set of CFR data and VMD result. **(A)** is the CFR data, **(B)** is the VMD result.

Therefore, a relationship exists between the voltage transfer function and the input impedance, and the correlation is apparent when the current transfer function is constant as follows (Piante et al., 2019):

$$\frac{\boldsymbol{H}_{NF}-\boldsymbol{H}_{fault}}{\boldsymbol{H}_{NF}}=\frac{\boldsymbol{Z}_{l}\boldsymbol{Y}_{in}\boldsymbol{H}_{I}-\boldsymbol{Z}_{l}\boldsymbol{Y}_{inf}\boldsymbol{H}_{If}}{\boldsymbol{Z}_{l}\boldsymbol{Y}_{in}\boldsymbol{H}_{I}}=\frac{\boldsymbol{Y}_{in}-\boldsymbol{Y}_{inf}\frac{\boldsymbol{H}_{If}}{\boldsymbol{H}_{I}}}{\boldsymbol{Y}_{in}} \quad (17)$$

where H_{NF} is the voltage transfer function under normal conditions, H_{fault} is the voltage transfer function under fault conditions. Furthermore, H_I is the current transfer function under normal conditions, H_{If} is the current transfer function under fault conditions, and the change of input impedance before and after a fault is apparent,Y_{in} is the admittance value of the first part of the receiver. The fault can be monitored using the input impedance; as expressed in Eq. 17, the voltage transfer function can be used to observe the fault, and the frequency domain of the voltage transfer function is the CFR. Therefore, the fault can be detected from the perspective of the CFR, which can be measured by the PLC equipment.

Therefore, the input impedance and CFR allow the detection of faults, as shown below:

$$\boldsymbol{\Delta}(\boldsymbol{IN})=\frac{|\boldsymbol{Z}_{NF}|-|\boldsymbol{Z}_{fault}|}{|\boldsymbol{Z}_{NF}|}\times\boldsymbol{100}(\%) \quad (18)$$

$$\boldsymbol{\Delta}(\boldsymbol{CFR})=\frac{|\boldsymbol{H}_{NF}(\boldsymbol{f})|-|\boldsymbol{H}_{fault}(\boldsymbol{f})|}{|\boldsymbol{H}_{NF}(\boldsymbol{f})|}\times\boldsymbol{100}(\%) \quad (19)$$

Fault location theory

After fault detection, fault location should be determined. When the network topology changes due to faults, enough fault information can be obtained from Eqs 18, 19, which can be used to determine the fault location. Since CFR is greatly affected, the fault can be determined from the perspective of input impedance. Moreover, the input impedance is obtained by using the impedance estimation technique, which does not require additional measurement equipment and is presented in Chapter three. After obtaining the input impedance, only the input impedance is subjected to the inverse fast Fourier transform (IFFT):

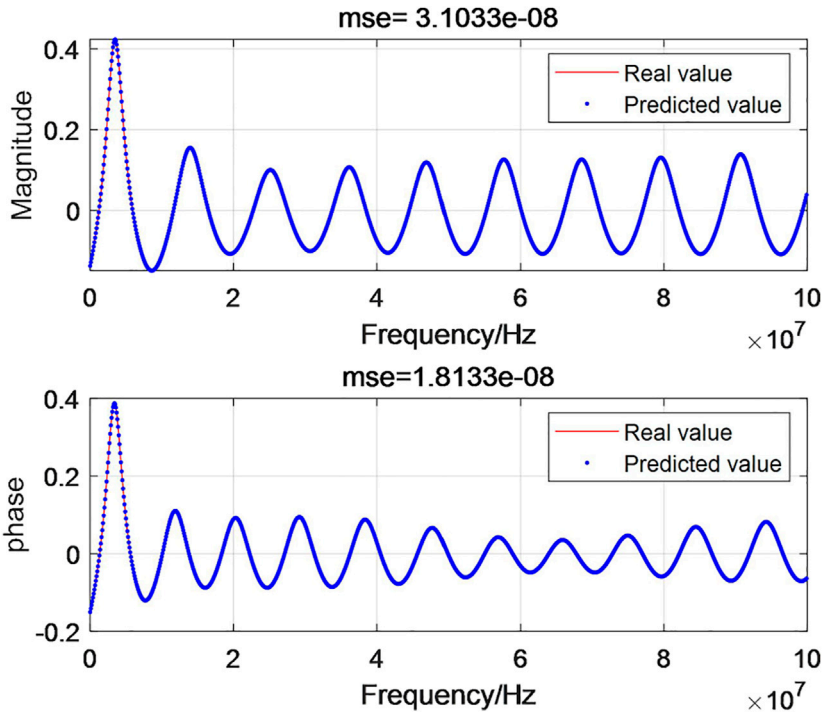

FIGURE 6
Predicted results of impedance estimation.

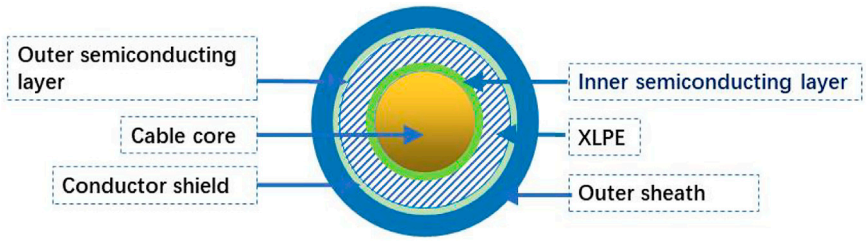

FIGURE 7
Simplified structure diagram of single-core cable.

$$\Delta(IN) \xrightarrow{IFFT} \Delta(t) \tag{20}$$

To achieve fault positioning, the electromagnetic wave propagation speed in the cable should be calculated at high frequency. The faster the wave propagation speed is, the highest is close to the speed of light. At high frequencies, the propagation speed of electromagnetic waves is independent of frequency and is mainly determined by the primary transmission constants L and C of the cable line, and the electromagnetic wave speed can be expressed as follows:

$$v = \frac{1}{\sqrt{LC}} \tag{21}$$

Combining the wave velocity (21) with the input impedance Eq. 20 in time domain yields a function of distance.

$$d(vt) = \Delta(t \times v) \tag{22}$$

Therefore, The obtained equation is a function of distance and variation, from which information about the fault location can be obtained. The input impedance is obtained through iteration easily by using the modeling process. When a fault occurs, the input impedance at the fault point and the input impedance of the node after the fault point change. Therefore, the fault location can be determined according to this characteristic.

Technical route and impedance estimation

According to the method proposed in (Liang et al., 2019), CFR is used to predict the impedance, that is, impedance estimation technology. Obtain CFR in real time through PLC equipment. According to the relationship between CFR and impedance

TABLE 1 The parameters of XLPE cable.

	Radius	Resistivity
Cable core	Rc = 9.2 mm	Pc = 1.75*10−8 Ω m
Shielding layer	Rs = 14.5 mm	Ps = 1.75*10−8 Ω m

TABLE 2 The properties of XLPE.

Relative dielectric constant (F·m)	ε = 2.11
Conductivity (S·m)	δ = 1*10−16
Vacuum permeability (H/m)	μ_0 = 4π*10−7
Absolute dielectric constant (F·m)	ε0 = 8.85*10−12

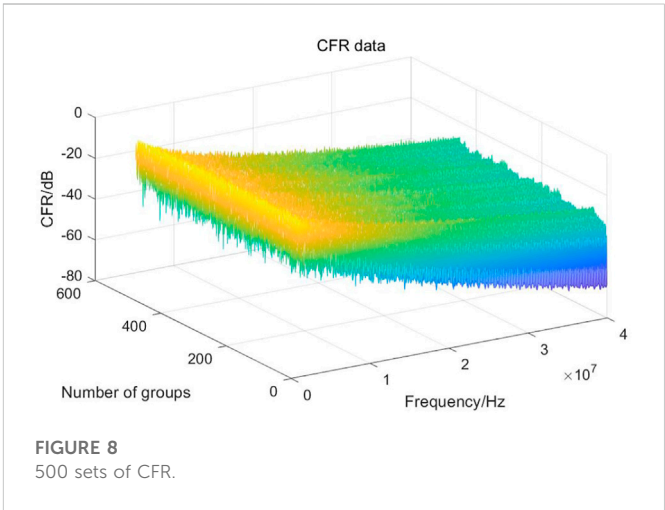

FIGURE 8
500 sets of CFR.

spectrum, the characteristics of CFR are extracted by variational modal decomposition (VMD), and the key factors affecting impedance are obtained. The impedance estimation model is obtained by using the decision tree machine learning algorithm model.

Impedance estimation

The impedance estimation technique is categorized into the following steps, as displayed in Figure 4.

First, the CFR is obtained by modeling the channel in a bottom-up approach. A close relationship exists between the input impedance and CFR; therefore, machine learning techniques are used to predict the input impedance, using the CFR as the input and the input impedance as the output. However, some error exists when using the CFR directly as the input. Therefore, feature extraction is performed for the CFR using VMD. In this study, the impedance estimation technique was introduced using a set of CFR data as an example, and a set of channel frequency response data is displayed in Figure 5.

The CFR was then subjected to VMD decomposition and performed on the CFR data in Figure 5A to obtain six sets of eigenmode functions (IMF components), as displayed in Figure 5B. High-frequency components exist in the IMF of Figure 5B, and the high-frequency components are used as the input produces errors in the prediction results. Therefore, the IMF should be analyzed. Experimental results revealed that the first three components of the VMD decomposition were selected for superior prediction.

In the third step, machine learning is used to predict impedance. Experimental results have revealed the first three quantities in the IMF after decomposition using VMD are closely related to the impedance; therefore, after removing the curve's high frequency noise, the first three quantities are selected as the input to the decision tree, and the amplitude and phase of the impedance are used as the output. The data from the preliminary modeling are compared to verify the accuracy of the impedance estimation technique. The results are displayed in Figure 6, which revealed that the impedance estimation technique exhibits excellent impedance prediction results; The results show that the predicted value from the simulation procedure is also in line with the set real value.

Impedance estimation techniques can predict impedance accurately, and the expected input impedance can be used for fault detection. When the CFR is obtained, the CFR can be used for fault detection. The impedance estimation technique can be used predict the impedance, and the input impedance can be used for fault detection and location. By contrast, the CFR can be obtained directly by using power line communication equipment.

Simulation

In this chapter, The simulation model is built in matlab software, and the transmission line model is modeled and processed by combining the bottom-up modeling method and the theory of transmission line. Combined with the change of network topology under fault conditions, the CFR of the receiving end is changed. According to the relationship between CFR and input impedance, the VMD and machine learning methods are used to predict the impedance. Then, according to the change of impedance spectrum under normal and fault conditions, the fault is monitored and the fault is located. First, a random topology using measured load data and random trunk and branch lengths is constructed, and then any set of data from it is taken for detailed analysis. Second, the fault detection is performed by CFR data and impedance data, and the fault detection effects of the two different methods are compared and analyzed, and finally, the fault location effect using the predicted input impedance is demonstrated.

The subsequent simulation will use a single-core power cable as the object of study, and simulations have been performed based on the actual parameters of the cable, and Figure 7 shows the simplified structure of the single-core cable (Wagenaars et al., 2010).

The parameters of 240-mm^2 single-core cross-linked polyethylene cable (XLPE cable) are presented in Table 1, and the properties of XLPE cable are listed in Table 2.

Given the above parameters, the cable can be modeled according to the cable modeling method described previously.

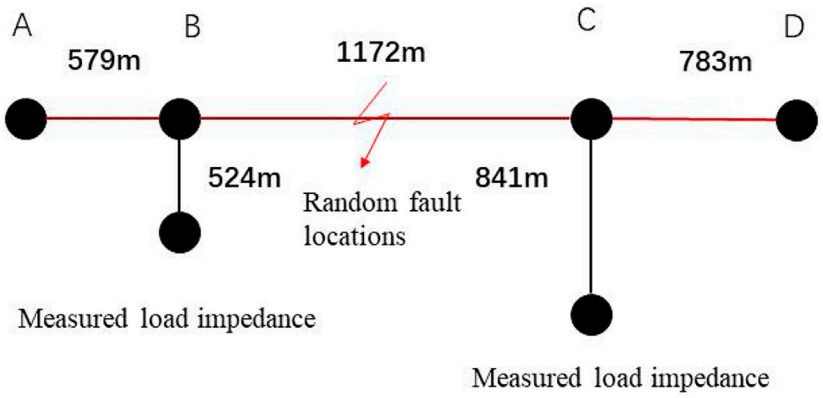

FIGURE 9
Topological network structure diagram.

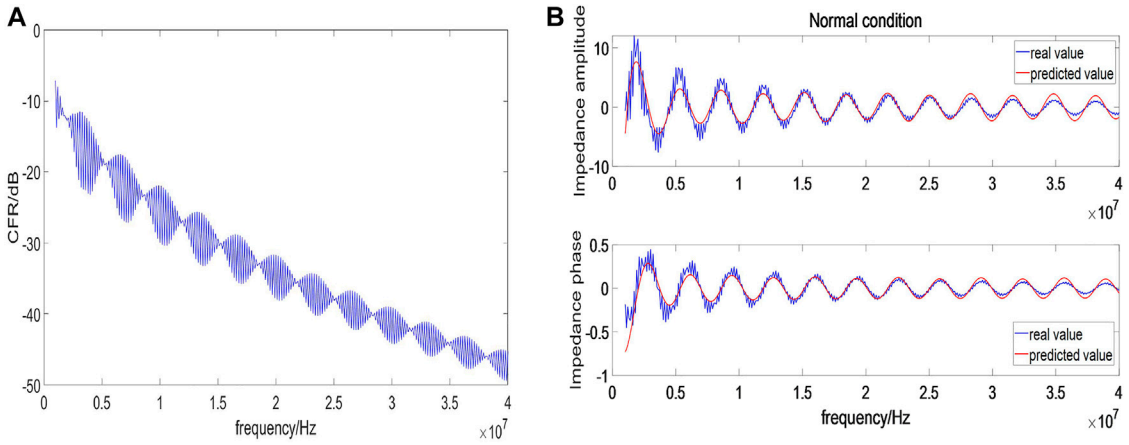

FIGURE 10
The data under normal conditions, **(A)** is the CFR data under normal conditions, **(B)** is the impedance date under normal conditions.

First, 500 sets of CFR data under normal conditions are generated. The trunk length of each basic unit is randomly generated in the range of 1000m–2000m, the branch length is randomly generated in the range of 500m–1000m, and the load impedance is set to the measured load impedance data Xiaoxian et al. (2007). The 500 group CFR data is shown in Figure 8, each set of CFR data showed a trend of oscillation attenuation with the increase of frequency.

Fault detection

To reflect the randomness of the extraction model, taking out any group from 500 groups of random data, and its topology is shown in Figure 9. The total length of the network backbone was 2591m, with two branches; branch lengths were 524 and 841 m respectively. The red color represents the backbone network, and it is divided into 579 m AB segment, 1172 m BC segment, and 783 m CD segment.

First, the network displayed in Figure 9 is simulated to obtain the CFR under normal conditions, as displayed in Figure 10A.

Based on the impedance estimation technique verified above, the system input impedance under normal conditions is predicted, and the prediction effect is shown in Figure 10B.

The input impedance changes when a grid ground fault occurs. By monitoring the input impedance at point B in Figure 9, a fault between BD can be observed because when a fault occurs in the BD segment, it causes the input impedance at point B to change. A 500-Ω high-impedance fault and a 50-Ω low-impedance fault are set in the BD segment, and the fault distance is set randomly in the BD segment; 300 sets are set in the BC segment, and 200 groups are set in the CD segment; therefore, 500 sets of fault data are generated, and 500 sets of input impedance and CFR data are shown in Figures 11A, B.

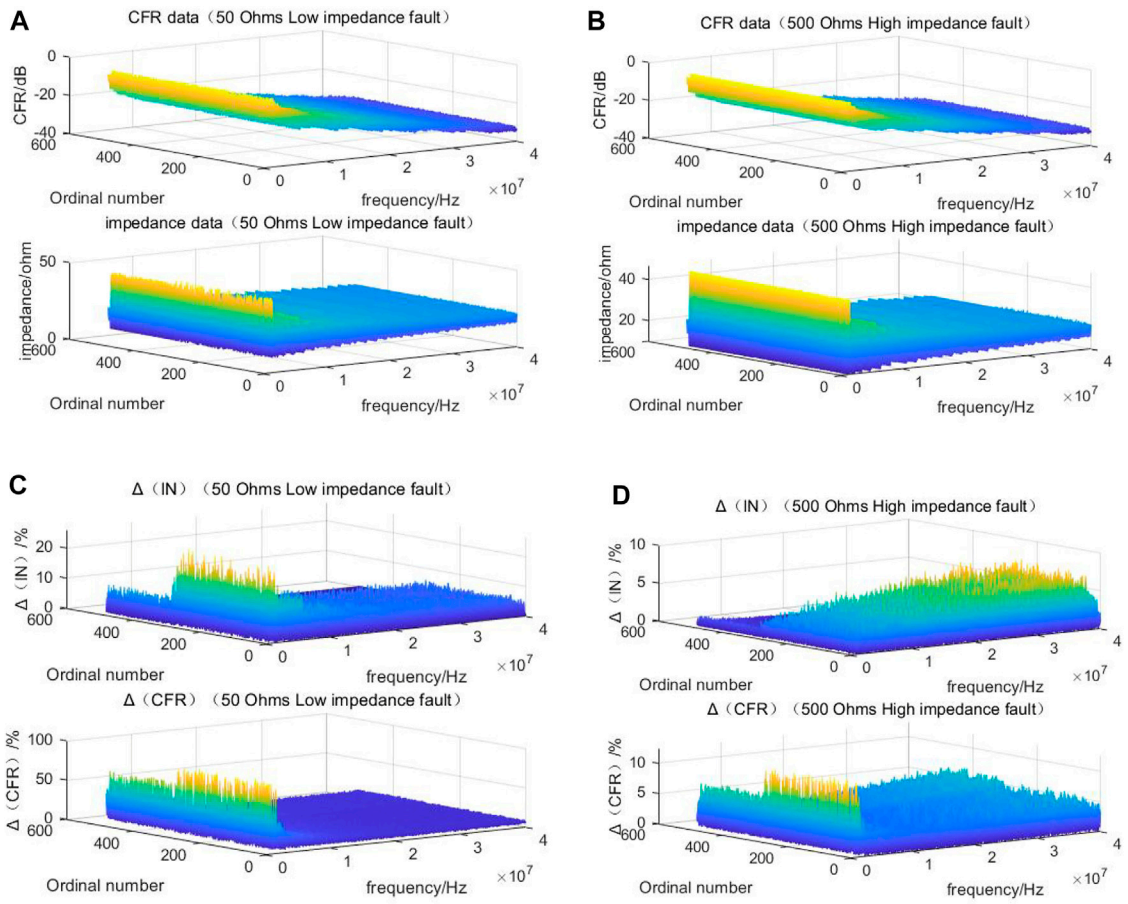

FIGURE 11
500 sets of CFR, impedance data and Δ values. **(A, B)** are CFR data and impedance data for low impedance and high impedance fault, respectively**(C, D)** are Δ values for low impedance and high impedance fault, respectively.

Figure 11A displays a low-impedance fault with a fault impedance of 50 Ω, and Figure 11B displays a high-impedance fault with a fault impedance of 500 Ω. The 500 sets of CFR data and 500 sets of input impedance amplitude data used in the study are shown. When the CFR data and the input impedance data are obtained, the data are calculated by using Eqs 18, 19 above to obtain the Δ value characterizing the system variation obtained from the CFR and input impedance, respectively. The Δ-values for the low-impedance fault and high-impedance fault cases are displayed in Figures 11C, D.

Figure 11C details a low impedance fault with a fault impedance of 50 Ω, and Figure 11D indicates a high-impedance fault with a fault impedance of 500 Ω. Five hundred sets of Δ(CFR) and Δ(IN), obtained from CFR and input impedance, respectively.

When the Δ value is obtained, Δ(CFR) and Δ(IN) are analyzed separately. If the peak value of Δ is more significant, the system exhibits more apparent changes and can be easily monitored. The peak values of 500 sets of Δ data are illustrated in Figure 12. Eventually, the Δ data can be analyzed to obtain fault information.

Figure 12A shows the data for Δ(CFR), Figure 12B shows the data for Δ(IN), and Figure 12C displays a comparison between Δ(CFR) and Δ(IN) for the low-impedance case. A comparison of the effectiveness of two of these techniques for monitoring faults is shown in Table 3 Figures 12A, B reveal that both different technologies have good monitoring results for high and low resistance faults, the peak value of low impedance faults is always higher than that of high impedance faults, so low impedance faults are easier to monitor. This method can be applied to monitor LIFs and HIFs. As displayed in Figure 12C, a branch exists at 1751 m in the topology. When using the input impedance for fault detection, a clear stratification is observed in Δ(IN), and also can roughly identify the fault before or after the branch; however, this effect is not clear when using CFR. And the Δ(CFR) is more significant than Δ(IN) when using CFR for fault detection. As illustrated in Figures 12C, D and Figure 12, 500 groups of random faults Δ Values have specific peaks; therefore, Δ Value can be used to detect faults.

Fault location

When using the aforementioned location method for fault location, the input impedance changes when the network changes; which provides sufficient information about fault location. The topological network displayed in Figure 9 was used for fault

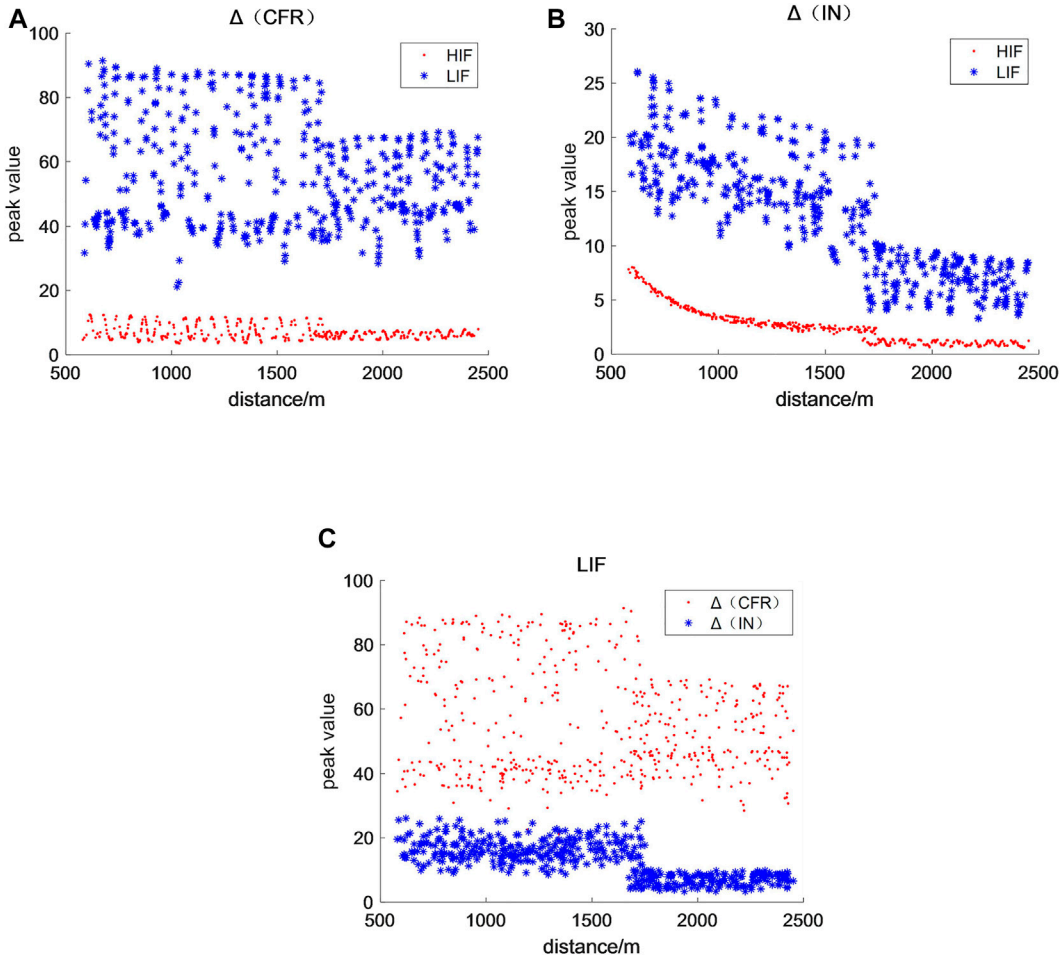

FIGURE 12
Comparison of 500 sets of Δ data. **(A)** is the Δ data comparison of CFR in the case of HIF and LIF. **(B)** is the Δ data comparison of IN in the case of HIF and LIF. **(C)** is the comparison of CFR and IN under LIF.

TABLE 3 Comparison of the effectiveness of different technologies for monitoring faults.

	LIFs	HIFs
Δ(CFR)	Significant (better)	Normal
Δ(IN)	Significant	Normal

location. Figure 13 shows the input impedance data (with actual as well as predicted values) for faults occurring at 1,000 and 1,500 m with 50 and 500 Ω. The input impedance predicted using impedance estimation techniques is then used for fault location.

When fault location is performed, the PLC device acquires the real-time CFR and estimates the current input impedance waveform from the real-time CFR. Then the IFFT of the impedance is obtained from Eq. 20. The wave speed can be obtained from Eq. 21. From the wave speed, a function (22) of distance can be obtained, by which the fault point can be located. Figure 14 shows the localization results for different fault impedances.

The figure shows that there is a clear wave peak at the location of the 1,000 and 1,500 m point, the peak contains the location information of the fault point, the position corresponding to the peak is the position of the fault point, so the fault can be located by peak finding. Among them, the results of fault impedance localization are shown in Table 4.

As presented in the table, the positioning, although a specific error exists, from the perspective of using the input impedance to locate the fault, the fault can be an approximate location of the calculation. This fault monitoring and location algorithm has a positive effect on high and low resistance fault monitoring and can be applied in fault monitoring.

If the fault occurs on the branch, the above method can also be used to detect and locate the fault. First, the receiver is connected to the branch end, the position of the transmitter remains unchanged, and the original network topology is changed. The original branch part can be regarded as the backbone part of the new topology. Then, the same method as above is used to achieve Fault detection and location.

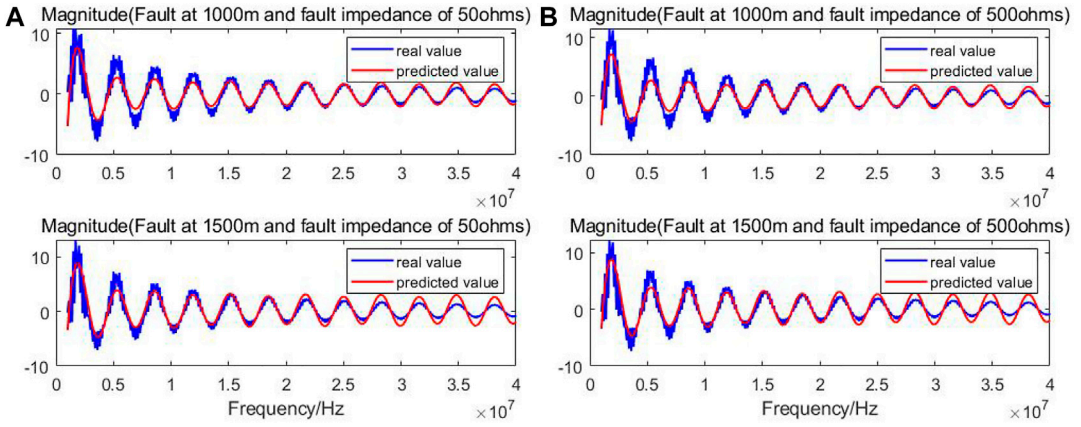

FIGURE 13
Input impedance values of different faults at different locations.

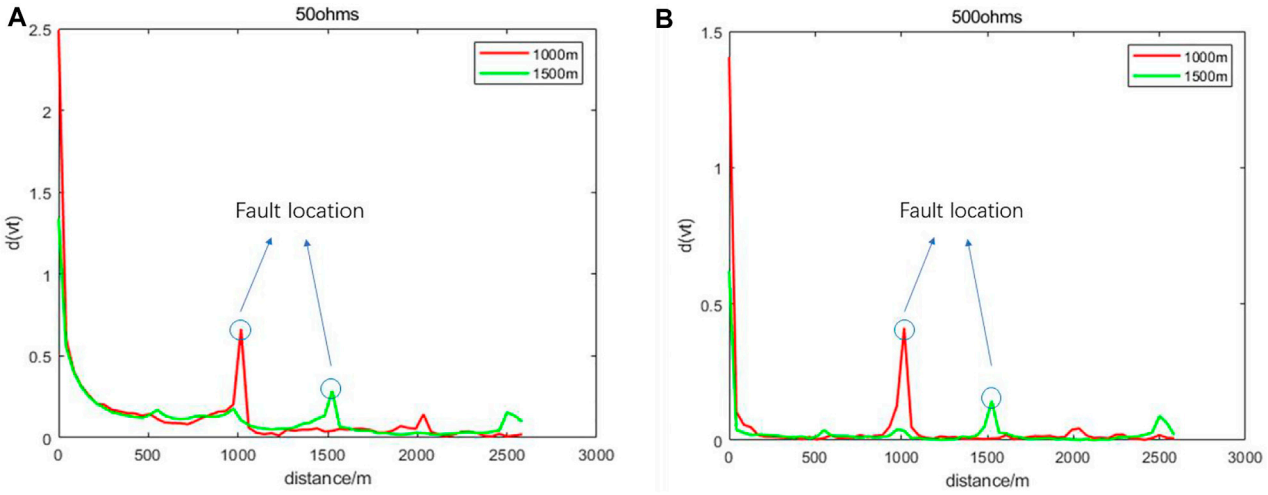

FIGURE 14
Positioning effect under different conditions. **(A)** is the fault location effect under LIF. **(B)** is the fault location effect under HIF.

TABLE 4 Localization results of different fault impedances at different distances.

Fault impedance Rf (ohm)	Assumed fault location (m)	Positioning fault position (m)	Positioning relative error (%)
50	1,000	1,016.9	1.69
500	1,000	1,021.3	2.13
50	1,500	1,525.4	1.693
500	1,500	1,531.9	2.126

Conclusion

An enhanced fault monitoring method based on power line carrier communication was proposed. In this method, an impedance estimation algorithm was used to monitor real-time impedance fluctuations to accomplish accurate fault location. The following conclusions were verified through theory and simulation.

1) The fault can be monitored in real time using the impedance estimation information only by computing and comparing the Δ value, and impedance positioning can be carried out in real time and with high

precision within the access network, without the need for additional equipment, making it an ideal option for ground fault monitoring.

2) For high and low impedance faults occurring at 1,500–2,500 m, the proposed method can be used to achieve complete monitoring success with a localization error of approximately 50 m, while at fault locations closer than 1,500 m, the proposed method has better monitoring results and high localization accuracy. The method is not affected by fault current.

3)Although the peak value of CFR technology in monitoring high and low impedance faults is higher than that of input impedance technology, the technology proposed in this paper can not only realize the correct monitoring of high and low resistance faults, but also achieve better positioning effect. The positioning error is less than 2.13%, and online monitoring and positioning can be realized only by relying on the carrier equipment on the existing power grid.

Data availability statement

The original contributions presented in the study are included in the article/supplementary material, further inquiries can be directed to the corresponding author.

Author contributions

DL put forward the research direction, organized the research activities, provided theory guidance, and completed the revision of the article. KZ completed the principal analysis and the method design, performed the simulation, and drafted the article. All five were involved in revising the paper. All authors have read and agreed to the published version of the manuscript.

Funding

This research was supported by the National Natural Science Foundation of China (Grant No. 51707154) and the Provincial Education Department (Program No. 15JK1511).

Conflict of interest

The authors declare that the research was conducted in the absence of any commercial or financial relationships that could be construed as a potential conflict of interest.

Publisher's note

All claims expressed in this article are solely those of the authors and do not necessarily represent those of their affiliated organizations, or those of the publisher, the editors and the reviewers. Any product that may be evaluated in this article, or claim that may be made by its manufacturer, is not guaranteed or endorsed by the publisher.

References

Aucoin, B. M., and Russell, B. D. (1982). Distribution high impedance Fault Detection utilizing high frequency current components. *IEEE Power Eng. Rev.* 2 (6), 46–47. doi:10.1109/MPER.1982.5521003

Balser, S. J., Clements, K. A., and Lawrence, D. J. (1986). A microprocessor-based technique for detection of high impedance faults. *IEEE Trans. Power Deliv.* 1 (3), 252–258. doi:10.1109/TPWRD.1986.4308000

Bhandia, R., Chavez, J. d. J., Cvetković, M., and Palensky, P. (2020). High impedance Fault Detection using advanced distortion detection technique. *IEEE Trans. Power Deliv.* 35 (6), 2598–2611. doi:10.1109/TPWRD.2020.2973829

Cao, A., Zeman, T., and Hrad, J. (2016). "Medium-voltage faults location and handling with the help of powerline communication systems," in 2016 17th International Conference on Mechatronics - Mechatronika (ME), Prague, Czechia, 1–4.

Chul-Hwan Kim, Hyun Kim, Ko, Young-Hun, Byun, Sung-Hyun, Aggarwal, R. K., and Johns, A. T. (2002). A novel fault-detection technique of high-impedance arcing faults in transmission lines using the wavelet transform. *IEEE Trans. Power Deliv.* 17 (4), 921–929. doi:10.1109/TPWRD.2002.803780

Costa, F. B., Souza, B. A., Brito, N. S. D., Silva, J. A. C. B., and Santos, W. C. (2015). Real-time detection of transients induced by high-impedance faults based on the boundary wavelet transform. *IEEE Trans. Industry Appl.* 51 (6), 5312–5323, Nov. doi:10.1109/TIA.2015.2434993

García, J. C., García, V. V., and Kagan, N. (2014). "Detection of high impedance faults in overhead multi grounded networks," in 2014 11th IEEE/IAS International Conference on Industry Applications, Juiz de Fora, Brazil, 1–6. doi:10.1109/INDUSCON.2014.7059480

Guillen, D., Olveres, J., Torres-García, V., and Escalante-Ramírez, B. (2022). Hermite transform based algorithm for detection and classification of high impedance faults. *IEEE Access* 10, 79962–79973. doi:10.1109/ACCESS.2022.3194525

Huo, Y., Prasad, G., Lampe, L., and Leung, V. C. M. (2020). "Advanced Smart Grid Monitoring: Intelligent Cable Diagnostics using Neural Networks," in 2020 IEEE International Symposium on Power Line Communications and its Applications (ISPLC), Malaga, Spain, 1–6. doi:10.1109/ISPLC48789.2020.9115403

Huo, Y., Prasad, G., Atanackovic, L., Lampe, L., and Leung, V. C. M. (2018). "Grid surveillance and diagnostics using power line communications," in 2018 IEEE International Symposium on Power Line Communications and its Applications (ISPLC), Manchester, UK, 1–6. doi:10.1109/ISPLC.2018.8360200

Huo, Y., Prasad, G., Lampe, L., Leung, V. C. M., Vijay, R., and Prabhakar, T. (2021). "Measurement Aided Training of Machine Learning Techniques for Fault Detection Using PLC Signals," in 2021 IEEE International Symposium on Power Line Communications and its Applications (ISPLC), Aachen, Germany, 78–83. doi:10.1109/ISPLC52837.2021.9628699

Jia, K., Bi, T., Ren, Z., Thomas, D. W. P., and Sumner, M. (2018). High frequency impedance based fault location in distribution system with DGs. *IEEE Trans. Smart Grid* 9 (2), 807–816. doi:10.1109/TSG.2016.2566673

Lai, T. M., Snider, L. A., Lo, E., and Sutanto, D. (2005). High-impedance fault detection using discrete wavelet transform and frequency range and RMS conversion. *IEEE Trans. Power Deliv.* 20 (1), 397–407. doi:10.1109/TPWRD.2004.837836

Lee, R. E., and Osborn, R. H. (1985). A microcomputer based data acquisition system for high impedance fault analysis. *IEEE Power Eng. ReviewPER-* 5 (10), 35. doi:10.1109/MPER.1985.5528687

Liang, D., Guo, H., and Zheng, T. (2019). Real-time impedance estimation for power line communication. *IEEE Access* 7, 88107–88115. doi:10.1109/ACCESS.2019.2925464

Liang, D., Wang, Y., Guo, H., Huo, Y., and Huang, C. Intelligent sensing strategy for grid anomalies using power line communication devices. *IEEE Sensors J.* doi:10.1109/JSEN.2022.3166899

Lu, Honggang, Qin, Jian, and Chen, Xiangxun (2004). Overview of power cable fault location. *Power Syst. Technol.* 28 (20), 58–63. (in chinese).

Lu, H., Zhang, W. -H., Wang, Y., and Xiao, X. -Y. (2022). Cable Incipient Fault Identification method using power disturbance waveform feature learning. *IEEE Access* 10, 86078–86091. doi:10.1109/ACCESS.2022.3197200

Meng, H., Chen, S., Guan, Y. L., Law, C. L., So, P. L., Gunawan, E., et al. (2004). Modeling of transfer Characteristics for the broadband power line communication channel. *IEEE Trans. Power Deliv.* 19 (3), 1057–1064. doi:10.1109/TPWRD.2004.824430

Michalik, M., Lukowicz, M., Rebizant, W., Lee, S. -J., and Kang, S. -H. (2008). New ANN-based algorithms for detecting HIFs in multigrounded MV networks. *IEEE Trans. Power Deliv.* 23 (1), 58–66. doi:10.1109/TPWRD.2007.911146

Michalik, M., Lukowicz, M., Rebizant, W., Lee, S. -J., and Kang, S. -H. (2007). Verification of the wavelet-based HIF detecting algorithm performance in solidly grounded MV networks. *IEEE Trans. Power Deliv.* 22 (4), 2057–2064. doi:10.1109/TPWRD.2007.905283

Milioudis, A. N., Andreou, G. T., and Labridis, D. P. (2015). Detection and location of high impedance faults in multiconductor overhead distribution lines using power line communication devices. *IEEE Trans. Smart Grid* 6 (2), 894–902. doi:10.1109/TSG.2014.2365855

Milioudis, A. N., Andreou, G. T., and Labridis, D. P. (2012a). Enhanced protection scheme for Smart grids using power line communications techniques—Part I: Detection of high impedance fault occurrence. *IEEE Trans. Smart Grid* 3 (4), 1621–1630. doi:10.1109/TSG.2012.2208987

Milioudis, A. N., Andreou, G. T., and Labridis, D. P. (2012b). Enhanced protection scheme for Smart grids using power line communications techniques—Part II: Location of high impedance fault position. *IEEE Trans. Smart Grid* 3 (4), 1631–1640. doi:10.1109/TSG.2012.2208988

Niu, L., Wu, G., and Xu, Z. (2021). Single-phase fault line selection in distribution network based on signal injection method. *IEEE Access* 9, 21567–21578. doi:10.1109/ACCESS.2021.3055236

Papaleonidopoulos, I. C., Capsalis, C. N., Karagiannopoulos, C. G., and Theodorou, N. J. (2003). "Statistical analysis and simulation of indoor single-phase low voltage power-line communication channels on the basis of multipath propagation," in IEEE Transactions on Consumer Electronics 49 (1), 89–99. doi:10.1109/TCE.2003.1205460

Passerini, F., and Tonello, A. M. (2017). "Power line fault detection and localization using high frequency impedance measurement," in 2017 IEEE International Symposium on Power Line Communications and its Applications (ISPLC), Madrid, Spain, 1–5. doi:10.1109/ISPLC.2017.7897102

Passerini, F., and Tonello, A. M. (2019). Smart grid monitoring using power line modems: Anomaly detection and localization. *IEEE Trans. Smart Grid* 10 (6), 6178–6186, Nov. doi:10.1109/TSG.2019.2899264

Paul, C. R. (2008). *Analysis of multiconductor transmission lines*. Hoboken, NJ, USA: John Wiley and Sons.

Paul, Clayton R. (1994). *Analysis of multiconductor transmission lines*. Newyork, NJ, USA: John Wiley.

Piante, M. D., and Tonello, A. M. (2019). "Channel and Admittance Dependence Analysis in PLC with Implications to Power Loading/Savings," in 2019 IEEE International Symposium on Power Line Communications and its Applications (ISPLC), Prague, Czech, 1–6. doi:10.1109/ISPLC.2019.8693391

Prasad, G., Huo, Y., Lampe, L., and Leung, V. C. M. (2019). "Machine Learning Based Physical-Layer Intrusion Detection and Location for the Smart Grid," in 2019 IEEE International Conference on Communications, Control, and Computing Technologies for Smart Grids (SmartGridComm), Beijing, China, 1–6. doi:10.1109/SmartGridComm.2019.8909779

Routray, P., Mishra, M., and Rout, P. K. (2015). "High Impedance Fault detection in radial distribution system using S-Transform and neural network," in 2015 IEEE Power, Communication and Information Technology Conference (PCITC), Bhubaneswar, India, 545–551. doi:10.1109/PCITC.2015.7438225

Sedighi, A. . -R., Haghifam, M. . -R., Malik, O. P., and Ghassemian, M. . -H. (2005). High impedance fault detection based on wavelet transform and statistical pattern recognition. *IEEE Trans. Power Deliv.* 20 (4), 2414–2421. doi:10.1109/TPWRD.2005.852367

Stefanidis, P. D., Papadopoulos, T. A., Arsoniadis, C. G., Nikolaidis, V. C., and Chrysochos, A. I. (2019). "Application of Power Line Communication and Traveling Waves for High Impedance Fault Detection in Overhead Transmission Lines," in 2019 54th International Universities Power Engineering Conference (UPEC), Bucharest, Romania, 1–6. doi:10.1109/UPEC.2019.8893519

Teng, J. -H., Huang, W. -H., and Luan, S. -W. (2014). Automatic and fast faulted line-section location method for distribution systems based on fault indicators. *IEEE Trans. Power Syst.* 29 (4), 1653–1662. doi:10.1109/TPWRS.2013.2294338

Tonello, A. M., and Zheng, T. (2009). "Bottom-up transfer function generator for broadband PLC statistical channel modeling," in 2009 IEEE International Symposium on Power Line Communications and Its Applications, Dresden, Germany, 7–12. doi:10.1109/ISPLC.2009.4913395

van der Wielen, P. C. J. M., and Steennis, E. F. (2008). *A centralized condition monitoring system for MV power cables based on on-line partial discharge detection and location*. Beijing, China: International Conference on Condition Monitoring and Diagnosis, 1166–1170. doi:10.1109/CMD.2008.4580495

Versolatto, F., and Tonello, A. M. (2010). *Analysis of the PLC channel statistics using a bottom-up random simulator*. Rio de Janeiro, Brazil: ISPLC2010, 236–241. doi:10.1109/ISPLC.2010.5479902

Wagenaars, P., Wouters, P. A. A. F., Van Der Wielen, P. C. J. M., and Steennis, E. F. (2010). Approximation of transmission line parameters of single-core and three-core XLPE cables. *IEEE Trans. Dielectr. Electr. Insulation* 17 (1), 106–115. doi:10.1109/TDEI.2010.5412008

Wang, B., Geng, J., and Dong, X. (2018). High-impedance Fault Detection based on nonlinear voltage–current characteristic profile identification. *IEEE Trans. Smart Grid* 9 (4), 3783–3791. doi:10.1109/TSG.2016.2642988

Xiaoxian, Y., Tao, Z., Baohui, Z., Fengchun, Y., Jiandong, D., and Minghui, S. (2007). Research of impedance characteristics for medium-voltage power networks. *IEEE Trans. Power Deliv.* 22 (2), 870–878. doi:10.1109/TPWRD.2006.881573

Xie, Min, Zhou, Kai, and Zhao, Shilin (2017). A new location method of local defects in power cables based on reflection coefficient spectrum. *Power Syst. Technol.* 41 (09), 3083–3089. (in chinese). doi:10.13335/j.1000-3673.pst.2016.2859

frontiers | Frontiers in Energy Research

TYPE Original Research
PUBLISHED 17 January 2023
DOI 10.3389/fenrg.2022.1056604

OPEN ACCESS

EDITED BY
Srete Nikolovski,
Josip Juraj Strossmayer University of Osijek, Croatia

REVIEWED BY
Ravi Samikannu,
Botswana International University of Science and Technology, Botswana
Suwarno Suwarno,
Bandung Institute of Technology, Indonesia

*CORRESPONDENCE
Tian Tian,
titan9012@163.com

SPECIALTY SECTION
This article was submitted to Smart Grids, a section of the journal Frontiers in Energy Research

RECEIVED 29 September 2022
ACCEPTED 09 November 2022
PUBLISHED 17 January 2023

CITATION
Zhou X, Tian T, Liu N, Bai J, Luo Y, Li X, He N, Zhang P and Jun S (2023), Research on gas production law of free gas in oil-immersed power transformer under discharge fault of different severity.
Front. Energy Res. 10:1056604.
doi: 10.3389/fenrg.2022.1056604

Research on gas production law of free gas in oil-immersed power transformer under discharge fault of different severity

Xiu Zhou[1], Tian Tian[1]*, Ningbo Liu[2], Jin Bai[1], Yan Luo[1], Xiuguang Li[1], Ninghui He[1], Pengcheng Zhang[2] and Sun Jun[3]

[1]Power Science Research Institute of State Grid Ningxia Power Co., Yinchuan, China, [2]Shizuishan Power Supply Company of State Grid Ningxia Electric Power Co., Ltd., Shizuishan, China, [3]Wuhan Pandian Technology Co., Ltd., Wuhan, China

Dissolved gas analysis (DGA) is a common technology used in the on-site maintenance of oil-immersed power transformers in the power industry at present. However, when the content of dissolved gas in the oil reaches the attention value DGA method can effectively diagnose the operating state of the transformer. Due to the lack of gas production data of free gas which was detected when the faults occur, DGA method cannot timely diagnose the transformer status. To solve the above problem, an experimental platform is built for studying the free gas generation law in oil-immersed transformers under discharge faults, and the characteristic free gas information under discharge fault of transformer is obtained through the experiment. It is found that the existing DGA method cannot accurately analyze the types and severity of sudden serious insulation faults. When high-energy partial discharge fault occurred in the equipment, CO, CO_2, CH_4, and H_2 will be collected in large quantities on the oil surface. These four gases can be used as the basis for characterizing high-energy partial discharge faults. When spark discharge occurred in the equipment, C_2H_6, C_2H_4, and C_2H_2 also be collected on the oil surface which can be used as a diagnostic basis for spark discharge. Moreover, it is found that the existing three-ratio method cannot be used for accurate analysis of oil free characteristic gas, so it is necessary to explore new diagnostic methods. The aim of this study is to explore the pattern of free gas production law by experiments when discharge faults occur and to provide data for a new diagnostic method.

KEYWORDS

transformer, discharge faults, free gas, production law, DGA

Abbreviations: AC, alternating current; DGA, dissolved gas analysis; IEC, international electrical commission; UHV, ultra high votage.

Introduction

Oil-immersed transformer is one of the most critical and widely used equipment in power system, the reliability of the power grid mainly depends on the trouble-free operation of the equipment (Tao et al., 2021; Kaliappan and Rengaraj, 2021; Wang et al., 2020).

The oil paper insulation defect is the main reason for the insulation fault of oil-immersed transformer. The insulation fault of power transformer is mainly divided into two types: overheating and discharge, of which discharge fault accounts for a large proportion (Yang, 2010; Chang et al., 2018; Yu et al., 2020). According to the discharge energy density, discharge faults can be divided into three types: high-energy discharge, spark discharge and partial discharge (Zhang et al., 2022). Discharge insulation defects will cause decomposition of insulating oil (mostly mineral oil) and then generate characteristic gases such as CH_4, C_2H_6, C_2H_2 and H_2 (IEEE Power & Energy Society, 2009; International Electrotechnical Commission, 2015). Nowadays, the most common used method to evaluate the operation condition of oil immersed transformer is Dissolved Gas Analysis (DGA) (National Energy Administration, 2015; Li, 2021; Wani et al., 2021). When high-energy discharge occurs in the transformer, the characteristic gas often accumulates in the gas relay before it is dissolved in the oil causing the gas relay to act (Dai et al., 2017). Similarly, for sudden serious insulation faults, the generated characteristic gas is too late to dissolve in the oil and it will escape to the oil surface (Taha et al., 2021). As a result, DGA technology cannot forecast sudden severe insulation effectively (Ravi et al., 2021). The sudden serious insulation fault is the main reason for the explosion of oil-immersed transformer (Yu, 2018), such as the Ultra High Voltage (UHV) Transformer explosion safety accident of Hunan province's power grid in 2017. By studying the change law of free gas component content, sudden and serious faults can be timely diagnosed.

At present, there is little research on free gas in the power industry. Zhang et al. (2021) proposed a new protection method by studying the relationship between the volume of free gas and the development stage of discharge in 2021, the research results can effectively reduce the safety accidents of transformers, this literature only studies the volume of free gas and the development stage of discharge, and the volume of free gas generated is difficult to measure by current technical means. Zheng et al. (2021) studied the gas production law of free gas with corona discharge model, this literature only studied the free gas production law of the normal discharge defect model, lacks the gas production law of tangential discharge defect model, which is of insufficient significance in engineering.

Based on above situation, two defect models are designed firstly, one is the surface discharge model dominated by normal discharge, and the other is the oil gap discharge model dominated by tangential discharge, which makes up for the significance of research in engineering. Then, the free gas production law under different severity is obtained through experiments, and the existing gas sensors can easily detect the concentrations of seven characteristic gases (Aldhafeeri et al., 2020; Ward et al., 2021). The research results can be applied to the current power industry to reduce the probability of oil-immersed transformer accidents.

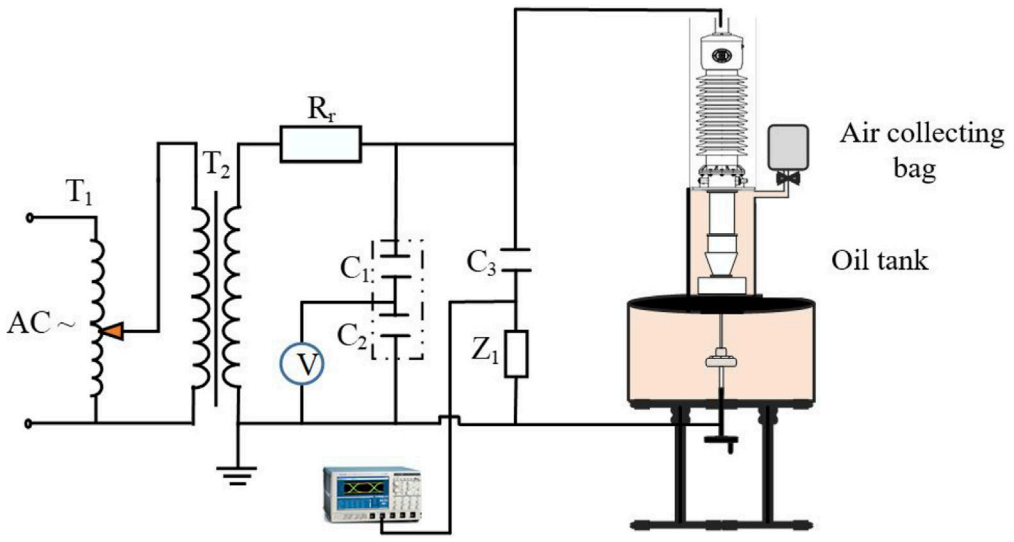

FIGURE 1
Analog experimental circuit for free gas detection of sudden and serious discharge fault of transformer.

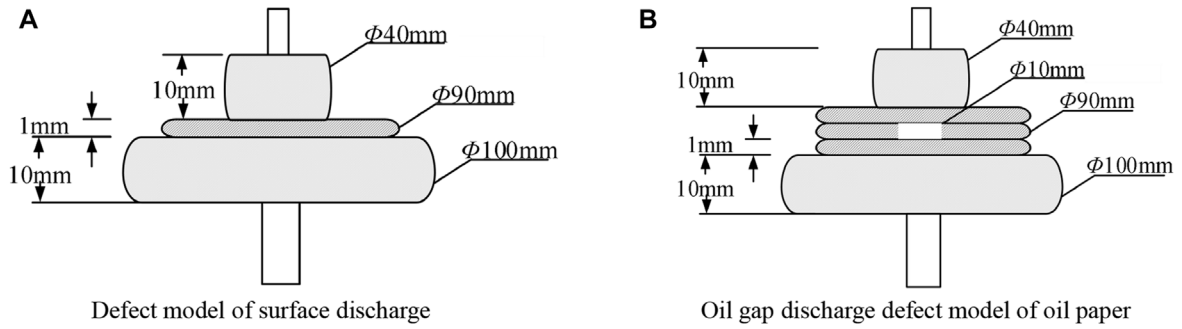

FIGURE 2
Discharge defect model of oil paper. **(A)** Defect model of surface discharge. **(B)** Oil gap discharge defect model of oil paper.

Materials and methods

Through the investigation on the escape path of fault characteristic gas of oil-immersed transformer, a simulation experiment platform for free gas detection of transformer sudden severe discharge fault is built, the test circuit is shown in Figure 1.

In Figure 1, T_1 is a voltage regulator with input 220 V power frequency Alternating Current (AC) voltage, T_2 refers to power frequency test transformer without partial discharge (YDTCW-1000/2 × 500), C_1 and C_2 are power frequency capacitive voltage dividers with a voltage division ratio of 1,000:1, R_r is the power frequency test protection resistance (GR1000-1/6), with a resistance value of 10kΩ, which is used to limit the short-circuit current when the test object breaks down; C_3 is the coupling capacitance, and its capacitance value is 413.7pf, Z_1 is the detection impedance. The air collecting bag is connected to the oil surface of the test object through a rubber hose. During the test, the ambient temperature shall be controlled at 20°C, and the temperature difference between day and night shall be ± 0.7°C.

Due to the complex insulation structure of the transformer, the possible internal discharge locations and types are as follows (Mahmud et al., 2015; Gang et al., 2018):

1. Oil gap discharge in oil diaphragm insulation in the middle of winding;
2. Oil gap discharge at winding end;
3. Partial discharge in oil paper insulation such as lead wire and bonding wire;
4. Partial breakdown of turn-to-turn insulation;
5. Flashover discharge of insulating paper along the surface.

According to the discharge form, characteristics of transformer internal insulation and International Electrical Commission (IEC) 60243 standard (IEC, 2013), two typical discharge defect models are designed. The structure and size of the model are shown in Figure 2.

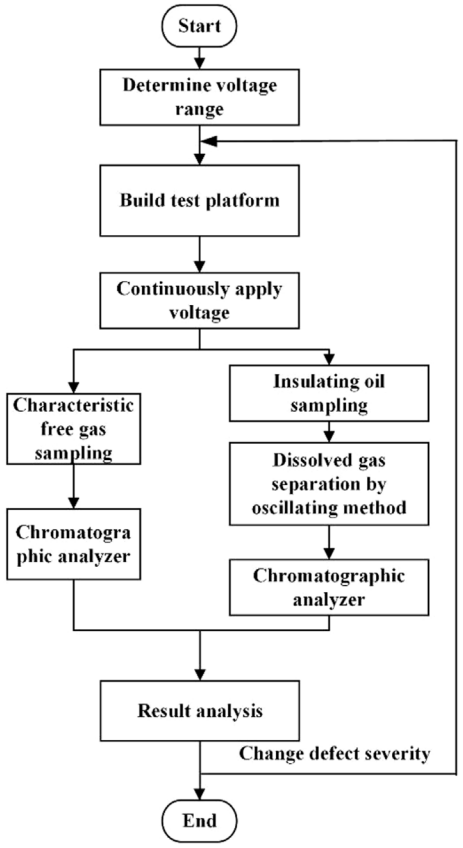

FIGURE 3
Flow chart of free gas detection simulation test for sudden serious discharge fault of transformer.

The surface discharge defect is composed of two copper plate electrodes with diameters of 100 mm and 40 mm and thicknesses of 10 mm and oil paper with single layer thickness of 1 mm and diameter of 90 mm (Guozhi et al., 2019; Zhang et al., 2022). The oil paper plate is fixed by two plate electrodes. There are two

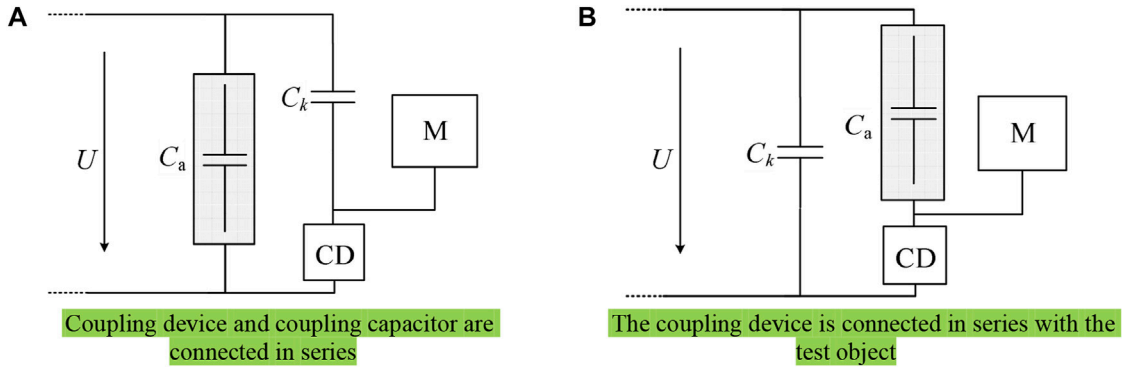

FIGURE 4
Typical pulse current PD measuring circuit. **(A)** Coupling device and coupling capacitor are connected in series. **(B)** The coupling device is connected in series with the test object.

40 mm diameter pole plates. One is connected to the high voltage terminal, the other is reliably grounded.

The oil gap defect is used to simulate the partial discharge of the oil gap in the oil paper inside the power transformer. The oil gap defect is composed of three layers of oil paper with a thickness of 1 mm. Through holes with a diameter of 10 mm are opened in the oil paper in the space layer. The superimposed oil paper is fixed by two copper plate electrodes with a diameter of 40 mm and 100 mm and a thickness of 10 mm.

In the discharge defect model, the insulating cardboard is dried at 60°C in the temperature control box for 3 days, and then the temperature is raised to 100°C for 3 days to ensure that the cardboard is fully dried without damaging the internal insulation structure. After vacuum oiling for 5 days, the insulating paperboard shall be polished with sandpaper in advance to ensure that the insulating paperboard is free of sharp corners or burrs.

Before the test, it is necessary to determine the initial discharge voltage and breakdown voltage of the oil paper surface discharge defect model and the oil paper oil gap discharge defect model. After placing the set defect in insulating oil, a step-by-step pressurization method is used. When the oscilloscope has a pulse current signal caused by defect's discharge, then maintain 5 min at this voltage level and observe whether there is a continuous pulsed discharge signal. If the pulse discharge signal persists, then record the voltage level as the initial discharge voltage, otherwise, until a continuous pulse discharge signal appears (Yang et al., 2022). After completing the above steps, continue increasing the voltage, until breakdown occurs in the oil tank. The voltage level at which the breakdown occurs is recorded as the breakdown discharge voltage. The specific test procedure is shown in Figure 3.

Pulse current method is the most commonly used insulation detection method for power equipment at present, the International Electrotechnical Commission has formulated a special standard for this method: IEC60270 (IEC, 2000). This method usually measures the electric pulse signal generated by device PD by connecting the coupling device (RL or RLC circuit) to the test object in series or to the coupling capacitor in series, the test method is shown in Figure 4.

After determining the initial discharge and breakdown voltages of both models, select the different levels of voltage between the initial voltage and the breakdown voltage as the test voltage. The defect model was continuously discharged using the constant voltage method, and the defect model is continuously discharged until breakdown. Statistical discharge information every half hour during the test. At the end of the test, the free gas and the dissolved gas were collected and component content was analysed by using a chromatography. Finally adjust the severity of defect discharge, repeating the above steps to obtain gas production laws with different severities.

Main results

Before the test, the initial discharge voltage of the surface discharge defect model is 14 kV, and the breakdown discharge voltage is 21 kV. The initial discharge voltage of the oil gap discharge defect model is 20 kV, and the breakdown discharge voltage is 25 kV.

Discharge characteristics of discharge defect model

Based on the measured initial discharge voltage and breakdown voltage, three test voltage levels of 15 kV, 17 kV, and 19 kV are selected as the test voltage for the surface discharge defect model; and 22 kV, 23 kV, and 24 kV are used as the test

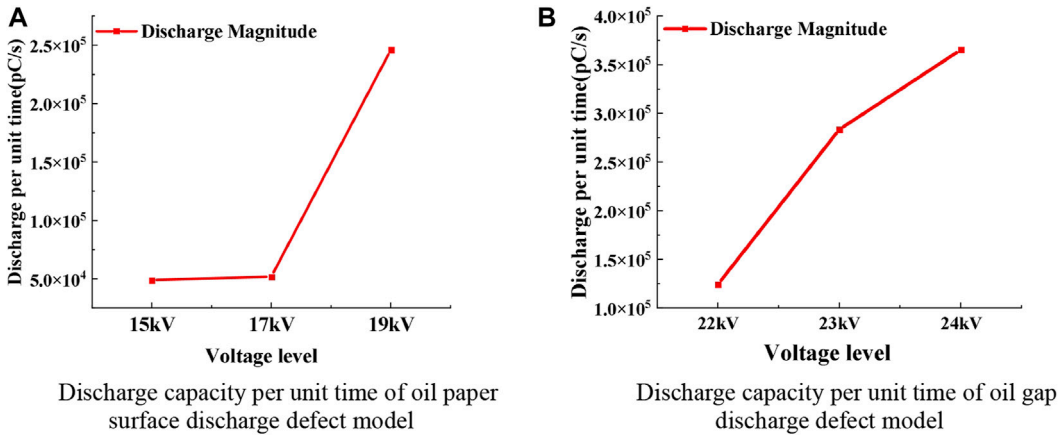

FIGURE 5
Unit time discharge of different voltage levels. **(A)** Discharge capacity per unit time of oil paper surface discharge defect model. **(B)** Discharge capacity per unit time of oil gap discharge defect model.

FIGURE 6
Spark discharge and bubble under test voltage grade 19 kV.

FIGURE 7
Carbonation trace of insulating cardboard.

voltage of oil gap discharge defect model; set the sampling frequency of the oscilloscope as 20 MS/s. Through calculation, the average discharge capacity per unit time of three test voltage levels of 15 kV, 17 kV, and 19 kV under the surface discharge defect model is 48932 pC/s, 51883 pC/s and 245873 pC/s respectively; under the oil gap discharge defect model, the average discharge capacity per unit time (Bo et al., 2016) of the three test voltage levels of 22 kV, 23 kV, and 24 kV are 124387 pC/s, 283376 pC/s and 365268 pC/s respectively, as shown in Figure 5. It can be seen that the discharge amount of the oil paper surface discharge defect model increases slightly at 15 kV–17 kV, and the discharge amount increases significantly near the breakdown voltage. The discharge quantity of oil gap discharge defect model increases with the increase of voltage level, the discharge amount of the oil gap discharge defect model increases with the increase of the voltage level, and the increment is obvious.

During the test, it was observed that electric sparks and bubbles will appear in the oil tank as shown in Figure 6. When the applied voltage of the oil paper surface discharge defect model is 19 kV. Once the test is completed, cut off the power. Taking out the insulating cardboard of the surface discharge defect model, it is found that there are obvious carbonization traces on the insulating cardboard. As shown in Figure 7, it indicates that

TABLE 1 Surface discharge defect model under different severity of oil surface gas and dissolved gas in oil (unit: *μL/L*).

	Before experiment		15 kV		17 kV		19 kV	
Gas	**Free gas**	**Dissolved gas**	**Free gas**	**Dissolved gas**	**Free gas**	**Dissolved gas**	**Free gas**	**Dissolved gas**
CO	0	0	139.1	2.05	421.18	7.0	1939.51	13.71
CO_2	0	2.63	87.89	3.68	110.08	97.89	293.83	324.31
CH_4	0	0	101.87	12.00	302.18	16.27	852.0	22.99
C_2H_6	0	0	0	0	0.24	0.69	33.29	16.74
C_2H_4	0	0	0.25	1.87	6.87	2.91	564.89	114.86
C_2H_2	0	0	0.28	0	11.28	3.48	2,557.14	252.57
H_2	0	8.7	78.97	12.82	297.65	20.12	1,182.78	55.91

TABLE 2 Oil gap discharge defect model under different severity of oil surface gas and dissolved gas in oil (unit: *μL/L*).

	Before experiment		22 kV		23 kV		24 kV	
Gas	**Free gas**	**Dissolved gas**	**Free gas**	**Dissolved gas**	**Free gas**	**Dissolved gas**	**Free gas**	**Dissolved gas**
CO	0	0	49.17	2.74	110.98	1.19	747.14	23.71
CO_2	0	2.63	0	2.63	4.32	3.01	142.13	7.28
CH_4	0	0	140.13	5.61	421.18	26.38	642.57	50.43
C_2H_6	0	0	0	0	0.25	0	5.88	0.3
C_2H_4	0	0	0	0	0	0	400.90	54.7
C_2H_2	0	0	0	0	0.28	0	531.47	49.17
H_2	0	8.7	391.12	43.31	3,314.55	261.23	8,498.32	304.11

the oil paper surface discharge under the test voltage level is spark discharge. In Figures 1, 6 is the bubble generated by test, 2 is the spark generated by spark discharge, 3 is the rod electrode of the surface discharge model, 4 is the insulating card board, 5 is the plate electrode of the surface discharge model.

Gas production law of characteristic gas under different severity of discharge defect model

At the end of the experiment, the collected free gas and dissolved gas are analyzed by oil chromatography respectively. The gas results obtained in the test are obtained through three measurements and the average value is taken. If the results of one measurement are far from those of other measurements, the measurement shall be repeated.

The analysis results are shown in Table 1 and Table 2. The obtained gas sample component concentration data into curves according to different voltage levels, as shown in Figures 8, 9.

It can be seen from Table 1 and Table 2 that the characteristic gas generated by the surface discharge defect under different test voltage levels will escape to the oil surface in the two defect models. Collecting and testing these gases reveals that the concentrations of some characteristic gases on the surface of the oil are much greater than the concentrations of dissolved gases, although the amount of insulating oil in the oil tank is less than that in the real power transformer. For surface discharge defects, when the discharge energy is low, the characteristic gas produced is mainly CO. But when the voltage level is close to the breakdown voltage, a large amount of C_2H_2 appears on the oil surface. Meanwhile, the content of C_2H_2 is the largest, and the severity of the fault can be judged according to the content of C_2H_2. For oil gap discharge defects, H_2 has always been the most productive characteristic gas, and is far greater than other characteristic gases. When the discharge energy is low, there is no C_2H_6, C_2H_4 and C_2H_2 on the oil surface. When the voltage level is 23 kV, a small amount of C_2H_6 and C_2H_2 will appear on the oil surface. When the voltage level reaches 24kV, the content of C_2H_6, C_2H_4 and C_2H_2 will increase. At this time, the severity of the fault can be judged according to the content of these three characteristic gases. The test results show that it is feasible to monitor

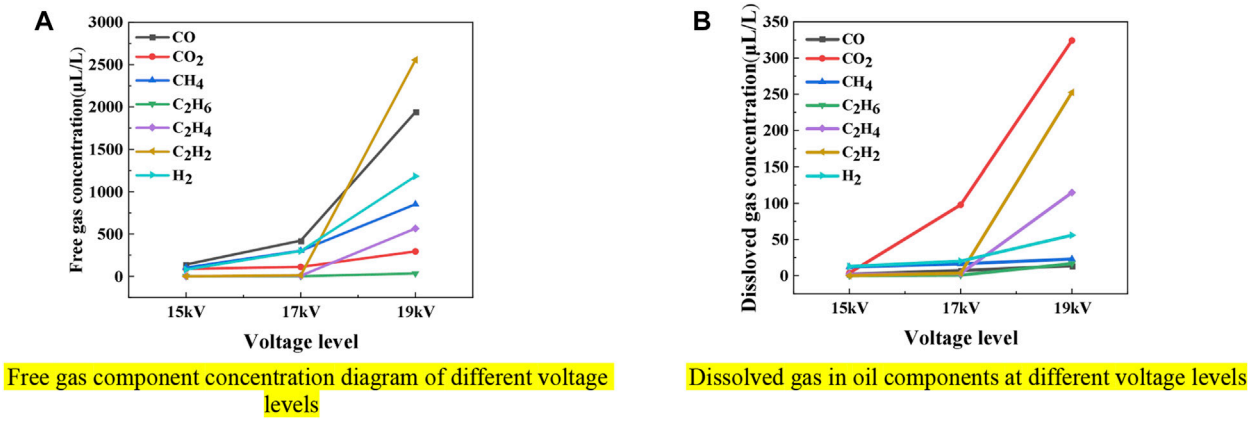

FIGURE 8
Concentration diagram of free characteristic gas and dissolved characteristic gas components in oil. **(A)** Free gas component concentration diagram of different voltage levels. **(B)** Dissolved gas in oil components at different voltage levels.

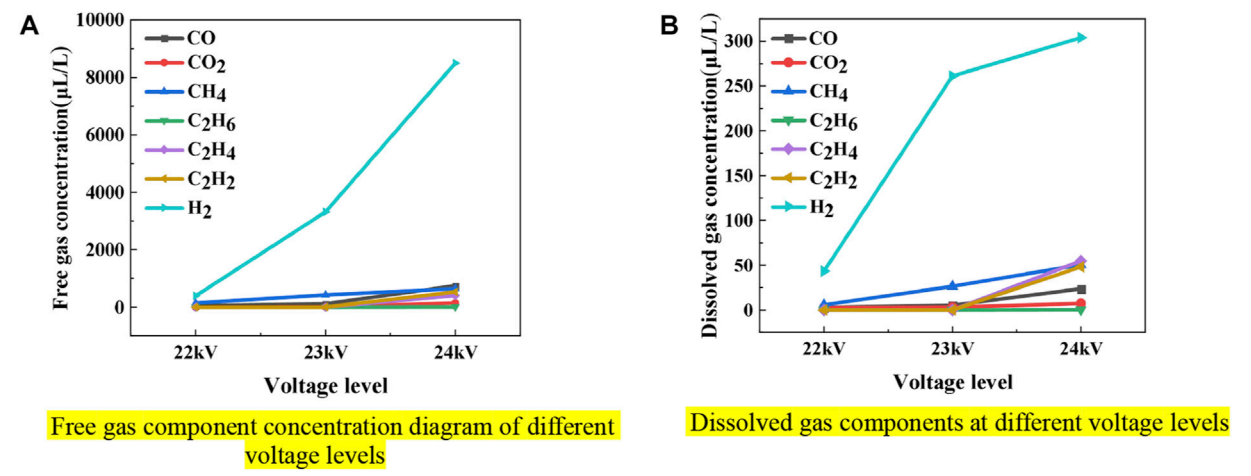

FIGURE 9
Concentration diagram of free characteristic gas and dissolved characteristic gas components in oil. **(A)** Free gas component concentration diagram of different voltage levels. **(B)** Dissolved gas components at different voltage levels.

the sudden serious discharge fault of oil-immersed power transformer by detecting the characteristic free gas.

To further, in order to explore whether the characteristic gas is dissolved in the insulating oil, the Ostwald coefficient *ki* corresponding to the characteristic gas under different discharge severity is calculated. The calculation formula of the Wald coefficient ki is as follows:

$$k_i = C_{oi} / C_{gi} \quad (1)$$

In Eq. 1, C_{oi} is the concentration of characteristic gas *i* dissolved in oil under equilibrium conditions; C_{gi} is the concentration of characteristic gas *i* in the gas phase under equilibrium conditions, and the unit of gas concentration is $\mu L/L$.

The comparison results of Ostwald coefficient corresponding to characteristic gas under different discharge severity calculated according to Eq. 1 and standard Ostwald coefficient at 50°C are shown in Table 3.

It can be seen from Table 3 that there is a great difference between the standard Ostwald coefficient when sudden severe discharge defects occur in the oil tank and when the temperature is 50°C and sudden severe discharge defects occur in the oil tank, which indicates that the generated characteristic gas cannot be dissolved in the insulating oil in time, and will escape to the oil surface under serious sudden discharge defects. The relationship between the two is no longer in line with the Ostwald coefficient.

TABLE 3 Ostwald coefficient corresponding to characteristic gas under different discharge severity.

Ostwald coefficient	CO	CO_2	CH_4	C_2H_6	C_2H_4	C_2H_2	H_2
50°C	0.12	1.00	0.40	1.80	1.40	0.90	0.05
15 kV	0.01	0.04	0.11	—	7.48	0	0.05
17 kV	0.01	0.86	0.05	2.88	3.67	0.31	0.03
19 kV	0.006	1.11	0.02	0.51	0.20	0.11	0.04
22 kV	0.05	—	0.04	—	—	—	0.05
23 kV	0.04	0.7	0.06	0	—	0	0.04
24 kV	0.03	0.05	0.078	0.05	0.14	0.09	0.03

TABLE 4 Diagnostic results of three direct ratio method of dissolved gas in oil and characteristic gas on oil surface.

Surface discharge defect	15 kV		17 kV		19 kV	
	Dissolved gas	Free gas	Dissolved gas	Free gas	Dissolved gas	Free gas
Code of three direct ratio	202	122	102	122	102	202
Fault type	Arc discharge	Spark discharge and overheating	Spark discharge	Spark discharge and overheating	Spark discharge	Arc discharge
Oil gap discharge defect	22 kV		23 kV		24 kV	
	Dissolved gas	Free gas	Dissolved gas	Free gas	Dissolved gas	Free gas
Code of three direct ratio	Unable	101	010	210	102	112
Fault type	—	Arc discharge	Partial discharge	Low energy discharge	Arc discharge	Arc discharge

In order to explore whether the dissolved gas in the oil and the characteristic free gas can be diagnosed and analyzed by the traditional three-ratio method (Tingfang et al., 2007), the dissolved gas and the characteristic free gas after the test are diagnosed by the three-ratio method. The diagnosis results are shown in Table 4.

It can be seen from Table 4 that for the dissolved gas was collected under the surface discharge defect model, the three-ratio method at 15 kV and 17 kV is diagnosed as arc discharge and spark discharge. However, no relevant phenomenon is observed in the oil tank. Although the three-ratio method is diagnosed as spark discharge at 19 kV, the main characteristic gas is not H_2 and C_2H_2 which are given in the guidelines to analyse and judge dissolved gas in transformer oil, and the content of H_2 does not reach the attention value. For characteristic free gas, the diagnostic results do not agree with the observed test phenomena. For the dissolved gas in the oil collected under the oil gap discharge defect model, when the fault degree is light, the characteristic gas does not reach the attention value, so the three direct ratio method cannot be used to judge the fault type.

In the case of serious fault, the three direct ratio method is diagnosed as arc discharge. But the actually observed phenomenon is not consistent with the phenomenon of arc discharge, so the existing DGA method cannot timely analyze the status of transformer, a new diagnostic method need to be explored.

In addition, when there is a high-energy partial discharge fault in the equipment, CO, CO_2, CH_4 and H_2 will gather in large quantities on the oil surface, and these four gases can be used as the basis for characterizing the high-energy partial discharge fault. When there is spark discharge in the equipment, the three characteristic gases C_2H_6, C_2H_4 and C_2H_2 will also converge on the oil surface, it can be used as the basis for spark discharge diagnosis.

Conclusion

In this paper, the discharge characteristics of typical defect models in oil-immersed transformers with different severity and the gas production law of free gas are studied. The component concentration of dissolved gas after the test is analyzed and the free gas is collected at the initial stage of the fault of the typical defects actually existing in the transformer. By setting up the test platform of two typical discharge defect model under different severity, the gas production law of free gas was explored of two typical discharge defects:

1. At the initial stage of the fault, the existing DGA technology is difficult to timely diagnose the transformer status. Up till the present moment, there is no method to diagnose the state of transformer according to the content change of free gas. In

this study, the free gas production law under discharge fault is obtained through experiments, and the change law of free gas with the aggravation of fault degree is studied.

2. Under the oil paper surface discharge defect model, the oil surface characteristic gas is mainly composed of four characteristic gases C_2H_2, CO, H_2 and CH_4. With the aggravation of the fault degree, the characteristic gases C_2H_4 and C_2H_6 as high-energy discharge are also collected and detected on the oil surface, and the concentration of the seven characteristic gases also increases with the aggravation of the fault degree.
3. It is found that the traditional three-ratio method cannot get the fault type and severity by analyzing the characteristic free gas. For the dissolved gas in oil, the analysis result of three-ratio method is not accurate because the concentration of dissolved characteristic gas is few at the initial stage of fault. This study provides data support for a new method of transformer status diagnosis by free gas.

Data availability statement

The original contributions presented in the study are included in the article/Supplementary Material, further inquiries can be directed to the corresponding author.

Author contributions

Conceptualization, XZ and TT; Methodology, NL; Software, JB and NL; Validation, PZ, TT, and YL; Formal analysis, YL; Investigation, XL; Resources, NH; Data curation, XL; Writing—original draft preparation, PZ; Writing—review and editing, SJ; Visualization, XZ; Supervision, XZ; Project administration, SJ.

Funding

Project Supported by State Grid Ningxia Electric Power Co., Ltd. (Item code: 5229DK20004S).

Conflict of interest

Authors XZ, TT, JB, YL, XL, and NH were empolyed by the company Power Science Research Institute of State Grid Ningxia Power Co. Authors PZ and NL were empolyed by the company Shizuishan Power Supply Company of State Grid Ningxia Electric Power Co., Ltd. Author SJ was empolyed by the company Wuhan Pandian Technology Co., Ltd.

The authors declare that this study received funding from Electric Power Institute of State Grid Ningxia Electric Power Co. Ltd. The funder had the following involvement in the study: Data acquisition and analysis.

Publisher's note

All claims expressed in this article are solely those of the authors and do not necessarily represent those of their affiliated organizations, or those of the publisher, the editors and the reviewers. Any product that may be evaluated in this article, or claim that may be made by its manufacturer, is not guaranteed or endorsed by the publisher.

References

Aldhafeeri, T., Tran, M. K., Vrolyk, R., Pope, M., and Fowler, M. (2020). A review of methane gas detection sensors: Recent developments and future perspectives. *Inventions* 5 (3), 28. doi:10.3390/inventions5030028

Bo, Q., Zhen, W., Chengrong, L., Qing, Y., Yi, G., and Xiaohan, Z. (2016). Surface discharge phenomena and characteristics of oil paper insulation in AC/DC composite electric fields [J]. *J. Electr. Eng.* 31 (10), 59–67. doi:10.19595/j.cnki.1000-6753.tces.2016.1007

Chang, S., Xiao, J., Zipin, L., Junran, Z. Y., and Shuwei, F. (2018). A CEEMDAN based noise diagnosis method for distribution transformer discharge fault. *High. Volt. Tech.* 44 (08), 2603–2611. doi:10.13336/j.1003-6520.hve.20180731019

Dai, J., Song, H., Sheng, G., and Jiang, X. (2017). Dissolved gas analysis of insulating oil for power transformer fault diagnosis with deep belief network. *IEEE Trans. Dielect. Electr. Insul.* 24 (5), 2828–2835. doi:10.1109/tdei.2017.006727

Gang, L., Ke, W., Shuqi, Z., Zhigang, Z., Jinzhong, L., Huanchao, C., et al. (2018). Development characteristics and phase identification method of surface discharge defects of transformer oil paper insulation. *Power Grid Technol.* 42 (10), 3451–3458. doi:10.13,335/j.1000-3673.pst.2018.0701

Guozhi, Z., Zhang, X., Xingrong, H., Jia, Y., Tang, J., Yue, Z., et al. (2019). On-line monitoring of partial discharge of less-oil immersed electric equipment based on pressure and UHF. *IEEE Access* 7, 11178–11186. doi:10.1109/access.2019.2892601

IEC (2013). *IEC 60243-1 Electrical stengtih of insulating materials test methods[S].*

IEC (2000). *IEC 60270 High voltage test technique-partial discharge measurement[S].* Paris.

IEEE Power & Energy Society (2009). *C57. 104-2008 IEEE guide for the interpretation of gases generated in oil-immersed transformers[S].* USA: IEEE.

International Electrotechnical Commission (2015). *IEC 60599 Mineral oil-impregnated electrical equipment in service-guide to the interpretation of dissolved and free gases analysis[S].* Geneva: IEC.

Kaliappan, G., and Rengaraj, M. (2021). Aging assessment of transformer solid insulation: A review[J]. *Mater. Today Proc.* 47, 272–277.

Li, K. (2021). *Fault diagnosis method of oil immersed transformer based on deep learning [D].* North China: North China Electric Power University.

Mahmud, S., Chen, G., Golosnoy, I. O., Wilson, G., and Jarman, P. (2015). Experimental studies of influence of DC and AC electric fields on bridging in contaminated transformer oil. *IEEE Trans. Dielect. Electr. Insul.* 22 (1), 152–160. doi:10.1109/tdei.2014.004573

National Energy Administration (2015). *DL/T 722-2014 Guide to the analysis and the diagnosis of gases dissolved in transformer oil[S].* Beijing: China Electric Power Press.

Ravi, V., Alazab, M., Srinivasan, S., and Arunachalam, A. (2021). Adversarial defense: DGA-based botnets and DNS homographs detection through integrated deep learning [J]. *IEEE Trans. Eng. Manag.* 99, 1–18. doi:10.1109/TEM.2021.3059664

Taha, I. B. M., Ibrahim, S., and Mansour, D. E. A. (2021). Power transformer fault diagnosis based on DGA using a convolutional neural network with noise

in measurements. *IEEE Access* 9, 111162–111170. doi:10.1109/access.2021.3102415

Tao, J., Fan, H., Jizhong, L., Hua, Y., Hong, L., Xiaoman, L., et al. (2021). Error analysis of winding structure simplification in calculation of hot spot temperature rise of oil immersed transformers [J]. *High. Volt. Appar.* 57 (11), 156–163+170. doi:10.13296/j.1001-1609.hva.2021.11.020

Tingfang, Y., Pei, L., Jinglu, L., and Yi, H. (2007). Diagnosis of transformer faults by FCM combined with IEC three ratio method [J]. *High. Volt. Tech.* 08, 66–70. doi:10.13,336/j.1003-6520.hve.2007.08.014

Wang, G., Liu, Y., Chen, X., Yan, Q., and Zhang, J. (2020). Power transformer fault diagnosis system based on Internet of Things[J]. *EURASIP J. Wirel. Commun. Netw.* 2021 (1), 1–24. doi:10.21203/rs.3.rs-71379/v1

Wani, SA, Rana, A. S., Sohail, S., Rahman, O., Parveen, S., and Khan, S. A. (2021). Advances in DGA based condition monitoring of transformers: A review. *Renew. Sustain. Energy Rev.* 149, 111347. doi:10.1016/j.rser.2021.111347

Ward, S. A., El-Faraskoury, A., Badawi, M., Ibrahim, S. A., Mahmoud, K., Lehtonen, M., et al. (2021). Towards precise interpretation of oil transformers via novel combined techniques based on DGA and partial discharge sensors. *Sensors* 21 (6), 2223. doi:10.3390/s21062223

Yang, J. (2010). *Study on partial discharge characteristics and gas production law of typical insulation defects in transformer[D]*. China, Chong Qing Shi: Chongqing University.

Yang, L., Ming, D., Yadong, X., Yizhuo, H., Yingjie, X., Ming, R., et al. (2022). Development law and phase characteristics of multiphysical signals of oil paper insulation surface discharge [J/OL]. *Chin. J. Electr. Eng.*, 1–12.

Yu, C. (2018). *Research on cross sensitivity suppression method of dissolved gas sensor array detection in transformer oil [D]*. China, Chong Qing Shi: Chongqing University.

Yu, C., Huijuan, H., Lei, S., Tao, Q., Gehao, S., and Xiuchen, J. (2020). Power transformer fault diagnosis method considering unbalanced case samples[J]. *High. Volt. Tech.* 46 (01), 33–41. doi:10.13336/j.1003-6520.hve.20191227004

Zhang, H., Zhang, G., Zhang, X., Tian, H., Lu, C., Liu, J., et al. (2022b). PD flexible built-in high-sensitivity elliptical monopole antenna sensor. *Sensors* 22 (13), 4982. doi:10.3390/s22134982

Zhang, S., Zhang, G., Lu, C., Tian, H., Liu, J., and Zhang, X. (2022a). Flexible planar monopole built-in GIS PD sensor based on meandering technology. *Sensors* 22 (11), 4134. doi:10.3390/s22114134

Zhang, Y., Hao, Z., Zheng, Y., Pan, S., Li, B., Xue, Z., et al. (2021). "Developing characteristics of oil-immersed transformer internal fault with dignostic method using convergence patterns of free gas[C]," in 2021 IEEE 2nd China International Youth Conference on Electrical Engineering (CIYCEE) (IEEE), 1–6.

Zheng, Y., Li, X., Wu, C., Pan, S., Long, F., et al. (2021). "Corona discharge characteristics and free gas generation law in insulating oil[C]," in 2021 11th International Conference on Power, Energy and Electrical Engineering (CPEEE), Shiga, Japan, 26-28 February 2021 (IEEE), 230–234.

frontiers | Frontiers in Energy Research

TYPE Original Research
PUBLISHED 19 January 2023
DOI 10.3389/fenrg.2023.1100789

OPEN ACCESS

EDITED BY
Mahamad Nabab Alam,
National Institute of Technology Warangal, India

REVIEWED BY
Anu Bhalla,
Indian Institute of Technology Roorkee, India
Hareshkumar Sabhadia,
Singapore Institute of Technology, Singapore
Monalisa Biswal,
National Institute of Technology Raipur, India

*CORRESPONDENCE
Kamal Kant,
2021rsee004@nitjsr.ac.in

SPECIALTY SECTION
This article was submitted to Smart Grids, a section of the journal Frontiers in Energy Research

RECEIVED 17 November 2022
ACCEPTED 09 January 2023
PUBLISHED 19 January 2023

CITATION
Kant K, Ansari S and Gupta OH (2023), An advanced short-circuit protection scheme for a bipolar DC microgrid.
Front. Energy Res. 11:1100789.
doi: 10.3389/fenrg.2023.1100789

An advanced short-circuit protection scheme for a bipolar DC microgrid

Kamal Kant*, Salauddin Ansari and Om Hari Gupta

Electrical Engineering Department, National Institute of Technology Jamshedpur, Jamshedpur, India

In order to provide quick and accurate fault detection in a DC microgrid, a new protection strategy is developed in this study. It is based on the multi-resolution analysis of travelling waves. The multi-resolution analysis of travelling waves is carried out using discrete wavelet transform (DWT). The dyadic filter bank theory is used to obtain the DWT coefficient of the voltage travelling wave. The energy of the DWT coefficient is then determined, and the fault will be identified if this energy content exceeds the predetermined threshold value. Initially, the efficacy of the proposed algorithm is verified on a 500 V ring-type bipolar DC microgrid test model, which is developed with MATLAB/Simulink environment. Then the results obtained were later validated with the real-time simulator Opal-RT. The various simulation results indicate that the proposed algorithm can successfully be implemented in both modes, i.e., grid-integrated and islanded. It can also provide protection against high resistance fault (HRF) up to 900 Ω in grid-integrated mode, and up to 1,300 Ω in islanded mode. The operating time of the proposed algorithm is also quite fast, i.e., 0.64 m.

KEYWORDS

DC microgrid, travelling wave, wavelet transform, high resistance faults, islanded mode protection

1 Introduction

Due to the global coal crisis and the rising price of crude oil in the global market, many emerging nations must now lessen their reliance on fossil fuels to meet their energy needs (Burke et al., 2018). The inception of renewable energy-based electricity generation and the introduction of an electric transportation system can help a country to become energy independent (Gielen et al., 2019). The introduction of a DC microgrid (DCMG) can also prove to be a crucial breakthrough in the process of electricity generation and utilization. The idea of a DCMG is feasible in the near future due to the significant increase in electronic loads and smart appliances that primarily use DC power (Al-Ismail, 2021).

DC microgrids have several advantages over AC microgrids like low effective resistance, absence of inductive and capacitive reactance, lesser number of power converting stages as compared to AC microgrids, no frequency related issues in DG integration, and many more (Justo et al., 2013). However, the AC microgrid persisted in being preferred over the DC microgrid because of lack of a well-defined standards, technological advancement, and trustworthy protective measures (Joos et al., 2017). The protection of DCMG is one of the challenging issues due to various reasons such as the absence of current-zero crossing points, lack of frequency-dependent parameters, absence of sequence components, quickly rising fault current, etc., (Augustine et al., 2018). As the DC microgrid possesses less physical inertia as compared to the AC system (Sun et al., 2022), hence the fault current in these systems rises

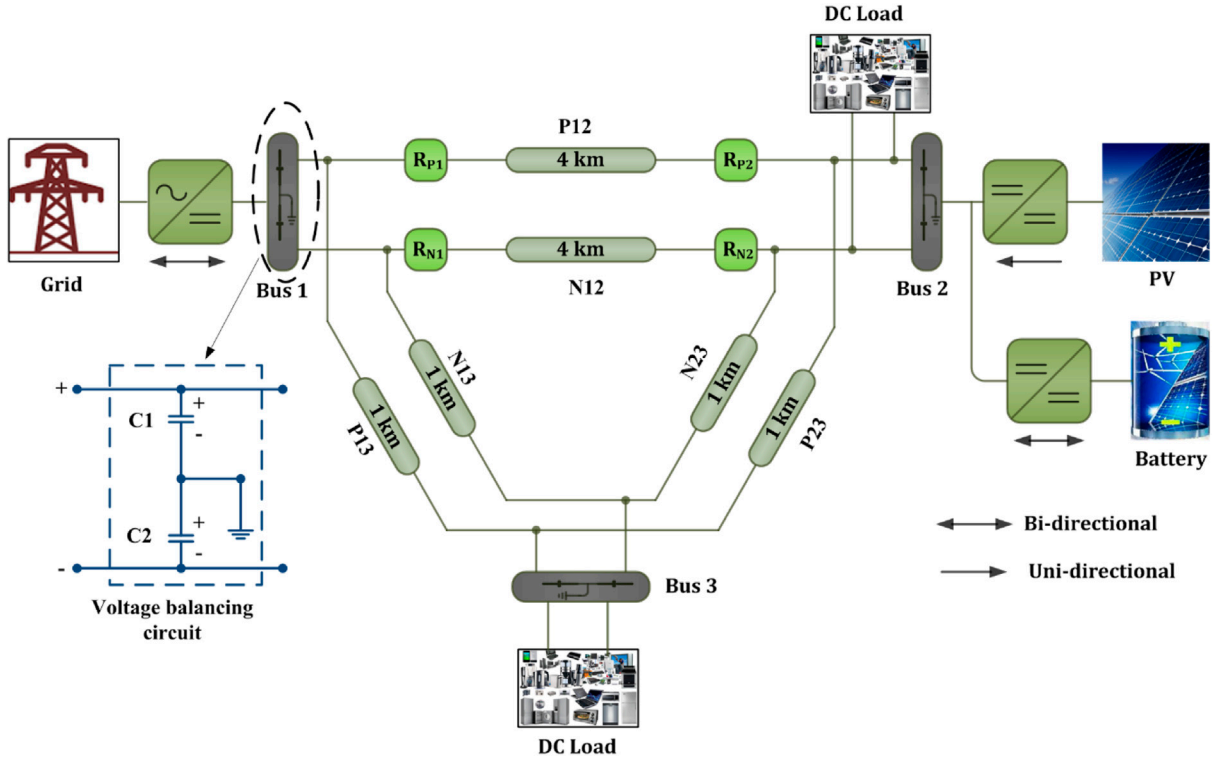

FIGURE 1
Bi-polar DC microgrid test system.

TABLE 1 Detailed description of the DC test system.

Sl.No.	Component name	Parameter name	Rating
1	DC Grid	DC grid voltage	500 V
2	DC Cable	Length	P12 & N12–4 km
			P13 & N13–1 km
			P23 & N23–1 km
		Resistance	12.7 mΩ/km
		Inductance	0.9337 mH/km
		Capacitance	12.74 nF/km
3	PV system	Power Rating	200 kW @1000 W/m2
4	Battery	Capacity	668 Ah
5	Grid side VSC	Power rating	0.2 MW
6	PV side DC-DC converter	Power rating	0.2 MW
7	Battery side converter	Power rating	0.2 MW
8	DC load	DC load	300 kW
9	Voltage balancing capacitors	C1 and C2	75 mF

rapidly to an intolerant level in a very short duration of time (Beheshtaein et al., 2019). This necessitates the requirement of very fast protection schemes for DC microgrids.

In the past various conventional protection schemes such as over-current protection (Shabani and Mazlumi, 2020), rate of change of current-based protection (Chauhan et al., 2022), differential protection (Dhar et al., 2018), resistance-based protection (Kesava Rao and Jena, 2022), (Yadav and Tummuru, 2020), etc., Have been suggested for the relaying of DC microgrid. Some of the merits of conventional relaying schemes are easy

implementation and low computational burden. However, the issues associated with these conventional protection schemes are slow response; high sensitivity for temporary faults; unable to protect against high resistance faults (HRF); And poor selectivity towards temporary faults (Kant and Gupta, 2022). To attain the objective of a faster response, a travelling wave (TW)-based relaying scheme has been proposed in various works of literature. The application of TW-based schemes for the protection of high voltage DC (HVDC) transmission systems has been reported in various kinds of literature. The fact that TW-based schemes do not rely on the magnitude of the fault current is one of their key advantages; as a result, these schemes function satisfactorily against HRFs (Zhang et al., 2012). Although there are various TW-based relaying schemes available for HVDC systems, the application of TW-based protection in low and medium-voltage DC systems (MVDC) is still an unexplored area. In (Saleh et al., 2019), a TW-based relaying strategy has been suggested for an MVDC microgrid. The proposed scheme in this literature is independent of the arrival times of the travelling wave and utilizes waveshape properties of the very first TW initiated by the fault. Due to the requirement of single-ended measurement only, no communication link is required to implement such schemes. Nowadays, many advanced techniques such as wavelet transform (WT), fuzzy logic, artificial neural network (ANN), etc. Are also being applied to improve the performance of the conventional DCMG protection schemes. As discussed in (Sharma et al., 2021), machine learning (ML) techniques are also used in combination with differential protection scheme for quick fault detection. This method uses a ML based support vector machine (SVM) classifier to increase the scheme's resilience to transient or momentary faults. The problem with this scheme is that it can detect faults up to 10Ω resistance only. In (Mohanty et al., 2021), a cosine similarity-based relaying strategy has been presented for DCMG protection. The operating time of the proposed scheme is 3 m. But again, it can detect faults up to 10Ω resistance only. In (Jayamaha et al., 2019), a WT and ANN-based relaying strategy for a DCMG has been proposed. The proposed scheme can detect the ground fault with a maximum resistance up to 300Ω, but the operating time varies between 3–5.5 m, depending on the type of fault.

Overall, there are a few things, in the available schemes, that may be improved and therefore, in this paper, an advanced short-circuit protection scheme for a DCMG is proposed. The key matters identified with previously discussed methods are a) the operating time of the relay; b) protection against HRFs; c) robustness during external fault or disturbances; and d) the operation during islanded operation. The proposed scheme is developed keeping all these issues into consideration and therefore, the main contributions of the developed scheme are as follows:

- It is an ultra-fast relaying scheme that performs a multi-resolution analysis of TW using the DWT.
- It works successfully under the grid-integrated as well as the islanded mode of DCMG.
- It can successfully detect and classify faults.
- It works effectively for pole-to-pole (PP) and pole-ground (PG) faults for HRFs up to 900 Ω.
- Even in islanded mode, it can successfully detect HRFs up to 1,300 Ω.
- It discriminates between faulty and non-fault conditions such as islanding and load switching events.
- The results obtained are validated using a lab setup with the real-time simulator, i.e., Opal-RT.

The remainder of the paper is structured as follows: Section 2 describes the DC microgrid test system in detail; Section 3 offers a brief explanation on the TW and DWT; Section 4 introduces the suggested algorithm; and Section 5 includes the simulation results and analysis. Section 6 presents the real-time validation of the results, Section 7 presents a comparison of the proposed scheme with the existing schemes, and Section 8 presents the conclusion.

2 DC microgrid test system description

In this study, a 500V ring-main bipolar DCMG architecture, as shown in Figure 1, has been considered for the implementation of the suggested scheme. This test system is a modification of the system considered in (Chauhan et al., 2022). The distributed generation (DG) sources, i.e., PV and battery are connected at bus two through appropriate DC-DC converters. The system is integrated to the grid at bus 1 with the help of a bi-directional voltage source converter (VSC). The bi-directional VSC, connected at the grid interface, enables the power transfer from/to DCMG. When connected to grid, the system voltage is maintained by the grid; and in islanded mode, it is maintained by the local sources. The battery is coupled to the bi-directional DC-DC converter, which is controlled to allow the battery to either absorb or supply power from/to the DC system. The PV-side DC-DC converter is managed to provide the DC system with the maximum real power available. To maintain the positive and negative pole voltage, a voltage balancer circuit is used at each bus. The grounding on the DC side is provided at each bus at the mid-point of voltage balancing capacitors (C1 & C2). A total load of 300 kW (200 kW on bus 3 & 100 kW on bus 1) is connected to the DC system. A detailed description of the components connected to this test system is given in Table 1. The proposed scheme has been implemented for the protection of positive and negative pole lines between bus 1 and bus 2, i.e., lines P12 and N12, respectively. Hence the relays are connected at each terminal of both lines, i.e., R_{P1}, R_{P2}, R_{N1}, and R_{N2}, as shown in Figure 1. Any fault outside this protected zone is considered an external fault.

3 Preliminaries of TW and DWT

3.1 Travelling wave

Travelling waves (TWs) are electromagnetic transients that are generated at the fault point upon the occurrence of the fault and propagate along the lines at a very high speed, nearly at the speed of light (Aftab et al., 20182020). These propagating TWs are captured at line terminals to design an ultra-fast relaying scheme. The TW-based relaying schemes are not new and widely employed for the protection of high voltage AC (HVAC) and HVDC transmission lines. But the application of these schemes in active distribution networks such as AC or

DC microgrids needs to be investigated. The benefits such as ultra-fast operation and the independence of the fault current make the TW-based schemes very suitable for DC microgrid protection.

3.2 Discrete wavelet transform (DWT)

A signal can be processed using the sophisticated mathematical tool known as the wavelet transform (WT) (Pukhova et al., 2017). The WTs can be classified in two categories, viz., continuous wavelet transform (CWT) and discrete wavelet transform (DWT). The scales and locations used by the CWT are unlimited. In contrast, the DWT employs a finite collection of wavelets that have been specified at a specific set of scales and locations. In this study, the DWT has been applied.

Mathematically, the DWT of a signal is given as (Bentley and McDonnell, 1994).

$$DWT(m,k) = \frac{1}{\sqrt{a_0^m}} \sum_{k=1}^{N} f[n]^* g\left[\frac{k - na_0^m b_0}{a_0^m}\right] \quad (1)$$

Where f[n] is the input signal, g[n] is the mother wavelet, k is the present sample, a_0^m is a scale parameter, and b_0 is the location parameter.

The DWT decomposes the input signal into the detail coefficient (D) and approximation coefficient (A) at each decomposition level. The detail coefficient (D) is the high-frequency component, and the approximation coefficient (A) is the low-frequency component of the input signal (Manohar et al., 2019).

4 Proposed algorithm

The proposed algorithm is developed by combining the concept of TW and DWT. This algorithm does not utilize the timing of the incident wave at the line terminals. Instead, this algorithm is based on the waveshape properties of the travelling waves. The travelling waves were calculated by Eqs 2, 3 (Tiwari et al., 2022).

$$V_{twf}(k) = \frac{1}{2}\left[\Delta V_f(k) + Z_s{}^*\Delta i_f(k)\right] \quad (2)$$

$$V_{twb}(k) = \frac{1}{2}\left[\Delta V_b(k) - Z_s{}^*\Delta i_b(k)\right] \quad (3)$$

Where subscript f and b denote the forward and backward wave quantities, respectively. $V_{tw}(k)$ is the voltage travelling wave at sample k and Z_s is the surge impedance of the dc cable. The change in voltage and current at the i^{th} bus can be calculated as in Eqs 4, 5.

$$\Delta V_i(k) = V_i(k) - V_i(k-1) \quad (4)$$

$$\Delta I_i(k) = I_i(k) - I_i(k-1) \quad (5)$$

The schemes based on the incident time of travelling waves require high frequency transient recorders to capture the travelling waves at the line terminals, and use of such costly equipment is not very economical for distribution lines. Hence in this study, the properties of the travelling are extracted by employing the signal processing tools, i.e., wavelet transform. The first incident forward voltage travelling wave is decomposed into the various high-frequency and low-frequency components by using the DWT's dyadic filter bank theory, as shown in Figure 2. The selection of the mother wavelet is also an important criterion for the implementation of WT. Some of the literature available (Sabug et al., 20192020) suggest that Daubechies as mother wavelet gives better result in the case of power system studies. The details of the DWT used in this algorithm have been provided in Table 2.

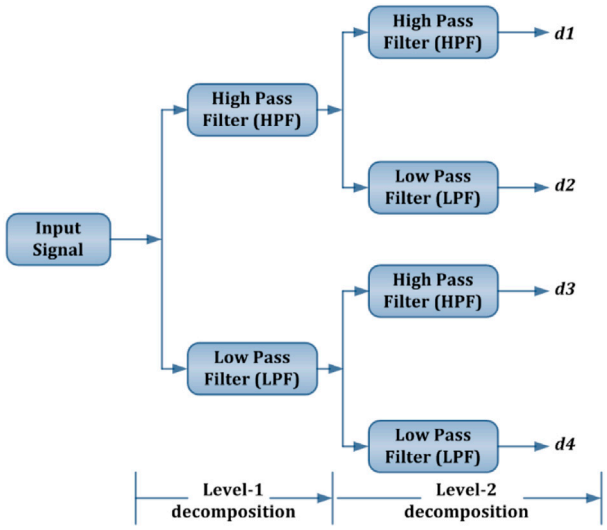

FIGURE 2
Decomposition tree of DWT using dyadic filter bank theory.

TABLE 2 Details of the DWT used in this algorithm.

Sl. No.	DWT components	Remarks
1	Mother wavelet	Daubechies
2	Wavelet order	2
3	No. of levels	2
4	Decomposition tree structure	Symmetric
5	Sampling frequency	200 kHz

The energy content of the extracted DWT coefficients of the voltage travelling wave is calculated by Eq 6.

$$E_{twf} = \sum_{i=1}^{N} |d_{twi}|^2 \quad (6)$$

Where d_{tw} is the high-frequency detail coefficient of the voltage travelling wave (V_{tw}), and N is the number of samples. In this case, N is taken as 16 samples. The number of samples (N) were decided based on the rigorous simulation studies. The energy content of the DWT coefficient (d_3) following a PG fault and PP fault is presented in Table 3.

If this energy content is more than the pre-set value, then the fault will be detected. The proposed algorithm is also able to classify the faults. With PP fault, the energy content of the DWT coefficient at

TABLE 3 Energy of travelling wave at positive and negative poles during different types of faults.

Fault type	Energy of positive pole voltage (EtwP)	Energy of negative pole voltage (EtwN)	| EtwP–EtwN|
PPG	2793.6	1.0008	2792.6
NPG	1.1726	2777.1	2775.93
PP	2765.3	2763.6	1.7

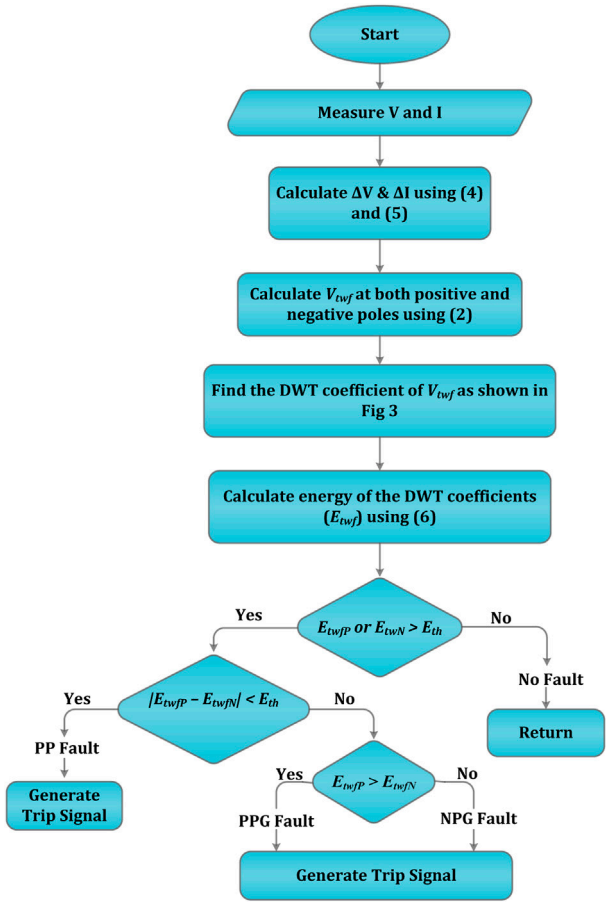

FIGURE 3
Flow chart of the proposed algorithm.

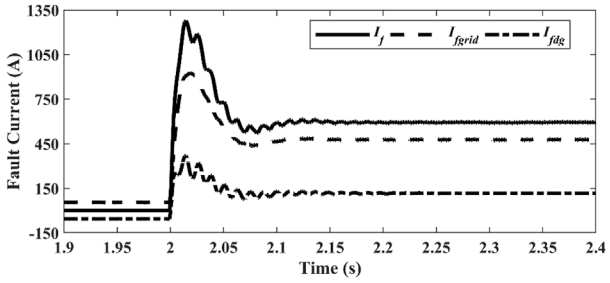

FIGURE 4
Fault current following a PPG fault at t = 2 s.

both positive and negative poles (i.e., E_{twP} and E_{twN}) will almost be the same. Hence, the difference between both energies will be very small. If this difference energy is less than the pre-specified value, the fault will be a PP fault. While in the case of PG-fault, this energy difference will be more than the pre-set value. The pre-specified threshold value has been determined by simulating the test model for different fault and non-fault conditions and then observing the energy content of the DWT coefficients in each case. The flow chart of the proposed algorithm is shown in Figure 3.

5 Simulation results and discussion

The DCMG test system, as illustrated in Figure 1, is simulated in the MATLAB/SIMULINK environment for the validation of the proposed algorithm. The performance of the suggested algorithm is evaluated in both fault- and non-fault-related scenarios.

5.1 Fault conditions

The performance of the proposed scheme for various fault conditions has been presented in this section.

5.1.1 Pole-to-ground (PG) fault simulation

To investigate the performance of the suggested algorithm for PG-fault, a positive pole-to-ground (PPG) fault with a fault resistance (R_f) of 0.1Ω were simulated on the line P12, and the results have been discussed here. The fault current contribution from the grid (I_{fgrid}) and DG (I_{fdg}), and the total fault current (I_f) following the PPG fault at the mid-point of line P12 are shown in Figure 4. The total fault is equal to the sum of the fault currents supplied from the grid and the DG. As shown in Figure 4, the fault current initially rises to a value greater than 1200 A in very short time duration, i.e., within 15 m, and then quickly settles down to a value around 600 A. For, this test system, normal current in the line P12 is around 55 A. So, the peak fault current is about 22 times the normal line current. That means if the fault current is allowed to reach the peak value, then it can pose some serious damage to the instruments present in the system. Hence, the relaying scheme must clear the fault well before the current reaches its peak value.

The energy content of the DWT coefficient of forward voltage travelling wave (E_{twfP}) is shown in Figure 5A. As soon as this energy content crosses the pre-set value (E_{th}), the fault is detected, and a trip signal is generated by relays R_{P1} and R_{P2} to isolate the faulty line P12. The status of the trip signal from relays R_{P1} and R_{P2} is shown in Figure 5B. As shown in Figure 5B, the trip signal becomes high at t = 2.00064 s which means the proposed scheme can detect the PPG fault within 0.64 m, which is quite fast.

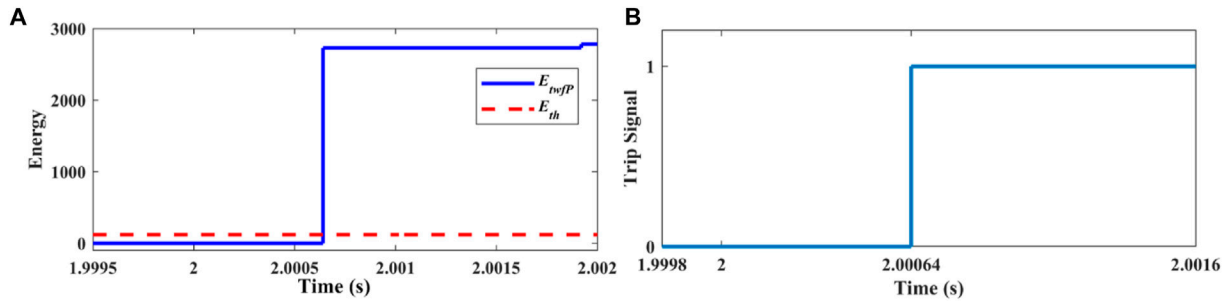

FIGURE 5
(A) Energy of forward voltage travelling wave, **(B)** Status of trip signal for relays R_{P1} and R_{P2} following a PPG fault on line P12 at t = 2 s.

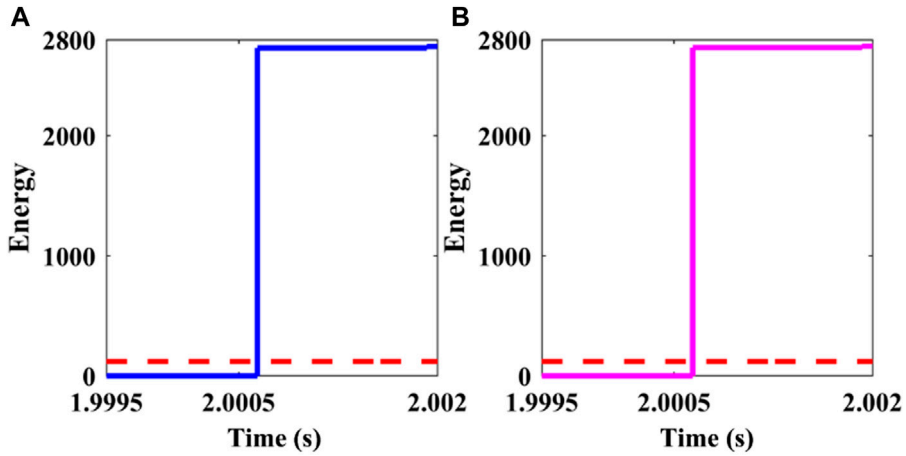

FIGURE 6
Energy content of DWT coefficient V_{twf} following a PP-fault at t = 2 s, **(A)** Energy at the positive pole (E_{twfP}), **(B)** Energy at the negative pole (E_{twfN}).

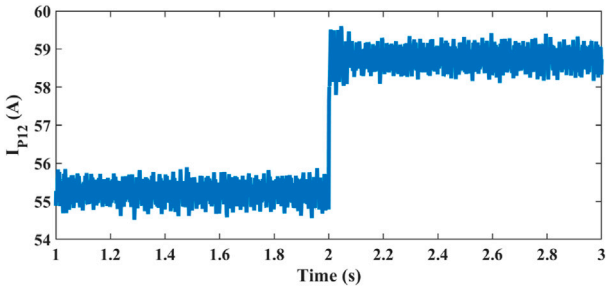

FIGURE 7
Current in line P12 following a PPG fault with R_f = 50 Ω at t = 2 s.

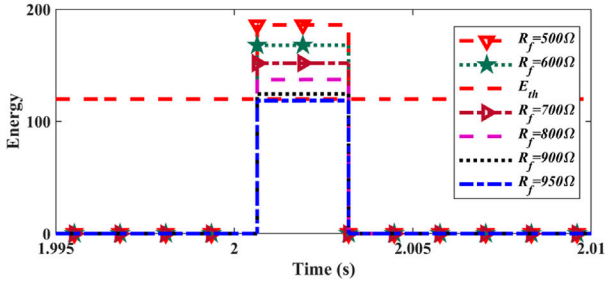

FIGURE 8
Energy content of DWT coefficient following a PPG fault with different fault resistances.

5.1.2 Pole-to-pole (PP) fault simulation

The performance of the proposed algorithm has been evaluated by simulating a pole-to-pole (PP) fault with R_f = 0.1 Ω on the mid-point of the lines P12 and N12. In this case, the forward voltage travelling wave (V_{twf}) is calculated at both positive and negative poles. The energy content of the DWT coefficient of the V_{twf} is shown in Figure 6. As shown in Figure 6, in the case of a PP fault, the energy of the DWT coefficient at both positive and negative poles is greater than the pre-set value. Hence, in this case, the trip signal will be generated by all four relays (i.e., two positive pole relays R_{P1} & R_{P2}, and two negative pole relays R_{N1} & R_{N2}).

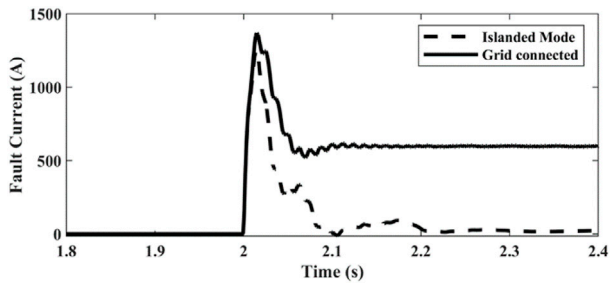

FIGURE 9
Fault current following a PPG fault at t = 2 s in grid-integrated and islanded operation.

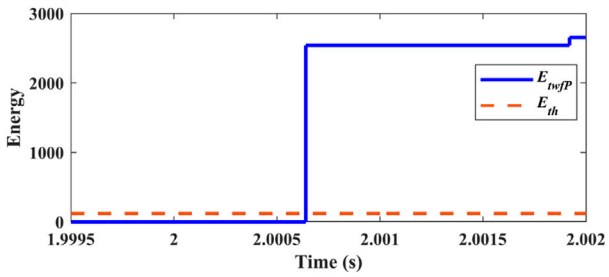

FIGURE 10
Energy of DWT coefficient of V_{twf} following a PPG fault with R_f = 1 Ω at t = 2 s during islanded operation of DCMG.

TABLE 4 Summary of the different cases considered in this study for the verification of the proposed algorithm.

Sl. No.	Operating events	Energy of DWT coefficient (joule)		Relay tripping status (1-high, 0-low)				Operating time (milli-seconds)
		EtwfP	EtwfN	RP1	RP2	RN1	RN2	
1	Fault in grid-integrated mode							
1A	PPG fault with Rf = 0.1 Ω	2793.6	1.0008	1	1	0	0	0.64
1B	NPG fault with Rf = 0.1 Ω	1.1726	2777.1	0	0	1	1	0.64
1C	PP fault with Rf = 0.1 Ω	2765.3	2763.6	1	1	1	1	0.64
1D	PPG fault with Rf = 50 Ω	1103.3	1.0008	1	1	0	0	0.64
1E	PPG fault with Rf = 100 Ω	613.713	1.0008	1	1	0	0	0.64
1F	PPG fault with Rf = 200 Ω	316.035	1.0008	1	1	0	0	0.64
1G	PPG fault with Rf = 500 Ω	186.062	1.0008	1	1	0	0	0.64
1H	PPG fault with Rf = 600 Ω	168.01	1.0008	1	1	0	0	0.64
1I	PPG fault with Rf = 700 Ω	151.97	1.0008	1	1	0	0	0.64
1J	PPG fault with Rf = 800 Ω	137.37	1.0008	1	1	0	0	0.64
1K	PPG fault with Rf = 900 Ω	124.50	1.0008	1	1	0	0	0.64
1L	PPG fault with Rf = 950 Ω	118.622	1.0008	0	0	0	0	—
2	Fault in islanded operation							
2A	PPG fault with Rf = 1 Ω	2654.7	0.3161	1	1	0	0	0.64
2B	NPG fault with Rf = 1 Ω	0.3092	2652.0	0	0	1	1	0.64
2C	PPG fault with Rf = 100 Ω	559.807	0.3161	1	1	0	0	0.64
2D	PPG fault with Rf = 200 Ω	267.68	0.3161	1	1	0	0	0.64
2E	PPG fault with Rf = 500 Ω	207.15	0.3161	1	1	0	0	0.64
2F	PPG fault with Rf = 600 Ω	198.56	0.3161	1	1	0	0	0.64
2G	PPG fault with Rf = 700 Ω	187.39	0.3161	1	1	0	0	0.64
2H	PPG fault with Rf = 800 Ω	175.17	0.3161	1	1	0	0	0.64
2I	PPG fault with Rf = 900 Ω	162.89	0.3161	1	1	0	0	0.64
2J	PPG fault with Rf = 1,000 Ω	151.15	0.3161	1	1	0	0	0.64
2K	PPG fault with Rf = 1.2kΩ	130.14	0.3161	1	1	0	0	0.64

(Continued on following page)

TABLE 4 (*Continued*) Summary of the different cases considered in this study for the verification of the proposed algorithm.

Sl. No.	Operating events	Energy of DWT coefficient (joule)		Relay tripping status (1-high, 0-low)				Operating time (milli-seconds)
		EtwfP	EtwfN	RP1	RP2	RN1	RN2	
2L	PPG fault with Rf = 1.3 k Ω	120.999	0.3161	1	1	0	0	0.64
2M	PPG fault with Rf = 1.35kΩ	116.74	0.3161	0	0	0	0	—
2N	PP fault with Rf = 0.1 Ω	2648.5	2648.5	1	1	1	1	0.64
3	External faults							
3A	LLL-fault on AC side	13.74	11.34	0	0	0	0	—
3B	LL-fault on AC side	5.154	6.119	0	0	0	0	—
3C	LLG-fault on AC side	5.415	7.973	0	0	0	0	—
3D	LG-fault on AC side	6.034	0.089	0	0	0	0	—
3E	Close-in external PPG fault	38.96	18.544	0	0	0	0	—
4	Non-fault operation							
4A	Grid outage	0.0181	0.0168	0	0	0	0	—
4B	Load switching-Scenario-I	0.04579	0.01993	0	0	0	0	—
4C	Load switching-Scenario-II	0.1202	0.07788	0	0	0	0	—
4D	DG uncertainty	0.077	0.075	0	0	0	0	—
4E	Tripping of other distribution lines	0.7089	0.3394	0	0	0	0	—
4F	DG outage	10.45	10.29	0	0	0	0	—

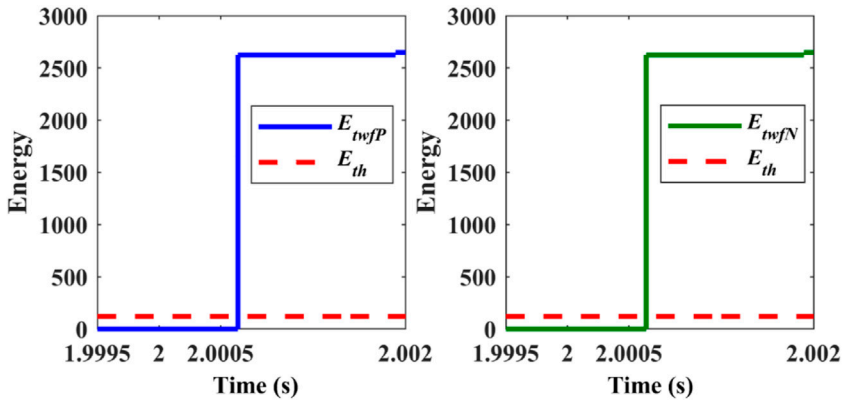

FIGURE 11
Energy of DWT coefficient of V_{twf} at both positive and negative pole following a PP fault with R_f = 0.1 Ω at t = 2 s during islanded operation of DCMG.

5.1.3 Protection against HRF fault

In case of an HRF, the post-fault current in the affected line is very close to the pre-fault current in the line. Hence, it is very difficult to detect these types of faults using conventional overcurrent relays. A conventional protection scheme may treat HRF as an overload condition. Hence, an effective protection scheme must be able to distinguish between the fault and the overload case. To examine the operation of the suggested scheme under HRF, a PPG fault with different fault resistance is simulated on the mid-point of line P12. The current in line P12 (I_{p12}) following a PPG fault with R_f equal to 50 Ω is shown in Figure 7. As the post-fault current in line P12 is very close to the pre-fault current, the current-based protection scheme may not be able to detect this fault. The energy content of the DWT coefficient of the forward voltage travelling wave at the positive pole (E_{twfP}) following a PPG fault with different fault

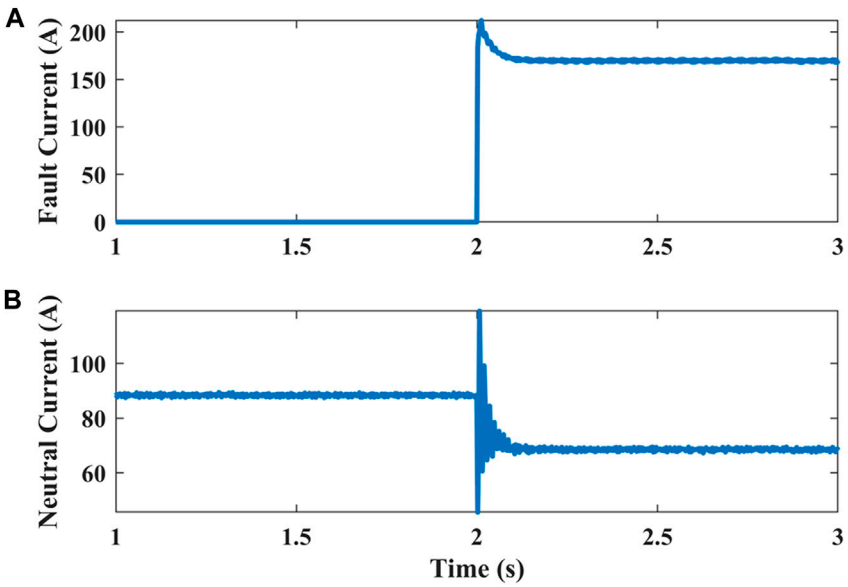

FIGURE 12
Current following a PPG fault with R_f = 10 Ω **(A)** Fault current **(B)** Neutral current.

resistances has been presented in Figure 8. As presented in Figure 8, the proposed algorithm can successfully detect a PG fault of fault resistance up to 900Ω. From Figure 8, it can also be interpreted that the operating time of the proposed algorithm is independent of the fault resistance. The operating time of this algorithm for each fault resistance is 0.64 m.

5.1.4 Protection in Islanded mode operation

During islanded mode operation, the power from the grid is not available and the total load connected to the system must be supplied by the DG only. The variation in fault current during islanded and grid-integrated operations can be observed in Figure 9. In islanded operation, the fault current rises rapidly, reaches up to the peak value, and then quickly settles down to an extremely low value as compared to the grid-integrated mode. Hence, a fault in islanded mode must be detected before it settles down to a low value. The performance of the suggested algorithm has been examined by simulating a PPG and PP fault during islanded operation of the DCMG. The fault current following a PPG fault with R_f = 1 Ω during islanded operation is shown in Figure 9. The energy content of the DWT coefficient of V_{twf} at the positive pole is shown in Figure 10. As soon as this energy content becomes higher than the threshold energy the trip signal is generated by relay R_{P1} and R_{P2}.

To evaluate the performance against a PP fault, a PP fault with R_f equal to 0.1 Ω is simulated between lines P12 and N12. To generate the trip signal for both positive and negative pole relays, the energy of the DWT coefficient of the V_{twf} at both positive and negative poles (i.e., E_{twfP} and E_{twfN}) is calculated using Eq 6. In the case of a PP fault, both E_{twfP} and E_{twfN} will almost be the same, and in this case, as these values are greater than the pre-set value, as shown in Figure 11, the trip signal will be generated by relays R_{P1}, R_{P2}, R_{N1}, and R_{N2}. To examine the performance of the proposed algorithm against HRF, a PPG fault at line P12 with different fault resistance has been simulated, and the energy of the DWT coefficient of V_{twf} is calculated for each case. The simulation results for these cases are presented in Table 4. The data obtained from Table 4 shows that in the islanded mode, the proposed algorithm can protect HRF up to 1,300 Ω.

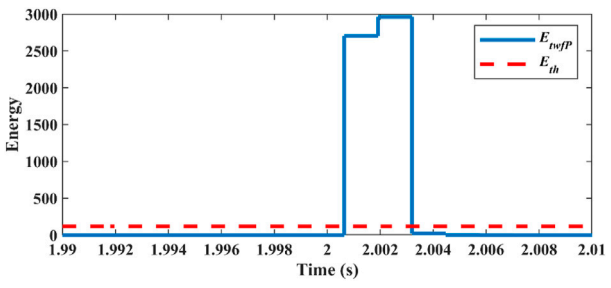

FIGURE 13
Energy of DWT coefficient of V_{twf} following a PPG fault with R_f = 10Ω at t = 2 s with unbalanced loading condition.

5.1.5 Protection during unbalanced loading condition

Till now the utility of the proposed scheme for the balanced network conditions have been presented. In this section, the effectiveness of this scheme during the unbalanced network condition have been presented. To create a unbalance in the system a load of 100 kW is connected at bus-2 between the positive pole and neutral. This load is connected at voltage level of 250 V. The simulation result associated with a PPG fault with R_f = 10 Ω is presented in Figures 12, 13. In balanced condition there will be no current through the neutral during the

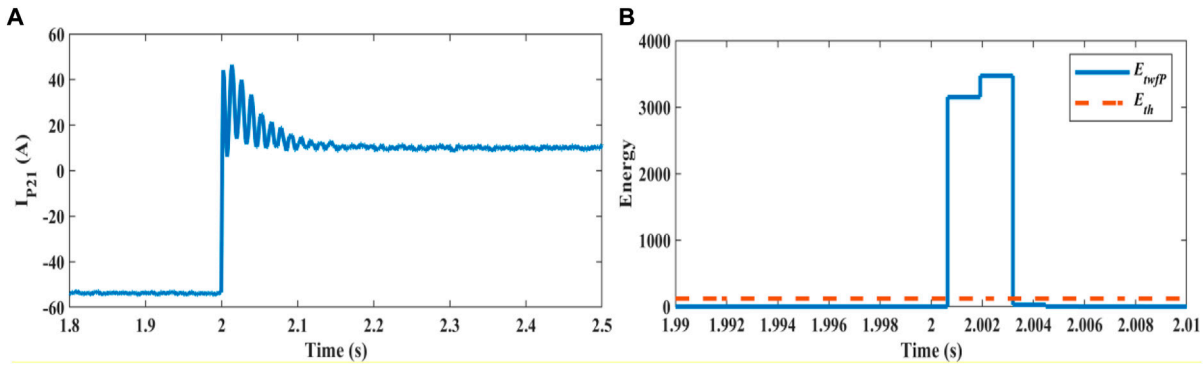

FIGURE 14
(A) Current in cable P21 with SNR 40 dB **(B)** Energy of V_{twf} following the PPG fault.

normal operation. The current in neutral will only if the network is unbalanced, as shown in Figure 12B. The energy of the DWT coefficients presented in Figure 13 confirms the operation of the proposed scheme during the unbalanced loading conditions.

5.1.6 Impact of noise (SNR 40 dB)

To verify the impact of noise, a noise of SNR 40 dB is added to the current signal measured at relay point R_{P2}. A PPG fault with R_f = 1 Ω is create on the cable P21. The simulation result presented in Figure 14 following this fault confirms that the proposed scheme works successfully under the noisy environment also.

5.2 External fault condition

5.2.1 AC side fault

A fault on the AC side of the DCMG may also affect the voltage and current on the DC side. But a protection scheme employed for DCMG protection should not respond to these external faults. To demonstrate the effect of AC side faults on the proposed algorithm, an LLL fault on the AC side has been created at t = 2 s. To see the impact of this fault on the status of trip signals for both positive and negative pole relays, the energies of the DWT coefficients of the V_{twf} (i.e., E_{twfP} & E_{twfN}) are calculated at both positive and negative poles and presented in Figure 15. As shown in the figure, the energies E_{twfP} and E_{twfN} are significantly less than the threshold value E_{th} which is equal to 120. Hence, the trip signal stays low and the protection scheme will not treat this event as a fault.

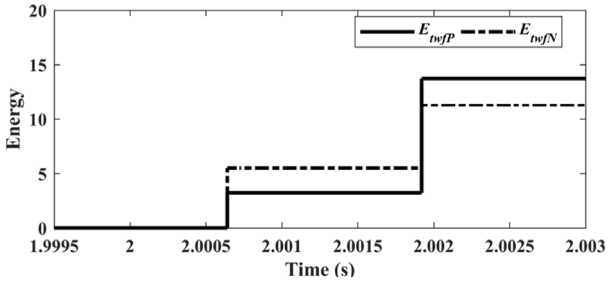

FIGURE 15
Energy content of DWT coefficients of V_{twf} at both positive and negative poles following an LLL-fault on the AC side.

5.2.2 External close-in fault

To verify the effect of close-in external fault on the nearby relays, a PPG fault is simulated closer to the relay R_{P2} outside its protection zone, as shown in Figure 16A.

To see the effect of this fault on the tripping status of the relay RP2, the energy of the DWT coefficients of the voltage travelling wave is calculated, and the same has been presented in Figure 16B. As the energy of the DWT coefficient at this point is less than the threshold value, the trip signal for the relay R_{P2} stays low. It means that the relay R_{P2} remains unaffected during this external fault.

5.3 Non-fault conditions

A decent protection algorithm needs to be discriminatory enough to distinguish between a fault and a no-fault state. Therefore, several non-fault scenarios such as: grid outage; load switching; DG uncertainty; DG outages; and disconnection of any other distribution line, were simulated and the results have been presented in Table 4. The results presented in Table 4 confirm the selectivity of the proposed approach for non-fault conditions, as this scheme remains unaffected from these non-fault operations.

5.4 Summary

In the previous section, the effectiveness of the proposed algorithm has been verified by implementing this for various fault and non-fault scenarios, and a summary of the same has been presented in Table 4. The proposed algorithm can effectively detect PPG, NPG, and PP faults during both islanded and grid-integrated operations. In grid-integrated mode, it can provide protection against HRF of up to 900 Ω. While during islanded operation, it can detect HRF up to 1,300 Ω. The operating time of the presented scheme is 0.64 m, which is quite fast. In the case of

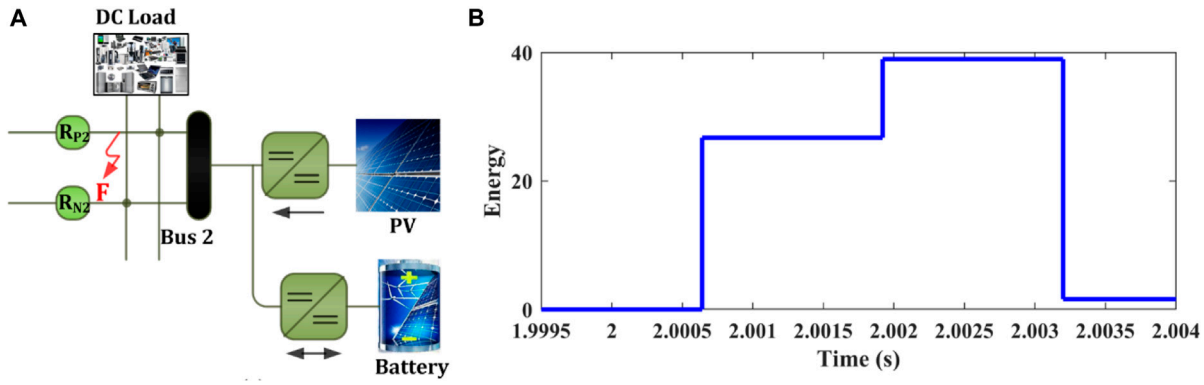

FIGURE16
(A) Close-in external fault; **(B)** Energy of voltage travelling wave at positive pole following a close-in external PPG fault.

TABLE 5 Effect of sampling frequency and no. of samples (N) on the fault detection time of the proposed scheme.

Sampling frequency (kHz)	Fault detection time (ms)				
	N = 64	N = 32	N = 16	N = 8	N = 4
200	2.56	1.28	0.64	—	—
20	3.2	1.6	0.8	0.4	0.4
10	—	3.2	1.6	0.8	0.8
4	—	8	4	2	2

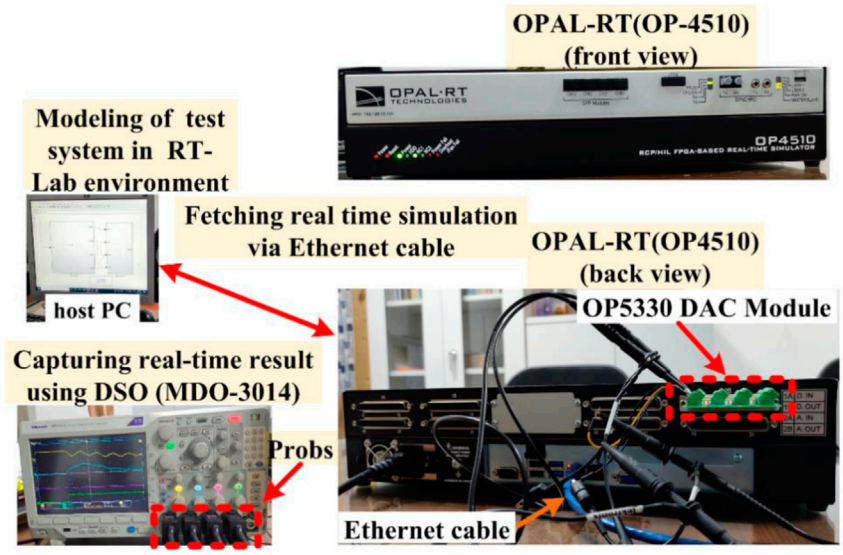

FIGURE 17
Laboratory set-up for real-time validation of the proposed algorithm.

MRA-based schemes, the operating time does not depend on the type of fault and the fault resistances, it mainly depends on the sampling frequency and the no. of samples considered for evaluation. Table 5 shows the effect of sampling frequency and no. of samples on the fault detection time of the proposed scheme. The information presented in the table shows that the proposed

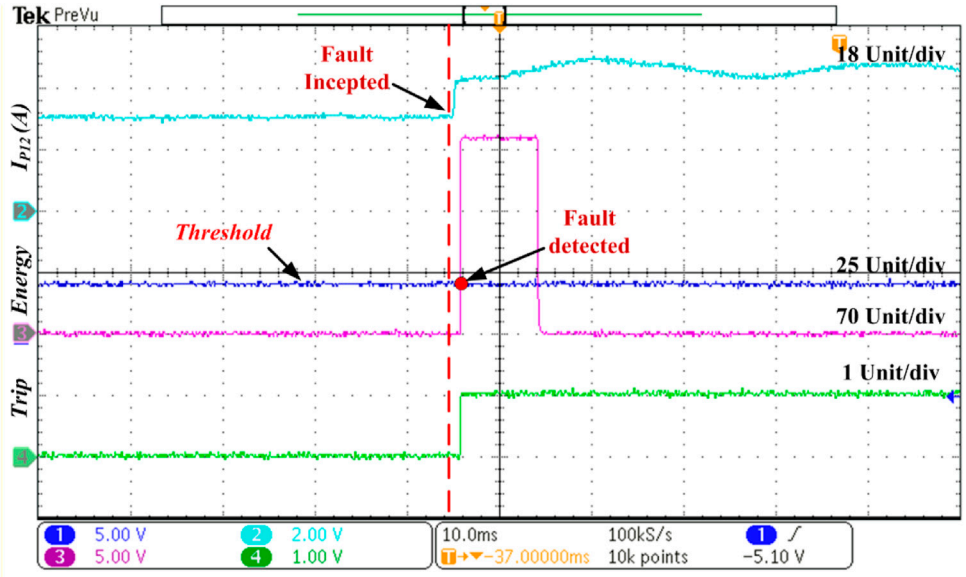

FIGURE 18
Real-time result for PPG fault at the middle of the line P12 with R_f = 50 Ω during the grid-integrated mode.

TABLE 6 Comparison of the proposed algorithm with existing methods.

Parameters/ Operation of the relay	Proposed scheme	Existing methods						
		Chauhan et al. (2022)	Dhar et al. (2018)	Kesava Rao and Jena, (2022)	Wang et al. (2021)	Saleh et al. (2017)	Mohanty et al. (2021)	Jayamaha et al. (2019)
Relay operating time (ms)	0.64	1	<100	3	1	3	3	3–5.5
HRF in grid connected mode	900 Ω	1 Ω	2 Ω	30 Ω	10 Ω	200 Ω	10 Ω	300 Ω
Protection in islanded mode	Yes	Yes	×	×	×	×	×	Yes
HRF in islanded mode	1,300 Ω	×	×	×	×	×	×	×
AC side faults	No	No	×	×	×	Yes	×	×
Grid outage	No	No	×	×	×	×	×	×
Close-in external fault	No	No	×	No	×	Yes	×	×
DG outage	No	No	×	×	×	×	×	×
DG uncertainty	No	No	×	No	×	×	×	×

×, Not Considered.

scheme works satisfactorily (with slight compromise in fault detection time, i.e., 0.8 m) up to the sampling frequency as low as 10 kHz.

6 Real-time validation

The operational validation of the proposed algorithm is conducted with the OPAL-RT time simulator. The laboratory set-up for the real-time validation is shown in Figure 17. The test system shown in Figure 1 is used for real-time simulation. Several cases were simulated for real-time validation of the proposed scheme, and the result of one such case has been presented here.

6.1 Case: PPG fault with R_f = 0.1 Ω in grid-integrated mode

The real-time result of a PPG fault in grid-integrated mode, with R_f = 50 Ω, is shown in Figure 18. As seen in the figure, the wavelet energy (E_{twf}) increases up on the fault inception, and as soon as this energy becomes greater than the threshold value, the trip signal

becomes high. The change in fault current (I_f) and the variation in positive pole voltage at bus-2 (V_{B2P}) following the PPG fault inception can also be observed in Figure 18.

7 Comparative study

In Table 5, the performance of the suggested algorithm is contrasted with that of other currently available techniques. Table 6 shows that the suggested algorithm can identify a ground fault up to a fault resistance of 900 Ω in the grid-integrated mode, which is greater than the other approaches stated in the literature. The suggested algorithm operates in 0.64 m, which is faster than the majority of the algorithms described in the literature. The suggested system does not malfunction in the presence of an outside disturbance like an AC side fault, a grid outage, or a DG outage. Since it is unaffected by external or non-fault situations, this protection strategy offers superior stability than others. Investigating whether a protection strategy is adaptable enough to function well in both grid-integrated and islanded modes is another crucial situation. This situation has not been taken into account by the numerous protection strategies studied in the literature. However, the efficiency of the suggested algorithm has been carefully examined for both grid-integrated and islanded operations. The study's findings confirm that the suggested strategy can properly function in both operating modes. Additionally, in islanded mode, it is capable of detecting PG faults up to 1,300 Ω fault resistance. As a result, the suggested scheme proves to be superior to the other existing schemes in many aspects.

8 Conclusion

For the preservation of DCMG, a novel protection system has been described in this study. In order to verify the effectiveness of the suggested approach, a test model for a 500 V ring-main bipolar DCMG was created in the MATLAB/Simulink environment. Faults such as PPG, NPG, and PP were then simulated. The suggested algorithm has been shown to be a very efficient solution for the protection of DC microgrids and can function well in both grid-integrated and islanded modes. Additionally, it is capable of detecting HRFs of up to 900Ω in grid-integrated mode and 1,300 Ω in islanded mode. The operating time of the proposed algorithm is independent of the type of faults and fault resistances, and it can detect all types of faults in 0.64 m, which is quite fast. The suggested algorithm's resilience has been tested during faults and external disturbance transients, and it has been discovered that this scheme is unaffected by these external disturbances. The suggested approach is therefore very robust, accurate, and highly selective and offers a quick, stable, and trustworthy solution for the protection of DC microgrids.

Data availability statement

The raw data supporting the conclusion of this article will be made available by the authors, without undue reservation.

Author contributions

KK, SA, and OG has contributed to the conception and design of this work. KK has done the statistical analysis and prepared the first draft of the manuscript. All authors contributed to manuscript revision, read, and approved the submitted version.

Conflict of interest

The authors declare that the research was conducted in the absence of any commercial or financial relationships that could be construed as a potential conflict of interest.

Publisher's note

All claims expressed in this article are solely those of the authors and do not necessarily represent those of their affiliated organizations, or those of the publisher, the editors and the reviewers. Any product that may be evaluated in this article, or claim that may be made by its manufacturer, is not guaranteed or endorsed by the publisher.

References

Aftab, M. A., Hussain, S. M. S., Ali, I., and Ustun, T. S. (2018). Dynamic protection of power systems with high penetration of renewables: A review of the traveling wave based fault location techniques. *Int. J. Electr. Power Energy Syst.* 114, 105410. doi:10.1016/j.ijepes.2019.105410

Al-Ismail, F. S. (2021). DC microgrid planning, operation, and control: A comprehensive review. *IEEE Access* 9, 36154–36172. doi:10.1109/ACCESS.2021.3062840

Augustine, S., Quiroz, J. E., Reno, M. J., and Brahma, S. (2018). "DC microgrid protection: Review and challenges,". SAND2018-8853 (Albuquerque, NM: Sandia National Laboratories). doi:10.2172/1465634

Beheshtaein, S., Cuzner, R. M., Forouzesh, M., Savaghebi, M., and Guerrero, J. M. (2019). DC microgrid protection: A comprehensive review. *IEEE J. Emerg. Sel. Top. Power Electron.*, 1. in press. doi:10.1109/jestpe.2019.2904588

Bentley, P. M., and McDonnell, J. T. E. (1994). Wavelet transforms: An introduction. *Electron. Commun. Eng. J.* 6 (4), 175–186. doi:10.1049/ecej:19940401

Burke, P. J., Stern, D. I., and Bruns, S. B. (2018). The impact of electricity on economic development: A macroeconomic perspective. *Int. Rev. Environ. Resour. Econ.* 12 (1), 85–127. doi:10.1561/101.00000101

Chauhan, P., Gupta, C. P., and Tripathy, M. (2022). A novel adaptive protection technique based on rate-of-rise of Fault Current in DC microgrid. *Electr. Power Syst. Res.* 207, 107832–107913. doi:10.1016/j.epsr.2022.107832

Dhar, S., Patnaik, R. K., and Dash, P. K. (2018). fault detection and location of photovoltaic based DC microgrid using differential protection strategy. *IEEE Trans. Smart Grid* 9 (5), 4303–4312. doi:10.1109/TSG.2017.2654267

Gielen, D., Boshell, F., Saygin, D., Bazilian, M. D., Wagner, N., and Gorini, R. (2019). The role of renewable energy in the global energy transformation. *Energy Strateg. Rev.* 24, 38–50. doi:10.1016/j.esr.2019.01.006

Jayamaha, D. K. J. S., Lidula, N. W. A., and Rajapakse, A. D. (2019). Wavelet-multi resolution analysis based ANN architecture for fault detection and localization in DC microgrids. *IEEE Access* 7, 145371–145384. doi:10.1109/ACCESS.2019.2945397

Joos, G., Reilly, J., Bower, W., and Neal, R. (2017). The need for standardization: The benefits to the core functions of the microgrid control system. *IEEE Power Energy Mag.* 15 (4), 32–40. doi:10.1109/MPE.2017.2690518

Justo, J. J., Mwasilu, F., Lee, J., and Jung, J. W. (2013). AC-microgrids versus DC-microgrids with distributed energy resources: A review. *Renew. Sustain. Energy Rev.* 24, 387–405. doi:10.1016/J.RSER.2013.03.067

Kant, K., and Gupta, O. H. (2022). DC microgrid: A comprehensive review on protection challenges and schemes. *IETE Tech. Rev.* 210, 1–17. doi:10.1080/02564602.2022.2136271

Kesava Rao, G., and Jena, P. (2022). Unit protection of tapped line DC microgrid. *IEEE J. Emerg. Sel. Top. Power Electron.* 10 (4), 4680–4689. doi:10.1109/JESTPE.2022.3143525

Manohar, M., Koley, E., and Ghosh, S. (2019). "A wavelet and ANFIS based reliable protection technique for Microgrid," in Proceedings of the 2019 8th International Conference on Power Systems: Transition towards Sustainable, Smart and Flexible Grids ICPS, 1–6. doi:10.1109/ICPS48983.2019.9067617Jaipur, India December 2019

Mohanty, R., Sahoo, S., Pradhan, A. K., and Blaabjerg, F. (2021). A cosine similarity-based centralized protection scheme for dc microgrids. *IEEE J. Emerg. Sel. Top. Power Electron.* 9 (5), 5646–5656. doi:10.1109/JESTPE.2021.3060587

Pukhova, V., Gorelova, E., Ferrini, G., and Burnasheva, S. (2017). "Time-frequency representation of signals by wavelet transform," in Proc. 2017 IEEE Russ. Sect. Young Res. Electr. Electron. Eng. Conf. ElConRus, Moscow, Russia, April. 2017, 715–718. doi:10.1109/EICONRUS.2017.7910658

Sabug, L., Musa, A., Costa, F., and Monti, A. (2019). Real-time boundary wavelet transform-based DC fault protection system for MTDC grids. *Int. J. Electr. Power Energy Syst.* 115, 105475. doi:10.1016/j.ijepes.2019.105475

Saleh, K. A., Hooshyar, A., and El-Saadany, E. F. (2017). Hybrid passive-overcurrent relay for detection of faults in low-voltage DC grids. *IEEE Trans. Smart Grid* 8 (3), 1129–1138. doi:10.1109/TSG.2015.2477482

Saleh, K. A., Hooshyar, A., and El-Saadany, E. F. (2019). Ultra-high-speed traveling-wave-based protection scheme for medium-voltage DC microgrids. *IEEE Trans. Smart Grid* 10 (2), 1440–1451. doi:10.1109/TSG.2017.2767552

Shabani, A., and Mazlumi, K. (2020). Evaluation of a communication-assisted overcurrent protection scheme for photovoltaic-based DC microgrid. *IEEE Trans. Smart Grid* 11 (1), 429–439. doi:10.1109/TSG.2019.2923769

Sharma, N. K., Saxena, A., and Samantaray, S. R. "An intelligent differential protection scheme for DC microgrid," in Proceedings of the 2021 9th IEEE International Conference on Power Systems (ICPS), Moscow, Russia, December 2021, 1–6. doi:10.1109/icps52420.2021.9670330

Sun, S., Tang, C., Hailati, G., and Xie, D. (2022). Voltage monitoring based on ANN-aided nonlinear stability analysis for DC microgrids. *Front. Energy Res.* 1, 1–14. doi:10.3389/FENRG.2022.1045809

Tiwari, R. S., Gupta, O. H., and Sood, V. K. (2022). fault detection using backward propagating traveling waves for bipolar LCC-HVDC lines. *Electr. Power Components Syst.* 50 (1), 1–14. accepted. doi:10.1080/15325008.2022.2136788

Wang, T., Liang, L., Gurumurthy, S. K., Ponci, F., Monti, A., Yang, Z., et al. (2021). Model-based fault detection and isolation in DC microgrids using optimal observers. *IEEE J. Emerg. Sel. Top. Power Electron.* 9 (5), 5613–5630. doi:10.1109/JESTPE.2020.3045418

Yadav, N., and Tummuru, N. R. (2020). A real-time resistance based fault detection technique for zonal type low-voltage DC microgrid applications. *IEEE Trans. Ind. Appl.* 56 (6), 6815–6824. doi:10.1109/TIA.2020.3017564

Zhang, Y., Tai, N., and Xu, B. (2012). Fault analysis and traveling-wave protection scheme for bipolar HVDC lines. *IEEE Trans. Power Deliv.* 27 (3), 1583–1591. doi:10.1109/TPWRD.2012.2190528

frontiers | Frontiers in Energy Research

TYPE Original Research
PUBLISHED 23 January 2023
DOI 10.3389/fenrg.2022.1081826

OPEN ACCESS

EDITED BY
Tahir Khurshaid,
Yeungnam University, South Korea

REVIEWED BY
Liansheng Huang,
Hefei Institutes of Physical Science (CAS), China
Tohid Rahimi,
Carleton University, Canada

*CORRESPONDENCE
Jin Zhu,
zhujin@mail.iee.ac.cn

SPECIALTY SECTION
This article was submitted to Smart Grids,
a section of the journal
Frontiers in Energy Research

RECEIVED 27 October 2022
ACCEPTED 28 November 2022
PUBLISHED 23 January 2023

CITATION
Zeng Q, Zhu J, Guo X, Huo Q, Yin J and Wei T (2023), A low-cost current flow controlling interline hybrid circuit breaker combined with SCR and H-bridge sub-module.
Front. Energy Res. 10:1081826.
doi: 10.3389/fenrg.2022.1081826

A low-cost current flow controlling interline hybrid circuit breaker combined with SCR and H-bridge sub-module

Qingpeng Zeng[1,2], Jin Zhu[1]*, Xinming Guo[1,2], Qunhai Huo[1,2], Jingyuan Yin[1] and Tongzhen Wei[1,2]

[1]Institute of Electrical Engineering, Chinese Academy of Sciences, Beijing, China, [2]University of Chinese Academy of Sciences, Beijing, China

A massive number of DC circuit breaker is usually necessary to be installed to protect HVDC grids from DC faults, this will lead to high capital costs because large number of expensive IGBT-in-series are used. In this paper, an interline hybrid circuit breaker is proposed by the combination of SCR string and a small number of H-bridge modules (SCR-IHCB). The proposed SCR-IHCB has the capacity of blocking DC fault of two adjacent lines respectively by sharing only one main breaker branch (MB) mainly composed of low-cost SCR string and H-bridge module instead of IGBT-in-series string. The interline current flow control function is also integrated. Hence it has advantages of simple and compact topology, economical design compared with typical IGBT based HCB solutions. The operation process of the proposed SCR-IHCB is discussed in detail, and the performance is verified by MATLAB Simulink simulation and scale-down prototype experiment.

KEYWORDS

hybrid circuit breaker, interline, SCR string, current flow control, H-bridge submodule

1 Introduction

Nowadays, HVDC grids have attracted significant attention, due to its inherent advantages such as flexible control of active and reactive power, low loss, system redundancy, and power reliability (Flourentzou et al., 2009; Akhmatov et al., 2014). While the HVDC grid offers several advantages, its engineering application still faces several challenges, one of which is the DC fault handling. The DC circuit breakers (DCCBs) is considered as an essential technology to isolate the fault area and maintain normal operations of non-fault areas in HVDC grids. There are three main groups of DCCB: mechanical DCCBs (Shi et al., 2015; Lin et al., 2016), solid-state DCCBs (Corzine and Ashton, 2012; Sano and Takasaki, 2014; Chang et al., 2016; Keshavarzi et al., 2017; Li et al., 2019; Wang et al., 2019; Shu et al., 2020; Zhang et al., 2020; Xu et al., 2021), and hybrid DCCBs(HÄFNER and JACOBSON, 2011; Sander et al., 2018). The hybrid DCCBs combine the merits of mechanical DCCBs and solid-state DCCBs and therefore is considered as an acceptable solution in HVDC grids. The classic hybrid DCCB

(HCB) topology contains a main breaker branch (MB), an energy absorption branch and a transfer branch, the transfer branch consists of an ultra-fast mechanical disconnector (UFD) in series with load current switch (LCS). There are two main groups of HCBs based on the different MB technical routes.

One of the technical routes is IGBT based MB, the classic IGBT-in-series based HCB has been proposed by ABB and successfully tested (HÄFNER and JACOBSON, 2011; Sander et al., 2018). The State Grid Corporation of China (SGCC) proposed a full-bridge modular based MB to avoid the problem of IGBT-in-series synchronization control and has been used in Zhangbei four-terminal MMC-HVDC (Jia et al., 2020; Jinkun et al., 2020.). In order to further reduce the system cost, some integration solutions are proposed, multi-line DC circuit breakers are integrated into one equipment to reduce the number of unidirectional MBs (Liu et al., 2017; Majumder et al., 2017; Mokhberdoran et al., 2018a; Kontos et al., 2018; Li and Wang, 2018; Xiao et al., 2020; Guo et al., 2021; Wang et al., 2022), another solution integrated HCBs and current flow controllers (CFCs) into one equipment is proposed in (Cwikowski et al., 2018; Mokhberdoran et al., 2018b; Zhu et al., 2022.) to reduce the system loss. But there are still some drawbacks to the hybrid DCCB topology as follows:

(1) Large number of series connected full-controlled semiconductors, such as IGBTs or IGCTs, in the main breaker increase the investment severely (Chen et al., 2018).
(2) In future, large DC grids fault currents may exceed the interruption capacity of IGBT under serious fault conditions. The parallel connection of IGBTs is needed but also introduces challenges in terms of construction cost (Dong et al., 2021).

Another technical route is SCR based MB, The SCR based MB has advantages of larger capacity, and lower price. Since the current conducted through the SCR need to reach a value below its threshold current during the turn-off process of SCR, apply a reverse voltage is one of the possible solutions to ensure fast transition from conducting to blocking. The most important issue when designing an SCR-based HCB is reliably to generate a reverse voltage on SCR during the turn-off process so as to make the current conducted through the SCR reach a value below its threshold current(Jamshidi Far and Jovcic, 2018).

Coupled inductors or Z-source schemes are used to generate the required reverse voltage on SCR during the turn-off process in (Ray et al., 2019). In those schemes, the transient fault current through capacitors is used to generate a reverse voltage on SCRs, hence those schemes can only be passively turned-off in the condition of the high current rising rate.

A thyristor full-bridge based HCB topology is proposed in (Guo et al., 2020), which can pre-charge the capacitor with DC system voltage, and the reverse voltage is generated by discharge process of pre-charged capacitor. The full-bridge structure is used to pre-charge the capacitor with dc system voltage and switch the fault current path, the use of large number of thyristor strings also increases the system cost.

A SCR-HCB with multiple branches is proposed by Alstom in (Grieshaber et al., 2015), the capacitance voltage difference of different branches is used to generate the required reverse voltage. The inductor is no longer needed, but if n branches are required for each HCB, 2n number of thyristor strings are required for two adjacent lines, which also increases the number of components in the whole DC grid system.

A DCCB topology combing many SCRs with a few IGBTs-in-series is proposed in (Shu et al., 2020). The required reverse voltage can be generated by controlled IGBT. However, each DCCB requires two additional IGBT strings, the utilization of the device needs to be increased in multi-terminal system.

In this paper, an interlink hybrid DC circuit breaker (IHCB) based on the concept of sharing only one SCR string MB between two lines is proposed (SCR-IHCB) to increase the utilization of the device. Only a few H-bridge submodule is embedded in to generate the required reverse voltage of SCR turn-off process, and the current flow controlling function is also integrated into the IHCB. No additional capacitor pre-charge circuits and inductors are required, the proposed solution can interrupt the short circuit current of two lines independently and control the current flow if necessary. Therefore, compared to the traditional DCCB/CFC schemes, the proposed topology is simple and economical.

2 Proposed topology

2.1 Basic structure of proposed SCR-IHCB

A novel IHCB is proposed in this paper and its detailed structure is shown in Figure 1. MB is composed of an anti-parallel SCR string and a H-bridge sub module, connecting line 12 and line 13. MOV_2 is used to protect IGBTs in H-bridge sub module. The transfer branch consisting of LCS and UFD is installed on each line. C_1 can be charged through T_1 to the limiting voltage of MOV_1 to block the fault current and absorb the residual energy of the system.

There are three modes of operation: normal operation without current flow controlling (bypass mode), normal operation with current flow controlling (CFC mode), fault current blocking mode. Obviously, higher system integration, lower volume and cost are achieved because only 1 MB mainly based on low-cost SCR string is used, and CFC function are integrated together.

2.2 Operation principles in different mode

2.2.1 Bypass mode

When the multiterminal HVDC (MT-HVDC) system is running normally, LCS_1/LCS_2 and UFD_1/UFD_2 are all

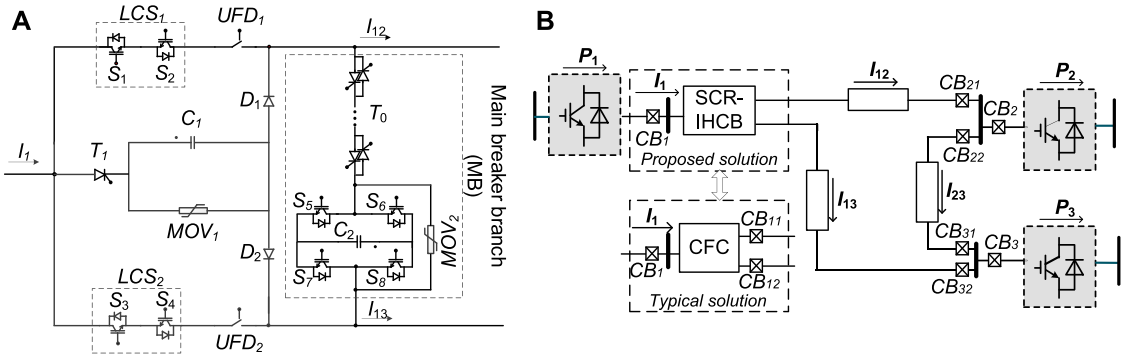

FIGURE 1
Proposed SCR-IHCB topology and installation position in system. **(A)** Proposed topology; **(B)** Three-terminal meshed HVDC system under study.

TABLE 1 Switching states for CFC mode.

State	S_1	S_2	S_3	S_4	S_5	S_6	S_7	S_8	V_1	V_2	V_{C2}
Bypass Mode											
0	1	1	1	1	0	0	0	0	0	0	–
CFC Mode (I_{12} and I_{13} are going out the CFC and I_1 is entering)											
1	1	0	0	0	0	0	0	0	0	$-E$	↑
2	0	0	1	0	0	1	1	0	E	0	↓
3	1	0	0	0	1	0	0	1	0	E	↓
4	0	0	1	0	0	0	0	0	$-E$	0	↑
CFC Mode (I_{12} and I_{13} are entering the CFC and I_1 is going out)											
5	0	0	0	1	0	0	0	0	$-E$	0	↑
6	0	1	0	0	0	1	1	0	0	E	↓
7	0	0	0	1	1	0	0	1	E	0	↓
8	0	1	0	0	0	0	0	0	0	$-E$	↑

E is the reference value of voltage over C_2.

conducted, the SCR string (T_0) and H-bridge submodule are bypassed. There is no additional conduction loss and switching loss of semiconductor devices except LCS_1/LCS_2.

2.2.2 Current flow control mode

When the current flow needs to be adjusted, the proposed SCR-IHCB can work in CFC mode, the working principle is similar with other interline power flow controllers as shown in (Balasubramaniam et al., 2015; Sau-Bassols and Gomis-Bellmunt, 2017). The possible states concerning the available switches are summarized in Table 1.

Where "1" represents the switch is ON and "0" represents the switch is OFF. In Figure 2, one pair of states (state1 and state 2 in Table 1)f of current flow scenarios (I_{12} and I_{13} are going out the SCR-IHCB and I_1 is entering) are considered as an example. In order to transfer power from line13 to line 12, the CFC should switch continuously in state 1 and state 2 by alternating conduction of S_1 and S_3.

Below, the analytical analysis of the SCR-IHCB is performed for the pair of states (state 1 and state 2) presented before. Then, the analysis can be extended to the whole range of current configurations.

Taking state 1 as an example, capacitor C_2 is charged by I_{13}, which is equivalent to inserting a negative voltage in series with line 13. In state 2, capacitor C_2 is discharged by I_{12}, which is equivalent to inserting a positive voltage in series with line 12.

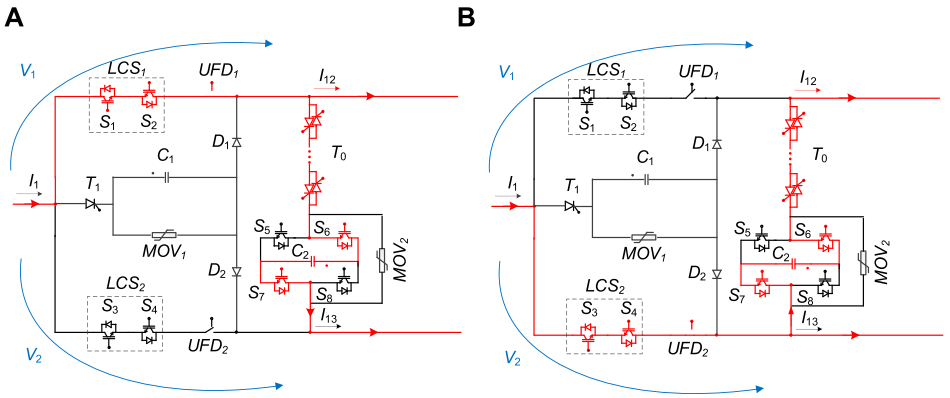

FIGURE 2
Operation stages of SCR-IHCB. **(A)** State 1; **(B)** State 2.

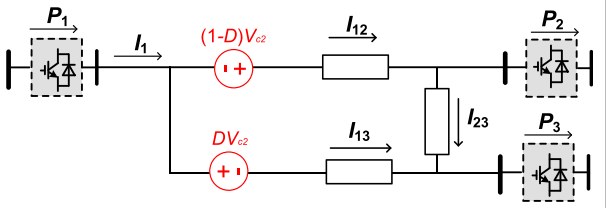

FIGURE 3
Average model of three-terminal DC grid with SCR-IHCB in current control mode.

Assuming D is the duty cycle of state 1. The average model of the three-terminal system with SCR-IHCB can be described as Figure 3.

2.2.3 Fault blocking mode

Take the DC short circuit fault of line12 when SCR-IHCB works in bypass mode as an example, the DC fault current blocking principle is given in Figure 4. Before the fault occurs, the load currents may flow through the low-loss transfer branches in bypass mode as shown in Figure 4A or in CFC mode such as shown in Figure 2.

Stage 1(t_1-t_3): If a fault occurs on line12 at t_1 and is detected at t_2, S_5, S_7 and T_0 will be switch on immediately, and then the IGBTs in LCS_1 will all be switched off at t_3, as shown in Figure 4B. The fault current is then commutated from transfer branch to the main breaker branches, and UFD_1 will open within 2 m.

Stage 2(t_3-t_5): With UFD_1 in open position at t_4 as shown in Figure 4C. Then S_7 switched off, and the S_8 will be switched on, thyristor T_1 will also be turned on immediately as shown in Figure 4D. Initially, T_0 still is on-state, capacitor voltage V_{c2} may suddenly increase in a short time, but its maximum value is strictly limited to the protection voltage V_{MOV2} by the parallel MOV_2, that will protect the IGBT S_5-S_8 from exceeding its maximum withstand voltage. Fault current will keep charging C_1 from zero-voltage state. The capacitor voltage V_{c1} gradually increases from zero but it is smaller than the capacitor voltage of V_{c2} which has been pre-charged in interline CFC mode, and a reverse voltage V_{T0} ($V_{T0} = V_{c1}(t) - V_{c2}$) will hereby be generated, the equivalent circuit is shown in Figure 5. The duration of reverse voltage should be larger than the requested recovery time, and the SCR string will be turn off reliably at t_5 as shown in Figure 4E.

Stage 3(t_5-t_7): The fault current continuously charges C_1. When V_{c1} reaches the protection voltage of MOV_1 at t_6, the current flowing through C_1 is transferred to MOV_1 as shown in Figure 4F. Until fault current decreases to value that no longer maintain D_1 conduction, the fault is cleared at t_7.

3 Parameters design and analysis

3.1 Analysis of current commutation

Based on the fault blocking mode described in Section 2, the process of current commutation starts when the IGBTs in LCS_1 are switched off at t_3. Prior to the capacitor C_1 is inserted at t_4, the fault current is fed into the fault node through healthy nodes, it means the current of other stations will inject into line12, the equivalent circuit is given in Figure 5A. Ignoring the resistance of the IGBTs and thyristor which are much less than line resistance, the fault current i_{fault} can be written as below:

$$i_{fault}(t) = i_{12}(t) + i_{13}(t) = \frac{V_1}{R_{12}}\left(1 - e^{\frac{-tR_{12}}{L_{12}}}\right) + \frac{V_3}{(R_{12}+R_{13})}\left[1 - e^{\frac{-t(R_{12}+R_{13})}{(L_{12}+L_{13})}}\right] \quad (t_1 \le t \le t_4) \tag{1}$$

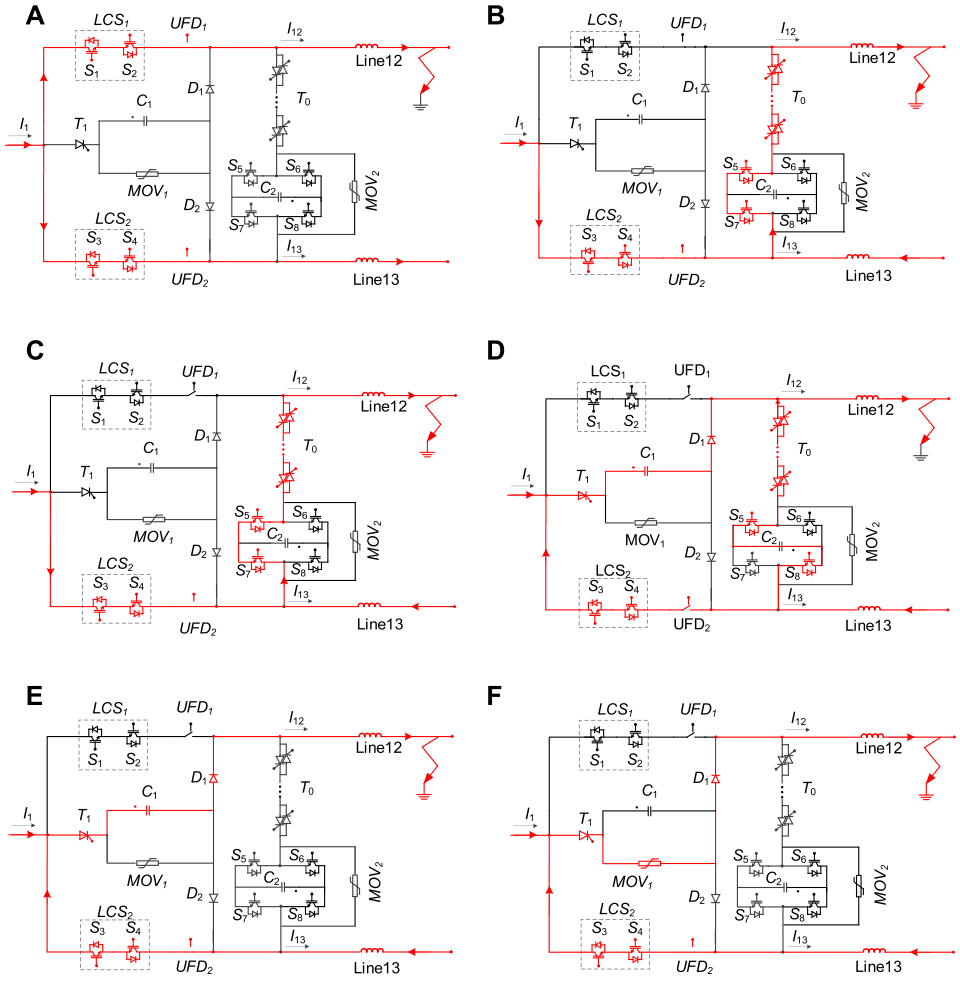

FIGURE 4
Operation of the SCR-IHCB for the transmission line fault. **(A)** Before t_2. **(B)** t_2-t_3. **(C)** t_3-t_4 **(D)** t_4-t_5 **(E)** t_5-t_6 **(F)** t_6-t_7.

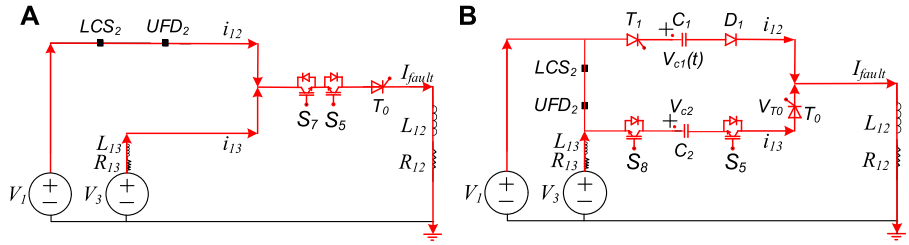

FIGURE 5
Implified equivalent circuit of current commutation process. **(A)** t_3-t_4 **(B)** t_4-t_5.

Where V_1 and V_3 are the voltage of station 1 and station 3 that assumed to remain constant value throughout the process, R_{12} and L_{12} is the resistance and inductance value of line12 to fault point, R_{13} and L_{13} is the resistance and inductance value of line13.

From t_4 to t_5, the capacitor C_1 and C_2 are inserted into the system, the simplified equivalent circuit can be seen in Figure 5B. For capacitor C_2, its voltage has a sudden increase in a short time and the maximum value is the clamping voltage of MOV_2. The

current i_{12} will charge the capacitor C_1 from zero until trigger the clamping voltage of MOV_1 at t_6. According to Figure 5B, the differential equations from t_4 to t_5 can be expressed as:

$$\begin{cases} L_{12}\dfrac{\mathrm{d}i_{12}}{\mathrm{d}t} + V_{\mathrm{c1}} = V_1 \\ i_{12} = \mathrm{C}_1\dfrac{\mathrm{d}u_{\mathrm{c_1}}}{\mathrm{d}t} \\ V_{\mathrm{c1}}(0) = 0 \\ V_{\mathrm{c2}} = V_{\mathrm{clamp2}} \\ i_{12}(0) = i_{12}(t_4) \end{cases} \tag{2}$$

where V_{clamp2} is the clamping voltage of MOV_2, the voltage of the capacitor C_1 from t_4 can be obtained:

$$V_{\mathrm{c1}}(t) = V_1 - V_1\cos\frac{1}{\sqrt{L_{12}C_1}}t + \sqrt{\frac{L_{12}}{C_1}}i_{12}(t_4)\sin\frac{1}{\sqrt{L_{12}C_1}}t \quad (t_4 \le t \le t_5) \tag{3}$$

Assuming T_{scr} is the minimum recovery time of SCR string, the SCR voltage V_{T0} can be expressed as:

$$V_{T0} = V_{\mathrm{c1}}(t) - V_{\mathrm{c2}} = V_1 - V_1\cos\frac{1}{\sqrt{L_{12}C_1}}t + \sqrt{\frac{L_{12}}{C_1}}i_{12}(t_4)\sin\frac{1}{\sqrt{L_{12}C_1}}t - V_{clamp2} \le 0\,(t_4 \le t \le t_4 + T_{scr}) \tag{4}$$

The most important issue of parameter design of the proposed topology is to make sure that the duration of reverse voltage on the SCR string T_0 must be larger than the minimum requested recovery time to make sure the current conducted thought the SCR reach a value below its threshold current and last long enough, thus the thyristor can be switched off reliably.

To meet the minimum recovery time of SCR under the worst situation, and the calculation process can be simplified:

$$T_{rv} = \frac{C_1 V_{C2}}{I_{\max}} \ge \alpha T_{scr} \tag{5}$$

The capacitor C_1 and voltage of C_2 can be chosen as:

$$\begin{cases} C_1 \ge \dfrac{\alpha T_{scr} I_{\max}}{V_{C2}} \\ V_{C2} \ge \dfrac{\alpha T_{scr} I_{\max}}{C_1} \end{cases} \tag{6}$$

Where T_{rv} is the required reverse voltage time, T_{scr} is the minimum recovery time of T_0. I_{max} is the maximum allowed breaking current of SCR-IHCB. α is a redundancy factor and must be larger than 1.

According to Eqs. 5, 6, a larger redundancy factor α increases the reliability of SCR-IHCB, but the capacitor value C_1 and V_{c2} becomes larger. A redundancy factor of 1.5~2 is generally preferred. When the value of α is determined, the value of C_1 and V_{C2} should be designed together, A smaller value of C_1 means a faster blocking speed (t_b in Figure 6) of the fault current because V_{c1} can rise to V_{DC} faster, but it also means that a higher V_{C2} value is required; a higher V_{c2} value also means higher withstand voltage of S_5-S_7, IGBT-in-series or cascaded multi submodule topology can be used, but the cost and loss of the system will also increase. There exists a trade-off between system economy and fault current blocking speed, as shown in Figure 6.

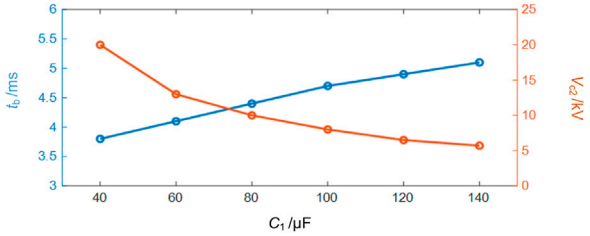

FIGURE 6
The relationship between C_1, t_b and V_{c2}.

3.2 Parameters calculation of MOV

The rated voltage for the MOVs of the typical HCB should be greater than 1.5 times the system voltage to quickly reduce the fault current to zero:

$$V_{MOV} \ge 1.5V_{DC} \tag{7}$$

The total absorbing energy E_{MOV} of MOV is associated with the energy storage components of system, which can be given by:

$$E_{MOV} = \frac{1}{2}L_{DC}I_{\max}^2 - \frac{1}{2}C_1\left(V_{mov}^2 - V_{DC}^2\right) \tag{8}$$

where L_{DC} is the value of system equivalent inductance, I_{max} is the maximum value of fault current.

3.3 Device cost and loss analysis

In order to compare the improvements of the proposed SCR-IHCB, it is compared with the typical HCB+CFC solution which is not integrated (three ABB's HCB solution (Häfner and Jacobson, 2011) in three lines with one CFC (Sau-Bassols and Gomis-Bellmunt, 2017)) in 10kV/1 kA three-port system, as shown in Figure 7. 4.5 kV IGBT(5SNA1200G452300) and 5.2 kV thyristor(T1451N) are selected in the comparison. The relative conduction loss and device cost of two solutions in the same voltage level are shown in Figure 8, where the ordinate is a relative value and "1" represents the maximum.

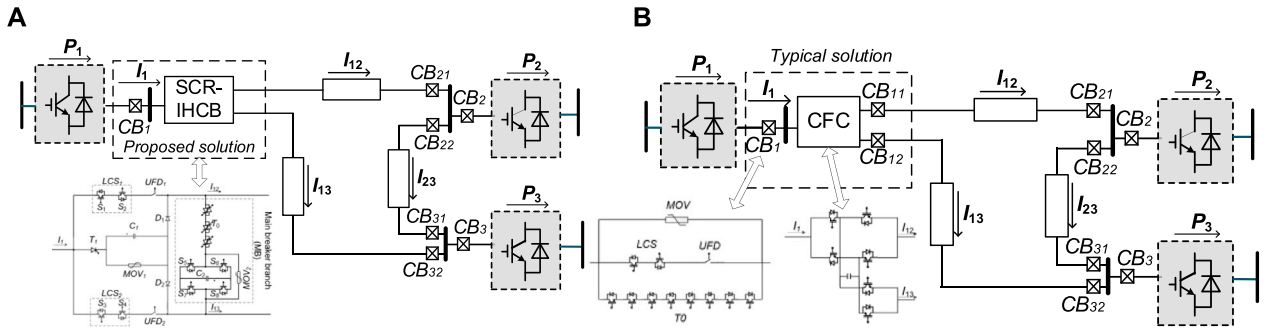

FIGURE 7
Detailed topologies of two solutions in 10kV/1 kA three-port system **(A)** Proposed SCR-IHCB; **(B)** Typical HCB+CFC solution.

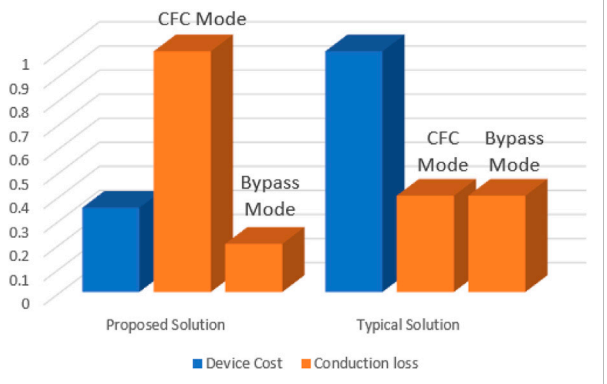

FIGURE 8
Economic comparison with two solutions in 10 kV three-port system.

As can be seen in Figure 8, the device cost of the proposed solution is much lower than that of typical HCB+CFC solution, because less HCBs are used and large number of fully-controlled semiconductor devices have been replaced by semi-controlled semiconductor devices.

The conduction loss in the proposed SCR-IHCB is much higher in CFC mode, but is lower in bypass mode compared with typical IGBT based HCB + CFC solution. Because in bypass mode, only the conduction loss of LCS is added with the proposed solution, but both conduction loss of IGBTs in LCS and CFC parts are added with the typical solution. Considering the investment and conduction loss in different mode together, the comprehensive cost during operation strongly depends on how often the SCR-IHCB need to operate in CFC mode to ensure stable grid conditions, therefore the comprehensive cost could be much lower than the typical solution in the application scenario where inter line power flow control is only needed occasionally.

4 Modeling and control methodology of CFC

In this section, the dynamic model of the proposed CFC is presented, using averaging technique where the terminals voltages are taken into consideration as setting values. Taking the first scenario for example, and the analysis can be extended to the rest of possible current configurations. We can see the current flow of the first scenario in the Figure 2.

The following set of equations describes the circuit of Figure 2A. This equivalent circuit was developed based on a reduction of the physical circuit layout, where: r_{xx} and L_{xx} are the resistance and the inductance of the line xx originated from the CFC bus and carrying an instantaneous current i_x, V_{c1} is the capacitor voltage, V_1 is the voltage at the bus where the CFC is connected to, V_2 and V_3 are the voltages at the end terminals of the lines, respectively.

$$\begin{bmatrix} L_{12} & 0 & 0 \\ 0 & L_{13} & 0 \\ 0 & 0 & C_1 \end{bmatrix} \dot{X} = \begin{bmatrix} -r_{12} & 0 & 0 \\ 0 & -r_{13} & -1 \\ 0 & 1 & 0 \end{bmatrix} X + \begin{bmatrix} 1 & -1 & 0 \\ 1 & 0 & -1 \\ 0 & 0 & 0 \end{bmatrix} U \quad (9)$$

$$X = \begin{bmatrix} i_{12} \\ i_{13} \\ V_{c1} \end{bmatrix}, \; U = \begin{bmatrix} V_1 \\ V_2 \\ V_3 \end{bmatrix} \quad (10)$$

Similarly, the state equations of Figure 2B, where the capacitor is discharging into line12, are as follows:

$$\begin{bmatrix} L_{12} & 0 & 0 \\ 0 & L_{13} & 0 \\ 0 & 0 & C \end{bmatrix} \dot{X} = \begin{bmatrix} -r_{12} & 0 & -1 \\ 0 & -r_{13} & 0 \\ -1 & 0 & 0 \end{bmatrix} X + \begin{bmatrix} 1 & -1 & 0 \\ 1 & 0 & -1 \\ 0 & 0 & 0 \end{bmatrix} U \quad (11)$$

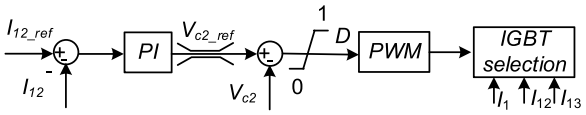

FIGURE 9
PI controller for CFC mode of SCR-IHCB.

Assume the duty ratio of the charging mode1 is D. Multiplying Eqs. 8, 10 by D and $(1–D)$, respectively, and adding the results to obtain the average model for the CFC for the scenario as follows:

$$\begin{bmatrix} L_{12} & 0 & 0 \\ 0 & L_{13} & 0 \\ 0 & 0 & C_1 \end{bmatrix} \dot{X} = \begin{bmatrix} -r_{12} & 0 & -1+D \\ 0 & -r_{13} & -D \\ -1+D & D & 0 \end{bmatrix} X + \begin{bmatrix} 1 & -1 & 0 \\ 1 & 0 & -1 \\ 0 & 0 & 0 \end{bmatrix} U \tag{12}$$

At steady state, Eq. 11 can be written as Eq. 12:

$$\begin{bmatrix} -r_{12} & 0 & -1+D \\ 0 & -r_{13} & -D \\ -1+D & D & 0 \end{bmatrix} X + \begin{bmatrix} 1 & -1 & 0 \\ 1 & 0 & -1 \\ 0 & 0 & 0 \end{bmatrix} U = 0 \tag{13}$$

Solving Eq. 12, the steady-state value of capacitor voltage is obtained as:

$$V_c = \frac{(V_1 - V_2) - r_{12} i_{12}}{1 - D} = \frac{(V_1 - V_3) - r_{12} i_{12}}{D} \tag{14}$$

Eq. 13 gives an expression for the capacitor voltage as a function of the network parameters and the voltage drops across the cables connected to the CFC which represents the loading condition of the grid.

Given that the power taken from one line is equal to the power added to the other line, the power balancing between state 1 and state 2 as shown in Figure 2 is given by:

$$V_{c2\_ref}(1 - D) I_{12} - V_{c2\_ref} D I_{13} = 0 \tag{15}$$

The relationship between I_{12} and I_{13} can be obtained from the above formula:

$$\frac{I_{12}}{I_{13}} = \frac{D}{1 - D} \tag{16}$$

From the previous analysis the voltage ripple can be deduced and it is given by Eq. 16.

$$\Delta U = \frac{D I_{13}}{C_2 f} = \frac{(1 - D) I_{12}}{C_2 f} \tag{17}$$

where f is the switching frequency of the CFC.

A block diagram for the control scheme is shown in Figure 9. The control system has two nested PI controllers: an inner capacitor voltage controller and outer DC current controller. The outer controller regulates the DC line current by feeding a reference voltage to the inner voltage controller. The inner controller achieves the required capacitor voltage level by controlling the duty cycle.

TABLE 2 Parameter of three-terminal HVDC system.

Line parameter	R (Ω Ω/km)	0.01105
	L(MH/km)	3.245
	C(μF/km)	0.382
Station	Length/km	
A1 to A2	200	
A1 to A3	300	
A2 to A3	200	
Converter Parameter	AC voltage	110 kV
	DC voltage	200 kV
	Limiting current inductor	100 mH
SCR-IHCB Parameter	Capacitor C_1	120 μF
	Capacitor C_2	1mF/6 kV
	Arrester protective voltage	250 kV

5 MTDC network Simulation Studies

In this section, a simplified three-terminal HVDC system is simulated. As shown in Figure 1, the proposed SCR-IHCB topology is equipped at station 1 to adjust the power of line 12 and line 13. The practical parameter of the three-terminal HVDC system is shown in Table 2.

The currents flowing from the DC bus of station 1 and the transmission lines in presence of the SCR-IHCB are depicted in Figure 10. The SCR-IHCB operates in the bypass mode for $0 < t <$ 2s. Thereafter, the CFC changes its operation mode to CFC mode at 2s. Figures 10A, B implies that the SCR-IHCB can adjust the current bidirectionally in CFC mode. The short-circuit fault in line12 happens at time $t = 4$s. It can be seen in Figures 10A, B that the SCR-IHCB can quickly isolate the fault on line 12, and the transmission between station 1 and station 3 returned to normal ($I_1 = I_{13}$).

As shown in Figure 10C, before the fault is detected in $t = 4.001$s, the SCR-IHCB is still working in CFC mode. when the system detects the fault, IHCB mode is activated, S_5 and S_7 conducts as mentioned above, the fault current goes through T_0, and I_{T0} started to rise rapidly. After 2 m (waiting for the UFD_1 completely open), the fault current was successfully transferred to charging path of the capacitor C_1, V_{c1} starts to rise (as shown in Figure 10E), in less than

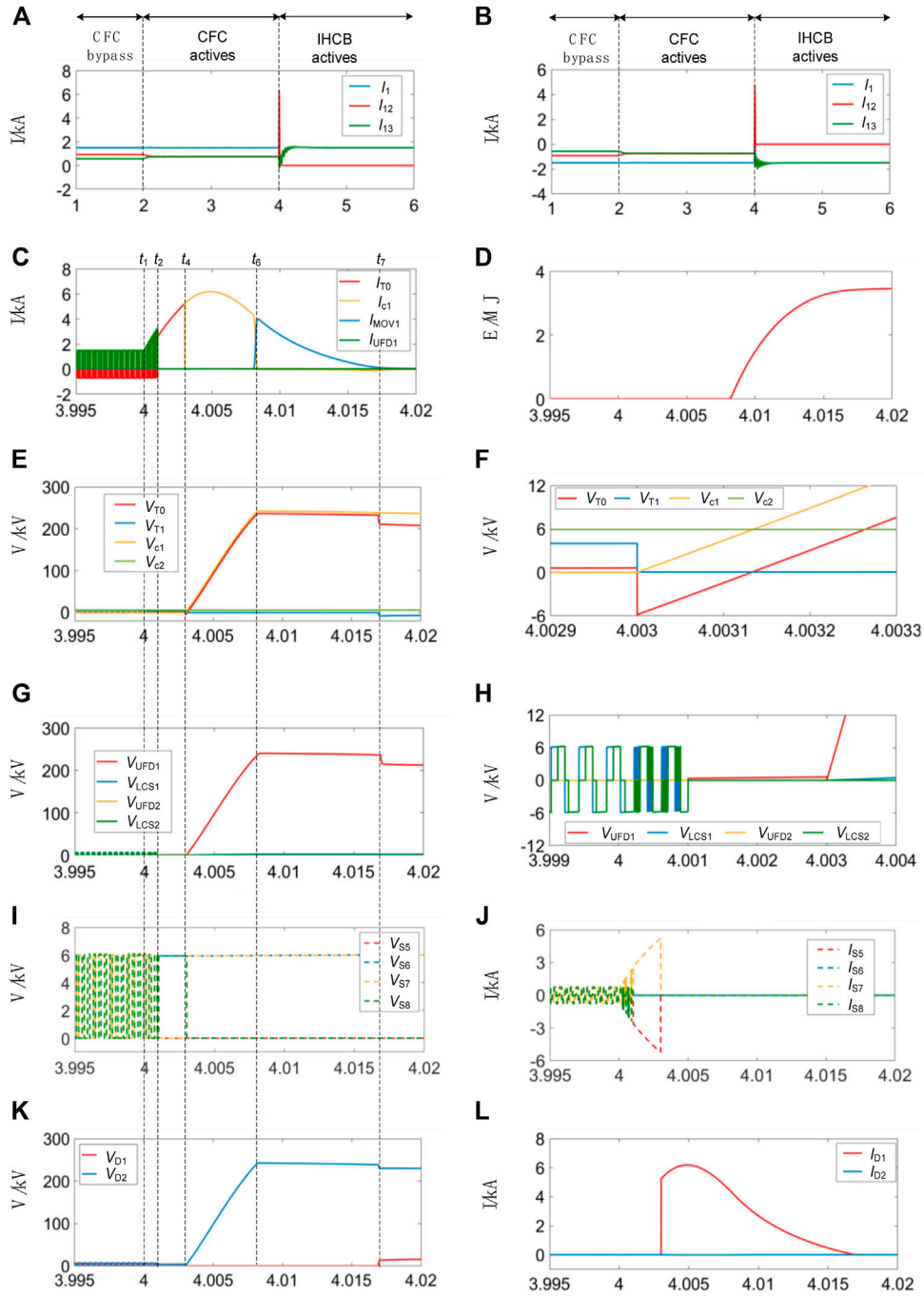

FIGURE 10
Performance of SCR-IHCB. **(A)** Current waveforms with forward power flow. **(B)** Reverse power flow. **(C)** Fault current transfer process. **(D)** Energy absorb by MOV_1. **(E)** V_{T0}, V_{T1}, V_{c1} and V_{c2}. **(F)** Details of V_{T0}, V_{T1}, V_{c1} and V_{c2}. **(G)** Voltage of transfer branches. **(H)** Details of voltage of transfer branches. **(I)** V_{S5}-V_{S8}. **(J)** I_{S5}-I_{S8}. **(K)** V_{D1} and V_{D2}. **(L)** I_{D1} and I_{D2}.

5 m, the fault current (I_{c1}, I_{D1}) reaches the peak value 6.1 kA. When V_{c1} reaches the protection voltage of MOV_1(250 kV as shown in Figure 10E), the fault current is transferred to MOV path (I_{mov1} in Figure 10C) and decreases to zero. The amount of absorbed energy of MOV_1 reaches almost 3.6 MJ as shown in Figure 10D. When the fault current drops to zero, the value of V_{T0} return to V_{DC}-V_{c2}, and the thyristor T_1 needs to withstand a reverse voltage of V_{c1}-V_{DC}, about 50 kV as shown in Figure 10E.

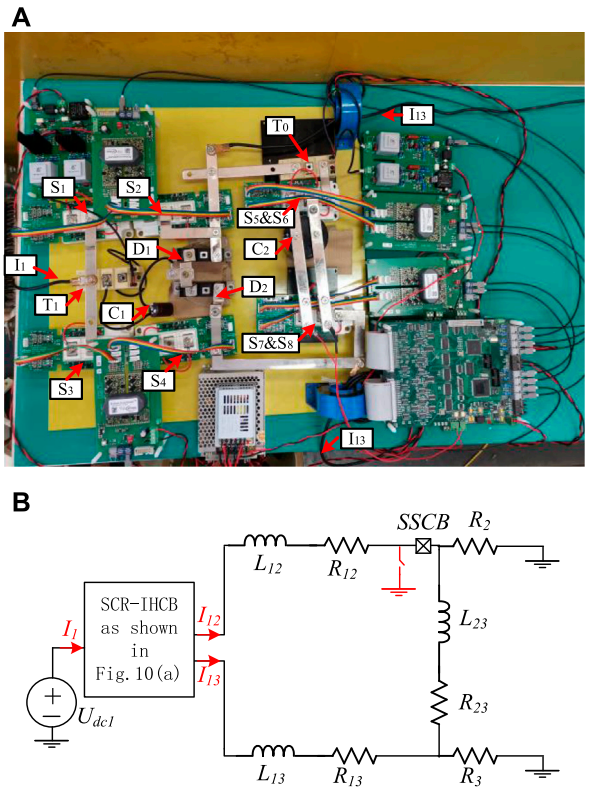

FIGURE 11
Experimental system. **(A)** Photograph of the scale down SCR-IHCB prototype. **(B)** Circuit diagram of three-terminal test platform.

Figure 10F shows that the reverse voltage V_{T0} ($V_{T0} = V_{c1} - V_{c2}$) is generated at 4.003s, and the duration time is about 140us, much larger than the minimum requested recovery time of SCR string in (Jamshidi Far and Jovcic, 2018).

Figures 10G, H show the voltage waveform of two transfer branch, LCS_1 and LCS_2 works in CFC mode before fault is detected. UFD_2 and LCS_2 remain on-state to keep transmission of station1 and station 3 after fault blocking, LCS_1 switch off at 4.001s, and the UFD_1 takes 2 m to completely open, then the voltage on UFD_1 increases with V_{c1}.

Figures 10I, J show the voltage and current of the S_5-S_7. Obviously, the operation sequence of S_5-S_8 is consistent with the theoretical analysis, and the maximum withstand voltage of S_5-S_8 is limited to the given voltage of V_{c2}, the maximum current is equal to the value when the fault current transferred from T_0 branch to C_1 branch.

Figures 10K, L show that the maximum withstand voltage and current of diode strings (D_1 and D_2) are consistent with the maximum voltage of V_{c1} and maximum fault current.

TABLE 3 Parameters of the experimental system.

Parameter	Value
U_{dc1}	200V
$L_{12}/L_{13}/L_{23}$	6mH/6mH/6 mH
R_{12}	6Ω
R_{13}	1.2Ω
R_{23}	4.8Ω
R_2	18.6Ω
R_3	18.6Ω
V_{c2_ref}	30V

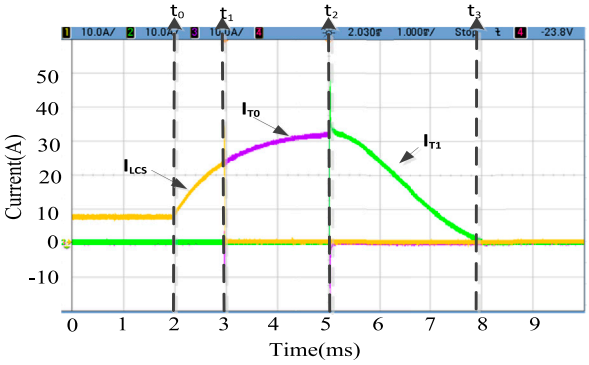

FIGURE 12
Measured fault-interrupting waveforms of the DC Fault Mode.

6 Experimental Studies

Considering that the proposed SCR-IHCB topology is a symmetrical structure for fault blocking of two adjacent lines; therefore, the verification for the current opening process of one line is enough. A scale-down prototype is built for verifying the concept of the feasibility of the SCR-IHCB, as shown in Figure 11A, the component marks in Figure 11A are consistent with those in Figure 1A. The diagram of the experimental system is depicted in Figure 11B and the system parameters are listed in Table 3.

6.1 Fault current blocking

The fault blocking waveforms of the SCR-IHCB are shown in Figure 12. It can be seen that after the fault occurs at t_0, after a detection time of 1 m, the IGBT in LCS is turned OFF, fault current is transferred to main breaker branch at t_1. A 2 m delay is

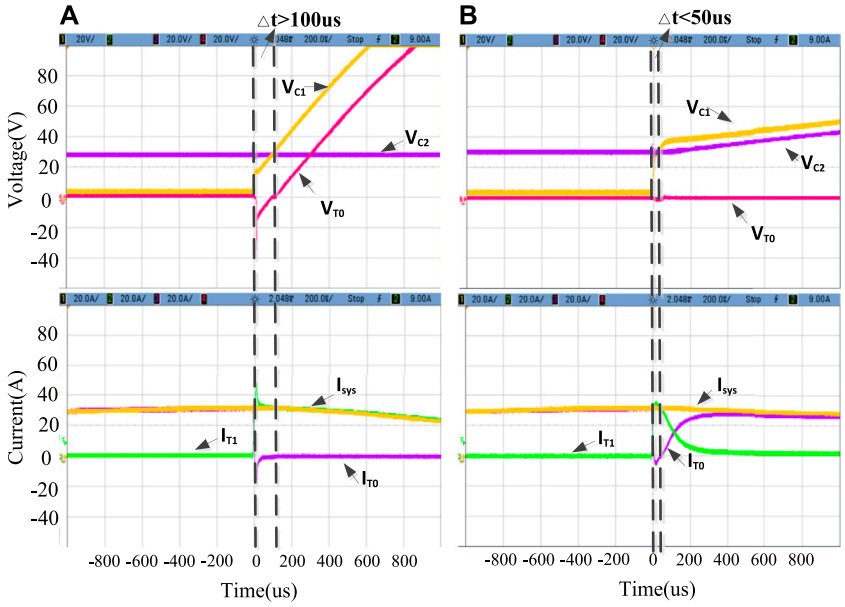

FIGURE 13
Measured waveforms during the thyristor recovery stage at **(A)** C_2 = 220μF; **(B)** C_2 = 100 μF.

set between t_1 and t_2 to simulate the opening time of mechanical switch. The IGBTs in main breaker branch is turned off at t_2, while C_1 is charged and the fault current is successfully interrupted eventually at t_3.

The detailed waveforms of the thyristor T_0 recovery stage is shown in Figure 13. When the value of 220 μF is chosen for C_2, the SCR-IHCB has Δt > 100us as shown in Figure 13A, and the thyristor is turned off successfully, the fault current of the system (I_{sys}) is quickly transferred from T_0 to T_1 (I_{T0} and I_{T1} in Figure 13A), the voltage of T_0 (V_{T0}) rises as C_1 is charged by the system fault current.

When the value of C_2 is reduced to 100 μF, the SCR-IHCB has Δt < 50us, smaller than t_q in datasheet of thyristor SKKT62 which is used in our experiment. It is obvious that the thyristor has failed to turn off, the fault current of the system (I_{sys}) continues to flow through T_0, Capacitor C_1 and capacitor C_2 are connected in parallel, and the voltage rises synchronously.

6.2 Current control

The CFC function is also verified by experiments, as shown in Figure 14. At the beginning, the current at line 12 (I_{12}) is 12A and at line 13 (I_{13}) is 6A at first. At t = 10 m, the CFC begins to work and the current at line 13 (I_{13}) begins to increase and the current at line 12 (I_{12}) decreases meanwhile. After 5 m, the line current forms a new steady state. It can be found that the controller can keep capacitor voltage constant at 30V (V_{c2}) during current regulation.

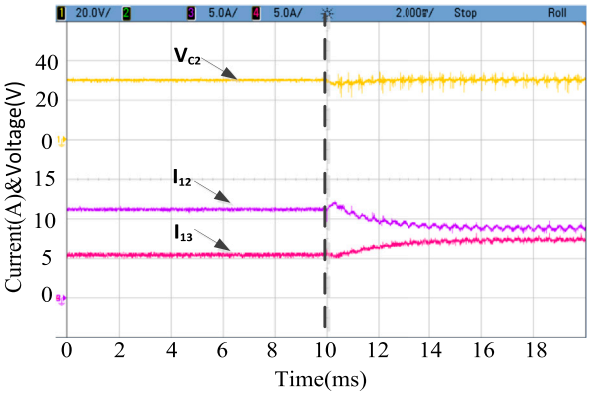

FIGURE 14
Measured fault-interrupting waveforms of the current control mode.

7 Conclusion

In this paper, a SCR string and H-bridge module based interline hybrid circuit breaker topology with current flow control function is proposed. The operation principles in normal operation mode and DC fault mode are analyzed, the parameters design principle is also presented in detail. The simulation and experiment results from a meshed HVDC grid model confirm the operational performance of the proposed topology. Compared with other solutions, the topology design is more economical and simpler because only one bidirectional

SCR string and only one H-bridge module is needed for two adjacent lines, no additional capacitor pre-charge circuits and inductors are required, the current flow control function is also integrated without additional components.

Data availability statement

The original contributions presented in the study are included in the article/Supplementary Material; further inquiries can be directed to the corresponding author.

Author contributions

QZ: Writing—Original Draft, Experimental Studies and Visualization. JZ: Conceptualization, Methodology and Supervision. XG: Writing—Original Draft and Simulation Studies. QH: Editing, Parameters Design. JY: Process Analysis, Supervision. TW: Supervision.

Funding

This work was supported in part by the National Natural Science Foundation of China under Grant 51607171, in part by The Institute of Electrical Engineering, CAS under Grant E155610301 and E155610201.

Acknowledgments

This is a brief acknowledgement of the contributions of individual colleagues, institutions, or agencies that assisted the writers' efforts in the writing of this article.

Conflict of interest

The authors declare that the research was conducted in the absence of any commercial or financial relationships that could be construed as a potential conflict of interest.

Publisher's note

References

Akhmatov, V., Callavik, M., Franck, C. M., Rye, S. E., Ahndorf, T., Bucher, M. K., et al. (2014). Technical guidelines and prestandardization work for first HVDC grids. *IEEE Trans. Power Deliv.* 29 (1), 327–335. doi:10.1109/TPWRD.2013.2273978

Balasubramaniam, S., Liang, J., and Ugalde-Loo, C. E. (2015). "Control, dynamics and operation of a dual H-bridge current flow controller," in IEEE Energy Conversion Congress and Exposition (Montreal, Canada: ECCE). doi:10.1109/ecce.2015.7309996

Chang, A. H., Sennett, B. R., Avestruz, A.-T., Leeb, S. B., and Kirtley, J. L. (2016). Analysis and design of DC system protection using Z-source circuit breaker. *IEEE Trans. Power Electron.* 31 (2), 1036–1049. doi:10.1109/TPEL.2015.2415775

Chen, Z., Yu, Z., Zhang, X., Wei, T., Lyu, G., Qu, L., et al. (2018). Analysis and experiments for IGBT, IEGT, and IGCT in hybrid DC circuit breaker. *IEEE Trans. Ind. Electron.* 65 (4), 2883–2892. doi:10.1109/TIE.2017.2764863

Corzine, K. A., and Ashton, R. W. (2012). A new Z-source DC circuit breaker. *IEEE Trans. Power Electron.* 27 (6), 2796–2804. doi:10.1109/tpel.2011.2178125

Cwikowski, O., Sau-Bassols, J., Chang, B., Prieto-Araujo, E., Barnes, M., Gomis-Bellmunt, O., et al. (2018). Integrated HVDC circuit breakers with current flow control capability. *IEEE Trans. Power Deliv.* 33 (1), 371–380. doi:10.1109/TPWRD.2017.2711963

Dong, Z., Ren, R., Zhang, W., Wang, F. F., and Tolbert, L. M. (2021). Instability issue of paralleled dies in an SiC power module in solid-state circuit breaker applications. *IEEE Trans. Power Electron.* 36 (10), 11763–11773. doi:10.1109/TPEL.2021.3068608

Flourentzou, N., Agelidis, V. G., and Demetriades, G. D. (2009). VSC-based HVDC power transmission systems: An overview. *IEEE Trans. Power Electron.* 24 (3), 592–602. doi:10.1109/TPEL.2008.2008441

Grieshaber, W., Davidson, C. C., Whitehouse, R. S., Dupraz, J.-P., and Barker, C. D. (2015). "A new ultra-fast HVDC Circuit breaker for meshed DC networks," in 11th IET International Conference on AC and DC Power Transmission (Birmingham, UK): Institution of Engineering and Technology), 047. doi:10.1049/cp.2015.0021

Guo, Y., Li, H., Gu, G., Zeng, D., and Wang, G. (2021). A multiport DC circuit breaker for high-voltage DC grids. *IEEE J. Emerg. Sel. Top. Power Electron.* 9 (3), 3216–3228. doi:10.1109/JESTPE.2020.3018646

Guo, Y., Wang, G., Zeng, D., Li, H., and Chao, H. (2020). A thyristor full-bridge-based DC circuit breaker. *IEEE Trans. Power Electron.* 35 (1), 1111–1123. doi:10.1109/TPEL.2019.2915808

Häfner, J., and Jacobson, B. (2011). "Proactive hybrid HVDC breakers-A key innovation for reliable HVDC grids," in Integrating Supergrids and Microgrids International Symposium (Bologna, Italy), 1–8.

Häfner, J., and Jacobson, B. (2011). "Proactive hybrid HVDC breakers-a key innovation for reliable HVDC grids," in Proceedings of the international symposium on integrating supergrids and microgrids (Bologna, Italy), 1–8.

Jamshidi Far, A., and Jovcic, D. (2018). Design, modeling and control of hybrid DC circuit breaker based on fast thyristors. *IEEE Trans. Power Deliv.* 33 (2), 919–927. doi:10.1109/TPWRD.2017.2761022

Keshavarzi, D., Ghanbari, T., and Farjah, E. (2017). A Z-source-based bidirectional DC circuit breaker with Fault Current limitation and interruption capabilities. *IEEE Trans. Power Electron.* 32 (9), 6813–6822. doi:10.1109/TPEL.2016.2624147

Kontos, E., Ramirez-Elizondo, L. M., Franck, C. M., Bauer, P., and Bauer, P. (2018). Multiline breaker for HVDC applications. *IEEE Trans. Power Deliv.* 33 (3), 1469–1478. doi:10.1109/TPWRD.2017.2754649

Li, C., and Wang, S. (2018). Interlink hybrid DC circuit breaker. *IEEE Trans. Ind. Electron.* 65 (11), 8677–8686. doi:10.1109/TIE.2018.2803778

Li, W., Wang, Y., Wu, X., and Zhang, X. (2019). A novel solid-state circuit breaker for on-board DC microgrid system. *IEEE Trans. Ind. Electron.* 66 (7), 5715–5723. doi:10.1109/TIE.2018.2854559

Lin, W., Jovcic, D., Nguefeu, S., and Saad, H. (2016). "Modelling of high power mechanical DC circuit breaker," in IEEE PES Asia-Pacific Power and Energy Engineering Conference (Brisbane, Australia: APPEEC), 1–5. doi:10.1109/APPEEC.2015.7381002

Liu, G., Xu, F., Xu, Z., Zhang, Z., and Tang, G. (2017). Assembly HVDC breaker for HVDC grids with modular multilevel converters. *IEEE Trans. Power Electron.* 32 (2), 931–941. doi:10.1109/TPEL.2016.2540808

Majumder, R., Barupati, P., Jonsson, T. U., and Velotto, G. (2017). An alternative method to build DC switchyard with hybrid DC breaker for DC grid. *IEEE Trans. Power Deliv.* 32 (2), 713–722. doi:10.1109/TPWRD.2016.2582923

Mokhberdoran, A., Gomis-Bellmunt, O., Silva, N., and Carvalho, A. (2018a). Current flow controlling hybrid DC circuit breaker. *IEEE Trans. Power Electron.* 33 (2), 1323–1334. doi:10.1109/TPEL.2017.2688412

Mokhberdoran, A., Van Hertem, D., Silva, N., Leite, H., and Carvalho, A. (2018b). Multiport hybrid HVDC circuit breaker. *IEEE Trans. Ind. Electron.* 65 (1), 309–320. doi:10.1109/TIE.2017.2719608

Ray, A., Rajashekara, K., Banavath, S. N., and Pramanick, S. K. (2019). Coupled inductor-based zero current switching hybrid DC circuit breaker topologies. *IEEE Trans. Ind. Appl.* 55 (5), 5360–5370. doi:10.1109/TIA.2019.2926467

Sander, R., Suriyah, M., and Leibfried, T. (2018). Characterization of a countercurrent injection-based HVDC circuit breaker. *IEEE Trans. Power Electron.* 33 (4), 2948–2956. doi:10.1109/TPEL.2017.2709785

Sano, K., and Takasaki, M. (2014). A surgeless solid-state DC circuit breaker for voltage-source-converter-based HVDC systems. *IEEE Trans. Ind. Appl.* 50 (4), 2690–2699. doi:10.1109/TIA.2013.2293819

Sau-Bassols, J., and Gomis-Bellmunt, O. (2017). Modelling and control of an interline current flow controller for meshed HVDC grids. *IEEE Trans. Power Deliv.* 32 (1), 11–22. doi:10.1109/TPWRD.2015.2513160

Shi, Z. Q., Zhang, Y. K., Jia, S. L., Song, X. C., Wang, L. J., and Chen, M. (2015). Design and numerical investigation of A HVDC vacuum switch based on artificial current zero. *IEEE Trans. Dielectr. Electr. Insul.* 22 (1), 135–141. doi:10.1109/TDEI.2014.004533

Shu, J., Wang, S., Ma, J., Liu, T., and He, Z. (2020). An active Z-source DC circuit breaker combined with SCR and IGBT. *IEEE Trans. Power Electron.* 35 (10), 10003–10007. doi:10.1109/TPEL.2020.2980543

Wang, S., Ming, W., Ugalde Loo, C. E., and Liang, J. (2022). A low-loss integrated circuit breaker for HVDC applications. *IEEE Trans. Power Deliv.* 37 (1), 472–485. doi:10.1109/TPWRD.2021.3063515

Wang, Y., Li, W., Wu, Xuanyu., and Wu, Xiaohua. (2019). A novel bidirectional solid-state circuit breaker for DC microgrid. *IEEE Trans. Ind. Electron.* 66 (7), 5707–5714. doi:10.1109/TIE.2018.2878191

Xiao, H., Xu, Z., Xiao, L., Gan, C., Xu, F., and Dai, L. (2020). Components sharing based integrated HVDC circuit breaker for meshed HVDC grids. *IEEE Trans. Power Deliv.* 35 (4), 1856–1866. doi:10.1109/TPWRD.2019.2955726

Xu, X., Chen, W., Liu, C., Sun, R., Li, Z., and Zhang, B. (2021). An efficient and reliable solid-state circuit breaker based on mixture device. *IEEE Trans. Power Electron.* 36 (9), 9767–9771. doi:10.1109/TPEL.2021.3067316

Zhang, X., Yu, Z., Chen, Z., Zhao, B., and Zeng, R. (2020). Optimal design of diode-bridge bidirectional solid-state switch using standard recovery diodes for 500-kV high-voltage DC breaker. *IEEE Trans. Power Electron.* 35 (2), 1165–1170. doi:10.1109/TPEL.2019.2930739

Zhu, J., Guo, X., Yang, X., Mi, Z., and Wei, T. (2022). Integrated topology of multi-line DC circuit breaker and power flow controller. *IEEE Trans. Power Deliv.* 37 (3), 2112–2121. doi:10.1109/TPWRD.2021.3104667

frontiers | Frontiers in Energy Research

TYPE Original Research
PUBLISHED 10 February 2023
DOI 10.3389/fenrg.2023.1103093

OPEN ACCESS

EDITED BY
Constantinos S. Psomopoulos,
University of West Attica, Greece

REVIEWED BY
George Ioannidis,
University of West Attica, Greece
Aneesh A. Chand,
University of the South Pacific, Fiji

*CORRESPONDENCE
Mohit Bajaj,
thebestbajaj@gmail.com
Tahir Khurshaid,
tahir@ynu.ac.kr
Ali Nauman,
anauman@ynu.ac.kr

SPECIALTY SECTION
This article was submitted to Smart Grids,
a section of the journal
Frontiers in Energy Research

RECEIVED 19 November 2022
ACCEPTED 31 January 2023
PUBLISHED 10 February 2023

CITATION
Vishnuram P, R N, P S, K V, Bajaj M, Khurshaid T, Nauman A and Kamel S (2023), A comprehensive review on EV power converter topologies charger types infrastructure and communication techniques.
Front. Energy Res. 11:1103093.
doi: 10.3389/fenrg.2023.1103093

A comprehensive review on EV power converter topologies charger types infrastructure and communication techniques

Pradeep Vishnuram[1], Narayanamoorthi R[1], Suresh P[1], Vijayakumar K[1], Mohit Bajaj[2,3,4]*, Tahir Khurshaid[5]*, Ali Nauman[6]* and Salah Kamel[7]

[1]Department of Electrical and Electronics Engineering, Electrical Vehicle Charging Research Centre, SRM Institute of Science and Technology, Chennai, Tamil Nadu, [2]Department of Electrical Engineering, Graphic Era (Deemed to be University), Dehradun, India, [3]Graphic Era Hill University, Dehradun, India, [4]Applied Science Research Center, Applied Science Private University, Amman, Jordan, [5]Department of Electrical Engineering, Yeungnam University, Gyeongsan, Republic of korea, [6]Department of Information and Communication Engineering Yeungnam University, Republic of korea, [7]Electrical Engineering Department, Faculty of Engineering, Aswan University, Aswan, Egypt

The energy transition is a crucial effort from many sectors and levels to create a more integrated, carbon-neutral society. More than 20% of all greenhouse gas emissions are attributed to the transportation sector, predominantly concentrated in metropolitan areas. As a result, various technological hurdles are encountered and overcome. It facilitates the adoption of electric vehicles (EVs) run on renewable energy, making them a practical option in the fight against climate change and the completion of the energy revolution. Recent developments suggest that EVs will replace internal combustion engine (ICE) during the next few months. The EV either gets all of its power from batteries and ultra capacitors or some of it from both. In a plug-in electric vehicle, the battery or ultra-capacitor is charged by an AC supply connected to a grid line. In a hybrid electric vehicle, the ICE charges the battery or ultra-capacitor. Regenerative braking is another way to charge the battery from the traction motor. In a plug-in electric vehicle, the energy from of the battery or ultra-capacitor is put back into the AC grid line. Electronic converters are essential to converting power from the grid line to the traction motor and back again. This paper examines the current state of the electric vehicle market throughout the world and its potential future developments. Power electronics converters (PEC) and energy storage devices significantly impact electric vehicles' efficiency. Furthermore, general opinions about EVs are soon in this sector, as well as research topics that are still open to industry and University researchers.

KEYWORDS

electric vehicle, DC-DC converter, DC-AC converter, bidirectional converter, electric market, on-boarding charging, off-board charging

1 Introduction

Recently, there has been significant growth in the number of initiatives aimed at increasing, establishing, and managing RES. Polluting, degrading, and adding to the greenhouse effect are all side effects of using conventional energy sources. Conventional vehicle significantly contributes to the transportation sector's air pollution and greenhouse gas emissions. Carbon dioxide (CO_2), sulphur dioxide (SO_2), and nitrogen oxide (NO_2) are released when gasoline, coal, or natural gas are burned in these automobiles, making them hazardous combustion vehicles. An internal combustion engine (ICE) loss is caused by friction and heat loss in the transferring section (Sharma and Sharma, 2019).

The replacement of ICE highlights the importance of EVs as the most incredible alternative for lowering emissions (Gryparis et al., 2020). Heavy-duty vehicle (HDV) energy efficiency is crucial due to its link to other policy instruments. Hence, this is critical because some HDVs, such as city buses and refuse trucks, are purchased in significant quantities by government organizations. Despite this, no technical comparison of the CO_2 emissions or fuel consumption of vehicles in the same class. Battery-powered EV propulsion demands a massive battery pack with a restricted range (Fontaras et al., 2016). Power electronic converters of various types are connected to energy storage systems (ESSs) in electric vehicles in various ways (Khalid et al., 2019). An EV's energy storage and control optimization are detailed (Islam and Pota, 2013).

Power management control (PMC) based on a fuzzy inference system has improved due to genetic algorithm (GA) assistance. To decrease the total size of the hybrid energy storage system and increase the EV range, the GA is used offline to optimise the lower and upper membership limitations. An accurate model for estimating the energy needs of EVs was created by Miri et al. Since the amount of power required to operate a vehicle's accessories varies widely, this estimation is included in the EV's design. Energy storage systems (ESSs) are charged by connecting them to an AC power source, such as the utility grid or a dedicated charging station (Wu et al., 2017). DC-DC converters are necessary to regulate the power flow in the EV (Elsayad et al., 2020).

An energy-harvesting and power-demanding bidirectional non-isolated DC-DC converter is designed (Navarro et al., 2020). It is challenging since it depends on the load characteristics, source voltage, and duty cycle (Fardahar and Sabahi, 2020). Kanamarlapudi et al. developed a novel full-bridge isolated DC-DC converter with a passive auxiliary circuit that offers zero voltage switching (ZVS) for every significant switch across the battery charging range (Kanamarlapudi et al., 2018). The creation of diverse energy sources reduces vehicle running costs and enhances efficiency. The hybrid electric vehicle (HEV) has developed as an effective alternative for minimizing greenhouse emissions due to transport. Compared to ICE vehicles, HEVs claim superior fuel economy by maintaining the state of charge (SOC) (Kumar and Jain, 2014). By using renewable energy to power EVs, green charging systems (GCSs) with lower CO_2 emissions and promote the use of RES in the energy sector (Najafi et al., 2021a).

Grid is the primary source for charging EVs, but in practice, they also use renewable energy sources and coal for their energy needs (Mamun et al., 2022). The main problems with HEVs seem to be the fuel tank and regenerative braking. Plug-in hybrid electric vehicles (PHEVs) with externally charged batteries can solve the above-said problem (Shakeri et al., 2018). The most recent technology has developed a carbon-free EV charging station utilizing solar energy, drastically reducing pollutants and the effect of EVs on the electrical network. The expansion of renewable energy will significantly accelerate the use of maximum power converters with much more efficient and reliable conversion of boundless energies into an electricity network. PHEVs address the issue of restricted driving range by providing vehicle-to-grid (V2G) functionality (Islam and Cirrincione, 2016).

Multiple communication connection qualities are necessary to suit the demands of various charging mechanisms. A component powered by multiple wireless connections is necessary for a large-scale EV charging system with static, dynamic, and quasi-dynamic charging to enable effective interaction among numerous network elements (Yu et al., 2019). Consequently, to maintain their economic performance in the coming years, several firms are doing more thorough research into BEV charging options (Verma and Singh, 2019). The battery management system (BMS) is notable in light of the challenging-to-attain safety and dependability standards (Momete, 2018). The new distribution network, driven by EVs and energy markets, is expected to play a significant role in autonomous charging stations at a port, public parking lots, and quick charging infrastructure (Nunes et al., 2016). This article put forth a comprehensive review of EV technology, which includes selection of motors, battery requirements, power electronic converters, charging technologies, different charging methods, EV market and charging infra structure, with future directions. This article will help the kindle researchers who wish to work in EV technologies.

The course of the paper is organised as follows. The details of electric motors for EV applications are explained in Section 2, whereas in Section 3, the battery requirement for EVs is briefed. Power converters and charging communication technologies are elucidated in Sections 4, 5, respectively. Sections 6, 7 briefs about the conductive and inductive charging respectively. The electric vehicle market and Repercussions of electric vehicle charging infrastructure are briefed in Section 8, 9, respectively. The future direction of the research area is explained in Section 10, birds view. The conclusion of the paper is drafted in Section 10.

2 Electric motors for EV

An integral component of the EV is the electric motor, which includes power electronics and batteries. In EVs, where weight and space are constrained, more power and torque density enable improved driving characteristics in a small, straightforward design. The other factor, efficiency, is improved. Whenever the vehicle is in motion, the energy stored in the battery is wasted, resulting in a more excellent range despite the same storage space. According to multiple unique problems in motor design, the EV industry has applied a range of distinct options, comprising wound rotor, permanent magnet and induction. The rare metals used in permanent magnet motors are subject to price fluctuations, have a restricted geographical distribution system, and come with a unique mix of benefits and drawbacks in terms of development costs, dependability, and accessibility. DC motors offer a

TABLE 1 Performance comparison of different motors.

Types of motor/ parameters	Torque density (Nm/kg)	Power density (kW/kg)	Loading capacity factor	Remarks
IM	4	1.5	1.6–3.2	• Less cost
				• Simple construction
				• Established technology
				• Expensive controller
				• At constant power operation due to breakdown operation
PMSM	5	1.5	2 (approx.)	• Better efficiency
				• Compact size
				• Lesser weight
				• Demagnetisation issue
				• Costlier
SRM	4	1	High	• Less cost
				• Torque ripple is high
				• more acoustic noise
				• Suffers from mechanical losses
BLDC	3.5	1	1.8	• High operating speed
				• Maintenance free
				• High reliable
				• High costly
				• Rugged mechanical strength

straightforward monitoring system compared to AC motors. Again, contrasted to DC motor drives, there are several significant benefits of using AC motors, such as increased efficiency through less motor frictional loss, fewer maintenance requirements, robustness, and maximum power density.

Motors preferred for EV applications are induction motor (IM), permanent magnet (PM), switched reluctance motor (SRM) and brushless DC motor (BLDC). Though challenging, evaluating various versions of these machines is non-etheless a task. IM has a simplified construction, requires minimal, is less costly, and has better overloading performance than PM-based motors (Hannan et al., 2018). On the other hand, PM motors outperform IM in terms of effectiveness and portability. Its tiny size, high power densities, and efficiency make it superior to IM (Barkas et al., 2020).

However, its torque decreases with increasing speed when subjected to a load. Therefore, it can only be used to a certain extent. As the torque changes, there is an audible noise produced. Compared to the other types of motors discussed, the permanent magnet synchronous motor (PMSM) stands out well. It operates across a wide range of speeds, is extremely powerful and efficient, causes no harmonic distortion, and is simple to operate (Sun et al., 2019a). However, the cost of PMSM-based drives exceeds that of both BLDC and IM-based systems. The switched reluctance motor (SRM) has several benefits over the IM and PMSM, including a magnet-free and sturdy rotor design that enables incredible velocities and is highly reliable by construction. Ripple torque reduction is among the most important and challenging SRM design elements to handle whenever it relates to vehicle applications. The SRMs for significantly higher torque in EV with reduced ripple torque, disturbance, and auditory concerns (Lan et al., 2021). The performance comparison of different motors used for EV applications is given in Table 1.

3 Requirements of battery for EVs

Electric vehicles (EVs) charge their batteries, super capacitors, fuel cells, or internal combustion engine (ICE) to power internal electrical and electronic load functions (Chan and Chau, 1997; Amjadi and Williamson, 2010a; Naghizadeh and Williamson, 2013; OnarKobayashi and Khaligh, 2013; Cabezuelo et al., 2017). The automobile cannot be powered in fuel mode by the fuel cell's electricity. Consequently, the unidirectional boost converter boosts it (Jafri and Gupta, 2016). Several electrical and technological loads are placed on the car, enhancing its opulent characteristics and convenience.

A power converter supplies energy to specific electrical loads requiring higher AC voltage, such as air conditioners and automatic headlights. A DC motor-fed mirror and driving seat adjustments receive electricity from a battery or fuel cell through a DC-DC

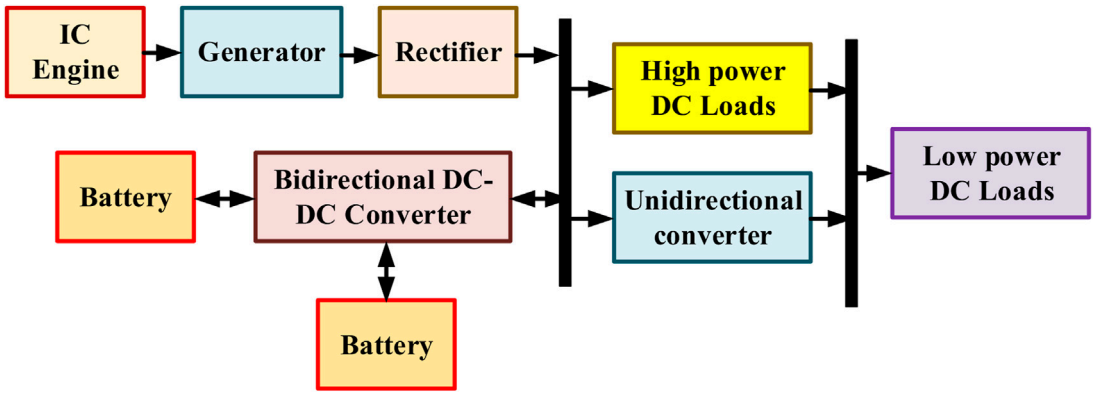

FIGURE 1
Block diagram of battery with the power converter.

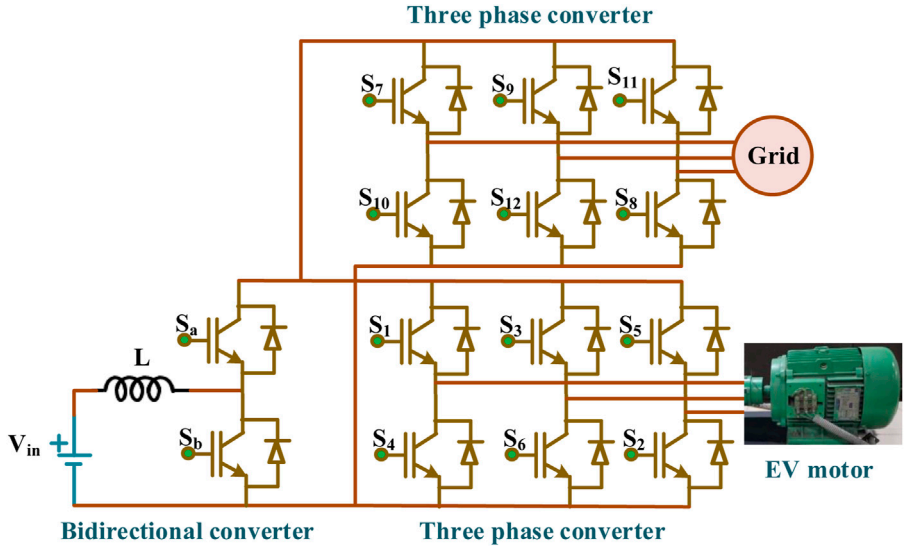

FIGURE 2
Overview of EV system with power electronic interface.

converter, which requires various voltage levels. The projection lamp needs 42 V, and the internal lighting needs 12 V to operate. Low voltage is required to function electronics components such as sensors, telecommunication networks, and tachometers. As the electrical/electronic load on the car rises, separate voltage output feeds are required, which are not achievable with a unified battery. The effectiveness of a vehicle powered by a single charge decreases as the quantity of DC-DC converters grows with rising diverse rating loads. The combination automotive system uses two forms of design (AdamsKlobodu and Apio, 2018). The other is a solitary, ICE- or fuel-cell-powered vehicle system (36 V). A different type is an ICE, or fuel cell, that uses two batteries (14 V and 42 V).

Figure 1 illustrates the block diagram of the battery with the power converter. This scheme uses a dual battery to deliver power to low-voltage electrical equipment (Cabezuelo et al., 2017). 12 V and 36 V batteries are used for low and mid-voltage applications. Nevertheless, for the driving and high voltage applications, the 36 V from the battery is raised to 42 V. Overview of the EV system with the power electronic interface is illustrated in Figure 2. The voltage from the grid/generator charges the battery through the rectifier and DC-DC converter (Elnozahy and Salama, 2014), (Yong et al., 2015). The bidirectional DC-DC converter boosts the battery voltage and feeds to high-voltage DC loads. Then it is inverted using a three-phase inverter to get variable voltage and frequency supply for feeding to motors. Modern electric vehicles can recharge batteries using the energy lost during braking and de-acceleration. During that mode, the converter acts as a rectifier and the battery charges with the

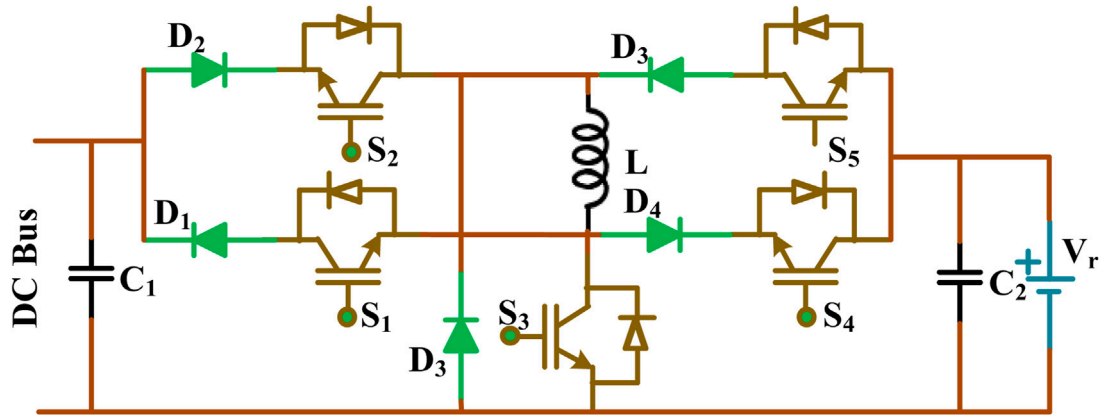

FIGURE 3
Bidirectional DC-DC converter.

TABLE 2 Modes of the operation.

Switches/modes	Source to Load		Load to source	
	Buck	Boost	Buck	Boost
S_1	Control	ON	OFF	OFF
S_2	OFF	OFF	ON	ON
S_3	OFF	OFF	Control	ON
S_4	ON	ON	OFF	OFF
S_5	OFF	Control	OFF	Control

bidirectional converter (Amjadi and Williamson, 2010a), (Chung et al., 2000; Di Napoli et al., 2002; KhanAhmedHusain et al., 2015; Lulhe and Date, 2015; Choubey and Lopes, 2017).

In the current EV system, the converter act as an inverter at the normal operating condition and a rectifier during the braking period. The controller fixes the operating mode upon the operation of the motor and produces the triggering pulses for the converter. The produced signal decides the operation of the converter, either in rectifier or inverter mode. The controller maintains the state of the charge (SOC) of the battery by monitoring it continuously. DC-DC converter regulates the output voltage by comparing the actual battery voltage with the reference voltage set by the user. Thus, the closed system maintains the battery voltage and speed of the motor.

4 Power converters for EV applications

The power converter plays a vital role in EV applications. As discussed in the previous section, Bi-directional DC-DC converters with boost and buck modes are preferred. In boost mode, the input voltage is boosted and fed to the motor, whereas the generated voltage from the motor during regenerative braking is bucked and fed to the battery. One of the well-known bidirectional DC-DC converter is illustrated in Figure 3, and the modes of operation are included in Table 2 (OnarKobayashi and Khaligh, 2013). The converter can operate in buck and boost modes upon selecting the proper switching pattern. Besides the basic topologies, several bi-directional converters are developed with single/multi-input, single/multistage and non-isolated multiphase converters.

In (Amjadi and Williamson, 2010b), Authors have developed a novel single-input bi-directional buck-boost converter, as shown in Figure 4A. The developed topology can be operated in both buck and boost modes by selecting the proper switching pattern. The topology includes two controlled switches and three passive elements. In this topology, the output current ripple is high, which may damage the battery and discontinuous operation in boost mode results in the increased size of the filter capacitor. Emadi proposed a modified buck-boost converter with an anti-parallel diode as shown in Figure 4B (Emadi, 2005). The diode connected in parallel with the power switches decreases the voltage stress across the switches, increasing system efficiency. The circuit diagram of the H-bridge converter is shown in Figure 4C. They maintain the SOC as the desired value and charge the battery during the regenerative braking (Waffler and Kolar, 2009; WuLuShi and Xing, 2012; Choubey and Lopes, 2017; Bharathidasan et al., 2022). This topology results in more semiconductor switches. The circuit diagram of DC-DC CUK and SEPIC with Luo converter is illustrated in Figures 4D, E, respectively (Amjadi and Williamson, 2010a). The developed topology can buck and boost the output voltage, and a bidirectional current flow is also possible. The input and output current ripple is minimum. But the output current is discontinuous in the Luo converter, which requires a bulky output capacitor. Elements in non-isolated single-input converters are summarised in Table 3.

The multiple-input fed bidirectional converter and single-input converters are developed for EV applications. The circuit diagram of the developed topology is illustrated in Figure 5. The input fed to the converter may be a battery, super capacitor or fuel cell in which battery-operated EV yield better response when compared with others (KhanAhmedHusain et al., 2015). A DC bus is maintained using a buck-boost converter with the battery and ultra-capacitor, as shown in Figure 5A. As two sources are used, voltage control is essential to maintain the value and to avoid circulating currents. A DC-DC converter with multiple sources is illustrated in Figure 5B

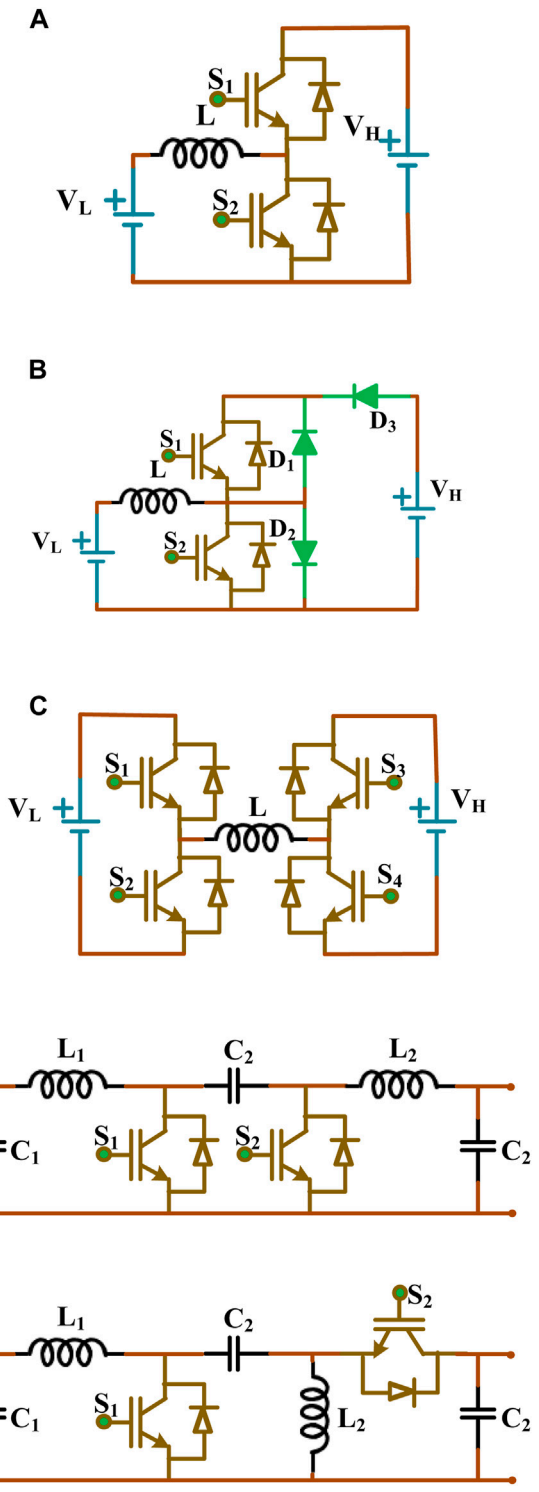

FIGURE 4
Non-isolated single input converters **(A)** buck-boost **(B)** modified buck-boost **(C)** H-bridge **(D)** CUK **(E)** SEPIC with Luo.

(Khaligh, 2008). The converter can handle multiple different sources that possess different VI characteristics. Figure 5C illustrates the cascaded bidirectional converter for fuel cell-operated EVs. The converter can boost the input voltage with high gain (Marchesoni and Vacca, 2007). The prime disadvantage of this topology is that DC link voltage should be maintained more significant than the sum of source voltage to avoid circulating current. They possess higher efficiency if the sources are connected in the same direction. Figure 5D shows the circuit diagram of the multi-level power electronic converter (Di Napoli et al., 2002; Onwuchekwa and Kwasinski, 2011; Dusmez, 2012). The converters can operate buck and boost modes to maintain the DC bus voltage constant. Elements in non-isolated multiple-input converters are summarised in Table 4.

Figure 6 depicts the non-isolated multiphase DC-DC converters used for electric vehicle applications. Figure 6A depicts the circuit diagram of interleaved boost three-phase converter (Khaligh and Li, 2010)- (YangGuanZhangJiang and Huang, 2018). The interleaved converter minimizes the input-output current ripples, significantly improving over the traditional bidirectional DC-DC converter. When there are multiple phases, the current ripple will decrease. Still ultimately, this will result in a fall in efficiency due to the increased number of passive and active elements required for each phase. Figure 6B illustrates the several structures in an interleaved converter (Ni et al., 2012). As the number of stages grows, the input/output filter gets smaller. This structure includes more active and passive elements than Figure 6A.

Figure 7 depicts electric vehicles' various switched capacitor (SC) circuit configurations. Figure 7A depicts the circuit diagram of SC converter (Amjadi and Williamson, 2010a), (Ni et al., 2012), (Chung et al., 2000). The SC structure possesses the capabilities of buck, boost, and buck-boost power flow operation in either direction. The topology supports both mode A (buck operation) and mode B (boost operation) of operation. Mode-efficiency A's of the illustrated topology is 85%, whereas mode-efficiency B's is 80%. Figure 7B, C demonstrate quasi-resonant converter of single-level and two-level topologies (Lee and Chiu, 2005). By utilizing an SC structure and a single inductor, the topology helps to alleviate the issue of current stress. The converter can achieve soft switching with the assistance of L and C, which decreases the losses. As a result, the MOSFET semiconductor device being switched ON and OFF in a condition with zero current, the EMI issue is significantly mitigated. The efficacy of the topology is 93%. Higher voltage conversion ratios require more SC stages. Table 5 lists the summary of various converter topologies for EV applications.

5 Charging communication technologies

Dynamic wireless charging necessitates a distinct communication network with an exceptionally low delay and high dependability to enable effective connection with the fast charging arrangement through the car's on-road capabilities (Abboud et al., 2016). The ability of the communications network is an essential factor that is determined by the amount of data that has to be sent and is reliant on this factor. Methods of good communication, whereby a network connection is built between the charging station and EV, are necessary to accomplish and control efficient synchronization of EVs on the internet of electric cars. It has been the impetus for developing 5G V2X innovation, which builds upon existing LTE, LTE-advanced (LTE-A), and LTE C-V2X networks. It also solves certification

TABLE 3 Elements in non-isolated single-input converters.

Ref. no	Converter topology	Active switch	Diode	Inductor	Capacitor
Amjadi and Williamson, (2010b)	Buck-boost	2	-	1	-
Emadi, (2005)	Modified buck-boost	2	3	1	-
Choubey and Lopes, (2017)	H-bridge	4	-	1	-
Amjadi and Williamson, (2010a)	CUK	2	-	2	3
Amjadi and Williamson, (2010a)	SEPIC with Luo	2	-	2	3

requirements such as super reliability, better portability, lower energy consumption, and more extensive density interconnections (Dai et al., 2018). Millimetre-wave (mmWave) technology is used to investigate the massive multiple-input multiple-output (MMIMO) technique (Busari et al., 2019). Several communication technologies, such as mmWave, D2D, MMIMO, and software-defined networks (SDN), are used for communications (Chen et al., 2017; Ahmed et al., 2019; Dagdougui et al., 2019; Zhang et al., 2020).

Static synchronization is concerned chiefly with task scheduling of driven automobiles at access points or in commercial parking areas (Zhang et al., 2020). Consequently, the vehicle's manoeuvrability is disregarded. The coordination that takes mobility into account considers not only the packages that need to be delivered but also where they need to be sent, how far they need to go, and how much energy they need before they get charged (Wang et al., 2019). Assessed is the best battery charging plan that may be used for EBs within a BSS (You et al., 2016). Several approaches to charging synchronization and routing management have been discussed in the research that has been published. The most current developments in 802.11bd and NR V2X standards have been analyzed (Kosmanos et al., 2018), (Naik et al., 2019). The United States National Institute of Standards and Technology (NIST) created a cyber-security structure that offers businesses recommendations on avoiding, detecting, and preventing cybersecurity risks. Recent years have seen a rapid increase in the purchase of electric vehicles, even though the overall cost of owning an EV is more than owning an internal combustion engine version of the same vehicle type (Forocoches Electricos, 2017).

DSRC's dependability quickly crumbles in highly congested systems due to severe network problems in inter-cluster communication (Framework Convention on Climate Change, 2015). Consequently, problems with quasi-dynamic charger synchronization develop, particularly in situations where electric vehicles benefit from high vehicle concentrations to increase their efficient charging duration and enhance the amount of electricity collected. Standards committee recommendation for IEEE 802.11bd, the problems of interference and non-line of sight (NLOS) functioning that plague DSRC based on IEEE 802.11p are addressed in the DSRC technique known as DSRC. To improve channel estimates with the rapidly changing channels seen in a moving vehicle, the latest revision of IEEE 802.11bd includes a new feature called midambles, which function similarly to opening paragraphs but are put amid the frame (Forocoches Electricos, 2017). In addition, unlike IEEE 802.11p, IEEE 802.11bd allows for many packet forwarding to ensure a steady connection. On the other hand, the physical layer delay also referred to as issues that limit inside the wireless medium, is shorter for IEEE 802.11bd than for IEEE 802.11p.

6 Conductive charging technologies

The electricity is transferred to an electric vehicle by conductive charging by a direct copper connection between the grid system and the EV. This charging technique is very reliable and has a high-efficiency level. There are two main types of conductive charging infrastructure: on-boarding and off-boarding. Slow charging is often performed using onboard charging infrastructures, wherein the charger facilities and battery storage system are housed within the electric vehicle's chassis. On the other hand, off-board charging infrastructures are made to charge electric cars quickly. Parking garages, shopping malls, hospitals, universities, and interstates are familiar places to find off-board charging infrastructures. Electrified automobiles use a conductive charging method, such as the Tesla Roadster, Nissan Leaf, and Chevrolet Volt. Figure 8 displays on-board and off-board charging facilities. The Society of Automatic Engineers (SAE) has established various charging levels for electric vehicles, outlined in Table 6.

As previously established, power quality measurements for EV chargers are crucial. One such indication is the total harmonic distortion (THD), which quantifies the amount of harmonic distortion delivered into the AC input by the charger (PF). For recharging electric vehicles, (Bai and Lukic, 2013), presents a 12-pulse rectifier and two buck-boost converters. To lessen the input current's harmonics, the virtual impedance injection technique is explained. Improved input power factor and 3.34 percent total harmonic distortion of the input line current are the results of this modification. The authors propose (Rivera et al., 2015; Rivera and Wu, 2017) that a bipolar dc structure be formed at the output of a grid-tied neutral point-clamped converter in order to charge electric vehicles. Because of its bidirectional energy conversion capabilities, it is well suited for use in linking electric vehicle power to the utility grid. Under balanced load conditions, the THD was found to be 5.8 percent, whereas under unbalanced load conditions, it was found to be 7.3 percent.

The development of the two-stage, bidirectional dc rapid charging facilities in MATLAB/Simulink (Arancibia and Strunz, 2012; Reed et al., 2012; Gjelaj et al., 2017). On the other hand, the efficacy of the chargers in addressing the problems with the power quality is not present. The two-stage energy conversion procedure is proposed to facilitate the integration of a flywheel energy storage

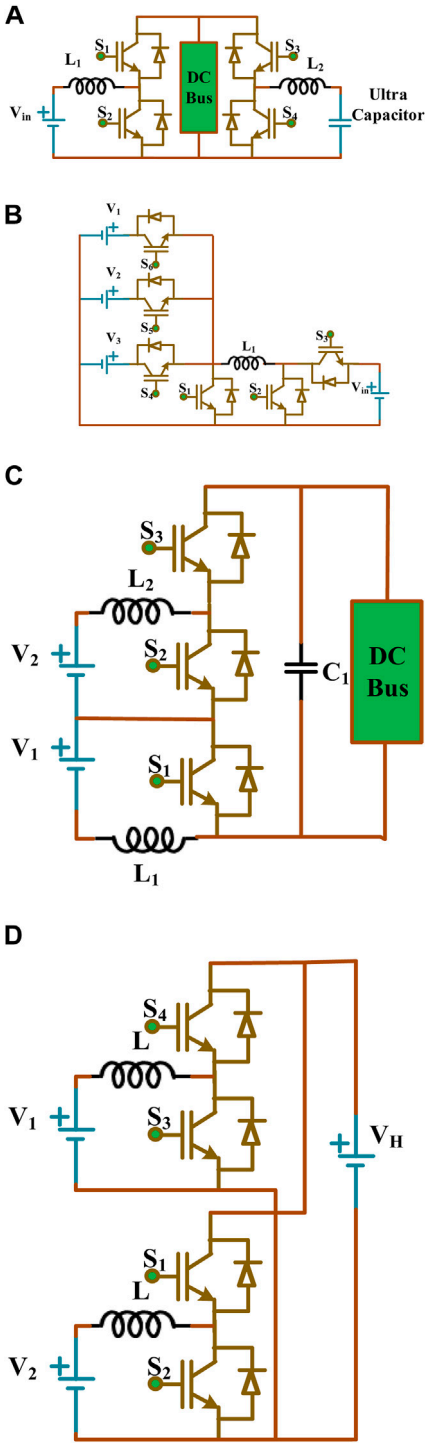

FIGURE 5
Non-isolated multi-input converters **(A)** buck-boost **(B)** DC-DC **(C)** cascaded **(D)** multi-level.

system with a charging system for electric vehicles (Sun et al., 2016). On the other hand, none of the power-quality concerns raised by the suggested charging scheme is addressed. Several distinct designs for EV chargers are explored, each involving low-frequency or high-frequency (LF or HF) transformers for electrical isolation (Aggeler et al., 2010). For charging electric vehicles during peak demand on the electric grid, a two-stage, bidirectional charging structure is considered together with a dynamic load control approach (Ahmadi et al., 2015).

For electric vehicle charging stations, Bai. et al. have proposed ac-to-dc converters with 6, 12, or 18 pulses and the difficulty of constructing the necessary specialized transformers to get that many pulses (Bai et al., 2010). The THD in the input line current for a 12-pulse converter is 11.5%. A dc-active power filter (dc-APF) circuit is developed using a 12-pulse rectifier for recharging electric vehicles (Bai and Lukic, 2011). When looking at the power quality of the input line current, the stated findings were highly promising. However, a significant heating issue is introduced by high-frequency switching in dc-APF to transform the input current into a sinusoidal waveform. In (Joy et al., 2013), it is detailed how a two-step, two-way charging setup for electric vehicles may work. High-frequency switching is a part of this design. However, it doesn't appear appropriate for a charging setup for electric vehicles that requires a lot of energy (in the MW range).

A bidirectional, multilayer cascaded converter with a medium switching frequency of 2880 Hz is proposed (Crosier et al., 2012) for use in EV charging stations. The authors propose a two-stage charging process for EVs. Because the dc/dc converter provides isolation in this charger, the isolation transformer may be smaller (Vasiladiotis et al., 2012), (Prakash et al., 2022). The switching frequency of this design is 10 kHz, and the circuit uses thirteen DC-DC converters linked in parallel. It is proposed to build a high-power bidirectional EV charger using a matrix converter and two inverters (Waltrich et al., 2012). On the other hand, this design uses many power electronics switches operating at high frequencies.

Slow charging uses a typical 120 V AC single-phase outlet with a 15 A–20 A current capability. One end of a typical electric socket is NEMA5-15R/20R, while the other is a standard SAEJ1772 connection. This level's power consumption ranges between 1.4 and 1.9 kW, depending on the current drawn from the grid. Typically, it takes 8–16 h to charge the battery altogether (Introduction, 2014). The price range for facilities at this degree of charge ranges from $500 to $880 (Morrow, 2008).

The semi-fast charging technique is typically implemented in private and public institutions, including hospitals, universities, and retail malls. Private equipment utilizes 1 ϕ 230 V_{AC} plug with a 40 A current size, whereas public facilities utilize a three-phase 400 V_{AC} output having an 80 A existing size (Bai and Lukic, 2013). This charging level uses SAEJ1772 (Plug-in electric vehicle, 2013). This charge level has a power rating of 7.7–25.6 kW, and it typically takes 4–8 h to fully charge the battery of an electric vehicle (Introduction, 2014). Costs associated with semi-charging construction are significant, anywhere between $2150 and $2300 on average (Morrow, 2008).

Public and private charging stations alike must adhere to the rapid charging requirement. This charging protocol mimics ICE fueling stations that use fossil fuels. The longest time an EV may spend charging at this rate is 10–15 min, at which point it will have been charged to 80% of its theoretical capacity. Only up to 80% of the entire capacity of an EV battery is considered to be charged using this approach (Braunl, 2012). Charging the remaining 20% needs charging at constant voltage, which takes time. A three-phase power supply between 208 V and 600 V alternating current and a maximum current capacity of 200 A is required for this level of

TABLE 4 Elements in non-isolated multiple-input converters.

Ref. no	Converter topology	Active switch	Inductor	Capacitor
KhanAhmedHusain et al. (2015)	Buck-boost	4	2	1
Khaligh, (2008)	DC-DC	6	1	-
Marchesoni and Vacca, (2007)	Cascaded	3	2	1
Onwuchekwa and Kwasinski, (2011)	Multi-level	4	2	-

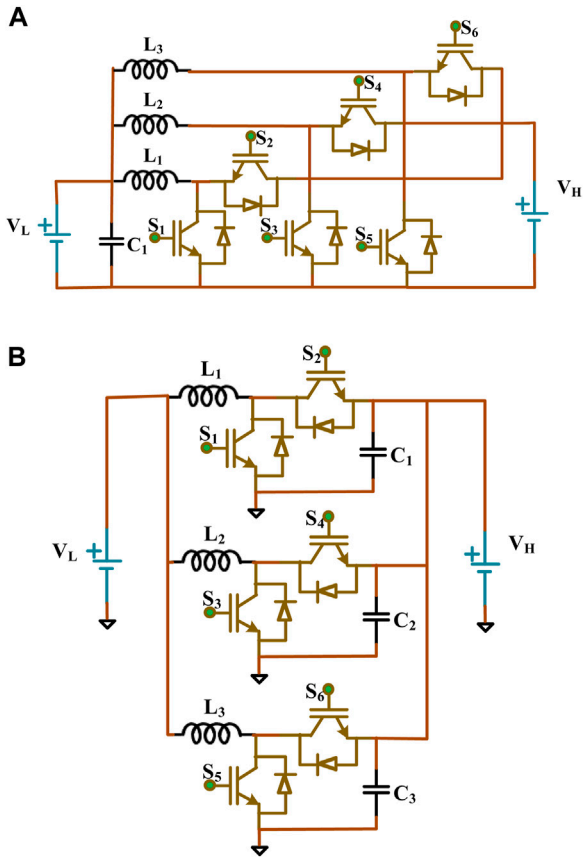

FIGURE 6
Non-isolated multiphase converters **(A)** interleaved boost **(B)** sixteen phase.

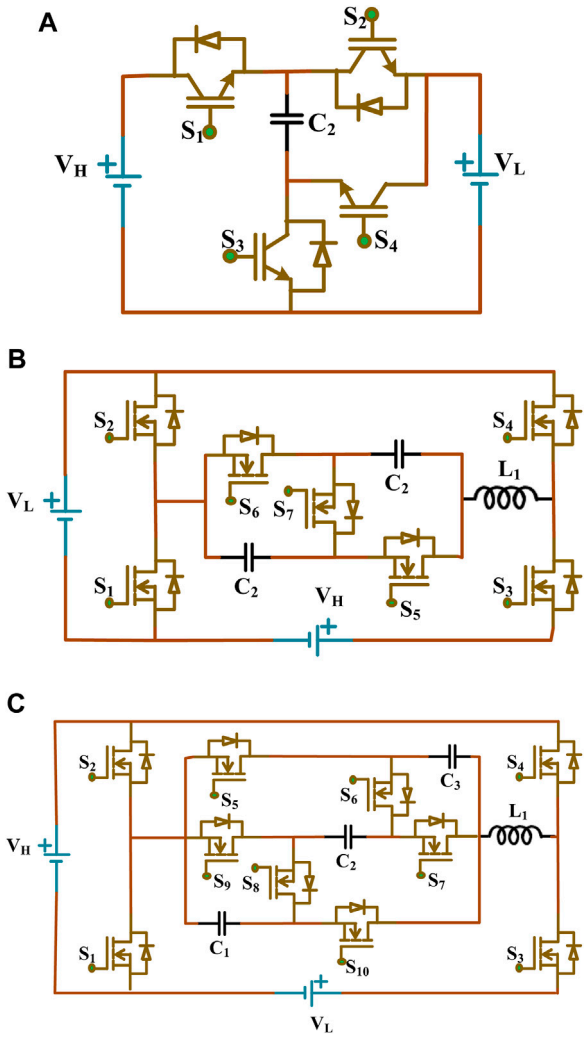

FIGURE 7
Switched capacitor converters **(A)** bidirectional **(B)** single-level quasi-resonant **(C)** two-level quasi-resonant.

charging. Due to the lighter weight of an electric vehicle, batteries with a higher energy density may be employed (Rawson, 1999). Only the SAE J1772 Combo standard and the Japanese CHAdeMO benchmark are in use for rapid charging of electric vehicles throughout the world (Braunl, 2012). It is estimated that between $50,000 and $160,000 would be needed to set up rapid charging infrastructure.

7 Inductive charging technologies

The concept of mutual induction is utilised by inductive charging infrastructures to carry power from the utility grid to the EV. There is no physical connection between the EV and the utility grid. In addition, unlike conductive chargers, they might not need bulky isolation transformers for further safety (Bryan et al., 2015). While convenient, inductive charging infrastructure suffers inefficiency because of power transmission coil mismatch. Infrastructure for inductive charging is categorized into three groups. a) Static inductive charging, b) Dynamic inductive

TABLE 5 Summary of various converter topologies for EV applications.

Ref	Topologies	Objective	Voltage gain	Advantage	Disadvantage	Remarks
MartmezMartinez-Salamero et al. (1998)	CUK	• To improve the efficiency	$\frac{-D}{1-D}$	• Minimum inductor ripple • Continuous conduction operation	• Unstable • underdamped oscillation	• Ripple free output
Zhang et al. (2019)	Switched Capacitor Bidirectional Converter	• To increase the gain and efficiency	$\frac{2}{1-D}$	• Minimum cost • Compact size • Reduced output current	• High current ripple • Less efficiency for wide range input variations	• Efficacy is greater than 90%
Babaei et al. (2019)	Couple Inductor Bidirectional Converter	• To minimize the inductor and load current ripple	$\frac{2+N-D}{1-D}$	• Reduced sie • Low cost • Minimum ripple	• Output voltage ripple	• Improved efficiency due to enhanced coupling coefficient
Wu et al. (2019)	Quasi-Z-source Converter	• To get high voltage gain with common ground	$\frac{1+D}{1-D}$	• Minimize the switching stress • Reduced components	• Discontinuous source current • High voltage stress in capacitor	• Efficiency varies between 88.17% and 96.44%
Mirzaei et al. (2010)	Multi-Device Interleaved Bidirectional Converter	• To minimize the circuit components • To minimize the inductor and load current ripple • Better transient response	$\frac{1}{1-ND}$	• Minimum current stress • Easy design • Compact size	• Complex to control • More sensitive to the duty cycle	• Minimum electromagnetic interference • Reduced voltage and current ripple
Lee et al. (2019)	Flyback Converter	• To handle the wide variations in input voltage	$\frac{ND}{1-D}$	• Primary and secondary is isolated • Regulated multiple outputs	• High current ripple • More losses • Requires bulky filters • Converter is unstable	• Leakage inductance is within allowable limits
Lee and Chiu (2005)	Zero Voltage Switching Converter	• To develop the adaptive load controller • To achieve zero voltage switching • To reduce the circuit components	$\frac{2}{\pi}D(1-D)$	• Minimum electromagnetic interference • Minimum switching losses • A clamping circuit is not required	• Requires bulky capacitor • Less fault-tolerant capacity	• Wide range of soft switching
D- Duty ratio, N- Turns ratio						

charging, and c) Quasi- Dynamic inductive charging (Miller et al., 2015; Chen et al., 2016; Li et al., 2016; Vu et al., 2018).

Figure 9 depicts the concept of electric car static and roadbed inductive charging. For static charging, one coil is located in an external charger, while the other is built within the electric vehicle itself. Both coils need to be positioned correctly for maximum efficiency (Khaligh and Dusmez, 2012). As the EV drives, inductive charging pads embedded in the road surface top up its battery. With this charging, dedicated charging tracks are set out on the roadways, most commonly on highways. As a result, the electric vehicle's driving range is improved, and the size of the battery pack is decreased (Budhia and Covic, 2487). In

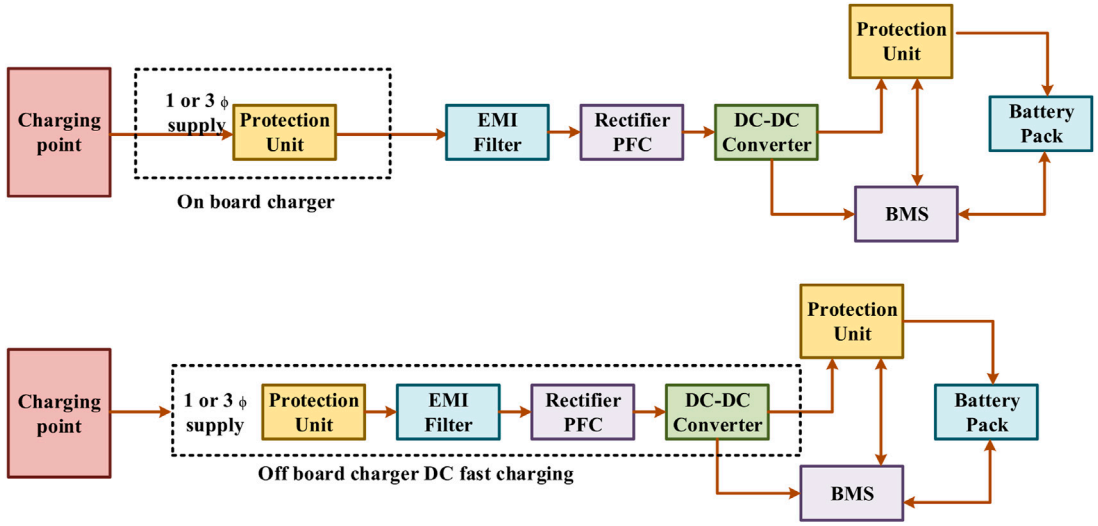

FIGURE 8
On-board and off-board charging facilities.

TABLE 6 Various charging levels for electric vehicles.

Charging	Slow	Semi fast	Fast
Typical voltage (V)	120	240	208–600
Typical current (A)	16	80	400
Duration (h)	4–12	2–6	0.2–1
Type	On-board	On-board	Off-board
Location	Home	Home/Commercial	Commercial

the process known as quasi-dynamic inductive charging, the electric vehicle obtains a charge anytime it comes to a halt for a brief period, such as at a traffic light (Honda accord plug-in hybrid, 2017).

8 Electric vehicle market

Five primary research issues are evaluated and correspond to the findings from the existing studies: 1) estimating the percentage of plug-in electric vehicles (PEVs) sold in a specific region; 2) identifying the inputs, 3) promising policies, 4) expected outcomes effects of widespread PEV market penetration 5) a new modelling strategy. Research questions about the above scenario are displayed in Figure 10 in chronological order, beginning with the most recently published. Most publications seek to identify the factors contributing to spreading PEVs in a specific market or geographic region. Research questions about adopting a new technique, with an emphasis on the methodology instead of the predicted market proliferation, often play a role. In recent years, interest has been raised in determining crucial policies and the influence of the PEV market's spread (for instance, on the power grid). The maturation of modelling tools or the need to incorporate policy initiatives to expedite markets may account for the current emphasis on examining effects and strategies.

A straightforward classification is utilized when comparing models because the above-mentioned categories do not adequately describe most models. To show model detail, they are categorized by aggregation: 1) Very consolidated models that analyze simply the vehicle stock; 2) more differentiated methods that predict vehicle sales and distinguish several markets or customer categories; 3) the most differentiated techniques model people and integrate them for vehicle sales. Every analysis has found that by 2020, PHEVs will have captured a more significant percentage of the market than BEVs. This indicates the state of affairs in the world's largest auto markets, where PHEVs are selling at a premium due to their more excellent range. But as battery prices continue to drop, more powerful batteries could be within reach (Nykvist and Nilsson, 2015)- (Gallagher et al., 2014). In light of this shift, several analyses (Gnann, 2015; Liu and Lin, 2017) suggest that between 2030 and 2050, BEVs will have a more significant percentage of the market than PHEVs. However, this shift in finest has to coincide with either consumers' diminishing range concern or the capacity to recharge during long-distance travels.

As seen below, only two scenarios that project 2050 seriously consider the problems mentioned above. Both Pasaoglu et al. and Shepherd et al. omit to charge infrastructure from their model. Therefore, it cannot account for "restricted range variables" (Pasaoglu et al., 2016)- (Shepherd et al., 2012). Both studies have strong models, but these two elements will determine how quickly the BEV industry expands in the future. The emphasis on the most cost-effective option for the foreseeable is one criticism levelled at the fourth research out to 2050 (Yabe et al., 2012). It may be inaccurate to focus on price until 2050, as virtually all research

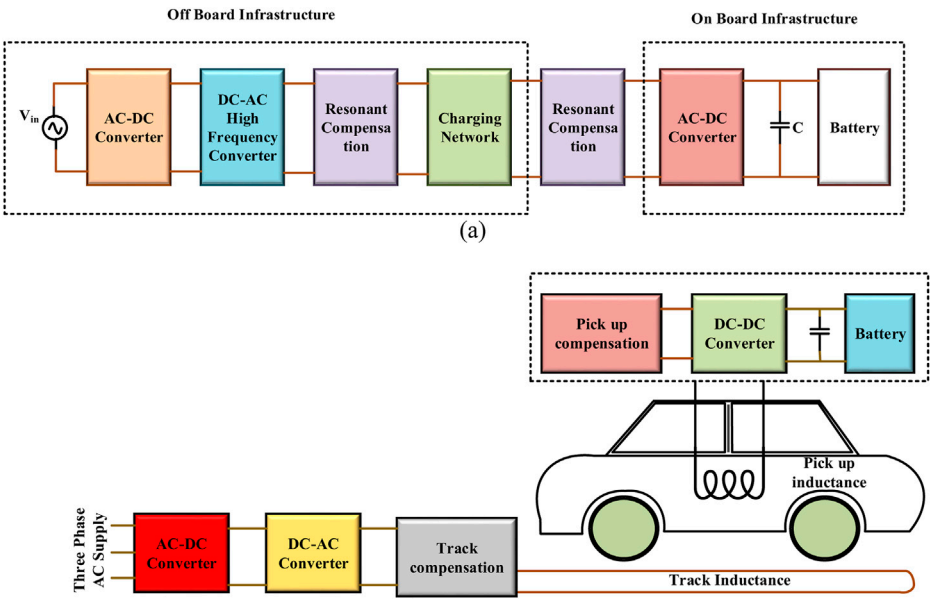

FIGURE 9
Electric car static and roadbed inductive charging.

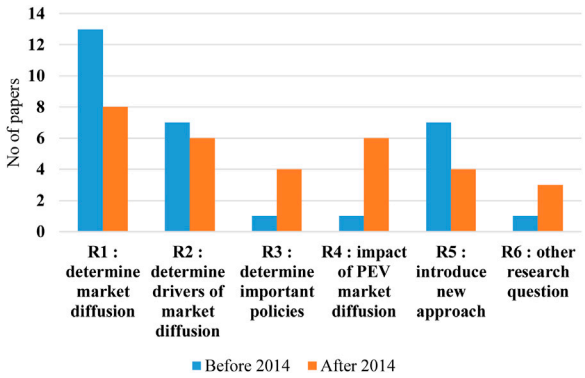

FIGURE 10
Research questions about PEV.

on PEV market spread includes combating climate change and reducing GHG emissions as critical drivers of PEV industry diffusion. Although BEV market shares may rise significantly in the long run, projections beyond the next few years are highly dependent on several factors. Four groupings of qualities are included in the simulations to look at the specific characteristics more carefully and to develop recommendations for future modelling attempts: Considerations unique to PEVs include, but are not limited to, the following: (1) elements directly connected to the purchasing decision; (2) vehicle qualities that are included in the models; (3) characteristics to define customer traits; and (4) aspects specifically relevant for PEVs.

9 Repercussions of electric vehicle charging infrastructure

This section investigates the various electric grid components affected by EV chargers and discusses efforts to mitigate these effects.

9.1 Effects of utilizing alternative energy sources

Renewable energy sources are challenging for utilities to incorporate because of their intermittent nature. Still, advances in PEC and high-energy-density storage systems have resolved the problem of inconsistent power and made it less complicated to link EV chargers (Yabe et al., 2012). Wind energy resources that are linked to the utility grid are susceptible to being dispatched. It regulates the flow of energy when an electric vehicle is being charged or discharged. This approach is provided as an alternative. A similar strategy may be found in (FraukeHeider, 2009), which details an investigation into how to keep the power constant at the feeder while linking it to both electric vehicles and renewable sources (El Chehaly et al., 2009). The successful functioning of an isolated grid is demonstrated (Pecas Lopes et al., 2009). About 59% of the total utility grid generation capacity is accounted for by wind energy in this analysis, which involves 323 EVs (Xin et al., 2009; Bedir et al., 2010; Gamboa et al., 2010). Research demonstrating the viability of solar-powered EV charging is reported (Xin et al., 2009). This research accounts for the typical 40-mile commute that North Americans do in their SUVs daily.

9.2 Effects on the reliability of the power system

Since many power grids are already suffering on the edge of instability, a stability study must be performed before increasing the electric vehicles. The EV demand is must be modelled as a continuous power demand, with the resistive load to identify the utility grid's reliability. The research concludes that modelling Electric vehicle charging stations as the constant resistance load since the integral to maintaining is higher, when the EV is treated as a continuous power load (Das and Aliprantis, 2008). Also, modelling EV chargers as the steady impedance load is preferable with artificial intelligence algorithms because the firm reliance is increased (Jingyu et al., 2010). The stability of the IEEE-24 bus system is analyzed with the aid of EVs employed as a power source (V2G mode), and it is observed that the usage of EVs as a power source assists in increasing the system's stability. So, it follows that EVs are better for the utility system's stability while they're the power supply, but they can cause significant problems when they're the load (El Chehaly et al., 2009).

9.3 Effects of source harmonics on the power system

The power electronics that are a part of the electric vehicle charger directly influence the harmonics that are produced by the charger. An elementary investigation has revealed that the design of the electric vehicle chargers is to blame for introducing a particular harmonic order into the electrical grid. The electric grid has demonstrated that it typically incorporates odd-order harmonics into its operations (Bradley, 1981). An investigation describes the design of electric vehicle chargers, which include regulated rectifiers and flattening line current inductors (Orr et al., 1982). Adjusting the control angle of the rectifiers demonstrates that it is possible to diminish or even eliminate the presence of the third harmonic in the line current. The architecture of the chargers at each of the 26 distinct charging stations is analyzed. The results demonstrate that the total harmonic distortion (THD) in the line current can range from 10% to 100%, depending on the architecture of the charger (Karady et al., 1994). Harmonics are introduced into the line current by electric vehicle chargers that are available for purchase, and the range of these harmonics is around 7%–99%. In addition, the results of this study indicate that it is possible to incorporate approximately fifty percent of EVs into the system without going over the voltage harmonics limit if capacitor banks are utilized. However, if capacitor banks are not utilized, it is only possible to incorporate thirty percent of EVs into the system (Staats, 1997). The dropout voltage of a transformer occurs primarily due to a decrease in its original current. It mainly relies on the amount of time the charging process is allowed to take. The total harmonic distortion of the line current has a quadratic relationship with the transformer's lifespan. The lifespan of a transformer is not significantly impacted when the THD is maintained between 25 and 30 percent of the total output.

9.4 Effects of losses on the power system

When electric vehicle load is incorporated into the existing distribution system, the losses in the power system are another significant factor to consider. During the off-peak charging time, the system experiences losses of around 40% when there is a penetration of EV load of 62%. It has also been demonstrated that the system's losses are proportional to the amount of EV demand and are not contingent on the geographic location (Bradley, 1981). The higher the load from electric vehicles, the higher the current in the system. As a result, the system sufferes from higher the losses across all utility system components, including transmission lines, transformers, etc.

10 Birds view

Initially, a motor provides propulsion in EVs rather than a mechanical or hydraulic shaft. Increasing the efficiency of a hybrid electric vehicle (HEV) can be achieved by carefully considering the optimal ICE and fuel cell or battery combination. PECs play an essential role in maximizing efficiency in the battery or fuel mode by making the right power converter choice. The input power and load requirements determine which converters are used. The number of components, control methods, and EMI effects all affect how well PEC works.

A critical factor in EVs' reliability is their electrical system's longevity. Consistently regulating the charging and discharging level with the aid of the voltage controller boosts the battery's lifetime. Semiconductor components determine how long PEC will last. The converter must be able to withstand excessive vibration and temperature. The difficulties arise when deciding on a converter that meets all your needs simultaneously: it must be very efficient, highly rigid, cheap, and compact.

One of the most challenging trends in today's vehicle system is the need for rapid and highly effective industrial motion control. High performance in EVs is accomplished by combining the PE method with digital signal processing.

Modern electric vehicles place greater emphasis on passenger conveniences. There is a specific minimum voltage requirement for each use case. Whether a multistage or multioutput DC-DC converter, it is a power source for DC appliances with varying ratings. The 3-ϕ inverter supplies energy to the AC load.

Traction motor health monitoring is as important as power conversion and propulsion regulation for spotting problems like faulty stators, rotors, and bearings. There is a need for robust actuators in advanced EVs to power systems like ABS and airbags. Future EVs may have better built-in safety measures thanks to the PEC with the DSP method.

The expense of the electrical system in EVs is defined by the number of inverter units and components used. The higher the luxury load, the more PEC is required to propel the car. The difficulty is reducing the vehicle's price by deciding on fewer power conversion units to handle more opulent loads.

11 Conclusion

The purpose of this concise study is to supply readers with more recent data on studies involving EV adoption with RE systems. Electric vehicles (EVs) have a lot of potentials to be the future of transportation and a saviour from the looming tragedies caused by global warming. The following recommendations are also provided for resolving the issues highlighted by this analysis.

- V2G is a prospective method that allows idle or parked EVs to act as dispersed resources that may store or generate power at suitable periods, allowing the grid and EV to interchange power.
- Improving asymmetric estimating methods and variable extraction approaches is essential for their usefulness in practice, accountability, and computing performance.
- To ensure long-term profitability and environmentally benign transportation, governments in practically all industrialized countries continually create new legislation to promote EV use.
- Battery life may be improved for many uses by developing estimation algorithms.
- The pace at which the EV battery may be charged or discharged is slow because of the power constraint of traditional silicon devices.
- The demand for faster and more powerful charging methods and more advanced inductive charging technology will increase as battery capacities increase.

This study addresses the currently available and commonly used architectures with back-to-back ac/dc/dc converters, constructions with multiple dc ports and a shared ac connection, and constructions without an isolation transformer. These buildings may be further classified by whether they use conductive or inductive charging. In addition, several forms of energy used by these structures are extensively outlined. This study delves deeply into several essential topics, including their adverse effects on renewable energy resources, the stability of the utility grid, the supply and demand balance, the assets of the utility system, voltage and phase, the current harmonics of the utility grid, and the utility system losses.

Data availability statement

The raw data supporting the conclusions of this article will be made available by the authors, without undue reservation.

Author contributions

All authors listed have made a substantial, direct, and intellectual contribution to the work and approved it for publication.

Funding

This work was supported in part by the Government of India, Department of Science and Technology (DST), Research Board (SERB) Core Research, under Grant CRG/2020/004073.

Conflict of interest

The authors declare that the research was conducted in the absence of any commercial or financial relationships that could be construed as a potential conflict of interest.

Publisher's note

All claims expressed in this article are solely those of the authors and do not necessarily represent those of their affiliated organizations, or those of the publisher, the editors and the reviewers. Any product that may be evaluated in this article, or claim that may be made by its manufacturer, is not guaranteed or endorsed by the publisher.

References

Abboud, K., Omar, H. A., and Zhuang, W. (2016). Interworking of DSRC and cellular network technologies for V2X communications: A survey. *IEEE Trans. Veh. Technol.* 65 (12), 9457–9470. doi:10.1109/tvt.2016.2591558

AdamsKlobodu, S. E. K. M., and Apio, A. (2018). Renewable and non-renewable energy, regime type and economic growth. *Renew. Energy* 125, 755–767. doi:10.1016/j.renene.2018.02.135

Aggeler, D., Canales, F., Zelaya-De La Parra, H., Coccia, A., Butcher, N., and Apeldoorn, O. (2010). "Ultra-fast DC-charge infrastructures for EV-mobility and future smart grids," in 2010 IEEE PES innovative smart grid technologies conference europe (ISGT europe) (gothenberg: IEEE), 1e8.

Ahmadi, M., Mithulananthan, N., and Sharma, R. (2015). "Dynamic load control at a bidirectional DC fast charging station for PEVs in weak AC grids," in 2015 IEEE PES asia-pacific power and energy engineering conference (APPEEC) (brisbane: IEEE), 1e5. QLD.

Ahmed, I., Ismail, M. H., and Hassan, M. S. (2019). Video transmission using device-to-device communications: A survey. *IEEE Access* 7, 131019–131038. doi:10.1109/access.2019.2940595

Amjadi, Z., and Williamson, S. S. (2010). A novel control technique for a switched-capacitor-converter-based hybrid electric vehicle energy storage system. *IEEE Transactions Industrial Electron.* 57 (3), 926–934. doi:10.1109/tie.2009.2032196

Amjadi, Z., and Williamson, S. S. (2010). Power-electronics-based solutions for plug-in hybrid electric vehicle energy storage and management systems. *IEEE Trans. Industrial Electron.* 57 (2), 608–616. doi:10.1109/tie.2009.2032195

Arancibia, A., and Strunz, K. (2012). "Modeling of an electric vehicle charging station for fast DC charging," in 2012 IEEE international electric vehicle conference (greenville, SC, 1e6.

Babaei, E., Zarbil, M. S., and Asl, E. S. (2019). A developed structure for DC–DC quasi-Z-source converter with high voltage gain and high reliability. *J. Circuits Syst. Comput.* 28 (01), 1950012. doi:10.1142/s0218126619500129

Bai, S., and Lukic, S. (2011). "Design considerations for DC charging station for plug-in vehicles," in 2011 IEEE vehicle power and propulsion conference (chicago, IL, 1e6.

Bai, S., and Lukic, S. M. (2013). Unified active filter and energy storage system for an MW electric vehicle charging station. *IEEE Trans. Power Electron Dec* 28, 579312–585803. doi:10.1109/tpel.2013.2245146

Bai, S., Yu, D., and Lukic, S. (2010). "Optimum design of an EV/PHEV charging station with DC bus and storage system," in 2010 IEEE energy conversion CongreCss and exposition (atlanta, ga, 1178e84.

Barkas, D. A., Ioannidis, G. C., Psomopoulos, C. S., Kaminaris, S. D., and Vokas, G. A. (2020). Brushed dc motor drives for industrial and automobile applications with emphasis on control techniques: A comprehensive review. *Electronics* 9, 887. doi:10.3390/electronics9060887

Bedir, A., Ozpineci, B., and Christian, J. E. (2010). "The impact of plug-in hybrid electric vehicle interaction with energy storage and solar panels on the grid for a zero energy house," in Transmission and Distribution Conference and exposition (IEEE PES), 1e6.

Bharathidasan, M., Indragandhi, V., Suresh, V., Jasiński, M., and Leonowicz, Z. (2022). A review on electric vehicle: Technologies, energy trading, and cyber security. *Energy Rep.* 8 (2022), 9662–9685. doi:10.1016/j.egyr.2022.07.145

Bradley, W. G. (1981). "Electric vehicle battery charger-power line interface," in Southeastcon '81. Conference proceedings, 430e4.

Braunl, T. EVChargingStandards. 2012. p. 1e5.

Bryan, E., Sid-Ahmed, M., and Narayan, C. (2015). A comparative study ofpower supply architectures in wireless EV charging systems. *IEEE Trans. Power Electron* 30 (11), 6408–6422. doi:10.1109/tpel.2015.2440256

Budhia, J. B. M., and Covic, G. "A new IPT magnetic coupler for electric vehicle charging systems," in IECON proceedings (industrial electronics conference), 2487e2492.

Busari, S. A., Khan, M. A., Huq, K. M. S., Mumtaz, S., and Rodriguez, J. (2019). Millimetre-wave massive MIMO for cellular vehicle to infrastructure communication. *IET Intell. Transp. Syst.* 13 (6), 983–990. doi:10.1049/iet-its.2018.5492

Cabezuelo, D., Andreu, J., de Alegría, I. M., and Robles, S. (2017). "Powertrain systems of electric, hybrid and fuel-cell vehicles: State of the technology," in Proceedings of the IEEE 26th international symposium on industrial electronics (ISIE) (IEEE), 1445–1450.

Chan, C. C., and Chau, K. T. (1997). An overview of power electronics in electric vehicles. *IEEE Trans. Industrial Electron.* 44 (1), 3–13. doi:10.1109/41.557493

Chen, Nan, Wang, M., Zhang, N., Shen, X. S., and Zhao, D. (2017). SDN-based framework for the PEV integrated smart grid. *IEEE Netw.* 31 (2), 14–21. doi:10.1109/mnet.2017.1600212nm

Chen, Z. S. W., Liu, C., Lee, C., and Shan, Z. (2016). Cost-effectiveness comparison of coupler designs of wireless power transfer for electric vehicle dynamic charging. *Energies* 9 (11), 906. doi:10.3390/en9110906

Choubey, A., and Lopes, L. A. C. (2017). "A tri-state 4-switch bi-directional converter for in-terfacing supercapacitors to DC micro-grids," in Proceedings of the IEEE 8th international symposium on power electronics for distributed generation systems (PEDG) (IEEE), 1–6.

Chung, H. S. H., Chow, W. C., Hui, S. Y. R., and Lee, S. T. S. (2000). Development of a switched-capacitor DC-DC converter with bidirectional power flow. *IEEE Trans. Circuits Syst. I Fundam. Theory Appl.* 47 (9), 1383–1389. doi:10.1109/81.883334

Crosier, R., Wang, S., and Jamshidi, M. A. (2012). "4800-V grid-connected electric vehicle charging station that provides STACOM-APF functions with a bi-directional, multi-level, cascaded converter," in 2012 twenty-seventh annual IEEE applied power electronics conference and exposition (APEC) (orlando, FL: IEEE), 1508e15.

Dagdougui, H., Ouammi, A., and Dessaint, L. A. (2019). Peak load reduction in a smart building integrating microgrid and V2B-based demand response scheme. *IEEE Syst. J.* 13 (3), 3274–3282. doi:10.1109/jsyst.2018.2880864

Dai, P., Liu, K., Wu, X., Liao, Y., Lee, V. C. S., and Son, S. H. (2018). Bandwidth efficiency and service adaptiveness oriented data dissemination in heterogeneous vehicular networks. *IEEE Trans. Veh. Technol.* 67 (7), 6585–6598. doi:10.1109/tvt.2018.2812742

Das, T., and Aliprantis, D. C. (2008). "Small-signal stability analysis of power system integrated with PHEVs," in Energy 2030 conference (IEEE), 1e4. ENERGY 2008.

Di Napoli, A., Crescimbini, F., Solero, L., Caricchi, F., and Capponi, F. G. (2002). "Multiple-input DC-DC power con-verter for power-flow management in hybrid vehicles," in Proceedings of the confer- ence record of the IEEE industry applications conference (IEEE), 1578–1585. 37th IAS Annual Meeting (Cat. No.02CH37344), 3.

Dusmez, S. (2012). Comprehensive topological analysis of conductive and inductive charging solutions for plug-in electric vehicles. *IEEE Trans. Veh. Technol.* 61 (8), 3475–3489. doi:10.1109/tvt.2012.2213104

El Chehaly, M., Saadeh, O., Martinez, C., and Joos, G. (2009). "Advantages and applications of vehicle to grid mode of operation in plug-in hybrid electric vehicles," in Electrical power & energy conference (EPEC) (IEEE), 1e6.

Elnozahy, M. S., and Salama, M. (2014). A comprehensive study of the impacts of PHEVs on residential distribution networks. *IEEE Trans. Sustain. Energy* 5, 332–342. doi:10.1109/tste.2013.2284573

Elsayad, N., Moradisizkoohi, H., and Mohammed, O. A. (2020). A new hybrid structure of a bidirectional DC-DC converter with high conversion ratios for electric vehicles. *IEEE Trans. Veh. Technol.* 69 (1), 194–206. doi:10.1109/tvt.2019.2950282

Emadi, A. (2005). *Handbook of automotive power electronics and motor drives*. 1st ed. New York: Taylor & Francis.

Fardahar, S. M., and Sabahi, M. (2020). New expandable switched capacitor/switched-inductor high-voltage conversion ratio bidirectional DC–DC converter. *IEEE Trans. Power Electron.* 35 (3), 2480–2487. doi:10.1109/tpel.2019.2932325

Fontaras, G., Grigoratos, T., Savvidis, D., Anagnostopoulos, K., Luz, R., Rexeis, M., et al. (2016). An experimental evaluation of the methodology proposed for the monitoring and certification of CO_2 emissions from heavy-duty vehicles in Europe. *Energy* 102, 354–364. doi:10.1016/j.energy.2016.02.076

Forocoches Electricos (2017). *Los incentivos Al coche eléctrico están creciendo en toda europa*. Europe: Forocoches Electricos.

Framework Convention on Climate Change (2015). *Adoption of the paris agreement*. Paris: UNFCCC.

FraukeHeider, M. B. (2009). "Vehicle to grid: Realization of power management for the optimal integration of plug-in electric vehicles into the grid," in EVS24 international battery, hybridand fuel cell electric vehicle symposium stavanger (Norway, 1e12.

Gallagher, K. G., Goebel, S., Greszler, T., Mathias, M., Oelerich, W., Eroglu, D., et al. (2014). Quantifying the promise of lithium–air batteries for electric vehicles. *Energy Environ. Sci.* 7 (5), 1555–1563. doi:10.1039/c3ee43870h

Gamboa, G., Hamilton, C., Kerley, R., Elmes, S., Arias, A., Shen, J., et al. (2010). "Control strategy of a multi-port, grid connected, direct-DC PV charging station for plug-in electric vehicles," in Energy ConversionCongress and exposition (ECCE) (IEEE), 1173e7.

Gjelaj, M., Træholt, C., Hashemi, S., and Andersen, P. B. (2017). "Optimal design of DC fastcharging stations for EVs in low voltage grids," in 2017 IEEE transportation electrification conference and expo (ITEC) (chicago, IL, 684e9.

Gnann, T. (2015). *Market diffusion of plug-in electric vehicles and their charging infrastructure*. Germany: Fraunhofer-Verlag Stuttgart.

Gryparis, E., Papadopoulos, P., Leligou, H. C., and Psomopoulos, C. S. (2020). Electricity demand and carbon emission in power generation under high penetration of electric vehicles. A European Union perspective. *A Eur. Union perspect. Energy Rep.* 6 (6), 475–486. doi:10.1016/j.egyr.2020.09.025

Hannan, M. A., Ali, J. A., Mohamed, A., and Hussain, A. (2018). Optimization techniques to enhance the performance of induction motor drives: A review. *Renew. Sustain. Energy Rev.* 81, 1611–1626. doi:10.1016/j.rser.2017.05.240

Honda accord plug-in hybrid 2017 "'Honda accord plug-in hybrid PluginCars.com.'".

Introduction, A. (2014). *Installation guide for electric vehicle supply equipment*. Massachusetts: Evse.

Islam, F., and Pota, H. (2013). Plug-in-hybrid electric vehicles park as virtual DVR. *Electron. Lett.* 49, 211–213. doi:10.1049/el.2012.3569

Islam, F. R., and Cirrincione, M. (2016). Vehicle to grid system to design a centre node virtual unified power flow controller. *Electron. Lett.* 52, 1330–1332. doi:10.1049/el.2016.0534

Jafri, N. H., and Gupta, S. (2016). "An overview of fuel cells application in transportation," in Proceedings of the IEEE transportation electrification conference and expo (IEEE).

Jingyu, Y., Xu, G., Qian, H., and Xu, Y. (2010). "Battery fast charging strategy based on model predictive control," in Vehicular technology conference fall (VTC 2010-fall) (IEEE 72nd), 1e8.

Joy, T., Thirugnanam, K., and Kumar, P. (2013). "A multi-point Bidirectional Contactless Charging System in a charging station suitable for EVs and PHEVs applications," in 2013 annual IEEE India conference (INDICON) (Mumbai: IEEE), 1e6.

Kanamarlapudi, V. R. K., Wangenfei, B., Kandasamy, N. K., and So, P. L. (2018). A new ZVS full-bridge DC–DC converter for battery charging with reduced losses over full-load range. *IEEE Trans. Ind. Appl.* 54 (1), 571–579. doi:10.1109/tia.2017.2756031

Karady, G. G., Berisha, S. H., Blake, T., and Hobbs, R. (1994). "Power quality problems at electric vehicle's charging station," in *International congress & exposition, february 1994, session.* (MI, USA: International Congress & Exposition Detroit).

Khalid, M. R., Alam, M. S., Sarwar, A., and Jamil Asghar, M. S. (2019). A Comprehensive review on electric vehicles charging infrastructures and their impacts on power-quality of the utility grid. *eTransportation* 1, 100006. doi:10.1016/j.etran.2019.100006

Khaligh, A. (2008). "A multiple-input dc-dc positive buck-boost converter topology," in Proceedings of the Twenty-third annual IEEE applied power electronics conference and exposition (IEEE), 1522–1526. doi:10.1109/APEC.2008.4522926

Khaligh, A., and Dusmez, S. (2012). Comprehensive topological analysis of conductive and inductive charging solutions for plug-in electric vehicles. *IEEE Trans. Veh. Technol.* 61 (8), 3475e3489.

Khaligh, A., and Li, Z. (2010). Battery, ultracapacitor, fuel cell, and hybrid energy storage systems for electric, hybrid electric, fuel cell, and plug-in hybrid electric vehicles: State of the Art. *IEEE Trans. Veh. Technol.* 59 (6), 2806–2814. doi:10.1109/tvt.2010.2047877

KhanAhmedHusain, M. A. A. I., Sozer, Y., and Badawy, M. (2015). Performance analysis of bidirectional DC–DC converters for electric vehicles. *IEEE Trans. Industry Appl.* 51 (4), 3442–3452. doi:10.1109/tia.2015.2388862

Kosmanos, D., Maglaras, L. A., Mavrovouniotis, M., Moschoyiannis, S., Argyriou, A., Maglaras, A., et al. (2018). Route optimization of electric vehicles based on dynamic wireless charging. *IEEE Access* 6, 42551–42565. doi:10.1109/access.2018.2847765

Kumar, L., and Jain, S. (2014). Electric propulsion system for electric vehicular technology: A review. *Renew. Sustain. Energy Rev.* 29, 924–940. doi:10.1016/j.rser.2013.09.014

Lan, Y., Benomar, Y., Deepak, K., Aksoz, A., Baghdadi, M. E., Bostanci, E., et al. (2021). Switched reluctance motors and drive systems for electric vehicle powertrains: State of the art analysis and future trends. *Energies* 14 (8), 2079. doi:10.3390/en14082079

Lee, W-S., Kim, J. H., Lee, J-Y., and Lee, I-O. (2019). Design of an isolated DC/DC topology with high efficiency of over 97% for EV fast chargers. *IEEE Trans. Veh. Technol.* 68 (12), 11725–11737. doi:10.1109/tvt.2019.2949080

Lee, Y. S., and Chiu, Y. Y. (2005). Zero-current-switching switched-capacitor bidirectional DC-DC converter. *Proc. IEE Electr. power Appl.* 152, 1525–1530. doi:10.1049/ip-epa:20050138

Li, Z. C. S., Liu, Z., Zhao, H., Zhu, L., Shuai, C., and Chen, Z. (2016). Wireless power transfer by electric field resonance and its application in dynamic charging. '" *IEEE Trans. Ind. Electron* 63, 6602–6612. doi:10.1109/tie.2016.2577625

Liu, C., and Lin, Z. (2017). How uncertain is the future of electric vehicle market: Results from Monte Carlo simulations using a nested logit model. *Int. J. Sustain Transp.* 11 (4), 237–247. doi:10.1080/15568318.2016.1248583

Lulhe, A. M., and Date, T. N. (2015). "A technology review paper for drives used in electrical vehicle (EV) & hybrid electrical vehicles (HEV)," in proceedings of the international conference on control, instrumentation, communication and computational technologies (ICCI- CCT) (IEEE), 632–636.

Mamun, K. A., Islam, F. R., Haque, R., Chand, A. A., Prasad, K. A., Goundar, K. K., et al. (2022). Systematic modeling and analysis of on-board vehicle integrated novel hybrid renewable energy system with storage for electric vehicles. *Sustainability* 14 (5), 2538. doi:10.3390/su14052538

Marchesoni, M., and Vacca, C. (2007). New DC-DC converter for energy storage system interfacing in fuel cell hybrid electric vehicles. *IEEE Trans. Power Electron.* 22 (1), 301–308. doi:10.1109/tpel.2006.886650

MartmezMartinez-Salamero, L., Calvente, J., Giral, R., Poveda, A., and Fossas, E. (1998). Analysis of a bidirectional coupled-inductor cuk converter operating in sliding mode. *IEEE Trans. Circuits Syst. Fundam. Theory Appl.* 45, 355–363. doi:10.1109/81.669058

Miller, O. C. O. J. M., Jones, P., Li, J. M., and Onar, O. C. (2015). ORNL experience and challenges facing dynamic wireless power charging of EV's. '" *IEEE Circuits Syst. Mag.* 15 (2), 40–53. doi:10.1109/mcas.2015.2419012

Mirzaei, A., Jusoh, A., Salam, Z., Adib, E., and Farzanehfard, H. (2010). "Analysis and design of a high efficiency bidirectional DC-DC converter for battery and ultracapacitor applications," in 2010 IEEE International Conference on Power and Energy (IEEE), 803–806.

Momete, D. C. (2018). Analysis of the potential of clean energy deployment in the European Union. *IEEE Access* 6, 54811–54822. doi:10.1109/access.2018.2872786

Morrow, K. U. S. (2008). *Department of energy vehicle technologies program e advanced vehicle testing activity plug-in hybrid electric vehicle charging infrastructure review*, 58517.

Naghizadeh, N., and Williamson, S. S. (2013). "A comprehensive review of power electronic converter topologies to integrate photovoltaics (PV), AC grid, and electric vehicles," in Proceedings of the IEEE Transportation Electrification Conference and Expo (ITEC) (IEEE), 1–6.

Naik, G., Choudhury, B., and Park, J-M. (2019). IEEE 802.11bd & 5G NR V2X: Evolution of radio access technologies for V2X communications. *IEEE Access* 7, 70169–70184. doi:10.1109/access.2019.2919489

Najafi, A., Jasinski, M., et al. (2021a). "A distributed framework for optimal operation of EV aggregators problem," in 2021 IEEE International Conference on Environment and Electrical Engineering and 2021 IEEE Industrial and Commercial Power Systems Europe, EEEIC/I & CPS Europe (IEEE), 1–5.

Navarro, G., Francisco, J., Yebra, L. J., and MedinaGomezGimenez-Fernandez, F. J. A. (2020). DC-DC linearized converter model for faster simulation of lightweight urban electric vehicles. *IEEE Access* 8, 85380–85394. doi:10.1109/access.2020.2992558

Ni, L., Patterson, D. J., and Hudgins, J. L. (2012). High power current sensorless bidirectional 16-phase interleaved DC-DC converter for hybrid vehicle application. *IEEE Trans. Power Electron.* 27 (3), 1141–1151. doi:10.1109/tpel.2011.2165297

Nunes, P., Figueiredo, R., and Brito, M. C. (2016). The use of parking lots to solar-charge electric vehicles. *Renew. Sustain. Energy Rev.* 66, 679–693. doi:10.1016/j.rser.2016.08.015

Nykvist, B., and Nilsson, M. (2015). Rapidly falling costs of battery packs for electric vehicles. *Nat. Clim. Change* 5 (4), 329–332. doi:10.1038/nclimate2564

OnarKobayashi, O. C. J., and Khaligh, A. (2013). A fully directional universal power electronic interface for EV, HEV, and PHEV applications. *IEEE Trans. Power Electron.* 28 (12), 5489–5498. doi:10.1109/tpel.2012.2236106

Onwuchekwa, C. N., and Kwasinski, A. (2011). "Analysis of boundary control for a multi-ple-input DC-DC converter topology," in Proceedings of the 26th annual IEEE applied power electronics conference and exposition (APEC) (IEEE), 1232–1237.

Orr, J. A., Emanuel, A. E., and Pileggi, D. G. (1982). in Current harmonics, voltage distortion, and powers associated with battery chargers Part I: comparisons among different types of chargers, PAS-101. Power Apparatus and Systems (IEEE Transactions on), 2703e10.

Pasaoglu, G., Harrison, G., Jones, L., Hill, A., Beaudet, A., and Thiel, C. (2016). A system dynamics based market agent model simulating future powertrain technology transition: Scenarios in the EU light duty vehicle road transport sector. *Technol. Forecast Soc. Change* 104, 133–146. doi:10.1016/j.techfore.2015.11.028

Pecas Lopes, J. A., Rocha Almeida, P. M., and Soares, F. J. (2009). "Using vehicle-to-grid to maximize the integration of intermittent renewable energy resources in islanded electric grids," in Clean electrical Power,2009 international conference on (IEEE), 290e5.

Plug-in electric vehicle (2013). *Plug-in electric vehicle handbook for public charging station hosts*. Washington, D.C: U.S department of energy.

Prakash, K., Ali, M., Siddique, M. N. I., Chand, A. A., Kumar, N. M., Dong, D., et al. (2022). A review of battery energy storage systems for ancillary services in distribution grids: Current status, challenges and future directions. *Front. Energy Res.* 10, 971704. doi:10.3389/fenrg.2022.971704

Rawson, M. K. S. (1999). "Electric vehicle charging equipment design and health and safety codes," in *SAE technical paper 1999-01-2941*. doi:10.4271/1999-01-2941

Reed, G. F., Grainger, B. M., Sparacino, A. R., Kerestes, R. J., and Korytowski, M. J. (2012). *Advancements in medium voltage DC architecture development with applications for powering electric vehicle charging stations*. Cleveland, OH: IEEE Energytech, 1e8.

Rivera, S., and Wu, B. (2017). Electric vehicle charging station with an energy storage stage for split-DC bus voltage balancing. *IEEE Trans. Power Electron March* 32, 2376–2386. doi:10.1109/tpel.2016.2568039

Rivera, S., Wu, B., Kouro, S., Yaramasu, V., and Wang, J. (2015). Electric vehicle charging station using a neutral point clamped converter with bipolar DC bus. *IEEE Trans. Ind. Electron April.* 62, 1999–2009. doi:10.1109/tie.2014.2348937

Shakeri, M., Shayestegan, M., Reza, S. S., Yahya, I., Bais, B., Akhtaruzzaman, M., et al. (2018). Implementation of a novel home energy management system (HEMS) architecture with solar photovoltaic system as supplementary source. *Renew. Energy* 125, 108–120. doi:10.1016/j.renene.2018.01.114

Sharma, A., and Sharma, S. (2019). Review of power electronics in vehicle-to-grid systems. *J. Energy Storage* 21, 337–361. doi:10.1016/j.est.2018.11.022

Shepherd, S., Bonsall, P., and Harrison, G. (2012). Factors affecting future demand for electric vehicles: A model based study. *Transp. Policy* 20, 62–74. doi:10.1016/j.tranpol.2011.12.006

Staats, P. T. (1997). "The harmonic impact of electric vehicle battery charging," in *Faculty of the graduate school. vol. Doctor of Philosophy Austin* (Texas: The university of Texas), 195.

Sun, B., Dragi_cevi_c, T., Freijedo, F. D., Vasquez, J. C., and Guerrero, J. M. (2016). A control algorithm for electric vehicle fast charging stations equipped with flywheel energy storage systems. *IEEE Trans. Power Electron Sept.* 31, 6674–6685. doi:10.1109/tpel.2015.2500962

Sun, X., Shi, Z., Lei, G., Guo, Y., and Zhu, J. (2019a). Analysis and design optimization of a permanent magnet synchronous motor for a campus patrol electric vehicle. *IEEE Trans. Veh. Technol.* 68 (11), 10535–10544. doi:10.1109/tvt.2019.2939794

Vasiladiotis, M., Rufer, A., and B_eguin, A. (2012). "Modular converter architecture for medium voltage ultra fast EV charging stations: Global system considerations," in 2012 IEEE international electric vehicle conference (greenville, SC: IEEE), 1e7.

Verma, A., and Singh, B. (2019). Multi-objective reconfigurable three-phase off-board charger for EV. *IEEE Trans. Ind. Appl.* 55 (4), 4192–4203. doi:10.1109/tia.2019.2908950

Vu, V., Tran, D., and Choi, W. (2018). Implementation of the constant current and constant voltage charge of inductive power transfer systems with the double-sided LCC compensation topology for electric vehicle battery charge applications. *IEEE Trans. Power Electron Sept.* 33, 73989–77410. doi:10.1109/tpel.2017.2766605

Waffler, S., and Kolar, J. W. (2009). A novel low-loss modulation strategy for high-power bidirectional buck ${\bm +}$ boost converters. *IEEE Trans. Power Electron.* 24 (6), 1589–1599. doi:10.1109/tpel.2009.2015881

Waltrich, G., Duarte, J. L., and Hendrix, M. A. M. (2012). Multiport converter for fast charging of electrical vehicle battery. *IEEE Trans. Ind. Appl. Nov.-Dec.* 48, 2129–2139. doi:10.1109/tia.2012.2226694

Wang, Y., Su, Z., Xu, Q., Yang, T., and Zhang, N. (2019). A novel charging scheme for electric vehicles with smart communities in vehicular networks. *IEEE Trans. Veh. Technol.* 68 (9), 8487–8501. doi:10.1109/tvt.2019.2923851

Wu, J., Wu, Z., Wu, F., and Mao, X. (2017). A power balancing method of distributed generation and electric vehicle charging for minimizing operation cost of distribution systems with uncertainties. *Energy Sci. Eng.* 5 (3), 167–179. doi:10.1002/ese3.157

Wu, Q., Wang, M., Zhou, W., Wang, X., and Wang, Q. (2019). "One zero-voltage-switching voltage-fed three-phase push-pull DC/DC converter for electric vehicle applications," in 2019 IEEE Transportation Electrification Conference and Expo (ITEC. IEEE), 1–5.

WuLuShi, H. J. W., and Xing, Y. (2012). Nonisolated bidirectional DC–DC converters with negative-coupled inductor. *IEEE Trans. Power Electron.* 27 (5), 2231–2235. doi:10.1109/tpel.2011.2180540

Xin, L., Lopes, L. A. C., and Williamson, S. S. (2009). "Power & energy society general meetingPES '09," in On the suitability of plug-in hybrid electric vehicle (PHEV) charging infrastructures based on wind and solar energy (IEEE), 1e8.

Yabe, K., Shinoda, Y., Seki, T., Tanaka, H., and Akisawa, A. (2012). Market penetration speed and effects on CO_2 reduction of electric vehicles and plug-in hybrid electric vehicles in Japan. *Energy Policy* 45, 529–540. doi:10.1016/j.enpol.2012.02.068

YangGuanZhangJiang, Y. T. S. W., and Huang, W. (2018). More symmetric four-phase inverse coupled inductor for low current ripples & high-efficiency interleaved bidirec-tional buck/boost converter. *IEEE Trans. Power Electron.* 33 (3), 1952–1966. doi:10.1109/tpel.2017.2745686

Yong, J. Y., Ramachandaramurthy, V. K., Tan, K. M., and Mithulananthan, N. (2015). Bi-directional elec-tric vehicle fast charging station with novel reactive power compensation for voltage regulation. *Int. J. Electr. Power & Energy Syst.* 64, 300–310. doi:10.1016/j.ijepes.2014.07.025

You, P., Yang, Z., Zhang, Y., Low, S. H., and Sun, Y. (2016). Optimal charging schedule for a battery switching station serving electric buses. *IEEE Trans. Power Syst.* 31 (5), 3473–3483. doi:10.1109/tpwrs.2015.2487273

Yu, Y., Zhao, L., and Zhou, C. (2019). Influence of rotor-bearing coupling vibration on dynamic behavior of electric vehicle driven by in-wheel motor. *IEEE Access* 7, 63540–63549. doi:10.1109/access.2019.2916554

Zhang, J., Pei, Y., Shen, J., Wang, L., Ding, T., and Wang, S. (2020). Charging strategy unifying spatial-temporal coordination of electric vehicles. *IEEE Access* 8, 74853–74863. doi:10.1109/access.2020.2987607

Zhang, Yun, Liu, Q., Gao, Y., Li, J., and Sumner, M. (2019). Hybrid switched-capacitor/switched-quasi-Z-source bidirectional DC–DC converter with a wide voltage gain range for hybrid energy sources EVs. *IEEE Trans. Ind. Electron.* 66 (4), 2680–2690. doi:10.1109/tie.2018.2850020

frontiers | Frontiers in Energy Research

TYPE Original Research
PUBLISHED 15 February 2023
DOI 10.3389/fenrg.2023.1091298

OPEN ACCESS

EDITED BY
Meng Yen Shih,
Autonomous University of Campeche, Mexico

REVIEWED BY
Ravi Samikannu,
Botswana International University of Science and Technology, Botswana
Jianquan Zhu,
South China University of Technology, China

*CORRESPONDENCE
Zhixiong Liu,
zxliu@whu.edu.cn

SPECIALTY SECTION
This article was submitted to Smart Grids, a section of the journal Frontiers in Energy Research

RECEIVED 06 November 2022
ACCEPTED 03 February 2023
PUBLISHED 15 February 2023

CITATION
Xiong H, Li J, Li W, Jiang X, Xiang B and Liu Z (2023), Overheating fault alarming for compact insulated busways in buildings by gas sensing.
Front. Energy Res. 11:1091298.
doi: 10.3389/fenrg.2023.1091298

Overheating fault alarming for compact insulated busways in buildings by gas sensing

Hu Xiong[1], Jiayuan Li[1], Wenpei Li[1], Xiaoguang Jiang[1], Bin Xiang[1] and Zhixiong Liu[2]*

[1]Electric Power Research Institute of State Grid Hubei Electric Power Co, Ltd., Wuhan, China, [2]School of Electrical Engineering and Automation, Wuhan University, Wuhan, China

Addressing the overheating fault detection and alarming of insulated busways in buildings, a system based on sensing volatile gases generated by the thermal degradation of the busduct insulation layer was proposed. By monitoring the concentration of volatile gases in the environment, the overheating fault of the busducts can be found early. The thermal degradation process of the busway insulating layer is analyzed, and the pyrolysis characteristic gas at low temperature is studied. The experimental platform has been built, by which the relation between the concentration of volatile gases and temperature of the insulated layer has been studied. By testing, the concentration of volatile organic compounds (VOCs) is proposed as the basis for judging the overheating fault in the alarming system. With the collected samples for training and testing, the AdaBoost classifier is used to identify the overheating fault. Finally, the design of the overheating fault alarming system is given.

KEYWORDS

compact insulated busway, thermal degradation, overheating fault, AdaBoost, alarming

1 Introduction

The busway is an efficient high-current conductor and has become very popular in recent years, due to the fact that it can offer the predictable electrical and mechanical characteristics (Wood and McGoldrick, 1985; Rana et al., 2017). Compared with the cable, it has many advantages, such as large current capacity, small voltage drops, strong short-circuit load capacity, high safety, and reliability and it does not burn easily. It is also easy to maintain, with a beautiful appearance. Therefore, it is widely used in the power distribution network, especially in the power supply system of high-rise buildings.

Busway trunkings can be divided into two categories: the air insulated type and the compact insulated type. The busbars of the former are insulated by an air medium, and the latter is covered with an insulating layer. Nowadays, the AC compact insulated busduct trunkings are used in buildings commonly, which replace the traditional cables on a large scale. In the power supply system of buildings, the AC busducts are suitable for three-phase four-wire power supply and distribution system engineering and can work with frequencies of 50–60 Hz, rated voltage of 380 V, and rated current of 250–4000 A.

When the busway is working under overload current, its temperature will increase accordingly. Then, some parts of it, especially the joints, will be seriously overheated. The insulating layer of the busbar may be melted and deformed by high temperatures. Particularly, the aging of the bus insulation layer or the poor factory quality of the insulation layer will speed up this process. If the busway works in an overheated state

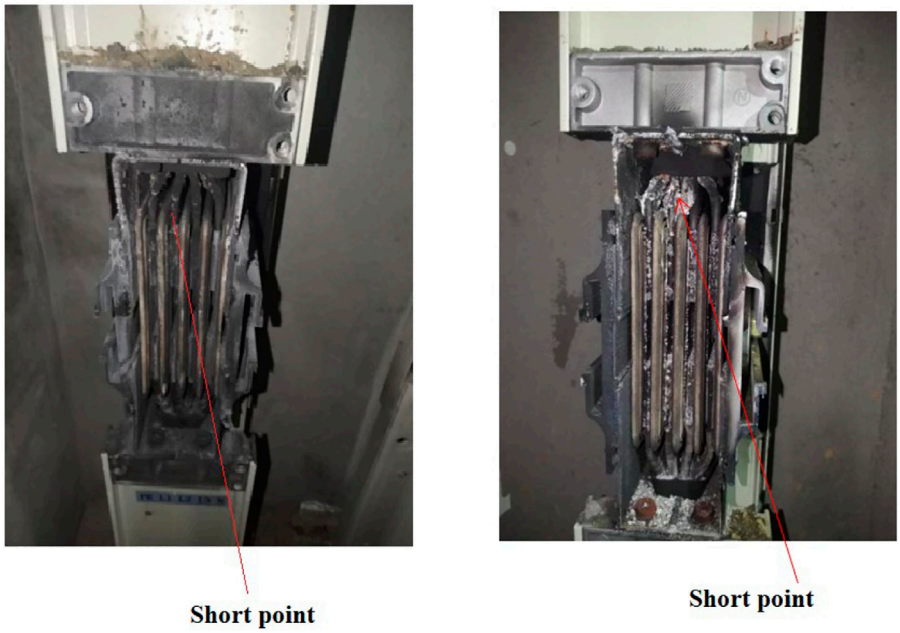

FIGURE 1
Fault busways with short circuit in buildings.

for a long time, its insulation layer will be physically damaged and the insulation performance will be reduced, which will result in the breakdown of the insulating layer and cause a short-circuit fault, which will cause fire or even explosion, as shown in Figure 1.

The short circuit caused by overheating will damage the electrical equipment, stop power supply of the building, and cause economic losses. The infrared imager can sense the surface temperature of electrical equipment, which is an effective way for monitoring overheating (Gao et al., 2021; Wang et al., 2021; Chen et al., 2022). During daily patrol inspection, the busduct can be inspected with an infrared imager. However, the working environment of the busway in buildings is relatively narrow, and the field vision of the camera is narrow. For achieving effective detection performance, we need to install many infrared cameras along the busduct trunkings, which is expensive.

Recently, some researchers proposed installing temperature sensors or thermo-couples inside the busduct to measure the inside temperature (Yun, 2013; Xu et al., 2019) and then used wireless or optical fiber communication to send data to the control device for analysis and alarm. However, the compact insulating busduct is a closed structure, its internal parts have been sealed and fixed, and the busbars in it are also wrapped by an insulation layer. If the sensors are installed in it, it will cause structural damage and affect the insulation and conductivity of the busduct. Therefore, it is not an appropriate choice to install temperature sensors inside the busduct.

Installing thermometers in the building wiring room to monitor the ambient temperature is also a choice. However, due to the closed structure of the busduct and the busbar which is wrapped by the insulated side, even the temperature of the busbar is very high, and the temperature rise of the busduct shell is not obvious. According to our testing, when the temperature of the busbar is as high as 130 °C, the busway is in a serious overheating state, but the external temperature of the compact insulated busway is only about 60 °C. Therefore, even if the busduct is overheated, the environmental temperature increase of the building wiring room is not significant. We also cannot get the ideal early warning effect only by monitoring the ambient temperature.

There are some similarities between the busway overheating fault warning study and fire warning study. Over the last decade, many early fire warning technologies have been studied (Fonollosa et al., 2018; Khan et al., 2022; Kuznetsov et al., 2022). Various elements such as image (including the inferred image), temperature, smoke, heat, and gases (CO, CO_2, etc.) are detected by multiple sensors and used for decision in fire alarm (Chen and Fu, 2012; Lin and Wang, 2017; Sarwar et al., 2018; Luo et al., 2019; Nakip et al., 2021; Wu et al., 2021; Dai et al., 2022; Kewon et al., 2022; Li et al., 2022). With the development of modern sensor technology, especially the application of high-sensitivity gas sensors in fire alarm systems, we can reduce the false alarms caused by other signal interference and get better accuracy than before. In these fire early warning systems, some machine learning algorithms are used such as Bayesian estimation (Chen and Fu, 2012), Fuzzy theory (Sarwar et al., 2018), Kalman filter (Lin and Wang, 2017), neural network, and deep learning (Kuznetsov et al., 2022) (Luo et al., 2019; Nakip et al., 2021; Wu et al., 2021; Dai et al., 2022; Kewon et al., 2022; Li et al., 2022).

Chen and Fu (2012) elaborated the logic relationship between the fire alarm and the physical–chemical characteristics generated in the process of fire burning and used the Bayesian network (BN) to analyze fire alarm systems. Sarwar et al. (2018) used a multi-sensor solution and presented an intelligent fire monitoring and warning system (FMWS) that is based on Fuzzy logic, which could send alert to the FMWS. Lin and Wang (2017) utilized the real-time sensor

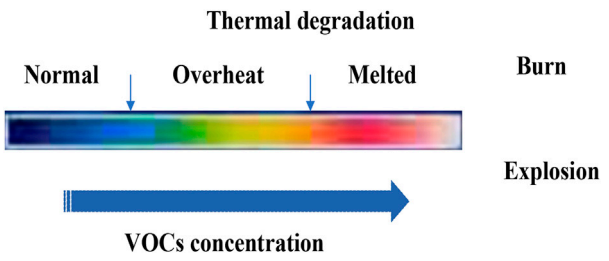

FIGURE 2
Thermal degradation process of the insulation layer.

data from thermocouple trees in each room and estimated the spread of building fire and forecasted smoke dispersion in real time by Kalman filter. Luo et al. (2019) proposed strategies to make the deep neural network (DNN) model smaller and improve its accuracy for detecting smoke from visual sensors. Nakip et al. (2021) used a recurrent trend predictive neural network for fire detecting based on fusion of multi-sensor readings. Kewon et al. (2022) designed a wireless fire prevention system that can detect and notify the fire risk by detecting the concentration of carbon dioxide (CO_2) near the gas stove. Wu et al. (2021) proposed an indoor fire early warning algorithm based on the back propagation (BP) neural network, which fused the data of temperature, smoke concentration, and carbon monoxide, and output the probability of fire occurrence. Li et al. (2022) proposed an indoor fire perception algorithm based on multi-sensor fusion. It extracted the sensor data features by an improved temporal convolutional network (TCN), and the fire classification was realized by the support vector machine (SVM) classifier. Dai et al. (2022) used Yolo v3 to obtain multi-size image information and proposed a flame detection algorithm that is more sensitive to small flames.

In these aforementioned studies, the fire can also be divided into three stages: no fire, smoke, and flame. The smoke stage means the initial fire stage in these studies, so it can provide the chance of taking protective measures to avoid the occurrence and expansion of the fire. However, in our study, the goal is to find the overheating fault of the busduct before it fired or smoked, which is different from the aforementioned fire warning studies.

At present, some studies focus on very early electrical fire detection (before combustion) under low temperature, which is described as follows.

Li (2014) observed the PVC insulation sheath releases gas substances, mainly including plasticizer DOP when the temperature rises to about 150 °C, which can be used as a judgment for early fire detection of PVC cables. Chen and Yi (2019) also analyzed the compositions of the vapors from PVC insulation at different temperatures, conducted gas sensing tests for the main component, and pointed out that DOP could be considered as the signature gas for early detection of PVC cable fires. Han et al. (2019) identified the major volatile species for overheated PVC cables and verified their potential as fire signatures with metal oxide gas sensors, which could effectively detect the cable overheating at an early stage. Nie et al. (2008) utilized chemical sensors for the application of detecting the vapors produced by electrical heating of wire insulation to provide alarm function.

Benes et al. (2004) studied the thermal degradation process in the range 200–340 °C of the PVC cable insulation sample, which is accompanied by the release of HCl, H_2O, CO_2, and benzene. McNeil et al. (1995) showed during the first stage of PVC thermal degradation between 200 and 360 °C, the main compositions are HCl and benzene and very little alkyl aromatic or condensed ring aromatic hydrocarbons. Babrauskas (2006) tracked the proximate cause of ignition involved with different mechanisms for the low-voltage PVC insulated electrotechnical products and pointed out that PVC required only approximately 160 °C for the material to become semiconducting during short-term exposure (around 10 h), while longer-term exposure (around 1 month) may cause failures at temperatures as low as 110 °C.

However, these aforementioned studies mainly focused on PVC cables. Addressing the detection of the overheating fault of compact insulated busducts in buildings, we proposed an overheating fault warning system based on the VOC sensor. VOCs usually refer to organic compounds which are volatile and can participate in atmospheric photochemical reactions. Usually, their boiling point is low and will cause harm to the environment. The basic principle of the proposed method is as follows.

There is an insulating layer which surrounded the busbar conductors in the busduct, and its component is PET (polyethylene terephthalate) film mixed with several different additives, which will be slowly pyrolyzed into gases of different compositions at high temperature. This thermal degradation process will be accelerated as the temperature increases (Dzieciol and Trzeszczy ski, 2001; Dzieciol and Trzeszczyn ski, 1998; Jiang et al., 2018). The wiring room of the building where the busduct is located is a relatively closed environment; then, considering that the temperature rise is a slow process, the concentration of VOCs in the air will increase gradually when the overheating of the busbar lasts for a period of time. As the VOC concentration reaches a certain value and is judged that an overheating fault has been occurred by our suggested algorithm, the alarm system will send a fault alarm signal to the operating staff.

Our study distinguishes itself from previous works in the following aspects:

- The proposed system can distinguish the overheating fault in compact insulated busduct of buildings by using the VOC centration data sampled by sensors, and send alarm message to the operation personnel. Many studies about early fire alarm systems (Wu et al., 2021; Dai et al., 2022; Kewon et al., 2022; Li et al., 2022) can identify the initial fire stage (smoke stage) effectively, by using the CO, CO_2, and other sensors. In other words, these mentioned studies are difficult to alarm before combustion, replaced by alarming on the early stage of combustion (smoke) only. In contrast, we designed an alarm system which can detect the overheating fault of busducts before the combustion of the insulating layer.
- The volatile gases generated by thermal degradation of the busbar insulation layer were analyzed by means of a variety of experiments with different sensors selectively. By experiment, we found that CO and CO_2 gases are not the typical gases in the early thermal degradation stage before the insulation layer melted. By experiment, the VOC concentration data have been selected as the input of the overheating fault early detecting system we designed.

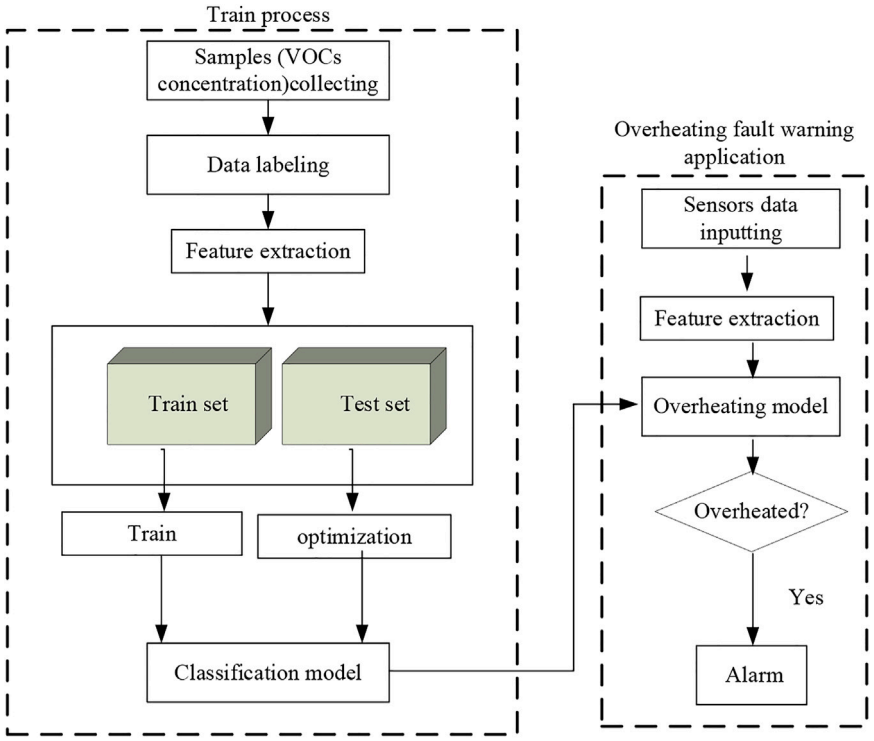

FIGURE 3
System architecture.

The rest of the paper is organized as follows: Section 2 studies the thermal degradation of the busbar insulation layer, Section 3 proposes the system architecture, and then, the data feature extraction and the AdaBoost algorithm used are introduced. Section 4 gives the experiment platform and analysis of the results. Finally, conclusions and future work are presented in Section 5.

2 Thermal degradation of the busbar insulation layer

Although the PET film has excellent chemical stability, its physical and chemical properties will be changed by thermal degradation under high-temperature environments, and then, its insulation performance will be reduced accordingly. When the current flowing through the busbar is too large, overheating will occur, especially in the joint of the busbar. As the temperature rises further, this fault will be intensified and finally lead to the damage of the insulating layer.

By experiments, we found that the status of the insulation layer of the busbar could be divided as the following stages: normal, overheat, melted, burn, or explosion with the increase in temperature. After the insulating layer is melted, short circuit will occur, which would lead to an explosion when the current flowing through the busbar is too large. In other words, the insulating layer would be burned when the current is not large enough. The thermal degradation process of the insulation layer of the busbar is shown in Figure 2.

The goal of our study is to detect the overheating fault of busducts and give alarms to operation personnel. It means we should identify the overheat stage before the insulation layer is melted.

The PET films are widely used in electrical engineering for their excellent insulating performance. The chemical formula of the PET is [OCH_2-$CH_2OCOC_6H_4CO$]. At high temperature, it will pyrolyze to produce various gases. Many studies and experiments have been carried out on the volatile toxic substances emitted within the temperature range 200–700 °C (Dzieciol and Trzeszczy ski, 2001; Dzieciol and Trzeszczyn ski, 1998). Studies have shown that acetaldehyde and formaldehyde are the main degradation products at temperatures 200–300 °C. At higher temperatures (400–700 °C), the decomposition products are very complex, which include carbon oxides, aldehydes, hydrocarbons, and aromatic acids and their esters, which depend on the temperature, atmosphere, or time. In our study about thermal degradation of the busway insulting layer, we face two problems different from these studies:

- The composition of the insulation layer in the busduct is not only PET films. In fact, in order to ensure various properties of the insulating layer, several types of additives are added for getting better performance during the manufacturing of the busduct insulated layer. Moreover, the composition of these additives is slightly different from manufacturer to manufacturer. Therefore, the composition of the insulating layer material is very complex, and its physical and chemical

FIGURE 4
Experimental platform.

properties are different from those of the commonly used PET films. Consequently, the thermal degradation process of the busbar insulation layer and the volatile substances emitted are different from those of pure PET films, and the compositions of these additives are kept secret by the manufacturers, which makes it difficult to analyze the pyrolysis products by chemical methods.

- Our goal is to detect the overheating fault, that is, the early stage of pyrolysis which is between the normal state and the melted state. Generally, the overheating stage occurs under 200 °C.

In this study, the VOC sensors were used to identify the overheating fault instead of the generally used CO and CO_2 sensors in other studies (Chen and Fu, 2012; Fonollosa et al., 2018; Khan et al., 2022) (Luo et al., 2019; Nakip et al., 2021; Wu et al., 2021; Kewon et al., 2022; Li et al., 2022), by a variety of experiments with different sensors selectively. We found that the VOC concentration was significantly changed during the overheating stage when the insulation layer of the busway worked under high temperature.

3 Overheating fault detecting system

3.1 System architecture

An overheating fault alarming system has been designed for the compact insulated busducts of buildings. In the designed system, the VOCs produced by pyrolysis in the thermal degradation of the insulation layer have been measured by sensors and as input of the classification model, which is used to identify the overheating fault of the busducts. Before the classification model is applied, it must be trained and tested with samples to determine its parameters. The train process is shown in Figure 3.

First, the collected samples have been labeled as positive and negative samples, and then, features were extracted from the samples to form a feature set. Then, the feature set was divided into a training set and a testing set according to a certain proportion. The training set is used to preliminarily determine the parameters of the model, and the testing set is used to optimize the parameters of the model. During the model testing, the samples of the testing set are input and classified by the trained classifier model and then the output classify results are used to compare with the correct labels, by which the model is evaluated and its parameters could be adjusted accordingly.

In the application system, the data series of various sensors are input into the trained model after feature extraction; finally, the classification results are obtained. If the model judges that it is currently in an overheated state, the system will send an alarm message to the operating staff.

3.2 AdaBoost classifier for overheating identification

The identification of the busduct overheating fault is essentially a two-classification problem in machine learning, that is, identifying the normal state and overheating state. In recent years, many classification algorithms have emerged in machine learning (Xiang et al., 2020), such as KNN (K-nearest neighbor) (Cover and Hart, 1967), SVM (support vector machine) (Schölkopf and Smola, 2002), Naive Bayes (Murphy, 2006), decision tree (Quinlan, 1986), random forest (Breiman, 2001), and AdaBoost (Freund and Schapire, 1995). Among them, AdaBoost has been proven to be extremely successful in generating accurate classifiers, especially, applied to two-classification problems (Zhu et al., 2009).

The AdaBoost algorithm is an iterative algorithm. It trains different classifiers (weak classifiers) for the same training set and then combines these weak classifiers to form a stronger final classifier (strong classifier). An AdaBoost classifier is a meta-estimator that begins by fitting a classifier on the original dataset and then fits additional copies of the classifier on the same dataset but where the weights of incorrectly classified instances are adjusted such that subsequent classifiers focus more on difficult cases. This implementing algorithm generally used is known as AdaBoost-SAMME (Zhu et al., 2009), and its procedure is shown as follows:

1) Initialize the weights $w_i = 1/n, i = 1, 2, \ldots, n$.
2) For m = 1 to M,

(a) Use the training data to fit a classifier $T^{(m)}(x_i)$ with weights w_i.
(b) Compute

$$err^{(m)} = \sum_{i=1}^{n} w_i \prod (c_i = T^{(m)}(x_i)) \Big/ \sum_{i=1}^{n} w_i. \quad (1)$$

(c) Compute

TABLE 1 Part of experiment records.

Time	Current (A)	Copper temperature (^{0}C)	C_6H_6 (ppm)	CO (ppm)	C_2H_4O (ppm)	H_2S (ppm)
09:50	350	38.2	0.20	1.45	0.20	0.12
09.55	350	54.7	0.18	1.46	0.17	0.12
10:00	350	57.6	0.18	1.47	0.21	0.12
10:10	350	63.2	0.20	1.46	0.17	0.12
10:20	350	64.5	0.20	1.71	0.20	0.12
10.30	350	67.2	0.20	1.46	0.20	0.12
10:40	400	74.7	0.20	1.46	0.17	0.12
10:50	400	78.5	0.20	1.71	0.19	0.12
11:00	400	81.0	0.20	1.48	0.17	0.12
11:10	400	82.8	0.20	1.46	0.16	0.12
11:20	400	83.4	0.20	1.48	0.17	0.12
11:30	450	90.7	0.20	1.45	0.17	0.12
11:40	450	97.0	0.18	1.71	0.20	0.15
11:50	450	98.2	0.20	1.72	0.20	0.15
12:00	450	98.4	0.20	1.71	0.17	0.15
13:10	450	92.5	0.20	1.47	0.17	0.12
13:50	450	97.0	0.20	1.74	0.20	0.15
14:10	450	98.3	0.20	1.71	0.20	0.12
14:20	450	98	0.40	1.95	0.20	0.15
14:30	450	98.3	0.20	1.93	0.17	0.15
14:40	500	103.3	0.20	1.96	0.18	0.15
14:50	500	117.0	0.20	1.88	0.19	0.17
15:00	500	120.0	0.20	1.71	0.17	0.12
15:10	500	122.0	0.20	1.95	0.20	0.15
15:20	500	123.0	0.20	1.22	0.15	0.12
15:30	500	124.0	0.20	1.46	0.20	0.15
15:40	550	129	0.20	1.46	0.18	0.12

$$a^{(m)} = \log\frac{1 - err^m}{err^m} + \log(K - 1). \tag{2}$$

(d) Set

$$w_i \leftarrow w_i \cdot \exp\left(a^m \cdot \prod\left(c_i = T^{(m)}(x_i)\right)\right) \quad i = 1, 2, ..., n. \tag{3}$$

(e) Renormalize w_i.

3) Output classifier

$$C(x) = \arg\max_k \sum_{m=1}^{M} a^{(m)} \cdot \prod\left(T^{(m)}(x) = k\right), \tag{4}$$

where $C(x)$ is the classification rule. $T(x)$ denotes a weak multi-class classifier that assigns a class label to x.

3.3 Feature extraction of samples

In the early stage of thermal degradation, the concentration of VOCs is small, and it increases gradually with the increase in the busbar temperature, so the time series can better express this process. We use the statistical values of gas concentration from the VOC sensor and its trend values (Wu et al., 2021) as the features input to the model.

Assuming a time series of VOC centration data with length N is $\boldsymbol{G} = \{x(0), x(1), \cdots, x(N)\}$, the features are extracted as follows:

1) The trend value of time series contains the amount of change and the direction of change, which can be obtained by the kendall τ formula:

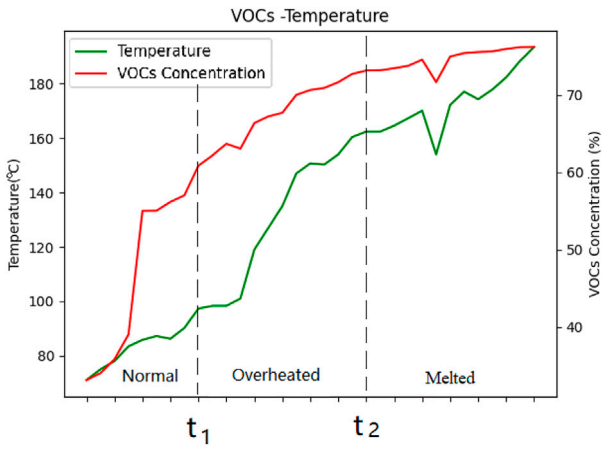

FIGURE 5
VOC concentration and copper temperature.

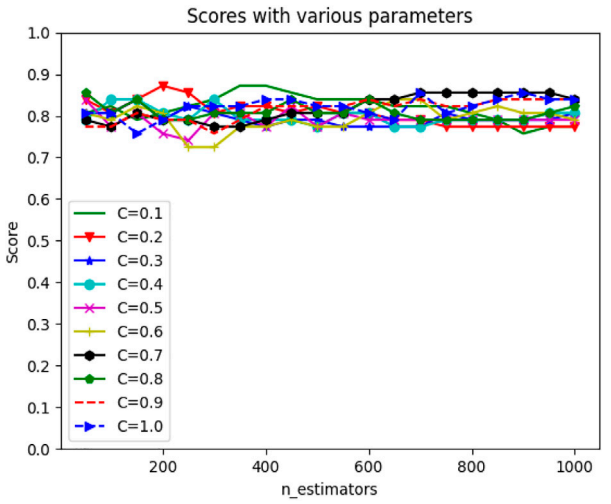

FIGURE 6
Score results of various parameters of AdaBoost.

$$y(n) = \sum_{i=0}^{N-1} \sum_{j=0}^{N-1} u(x(n-i) - x(n-j)), \tag{5}$$

where n is the discrete time variable, N is the window length, and $u(x)$ is the unit step function.

In order to better detect the rising and falling trends of fire signals, the kendall τ algorithm can modified as follows (Wu et al., 2021):

$$y(n) = \sum_{i=0}^{N-1} \sum_{j=i+1}^{N-1} \mathrm{sgn}(x(n-i) - x(n-j)), \tag{6}$$

where $y(x)$ is the sum of $\mathrm{sgn}(x)$, which contains the $N(N-1)/2$ terms. This can be normalized to section $[-1, +1]$.

$$\tau(n) = \frac{y(n)}{N(N-1)/2}. \tag{7}$$

TABLE 2 Recognition results.

	Precision (%)
Category 0	93.42
Category 1	84.98
Average	89.20

So, after the aforementioned modification, Eq. 5 is modified as a recursive formula:

$$y(n) = y(n-1) + \sum_{i=0}^{N-1} \mathrm{sgn}(x(n) - x(n-j)) - \sum_{i=0}^{N-1} \mathrm{sgn}(x(n-1-j) - x(n-N)). \tag{8}$$

Then, the trend value series TR can be obtained from VOC time series G by Eq. 8.

2) The statistical values of ***G*** and ***TR*** are selected as the features of the gas data input to the model, namely, the maximum, the minimum, the mean, and the variance. So, for a VOC concentration time series with length N captured from a sensor, it can extract two features arrays:

$$F_G = \{\max(G),\ \min(G), \mathrm{mean}(G), \mathrm{var}(G)\}, \tag{9}$$

$$F_{TR} = \{\max(TR),\ \min(TR), \mathrm{mean}(TR), \mathrm{var}(TR)\}. \tag{10}$$

3) The final feature set F is obtained by merging F_G and F_{TR}; then,

$$F = \{F_G, F_{TR}\}. \tag{11}$$

So, there are eight features in a dataset used to identify the overheating in the application.

4 Experiment

4.1 Experiment platform

For the study, we built an experimental platform which can provide large current with a maximum of AC 600 A, as shown in Figure 4. The experimental device has a transparent shell, which is a closed structure simulating the wiring room of high-rise buildings. The insulated busduct is placed in the shell. A VOC sensor is installed on top of the cover. During testing, the temperature of the busbar is controlled by adjusting the magnitude and duration of the passing current. When an increasing large current passes through the busbar and lasts a certain time, the insulation layer will be overheated and pyrolyzed gradually. By this means, we can simulate the various overheating statuses by changing the working current of the busduct and collect samples under different statuses.

4.2 Characteristic gas selection

In the experiment, the copper bars in the busduct are 4 mm*20 mm, which are covered with the isolated layer (PET).

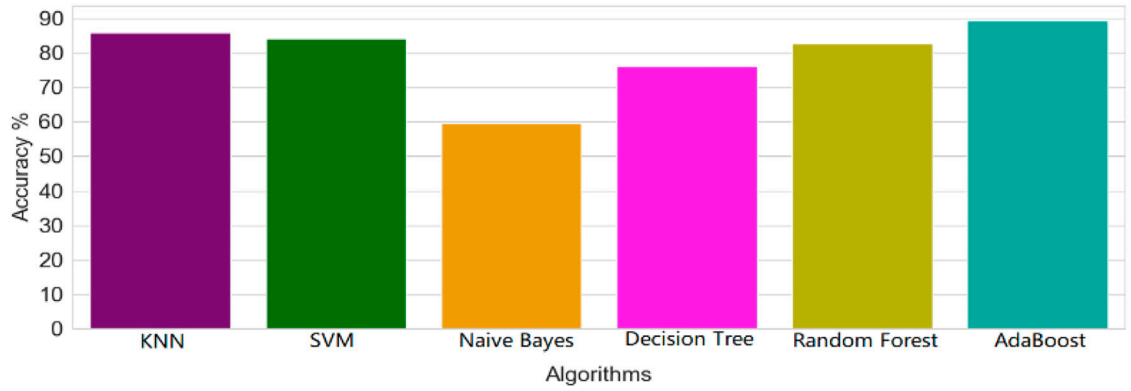

FIGURE 7
Accuracy comparison of different classifiers.

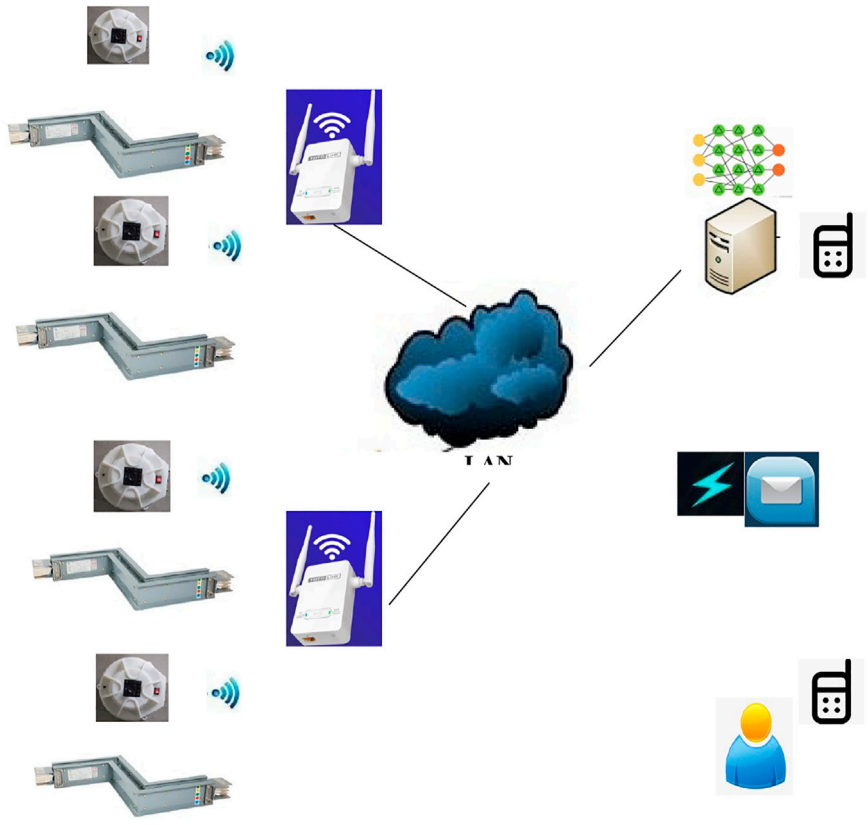

FIGURE 8
Overheating alarm system for busducts.

The rated current of the testing busduct is 200 A. We gradually apply different currents to the busbars from small to large and measure various gases' concentration by using different sensors. The commonly used detection gases in cable fire studies, such as carbon dioxide, formaldehyde, benzene, hydrogen sulfide, ethylene oxide, chlorine, and ammonia, are all detected in our experiment. We found that the concentrations of these gases had no obvious change both in the normal stage and the overheated stage during the temperature rise. Part of records are shown in Table1.

However, the measured values of the VOC sensor have been changed obviously and regularly during this period. Part of experiment records are described in Figure 5. From time t_1 , we can smell a special smell, which comes from thermally decomposed gases. This time can be considered as the initial stage of thermal

decomposition of the insulating layer. When the current is increased gradually, the temperature of the insulating layer is higher and the concentration of VOCs is also larger. From time t_2, we can see with the naked eye that the insulating layer is beginning to melt.

As shown in Figure 5, with the increase in the current flowing through the busbar, the temperature of the busbar gradually rises, and the concentration of VOCs increases accordingly. It can be divided into three different stages which correspond to different concentrations of VOCs: normal, overheated, and melted. Consequently, we selected VOCs as the characteristic gas for the overheating fault warning study.

4.3 Training and testing

In order to verify the effectiveness of the proposed method, we collected 3,000 samples that include two categories, which correspond to normal condition and overheated condition. The data sampling frequency is 2 s/time, and every five sampled data are grouped as a sample. Then, we labeled these samples and extracted features according to Eqs 6–10. Finally, the sample set has been made for training and testing. In our experiment, 80% of the samples were used as the training set and 20% of the samples were used as the test set.

The programming of the AdaBoost algorithm is available in Scikit-Learn, a powerful machine learning library written in Python. The classifier function is AdaBoostClassifier (), and its main input parameters are n_estimators (int) and learning_rate (float). "n_estimators" represents the maximum numbers of estimators at which boosting is terminated. In case of perfect fit, the learning procedure is stopped early. "learning_rate(C)" is the weight applied to each classifier at each boosting iteration. A higher learning rate increases the contribution of each classifier. There is a trade-off between the "n_estimators" and "learning_rate" parameters. The score results with various parameters are shown in Figure 6. By training and optimization, an average score of 89.2% is obtained when "n_estimators" = 200 and "C" = 0.2. The recognition results are shown in Table 2. Since the overheating stage (early thermal degradation stage) occurs before the melting of the insulating layer, the characteristics are not very obvious, so the identification rate is lower than that of the normal stage.

For comparison, other machine learning classification algorithms are used, and the classification accuracies are compared and shown in Figure 7. In our testing, the AdaBoost, KNN, and SVM classifiers have shown higher accuracy than others.

4.4 Application system designed

The overheating fault alarming system is designed as in Figure 8. For the application, we have made a VOC sensing device which integrates a VOC sensor, MCU, and WIFI communication module. In the wiring room of the building, the VOC sensing devices are installed. All VOC data of sensors are sent to the server through the WIFI network. By the VOC data samples collected in the experiment, the AdaBoost model was trained and its parameters were optimized before it was put into practice. After the server has received the VOC contraction data in application, it will use the trained AdaBoost model to output the classification results. If it is judged that an overheating fault has been occurred, it will notify the operating staff through phone call, email, APP, etc. In the designed system, the AdaBoost classifier is used to recognize the overheat status of the busducts.

5 Conclusion and future work

Aiming at the overheating fault warning of compact insulted busways in buildings, this paper proposed a fault warning system based on pyrolysis gases which came from thermal degradation of the busduct insulation layer. Although there are many studies on early warning of fire, little attention is paid to the overheating stage of fire. Few similar studies on cable overheating warning focus on PVC cables (Nie et al., 2008; Li, 2014; Chen and Yi, 2019; Han et al., 2019), but not on busways in buildings. The architecture of the recognition system based on the AdaBoost classification model was designed, and the method of feature extraction was also given. The experimental platform was built, and it is pointed out that VOC gas could be used as the characteristic gas for overheating fault warning by testing. The experimental results showed that the AdaBoost classifier could get high classification accuracy than other commonly used classifiers in machine learning. Finally, the design and implementation of the system are given.

In the future work, the specific chemical components of the thermal decomposition gas will be analyzed in detail by chemical instruments, and more representative characteristic gases will be selected according to the analysis results to improve the identification accuracy. In engineering applications, some problems will continue to be studied, such as the installation location and number of sensors. The proposed method and the designed system are further optimized and improved in practical application.

Data availability statement

The original contributions presented in the study are included in the article/Supplementary Material; further inquiries can be directed to the corresponding author.

Author contributions

This paper is a result of the collaboration of all co-authors. HX was responsible for the research organization and experiment. ZL provided the theory and conceived and revised the manuscript. JL, XJ, WL, and BX helped in testing and analysis.

Conflict of interest

Authors HX, JL, WL, XJ, and BX were employed by the Electric Power Research Institute of State Grid Hubei Electric Power Co., Ltd.

The remaining authors declare that the research was conducted in the absence of any commercial or financial relationships that could be construed as a potential conflict of interest.

Publisher's note

References

Babrauskas, V. (2006). Mechanisms and modes for ignition of low-voltage, PVC-insulated electrotechnical products. *Fire Mater.* 30 (2), 151–174. doi:10.1002/fam.900

Benes, M., Milanov, N., Matuschek, G., Kettrup, A., Placek, V., and Balek, V. (2004). Thermal degradation of PVC cable insulation studied by simultaneous TG-FTIR and TG-EGA methods. *J. Therm. Analysis Calorim.* 78 (2), 621–630. doi:10.1023/B:JTAN.0000046123.59857.ad

Breiman, L. (2001). Random forests. *Mach. Learn.* 45 (1), 5–32. doi:10.1023/A:1010933404324

Chen, J., and Fu, J. (2012). Fire alarm system based on multi-sensor Bayes network. *Procedia Eng.* 29, 2551–2555. doi:10.1016/j.proeng.2012.01.349

Chen, L., Lin, F., Chen, M., Huang, X., He, R., and Zheng, Y. (2022). Influence for ambient relative humidity and pollution on infrared detection of zero resistance insulators. *Front. Energy Res.* 8 (17), 942408. doi:10.3389/fenrg.2022.942408

Chen, W., and Yi, J. (2019). Identification and gas sensor testing of volatile signature gas for early detection of PVC cable fires. *Fire Saf. Sci.* 28 (2), 94–100. doi:10.3969/j.issn.1004-5309.2019.02.04

Cover, T. M., and Hart, P. E. (1967). Nearest neighbor pattern classification. *IEEE Trans. Inf. Theory* 13 (1), 21–27. doi:10.1109/TIT.1967.1053964

Dai, P., Zhang, Q., Lin, G., Shafique, M. M., Huo, Y., Tu, R., et al. (2022). Multi-scale video flame detection for early fire warning based on deep learning. *Front. Energy Res.* 10, 848754. doi:10.3389/fenrg.2022.848754

Dzieciol, M., and Trzeszczy ski, J. (2001). Temperature and atmosphere influences on smoke composition during thermal degradation of Poly (ethylene terephthalate). *J. Appl. Polym. Sci.* 81, 3064–3068. doi:10.1002/app.1757

Dzieciol, M., and Trzeszczyn ski, J. (1998). Studies of temperature influence on volatile thermal degradation products of Poly (ethylene terephthalate). *J. Appl. Polym. Sci.* 69, 2377–2381. doi:10.1002/(sici)1097-4628(19980919)69:12<2377::aid-app9>3.0.co;2-5

Fonollosa, J., Solórzano, A., and Marco, S. (2018). Chemical sensor systems and associated algorithms for fire detection: A review. *Sensors* 18, 553. doi:10.3390/s18020553

Freund, Y., and Schapire, R. E. (1995). A desicion-theoretic generalization of on-line learning and an application to boosting. *Lect. Notes Comput. Sci.* 904, 23–37. doi:10.1007/3-540-59119-2_166

Gao, X., Boecklin, M. V., Ermanoski, I., and Stechel, E. B. (2021). Low-Cost radiant heater for rapid response, high-temperature heating. *Front. Energy Res.* 9, 652203. doi:10.3389/fenrg.2021.652203

Han, J., Chen, W., Yu, A., and Yi, J. (2019). Detection of semi-volatile plasticizers as a signature of early electrical fire. *Front. Mater.* 6, 250. doi:10.3389/fmats.2019.00250

Jiang, X., Sun, P., Peng, Q., and Sima, W. (2018). Isothermal relaxation current and microstructure changes of thermally aged polyester films impregnated by epoxy resin. *J. Phys. D Appl. Phys.* 51, 015306. doi:10.1088/1361-6463/aa9a6e

Kewon, S. J., Park, J. R., Park, C. O., Yoo, H. J., and Ha, S. (2022). Wireless kitchen fire prevention system using electrochemical carbon dioxide gas sensor for smart home. *Sensors* 22 (11), 3965. doi:10.3390/s22113965

Khan, F., Xu, Z., Sun, J., Ahmed, A., and Zhao, Y. (2022). Recent advances in sensors for fire detection. *Sensors* 22, 3310. doi:10.3390/s22093310

Kuznetsov, G., Kopylov, N., Sushkina, E., and Zhdanova, A. (2022). Adaptation of fire-fighting systems to localization of fires in the premises: Review. *Energies* 15 (2), 522. doi:10.3390/en15020522

Li, N. (2014). Study on new electrical fire monitoring technology for low-voltage distribution cabinet. *Build. Electr.* 33 (7), 26–29. doi:10.3969/j.issn.1003-8493.2014.07.007

Li, Y., Su, Y., Zeng, X., and Wang, J. (2022). Research on multi-sensor fusion indoor fire perception algorithm based on improved TCN. *Sensors* 22 (12), 4550. doi:10.3390/s22124550

Lin, C., and Wang, L. (2017). Real-time forecasting of building fire growth and smoke transport via ensemble Kalman filter. *Fire Technol.* 53 (3), 1101–1121. doi:10.1007/s10694-016-0619-x

Luo, S., Zhang, X., Wang, M., and Xu, J. H. (2019). A slight smoke perceptual network. *IEEE Access* 7, 42889–42896. doi:10.1109/ACCESS.2019.2906695

McNeil, L. C., Memetea, L., and Cole, W. J. (1995). A study of the products of PVC thermal degradation. *Polym. Degrad. Stab.* 49 (1), 181–191. doi:10.1016/0141-3910(95)00064-S

Murphy, K. P. (2006). *Naive Bayes classifiers*. Canada: University of British Columbia.

Nakip, M., Guzelis, C., and Yildiz., O. (2021). Recurrent trend predictive Neural Network for multi-sensor fire detection. *IEEE Access* 9, 84204–84216. doi:10.1109/ACCESS.2021.3087736

Nie, M., Stetter, J. R., and Buttner, W. J. (2008). Orthogonal gas sensor arrays with intelligent algorithms for early warning of electrical fires. *Sensors Actuators B* 130, 889–899. doi:10.1016/j.snb.2007.10.070

Quinlan, J. R. (1986). Induction of decision trees. *Mach. Learn.* 1 (1), 81–106. doi:10.1007/bf00116251

Rana, B., Mallick, P., and Rana, T. K. (2017). "Efficient and superior elbow joint for high power busway trunking System," in In proceedings of the 8th Annual Industrial Automation and Electromechanical Engineering Conference (IEMECON), Bangkok, Thailand, 16-18 August 2017.

Sarwar, B., Bajwa, I. S., Ramzan, S., Ramzan, B., and Kausar, M. (2018). Design and application of fuzzy logic based fire monitoring and warning systems for smart buildings. *Symmetry* 10, 615. doi:10.3390/sym10110615

Schölkopf, B., and Smola, A. J. (2002). *Learning with kernels: Support Vector Machines, regularization, optimization and beyond. adaptive computation and machine learning*. Cambridge, MA: MIT Press.

Wang, H., Wang, B., Li, M., Luo, P., Ma, H., and Ma, F. (2021). Insulator contamination perception based on feature fusion of infrared image and meteorological parameters. *Front. Energy Res.* 9, 746378. doi:10.3389/fenrg.2021.746378

Wood, R. H., and McGoldrick, G. A. (1985). Busway short circuit testing procedures. *IEEE Trans. Industry Appl.* 21 (4), 873–875. doi:10.1109/TIA.1985.349534

Wu, L., Chen, L., and Hao, X. (2021). Multi-sensor data fusion algorithm for indoor fire early warning based on BP neural network. *Information* 12, 59. doi:10.3390/info12020059

Xiang, B., Liu, Z., and Zhang, K. (2020). Flagging implausible inspection reports of distribution transformers via anomaly detection. *IEEE Access* 8, 75798–75808. doi:10.1109/ACCESS.2020.2989330

Xu, Q., Xie, W., Jiang, S., Zeng, C., and Jiang, D. (2019). A wireless sensor dynamic sampling strategy for monitoring temperature rise signals of busway. *Power Syst. Prot. Control* 47 (8), 106–112. doi:10.7667/PSPC180541

Yun, Q. (2013). Design of fiber distributed busway temperature monitoring system. *Adv. Mater. Res.* 694-697, 1114–1117. doi:10.4028/www.scientific.net/amr.694-697.1114

Zhu, J., Rosset, S., Zhou, H., and Zou, H. (2009). Multi-class adaBoost. *Statistics its Interface* 2 (3), 349–360. doi:10.4310/SII.2009.v2.n3.a8

frontiers | Frontiers in Energy Research

TYPE Original Research
PUBLISHED 17 February 2023
DOI 10.3389/fenrg.2023.1069119

OPEN ACCESS

EDITED BY
Srete Nikolovski,
Josip Juraj Strossmayer University of Osijek, Croatia

REVIEWED BY
Arturo García Pérez,
University of Guanajuato, Mexico
Sherif S. M. Ghoneim,
Taif University, Saudi Arabia

*CORRESPONDENCE
Na Qu,
11502332@qq.com

SPECIALTY SECTION
This article was submitted to Smart Grids, a section of the journal Frontiers in Energy Research

RECEIVED 13 October 2022
ACCEPTED 07 February 2023
PUBLISHED 17 February 2023

CITATION
Shuai Z, Qu N, Zheng T, Hu C and Lu S (2023), Research on arc fault detection using ResNet and gamma transform regularization.
Front. Energy Res. 11:1069119.
doi: 10.3389/fenrg.2023.1069119

Research on arc fault detection using ResNet and gamma transform regularization

Zhang Shuai[1], Na Qu[1]*, Tianfang Zheng[1], Congqiang Hu[1] and Senxiang Lu[2]

[1]School of Safety Engineering, Shenyang Aerospace University, Shenyang, China, [2]Northeastern University, Shenyang, China

Series arc fault is the main cause of electrical fire in low-voltage distribution system. A fast and accurate detection system can reduce the risk of fire effectively. In this paper, series arc experiment is carried out for different kinds of electrical load. The time-domain current is analyzed by Morlet wavelet. Then, the multiscale wavelet coefficients are expressed as the coefficient matrix. In order to meet the data dimension requirements of neural networks, a color domain transformation method is used to transform the feature matrix into an image. A regularization method based on gamma transform is proposed for small sample data sets. The results showed that the proposed regularization method improved the validation set accuracy of ResNet50 from 66.67% to 96.53%. The overfitting problem of neural network was solved. In addition, this method fused fault features of 64 different scales, and provided a valuable manually labeled arc fault dataset. Compared with the threshold detection method, this method was more objective. The use of image features increased intuitiveness and generality. Compared with other typical lightweight networks, this method had the best detection performance.

KEYWORDS

morlet continuous wavelet, arc fault, ResNet, regularization, color index

1 Introduction

1.1 Introduction to arc faults

Arc is a kind of abnormal discharge phenomenon in insulating medium. The arc can keep burning when the circuit voltage is higher than 20 V and the current is greater than 0.1A (Qu and Wang, 2018). It is easy to injure people or produce electrical fire. In low-voltage power distribution system, arc fault may be caused by irregular circuit connection and the aging electronic equipment. When series arc fault occurs, the residual current of the circuit is usually less than the cut-off threshold of low-voltage circuit breaker. The circuit cannot be cut off in time. A real-time and accurate arc fault detection system can reduce the risk of fire effectively.

Abbreviations: f_s, Non-destructive sampling frequency; $Var[x^{(k)}]$, Variance; f_m, Highest harmonic frequency; $\mathcal{L}(\cdot)$, Specific loss function; $\psi(t)$, The mother wavelet; $\hat{h}$, Theoretical assumption optimal value; $f(t)$, Time domain signal; h^*, Constraint value; C, Approximate coefficient; S, Gray value; w_0, Center frequency; γ, Gamma influence factor; A, Scale coefficient; B, Translation coefficient; $E[x^{(k)}]$, Expectation.

In the 1940s, Cassie and Mayr established the arc model by studying the relationship between arc dissipated power and current. Since then, the research on arc faults mainly focuses on the simulation of arc models. As these two arc models are suitable for circuits with different voltages, some studies are aimed at improving and integrating the arc model to make it applicable to more occasions (Xiang and Wang, 2019) (Shu and Wang, 2018).

1.2 Research gap

In recent years, the researches of arc fault detection are not limited to the arc mathematical model. In fact, some circuit parameters may have a mutation when an arc fault occurs. The purpose of fault detection can be achieved by identifying the circuit parameters as features. In practical application, it is difficult to collect the photothermal physical characteristics of the arc in real time due to the random arc generation. As a result, the common feature extraction method is time-frequency domain analysis of voltage or current. Fast Fourier analysis (FFT) is the main method of frequency domain analysis. In addition, literature (Humbert et al., 2021) realizes the detection of series arc faults of different loads through the change rate of voltage spectral dispersion index (SDI) of low-voltage power line. Literature (Chu et al., 2020) designed a high-frequency coupling sensor to detect the high-frequency characteristics of arc generation, and established a fault identification model according to the different high-frequency characteristics of different loads. In literature (Joga et al., 2021), time-domain information and frequent-domain information are fused by wavelet analysis. The fused features are fed into the convolutional neural network for detection.

The extraction of time domain features has also changed from the original phase analysis to empirical mode analysis (EMD) or noise processing (Ji et al., 2020; Lala and Subrata, 2020; Cui and Tong, 2021). However, a single feature has great uncertainty in the face of arc faults with many singularities. The fusion of fault feature has become a new challenge in the research of detection method.

As a time-frequency analysis method, the multi-resolution characteristic of wavelet analysis is efficient in many fields. The fusion of fault features in time-frequency domain ensures the real-time detection (Xiong and Chen, 2020) (Liu and Du, 2017).

In addition, some statistics of the circuit can also be used as fusion features, such as information entropy wavelet energy entropy and power spectrum entropy of signal (Cui and Li, 2021a) or the fusion of proportional coefficient of arc zero rest time and normalization coefficient of low-pass filter (Zhao and Qin, 2020). These features detect the fault state of the circuit by setting the weight and threshold of parameters. Due to the limitation of experimental conditions, threshold setting is faced with the disadvantages of poor reliability and low efficiency. In order to improve the accuracy of detection, the fault feature data of arc can be input into machine learning algorithm for processing (Miao et al., 2023). Machine learning can be subdivided into unsupervised learning and supervised learning. Typical unsupervised learning including cluster analysis, principal component analysis (PCA) (Ku et al., 1995) and singular value decomposition (SVD) (Vozalis and Margaritis, 2006), etc. As a basic algorithm, SVD plays a role in many machine learning algorithms, especially in the current era of big data, SVD can realize parallelization with many algorithms. Common applications include DWT-SVD, RDWT-SVD and K-SVD dictionary learning (Chen et al., 2014; Kadian et al., 2019; De et al., 2021). PCA is widely used as a data dimension reduction method. In literature (De et al., 2021) the high-dimensional phase plane at the center of the moment, the radius vector offset, Correlation dimension and K-entropy were used as fusion features. Then PCA is used to reduce the dimension of features to extract the main features of fault detection. In addition, PCA is applied to data preprocessing as a way of dimensionality reduction (Xia et al., 2022). The effect of unsupervised learning is affected by the sparsity of data and singular value points to some extent. The randomness of arc fault data brings great challenges to the use of unsupervised learning.

With the good performance of supervised learning in various fields, neural networks and support vector machines (SVM) have also been applied to arc fault detection. As an example, the authors of literature (Cui and Li, 2021b) proposed a method to input the fusion features of variational modal decomposition (VMD) and multi-scale fuzzy entropy (IMFE) into SVM for classification, and the accuracy of classification was verified through experiments. Supervised learning is a data-driven algorithm. Fewer fault data samples may result in the accuracy decreasing of neural network. Literature (Wang et al., 2021) solved the impact of less fault data on the accuracy of neural network by using the method of adversarial data enhancement, and proved the effectiveness of data enhancement through the detection of convolutional neural network.

In fact, feature data can exist in the form of more intuitive images. As proposed in literature (Lu et al., 2021), quantitative recursive analysis (RQA) was performed on the sequential periodic phase space trajectory diagram of load faults to extract fault characteristics of different loads.

According to the questions above, the research of this paper aims to improving the performance of detection methods through the following three aspects:

1) Data acquisition and processing

The selection of fault features should consider both diversity and real-time. The arc fault data of different loads are obtained by experiments, and the wavelet coefficient matrix of 64 scales is obtained by Morlet-wavelet analysis. This means that the neural network can obtain a wider field of perception from the features.

2) Image conversion and algorithm construction

In order to handle fault features in an intuitive manner, we converted features into images and a computer vision network is built for classification. “A colormap index method” is proposed to transform fault features into image features, and the fault dataset is manually annotated. ResNet50 with better performance was used for classification and detection of image data. The data set can reduce the data cost of migration learning.

3) Optimization of detection algorithm

The randomness of arc fault results in a small number of experimental samples. Aiming at the phenomenon of neural

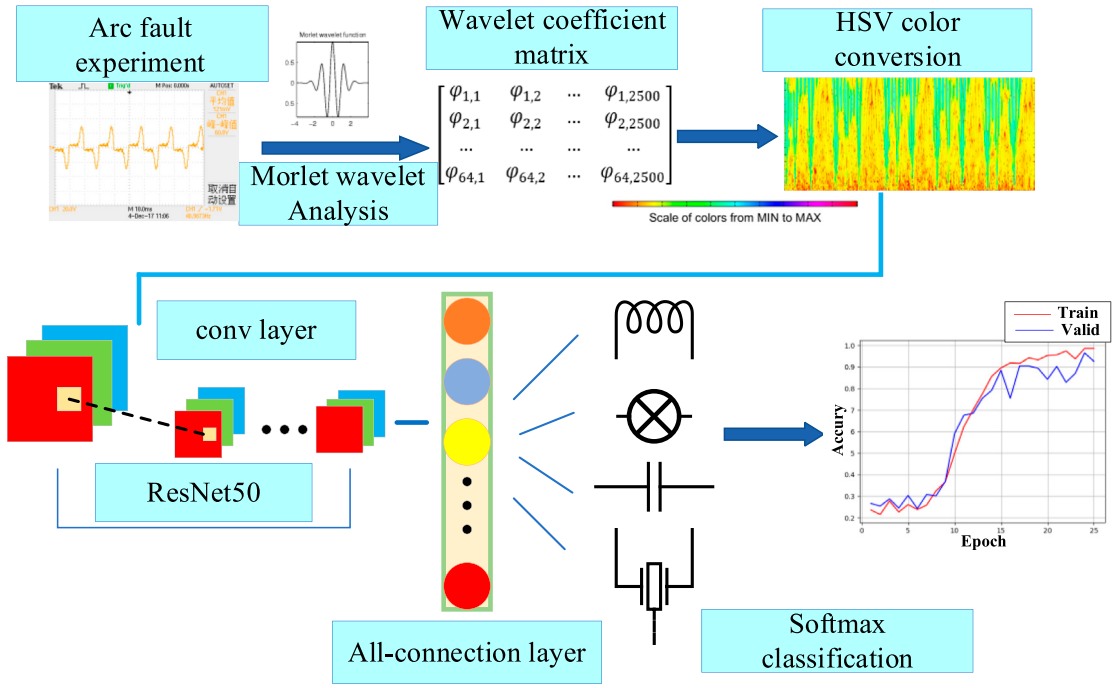

FIGURE 1
The process of arc fault detection method.

TABLE 1 Load parameters and sample resistance values.

Load name	Rated power (W)	The load type	The load properties	Sampling resistance(Ω)
Lamp	100	Resistive load	Linear load	100
Lamp and inductor in series	100	Resistive and inductive load	Linear load	100
Electric blower	500	DC motor load	Non-linear load	50
Induction cooker	1200	Eddy current load	Non-linear load	1
Computer	90	Switching power	Non-linear load	50
Hand drill	500	Series motor load	Non-linear load	50

network overfitting caused by small sample data a data enhancement method named "Gamma transform" is proposed. Compared with other regularization methods, the regularization method based on image feature enhancement can reduce the cost of neural network pre-training and improve the detection performance better.

This method also provides a new idea for regularization research based on data enhancement.

The research process of this paper is shown in Figure 1.

In Figure 1, the blue rectangle shows the specific content of the research steps, and the blue arrow shows the process of the research steps.

2 Experiment and data processing

In order to restore the real arc fault data, we set up an arc fault experiment platform according to the international standard UL1699. Six kinds of common loads in low-voltage circuits are connected with the arc fault generator in series. The sampling resistance method is used to measure the current time domain signals of six loads in normal working state and fault state. The load types and sampling resistance values are shown in Table 1.

In 220 V, 50 HZ power grid environment, the six kinds of loads above are tested in normal operation and fault state for 4 times respectively. In the power grid, harmonics have little influence on the signal with the harmonic frequency higher than 20 times. In view of this, the sampling frequency of the experimental current is set as 25 KHZ according to Nyquist sampling theorem. Nyquist's theorem can be expressed by Eq. 1:

$$f_s \geq 2f_m \tag{1}$$

Where f_s is the non-destructive sampling frequency and f_m is the highest harmonic frequency of the time domain signal.

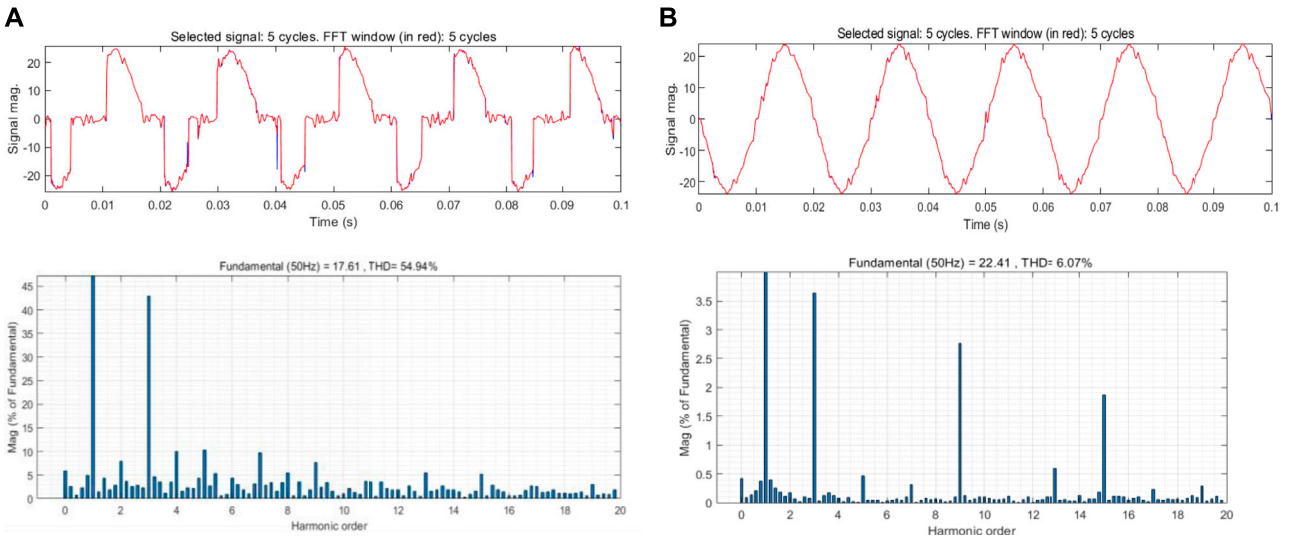

FIGURE 2
Experimental results, **(A)** is the time-frequency information under the failure of the incandescent lamp, **(B)** is the time-frequency information under the normal operation of the incandescent lamp.

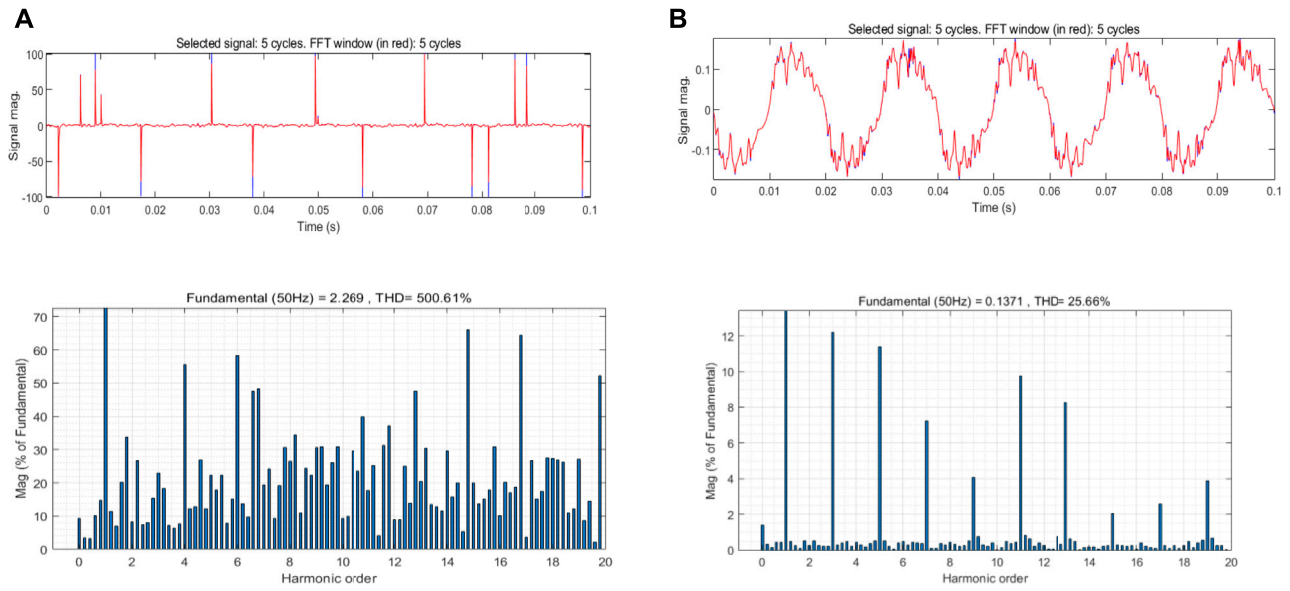

FIGURE 3
Experimental results, **(A)** is the time-frequency information under the failure of the computer, **(B)** is the time-frequency information under the normal operation of the computer.

The 48 groups of data obtained from the experiment are reproduced in Matlab. Taking incandescent lamp and computer of linear load and non-linear load as examples respectively, which experimental results are shown in Figures 2, 3.

The spectrum in the figure is obtained by fast Fourier analysis transform (FFT) of time-domain signals. It can be seen from the figure that the "flat shoulder" phenomenon occurs near the zero crossing of non-linear load when it fails. Ac arc in the current zero moment, the arc will automatically extinguished, and after the current zero, if the conditions are available, it will restart the arc. This phenomenon of the arc going out before and after the current crossing zero is known as the "zero-rest" of the AC arc. In the frequency spectrum, the linear load has a higher odd number of high harmonics during the failure. In addition, the total harmonic distortion (THD) rate reaches 54.94%, which is much higher than 6% under normal operation. By contrast, the time domain current of non-linear load presents high randomness, higher harmonic component and complete distortion of signal. In

normal operation, the non-linear load also produces odd high order harmonics and the harmonic amplitude is higher than that of the linear load. In the research of arc faults, fault features are usually combined with machine learning algorithms to ensure the accuracy and rigor of detection (Johnson and Kang, 2012) (Cao et al., 2013).

3 Morlet continuous wavelet analysis

By using FFT, we can obtain the frequency domain distribution of the continuous signal over the sampling period. At the end of Section 2, we verify that the arc fault of non-linear load cannot be judged by spectrum alone. The fault features used for detection need deep fusion as well as generality and typicality. Wavelet analysis can be used to process the time domain signal. For the multi-resolution characteristic of wavelet function, continuous wavelet analysis can obtain the overall and detailed features of signal at different scales. 1D wavelets are mainly used to process ordinary 1D signals, while 2D wavelets are mainly used to process image signals. In addition, the cost of1d wavelet analysis is lower. Therefore, Morlet 1D wavelet, which is more suitable for 1D current signal in this paper, is selected. The continuous wavelet transform can be expressed as:

$$T(a,b) = \frac{1}{\sqrt{a}}\int_{-\infty}^{\infty} f(t)\psi^{*}\left(\frac{t-b}{a}\right)dt \tag{2}$$

The meaning of Eq. 2 is as follows: After the mother wavelet ψ(t) is displaced by b, the inner product operation is carried out with the time domain signal f(t) at different scales a (Mallat and Zhong, 1992) (ByPaul, 2016). The "*" indicates that the complex conjugate of the wavelet function is used in the transform. In order to obtain more fault features at different scales, the typical Morlet continuous wavelet is selected to analyze the current signal (Ferracuti et al., 2021). The Morlet mother wavelet function is as follows:

$$\Psi(x) = Ce^{-x^2/2}\cos(5x) \tag{3}$$

Where C is the approximate coefficient. The continuous wavelet transform is an integral transform, which is the same as the Fourier transform. The continuous wavelet transforms the mother wavelet by continuous translation and scaling, and then the wavelet coefficient is obtained. The wavelet coefficient is a binary function composed of translation and scaling, and the continuous wavelet transform can be expressed as:

$$C(\text{Scale, Position}) = \int_{-\infty}^{\infty} f(t)\Psi(scale, position, t)dt \tag{4}$$

The Morlet continuous wavelet transform coefficient can be expressed as:

$$\Psi f(a,b) = \int_{-\infty}^{\infty} f(t)\,exp\left(-iw_0\left(\frac{t-b}{a}\right)\right)exp\left(-\frac{(t-b)^2}{2a^2}\right)dt \tag{5}$$

Where w_0 is the center frequency, a is the scale coefficient and b is the translation coefficient. The current time-domain signal obtained in the experiment was taken as the original signal for Morlet continuous wavelet analysis with the maximum scale of 64. Taking the incandescent lamp fault as an example, the wavelet coefficient with the change of time when the central scale a = 32 was shown in Figure 4:

Fusion of more features can improve the accuracy of the detection algorithm. In the next section, we try to use computer vision network to classify and detect fault features. Therefore, we try to transform fault features which fused with more scales into images. The wavelet coefficients obtained from each experiment are arranged into a 64 × 2500 matrix according to the scale of 1–64. The phase space depth diagram of continuous wavelet transform is made by mapping the coefficient matrix into the phase space of "hsv colormap", as shown in Figure 5. The method of "Colormap index" works by mapping matrix values onto a preset colormap. One thing to note, Different from the familiar HSV-color mode, the "hsv colormap" in Matlab is also coded by RGB mode (Gonzalez, Woods) (Hartley and Zisserman, 2003). By using this method, the image is convolved in the form of three-channel (RGB) respectively. A wider receptive field can be obtained during the traversal operation of the convolution kernel (Morteza et al., 2021), thus achieving higher recognition accuracy.

The significance of Figure 5 is that the color index at the bottom of the image represents the size of the wavelet coefficient from small to large. The horizontal axis is the sampling time axis, and the vertical axis is the scale axis. By adjusting the color value at the bottom of the image, the color domain of the phase space depth map can be changed to obtain different images. Figure 6 is the phase space map with the color domain changed. The above processing is applied to the data we obtained from 48 groups of experiments, and the 480 images are labeled artificially according to load types and working conditions. The data sets are set for subsequent classification detection. The use of "hsv colormap" will also be more convenient for the image enhancement method above.

By this way, we obtain the time-frequency domain characteristics of arc faults at various scales. Image transformation can fuse features better and meet the requirements of subsequent neural networks for data dimension. In addition, compared with complex data features and matrix feature, graph features is more friendly to users without prior knowledge. In fact, wavelet analysis can be combined with control algorithm to achieve the purpose of optimizing performance in engineering field. For example, combining with particle swarm optimization algorithm to adjust the wavelet parameters and improve the performance of pattern recognition algorithm, or using Morlet wavelet function as the activation function of neural network to fit the parameters of robot travel (Dutta et al., 2013) (Vázquez et al., 2015). We attempt to improve the performance of neural networks for small sample datasets from the perspective of image feature engineering in the following sections.

4 ResNet50 arc detection model

Deeper convolutional neural networks can learn deeper data features. The identity mapping of neural networks between network layers is realized by updating network weights. The learning process of neural networks is the process of updating the weights between network layers through the back propagation of gradients between network layers (Amora et al., 2022). According to the chain

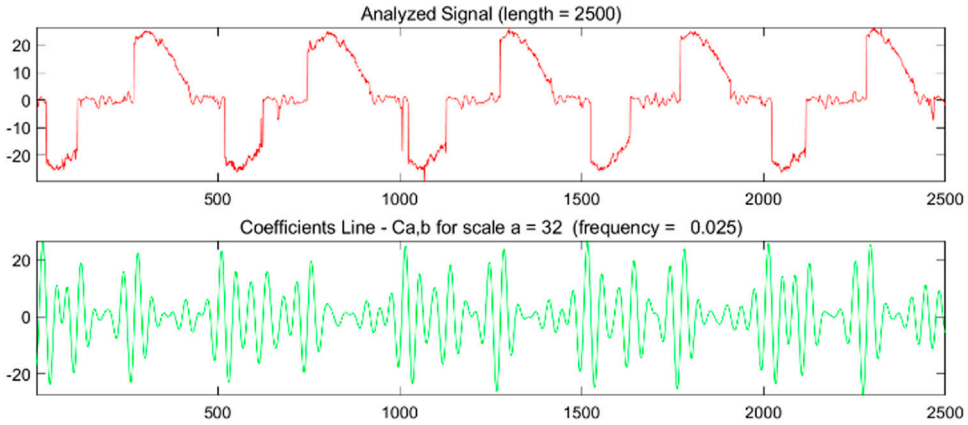

FIGURE 4
Original time domain signal and wavelet coefficient value curve of incandescent lamp fault.

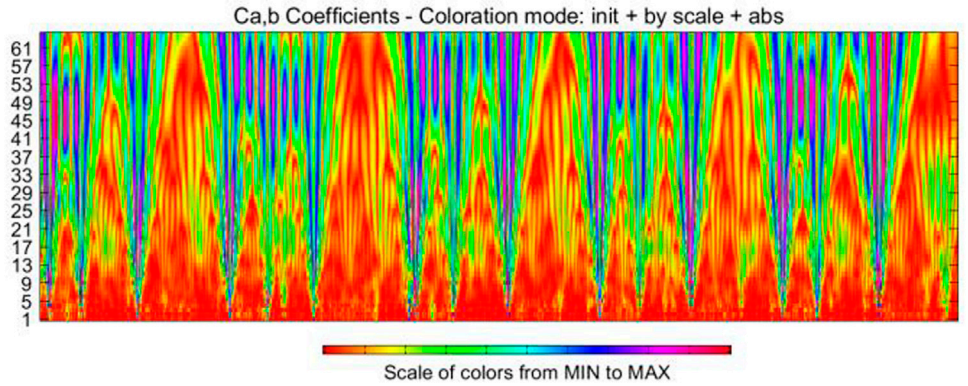

FIGURE 5
Depth map of phase space of continuous wavelet transform.

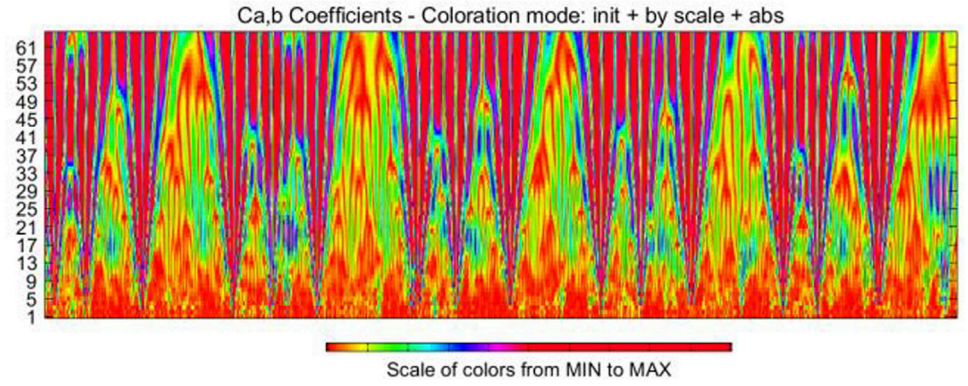

FIGURE 6
Phase space image of wavelet coefficients after changing color domain.

derivative rule, gradient disappearance or gradient explosion will occur with the increase of neural network layers. Normalization of data can alleviate this phenomenon.

4.1 Batch-normalization

In order to prevent the simple linear relationship between the input and output of neural network neurons, we use ReLU as the activation function to add non-linearity to the neurons. The processed function can approximate any non-linear function. ReLU function can be expressed as Eq. 6:

$$ReLU(x) = \begin{cases} x, & if\ x > 0 \\ 0, & if\ x \le 0 \end{cases} \tag{6}$$

For deep neural networks, the distribution of neuron input values will shift with the training process. The overall distribution will approach the extreme value of non-linear function generally. The addition of batch-normalization fixes the distribution of input values across layers to a standard normal distribution with an expectation of 0 and variance of 1 (Huang et al., 2021). One-hot labels are set for the four data sets, and 8 images in each sub-data set are used as mini-batch for training to improve training efficiency. Batch-normalization for input of neurons in layer K of neural network through input value X after activation function can be expressed as Eq. 6:

$$\hat{x}^{(k)} = \frac{x^{(k)} - E[x^{(k)}]}{\sqrt{Var[x^k]}} \tag{7}$$

Where, $E[x^{(k)}]$ and $V_{ar}[x^{(k)}]$ are the expectation and variance of the whole data set, and the normalized result $y^{(k)}$ can be obtained through network parameters $\gamma^{(k)}$ and $\beta^{(k)}$ changes:

$$y^{(k)} = \gamma^{(k)}\hat{x} + \beta^{(k)} \tag{8}$$

Accordingly, the variance and expectation in Eq. 6 should be the unbiased estimation of corresponding statistics in the mini-batch composed of every 8 images.

4.2 ResNet50 network structure

ResNet is a typical model in the field of computer vision. The proposal of ResNet enables convolutional neural network to avoid network degradation even when the number of network layers increases to a large extent (Qu et al., 2019a). As we known, deep neural networks take multi-convolutional layers as parameter mapping. According to the chain rule, deep networks face the problem of gradient explosion or gradient disappearance when calculating gradients. The idea of ResNet is to make the deep network obtain the gradient of the shallow network through the mapping of residuals. When the input parameter X maps to $H(X)$, the residual can be expressed as:

$$F(x) = H(x) - x \tag{9}$$

ResNet takes the residuals as a mapping. The input and output of the network layer are identical mappings even when gradient disappearance occurs, thus preventing the network performance degradation caused by gradient disappearance. In practical applications, the residual is usually not 0, so the network layer can learn new features from the input features to improve the accuracy of the network. The convolutional block structure of ResNet50 can be expressed in Figure 7.

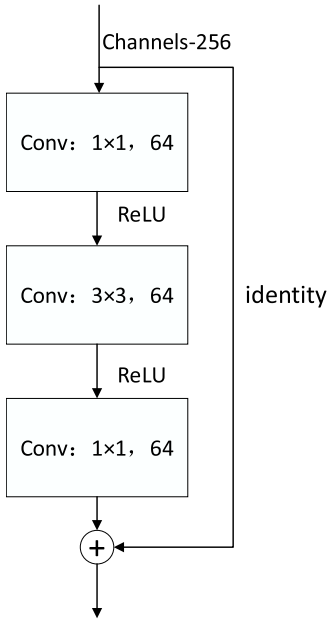

FIGURE 7
ResNet50 convolutional block structure.

TABLE 2 ResNet50 detects network structure.

Layer name	50-layer
Conv1	7 × 7,6, stride 2
Conv2_x	3 × 3, max pool, stride 2
	$\begin{bmatrix} 1\times1, 64 \\ 3\times3, 64 \\ 1\times1.256 \end{bmatrix} \times 3$
Conv3_x	$\begin{bmatrix} 1\times1, 128 \\ 3\times3, 128 \\ 1\times1, 512 \end{bmatrix} \times 4$
Conv4_x	$\begin{bmatrix} 1\times1, 256 \\ 3\times3, 256 \\ 1\times1, 1024 \end{bmatrix} \times 6$
Conv5_x	$\begin{bmatrix} 1\times1, 512 \\ 3\times3, 512 \\ 1\times1, 2048 \end{bmatrix} \times 3$
	average pool,1000-d fc, softmax

ResNet can be expressed as the mathematical model shown in Eq. 10:

$$y = F(x, \{W_i\}) + x \tag{10}$$

Where x is the input vector, y is the output vector, and F is the residual mapping, which is part of network training. The convolutional Block in Figure 7 skips two layers, and its residual mapping can be expressed as:

TABLE 3 Neural network training hyperparameters.

Hyperparameter	Value
Image size	100 × 100
Batch size	8
Epoch	20
Target category	4

$$F = W_3\sigma(W_2\sigma(W_1x)) \tag{11}$$

We use different convolution kernels for convolution with step 2 and maximum pooling respectively, and then restore ResNet using convolution block as shown in Figure 7. Softmax layer is added in the output layer of the network to predict the type of feature and the maximum value is the prediction category. The specific model of the network is shown in Table 2:

4.3 Implementation of the detection method

The process of arc fault detection can be summarized as the following steps:

1. The arc fault current data of different loads are obtained by experiments.
2. The fault features of 64 scales were obtained by Morlet wavelet analysis.
3. "Colormap index method" is used to convert numerical features into image features. Image data is preprocessed using data enhancement graph.
4. The fault dataset is put into ResNet50 for classification detection.

4.4 Classification and detection results of arc fault

The image data set is divided into training set and test set according to the ratio of 9:1, and the hyperparameters of the neural network are adjusted through repeated training so that the neural network can obtain higher classification accuracy. Since 480 images are relatively small image samples, Adam algorithm is added to dynamically adjust the learning rate of neural network in order to prevent the increase of loss caused by uneven distribution of image samples in each iteration. Hyperparameters are adjusted through several experiments. The pre-trained model with the highest accuracy is selected as the result. The final neural network hyperparameters are shown in Table 3.

All the algorithms above are implemented based on Keras platform interface Tensorflow. The neural network is trained on Intel I7-9750H processor (8G RAM) and the graphics card is NVIDIA RTX 2060 (6G).

In order to reflect the changes in the accuracy of training set and validation set in each epoch during the training process, the average accuracy and loss changes in each epoch are made into curves, and the training results were shown in Figure 8.

The accuracy rate in the figure is the average of each epoch, and the image on the right is the change curve of the cross-entropy loss function.

In order to compare the training connection of the network, the accuracy of training set better, the accuracy of verification set and the loss value of epoch18-20 are expressed in numbers, as shown in Table 4:

As can be seen from Figure 8, the accuracy of the verification set began to be lower than that of the training set since the epoch is 11. When the epoch is 20, the accuracy of the training set still showed an upward trend, while the loss tended to converge. The accuracy of the verification set is 30% lower than that of the training set, which indicates that the network has a certain over-fitting phenomenon. Due to the small number of samples in the dataset and the image data obtained through color domain transformation, many images may have certain similarity. Insufficient sparsity of data samples may lead to uneven distribution of samples.

5 Image data enhancement

5.1 Image preprocessing

Neural networks achieve the purpose of classification by fitting the distribution of the training dataset. Suppose the data distribution P (x, y) is known, where x is the feature, y is the label, Given a specific loss function $\mathcal{L}(\cdot)$, for a model assuming h$\in \mathcal{H}$. We expect a machine learning algorithm to minimize its expected risk, which is defined as Eq. 12.

$$R(h) = \int \mathcal{L}(h(x), y)dp(x, y) = \mathbb{E}[\mathcal{L}(h(x), y)] \tag{12}$$

In fact, the data distribution P (x, y) is usually unknown, so it is difficult to be integrated. Propose that the number of samples with labels is I. We approximate this distribution with the sampling results, and seek to minimize the empirical risk. Here, "experience" means the data set obtained by sampling. Eq. 12 can be rewritten as Eq. 13

$$R_I(h) = \frac{1}{I}\sum_{i=1}^{I}\mathcal{L}(h(x_i), y_i) \tag{13}$$

The parameter h can be represented in the following ways:

$$\hat{h} = arg_h^{min}R(h) \tag{14}$$

Where $\hat{h}$ is the theoretical assumption optimal value. Because the data distribution of the sample set is unknown, the value of $\hat{h}$ cannot be found.

$$h^* = arg_{h\in H}^{min}R(h) \tag{15}$$

Where h^* is the constraint value assumed to minimize the expected risk in the data space $h \in \mathcal{H}$.

$$h_I = arg_{h\in H}^{min}R_I(h) \tag{16}$$

This equation represents the optimal hypothesis h_I obtained by optimizing on a specified data set of amount I and minimizing the empirical risk under the specified hypothesis space h$\in \mathcal{H}$.

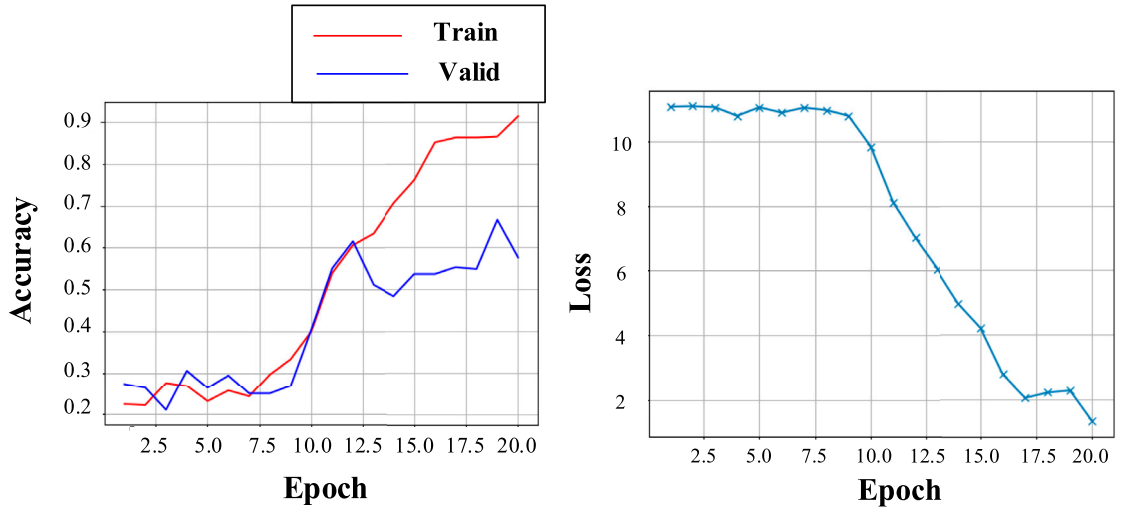

FIGURE 8
Training accuracy and loss curves of ResNet50.

TABLE 4 ResNet50 training accuracy rate and loss change table.

layers	Epoch	Train accuracy (%)	Valid accuracy (%)	loss
50	18	86.34	54.86	2.21
	19	86.57	66.67	2.28
	20	91.43	57.64	1.31

Two error forms of the assumed distribution and the actual distribution can be obtained through the three equations above.

$$\mathcal{E}_{app}(\mathcal{H}) = \mathbb{E}\left[R(h^*) - R\left(\hat{h}\right)\right]$$
$$\mathcal{E}_{est}(\mathcal{H}, I) = \mathbb{E}[R(h_I) - R(h^*)] \quad (17)$$

Where $\mathcal{E}_{app}$ denotes the difference between the optimal solution h^* of the hypothetical space $\mathcal{H}$ and the ideal value $\hat{h}$ under the expected loss. $\mathcal{E}_{est}$ represents the error between the data sample and the assumed data distribution. The performance of the network can be improved by reducing the above errors. When the amount of training data increases, the neural network will get more supervision information. $R(h_I)$ can approximates $R(h^*)$ better (Wang et al., 2019) (Zhang et al., 2021). The performance of the network can be improved by reducing the above errors. In order to solve the problem of neural network overfitting caused by small sample data sets. We used the following two kinds of non-linear image transformation methods to amplify the dataset.

1) Random gamma variation of the image

Gamma change is also known as the curve gray change of color image. In the field of image processing, gamma change of image is often used to adjust the contrast. Gamma change is a non-linear change acting on pixel gray value, which can be expressed mathematically as Eq. 18:

$$S = T(r) = Cr^{\gamma} \quad (18)$$

Where, S is the gray value after gamma changes, and C is the gray scale coefficient, which is 1 in this paper. "r" is the gray value of the image input, and its value range is [0,1]. γ is the gamma influence factor, we change the value of gamma randomly to amplify the original image. When the gamma value is greater than 1, the area of the image with lower gray value will be stretched, and the part with higher gray value will be compressed. For gamma values less than 1, the reverse action is performed. The image is converted to grayscale image to make the subsequent image computation less. The description of gray image, like color image, still reflects the distribution and characteristics of the overall and local chromaticity and highlight level of the whole image. The images after gamma changes are shown in Figure 9.

2) Random rotation of the image

Rotate the image at random Angle without changing the size of the image. Fill the free part of the rotation with black and the images after random Angle rotation are shown in Figure 10.

The original image is changed by the above two methods, and 5 new images are obtained for each image. The new dataset contains 960 images, which is two times the size of the original dataset.

5.2 Network training results after data enhancement

On the basis of not changing epoch and mini-Batch parameters, we use the enhanced data set to conduct neural network training of ResNet50. After training, the average accuracy and average loss of the training set and verification set on each epoch are shown in Figure 11:

When the epoch is 23–25, the classification training results of neural network can be expressed in Table 5:

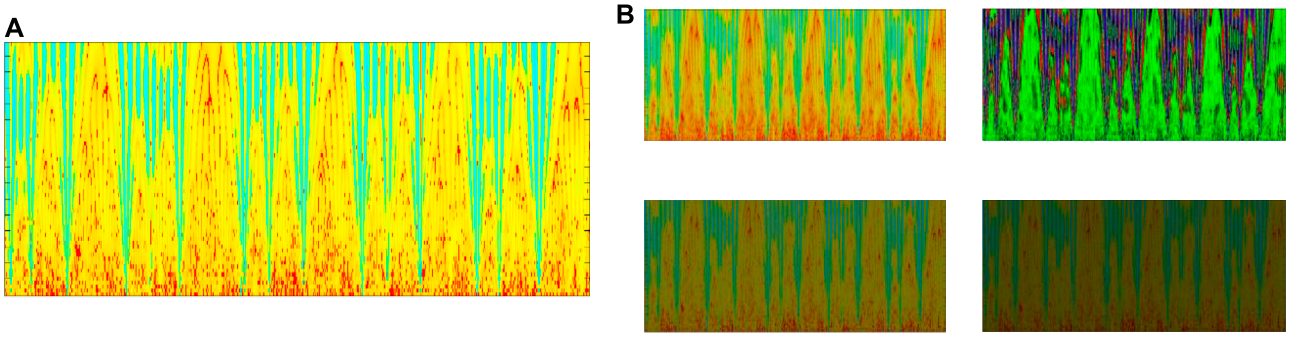

FIGURE 9
Gamma change of the image, **(A)** is the original image, and **(B)** is the image after gamma change.

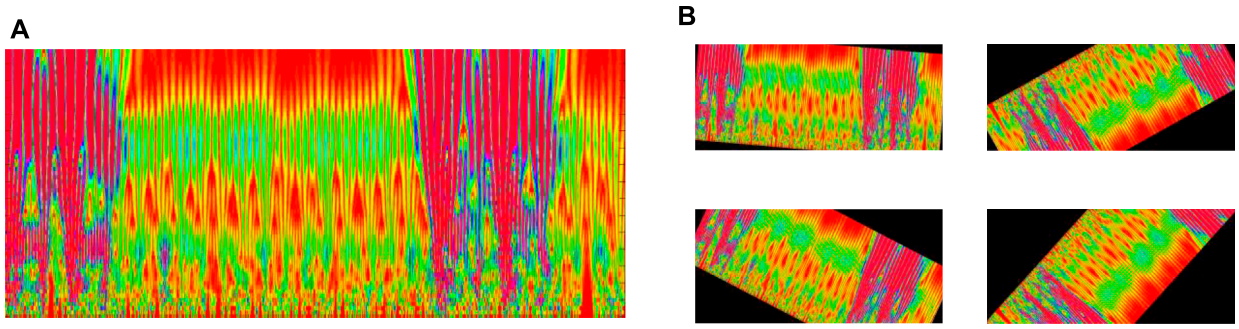

FIGURE 10
Random Angle changes of the image, **(A)** is the original image, **(B)** is the changed image.

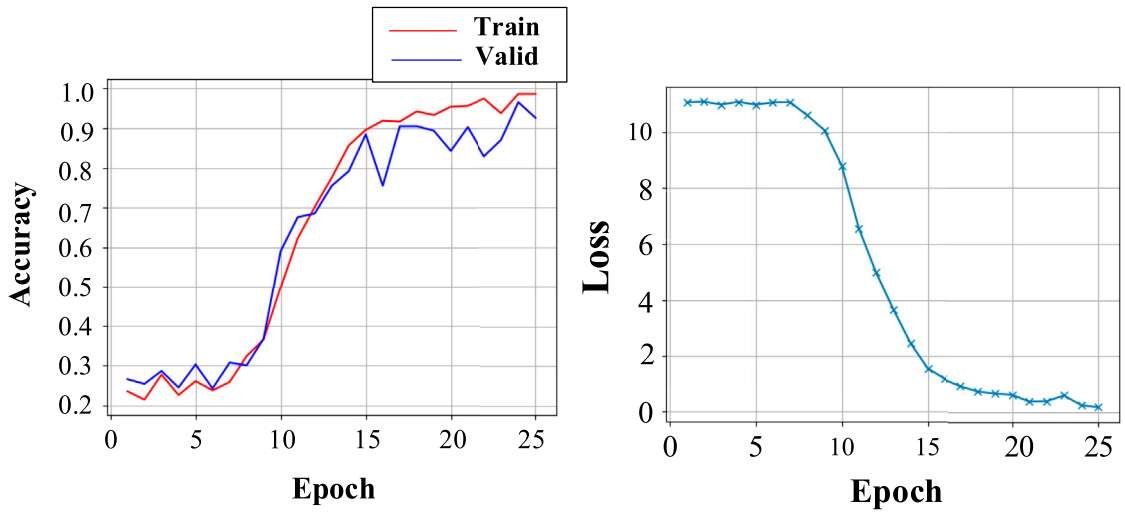

FIGURE 11
ResNet50 training results after data enhancement.

It can be seen that the over-fitting phenomenon of neural network is solved after adding data enhancement to the data set. The network obtained the highest accuracy of validation set and training set when the epoch is 24. Compared with Table 4, the loss value of the neural network is generally lower, indicating that the neural network had learned more image features and the

TABLE 5 ResNet50 classification training results after data enhancement.

layers	Epoch	Train accuracy (%)	Valid accuracy (%)	loss
50	23	93.75	87.04	0.60
	24	98.61	96.53	0.25
	25	98.61	92.59	0.18

TABLE 6 Other typical computer vision network pre-training results.

Network	Train accuracy (%)	Valid accuracy (%)	loss
ResNet50	98.61	96.53	0.25
AlxNet	24.77	12.5	11.09
InceptionV4	23.84	28.47	11.12
VGG19	24.68	12.5	11.09

preprocessing of the data set is effective (Li et al., 2021) (Qu et al., 2019b).

5.3 The comparison experiment

We set up a comparison method to verify the detection performance of ResNet50. In addition, we consider verifying whether our proposed method is suitable for classical lightweight networks including AlxNet, InceptionV4 and VGG19. The image data enhancement method also applied in the comparing methods. To ensure convergence of the loss function, we increased the hyperparameter epoch in the comparison test to 50. However, other neural networks showed serious overfitting phenomenon. Hence the "early stop" has been carried out. The network pre-training results are shown in Table 6.

It can be seen that the accuracy of other typical networks is maintained at 20%–30%. The loss function stays around 11 which suggests that the network is not learning the deeper features of the image. Due to the limitation of the fault conditions, it is difficult to obtain large numbers of fault samples. Compared with ResNet, the visual model above is prone to the problem of gradient disappearance/explosion when dealing with small samples and similar data.

6 Conclusion

This paper presents a series arc fault detection method combining Morlet wavelet analysis and computer vision. Common load arc fault current is sampled by sampling resistance method. The Morlet wavelet with the scale of 64 is applied to deep fault feature fusion.

The matrix composed of wavelet coefficients is mapped to images by HSV color index. The image data is used as the feature to establish the detection data set, and the data categories are annotated manually. ResNet50 is applied to feature image recognition. In addition, we propose a data enhancement method of image random gamma transform and random rotation. Experimental results show that data enhancement can effectively improve the over-fitting phenomenon of neural network, and improve the detection accuracy to 96.53%.

It is worth mentioning that the image feature extraction in this paper provides a new method for feature selection. More researches can be done on image features, such as dimensionality reduction of image level data, image preprocessing that can change network performance, and image expression of typical network regularization.

Computer vision has brought a lot of convenience to our life. Just like face recognition, we look forward to applying computer vision to fault arc detection.

Data availability statement

The original contributions presented in the study are included in the article/supplementary material, further inquiries can be directed to the corresponding author.

Author contributions

ZS is responsible for the main body of the article NQ a is responsible for directing the experiment CH and TZ are responsible for the revision and data processing of the article.

Funding

This work is supported in part by the National Natural Science Foundation of China under Grant 61901283 and National Natural Science Foundation of China (Grant No 62003080, U22A2055, 62273058), and the Fundamental Research Funds for the Central Universities (Grant No N2204011).

Conflict of interest

The authors declare that the research was conducted in the absence of any commercial or financial relationships that could be construed as a potential conflict of interest.

Publisher's note

References

Amora, D. J. A., Deocadiz, A. B., Sañejo, G. L., Santiago, C. J. R., Umali, M. G., and Arenas, S. U. (2022). "NPK prediction based on pH colorimetry utilizing ResNet for fertilizer recommender system," in IET International Conference on Engineering Technologies and Applications, Changhua Taiwan, 14-16 October 2022 (IET-ICETA), 1–2. doi:10.1109/IET-ICETA56553.2022.9971508

ByPaul, S. A. (2016). *The illustrated wavelet transform handbook introductory theory and applications in science, engineering, medicine and finance*, Boca Raton: CRC Press, 978.

Cao, Y., Li, J., Sumner, M., Christopher, E., and Thomas, D. (2013). "Arc fault generation and detection in DC systems," in IEEE PES Asia-Pacific Power and Energy Engineering Conference, Hong Kong, 08-11 December 2013 (APPEEC), 1–5. doi:10.1109/APPEEC.2013.6837123

Chen, H., Gan, Z., and Yang, H. (2014). "Realizing speech enhancement by combining EEMD and K-SVD dictionary training algorithm," in The 9th International Symposium on Chinese Spoken Language Processing, Singapore, 12-14 Sept. 2014 (IEEE), 378.

Chu, R., Schweitzer, P., and Zhang, R. (2020). Series AC arc fault detection method based on high-frequency coupling sensor and convolution neural network. *Sensors* 20 (17), 4910. doi:10.3390/s20174910

Cui, R., and Li, Z. (2021). arc fault detection and classification based on three-dimensional entropy distance and EntropySpace in aviation power system[J]. *Trans. China Electrotech. Soc.* 36 (04), 869–880. doi:10.19595/j.cnki.1000-6753.tces.191717

Cui, R., and Li, Z (2021)arc fault detection based on phase space reconstruction and principal component analysis in aviation power system. *Trans. China Electrotech. Soc.* 41(14):5054–5065. doi:10.13334/j.0258-8013.pcsee.201323

Cui, R., and Tong, D. (2021). Frequency domain analysis and feature extraction of aviation AC arc fault and crosstalk[j]. *Electr. Mach. Control* 25 (06), 18–26. doi:10.15938/j.emc.2021.06.003

De, P., Chatterjee, A., and Rakshit, A. (2021). Regularized K-SVD-Based dictionary learning approaches for PIR sensor-based detection of human movement direction. *IEEE Sensors J.* 21 (5), 6459–6467. doi:10.1109/jsen.2020.3040228

Dutta, S., Pal, S. K., Mukhopadhyay, S., and Sen, R. (2013). Application of digital image processing in tool condition monitoring: A review. *CIRP J. Manuf. Sci. Technol.* 6, 212–232. doi:10.1016/j.cirpj.2013.02.005

Ferracuti, F., Schweitzer, P., and Monteriù, A. (2021). Arc fault detection and appliances classification in AC home electrical networks using recurrence quantification plots and image analysis. *Electr. Power Syst. Res.* 201, 107503. doi:10.1016/j.epsr.2021.107503

Gonzalez, R. C., and Woods, R. E. (2021). *Digital image processing*. second edition. Upper Saddle River, New Jersey, United States: Prentice-Hall. 7-5053-7798.

Hartley, R., and Zisserman, A. (2003). *Multiple view geometry in computer vision*. Cambridge: Cambridge University Press, 655.

Huang, G., Qiao, L., Khanna, S., Pavlovich, P. A., and Tiwari, S. (2021). Research on fan vibration fault diagnosis based on image recognition. *J. Vibroengineering* 23 (6), 1366–1382. doi:10.21595/jve.2021.21935

Humbert, J. B., Schweitzer, P., and Weber, S. (2021). Serial-arc detection by use of Spectral Dispersion Index (SDI) analysis in a low-voltage network (270V HVDC) [J]. *Electr. Power Syst. Res.* 196, 107084.doi:10.1016/j.epsr.2021.107084

Ji, H., Kim, S., and GyungSuk, K. (2020). Phase analysis of series arc signals for low-voltage electrical devices. *Energies* 13 (20), 5481. doi:10.3390/en13205481

Joga, S. R. K., Sinha, P., and Maharana, M. K. (2021). Performance study of various machine learning classifiers for arc fault detection in AC microgrid. *IOP Conf. Ser. Mater. Sci. Eng.* 1131 (1), 012012. doi:10.1088/1757-899x/1131/1/012012

Johnson, J., and Kang, J. (2012). "Arc-fault detector algorithm evaluation method utilizing prerecorded arcing signatures," in 38th IEEE Photovoltaic Specialists Conference, Austin, TX, USA, 03-08 June 2012, 001378–001382. doi:10.1109/PVSC.2012.6317856

Kadian, P., Arora, N., and Arora, S. M. (2019). "Performance evaluation of robust watermarking using DWT-SVD and RDWT-SVD," in 6th International Conference on Signal Processing and Integrated Networks (SPIN), Noida, 07-08 March 2019, 987–991.

Ku, W., Storer, R. H., and Georgakis, C. (1995). Disturbance detection and isolation by dynamic principal component analysis. *Chem. Intel. Lab. Syst.* 30 (1), 179–196. doi:10.1016/0169-7439(95)00076-3

Lala, H., and Subrata, K. (2020). Classification of arc fault between broken conductor and high-impedance surface: An empirical mode decomposition and stockwell transform-based approach. *Transm. Distribution* 14 (22), 5277–5286. doi:10.1049/iet-gtd.2020.0340

Li, B., Zhang, Z., Duan, F., Yang, Z., Zhao, Q., Sun, Z., et al. (2021). Component-mixing strategy: A decomposition-based data augmentation algorithm for motor imagery signals. *Neurocomputing* 465, 325–335. doi:10.1016/j.neucom.2021.08.119

Liu, G., and Du, S. (2017). Research on LV arc fault protection and its development trends. *Power Syst. Technol.* 41 (01), 305–313. doi:10.13335/j.1000-3673.pst.2016.0804

Lu, S., Rui, M., Phung, T., Tharmakulasingam, S., Daming, Z., et al. (2021). Lightweight transfer nets and adversarial data augmentation for photovoltaic series arc fault detection with limited fault data[J]. *Int. J. Electr. Power Energy Syst.* 130, 107035. doi:10.1016/j.ijepes.2021.107035

Mallat, S., and Zhong, S. (1992). Characterization of signals from multiscale edges. *IEEE Trans. Pattern Analysis Mach. Intell.* 14 (7), 710–732. doi:10.1109/34.142909

Miao, W., Wang, Z., Wang, F., Lam, K. H., and Pong, P. W. T. (2023). Multicharacteristics Arc model and autocorrelation-algorithm based arc fault detector for DC microgrid. *IEEE Trans. Industrial Electron.* 70 (5), 4875–4886. doi:10.1109/TIE.2022.3186351

Morteza, S., Samir, K., Mohammad-Hadi, P., Ramazan-Ali, J-T., et al. (2021). Damage detection on rectangular laminated composite plates using wavelet based convolutional neural network technique. *Compos. Struct.* 278, 114656. doi:10.1016/j.compstruct.2021.114656

Qu, N, and Wang, J. (2018). A series arc fault detection method based on Cassie model and L3/4 norm[J]. *Power Syst. Technol.* 42 (12), 3992–3997. doi:10.13335/j.1000-3673.pst.2017.3091

Qu, N., Wang, J., and Liu, J. (2019). An Arc fault detection method based on current amplitude spectrum and sparse representation. *IEEE Trans. Instrum. Meas.* 68 (10), 3785–3792. Response to the editor and reviewer. doi:10.1109/tim.2018.2880939

Qu, N, Zuo, J., and Chen, J. (2019). Series Arc fault detection of indoor power distribution system based on LVQ-NN and PSO-SVM[J]. *IEEE Access* 2019(7), 184019–184027. doi:10.1109/ACCESS.2019.2960512

Shu, L., and Wang, P. (2018). Study on dynamic circuit model of DC icing flashover based on improved time-varying arc equation[J]. *Trans. China Electrotech. Soc.* 33 (19), 4603–4610. doi:10.19595/j.cnki.1000-6753.tces.171391

Vázquez, L. A., Jurado, F., and Alanís, A. Y. (2015). Decentralized identification and control in real-time of a robot manipulator via recurrent wavelet first-order neural network. *Math. Problems Eng.* 451049, 1–12. doi:10.1155/2015/451049

Vozalis, M. G., and Margaritis, K. G. (2006). Applying SVD on generalized item-based filtering. *IJCSA* 3 (3), 27–51.

Wang, L, Qiu, H., and Yang, P. (2021). arc fault detection algorithm based on variational mode decomposition and improved multi-scale fuzzy entropy. *Energies* 14 (14), 4137. doi:10.3390/en14144137

Wang, Y., Yao, Q., and Kwok, J. (2019). Generalizing from a few examples: A survey on few-shot learning,//arXiv: 1904.05046.

Xia, Z., Chen, Y., and Xu, C. (2022). Multiview PCA: A methodology of feature extraction and dimension reduction for high-order data. *IEEE Trans. Cybern.* 52, 11068–11080. doi:10.1109/tcyb.2021.3106485

Xiang, C., and Wang, H. (2019). Research on the combustion process of vacuum arc based on an improved pulse coupled neural network model[J]. *Trans. China Electrotech. Soc.* 34 (19), 4028–4037. doi:10.19595/j.cnki.1000-6753.tces.181158

Xiong, Q., and Chen, W. (2020). Review of research progress on characteristics, detection and localization approaches of fault arc in low voltage DC system. *Proc. CSEE [j]* 40 (18), 6015–6027. doi:10.13334/j.0258-8013.pcsee.200330

Zhang, C., Xia, K., Feng, H., Yang, Y., and Du, X. (2021). Tree species classification using deep learning and RGB optical images obtained by an unmanned aerial vehicle. *J. For. Res.* 32 (05), 1879–1888. doi:10.1007/s11676-020-01245-0

Zhao, H., and Qin, H., A series fault arc detection method based on the fusion of correlation theory and zero current feature. 2020,41(04):218–228. doi:10.19650/j.cnki.cjsi.J2006019

frontiers | Frontiers in Energy Research

TYPE Correction
PUBLISHED 14 December 2023
DOI 10.3389/fenrg.2023.1326226

OPEN ACCESS

APPROVED BY
Frontiers Editorial Office,
Frontiers Media SA, Switzerland

*CORRESPONDENCE
Na Qu,
11502332@qq.com

RECEIVED 23 October 2023
ACCEPTED 29 November 2023
PUBLISHED 14 December 2023

CITATION
Shuai Z, Qu N, Zheng T, Hu C and Lu S (2023), Corrigendum: Research on arc fault detection using ResNet and gamma transform regularization.
Front. Energy Res. 11:1326226.
doi: 10.3389/fenrg.2023.1326226

Corrigendum: Research on arc fault detection using ResNet and gamma transform regularization

Zhang Shuai[1], Na Qu[1]*, Tianfang Zheng[1], Congqiang Hu[1] and Senxiang Lu[2]

[1]School of Safety Engineering, Shenyang Aerospace University, Shenyang, China, [2]Northeastern University, Shenyang, China

KEYWORDS

morlet continuous wavelet, arc fault, ResNet, regularization, color index

A Corrigendum on
Research on arc fault detection using ResNet and gamma transform regularization

by Shuai Z, Qu N, Zheng T Hu C and Lu S (2023). Front. Energy Res. 11:1069119. doi: 10.3389/fenrg.2023.1069119

In the published article, there was a missing **affiliation**. A second author affiliation should be added as follows.

"[2]Northeastern University, Shenyang, China"

In the published article, there was an error in the **author list**, and author Senxiang Lu[2] was erroneously excluded. The corrected author list appears below.

"Zhang Shuai[1], Na Qu[1,*], Tianfang Zheng[1], Congqiang Hu[1], Senxiang Lu[2]"

Incorrect Funding

In the published article some **funding** information was not included. The corrected **Funding Statement** appears below.

Funding

This work is supported in part by the National Natural Science Foundation of China under Grant 61901283 and National Natural Science Foundation of China (Grant No 62003080, U22A2055, 62273058), and the Fundamental Research Funds for the Central Universities (Grant No N2204011).

The authors apologize for these errors and state that this does not change the scientific conclusions of the article in any way. The original article has been updated.

Publisher's note

frontiers | Frontiers in Energy Research

TYPE Original Research
PUBLISHED 24 March 2023
DOI 10.3389/fenrg.2023.1141235

OPEN ACCESS

EDITED BY
Shiping Wen,
University of Technology Sydney,
Australia

REVIEWED BY
Pradeep Vishnuram,
SRM Institute of Science and Technology,
India
Minh Quan Duong,
The University of Danang, Vietnam
Nima Rezaei,
Lakehead University, Canada

*CORRESPONDENCE
Paresh Kumar Nayak,
paresh@iitism.ac.in

SPECIALTY SECTION
This article was submitted
to Smart Grids,
a section of the journal
Frontiers in Energy Research

RECEIVED 10 January 2023
ACCEPTED 06 March 2023
PUBLISHED 24 March 2023

CITATION
Prabhu MS, Biswas S, Nayak PK,
Abdelaziz A and El-Shahat A (2023), An
intelligent protection scheme for series-
compensated transmission lines
connecting large-scale wind farms.
Front. Energy Res. 11:1141235.
doi: 10.3389/fenrg.2023.1141235

An intelligent protection scheme for series-compensated transmission lines connecting large-scale wind farms

M. S. Prabhu[1], Sauvik Biswas[2], Paresh Kumar Nayak[3]*, Almoataz Abdelaziz[4] and Adel El-Shahat[5]

[1]Electrical and Electronics Engineering, Vel Tech Rangarajan Dr Sagunthala R&D Institute of Science and Technology, Chennai, India, [2]Electrical Engineering, Indian Institute of Technology, Delhi, India, [3]Electrical Engineering, Indian Institute of Technology (ISM), Dhanbad, India, [4]Faculty of Engineering and Technology, Future University in Egypt, Cairo, Egypt, [5]Energy Technology Program, School of Engineering Technology, Purdue University, West Lafayette, IN, United States

Series-compensated transmission lines (SCTLs) are increasingly preferred for transmitting bulk amounts of electricity generated from the present-day large-scale wind farm to the utility grid due to several technical and economic benefits. However, when a fault occurs in such a wind farm-integrated SCTL, the impedance across the metal oxide varistor (MOV)-protected series capacitor varies non-linearly. Also, the fault current contributed from the wind farm side is quite different compared to the grid side. Consequently, the widely used fixed impedance-based distance relaying schemes showed limitations when used for protecting such crucial TLs. In this paper, the impacts of series compensation and wind farm integration on distance relay are investigated, and this paper proposes an intelligent relaying scheme using only the current measurements. In the proposed scheme, the fault detection task is performed using the signs of the half-cycle magnitude differences of the line end positive-sequence currents, and the fault classification task is performed using only the local current measurements processed through the Fourier–Bessel series expansion (FBSE) bagging ensemble (BE) classifier. The non-stationary components present in the current signal at the initiation of a fault are captured by calculating FBSE coefficients, and the singular value decomposition is applied for dimensionality reduction of the feature set. Finally, the extracted features are used by the BE classifier for fault classification. The method is evaluated in MATLAB/Simulink® on numerous fault and non-fault data simulated in two-bus systems and also validated through the OPAL-RT (OP4510) manufactured real-time digital simulation platform. The obtained results (response time for fault detection and classification $<10\,ms$), including the comparative assessment results (fault detection accuracy = 100% and fault classification accuracy = 99.37%), justify the effectiveness of the proposed relaying scheme in protecting the wind farm-integrated SCTLs.

KEYWORDS

series-compensated transmission line, DFIG-WTG, large-scale wind farm, distance relay, fault detection, fault classification, bagging ensemble classifier

1 Introduction

1.1 Background and motivation of the research

In recent years, a considerable growth has been observed in electricity generation using wind energy across the world (Chaurasiya et al., 2019). Currently, the doubly fed induction generator (DFIG) is one of the most accepted wind turbine generators (WTGs) due to its various technical and economic advantages (Lopez et al., 2007). The large-scale DFIG-based wind farms are usually integrated to the utility grid through high-voltage transmission lines (HV-TLs). However, the restrictions on building new transmission facilities due to environmental and economic reasons impose main barriers in harnessing the full potential of the wind energy. To get rid of the problem, series-compensated transmission lines (SCTLs) are increasingly preferred nowadays for transmitting the bulk amount of electricity generated from large-scale wind farms to the utility grid (Varma et al., 2008), (Varma and Moharana, 2013). However, the power electronics interfaced distributed energy resources, especially large-capacity solar photovoltaic plants (Hoang et al., 2022) or large-capacity DFIG-WTGs with low-voltage ride through (LVRT) capability (Li et al., 2018), have quite unusual fault patterns compared to conventional synchronous generators. Also, the non-linear functioning of the metal oxide varistor (MOV) protecting the series capacitor produces unusual fault currents and causes rapid variation in the line impedance, especially during the first one or two cycles after the initiation of the faults. Consequently, the widely used fixed impedance-based distance relaying schemes, when used for protecting such wind farm integrated SCTLs, show limitations in providing fast and reliable protection. Motivated by the previous issues, an improved relaying scheme is proposed in this paper with an intention of ensuring fast and reliable protection to SCTL connecting large-scale DFIG-based wind farms.

1.2 Literature review

In the last decade, several improved relaying schemes were reported in the literature in order to provide fast and reliable protection to large-scale DFIG-based wind farm-integrated HV-TLs compensated with/without series capacitors. The merits and demerits of each of the available methods are discussed in the following.

The detailed theoretical analysis of the dynamic behavior of the DFIG during symmetrical and asymmetrical voltage sags is studied by Lopez et al. (2007) and Ouyang and Xiong (2014) and Lopez et al. (2008) and Xiao et al. (2015), respectively. It is demonstrated that asymmetrical voltage sags are more dangerous than symmetrical voltage sags. Different adaptive trip boundary-setting techniques are proposed for distance relays protecting DFIG-based wind farm-connected TLs (Pradhan and Joos, 2007; Sadeghi, 2012; Dubey et al., 2014; Chen et al., 2017a; Ma et al., 2018; Prasad and Biswal, 2020; Prasad et al., 2020). In the study by Sadeghi (2012), an adaptive trip boundary-setting technique is proposed for distance relay protecting a wind farm-connected TL using an artificial neural network (ANN). In that scheme, line impedance is estimated using the wind farm-side voltage and current measurements first and then trained using a scaled conjugate gradient backpropagation technique. However, to obtain higher accuracy, a large dataset is built for the ANN. The adaptive distance relay setting for the line connecting the wind farm is proposed by Dubey et al. (2014). Line-end voltage and current signals are used for adaptive trip boundary setting. However, no information is provided about the type of generator and related wind farm control and protection strategies.

In Chen et al. (2017a), zone-2 of the distance relay is set adaptively using an adaptive branch coefficient according to the fault type and equivalent sequence impedances of WTGs. Another adaptive distance protection scheme is proposed by Ma et al. (2018) to protect low-voltage collector lines of DFIG-based wind farms using the phase relationship of the fault current. Recently, swarm intelligence-assisted adaptive threshold-based differential protection schemes have been proposed by Prasad and Biswal (2020), (Prasad et al., 2020), to protect DFIG wind farm-integrated TLs. However, all the previously conducted studies for adaptive distance relay settings are not specific to the fault characteristics of DFIG-WTGs and mostly require line-end voltage and current measurements to implement the adaptive protection schemes. The other protection schemes such as the time-domain-based distance relaying algorithm (Lopez et al., 2007), modified permissive overreach transfer trip method (Hooshyar et al., 2014), unit protection scheme (Ghorbani et al., 2017), transient-based distance protection scheme (Chen et al., 2017b), zero-sequence impedance-based relaying algorithm (Fang et al., 2018), and wavelet transform (WT)-based protection approach (Yang et al., 2020) are also proposed for the protection of DFIG-based wind farm-connected TLs.

The limitations of distance relay protecting SCTLs are documented in several research articles (Novosel et al., 1997; Altuve et al., 2009; Vyas et al., 2014; Hoq et al., 2021). Furthermore, newer solutions are reported in the literature to ensure improved protection for such SCTLs (Abdelaziz et al., 2005; Dash et al., 2006; Nayak et al., 2014; Mishra et al., 2019). Only (Sivov et al., 2016; Sahoo and Samantaray, 2017; Mishra et al., 2021; Mohamed et al., 2021), improved protection schemes are proposed for SCTLs (compensated with either a fixed series capacitor (FSC) or a thyristor-controlled series capacitor (TCSC)) connected with large-scale wind farms. In the study by Sivov et al. (2016), an adaptive zone setting method is proposed for the distance relay protecting a fixed series capacitor-compensated transmission line connected to the wind power plant. However, for the implementation of the adaptive setting, the method requires both end voltage and current measurements and current measurements before and after the series compensation. Thus, it requires a dedicated communication medium for implementation of the protection scheme. In the study by Sahoo and Samantaray (2017), a protection solution is proposed for TCSC-compensated lines connecting DFIG-based wind farms using line-end synchronized voltage and current measurements at a sampling frequency of 200 kHz. From a practical implementation point of view, such a high-frequency sampling may not be economically attractive. Another adaptive distance relaying scheme is proposed recently by Mohamed et al. (2021) for fast and reliable protection of TCSC-compensated HV-TL connecting wind farms using line-end voltage and current measurements received through a limited

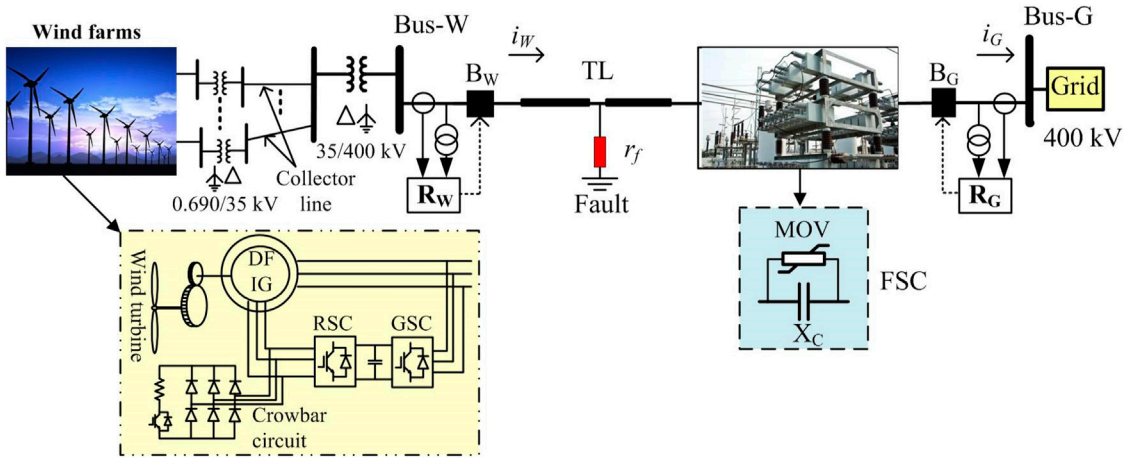

FIGURE 1
Single-line diagram of a two-bus test power system (in this study, the zone-1 reach of R_W and R_G is set equal to 80% length of the TL).

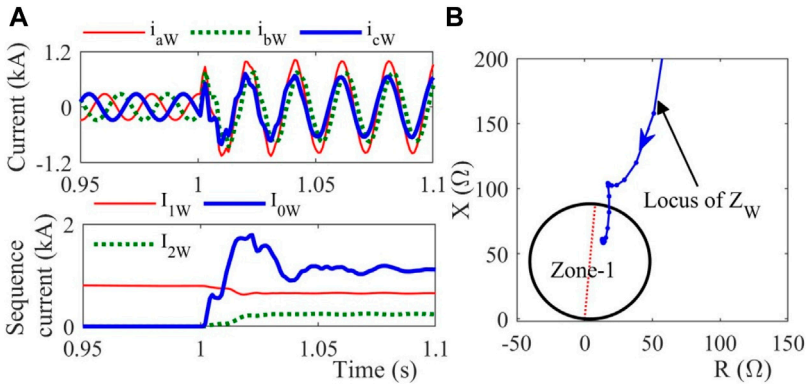

FIGURE 2
Demonstration of the impacts of unbalanced ground faults (cg-type) on relay R_W protecting the large-scale DFIG wind farm-connected TL.

communication facility. Another traveling wave-based fault location technique is proposed by Mishra et al. (2021) for an FSC-compensated TL connecting DFIG-based wind farm using line-end voltage measurements at a sampling frequency of 1,000 kHz.

The aforementioned study clearly shows that, in most of the published papers, the fault behaviors of large-scale DFIG-based wind farms and their impacts on distance relaying-based TL protection schemes are studied thoroughly and demonstrated through simulation results. Similarly, several articles are reported to provide enhanced protection to SCTLs. However, except a few, none of the methods have studied the simultaneous impacts of the integration of DFIG-based wind farms and series compensation on distance relaying-based TL protection schemes. Also, the relaying schemes proposed for improved protection of DFIG-based wind farm-integrated FSC/TCSC-compensated HV-TL require both end voltage and current measurements. Thus, efficacies of the available methods depend very much on the communication medium. Also, some of the schemes require data at a very high sampling frequency. Thus, from a practical implementation point of view, the available methods will be costlier. Hence, an economically feasible improved protection scheme is very much essential at this point for effective protection of the SCTL connecting large-scale DFIG-based wind farms.

1.3 Contribution and paper organization

In this paper, a new intelligent fault detection and classification technique is proposed for an FSC-compensated TL connecting large-scale DFIG-based wind farms. The main contributions including the novelty of the present work are highlighted as follows:

- The impacts of FSC compensation and DFIG-based wind farm integration on the performance of the distance relay are investigated rigorously through both analytical study and simulation results
- The use of the sign of the half-cycle magnitude difference of the line-end positive-sequence currents for fast and accurate detection of faults in the DFIG-based wind farm-integrated

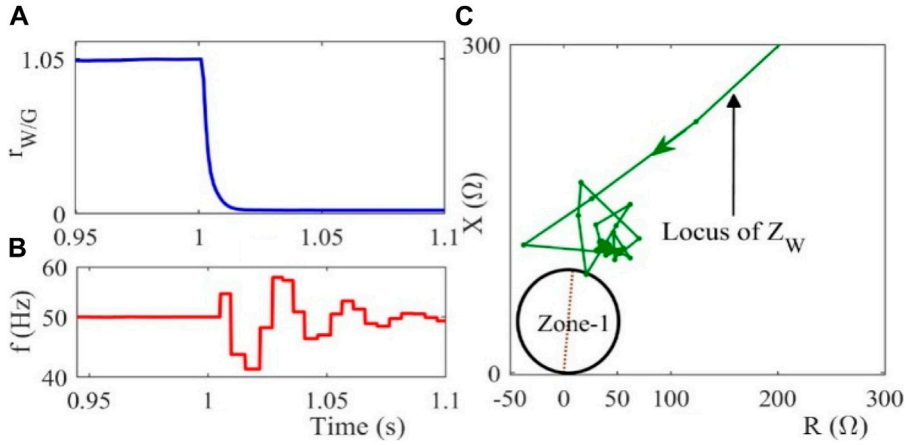

FIGURE 3
Demonstration of the impacts of three-phase faults on the performance relay R_W protecting the large-scale DFIG wind farm-connected TL.

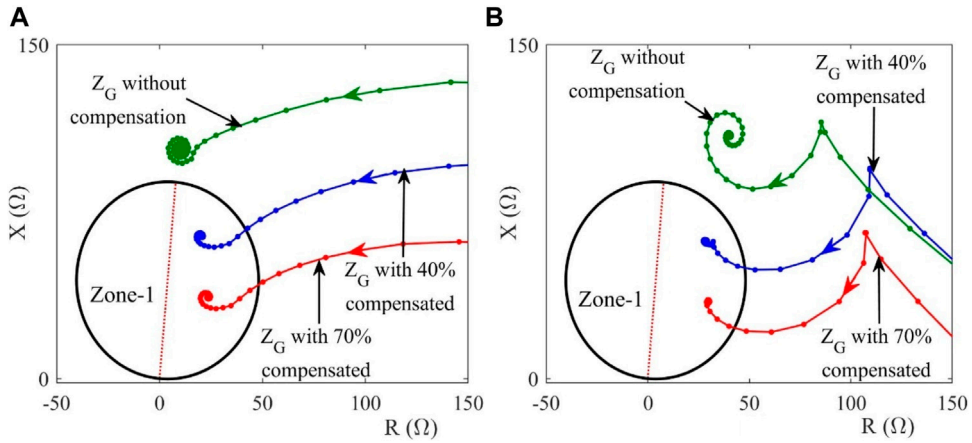

FIGURE 4
Demonstration of the impacts of balanced and unbalanced ground faults on relay R_G during **(A)** abcg-fault and **(B)** ag-fault.

FSC-compensated TL is the main novelty and contribution of the present work

- The extraction of useful features from the grid-side measured currents using an efficient time-frequency signal processing technique known as Fourier–Bessel series expansion (FBSE) and an efficient matrix decomposition technique, namely, the singular value decomposition (SVD), and furthermore, fast and accurate classification of the fault using a bagging ensemble classifier is another novelty and the second main contribution of the present work
- Validation and implementation of the proposed method through MATLAB/Simulink® and OPAL-RT (OP4510)-manufactured real-time digital simulation (RTDS) platforms on numerous fault and non-fault data simulated in a two-bus test system are another contribution of the present work

The rest of this paper is organized as follows. The impacts of the installation of FSC compensation and integration of DFIG-based windfarms on the conventional distance relay are investigated in detail in Section 2. The proposed fault detection and classification technique is elaborated in Section 3. Results and discussions and comparative results are provided in Sections 4 and Section 5, respectively. Validation of the proposed protection scheme in the RTDS platform is demonstrated in Section 6. Finally, the conclusion of the paper is provided in Section 7.

2 Protection challenges of FSC-compensated TLs connecting large-scale wind farms

The two-bus system, as shown in Figure 1, is simulated in MATLAB/Simulink® for evaluating the impacts of the FSC compensation and wind farm integration on distance relays. Specifications of each of the system components are provided in Appendix. As shown in the figure, the crowbar circuit is

installed on the rotor side of the DFIG-WTG to protect the rotor-side converter (RSC) during grid voltage sags. The wind farm with LVRT capability acts as a weak power system compared to the utility grid. Different converters (Nayak et al., 2022) and optimization techniques (Vishnuram et al., 2021) are considered for the study. In the present research, the large capacity DFIG-WTG satisfies LVRT capability during grid faults as per the requirement of the Indian grid code (Central Electricity Regulatory Commission, 2010). The DFIG-WTG with LVRT capability produces unusual sequence currents that generally affect the performance of the wind farm-side distance relay R_W (Lopez et al., 2007), (Pradhan and Joos, 2007). Furthermore, as series compensation is provided at the grid side of the line, the non-linear operation of the MOV protecting the series capacitor during a fault in the TL will result in a non-linear variation of the line impedance (Novosel et al., 1997; Abdelaziz et al., 2005; Altuve et al., 2009; Vyas et al., 2014; Hoq et al., 2021). Thus, it will affect the performance of the grid-side distance relay R_G. Therefore, the performance of both-side distance relays needs to be tested.

2.1 Impact study on wind farm-side relay R_W

The wind farm is usually connected to the grid through a star-grounded HV transformer, as shown in Figure 1. As the wind farm side is delta connected, it restricts the flow of zero-sequence current when a ground fault occurs in the interconnected TL. The zero-sequence current of the ground fault is limited only by the zero-sequence impedance of the HV transformer and the TL. Thus, higher magnitudes of zero-sequence current than positive- and negative-sequence currents exist as the wind farm side acts as a weak power supply system. The unusual sequence components of current during ground fault and the control action of the DFIG-WTGs with LVRT capability affect the performance of wind farm-side distance relay R_W.

To test the performance of relay R_W of Figure 1 during ground faults, a cg-fault (r_f = 10 Ω) is started at 1 s on the 400-kV line at a distance of 270 km (90% length of the line) from R_W with a wind speed v = 15 m/s and an FSC compensation level (*CL*) = 40%. The result for the fault case is shown in Figure 2. As shown in Figure 2A, the magnitude and wave shape of phase-c current and the sequence currents produced are pretty unusual due to the grounding arrangements and control actions of the DFIG-WTGs. Due to the high magnitude of zero-sequence current and the limited increase in fault current magnitude of phase-c, the impedance Z_W (= $\bar{V}_{cW}/(\bar{I}_{cW} + k_0\bar{I}_{0W})$, where $\bar{V}_{cW}$ and $\bar{I}_{cW}$ are the voltage and current phasors of phase-c; k_0 is the residual compensation factor; and $\bar{I}_{0W}$ is the zero-sequence current) seen at relay R_W is reduced compared to the impedance between the relay and the fault point. As a result, even if the fault has occurred outside of zone-1, the impedance seen at relay R_W enters its zone-1 characteristics. A similar result is also obtained for other types of ground faults. This shows that when used to protect TLs connecting large-scale DFIG-WTGs, the conventional distance relay will face an overreaching problem.

The apparent impedance Z_W seen at relay R_W (Figure 1) during a balanced three-phase fault can be computed as (Biswas and Nayak, 2021a)

$$Z_W = \frac{\bar{V}_W}{\bar{I}_W} = \left(Z_{Wf} + r_f\right) + \frac{r_f}{r_{W/G}} \tag{1}$$

where $r_{W/G} = \bar{I}_W/\bar{I}_G$. During faults in the interconnected TL, the contribution of current from the wind farm side is relatively low compared to the grid side due to the control action and weak system of the DFIG-WTG causing $r_{W/G} \ll 1$. As a result, the impedance seen at relay R_W due to even low fault resistance r_f is magnified, which may impose an underreach problem on R_W.

To test the performance of R_W, the result of a three-phase fault (r_f = 5 Ω) started at a distance of 210 km (70% length of the TL) from R_W with v = 15 m/s is shown in Figure 3. As observed in Figure 3A, during steady-state, $r_{W/G} \cong 1$ shows the power flow from the wind farm to the utility grid. However, at the inception of a three-phase fault at 1 s, $r_{W/G} \ll 1$ due to a significantly high contribution of $\bar{I}_G$ compared to $\bar{I}_W$.Also, the control action of DFIG-WTG produces subharmonics apart from the fundamental frequency component, which is evident from Figure 3B. The low current contribution from the wind side and high fluctuations in the frequency components introduce errors in the impedance calculation at relay R_W, resulting in underreach problems evident in Figure 3C.

2.2 Impact study on grid-side relay R_G

As in Figure 1, series compensation in the fault loop affects the apparent impedance measured by grid-side distance relay R_G. The apparent impedance Z_G measured at relay R_G for different faults (abc/abcg, ag, and ab/bag types) when occurring at *F* (Figure 1) can be computed as (Biswas and Nayak, 2019)

$$Z_{G(abcg)} = \frac{\bar{V}_{G1}}{\bar{I}_{G1}} = Z_{Gf} + \frac{\bar{V}_{FSC1}}{\bar{I}_{G1}} + \frac{\bar{I}_{f1}}{\bar{I}_{G1}} r_f \tag{2}$$

$$Z_{G(ag)} = \frac{\bar{V}_{Ga}}{\bar{I}_{Ga} + k_0\bar{I}_{G0}} = Z_{Gf} + \frac{\bar{V}_{FSCa}}{\bar{I}_{Ga} + k_0\bar{I}_{G0}} + \frac{\bar{I}_{fa}}{\bar{I}_{Ga} + k_0\bar{I}_{G0}} r_f \tag{3}$$

$$Z_{G(ab/abg)} = \frac{\bar{V}_{Ga} - \bar{V}_{Gb}}{\bar{I}_{Ga} - \bar{I}_{Gb}} = Z_{Gf} + \frac{\bar{V}_{FSCa} - \bar{V}_{FSCb}}{\bar{I}_{Ga} - \bar{I}_{Gb}} + \frac{\bar{I}_{fa} - \bar{I}_{fb}}{\bar{I}_{Ga} - \bar{I}_{Gb}} r_f \tag{4}$$

In (2)–(4), the voltage drops across the FSC, i.e., $\bar{V}_{FSC}$, varies non-linearly, especially during the first one or two cycles after the initiation of the fault due to the non-linear functioning of the MOV protecting the FSC. As a result, relay R_G will see variable impedance at least during the first one or two cycles after the initiation of the fault, where actually the distance relay takes the decision and hence can affect the performance of R_G.

To evaluate the performance of R_G, the results of two typical fault cases are demonstrated here. The first one is a three-phase fault (abcg-type) created at 270 km (90%-line length) away from R_G while v = 10 m/s and compensation levels are 40% and 70%, respectively. Results for the test cases are provided in Figure 4. It is evident from Figure 4A that the relay R_G faces an overreach problem due to the presence of series compensation in the fault loop. Another ag-fault is created, keeping the fault distance and wind speed the same. The characteristics of the relay R_G are shown in Figure 4B. In this fault case also, R_G faces an overreaching problem.

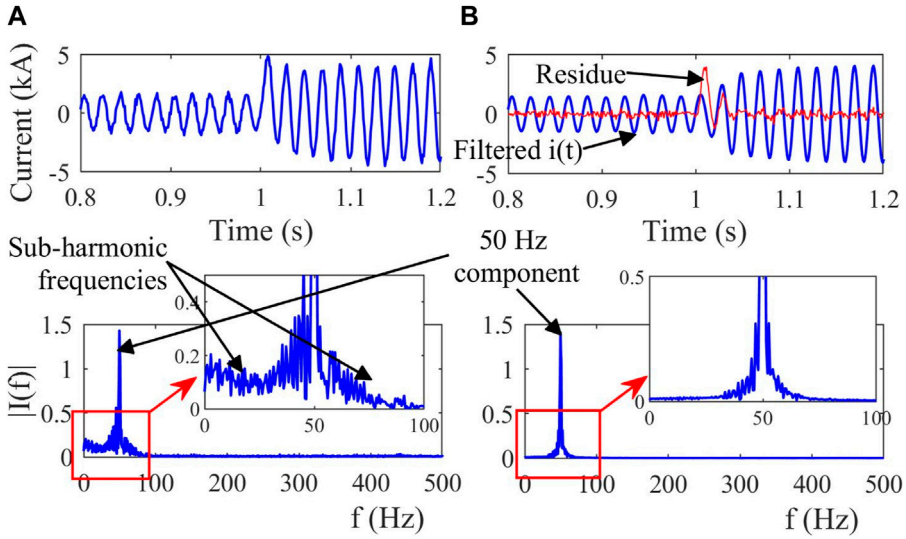

FIGURE 5
Demonstration of the elimination of subharmonic components from the contaminated fault current signal using the Weiner filter.

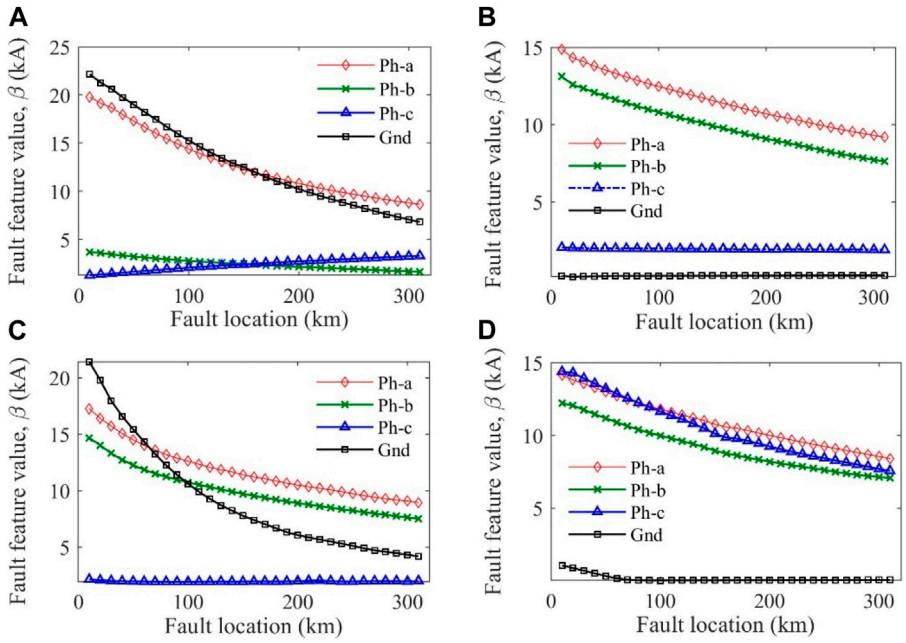

FIGURE 6
Demonstration of the variation of fault feature β with fault locations for **(A)** ag-fault, **(B)** ab-fault, **(C)** abg-fault, and **(D)** abc-fault.

3 Proposed protection scheme

In the present work, signs of the half-cycle magnitude differences of the line end positive-sequence currents are utilized for discriminating internal faults from external faults. Furthermore, the currents measured at the utility grid side are processed through FBSE and the SVD, and finally, the BE classifier is used for fault classification. The calculation steps of the proposed fault detection and classification scheme are provided in the following sections in detail.

3.1 Proposed fault detection technique

Let the three-phase currents of the grid side and wind farm side be denoted as $(\bar{I}_{aG}, \bar{I}_{bG}, \bar{I}_{cG})$ and $(\bar{I}_{aW}, \bar{I}_{bW}, \bar{I}_{cW})$,

TABLE 1 Parameter variation for the generated 6000 possible fault cases.

Parameters	Cases	No. of cases
Fault types (*FTs*)	ag, bg, cg, ab, bc, ca, abg, bcg, cbg, abc.	10
Fault resistance (R_f)	1, 10, 30, 200 Ω.	4
Fault location (L_f)	20%, 40%, 60%, 80%, 100% of line length.	5
Fault inception angle (*FIA*)*	0^0, 54^0, 90^0, 144^0, 180^0.	5
Compensation level (*CL*)	40%, 70%.	2
Wind speed (v)	5, 10, 15 m/s.	3
Total number of fault cases generated = **10** × **4** × **5** × **5** × **2** × **3** = **6000**		

*Fault inception angle is set about negative to positive zero crossing of phase-a voltage.

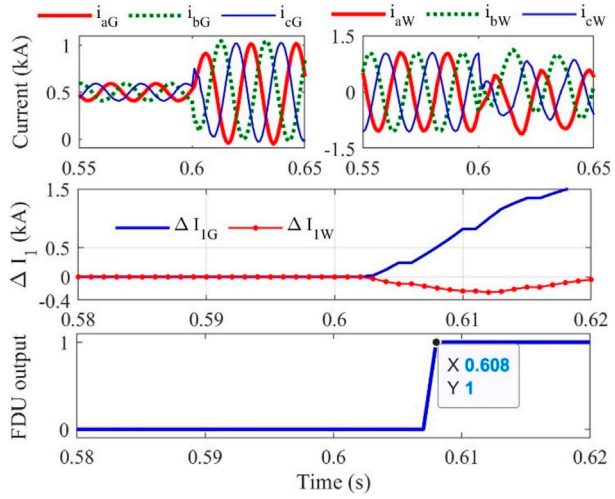

FIGURE 7
Result during a balanced 3ph-fault.

respectively. The positive-sequence currents at the grid side ($\bar{I}_{1G}$) and the wind farm side ($\bar{I}_{1W}$) are computed from three-phase currents using the Fortescue transform as follows (Fortescue, 1918):

$$\bar{I}_{1G} = \frac{1}{3}\left[\bar{I}_{aG} + \alpha\bar{I}_{bG} + \alpha^2\bar{I}_{cG}\right],\ \bar{I}_{1W} = \frac{1}{3}\left[\bar{I}_{aW} + \alpha\bar{I}_{bW} + \alpha^2\bar{I}_{aW}\right] \quad (5)$$

where $\alpha = e^{j2\pi/3}$. In the present work, phasor currents are computed from the measured time-domain currents using the full-cycle discrete Fourier transform (DFT). The half-cycle magnitude differences of the positive-sequence currents at the grid side and the wind farm side are calculated as follows (Biswas and Nayak, 2021b):

$$\begin{aligned}\Delta I_{1G}(n) &= \left|\bar{I}_{1G}(n)\right| - \left|\bar{I}_{1G}(n - P/2)\right| \text{ and } \Delta I_{1W}(n)\\ &= \left|\bar{I}_{1W}(n)\right| - \left|\bar{I}_{1W}(n - P/2)\right| \end{aligned} \quad (6)$$

where P represents the no. of samples/cycles.

It is observed from the simulation results that at the inception of an internal fault, there is a reduction in positive-sequence current magnitude from the wind farm side, whereas there is an increase in positive-sequence current magnitude from the grid side to the fault point. Consequently, the half-cycle magnitude differences of the positive-sequence current at the wind farm side become negative just after initiating an internal fault. On the other hand, the half-cycle magnitude differences of the positive-sequence current at the grid side become positive just after initiating an internal fault. As a result, the signs of ΔI_{1G} and ΔI_{1w} are opposite during the inception of an internal fault. This distinguishing feature, i.e., the signs of ΔI_{1G} and ΔI_{1w}, is utilized in this paper for discriminating internal faults from external faults and any other non-fault transients.

During steady-state system operating conditions, $|\Delta I_{1G}| = |\Delta I_{1w}| = 0$. However, due to frequency variations during the switching of loads, low magnitudes of ΔI_{1G} and ΔI_{1w} are observed. Thus, to make ΔI_{1G} and ΔI_{1w} zeros during normal operation/non-fault transients, a significantly small threshold $\varepsilon = 0.005$ is set as

$$\Delta I_{1G}, \Delta I_{1w} = \begin{cases} 0; & |\Delta I_{1G}| = |\Delta I_{1w}| < \varepsilon \\ \Delta I_{1G}, \Delta I_{1w}; & \text{otherwise} \end{cases} \quad (7)$$

Thus, the proposed fault detection unit (FDU) detects a fault when the criterion in (8) is satisfied.

$$sign(\Delta I_{1G}) \neq sign(\Delta I_{1W}) \rightarrow FDU\ output = 1 \quad (8)$$

Elimination of noise and subharmonics from the fault current signals using the Weiner filter

The use of anti-aliasing filters in DFT restricts the noise in the fault current signals. However, the DFT has a limitation in eliminating subharmonic components generated in the wind farm-side fault current due to the control actions of the DFIG. In this work, the Weiner filter removes subharmonics from the fault current (Tikhonov, 1963). Let an observed signal $i(t)$ consisting of an original signal $i_o(t)$ with additive zero-mean Gaussian noise η be expressed as follows:

$$i(t) = i_o(t) + \eta \quad (9)$$

Using Tikhonov regularization, $i_o(t)$ is recovered by the ill-posed inverse method as follows (Tikhonov, 1963):

$$\underset{i_o}{min}\left\{\|i_o - i\|_2^2 + \alpha\|\partial_t i_o\|_2^2\right\} \quad (10)$$

where α is the variance of noise η. The Euler–Lagrange equations are solved in the Fourier domain as follows:

$$\mathcal{F}\{i(\omega)\} = i/\left(1 + \alpha\omega^2\right) \quad (11)$$

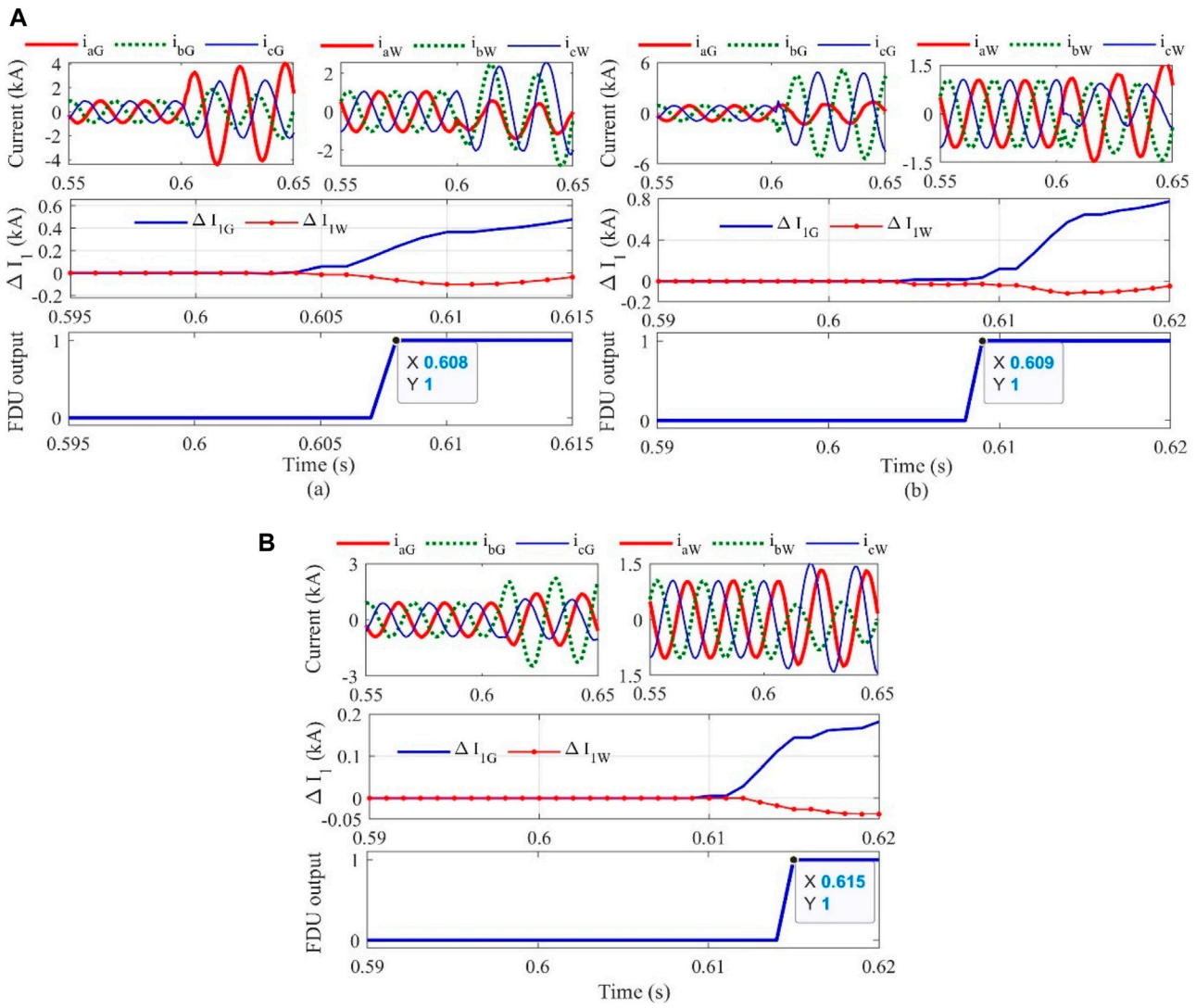

FIGURE 8
Results during **(A)** unbalanced fault, (a) ag-fault, (b) bc-fault and **(B)** high-resistance fault.

Here, the estimated signal i_o is a low-pass narrow-band selection of i around $\omega = 0$. For example, a noisy current signal $i(t)$ is chosen, and its corresponding fundamental and harmonic frequencies are shown in Figure 5A. It is evident that $i(t)$ is suffered from dominant subharmonic noise. However, the Weiner filter removes subharmonics from the current waveform, which is clearly evident from Figure 5B.

3.2 Proposed fault classification technique

The FBSE is an efficient time-frequency signal processing technique widely used to analyze non-linear and non-stationary signals. The main advantage of FBSE is that it has unique coefficients for a given signal, and the Bessel functions are aperiodic and decay over time (Pachori and Sircar, 2008). The synthesized signal from the FB coefficients has an inherent filtering property that helps reduce the noise in the low- and high-frequency regions of the spectrum. The various application areas of FBSE include speech-related applications (Gopalan, 2001), (Gopalan et al., 1997) and fault diagnosis studies (D'Elia et al., 2012), (Tran et al., 2013). In the fault diagnosis area, the FBSE and the Wigner–Ville distribution are used together to identify gear faults (D'Elia et al., 2012). Tran et al. (2013) used FBSE in association with generalized discriminant analysis and simplified fuzzy ARTMAP to diagnose induction motor faults. The mathematical backgrounds and the applicability of FBSE, SVD, and BE classifiers for TL fault classification are provided in the following.

3.3 Fourier–Bessel series expansion

As previously mentioned, the grid-side three-phase current signals are utilized for fault classification. Let the discrete-time-domain current signal of the grid side be denoted as $i_G(t)$. The FBSE

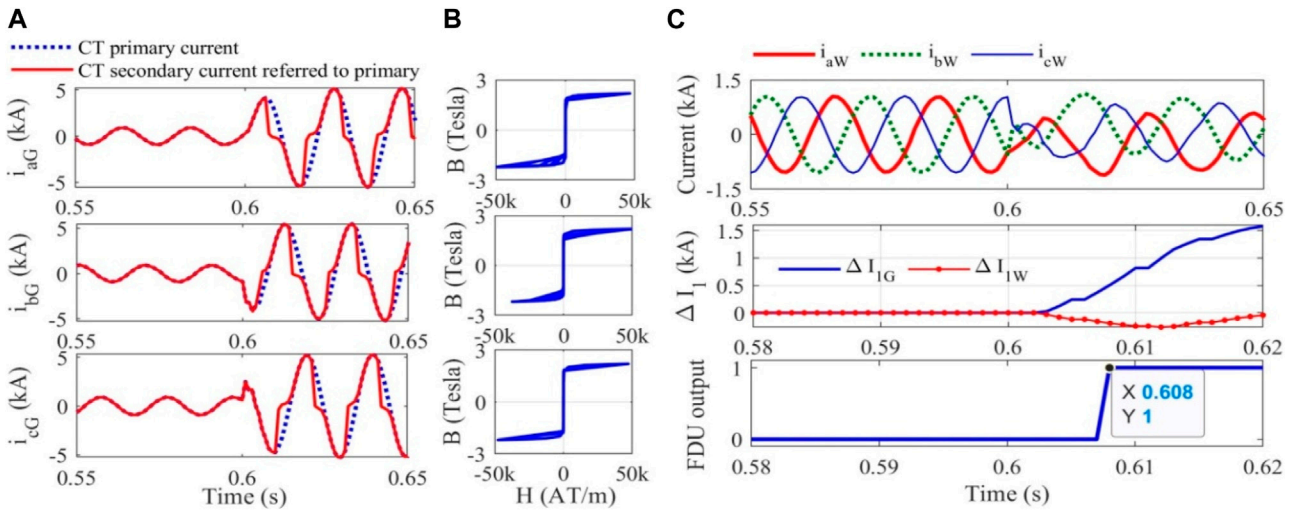

FIGURE 9
Performance of the proposed fault detection algorithm for faults producing CT saturation.

of $i_G(t)$ can be expressed using a zero-order Bessel function over some finite interval (0, a) as follows (Schroeder, 1993):

$$i_G(t) = \sum_{m=1}^{M} C_m J_0\left(\frac{\lambda_m t}{a}\right) \tag{12}$$

where $J_0(\cdot)$ are the zero-order Bessel functions, which are the solution of Bessel's differential equation.

Using the orthogonality of the set $J_0(\frac{\lambda_m t}{a})$, the FB coefficient C_m is computed as follows:

$$C_m = \frac{2\int_0^a t i_G(t) J_0\left(\frac{\lambda_m t}{a}\right) dt}{a^2 [J_1(\lambda_m)]^2} \tag{13}$$

where $J_1(\cdot)$ are the first-order Bessel functions. The integral in the numerator in the previous equation is known as the finite Hankel transform. In this paper, the values of FB coefficients C_m computed from the grid-side measured three-phase current signals are utilized as a feature. The mathematical details of FBSE for time-frequency domain analysis are provided by Gopalan (2001), Tran et al. (2013), and Schroeder (1993).

3.4 Singular value decomposition

Due to dimensionality issues, the direct use of FBSE coefficients as input feature vectors is computationally expensive. The SVD is an efficient matrix decomposition technique that can effectively reduce the vectors' dimensionality and capture the transient present in the measured time-domain signal (Pazoki, 2018). The SVD rearranges the FBSE coefficient matrix $A_{m\times n}$ into a product of three matrices as in the following equation:

$$A_{m\times n} = U_{m\times r} \Sigma_{r\times r} V^T_{n\times r} \tag{14}$$

where $U_{m\times r}$ is the orthogonal matrix, $V_{n\times r}$ is the orthogonal transpose matrix, and $\Sigma_{r\times r}$ is a diagonal matrix. $\Sigma_{r\times r}$ is expressed as follows (Mishra et al., 2018):

$$\Sigma_{r\times r} = \begin{bmatrix} \lambda_1 & 0 & \cdot & 0 & 0 \\ 0 & \lambda_2 & \cdot & 0 & 0 \\ \cdot & \cdot & \cdot & \cdot & \cdot \\ 0 & 0 & \cdot & \lambda_{r-1} & 0 \\ 0 & 0 & \cdot & 0 & \lambda_r \end{bmatrix} \tag{15}$$

where the diagonal elements $\lambda_i = (1, 2, \ldots . r)$ are called singular values of matrix $\Sigma_{r\times r}$. The singular values are all non-negative real numbers and arranged in decreasing order $(i.e, \lambda_1 \geq \lambda_2 \cdot \cdot \geq \lambda_r \geq 0)$.

In the present work, the FBSE coefficients calculated using (13) from the measured one-cycle local post-fault current signal are stored in the matrix $A_{m\times n}$. The high-frequency features stored in $A_{m\times n}$ contain the maximum energy and are susceptible to any change in the signal. Consequently, the highest change will be observed in the first singular value from the primary model characteristic of the matrix $A_{m\times n}$. Thus, in this work, the maximum value of $\Sigma_{r\times r}$, i.e., $\beta = max(\Sigma_{r\times r})$, is used as the final feature for fault classification.

The variation of the amplitudes of fault feature β derived from the grid-side three-phase currents and the zero-sequence currents concerning the location of faults for four different fault cases, i.e., ag-, ab, abg-, and abc-faults are shown in Figure 6. It is noticed that the faulty features have higher values than their healthy counterparts. This will enable faster fault classification through a suitable machine learning technique.

3.5 Bagging ensemble classifier

An ensemble-based learning algorithm has drawn considerable attention in classification and regression problems in recent years. The idea behind this learning process is to use several learners instead of a single learner and aggregate them. It produces the final decision from the collective voting from the decision of the individual learners. The BE classifier is an ensemble classifier that uses the collaborative approach of the bagging and decision tree

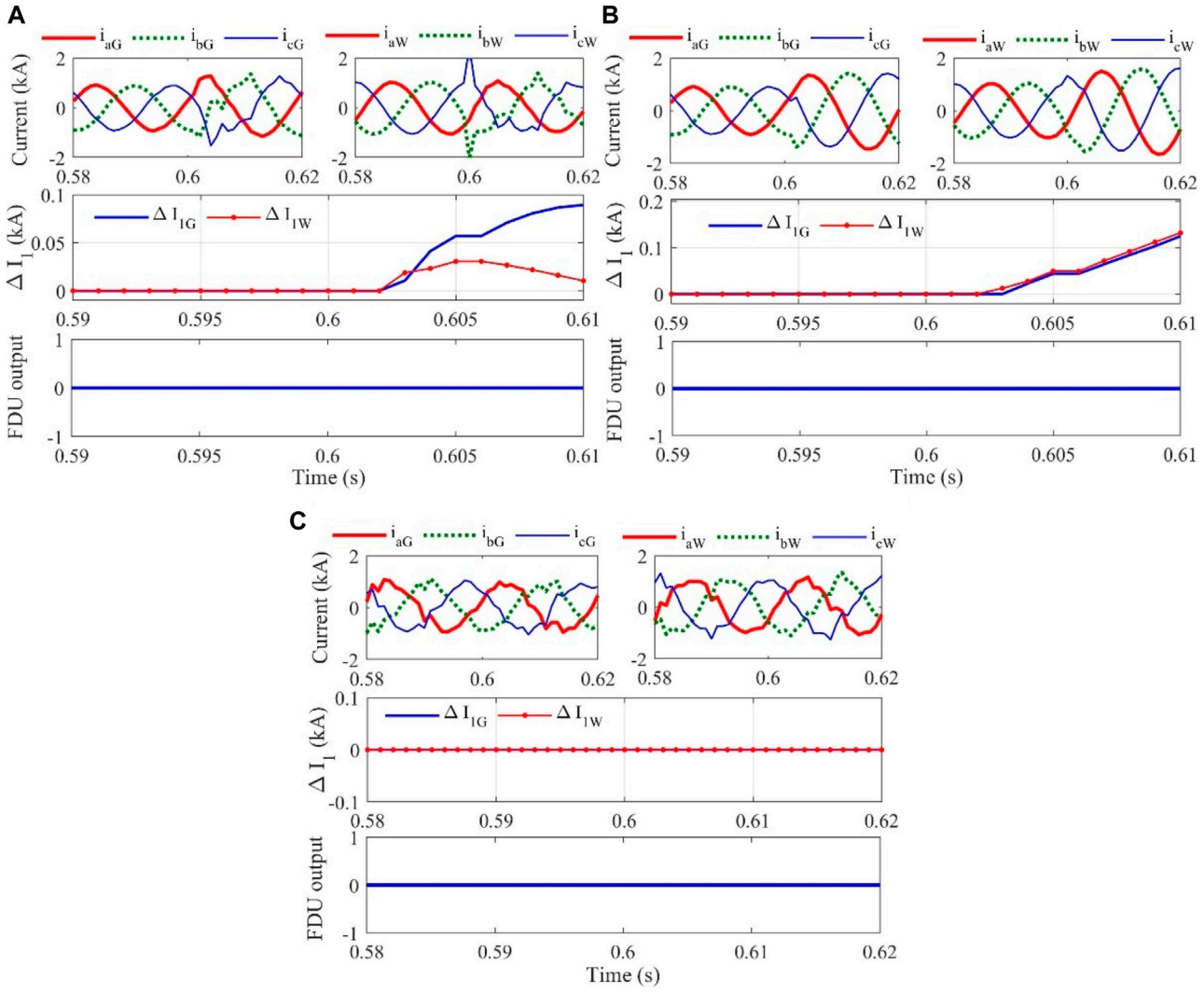

FIGURE 10
Results during switching transients: **(A)** capacitor switching, **(B)** load switching, and **(C)** presence of noise in the current signal.

(DT). The BE classifier predictor is explicitly given as follows (Ho, 1995):

$$F_{BE}^{N}(in, out) = \frac{1}{N}\sum_{i=1}^{N} T_i(in, out) \tag{16}$$

where (in, out) is the input–output set, N is the number of individual learners, and T is a single learner built from a subset of (in, out) by the bagging technique (Breiman, 2001). This bagged form of multiple learners grows in parallel and mitigates the limitations due to overfitting data with a single decision tree. The majority voting from the different bags is considered best suitable for the test set and is performed as follows:

$$S(in, out) = arg\max_{out}\left(\sum_{i=1}^{N} f\left(out = T_i(in, out)\right)\right) \tag{17}$$

Here, $f(out = T_i(in, out)) = 1$ for $out = T_i(in, out)$ is true; otherwise, $f(out = T_i(in, out)) = 0$.

4 Results and discussion

The performance of the proposed protection scheme is tested on numerous possible fault cases (= 6000 cases) simulated on the two-bus system (Figure 1) by varying different parameters as listed in Table 1. The data are generated at a sampling frequency of 1 kHz. Results of some typical fault and non-fault cases are demonstrated in the following.

4.1 Results of the proposed fault detection algorithm

4.1.1 Balanced fault

Results of a 3ph-fault initiated at 0.605 s with $L_{f=}$ 240 km away from relay R_G of Figure 1, $FIA = 90^0$, $CL = 40\%$, and $v = 10$ m/s are shown in Figure 7. As seen in the figure, the half-cycle magnitude differences of the line end positive-sequence currents ($\Delta \boldsymbol{I_{1G}}, \Delta \boldsymbol{I_{1w}}$)

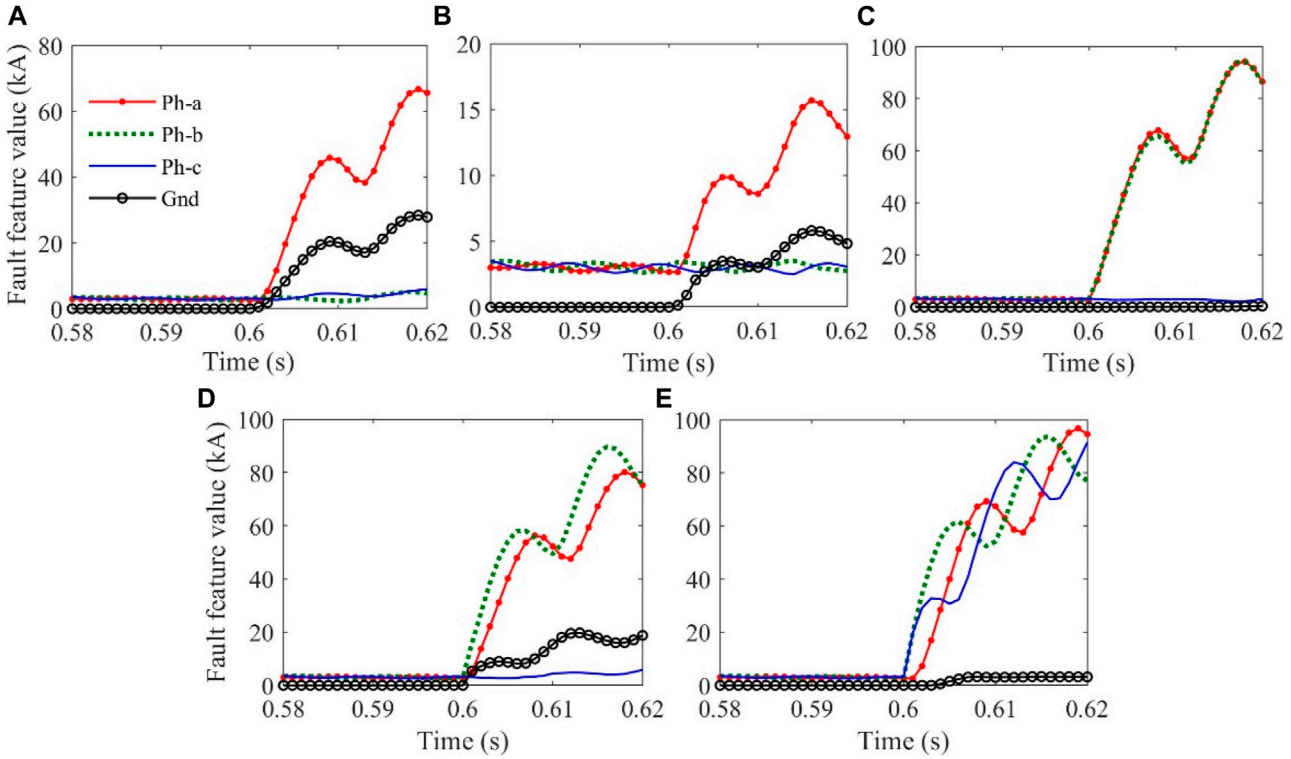

FIGURE 11
Demonstration of the variation of input fault features β to the BE classifier for few typical fault cases initiated at 0.6 s (60 km away from the grid side of Figure 1 with CL = 40%): **(A)** ag-fault (R_f = 10 Ω), **(B)** ag-fault (R_f = 200 Ω), **(C)** ab-fault, **(D)** abg-fault (R_f = 10 Ω), and **(E)** abc-fault.

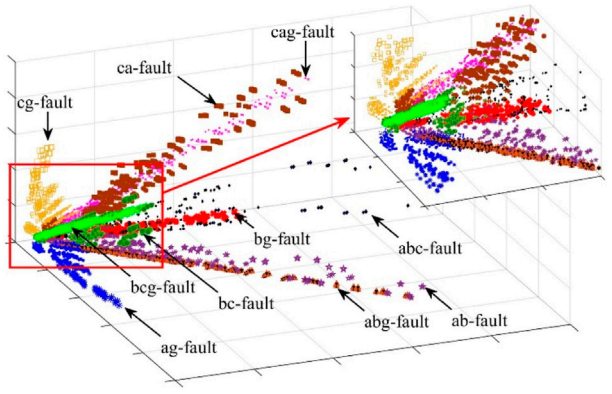

FIGURE 12
Distribution of input features for different fault cases.

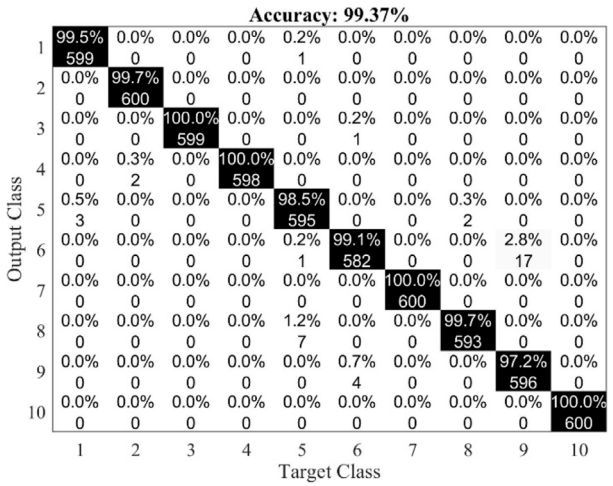

FIGURE 13
Overall confusion matrix of the BE classifier.

are of opposite signs, confirming the case of an internal fault in 3 ms only. Considering the 5 ms latency of the PLCC, the FDU activates the fault classification unit (FCU) in 8 ms.

4.1.2 Unbalanced fault

Performance is demonstrated for two different unbalanced faults: 1) an ag-fault initiated at 0.6 s (L_f = 270 km (90% length of the line) away from R_G with R_f = 10 Ω, $FIA = 0^0$, CL = 40%, and v = 5 m/s) and 2) a bc-fault initiated at 0.605 s (L_f = 210 km (70% length of the line) away from R_G with $FIA = 90^0$, CL = 40%, and v = 15 m/s. Results of the previous three fault cases are shown in Figures 8A,B,

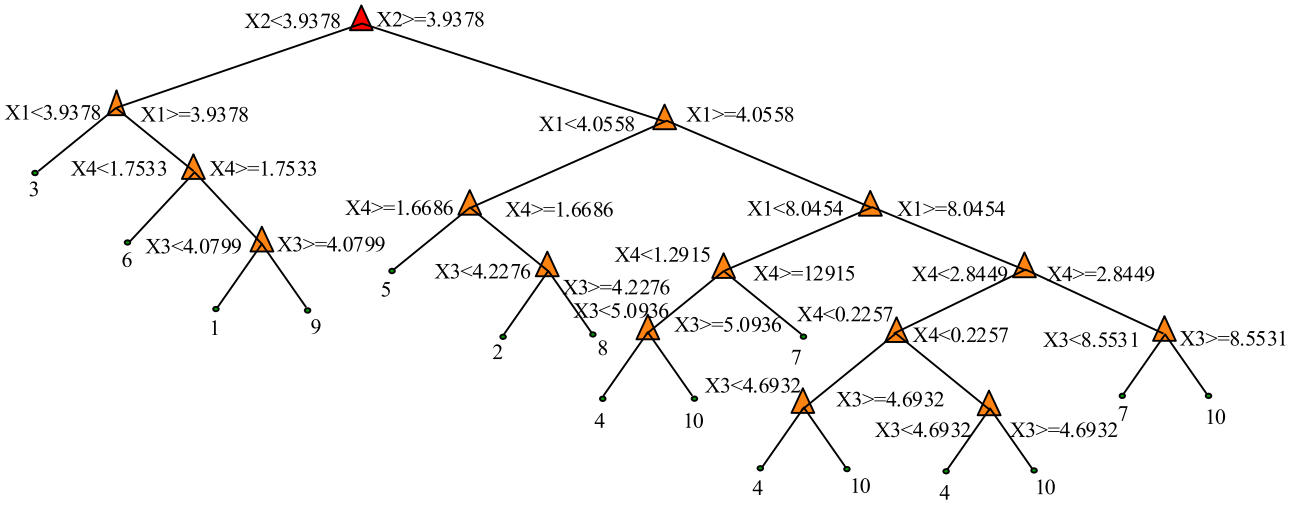

FIGURE 14
Final tree structure of the BE classifier.

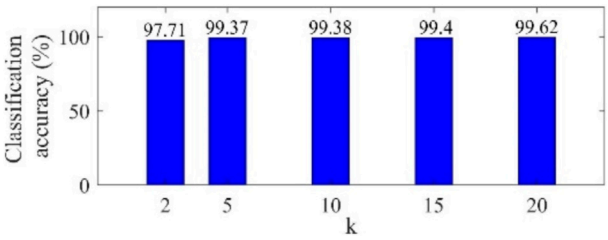

FIGURE 15
Variation of fault classification accuracies with *k*.

respectively. It is evident from Figure 8A that for all the unbalanced fault cases, signs of ΔI_{1G} and ΔI_{1w} are coming from the opposite direction. Thus, all three fault cases are internal faults in 8 ms and 3 ms, respectively. Including 5 ms PLCC latency, the FDU for these three fault cases activates the FCU after 13 ms and 8 ms, respectively.

4.1.3 High-resistance fault

Fault detection during high fault resistance is often difficult due to the possibility of minimal changes in the current magnitude. To test the efficacy during such fault situations, a bg-fault is initiated at 0.61 s with L_f = 240 km away from R_G, R_f = 200 Ω, $FIA = 180^0$, CL = 70%, and v = 10 m/s. Despite high fault resistance, the signs of ΔI_{1G} and ΔI_{1w} are opposite, and the proposed FDU detects and activates the FCU in 10 ms considering the 5 ms latency of PLCC (Figure 8B).

4.1.4 Performance during three-phase fault producing current transformer saturation

Sometimes, the core of the CT is saturated due to severe short circuit faults and the burden settings of the CT. In such a situation, the secondary currents of the CTs may not be replicated correctly as those of the primary currents. Due to the incorrect secondary current during CT saturation, the relay may find difficulty in correctly distinguishing internal faults from external faults. To test the performance during such a situation, a three-phase fault is created at 0.603 s with L_f = 210 km (70% length of the line) away from R_G while $FIA = 54^0$, CL = 40%, and v = 15 m/s. Here, the burden of grid-side CTs is chosen in such a way that the CT secondary current referred to as primary defers from the actual current, as shown in Figure 9A. The B-H curves of the three CTs shown in Figure 9B also confirm that the CT cores are saturated. Despite the CT saturation, the signs of the superimposed positive-sequence currents at Bus-G and Bus-W are opposite in polarity, and the proposed FDU detects and activates the FCU in 10 ms, considering 5 ms latency of PLCC. Thus, CT saturation is not an issue for the proposed fault detection algorithm.

4.1.5 Non-fault transients

The fault detector should remain silent during non-fault transients such as capacitor switching, load switching, and noise. Results during the initiation of three non-fault transients: 1) switching of a capacitor equivalent to 40% MVAr capacity of the line, 2) a load of 50% capacity of the total MW demand is switched on suddenly, and 3) the presence of noise in the current waveform with a signal-to-noise ratio of 15 db. During the initiation of the previous three non-fault transients, the wind speed was maintained at 15 m/s. As observed from the results (Figures 10A–C), the present fault detection scheme remains silent during the initiation of all the three non-fault transients.

4.2 Efficacy testing of the proposed fault classification scheme

The present work captures the current data for 6000 fault cases simulated in Figure 1 through MATLAB/Simulink® by changing the different parameters, as shown in Table 1. From the one-cycle post-fault three-phase current signals of all the generated fault cases, the valuable features are extracted using FBSE and SVD first. Out of the total generated data cases, 70% and 30% of the feature data cases are then used to train and test the BE classifier, respectively. The

TABLE 2 Comparative assessment result.

Parameter	Swetapadma et al. (2017)	Mohammad Taheri et al. (2018)	Mishra et al. (2019)	Prasad et al. (2020)	Proposed method
Method used	DWT, k-NN	DPASC, DT	FDOST, DT	PSO	FBSE, SVD, BE
System and sampling frequency	50 Hz & 1 kHz	50 Hz & 1 kHz	50 Hz & 1 kHz	60 Hz & 1.2 kHz	50 Hz &1 kHz
Data utilized	Current	Differential current	Voltage and current	Differential current	Current
Network consists of	FSC	FSC	FSC	Wind farm	FSC, Wind farm
Fault detection accuracy in %	100	100	99.9	NM	100
Fault classification accuracy in %	100	100	99.9	NM	100
Delay time in ms	<10	<10	<10	NM	<10
Max. R_f in Ω	100	300	200	NM	200
Affected by high R_f	No	No	No	No	No
Is it affected by CT saturation?	NM	NM	No	NM	No
Is it affected by load switching?	NM	NM	NM	NM	No
Affected by capacitor switching?	NM	NM	NM	NM	No
Affected by current inversion?	NM	NM	NM	NM	No
Affected by noise?	NM	NM	No	NM	No
Real-time validation	NM	NM	NM	NM	OPAL-RT

NM, not mentioned.

variations of the input fault feature β to the BE classifier for a few faults generated in Figure 1 are shown in Figure 11. With the initiation of faults, the fault features β of the faulted phase are increased from a lower value to a higher value, making a more straightforward estimation of fault types by the BE classifier.

The scatter plot of all the 6000-feature data generated, as demonstrated in Figure 12, clearly shows different feature datasets for different fault cases. The computed overall confusion matrix (Figure 13) shows that the classification accuracy of the proposed BE classifier for fault classification is 99.37%. Figure 14 shows the final tree structure of the BE classifier.

In the present work, *k*-fold cross-validation is used to counteract the bias-variance problem. Here, the *k*-fold cross-validation uses k = 2, 5, 10, 15, and 20. As evident from Figure 15, after $k = 5$, there is no such improvement in the classification accuracy. Thus, to avoid computational complexity and time, fault classification accuracy is calculated using $k = 5$.

5 Comparative assessment

The performance of the proposed method is compared with Prasad et al. (2020), Mishra et al. (2019), Swetapadma et al. (2017), and Mohammad Taheri et al. (2018) earlier used for the protection of either FSC-compensated TLs or DFIG wind farm-connected TLs. The summarized comparative study considering different attributes is provided in Table 2. The table clearly shows that the proposed approach's fault detection and classification accuracies are coming 100%. Similar accuracies are obtained earlier by Swetapadma et al. (2017) and Mohammad Taheri et al. (2018). However, the methods proposed by Swetapadma et al. (2017) and Mohammad Taheri et al. (2018) are tested only for FSC-compensated TLs. These protection schemes were not validated for large-scale DFIG wind farm integration. The control action of DFIG with LVRT capability and the grounding arrangement of DFIG produce unusual frequency components and unusual sequence currents, especially during ground faults. These characteristics will affect the performance of the existing methods.

Furthermore, the discrete wavelet transforms (DWTs), k-nearest neighbor (k-NN)-based method used in the study by Swetapadma et al. (2017), differential phase angle of superimposed current (DPASC), and DT-based method used in the study by Mohammad Taheri et al. (2018) are computationally not efficient compared to the proposed FBSE-SVD and BE classifier. Also, the methods proposed by Swetapadma et al. (2017) and Mohammad Taheri et al. (2018) have not been tested in the presence of non-fault transients such as significant load switching, switching on/off of capacitor banks, and CT saturation during severe short circuit faults. The method in the study by Mohammad Taheri et al. (2018) used the current differential principle. Such a scheme cannot ensure secure protection for TLs connecting large-scale DFIG

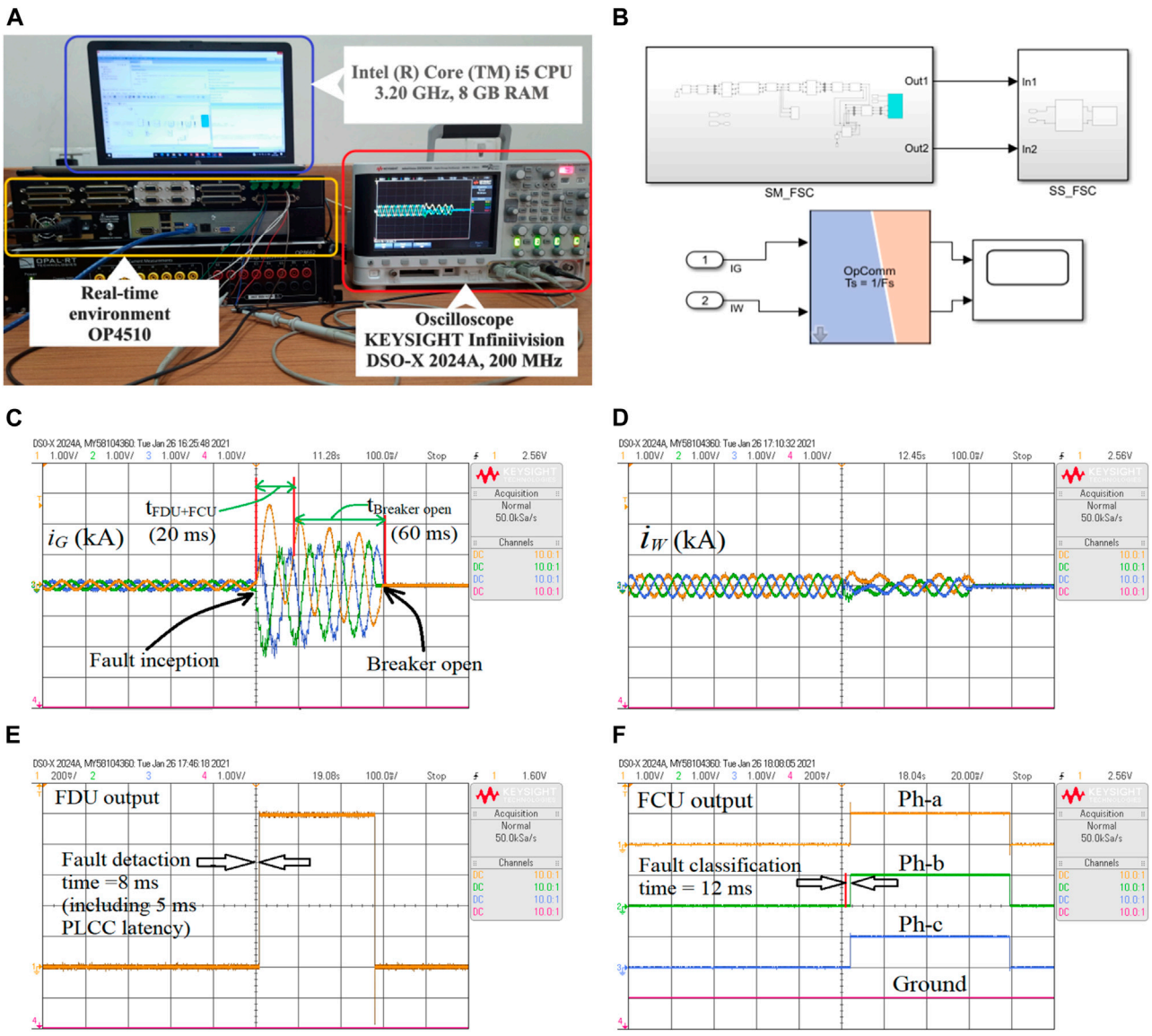

FIGURE 16
Results on the real-time environment: **(A)** real-time experimental setup, **(B)** Simulink in RT-LAB software, **(C)** grid-side current, **(D)** wind farm-side current, **(E)** FDU output, and **(F)** FCU output.

wind farms. The performance of the proposed protection scheme has immunity to such non-fault transients. This shows that the overall performance of the proposed protection scheme is superior compared to that the existing approaches, mainly when used for the protection of FSC-compensated TLs connected with large-scale DFIG wind farms.

6 Real-time validation through the OPAL-RT platform

The proposed protection scheme is tested on the RTDS platform manufactured by OPAL-RT (OP4510. The experimental setup is shown in Figure 16A (Biswas et al., 2022). As shown in Figure 16B, the test model of Figure 1 is simulated in MATLAB/Simulink® and compiled in RT-Lab software. The real-time data are generated and stored in the processor of OP4510. The real-time current at the grid side for a 3ph-fault (L_f = 240 km from relay R_G, CL = 70%, v = 5 m/s) provided in Figure 16C shows the fault detection and classification time of the proposed method is 20 ms. The real-time current at the wind farm site for the previous fault case is shown in Figure 16D. Considering 60 ms circuit breaker operating time, the faulted phases are finally tripped in 80 ms (Figures 16E,F). This shows that the proposed protection scheme can be implemented easily in real-time.

7 Conclusion

In the present paper, the limitations of distance relay protecting an FSC-compensated TL connecting large-capacity

DFIG-WTGs are studied, and an intelligent protection scheme is proposed for fast and reliable detection and classification of faults in such crucial TLs. The proposed scheme utilizes the signs of the half-cycle magnitude differences of the line-end positive-sequence currents for fault detection, and the fault classification is performed using the local current measurements processed through the combination of the FBSE-SVD-BE classifier. Performance is evaluated on 6000 fault cases simulated on the two-bus test system through MATLAB/Simulink®. The method is also validated in OPAL-RT (OP4510) manufactured RTDS platform. The marginal computational burden, feasibility for real-time implementation, fast fault detection and classification time (<10 ms), 100% fault detection accuracies, and comparatively higher fault classification accuracies (= 99.37% are the main merits of the proposed relaying algorithm. However, the proposed approach's efficacy is validated through the OPAL-RT-manufactured RTDS platform. It must be validated through the hardware-in-loop (HIL) experimental setup using OPAL-RT systems and field-programmable gate array (FPGA) boards with prototype relays and should be compared with existing relays used in fields such as SEL-421. This may be extended as future work.

Data availability statement

The original contributions presented in the study are included in the article/Supplementary Material; further inquiries can be directed to the corresponding author.

Author contributions

PM simulated the system and generated the data for training and testing the Fourier–Bessel series expansion (FBSE) bagging ensemble (BE) classifier for performing the fault classification task. He also wrote the initial draft of the manuscript. SB studied and tested the simultaneous impacts of the installation of series compensation and the integration of large-scale wind farms on distance relay performance. He also wrote the initial draft of Section 2 of the manuscript. PN edited the whole manuscript. AA provided guidence for the overall improvement of the manuscript. AS provided further guidence for the overall improvement of the manuscript.

Conflict of interest

The authors declare that the research was conducted in the absence of any commercial or financial relationships that could be construed as a potential conflict of interest.

Publisher's note

References

Abdelaziz, A. Y., Ibrahim, A. M., Mansour, M. M., and Talaat, H. E. (2005). Modern approaches for protection of series compensated transmission lines. *Electr. Power Syst. Res.* 75 (1), 85–98. doi:10.1016/j.epsr.2004.10.016

Altuve, H. J., Mooney, J. B., and Alexander, G. E. (2009). "Advances in series-compensated line protection," in 62nd Annual Conf. for Protective Relay Engineers, College Station, TX, USA, 30 March 2009 - 02 April 2009 (IEEE), 263–275.

Biswas, S., and Nayak, P. K. (2021). A fault detection and classification scheme for unified power flow controller compensated transmission lines connecting wind farms. *IEEE Syst. J.* 15 (1), 297–306. doi:10.1109/jsyst.2020.2964421

Biswas, S., and Nayak, P. K. (2019). An unblocking assistance to distance relays protecting TCSC compensated transmission lines during power swing. *Int. Trans. Elect. Energy Syst.* 29 (8), 1–21. doi:10.1002/2050-7038.12034

Biswas, S., and Nayak, P. K. (2021). A new approach for protecting TCSC compensated transmission lines connected to DFIG-based wind farm. *IEEE Trans. Indus. Infor.* 17 (8), 5282–5291. doi:10.1109/tii.2020.3029201

Biswas, S., Nayak, P. K., and Pradhan, G. (2022). A dual-time transform assisted intelligent relaying scheme for the STATCOM-compensated transmission line connecting wind farm. *IEEE Syst. J.* 16 (2), 2160–2171. doi:10.1109/jsyst.2021.3070448

Breiman, L. (2001). Random forests. *Mach. Learn.* 45 (1), 5–32. doi:10.1023/a:1010933404324

Sahoo, B., and Samantaray, S. R. (2017). An enhanced fault detection and location estimation method for TCSC compensated line connecting wind farm. *Int. J. Electr. Power Energy Syst.* 96, 432–441. doi:10.1016/j.ijepes.2017.10.022

Central Electricity Regulatory Commission (2010). Indian electricity grid code. Available: http://cercind.gov.in/2010/ORDER/February2010/IEGC_Review_Proposal.pdf.

Chaurasiya, P. K., Warudkar, V., and Ahmed, S. (2019). Wind energy development and policy in India: A review. *Energy Strategy Rev.* 24, 342–357. doi:10.1016/j.esr.2019.04.010

Chen, S., Tai, N., Fan, C., Liu, J., and Hong, S. (2017). Adaptive distance protection for grounded fault of lines connected with doubly-fed induction generators. *IET Gener. Transm. Distrib.* 11 (6), 1513–1520. doi:10.1049/iet-gtd.2016.1145

Chen, S., Yin, X., and Zhang, Z. (2017). Impacts of DFIG-based wind farm integration on its tie line distance protection and countermeasures. *IEEJ Trans. Electr. Electron. Eng.* 12 (4), 553–564. doi:10.1002/tee.22411

Dash, P. K., Samantaray, S. R., and Panda, G. (2006). Fault classification and section identification of an advanced series-compensated transmission line using support vector machine. *IEEE Trans. Power Deliv.* 22 (1), 67–73. doi:10.1109/tpwrd.2006.876695

D'Elia, G., Delvecchio, S., and Dalpiaz, G. (2012). "On the use of Fourier-Bessel series expansion for gear diagnostics," in *Condition monitoring of machinery in non-stationary operations* (Berlin, Germany: Springer), 267–275.

Dubey, R. K., Samantaray, S. R., and Panigrahi, B. K. (2014). Adaptive distance relaying scheme for transmission network connecting wind farms. *Electr. Power Compon. Syst.* 42 (11), 1181–1193. doi:10.1080/15325008.2014.921953

Fang, Y., Jia, K., Yang, Z., Li, Y., and Bi, T. (2018). Impact of inverter-interfaced renewable energy generators on distance protection and an improved scheme. *IEEE Trans. Ind. Electron.* 66 (9), 7078–7088. doi:10.1109/tie.2018.2873521

Fortescue, C. L. (1918). Method of symmetrical co-ordinates applied to the solution of polyphase networks. *Trans. Am. Inst. Electr. Eng.* 21 (2), 1027–1140. doi:10.1109/t-aiee.1918.4765570

Ghorbani, A., Mehrjerdi, H., and Al-Emadi, N. A. (2017). Distance-differential protection of transmission lines connected to wind farms. *Int. J. Electr. Power Energy Syst.* 89, 11–18. doi:10.1016/j.ijepes.2017.01.002

Gopalan, K., Anderson, T. R., and Cupples, E. J. (1997). "Speaker identification using features based on first-order Bessel function expansion of speech," in IEEE Pacific Rim Conference on Communications, Computers and Signal Processing, 10 Years Networking the Pacific Rim, 1987-1997, Victoria, BC, Canada, 20-22 August 1997 (IEEE), 589–592.

Gopalan, K. (2001). "Speech coding using Fourier-Bessel expansion of speech signals," in 27th Annual Conf. of the IEEE Indus. Electronics Society (Cat. No.

37243), Denver, CO, USA, 29 November 2001 - 02 December 2001 (IEEE), 2199–2203.

Ho, T. K. (1995). Random decision forests. in Proceedings of 3rd international conference on document analysis and recognition. Montreal, QC, Canada, 14-16 August 1995, IEEE, 278–282.

Hoang, T. T., Tran, Q. T., Le, H. S., Nguyen, H. N., and Duong, M. Q. (2022). "Impacts of high solar inverter integration on performance of FLIRS function: Case study for Danang distribution network," in 2022 11th International Conference on Control, Automation and Information Sciences (ICCAIS) (Hanoi, Vietnam: IEEE), 327–332.

Hooshyar, A., Azzouz, M. A., and El-Saadany, E. F. (2014). Distance protection of lines connected to induction generator-based wind farms during balanced faults. *IEEE Trans. Sustain. Energy* 5 (4), 1193–1203. doi:10.1109/tste.2014.2336773

Hoq, M. T., Wang, J., and Taylor, N. (2021). Review of recent developments in distance protection of series capacitor compensated lines. *Electr. Power Syst. Res.* 190, 106831. doi:10.1016/j.epsr.2020.106831

Li, B., Liu, J., Wang, X., and Zhao, L. (2018). Fault studies and distance protection of transmission lines connected to DFIG-based wind farms. *Appl. Sci.* 8 (4), 562. doi:10.3390/app8040562

Lopez, J., Gubia, E., Sanchis, P., Roboam, X., and Marroyo, L. (2008). Wind turbines based on doubly fed induction generator under asymmetrical voltage dips. *IEEE Trans. Energy Convers.* 23 (1), 321–330. doi:10.1109/tec.2007.914317

Lopez, J., Sanchis, P., Roboam, X., and Marroyo, L. (2007). Dynamic behavior of the doubly-fed induction generator during three-phase voltage dips. *IEEE Trans. Energy Convers.* 22 (3), 709–717. doi:10.1109/tec.2006.878241

Ma, J., Zhang, W., Liu, J., and Thorp, J. S. (2018). A novel adaptive distance protection scheme for DFIG wind farm collector lines. *Int. J. Electr. Power Energy Syst.* 94, 234–244. doi:10.1016/j.ijepes.2017.07.008

Mishra, P. K., Yadav, A., and Pazoki, M. (2018). A novel fault classification scheme for series capacitor compensated transmission line based on bagged tree ensemble classifier. *IEEE Access* 6, 27373–27382. doi:10.1109/access.2018.2836401

Mishra, P. K., Yadav, A., and Pazoki, M. (2019). FDOST-based Fault Classification scheme for fixed series compensated transmission system. *IEEE Syst. J.* 13 (3), 3316–3325. doi:10.1109/jsyst.2018.2890288

Mishra, S., Gupta, S., and Yadav, A. (2021). A novel two-terminal fault location approach utilizing traveling-waves for series compensated line connected to wind farms. *Elect. Power Syst. Res.* 198, 107362. doi:10.1016/j.epsr.2021.107362

Mohamed, A. R., Sharaf, H. M., and Ibrahim, D. K. (2021). Enhancing distance protection of long transmission lines compensated with TCSC and connected with wind power. *IEEE Access* 9, 46717–46730. doi:10.1109/access.2021.3067701

Mohammad Taheri, M., Seyedi, H., Nojavan, M., Khoshbouy, M., and Ivatloo, B. M. (2018). High-speed decision tree-based series-compensated transmission lines protection using differential phase angle of superimposed current. *IEEE Trans. Power Deliv.* 33 (6), 3130–3138. doi:10.1109/tpwrd.2018.2861841

Nayak, P. K., Pradhan, A. K., and Bajpai, P. (2014). Wide-area measurement-based backup protection for power network with series compensation. *IEEE Trans. Power Deliv.* 29 (4), 1970–1977. doi:10.1109/tpwrd.2013.2294183

Nayak, S., Kar, S. K., Dash, S. S., Vishnuram, P., Thanikanti, S. B., and Nastasi, B. (2022). Enhanced salp swarm algorithm for multimodal optimization and fuzzy based grid frequency controller design. *Energies* 15 (9), 3210. doi:10.3390/en15093210

Novosel, D., Phadke, A., Saha, M. M., and Lindahl, S. (1997). "Problems and solutions for microprocessor protection of series compensated lines," in Sixth International Conference on Developments in Power System Protection, Nottingham, UK, 25-27 March 1997 (IEEE), 18–23.

Ouyang, J., and Xiong, X. (2014). Dynamic behavior of the excitation circuit of a doubly-fed induction generator under a symmetrical voltage drop. *Renew. Energy* 71, 629–638. doi:10.1016/j.renene.2014.06.029

Pachori, R. B., and Sircar, P. (2008). EEG signal analysis using FB expansion and second-order linear TVAR process. *Signal process.* 88 (2), 415–420. doi:10.1016/j.sigpro.2007.07.022

Pazoki, M. (2018). A new fault classifier in transmission lines using intrinsic time decomposition. *IEEE Trans. Ind. Inf.* 14 (2), 619–628. doi:10.1109/tii.2017.2741721

Pradhan, A. K., and Joos, G. (2007). Adaptive distance relay setting for lines connecting wind farms. *IEEE Trans. Energy Convers.* 22 (1), 206–213. doi:10.1109/tec.2006.889621

Prasad, C. D., Biswal, M., and Abdelaziz, A. Y. (2020). Adaptive differential protection scheme for wind farm integrated power network. *Electr. Power Syst. Res.* 187, 106452. doi:10.1016/j.epsr.2020.106452

Prasad, C. D., and Biswal, M. (2020). Swarm intelligence-based differential protection scheme for wind integrated transmission system. *Comput. Electr. Eng.* 86, 106709. doi:10.1016/j.compeleceng.2020.106709

Sadeghi, H. (2012). A novel method for adaptive distance protection of transmission line connected to wind farms. *Int. J. Electr. Power Energy Syst.* 43 (1), 1376–1382. doi:10.1016/j.ijepes.2012.06.072

Schroeder, J. (1993). Signal processing via Fourier-Bessel series expansion. *Digit. Signal Process.* 3 (2), 112–124. doi:10.1006/dspr.1993.1016

Sivov, O., Abdelsalam, H., and Makram, E. (2016). Adaptive setting of distance relay for MOV-protected series compensated line considering wind power. *Electr. Power Syst. Res.* 137, 142–154. doi:10.1016/j.epsr.2016.03.048

Swetapadma, A., Mishra, P., Yadav, A., and Abdelaziz, A. Y. (2017). A non-unit protection scheme for double circuit series capacitor compensated transmission lines. *Electr. Power Syst. Res.* 148, 311–325. doi:10.1016/j.epsr.2017.04.002

Tikhonov, A. N. (1963). Solution of incorrectly formulated problems and the regularization method. *Sov. Math.* 4, 1035–1038.

Tran, V. T., Al Thobiani, F., Ball, A., and Choi, B.-K. (2013). An application to transient current signal-based induction motor fault diagnosis of Fourier–Bessel expansion and simplified fuzzy ARTMAP. *Expert Syst. Appl.* 40 (13), 5372–5384. doi:10.1016/j.eswa.2013.03.040

Varma, R. K., Auddy, S., and Semsedini, Y. (2008). Mitigation of subsynchronous resonance in a series-compensated wind farm using FACTS controllers. *IEEE Trans. Power Del.* 23 (3), 1645–1654. doi:10.1109/tpwrd.2008.917699

Varma, R. K., and Moharana, A. (2013). SSR in double-cage induction generator-based wind farm connected to series-compensated transmission line. *IEEE Trans. Power Syst.* 28 (3), 2573–2583. doi:10.1109/tpwrs.2013.2246841

Vishnuram, P., Ramachandiran, G., Sudhakar, T. B., and Nastasi, B. (2021). Induction heating in domestic cooking and industrial melting applications: A systematic review on modelling, converter topologies and control schemes. *Energies* 14 (20), 6634–34. doi:10.3390/en14206634

Vyas, B., Maheshwari, R. P., and Das, B. (2014). Protection of series compensated transmission line: Issues and state of art. *Electr. Power Syst. Res.* 107, 93–108. doi:10.1016/j.epsr.2013.09.017

Xiao, F., Zhang, Z., and Yin, X. (2015). Fault current characteristics of the DFIG under asymmetrical fault conditions. *Energies* 8 (10), 10971–10992. doi:10.3390/en81010971

Yang, Z., Jia, K., Fang, Y., Zhu, Z., Yang, B., and Bi, T. (2020). High-frequency fault component-based distance protection for large renewable power plants. *IEEE Trans. Power Electron.* 35 (10), 10352–10362. doi:10.1109/tpel.2020.2978266

Appendix

Parameters of the grid transmission line:

TL length: 300 km.

Positive-sequence impedance (Z_1): 0.03293 + j0.327 Ω/km.

Zero-sequence impedance (Z_0): 0.2587 + j1.1740 Ω/km.

Positive-sequence capacitive impedance: 280.1 MΩ/km.

Zero-sequence capacitive reactance: 461.2546 MΩ/km.

Parameters of DFIG wind farm:

Rating of wind farm: 0.690 kV, 50 Hz, 60 MW, 28 MVAr (40 Nos. × 2 MW each), slip = −0.25, and inertia constant: 4.32.

Collector lines: 30 km π-section, Z_1 = 0.115 + j0.33 Ω/km.

Transformer before collector line Y/Δ, 2.2 MVA, 0.690/35 kV, 50 Hz.

Transformer after collector line Δ/Y, 90 MVA, 35/400 kV, 50 Hz.

Parameters of the capacitor bank:

Capacitance: 80 μF (40% compensation), 45 μF (70% compensation); MOV voltage: 75 kV.

frontiers | Frontiers in Energy Research

TYPE Original Research
PUBLISHED 03 April 2023
DOI 10.3389/fenrg.2023.1171815

OPEN ACCESS

EDITED BY
Srete Nikolovski,
Josip Juraj Strossmayer University of Osijek, Croatia

REVIEWED BY
Pradeep Vishnuram,
SRM Institute of Science and Technology, India
Adel Oubelaid,
Université de Bejaia, Algeria

*CORRESPONDENCE
Jin Zhu,
zhujin@mail.iee.ac.cn

SPECIALTY SECTION
This article was submitted to Smart Grids, a section of the journal Frontiers in Energy Research

RECEIVED 22 February 2023
ACCEPTED 15 March 2023
PUBLISHED 03 April 2023

CITATION
He S, Zhu J, Zeng Q, Guo X, Yin J and Wei T (2023), Topology searching algorithm for multi-port hybrid circuit breakers based on graph theory. *Front. Energy Res.* 11:1171815. doi: 10.3389/fenrg.2023.1171815

Topology searching algorithm for multi-port hybrid circuit breakers based on graph theory

Songming He[1,2], Jin Zhu[1]*, Qingpeng Zeng[1,2], Xinming Guo[1,2], Jingyuan Yin[1] and Tongzhen Wei[1,2]

[1]Institute of Electrical Engineering, Chinese Academy of Sciences, Beijing, China, [2]University of Chinese Academy of Sciences, Beijing, China

Due to the significant advantages of low cost, integrated multi-port hybrid DC circuit breakers (M-HCBs) with a reduced number of devices have attracted extensive attention for fault blocking in multi-terminal VSC-HVDC system. However, the current topology exploration by researchers is random, uncertain, and time-consuming. In order to provide more new cost-effective topologies, this paper innovatively proposes a topology searching algorithm for the IGBT-type M-HCB and uses the concept of 'roadblock' to simplify the adjacency matrix. It can be used to significantly save time spent on proposing a new M-HCB topology because viable topologies can be quickly and rigorously carried out from a large number of directed graphs using computers. Performance characteristics of all derived topologies are simultaneously obtained, and a comparison can be easily conducted to meet the needs of actual application scenarios. A three-port M-HCB example-specific application is given, along with some detailed output topologies that prove the validity and feasibility of the proposed method.

KEYWORDS

hybrid DC circuit breaker, graph theory, topology searching algorithm, HVDC, circuit fault

1 Introduction

1.1 Motivation and literature review

The multi-terminal VSC-HVDC system plays an important role in the integration of renewable energy sources due to the advantages of decoupled active and reactive power control, lower power losses, high flexibility, and redundancy (Meah and Ula, 2007; Debnath et al., 2015). This has been reflected by recent practical projects (Tang et al., 2015; Li et al., 2017). The system is also efficient in meeting the growing demands in electric vehicle charging (Oubelaid et al., 2022a; Oubelaid et al., 2022b; Oubelaid et al., 2022c; Oubelaid et al., 2022d).

Although the multi-terminal DC transmission (MTDC) system has several advantages, the protection of MTDC systems against DC faults is a challenging issue. Various hybrid DC circuit breaker (HCB) topologies based on different types of semiconductor devices have been proposed and have attracted widespread attention by integrating the quick response of power electronic components with the low-loss performance of a mechanical switch.

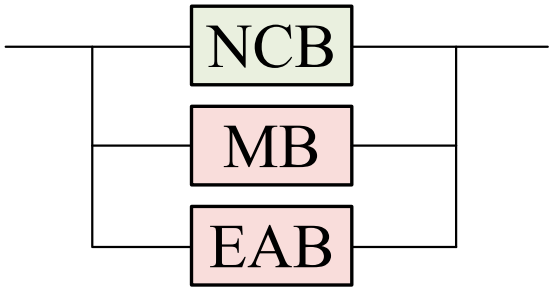

FIGURE 1
Typical HCB structure.

Most of the HCB topologies can be simplified into a parallel structure of the normal current branch (NCB), main break branch (MB), and energy absorption branch (EAB) (Guo et al., 2021), as shown in Figure 1. During normal operation, the NCB conducts the system current with low losses. When the short-circuit fault occurs, the fault current needs to be commutated to the MB and EAB to realize the final blocking.

According to different methods of commutating the fault current from the NCB to MB, the HCB can be denoted as the proactive HCB (P-HCB) and current-injection-HCB (C-HCB), respectively (Guo et al., 2021). In P-HCBs, the NCB is usually composed of ultra-fast disconnectors (UFDs) and a load commutation switch (LCS), and the fault current can be commutated to the MB by turning off the LCS, while the C-HCBs achieve the current commutating process by injecting a reverse current into the NCB.

No matter which topology is adopted, the required number of HCBs in the meshed VSC-HVDC system will increase significantly, leading to a huge cost. In order to further reduce the system cost, the multi-port hybrid DC circuit breaker (M-HCB) concept has been proposed and has been a research hotspot in recent years. The core idea is to share main breaker units among connected lines.

Most of the M-HCB topologies can also be mainly divided into two types according to the current commutation process; some M-HCB topologies are based on the C-HCB structure (C-M-HCB) (Qu et al., 2019; Wen et al., 2019; Guo et al., 2021; Wang et al., 2022). However, more topologies are mainly based on the P-HCB structure (P-M-HCB) (Kontos et al., 2018; Li et al., 2018; Mokhberdoran et al., 2018; He et al., 2020; Wang et al., 2020; Xiao et al., 2020; Zhang et al., 2021). Different topologies have different characteristics, as shown in Table 3, so they are suitable for different application scenarios.

However, the topology design of the M-HCB mainly relies on the experience of researchers; researchers may prefer to figure out some viable topology configurations from all possible connections by their experience instead of examining all configurations one by one (Wang et al., 2022). As a result, some preferred topologies are often not found, and it usually takes several years for an application field to gradually improve the topology design, for example, the topology exploration for the M-HCB has lasted for 5 years (Liu et al., 2017), and some new topologies are still emerging, [such as Wang et al. (2022)]. The innovation of the new M-HCB topology seems random and uncertain.

Some mathematical methods and programmable algorithms have been applied to power electronics topology design, such as duality theory (Liu and Lee, 1988; Ranjana et al., 2016), graph theory (Ogata and Nishi, 2003; Ogata and Nishi, 2005; Li et al., 2017), and a programmable algorithm (Chen et al., 2019; Li et al., 2019), for the DC–DC converter to improve the efficiency of the topology design. In Ogata and Nishi (2003), Ogata and Nishi (2005), and Li et al. (2017), electrical components of the DC–DC converter are abstracted as directed edge segments, according to the current flow direction; the circuit diagram is represented as the directed graph; and the state space equation is used to derive novel topologies. Chen et al. (2019) proposed a programmable topology searching algorithm for the integrated non-isolated three-port DC–DC converter based on the switching network unit. Li et al. (2019) proposed a programmable topology search algorithm for the DC–DC converter based on graph theory; a large number of potential topologies are obtained, and the invalid topology is then further screened out with the help of computers. Guo et al. (2022) proposed the idea of using graph theory in the M-HCB topology and obtained three new topologies by manually optimizing the existing topology.

As mentioned previously, research on the application of graph theory in power electronic topology design mainly focuses on the field of non-isolated DC–DC converters. Hybrid DC circuit breakers are essentially different from DC–DC converters in the operation principle, device type, and circuit composition. Although Guo et al. (2022) used graph theory to analyze the M-HCB, no computer algorithm was implemented. This article uses the computer algorithm to solve the problem that the process of the M-HCB topology proposed by researchers is random, uncertain, and time-consuming.

1.2 Contributions and organization

The main contributions of this paper are as follows:

1) A topology searching algorithm suitable for M-HCBs is proposed, which is different from the existing topology construction methods.
2) The concept of 'roadblock' is proposed and used to simplify the adjacency matrix, which can significantly reduce the difficulty of writing and running the algorithm.
3) A three-port P-M-HCB example-specific application through the computer algorithm is explained to show the basic working principle of the method. Several valuable new topologies are carried out by the proposed method.

This paper is organized as follows: Section 2 includes the graph theory representation of M-HCB topologies and their corresponding adjacency matrices are proposed; Section 3 introduces the whole topology searching algorithm including the directed graph construction, feasible path search, and filtering electrical rules; Section 4 shows some interesting output topologies from the three-port M-HCB example-specific application, followed by the conclusion in Section 5.

2 Graph theory of the M-HCB

In order to use computer language to derive M-HCB topologies and analyze them, this article first uses graph theory to abstract the M-HCB into the directed graph.

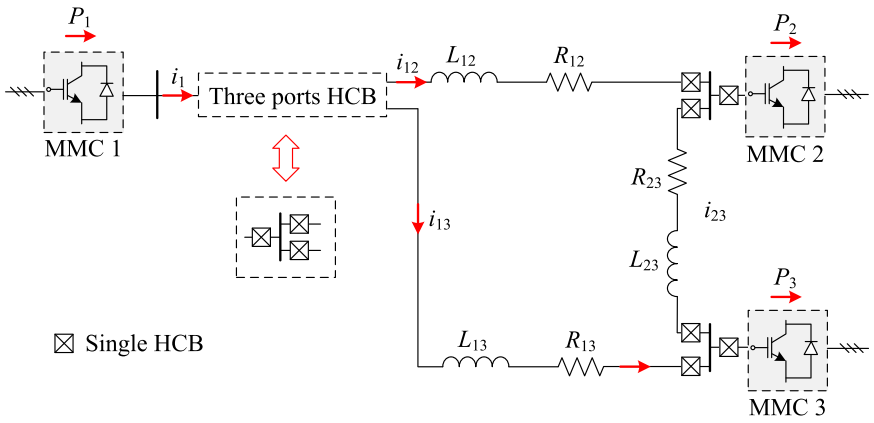

FIGURE 2
Typical three-terminal VSC-HVDC system with M-HCBs.

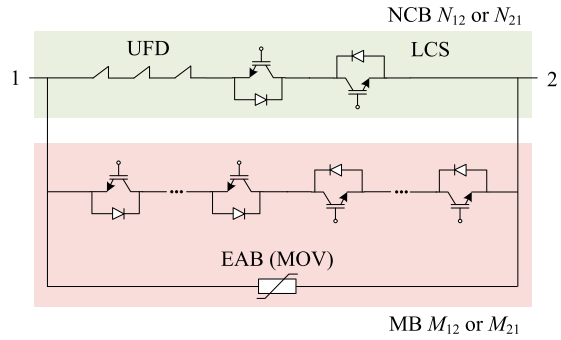

FIGURE 3
Structure of ABB's hybrid DC circuit breakers.

There are lots of M-HCB topologies, as mentioned previously, in recent research (such as P-M-HCB and C-M-HCB); this article considers the P-M-HCB topologies derived from ABB's hybrid DC circuit breakers applied in the three-terminal VSC-HVDC system as an example to explain the topology derivation principle, as shown in Figures 2, 3. Other types of M-HCB topologies can be derived from similar principles.

2.1 Basic concepts of graph theory

The directed graph is a data structure composed of a vertex set V and an edge set E, and $Graph = (V, E)$, abbreviated as $G = (V, E)$. $E = \{<v, w> | v, w \in V, \text{ and } P_{vw}\}$

P_{vw} defines the meaning of edge $<v, w>$. In this article, P represents the edge type and vw represents the edge direction (from v to w).

Then, if there are n vertexes in a directed graph, the adjacency matrix is established as

$$\boldsymbol{C} = [C_{vw}]_{n\times n}. \quad (1)$$

The detailed method for establishing the adjacency matrix will be described in subsection 2.3.

2.2 Graph representation of the M-HCB

The method to convert the M-HCB topology into the directed graph is defined as follows:

For vertex: In the three-port HCB, three port points must exist; in graph theory, it can be abstracted as V_P (port vertex), $V_P = 3$. The remaining common connection points can be abstracted as V_C (common vertex). The vertexes are usually expressed by numbers in the directed graph, the port points are numbered 1, 2, and 3, and the common connection points are sorted after the port points.

For edge: The NCB can be denoted by N_{vw} in the graph; the MB and EAB can be considered as a whole, represented by M_{vw}, as illustrated in Figure 3. In addition, in many topologies, there will also be diode branches, denoted by D_{vw}.

Summarizing the aforementioned definitions, the abstract rules are defined, as shown in Table 1.

The previous M-HCB topologies can be abstracted into directed graphs and are divided into several categories according to the number of common connection points:

1) $\boldsymbol{V_C}$ **= zero:** A unidirectional fault blocking solution proposed by Li et al. (2018) is abstracted into a directed graph, as shown in Figure 4A.
2) $\boldsymbol{V_C}$ **= one:** The directed graph in Figure 4B is a bidirectional fault blocking topology, as proposed by Li et al. (2018).
3) $\boldsymbol{V_C}$ **= two:** Three examples are explained here, as shown in Figure 4C–E. Although they belong to different design ideas, they are still regarded as the same type in graph theory.
4) $\boldsymbol{V_C}$ **= three:** The situation is more complicated due to more common connection points. In Figure 4F, only one unidirectional MB, whose blocking capacity is the system voltage, is used to block the fault current.

2.3 Corresponding adjacency matrix

In graph theory, the adjacency matrix can denote the relationship of the graph clearly. On the other hand, it is difficult

TABLE 1 Abstract rules of M-HCBs.

Legend	Designation	Category	Definition
●	V_P	Vertex	Port point
○	V_C	Vertex	Common connection point
⟷	N_{vw}	Edge	Bidirectional NCB
- - - →	M_{vw}	Edge	Unidirectional MB
⟶	D_{vw}	Edge	Diode branch

Note: The number of IGBTs in LCS is much less than that in MB, which has little impact on system cost. In order to simplify the derivation process of graph theory, it is tentatively assumed that all NCBs adopt a bidirectional LCS design.

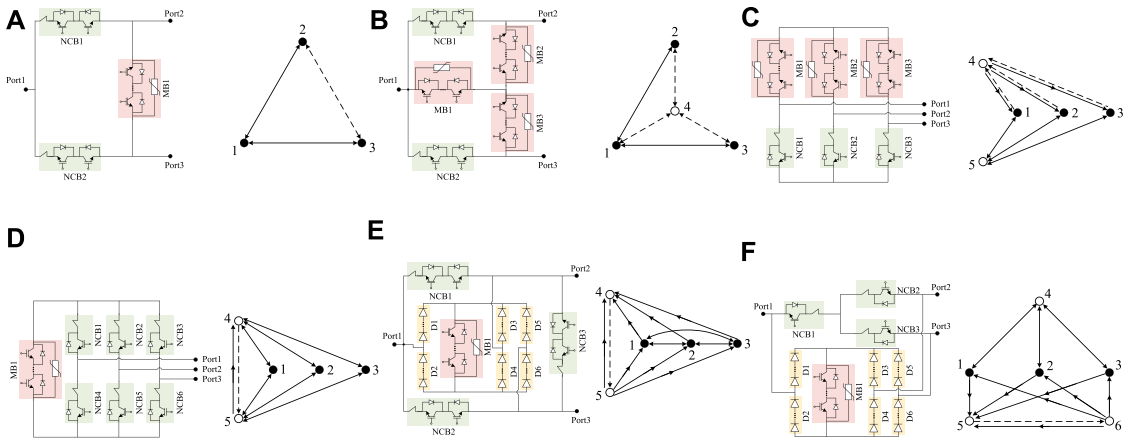

FIGURE 4
Previous three-port HCB topologies and their corresponding graphs: **(A)** topology proposed by Li et al. (2018), **(B)** topology proposed by Li et al. (2018), **(C)** topology proposed by Mokhberdoran et al. (2018), **(D)** topology proposed by Kontos et al. (2018), **(E)** topology proposed by He et al. (2020), and **(F)** topology proposed by Xiao et al. (2020).

for computers to recognize image statements but easy for math matrices.

As explained previously, *Graph* = (*V*, *E*), and the labels of vertexes in the graph are 1, 2, . . .*n*. An *n*×*n* matrix $\boldsymbol{C} = [C_{vw}]$ is named the adjacency matrix and

$$C_{vw} = \begin{cases} \inf & if < v, w > \notin E, \\ 0 & v = w, \\ P_{vw} & if < v, w > \in E, \end{cases} \tag{2}$$

where *P* represents the edge type from vertex *v* to vertex *w*, such as N_{vw}, M_{vw}, and D_{vw}.

The matrix elements do not consider the parallel multiple branch situation in the ABB scheme in Figure 3 because the core idea of the M-HCB is to share the main breaker branch.

However, like N_{vw}, M_{vw}, and D_{vw}, symbolic variables are hard to be identified in computers. It will present many difficulties in the subsequent M-HCB topology screening, such as the complex algorithm and inefficient operations in computers.

TABLE 2 'Roadblock' in M-HCB Topology.

Designation	Roadblock
N_{vw}	0.01
M_{vw}	100
D_{vw}	1

Inspired by the concept of resistance, this paper innovatively proposes the conception of a 'roadblock' to simplify adjacency matrices of M-HCB topologies. The purpose of setting the value with a difference of 100 times among three kinds of branches is to facilitate distinction and operation, as shown in Table 2.

The number of various types of branches on the path can be easily derived by 'roadblock,' and it will have a huge impact on proposing electrical rules in subsection 3.3. Moreover, the concept of 'roadblock' also fits the definition of the directed weighted adjacency matrix (Eq. 2) in graph theory.

TABLE 3 Characteristics and comparison of previous topologies.

V_C	Figure 4A	Figure 4B	Figure 4C	Figure 4D	Figure 4E	Figure 4F
	0	1	2			3
Unidirectional blocking	Y	Y	Y	Y	Y	Y
Bidirectional blocking	N	Y	Y	Y	Y	Y
Non-fault line recovery	N	N	Y	Y	Y	Y
Backup blocking	N	N	Y	Y	N	Y
Number of NCB(s)	2	2	3	6	3	3
Number of MB(s)[a]	2	3	3	1	1	1
Number of diode branches	0	0	0	0	6	6

Note: 'Y' represents yes, the topology has the ability; 'N' represents no, the topology does not have the ability.
[a]Equivalent to the unidirectional MB(s) that need to withstand the system voltage.

The adjacency matrices $\boldsymbol{C}$ are directly framed, as derived from abstract graphs. The following are the adjacency matrices corresponding to previous examples in Figure 4.

Figure 4A:

$$C_1 = \begin{bmatrix} 0 & 0.01 & 0.01 \\ 0.01 & 0 & 100 \\ 0.01 & 100 & 0 \end{bmatrix}, \tag{3}$$

Figure 4B:

$$C_2 = \begin{bmatrix} 0 & 0.01 & 0.01 & 100 \\ 0.01 & 0 & inf & 100 \\ 0.01 & inf & 0 & 100 \\ 100 & 100 & 100 & 0 \end{bmatrix}, \tag{4}$$

Figure 4C:

$$C_3 = \begin{bmatrix} 0 & inf & inf & 100 & 0.01 \\ inf & 0 & inf & 100 & 0.01 \\ inf & inf & 0 & 100 & 0.01 \\ 1 & 1 & 1 & 0 & inf \\ 0.01 & 0.01 & 0.01 & inf & 0 \end{bmatrix}, \tag{5}$$

Figure 4D:

$$C_4 = \begin{bmatrix} 0 & inf & inf & 0.01 & 0.01 \\ inf & 0 & inf & 0.01 & 0.01 \\ inf & inf & 0 & 0.01 & 0.01 \\ 0.01 & 0.01 & 0.01 & 0 & 100 \\ 0.01 & 0.01 & 0.01 & 1 & 0 \end{bmatrix}, \tag{6}$$

Figure 4E:

$$C_5 = \begin{bmatrix} 0 & 0.01 & 0.01 & 1 & inf \\ 0.01 & 0 & 0.01 & 1 & inf \\ 0.01 & 0.01 & 0 & 1 & inf \\ inf & inf & inf & 0 & 100 \\ 1 & 1 & 1 & 1 & 0 \end{bmatrix}, \tag{7}$$

Figure 4F:

$$C_6 = \begin{bmatrix} 0 & inf & inf & 0.01 & 1 & inf \\ inf & 0 & inf & 0.01 & 1 & inf \\ inf & inf & 0 & 0.01 & 1 & inf \\ 0.01 & 0.01 & 0.01 & 0 & inf & inf \\ inf & inf & inf & inf & 0 & 100 \\ 1 & 1 & 1 & inf & 1 & 0 \end{bmatrix}. \tag{8}$$

The aforementioned topologies are proposed at different times, so their performance and characteristics are also different. Four characteristics are summarized to evaluate M-HCB topologies, as shown in Table 3. They are applicable to different application scenarios, according to the different costs and functional requirements. These characteristics can also be analyzed through the adjacency matrix, as mentioned in Section 3. Therefore, the topology type is quickly deduced according to the actual application requirements through the programmable mathematical algorithm rather than spending years (2018–2022) relying on the experience of researchers. In addition, other characteristics can be proposed according to the requirements.

Non-fault line recovery: When the fault current is cleared, the non-fault lines can be restored to normal operation.

Backup blocking (Zhu et al., 2023): When the fault current is transferred to the MB, the line with short-circuit fault needs to open the UFD(s) to physically isolate the fault point. The backup blocking capacity represents that if corresponding UFD(s) have been broken, other UFD(s) could be used to isolate the fault point.

TABLE 4 Feasible path examples.

	Feasible path	Roadblock
Path 1	1-2	0.01
Path 2	1-3-4-2	0.03
Path 2	1-4-2	100.01

3 Topology searching algorithm

The flow diagram of the topology searching algorithm proposed in this paper is shown in Figure 5. It is divided into three parts: the construction of graphs, the search for feasible paths, and the filtering of electrical rules.

1) ***The construction of graphs:*** The number of port points, the number of common connection points, and the type of edge are input; then, the algorithm constructs M-directed graphs for all situations and generates the adjacency matrix of each graph.

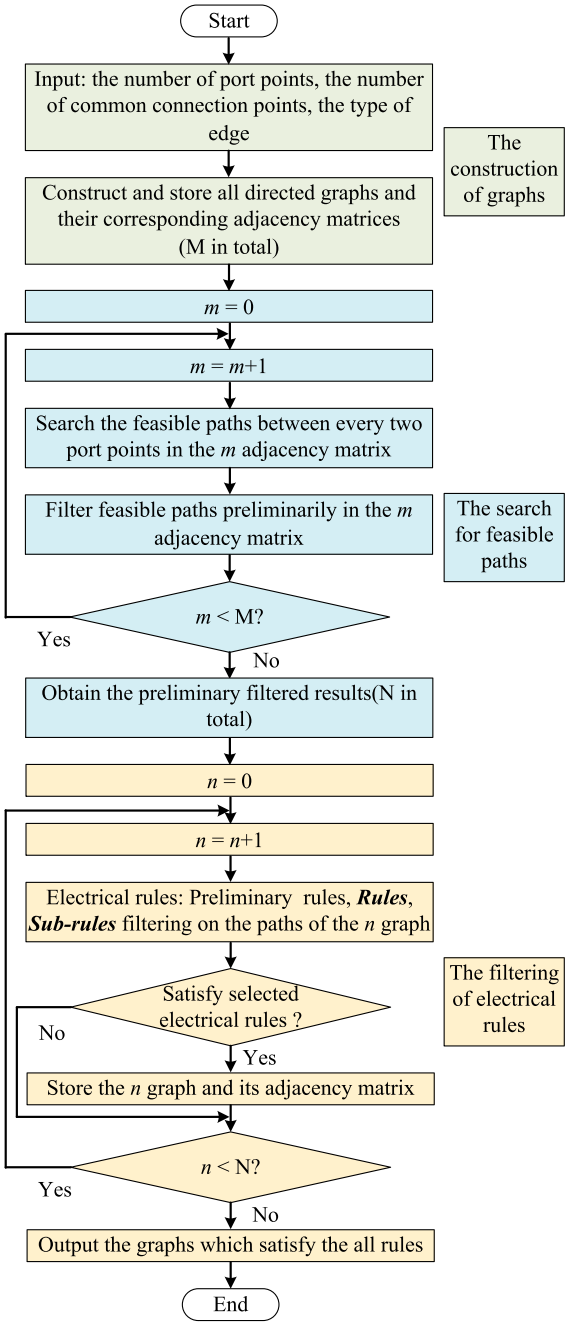

FIGURE 5
Topology searching algorithm flow diagram.

2) ***The search for feasible paths:*** According to the established adjacency matrix of each graph, the algorithm searches the feasible paths between every two port points of each graph and then filters feasible paths of each adjacency matrix preliminarily.
3) ***The filtering of electrical rules:*** Here, three kinds of rules are proposed: preliminary rules, ***Rules***, and ***Sub-rules***. Then, the algorithm filters the feasible paths between every two port points of each graph and outputs the graphs, which satisfy the selected electrical rules.

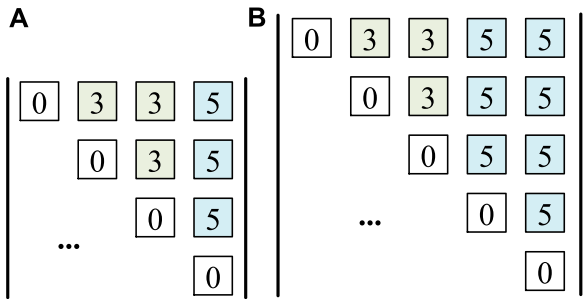

FIGURE 6
Generation algorithm principle diagram **(A)** one common connection point situation **(B)** two common connection points situation

3.1 The construction of graphs

In this paper, the M-HCB topologies take three ports as examples, so the number of port points is three.

In the previous section, the number of common connection points could take values of zero, one, two, and three. The cases are not considered where the number of common connection points is zero or three due to very little or much traversal numbers; the detailed reason and specific traversal number of the connection points will be described in Figure 6. In addition, very few topologies use three common connection points.

The algorithm is backward compatible, which means that one common connection point situation includes the zero common connection point situation without restrictions. However, different rules are flexibly applied to different common connection point situations in the following section.

Similarly, in the previous section, the type of edge could be divided into three categories: the bidirectional NCB, unidirectional MB, and unidirectional diode branch.

In order to reduce the complexity of the algorithm, the category 'unidirectional MB' is simplified to 'bidirectional MB'. Although the cost difference between the unidirectional MB and bidirectional MB is significant, the M-HCB topology using the unidirectional MB can meet the requirements of the circuit breaker better when changing to the bidirectional MB.

So there are five connection methods between every two points: the bidirectional NCB, bidirectional MB, diode branch (go), diode branch (back), and not being connected. If the algorithm is not simplified for the MB, connection methods will increase by two types: the unidirectional MB (go) and unidirectional MB (back). It is noted that there are only connection methods between every two points, and the total number of directed graphs is will exponentially grow.

For the one common connection point, the specific traversal number is $3^3 \times 5^3 = 3{,}375$, as shown in Figure 6A. The number of connection methods between every two port points is three because the branch between port points must be controllable, and the diode branch is an uncontrollable branch.

There are $3^3 \times 5^7 = 2109375$ adjacency matrices for two common connection points, as shown in Figure 6B. The detailed reason for abandoning the situation for three common connection points is as follows: using the generation algorithm proposed in this section, it is observed to be $5^5 \times 2109375$ adjacency matrices. An adjacency matrix example of Output 913 in Figure 9A is illustrated in Figure 7.

$$C = \begin{vmatrix} 0 & 0.01 & 0.01 & 100 \\ 0.01 & 0 & inf & 0.01 \\ 0.01 & inf & 0 & 0.01 \\ 100 & 0.01 & 0.01 & 0 \end{vmatrix}$$

FIGURE 7
Adjacency matrix example.

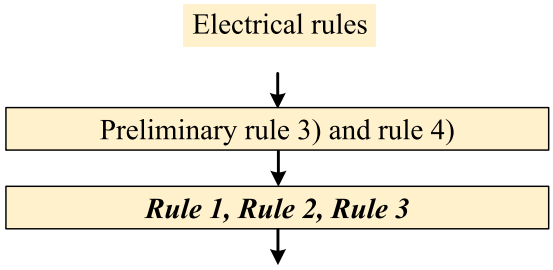

FIGURE 8
Electrical rules for one common connection point.

3.2 The search for feasible paths

The algorithm previously obtained 3,375 adjacency matrices and 2109375 adjacency matrices separately; many isomorphic graphs are hidden in them.

Reducing isomorphic graphs is a problem in graph theory; first, the rules of the generation algorithm are used to reduce part of isomorphic graphs and their corresponding adjacency matrices. The number of adjacency matrices is, respectively, reduced to 1,250 and 781,250 through this operation. The reduction efficiency is 63%.

The depth-first find-path algorithm is used to directly obtain all feasible paths between every two port points and their corresponding roadblocks in each adjacency matrix. The pseudocode for the find-path algorithm is illustrated in Algorithm 1.

```
Input: adjacency matrix, initial port point, terminate port point
Output: feasible paths and their roadblocks
Initialize path length, last point, next possible points (At the beginning, path length = 1, last point = initial port point)
If last point = terminate port point
return feasible paths and roadblocks
For each next possible point
  If next possible point = terminate port point
  Form feasible path and roadblock, remove it
  If next possible point is in the part path
  Remove this next possible point
For remaining next possible points
  Put the next possible point in the part path
Place the part path as initial port point and algorithmic recursion
Connect all feasible paths and roadblocks
Return feasible paths and their roadblocks
```

Algorithm 1: Depth-first find-path

The find-path algorithm runs six times for six port point combinations including 1 to 2, 2 to 1, 1 to 3, 3 to 1, 2 to 3, and 3 to 2 to obtain six sets of feasible paths and roadblocks.

Then, to filter feasible paths preliminarily after using the find-path algorithm, the adjacency matrices whose number of feasible paths is less than two between any two port points are removed because feasible paths between two port points include at least one MB and one NCB in M-HCB topologies.

After running the algorithm through this part, the algorithm obtains feasible paths and roadblocks in each adjacency matrix, and it also removes some unfeasible adjacency matrices. Now, the number of adjacency matrices is, respectively, reduced to 576 and 480,168. The feasible paths between 1 and 2 of Output 913 in Figure 9A are taken as examples to illustrate the principle, as shown in Table 4.

3.3 Electrical rules

In the algorithm, electrical rules are divided into three categories. They are preliminary rules, ***Rules***, and ***Sub-rules*** in the order of the algorithm, as illustrated in Figure 10. However, this section will introduce them according to their importance.

After obtaining the feasible paths, it is necessary to determine whether the feasible paths satisfy the electrical rules as an M-HCB or some characteristic requirements. The 'feasible path' is simplified as 'path' in this part.

For the adaptability and high performance of the output topologies, unidirectional blocking schemes are not considered in this article, and the generated topologies are all bidirectional blocking by default.

The MB and NCB are two important features of the M-HCB. The topology has three basic functions as an M-HCB:

1) Normal working function: When no fault occurs, the normal current is conducted through NCB(s) completely to reduce losses.
2) Blocking fault current function: When a short-circuit fault occurs, the fault current can be transferred to the MB(s) for UFD(s) in NCB(s) opening without the arc.
3) Blocking normal load current function: During normal operation, it has the ability to interrupt the normal load current by MB(s).

According to the aforementioned three basic functions, three basic rules are proposed.

Rule 1: There should be at least one path entirely composed of NCB(s) between every two port points to ensure the normal current

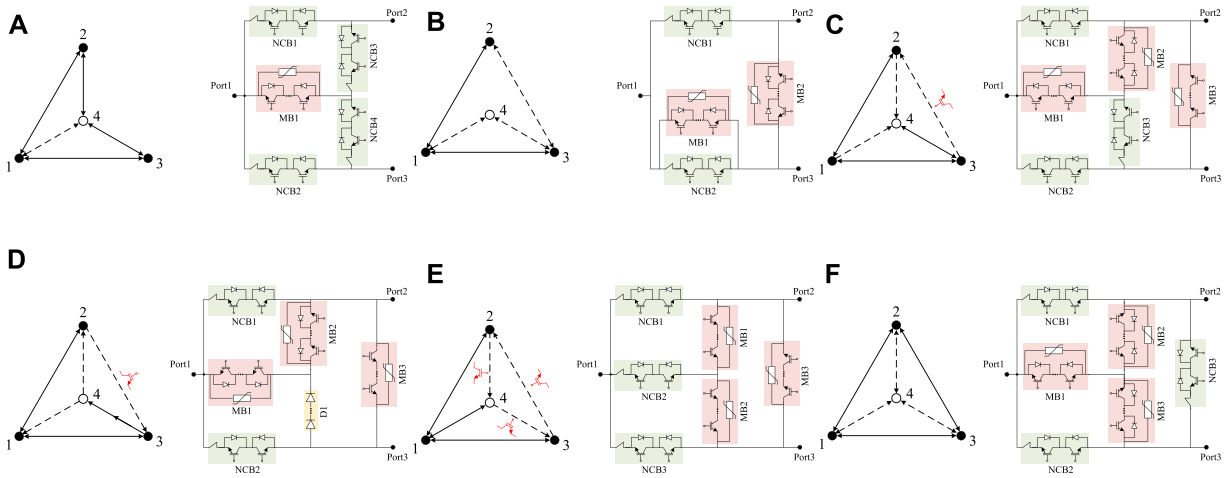

FIGURE 9
Three-port HCB topologies searched by the algorithm in the one common connection point situation: **(A)**Output 913, **(B)** Output 1,027, **(C)** Output 1,033, **(D)** Output 1,034, **(E)** Output 1,057, and **(F)** Output 1,157.

is flowing. 'Entirely' means that the path should not include the MB or diode branch due to their high on-state loss.

Although it is difficult for the algorithm to calculate the number of symbolic variables, due to the introduction of the roadblock concept, the algorithm could easily judge whether the path satisfies ***Rule 1***. For six sets of paths and roadblocks in each adjacency matrix, the condition of satisfying ***Rule 1*** is that there is at least one path in each set with a roadblock greater than 0 and less than 0.03. This restriction allows only one or two NCB(s) in the path, and the reason for no more NCBs is to reduce on-state loss.

Rule 2: There should be at least one path that contains MB(s) between every two port points, and the paths are used to block the fault current when the short-circuit fault occurs.

Judgment of existence seems easier than ***Rule 1***; at least one path in each set with a roadblock greater than 100 can satisfy ***Rule 2***. However, when the path contains another port point, the position of MB may result in fault current blocking failure. The solution given is that the path could pass another port point, but there should be at least 1 MB between the port point being passed and the short-circuit point. The pseudocode for MB judgment in the fault current algorithm is illustrated in Algorithm 2.

```
Input: adjacency matrix, paths, and roadblocks
Output: 0 or 1 (1 represents a valid MB path)
If roadblock < 100
return 0
Initialize another port point in path
If another port point = empty
return 1
else Initialize terminate port point in path; luzu1 = 0
  For another port point : 1 : terminate port point
Calculate the sum of luzu1
If luzu1 > 100
return 1
else return 0
```

Algorithm 2: MB judgment in the fault current

Rule 3: This rule is for blocking the normal load current; theoretically, satisfying ***Rule 2*** can block the fault current, and it can also easily block the normal load current. However, the direction of the fault current and normal load current is different: In most cases for three-port HCBs, the direction of the fault current is converging to a port point, while the direction of the normal load current is radiating outward from a port point.

So blocking the normal load current also has the problem of passing through another port point. It is the same problem as in ***Rule 2***; the pseudocode for MB judgment in the load current is shown in Algorithm 3.

```
Input: adjacency matrix, paths, and roadblocks
Output: 0 or 1 (1 represents a valid MB path)
If roadblock < 100
return 0
Initialize another port point in the path
If another port point = empty
return 1
else Initialize initial port point in the path; luzu2 = 0
  For initial port point : 1 : another port point
Calculate the sum of luzu2
If luzu2 > 100
return 1
else return 0
```

Algorithm 3: MB judgment in the load current

The aforementioned three rules are the main rules that must be satisfied by each output graph and its corresponding adjacency matrix from the algorithm. Moreover, some preliminary filtering rules in the front and ***Sub-rules*** for Table 3 in the back could be added according to the demand.

TABLE 5 Comparison in the one common connection point situation.

	907	913	1,027	1,033	1,034	1,057	1,157
Number of NCB(s)	2	4	2	3	2	3	3
Number of MB(s)[a]	3	2	4	3	3	3	3
Number of diode branches	0	0	0	0	1	0	0
Non-fault line recovery	N	Y	N	N	N	N	Y
Cost	++	+++	+	++	++	++	++

[a]Equivalent to unidirectional MB(s) that need to withstand the system voltage. More '+' means the corresponding topology performs better in the comparison.

Preliminary rules: 1) restrict the number of MBs, 2) restrict the number of NCBs, 3) remove the adjacency matrices with the existence of one degree point, and 4) remove the adjacency matrices with a pure diode branch between any two port points. Preliminary rules 1) and 2) are simply derived by calculating the number of '100' and '0.01' in the adjacency matrix. Preliminary rule 3) is judged by calculating the degree of every point, and preliminary rule 4) needs to determine whether there is a path consisting of only diode branches in each set before judging ***Rules*** by roadblock rounding and calculating the remainder.

Sub-rules are the same as ***Rules***, and they are still judged for six sets of paths and roadblocks in each adjacency matrix. Significantly, the graphs must satisfy ***Rules*** before making ***Sub-rule*** judgments; the output adjacency matrices from ***Rules*** are all bidirectional blocking; only two optional characteristics are explained in Table 3, and their corresponding ***Sub-rules*** are formulated in order.

Sub-rule 1 **(non-fault line recovery)**: If there is a path that satisfies ***Rule 1*** and does not pass through another port point between every two port points, the graph has non-fault line recovery ability.

Only the ideas of the first five lines of Algorithm 2 need to be used for judging ***Sub-rule 1***. The algorithm initializes '*another port point*' in the path, which satisfies ***Rule 1*** and then determines whether '*another port point*' is empty.

Sub-rule 2 **(backup blocking)**: If there is a path that satisfies ***Rule 1*** containing two or more NCBs between every two port points, the graph has the backup blocking ability.

To judge ***Sub-rule 2***, we calculated the number of NCBs in the path, which satisfies ***Rule 1*** by roadblock rounding and calculating the remainder.

After the filtering of ***Rule 1***, ***Rule 2,*** and ***Rule 3***, the search results should have the functions of bidirectional M-HCBs. As for the preliminary rules, ***Sub-rule 1*** and ***Sub-rule 2***, they are optional rules of the algorithm to satisfy the actual application requirements. If other characteristics are required in the future, extra corresponding ***Sub-rules*** will be added in the algorithm.

4 Novel M-HCB topologies

The overall topology searching algorithm, shown in Figure 5, was implemented using MATLAB and ran on AMD Ryzen 5800H CPU with 16GB RAM.

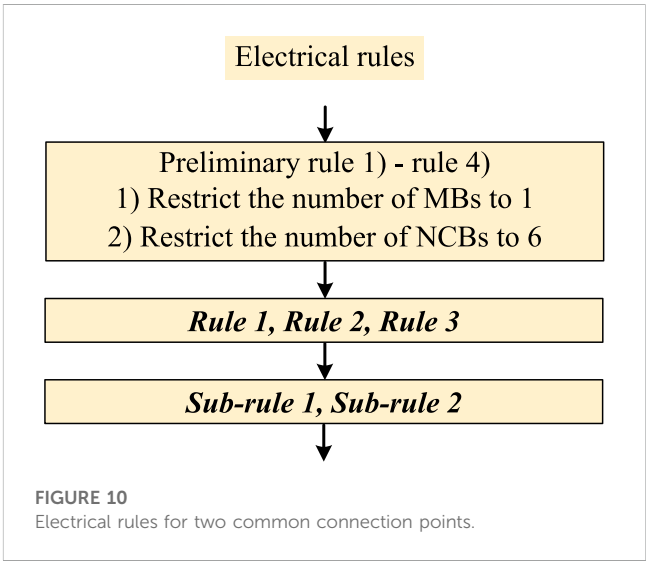

FIGURE 10
Electrical rules for two common connection points.

4.1 One common connection point

There are only 1,250 graphs, and their corresponding adjacency matrices need to be filtered for one common connection point situation. So, an appropriate reduction in rules could get more results that are worth analyzing. The rules used at this time are shown in Figure 8.

In the previously introduced computer configuration, running the topology searching algorithm takes approximately 1 s in this situation. The algorithm outputs 40 graphs and their adjacency matrices, and most of them are isomorphic due to the isomorphism problem; some outputs have no advantages over the proposed topologies. Here, some output topologies selected are shown in Figure 9.

MBs that must be packaged without anti-parallel diodes are indicated in the figures; other MBs are packaged with anti-parallel diodes by default.

Output 907 in Figure 4B is the topology proposed by Li et al. (2018), and it does not have the 'non-fault line recovery' ability when the fault occurs on port 1.

Output 913 in Figure 9A is the optimal performance topology in the one common connection point situation. It has the 'non-fault line recovery' ability for all port points after analysis, and only one bidirectional MB is required.

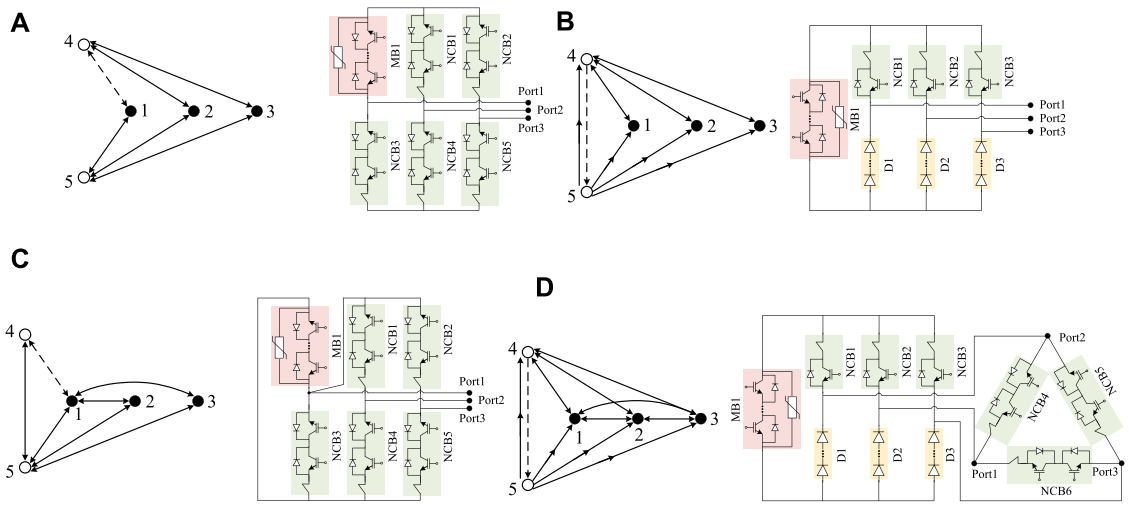

FIGURE 11
Three-port HCB topologies searched by the algorithm in two common connection point situations: **(A)**Output 23,436, **(B)** Output 39,372, **(C)** Output 562,813, and **(D)** Output 742,497.

TABLE 6 Comparison in two common connection points situation.

	23,436	39,062	39,372	562,813	742,497
Number of NCB(s)	5	6	3	5	6
Number of MB(s)[a]	2	1	1	2	1
Number of diode branches	0	0	3	0	3
Cost	+	++	+++	+	++

[a]Equivalent to unidirectional MB(s) that need to withstand the system voltage. More '+' means the corresponding topology performs better in the comparison.

Output 1,027 in Figure 9B is an improvement of Figure 4A, which can be simplified to a zero common connection point situation. It realizes bidirectional blocking by adding another bidirectional MB parallel to the existing NCB.

Outputs 1,033, 1,034, and 1,057 all require three unidirectional MBs to meet the selected electrical rules. They all use one or more MB(s) without anti-parallel diodes. Output 1,034 is the best cost among the three.

Output 1,157 in Figure 9F is an improvement of Output 907, and it has the 'non-fault line recovery' ability in all ports by adding one NCB. For the star structure of MBs in Output 907 and 1,157, three bidirectional MBs are equivalent to three unidirectional MBs, and the MOVs in bidirectional MB arrangement only need to withstand half the system voltage.

Through the aforementioned analysis, the algorithm can search for new topologies while verifying existing topologies and possibly find improvements to existing topologies. There is no limit on the NCB and MB number for the diversity of the output. The output topologies are all bidirectional blocking in terms of characteristics, and the comparison of them is shown in Table 5.

4.2 Two common connection points

Unlike the one common connection point situation, there are 781,250 graphs, and their corresponding adjacency matrices need to be filtered for two common connection point situations. All electrical rules are used from the previous section, as illustrated in Figure 10. Running the overall topology searching algorithm takes approximately 5.5 min. The algorithm outputs 195 graphs and their adjacency matrices; only some output topologies are displayed due to the same isomorphism problem.

Output 23,436, shown in Figure 11A, which uses a small number of branches, is a simple way to configure various branches. The MB located in 1–4 can be configured to replace any of the other five NCBs. Output 39,062 is the topology proposed by Kontos et al. (2018), as illustrated in Figure 4C and Table 3.

Output 39,372 in Figure 11B is the optimal performance topology in this situation. It reduces the cost by replacing three NCBs with three diode branches compared to Output 39,062.

Output 562,813 in Figure 11C is an improvement of Output 913 in the previous part. It obtains the 'backup blocking' ability by adding additional NCBs.

Output 742,497 in Figure 11D also shows good performance. The additional triangular configuration of NCBs provides low-loss branches when flowing through the normal load current and provides more feasible paths for blocking fault current.

In two common connection point situation, the proportion of output reduction is large (781,250–195) due to strict filtering rules. If the algorithm reduces the electrical rules appropriately, such as abandoning ***Sub-rule 2*** or reducing the limit on the NCB and MB

number, it may not only output more topologies but also increase the workload of filtering results. The output topologies are all bidirectional blocking, and they have 'non-fault line recovery' and 'backup blocking' abilities in terms of characteristics. The comparison of them is shown in Table 6.

5 Conclusion

A novel M-HCB topology searching algorithm based on graph theory is proposed in this paper. The algorithm uses 'roadblock' to simplify adjacency matrices in the mathematization of the topologies and then enumerates all matrices and filters them by electrical rules. Some new M-HCB topologies are obtained from the three-port example-specific application. This proves that the new method can search M-HCB topologies effectively. It greatly reduces the innovation time of the new M-HCB topology, which can be customized according to the actual requirements. The idea of the topology searching algorithm and the concept of 'roadblock' can be applied to find other types of circuit breaker topologies or even power supply topologies.

Data availability statement

The original contributions presented in the study are included in the article/Supplementary Material; further inquiries can be directed to the corresponding author.

Author contributions

SH: writing—original draft and algorithm implementation. JZ: idea and writing—original draft. QZ: drawing figures and editing. XG: drawing figures and editing. JY: process analysis and supervision. TW: supervision.

Funding

This work was supported in part by the National Natural Science Foundation of China under Grant 51607171 and the Institute of Electrical Engineering, CAS, under grants E155610301 and E155610201.

Acknowledgments

This is a brief acknowledgment of the contributions of individual colleagues, institutions, or agencies that assisted the writers' efforts in the writing of this paper.

Conflict of interest

The authors declare that the research was conducted in the absence of any commercial or financial relationships that could be construed as a potential conflict of interest.

Publisher's note

References

Chen, G., Jin, Z., Liu, Y., Hu, Y., Zhang, J., and Qing, X. (2019). Programmable topology derivation and analysis of integrated three-port dc–dc converters with reduced switches for low-cost applications. *IEEE Trans. Ind. Electron.* 66 (9), 1–6660. doi:10.1109/TIE.2018.2877159

Debnath, S., Qin, J., Bahrani, B., Saeedifard, M., and Barbosa, P. (2015). Operation, control, and applications of the modular multilevel converter: A review. *IEEE Trans. Power Electron.* 30 (1), 37–53. doi:10.1109/TPEL.2014.2309937

Guo, X., Zhu, J., Yin, J., Wang, W., and Wei, T. (2022). Topology optimization and evaluation of multiport hybrid dc circuit breaker based on graph theory. *Energy Rep.* 8, 1002–1012. doi:10.1016/j.egyr.2021.12.004

Guo, Y., Li, H., Gu, G., Zeng, D., and Wang, G. (2021). A multiport dc circuit breaker for high-voltage dc grids. *IEEE J. Emerg. Sel. Top. Power Electron.* 9 (3), 3216–3228. doi:10.1109/JESTPE.2020.3018646

He, J., Luo, Y., Li, M., Zhang, Y., Xu, Y., Zhang, Q., et al. (2020). A high-performance and economical multiport hybrid direct current circuit breaker. *IEEE Trans. Ind. Electron.* 67 (10), 8921–8930. doi:10.1109/TIE.2019.2947835

Kontos, E., Schultz, T., Mackay, L., Ramirez-Elizondo, L., Franck, C., and Bauer, P. (2018). Multi-line breaker for hvdc applications. *IEEE Trans. Power Del* 33 (3), 1469–1478. doi:10.1109/TPWRD.2017.275464933

Li, C., Liang, J., and Wang, S. (2018). Interlink hybrid dc circuit breaker. *IEEE Trans. Ind. Electron.* 65 (11), 8677–8686. doi:10.1109/TIE.2018.2803778

Li, H., Wang, W., Li, Y., Zeng, Y., Su, W., and Zhang, B. (2019). Programmable topology searching algorithm for $S^1D^1L^2C^1$ type DC-DC converters based on graph theory. *Proc. CSEE* 41 (16), 5670–5683. doi:10.13334/j.0258-8013.pcsee.201750

Li, K., Hu, Y., and Ioinovici, A. (2017b). Generation of the large dc gain step-up non-isolated converters in conjunction with renewable energy sources starting from a proposed geometric structure. *IEEE Trans. Power Electron.* 32 (7), 5323–5340. doi:10.1109/TPEL.2016.260950132

Li, Z., Tang, Y., Zhao, Z., Wu, X., Han, Y., Li, L., et al. (2017a). The model and parameters based on the operation mode of a 500kV multi-terminal flexible DC power grid. *Int. J. Power Eng. Eng. Thermophys.* 1, 16–24. doi:10.23977/poweet.2017.11003

Liu, G., Xu, F., Xu, Z., Zhang, Z., and Tang, G. (2017). Assembly hvdc breaker for hvdc grids with modular multilevel converters. *IEEE Trans. Power Electron.* 32 (2), 931–941. doi:10.1109/TPEL.2016.2540808

Liu, K., and Lee, F. (April, 1988). Topological constraints on basic PWM converters. IEEE Power Electronics Specialists Conference, Kyoto, Japan, 164–172. doi:10.1109/PESC.1988.18130

Meah, K., and Ula, S. (2007). Comparative evaluation of HVDC and HVAC transmission systems. *IEEE Power Eng. Soc. Gen. Meet.*, 1–5. doi:10.1109/PES.2007.385993

Mokhberdoran, A., Van Hertem, D., Silva, N., Leite, H., and Carvalho, A. (2018). Multi-port hybrid hvdc circuit breaker. *IEEE Trans. Ind. Electron.* 65 (1), 309–320. doi:10.1109/TIE.2017.2719608

Ogata, M., and Nishi, T. (2005). Graph-theoretic approach to the design of four-switch DC-DC converters. *IEEE Int. Symp. Circuits Syst.*, 768–771. doi:10.1109/ISCAS.2005.1464701

Ogata, M., and Nishi, T. (May, 2003). Topological criteria for switched mode DC-DC converters. IEEE International Symposium on Circuits and Systems. (ISCAS), Bangkok, Thailand, 184–187. doi:10.1109/ISCAS.2003.1204986

Oubelaid, A., Taib, N., Rekioua, T., Bajaj, M., Blazek, V., Prokop, L., et al. (2022d). Multi source electric vehicles: Smooth transition algorithm for transient ripple minimization. *Sustainability* 22 (18), 6772. doi:10.3390/s22186772

Oubelaid, A., Albalawi, F., Rekioua, T., Ghoneim, S., Taib, N., and Abdelwahab, S. (2022a). Intelligent torque allocation based coordinated switching strategy for comfort enhancement of hybrid electric vehicles. *IEEE Access* 10, 58097–58115. doi:10.1109/ACCESS.2022.3178956

Oubelaid, A., Alharbi, H., Humayd, A., Taib, N., Rekioua, T., and Ghoneim, S. (2022c). Fuzzy-energy-management-based intelligent direct torque control for a battery-supercapacitor electric vehicle. *Sustainability* 14 (14), 8407. doi:10.3390/su14148407

Oubelaid, A., Taib, N., Nikolovski, S., Alharbi, T., Rekioua, T., Flah, A., et al. (2022b). Intelligent speed control and performance investigation of a vector controlled electric vehicle considering driving cycles. *Electronics* 11 (13), 1925. doi:10.3390/electronics11131925

Qu, L., Yu, Z., Chen, Z., Zhang, X., Chen, J., Liu, Y., et al. (2019). Engineering application of three-terminal hybrid dc circuit breaker. *Automation Electr. Power Syst.* 43 (23), 141–146+154. doi:10.7500/AEPS20190509005

Ranjana, M., Mule, S., Arjun, H., and Kulkarni, R. (March, 2016). DC-DC buck converter through duality approach for current based loads. IEEE International Conference on Electrical, Electronics, and Optimization Techniques (ICEEOT), Chennai, India, 2622–2625. doi:10.1109/ICCPCT.2016.7530111

Tang, G., He, Z., Pang, H., Huang, X., and Zhang, X. (2015). Basic topology and key devices of the five-terminal dc grid. *CSEE J. Power Energy Syst.* 1 (2), 22–35. doi:10.17775/CSEEJPES.2015.00016

Wang, S., Ming, W., Ugalde-Loo, C. E., and Liang, J. (2022). A low-loss integrated circuit breaker for hvdc applications. *IEEE Trans. Power Del* 37 (1), 472–485. doi:10.1109/TPWRD.2021.3063515

Wang, S., Ugalde-Loo, C. E., Li, C., Liang, J., and Adeuyi, O. D. (2020). Bridge-type integrated hybrid dc circuit breakers. *IEEE J. Emerg. Sel. Top. Power Electron.* 8 (2), 1134–1151. doi:10.1109/JESTPE.2019.29004928

Wen, W., Li, B., Li, B., Liu, H., He, J., Ma, J., et al. (2019). Analysis and experiment of a micro-loss multi-port hybrid dccb for mvdc distribution system. *IEEE Trans. Power Electron* 34 (8), 7933–7941. doi:10.1109/TPEL.2018.2881000

Xiao, H., Xu, Z., Xiao, L., Gan, C., and Dai, L. (2020). Components sharing based integrated hvdc circuit breaker for meshed hvdc grids. *IEEE Trans. Power Del.* 35 (4), 1856–1866. doi:10.1109/TPWRD.2019.295572635

Zhang, S., Zou, G., Wei, X., and Sun, C. (2021). Diode-bridge multiport hybrid dc circuit breaker for multiterminal dc grids. *IEEE Trans. Ind. Electron.* 68 (1), 270–281. doi:10.1109/TIE.2020.2965459

Zhu, J., Zeng, Q., Guo, X., Jia, H., Cui, B., and Wei, T. (2022). Multiport current injection hybrid DC circuit breaker with simple bridge arm circuit. *IEEE Trans. Ind. Electron.*, 1–10. doi:10.1109/TIE.2022.3224138 Early Access

frontiers | Frontiers in Energy Research

TYPE Original Research
PUBLISHED 09 May 2023
DOI 10.3389/fenrg.2023.1125861

OPEN ACCESS

EDITED BY
Meng Yen Shih,
Autonomous University of Campeche, Mexico

REVIEWED BY
Fang Shi,
Shandong University, China
Ahmad Farid Abidin,
Faculty of Electrical Engineering UiTM, Malaysia

*CORRESPONDENCE
Abbas Ketabi,
aketabi@kashanu.ac.ir

SPECIALTY SECTION
This article was submitted to Smart Grids, a section of the journal Frontiers in Energy Research

RECEIVED 16 December 2022
ACCEPTED 29 March 2023
PUBLISHED 09 May 2023

CITATION
Nobakhti SM and Ketabi A (2023), A protection scheme based on impedance for LV and MV lines in microgrids with high-impedance fault detection capability.
Front. Energy Res. 11:1125861.
doi: 10.3389/fenrg.2023.1125861

A protection scheme based on impedance for LV and MV lines in microgrids with high-impedance fault detection capability

Seyyed Mohammad Nobakhti[1] and Abbas Ketabi[2]*

[1]Department of Electrical Engineering, Technical and Vocational University (TVU), Tehran, Iran, [2]Department of Electrical and Computer Engineering, University of Kashan, Kashan, Iran

Microgrid properties including bidirectional power flow in feeders, fault level decrease in the islanded mode, and intermittent nature of distributed generators (DGs) result in the malfunctioning of microgrid conventional protection schemes. In the present article, a protection scheme based on impedance is suggested for fault detection in LV and MV overhead and cable distribution lines in both grid-connected and islanded modes. To determine a fault detection index, new suggested equivalent circuits for doubly fed lines are applied. Relay location data and magnitude of positive sequence voltage of the other end of the line are used. It is simulated by PSCAD and MATLAB software in order to evaluate its performance and approve its validity. This scheme can detect even high-impedance faults in both grid connected and islanded modes in LV and MV overhead and cable distribution lines. In addition, it is robust against load and generation uncertainty and network reconfigurations. Low sampling rate and minimum data exchange are among the advantages of the proposed scheme.

KEYWORDS

active distribution line, distributed generator, distribution network, doubly fed line modeling, fault detection, impedance-based protection, microgrid

1 Introduction

Microgrids are made of medium- and low-voltage distribution systems including distributed generators (DGs) and loads, capable of operating in islanded and grid-connected modes in an organized and controlled way. Microgrids mainly improve the reliability and resiliency of the power system. An advantage of microgrids is their capability of facilitating more creative schemes to meet local demands flexibly with small-scale generators and consumers closely integrated (Mirsaeidi et al., 2016), (Teimourzadeh et al., 2016).

Regardless of the advantages of microgrids, extensive use of microgrids leads to protection and control challenges and coordination problems with the main network. Because of the presence of looped feeders, bidirectional power flow in the lines, and a considerable decrease in the fault level in the islanded mode, the conventional strategies of microgrid protection do not operate correctly (Blaabjerg et al., 2017).

Furthermore, in traditional distribution networks, if a fault occurs, the recloser disconnects the fault from the utility in a fast mode and reconnects after a short interval. It may cause fault self-clearing if it was temporary. However, in the distribution network with DGs, to ensure the correctness of automatic reclosing, DGs should be entirely disconnected before reconnecting. If during the disconnecting interval, a DG continues its

connection to the network, after the short break and utility reconnection, the fault may not be cleared because the DG has fed the arc during the disconnecting interval. In addition, after the break, the frequency changes are probable in the distribution network islanded part. So, by reclosing the switch, two operating systems consisting of active sources with different frequencies on both sides of one recloser are coupled (Jiao et al., 2015), (Adly et al., 2017). Therefore, new communication-based protection schemes with intelligent devices are required to protect these lines (Aminifar et al., 2014).

In general, microgrid protection schemes are configured in two classes: first, network modifying-based schemes modifying the behavior of the grid during the fault for correct performance of traditional protection schemes; second, protective strategy-based schemes modifying conventional protection schemes based on behaviors of microgrids.

A. Network modifying-based schemes

The fault current level changes considerably when the microgrid alters from grid-connected to islanded mode and *vice versa*. Some protection strategies use external devices for decreasing the main grid fault current contribution. These devices include fault current limiters, ultra-capacitors, flywheels, batteries, and ones installed between the microgrid and the main grid. Mostly, the implementation of these schemes needs high investment (Khederzadeh, 2012; Ghanbari and Farjah, 2013; Esmaeili Dahej et al., 2018).

Grounding strategy modification was suggested in Teimourzadeh et al. (2016) to avoid mal-operation of conventional protection strategies. To some extent, it affords correct operation conditions of relays at a low cost.

In Oureilidis and Demoulias (2016), a scheme was proposed for the protection of looped microgrids with a conventional protection system. The fault was detected by indirectly measuring the impedance of the microgrid. Then, the control system of DGs was adjusted to inject a current proportionate to the measured microgrid impedance, according to a droop curve. This meant that DGs closer to the fault injected a moderately larger current and provided selective coordination of the protection devices.

B. Protective strategy-based schemes

There are several kinds of microgrid protection schemes in this class. Adaptive strategies are one group. In these schemes, relay settings are modified automatically when the operation mode of the microgrid (islanded or grid-connected) is changed (Orji et al., 2017). A scheme for the protection of microgrids in both operation modes applying phasor measurement units (PMUs) on the basis of positive sequence impedance was presented in Mirsaeidi et al. (2016). However, it was required to update the values of pickup relays after a configuration change in the microgrid. In Laaksonen et al., 2014), a monitoring system was explained, in which online updating of the relay settings was based on the operating modes of the microgrid. It used communication links to collect data from smart electronic devices and send data to a central controller for real-time analysis.

One challenge of using these schemes is substituting all the existing relays with adaptive ones, which is costly and requires upgrading the present protection schemes of distribution systems. Moreover, adaptive relays usually need communication infrastructures.

Differential-based schemes as another group compare the currents entering and leaving the protected zone and operate when the differential between these currents exceeds a predetermined magnitude (Zeineldin et al., 2006), (Sortomme et al., 2010). A multi-agent microgrid protection scheme based on a variable tripping time differential protection was suggested by Aghdam et al. (2019) and would be capable of operating in both grid-connected and islanded modes. Moreover, in Kar et al. (2017), the differential features were extracted from the fault current and voltage by applying the discrete Fourier transform, and a decision-tree data mining model was proposed to decide ultimately.

Generally, differential schemes require a communication system and synchronized measurements. Moreover, transients and unbalanced loads may challenge the operation of the protection system.

Another group is voltage-based schemes. Some voltage-based protection schemes recognize the faults by detecting the fundamental voltage-positive sequence component. Some others apply the d–q transform. Loix presented a technique on the basis of the impact of different types of faults on the components of the voltage Park transform for protecting microgrids against different faults (Loix et al., 2009). Differential angle variations of the voltages of buses with the common coupling point voltage were used to propose a scheme for microgrid protection in Sharma and Samantaray (2019). This scheme required synchronous measuring of the angles of several bus voltages. This protection scheme recognized fault occurrence; however, it was not able to determine the faulty line of the microgrid.

Generally, in these schemes, the type of fault and voltage depth magnitude during the fault change the detection time. Hence, these schemes are mainly dependent on the operational mode of the microgrids. Incorrect protections may be triggered by voltage fluctuations owing to non-fault happenings in the islanded mode of microgrids.

In addition, the overcurrent schemes are another group in this class (Best et al., 2009). An overcurrent relay characteristic was proposed in Darabi et al. (2020) to reduce the time of operation of the overcurrent relay. Zero and negative sequence currents were applied for proposing the protection scheme in Zamani et al. (2011). Furthermore, in Furlan et al. (2018), unbalances of voltage were used to improve the overcurrent operation.

Usually, these schemes are highly dependent on wide-area communication systems and are affected by fault level changes.

In distance protection, impedance or admittance is utilized for fault detection. Here, for a fault occurrence downstream of the distance relay location where DGs are installed, the distance relay observes an impedance larger than the actual impedance of the fault. It causes an ostensibly increased distance in the fault because of the added voltage due to an infeed at the common bus. It may lead to a malfunction of the distance relays (Hooshyar and Iravani, 2017). The effects of the resistance of the fault and midway infeed on the performance of the distance protection system in the radial feeders of distribution grids were studied in Nikolaidis et al. (2018). In

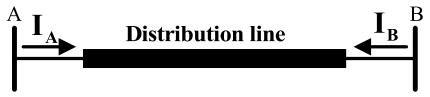

FIGURE 1
Doubly fed distribution line.

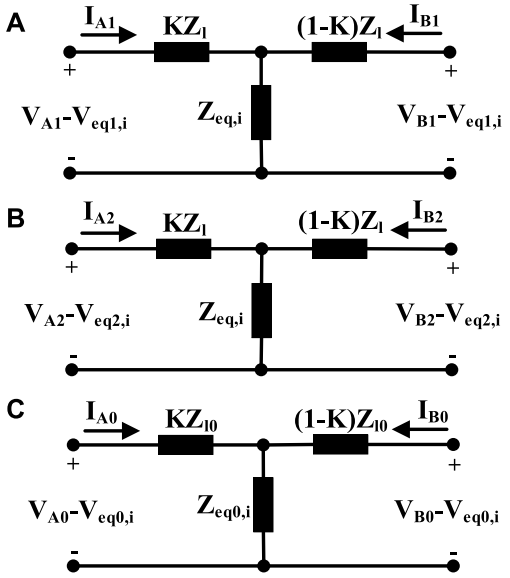

FIGURE 2
(A) SPS, simplified positive sequence circuit; **(B)** SNS, simplified negative sequence circuit; **(C)** SZS, simplified zero sequence circuit.

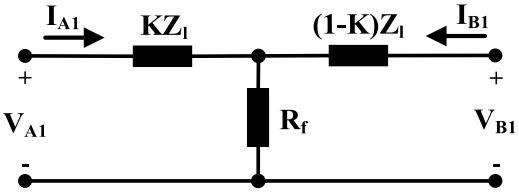

FIGURE 3
SPS circuit for three-phase fault.

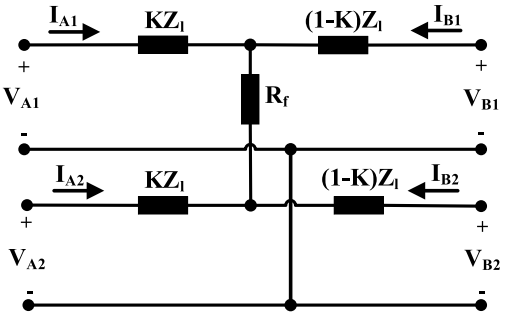

FIGURE 4
Conventional sequence equivalent circuits for line-to-line fault.

addition, the combined influence of fault resistance and infeed on the distance protection system was assessed, and resulting problems concerning suitable relay operations were illustrated. In Bottrell and Green (2013), faults were detected by applying the inverse-time tripping admittance. In addition, impedance differential and inverse-time low-impedance protection schemes were proposed in Huang et al. (2014) as the main and backup protection schemes, respectively. Furthermore, in Pandakov and Hoidalen (2017), a compensation scheme to omit errors due to impedances of faults and infeed currents was suggested. Biller and Jaeger (2018) proposed a voltage-free scheme for distance protection compatible with inter-infeed and closed-loop feeders to protect lines in the microgrids. This scheme was based on negative sequence currents measured at the relay location and remained unaffected by negative sequence current suppressing converter-connected DGs and fault resistances. In addition, in FangJia et al. (2019), an improved scheme on the basis of time delay and zero sequence impedance was presented.

The most important advantage of these schemes is their independence of change in the fault current in both microgrid operation modes, but the resistance of the fault and the infeed produced by DGs may cause some errors in the measured impedance. Furthermore, current transients may decrease the measurement precision. Optic fibers can be used for the communication link (Shabani and Mazlumi, 2020), and in long lines, PMUs can be placed on buses (Sharma and Samantaray, 2020) (Garcia et al., 2020).

In Wang et al. (2019), a high-impedance fault detection method based on variational mode decomposition was proposed, where the non-linear characteristics of high-impedance faults were modeled. In addition, in Nobakhti et al. (2021), protection algorithms were proposed for main and backup protection in LV microgrid lines, but their operations have not been studied for high-impedance faults. Moreover, the performance of the schemes was not evaluated in MV microgrids and cable lines.

Therefore, it seems a serious requirement for a protection scheme based on impedance for overhead and cable lines, with the least effect of infeed and impedance of the fault on its operation. In this article, a new impedance-based scheme for microgrid protection in grid-connected and islanded modes is proposed. It has the following features:

- High-impedance fault detection
- Correct performance in overhead and cable lines
- Fault detection capability in LV and MV lines
- Suitable detection time
- Low rate of sampling
- Minimal exchange of data
- Independence from uncertainties of load and generation
- Independence from grid reconfigurations

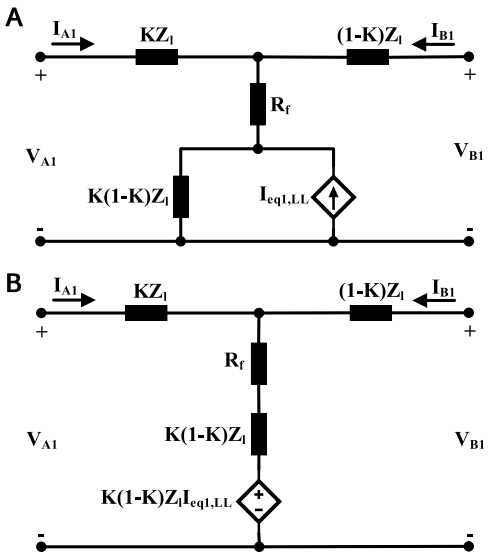

FIGURE 5
Simplified circuit for line-to-line fault. **(A)** simplified circuit of Figure 4 for line-to-line fault. **(B)** simplified circuit of Figure 5A.

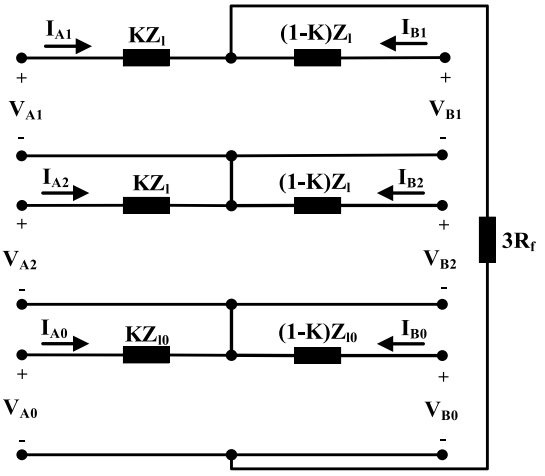

FIGURE 6
Conventional sequence equivalent circuits for single-line-to-ground fault.

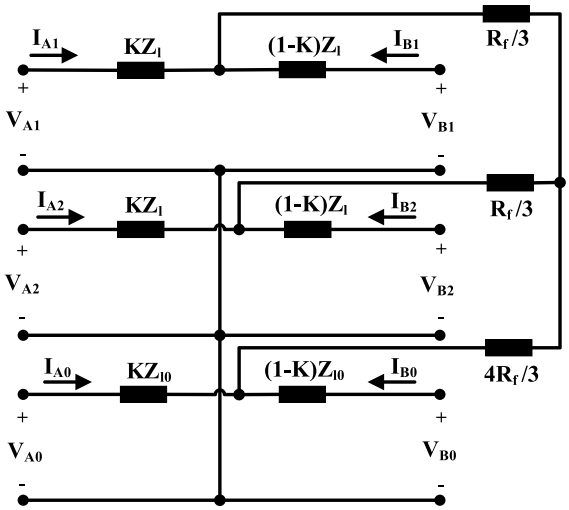

FIGURE 7
Conventional sequence equivalent circuits for double-line-to-ground fault.

This article comprises the following sections. Short-circuit fault types and their corresponding equivalent circuits used in the suggested protection scheme are presented in Section 2. In the next section, a new fault detection scheme for microgrids based on impedance is proposed. Section 4 elaborates on the simulation of the proposed strategy in PSCAD and MATLAB software to evaluate its performance. , Section 5 concludes the study.

2 Proposed doubly fed line equivalent circuits during short-circuit faults

Because of the presence of DGs, some distribution lines in microgrids are supplied from two ends. These doubly fed distribution lines are depicted in Figure 1. The sequence equivalent circuits of each type of short-circuit fault are required for studying faults.

In this section, the simplified positive sequence equivalent circuit, abbreviated as "SPS" circuit; simplified negative sequence circuit, abbreviated as "SNS" circuit; and simplified zero sequence circuit, abbreviated as "SZS" circuit, using the conventional sequence ones, are introduced, and they are described in Figure 2, where K is between 0 and 1 and indicates the location of the fault, and "i" may be substituted with "3P," "LL," "DLG," and "SLG" for three-phase, line-to-line, double-line-to-ground, and single-line-to-ground faults, respectively.

Also, positive, negative, and zero sequence will be symbolized by "1," "2," and "0" subscript, respectively. Z_l represents positive sequence line impedance, and Z_{l0} is zero sequence line impedance. $Z_{eq,i}$ and $Z_{eq0,i}$ represent sequence equivalent impedances, and $V_{eq1,i}$,$V_{eq2,i}$, and $V_{eq0,i}$ represent sequence equivalent voltages. The sequence equivalent impedances and voltages will be explicated for each fault type distinctively.

A.Three-phase fault

Here, three phases are grounded by resistance R_f. Figure 3 depicts the conventional equivalent circuit that contains the positive sequence. By comparing this figure and the SPS circuit in Figure 2A, $V_{eq1,3P}$ and $Z_{eq,3P}$ are obtained as follows:

$$\begin{cases} Z_{eq,3P} = R_f \\ V_{eq1,3P} = 0. \end{cases} \quad (1)$$

There are no SNS and SZS circuits in this fault type because of the absence of negative and zero sequence components.

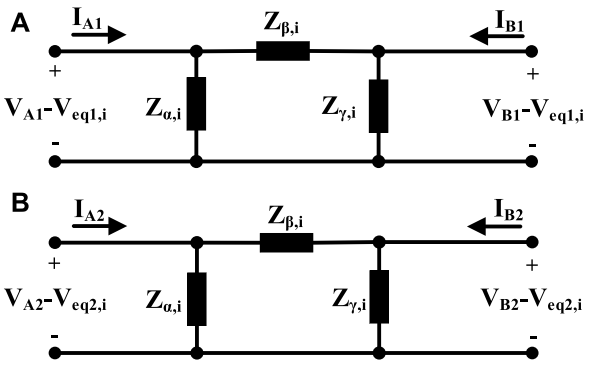

FIGURE 8
Transformed to equivalent delta circuits **(A)** SPS and **(B)** SNS.

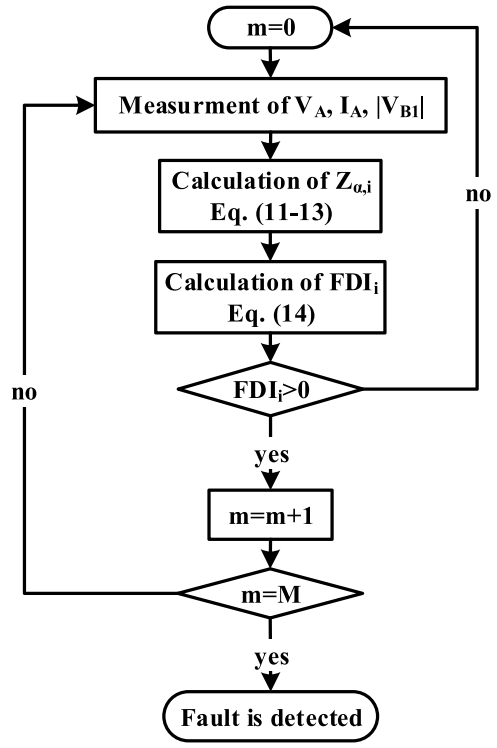

FIGURE 9
Proposed scheme flowchart.

B. Line-to-line fault

In the line-to-line fault, two phases are connected by resistant R_f. Figure 4 shows the conventional equivalent circuit for this fault comprising the positive and negative sequences.

If Thevenin equivalent circuits [V_{A2} series with impedance KZ_l and also V_{B2} series with impedance $(1-K)Z_l$] convert to the corresponding Norton equivalent, after simplifying the resulting circuit, Figure 5A will be attained, where

$$I_{eq1,LL} = \frac{V_{A2}}{K.Z_l} + \frac{V_{B2}}{(1-K).Z_l.} \quad (2)$$

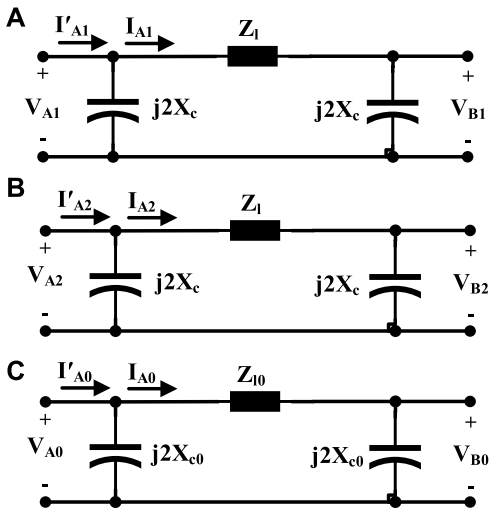

FIGURE 10
π model of the line. **(A)** positive sequence **(B)** negative sequence **(C)** zero sequence.

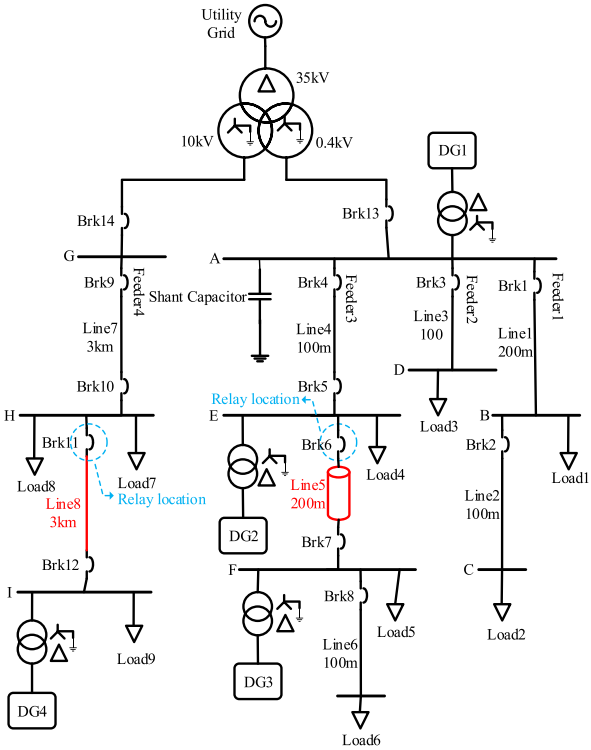

FIGURE 11
Case study system.

By altering the dependent current source parallel with impedance (Norton equivalent) to the corresponding dependent voltage source series with impedance (Thevenin equivalent) shown in Figure 5A, the circuit in Figure 5B is obtained. By subtracting voltage $K(1-K)Z_lI_{eq1,LL}$ from the voltages of both ends of the circuit, the dependent source in the

middle branch is removed. So, the SPS circuit for this fault type is achieved. $V_{eq1,LL}$ and $Z_{eq,LL}$ are obtained as follows:

$$\begin{cases} Z_{eq,LL} = R_f + K.(1-K).Z_{l,} \\ V_{eq1,LL} = (1-K).V_{A2} + K.V_{B2.} \end{cases}. \quad (3)$$

In the same way, the SNS circuit is achieved, in which

$$V_{eq2,LL} = (1-K).V_{A1} + K.V_{B1.}. \quad (4)$$

It is clear that there is no SZS circuit for the LL fault.

C. Single-line-to-ground fault

In this fault type, one of three phases is connected to the ground by resistant R_f. Figure 6 shows the sequence equivalent circuits of the single-line-to-ground fault. By simplifying the negative and zero sequence circuits, the SPS circuit is achieved. Similarly, SNS and SZS circuits are achieved:

$$\begin{cases} Z_{eq,SLG} = 3R_f + K.(1-K).(Z_l + Z_{l0}), \\ V_{eq1,SLG} = -(1-K).(V_{A2} + V_{A0}) - K.(V_{B2} + V_{B0}), \\ V_{eq2,SLG} = -(1-K).(V_{A1} + V_{A0}) - K.(V_{B1} + V_{B0}), \\ Z_{eq0,SLG} = 3R_f + 2K.(1-K).Z_l, \\ V_{eq0,SLG} = -(1-K).(V_{A1} + V_{A2}) - K.(V_{B1} + V_{B2}). \end{cases} \quad (5)$$

D. Double-line-to-ground fault

This fault will happen when two phases are connected together by resistant R_f and also to the ground by the same resistance. Figure 7 displays the sequence equivalent circuits of the double-line-to-ground fault. Parameters of SNS, SPS, and SZS equivalent circuits will be determined as follows:

$$\begin{cases} Z_{eq,DLG} = \dfrac{R_f}{3} + \\ \dfrac{\left(3K.(1-K).Z_{l0} + 4R_f\right).\left(3K.(1-K).Z_l + R_f\right)}{3\left(3K.(1-K).(Z_l + Z_{l0}) + 5R_f\right)} \\ V_{eq1,DLG} = M.((1-K).V_{A2} + K.V_{B2}) + \\ N.((1-K).V_{A0} + K.V_{B0}) \\ V_{eq2,DLG} = M.((1-K).V_{A1} + K.V_{B1}) + \\ N.((1-K).V_{A0} + K.V_{B0}) \\ Z_{eq0,DLG} = \dfrac{K.(1-K).Z_l + 3R_f}{2} \\ V_{eq0,DLG} = \dfrac{(1-K)}{2}(V_{A1} + V_{A2}) + \dfrac{K}{2}(V_{B1} + V_{B2}), \end{cases} \quad (6)$$

where M and N are achieved as follows:

$$\begin{cases} M = \dfrac{3K.(1-K).Z_{l0} + 4R_f}{3K.(1-K).(Z_l + Z_{l0}) + 5R_f}, \\ N = \dfrac{3K.(1-K).Z_l + R_f}{3K.(1-K).(Z_l + Z_{l0}) + 5R_{f.}} \end{cases} \quad (7)$$

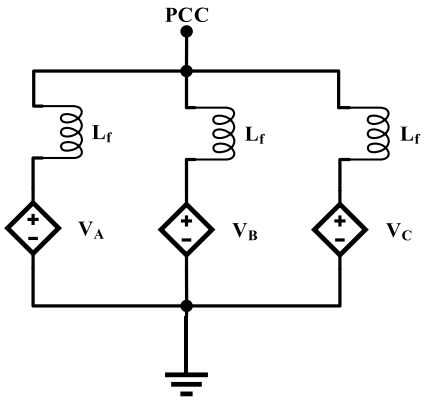

FIGURE 12
Equivalent circuit for DGs.

3 Proposed impedance-based protection scheme

Using Y-Δ transform, SPS and SNS circuits shown in Figure 2 are reformed to Figure 8, as follows:

$$Z_{\alpha,i} = K.Z_l + \frac{Z_{eq,i}}{1-K}, \quad (8)$$

$$Z_{\beta,i} = Z_l + \frac{K.(1-K).Z_l^2}{Z_{eq,i}}, \quad (9)$$

$$Z_{\gamma,i} = (1-K).Z_l + \frac{Z_{eq,i}}{K}. \quad (10)$$

Based on Eq. 8, by increasing R_f, the absolute value of $Z_{\alpha,LL}$ shall be increased. R_f is infinite under normal conditions, so the absolute value of $Z_{\alpha,LL}$ will be infinite, too, and its angle will be 0. However, during the fault, its absolute value will be decreased drastically and its angle will be increased at most about the angle of the positive sequence impedance of the line. Notably, the line impedance angle in distribution lines is small.

In addition, based on Eq. 9), under normal conditions, the absolute values and angles of impedance $Z_{\beta,LL}$ and impedance Z_l will be equal, and during the faults, the angle variations of impedance $Z_{\beta,LL}$ will be low. The absolute value variations of $Z_{\beta,LL}$ will be low, too, except for small R_f. The intensive reduction of $Z_{\alpha,i}$ during the fault can be a basis for fault detection.

Using KCL and KVL in circuits shown in Figure 8 and the SZS circuit, and substituting R_f and K with $Z_{\alpha,i}$ and $Z_{\beta,i}$, the absolute value of V_{B1} is obtained. If this value equals its sent value from the other line end, and $Z_{\beta,i}$ is substituted with Z_l (as its value in normal conditions), an equation with variable $Z_{\alpha,i}$ shall be attained.

For example, for the line-to-line fault, KCL leads to

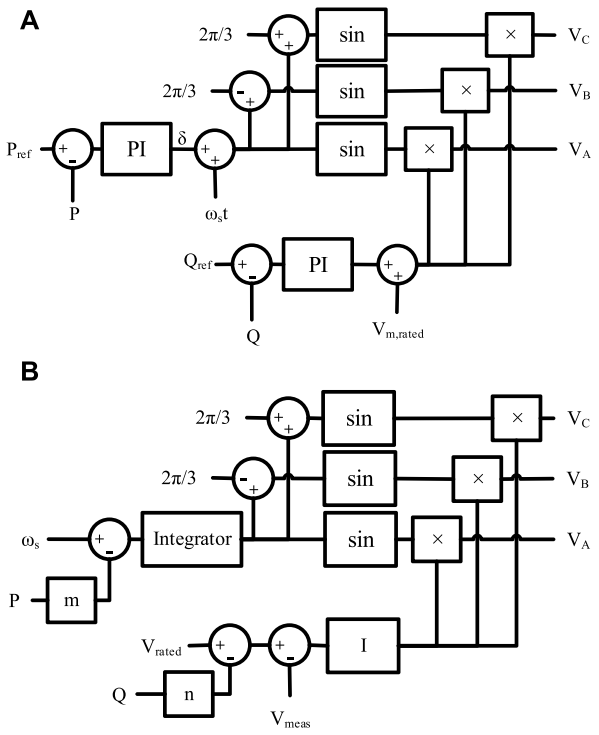

FIGURE 13
DG control system in **(A)** grid-connected mode and **(B)** islanded mode.

$$I_{A1} = \frac{V_{A1} - V_{B1}}{Z_{\beta,LL}} + \frac{V_{A1} - V_{eq1,LL}}{Z_{\alpha,LL}} = \frac{V_{A1} - V_{B1}}{Z_{\beta,LL}} + \frac{V_{A1} - (1-K).V_{A2} - K.V_{B2,}}{Z_{\alpha,LL}}$$
$$I_{A2} = \frac{V_{A2} - V_{B2}}{Z_{\beta,LL}} + \frac{V_{A2} - V_{eq2,LL}}{Z_{\alpha,LL}} = \ldots \quad (11)$$
$$\frac{V_{A2} - V_{B2}}{Z_{\beta,LL}} + \frac{V_{A2} - (1-K).V_{A1} - K.V_{B1.}}{Z_{\alpha,LL}}$$

.

Considering Eq. 8 and Eq. 9, K and Rf can be attained from the following equations:

$$Z_{\alpha,LL} = K.Z_l + \frac{Z_{eq,LL}}{1-K} = K.Z_l + \frac{R_f + K.(1-K).Z_l}{1-K},$$
$$Z_{\beta,LL} = Z_l + \frac{K.(1-K).Z_l^2}{Z_{eq,LL}} = Z_l + \frac{K.(1-K)Z_l^2}{R_f + K.(1-K).Z_l}. \quad (12)$$

By substituting calculated K and R_f in the KCL equations and also substituting $Z_{\beta,LL}$ with Z_l, V_{B1} is achieved as follows:

$$V_{B1} = \frac{Z_l V_{A1}}{Z_{\alpha,LL}} - \frac{Z_l V_{A2}}{Z_{\alpha,LL}} + V_{A1} - Z_l I_{A1.} \quad (13)$$

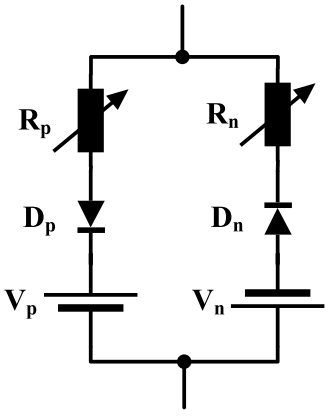

FIGURE 14
High-impedance fault model.

In the same way, V_{B1} is achieved for other faults. By supposing 0 for the angle of $Z_{\alpha,i}$, two answers will be found for $Z_{\alpha,i}$ (as a real number). One of them has an ineligible negative value. The other answer, for the external faults and normal conditions, is $+\infty$, and during the faults, it decreases to a positive value. So, considering this change, Fault Detection Index (FDI_i) can be described as follows:

$$FDI_i = \log\left(\frac{C_i}{Z_{\alpha,i}}\right). \quad (14)$$

Constant coefficient C_i is determined, which is slightly greater than the absolute value of $Z_{\alpha,i}$, for the fault near to the end B with considered maximum fault resistance.

FDI_i is negative under normal conditions and may transiently become positive for faults in the adjacent lines. Therefore, consecutive M positive samples of FDI_i will detect a fault.

In this scheme, the voltage and current of the line beginning and the positive sequence voltage absolute value of the line end are applied to line protection from the beginning of the line. Thus, only one quantity should be sent from the other side of the line, unlike the previously presented protection schemes, like Huang et al. (2014), that generally required the transmission of two quantities (absolute value and angle of a phasor quantity) or more. Hence, in the proposed scheme, the exchange of data decreases by 50%, which is an advantage. Figure 9 shows the flowchart of this scheme. Nowadays, intelligent digital relays are used extensively, and implementation of the proposed scheme is possible using them.

In this scheme, distribution lines were modeled by resistance and inductance, and the line capacitance was ignored. This assumption is acceptable in the overhead lines, but it may be challenged for cable lines in high-resistance faults. In order to modify this scheme for cable lines, the π model of the line is applied (illustrated in Figure 10). So, I_{A1}, I_{A2}, and I_{A0} in the proposed scheme should be substituted as follows:

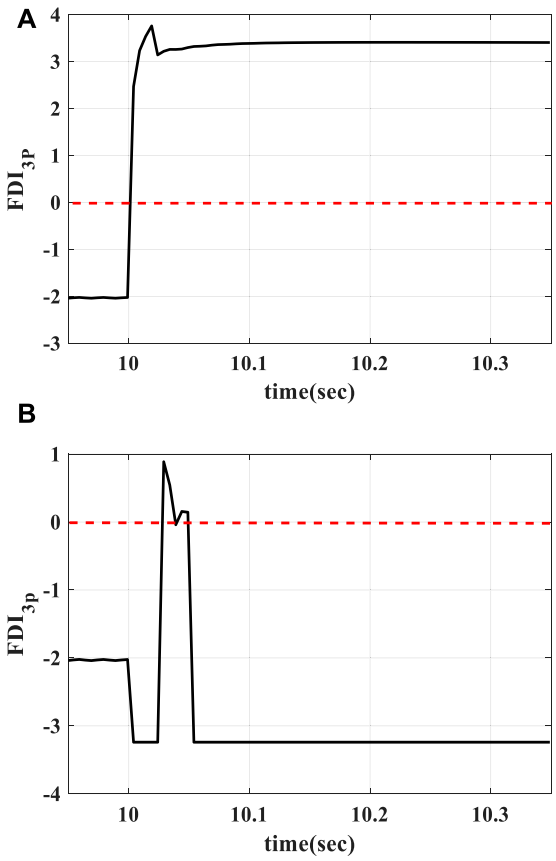

FIGURE 15
FDI$_{3P}$ curve for 3P fault in grid-connected operation mode with fault resistance 0.01 ohm at **(A)** 50% of Line 5 (constantly positive) and **(B)** 10% of Line 6 (temporary positive).

$$I_{A1} = I'_{A1} - \frac{V_{A1}}{j2X_c},$$
$$I_{A2} = I'_{A2} - \frac{V_{A2}}{j2X_c}, \quad (15)$$
$$I_{A0} = I'_{A0} - \frac{V_{A0}}{j2X_{c0}},$$

where X_c is the positive and negative sequence capacitive reactance of the line, and X_{c0} is zero sequence capacitive reactance. In addition, I'_{A1}, I'_{A2}, and I'_{A0} are positive, negative, and zero sequence input line currents, respectively.

4 Case study

A 50-Hz distribution network shown in Figure 11 was simulated in PSCAD and MATLAB software to evaluate the proposed scheme (Huang et al., 2014). Two 400-V and 10-kV networks are connected to the main grid (35 kV) by a transformer. In the coupling point with the main grid, the fault level and R/X ratio are 500 MV A and 0.1, respectively. There are three inverter-based DGs in the 400-V feeders. DG1 and DG2 have nominal powers of 200 kV A and 100 kV A, respectively. DG3 is a photovoltaic system with a nominal power of 50 kV A.

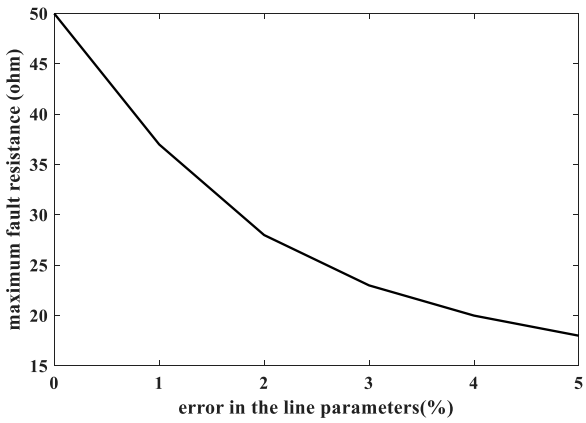

FIGURE 16
Maximum fault resistance for fault detection in the presence of line parameter errors.

The positive and negative sequence resistance of 400-V overhead lines (Lines 1 to 4 and Line 6) is 0.32 Ω/km, and this parameter in the cable line (Line 5) is 0.30 Ω/km. Zero sequence resistances of these overhead lines and the cable line are 1.1 Ω/km and 1 Ω/km, respectively. Moreover, the positive and negative sequence inductance of 400-V overhead lines and the cable line is 0.261 mH/km and 0.223 mH/km, respectively. Zero sequence inductances of these overhead lines and the cable line are 0.955 mH/km and 0.828 mH/km, respectively. In addition, the positive and negative sequence capacitance of the 400 V cable line is 0.07 μF/km, and the zero sequence capacitance is 0.02 μF/km. The nominal reactive power of the shunt capacitor in bus A is 20 kVAr. Load 1, Load 3, and Load 4 have a power of 40 kV A, and the powers of Load 2, Load 5, and Load 6 are 20, 5, and 25 kV A, respectively. The power factor of all loads in 400-V feeders is considered 0.9 lag.

The positive and negative sequence resistance of the 10-kV lines is 0.38 Ω/km, and the zero sequence resistance is 0.76 Ω/km. In addition, the positive and negative sequence inductance of these lines is 1.432 mH/km, and the zero sequence inductance is 4.2 mH/km. The nominal power of DG4 (inverter-based) at the end of the 10-kV feeder is 600 kV A. The power of Load 7 is 100 kV A, and the powers of Load 8 and Load 9 are 500 kV A. The power factor of loads in the 10-kV feeder is considered 0.85 lag.

A 400-V subsystem may be considered a microgrid that can operate in grid-connected or islanded operation mode. In this paper, the control system of DG1, DG2, and DG4 changes from active–reactive power (P–Q) to voltage–frequency (v-f) to support voltage and frequency in the islanded mode, but because of the nature of the photovoltaic system, DG2 retains P–Q control, irrespective of operation modes. The considered equivalent circuit for DGs is shown in Figure 12, which includes dependent voltage sources and inductors as filters.

When the microgrid is in the grid-connected mode, DGs operate in P–Q control mode. In this mode, the DG control system operates so that DG injects active power (Pref) equal to its nominal power and reactive power (Qref) of 0 to the grid. However, when the microgrid operates in the islanded mode, the DGs (except PV)

TABLE 1 Proposed scheme performance for three-phase faults.

Mode of operation	Fault type–fault res.	Location of the fault		Inside the prot. zone	FDI_{3P}	Correct perf.	Resp. time (msec)
Grid-connected	3P–0.01Ω	Line 5	10%	✓	4.24	✓	30
			50%	✓	3.22	✓	30
			90%	✓	3.01	✓	35
		Line 4	90%	✗	TP	✓	—
		Line 6	10%	✗	TP	✓	—
	3P–1Ω	Line 5	10%	✓	2.71	✓	30
			50%	✓	2.45	✓	30
			90%	✓	1.72	✓	30
	3P–10Ω	Line 5	10%	✓	1.71	✓	30
			50%	✓	1.46	✓	30
			90%	✓	0.76	✓	35
	3P–50Ω	Line 5	10%	✓	1.01	✓	30
			50%	✓	0.76	✓	35
			90%	✓	0.06	✓	50
Islanded	3P–0.01Ω	Line 5	10%	✓	4.05	✓	30
			50%	✓	2.45	✓	30
			90%	✓	3.06	✓	35
		Line 4	90%	✗	TP	✓	—
		Line 6	10%	✗	TP	✓	—
	3P–1Ω	Line 5	10%	✓	2.71	✓	30
			50%	✓	2.45	✓	30
			90%	✓	1.74	✓	35
	3P–10Ω	Line 5	10%	✓	1.71	✓	30
			50%	✓	1.46	✓	30
			90%	✓	0.75	✓	35
	3P–50Ω	Line 5	10%	✓	1.02	✓	35
			50%	✓	0.76	✓	35
			90%	✓	0.05	✓	50

TP, temporarily positive.

operate in a v–f control mode. In this mode, the DG control system operates for maintaining the voltage and angular frequency of the grid at or near the nominal values (Vrated and ωs). To share the power between DGs according to their nominal powers, the drop control method is applied. The considered DG control system in the grid-connected mode is shown in Figure 13A. In this figure, $V_{m,rated}$ is the nominal voltage amplitude, ωs is the nominal angular frequency, and t is time. In addition, the considered DG control system in the islanded mode is shown in Figure 13B, where m is the ratio of permissible angular frequency drop to DG rated power, n is the ratio of permissible rated DG drop to rated power and, V_{meas} is the measured terminal voltage. It should be mentioned that the output currents of DGs during the fault condition are limited to 1.5 times of nominal currents.

Optic fibers can be used for the communication link in the proposed scheme. Generally, total communication delay includes four components: transmission delay, queuing delay, propagation delay, and processing delay. Transmission and queuing delays are insignificant for advanced communication systems such as optic fiber with high bandwidth. The delay is around 0.1 ms with a bandwidth of 100–1,000 Mb/s. The propagation delay is small for LV systems with short lines (several μs) (Shabani and Mazlumi, 2020). The processing delay can be minimized using advanced routing. So, the total communication delay will be small enough

TABLE 2 Proposed scheme performance for double-line-to-ground faults.

Mode of operation	Fault type–fault res.	Location of the fault		Inside the prot. zone	FDI_{DLG}	Correct perf.	Resp. time (msec)
Grid-connected	DLG-0.01Ω	Line 5	10%	✓	4.28	✓	30
			50%	✓	3.50	✓	30
			90%	✓	2.57	✓	40
		Line 4	90%	✗	TP	✓	—
		Line 6	10%	✗	TP	✓	—
	DLG-1Ω	Line 5	10%	✓	2.71	✓	30
			50%	✓	2.43	✓	30
			90%	✓	1.71	✓	40
	DLG-10Ω	Line 5	10%	✓	1.71	✓	30
			50%	✓	1.46	✓	30
			90%	✓	0.76	✓	40
	DLG-50Ω	Line 5	10%	✓	1.01	✓	30
			50%	✓	0.76	✓	35
			90%	✓	0.06	✓	50
Islanded	DLG-0.01Ω	Line 5	10%	✓	4.29	✓	30
			50%	✓	3.52	✓	30
			90%	✓	2.57	✓	35
		Line 4	90%	✗	TP	✓	—
		Line 6	10%	✗	TP	✓	—
	DLG-1Ω	Line 5	10%	✓	2.71	✓	30
			50%	✓	2.43	✓	30
			90%	✓	1.71	✓	35
	DLG-10Ω	Line 5	10%	✓	1.71	✓	30
			50%	✓	1.46	✓	30
			90%	✓	0.76	✓	36
	DLG-50Ω	Line 5	10%	✓	1.02	✓	30
			50%	✓	0.76	✓	35
			90%	✓	0.05	✓	50

TP, temporarily positive.

to enable the data of the absolute value of positive sequence voltage to be transferred between the relays within a timescale <1 ms. For longer lines, PMUs can be located on the buses in IEEE C37.118.1 standard complied extended Kalman filter (EKF) algorithm-based PMUs. PMUs are classified into two types: class P and class M. Class P EKF-based PMUs have faster response times and are suitable for protection applications (Sharma and Samantaray, 2020), (Garcia et al., 2020).

To evaluate the performance of the proposed scheme in the presence of non-linear characteristics of high-impedance faults, the model in Figure 14 was applied (Wang et al., 2019). This model includes two DC sources, V_p and V_n, and corresponding diodes D_p and D_n to form positive and negative half cycle current paths. The two DC sources V_p and V_n simulate the voltage from the arc and are varied randomly and independently. When the instantaneous value v_{ph} is greater than V_p, current flows toward the ground and reverses when the instantaneous value v_{ph} is lower than –Vn. During –Vn < vph < Vp, no current flows. Changing the value of Vp and Vn increases the randomness and arc suppression time of the asymmetric fault. To simulate the arc resistance that causes the asymmetrical current, Rp and Rn take different values and change randomly and independently.

TABLE 3 Proposed scheme performance for line-to-line faults.

Mode of operation	Fault type-fault res.	Location of the fault		Inside the prot. zone	FDI_{LL}	Correct perf.	Resp. time (msec)
Grid-connected	LL-0.01Ω	Line 5	10%	✓	4.37	✓	30
			50%	✓	3.62	✓	30
			90%	✓	2.69	✓	40
		Line 4	90%	✗	TP	✓	—
		Line 6	10%	✗	TP	✓	—
	LL-1Ω	Line 5	10%	✓	2.71	✓	30
			50%	✓	2.44	✓	30
			90%	✓	1.73	✓	40
	LL-10Ω	Line 5	10%	✓	1.71	✓	30
			50%	✓	1.46	✓	30
			90%	✓	0.76	✓	40
	LL-50Ω	Line 5	10%	✓	1.02	✓	30
			50%	✓	0.76	✓	35
			90%	✓	0.06	✓	45
Islanded	LL-0.01Ω	Line 5	10%	✓	4.34	✓	30
			50%	✓	3.58	✓	30
			90%	✓	2.64	✓	35
		Line 4	90%	✗	TP	✓	—
		Line 6	10%	✗	TP	✓	—
	LL-1Ω	Line 5	10%	✓	2.71	✓	30
			50%	✓	2.44	✓	30
			90%	✓	1.73	✓	35
	LL-10Ω	Line 5	10%	✓	1.71	✓	30
			50%	✓	1.46	✓	30
			90%	✓	0.76	✓	35
	LL-50Ω	Line 5	10%	✓	1.02	✓	30
			50%	✓	0.76	✓	35
			90%	✓	0.06	✓	50

TP, temporarily positive.

In order to assess the proposed protection scheme, various fault types at Line 5 (cable line) were examined. In addition, faults at Lines 4 and 6 were studied for external faults. The frequency of sampling was considered 200 Hz, and the fault was initiated at t = 10 s.

Considering fault location K = 0.9 and fault resistance $R_f = 50\ \Omega$ in Eqs 1, 3, 5, and 6, the values of $Z_{eq,3P}$, $Z_{eq,LL}$, $Z_{eq,SLG,}$ and $Z_{eq,DLG}$ were obtained. If these values were substituted in Eq. 8 and their absolute values were calculated, then the values of $|Z_{\alpha,3P}|$, $|Z_{\alpha,LL}|$, $|Z_{\alpha,SLG}|$, and $|Z_{\alpha,DLG}|$ are 500, 500, 1,500, and 300, respectively. To ensure proper operation, Ci should be considered 15% greater than these values. Therefore, C_{3P}, C_{LL}, C_{SLG}, and C_{DLG} were considered 575, 575, 1,725, and 345, respectively.

5 Evaluation of the proposed scheme

FDI_{3P} curves for a 3P fault at 50% of line 5 and 10% of line 6 with a resistance 0.01 Ω in the grid-connected operation mode are shown in Figure 15. For a fault inside the protection zone (at Line 5), FDI_{3P} increases rapidly and holds a positive value. However, for a fault outside the protection zone (at 10% of Line 6), it increases transiently and decreases quickly. By studying different fault types at different locations, M (number of positive FDI_i to detect fault) was determined 6.

Tables 1–4 show FDI_i values and the proposed scheme response time for the relay at the beginning of Line 5. The

TABLE 4 Proposed scheme performance for single-line-to-ground faults.

Mode of operation	Fault type–fault res.	Location of the fault		Inside the prot. zone	FDI_{SLG}	Correct perf.	Resp. time (msec)
Grid-connected	SLG-0.01Ω	Line 5	10%	✓	4.42	✓	30
			50%	✓	3.77	✓	30
			90%	✓	2.91	✓	35
		Line 4	90%	✗	TP	✓	—
		Line 6	10%	✗	TP	✓	—
	SLG-1Ω	Line 5	10%	✓	2.71	✓	30
			50%	✓	2.44	✓	30
			90%	✓	1.75	✓	35
	SLG-10Ω	Line 5	10%	✓	1.71	✓	30
			50%	✓	1.46	✓	30
			90%	✓	0.75	✓	45
	SLG-50Ω	Line 5	10%	✓	1.02	✓	30
			50%	✓	0.77	✓	35
			90%	✓	0.07	✓	45
Islanded	SLG-0.01Ω	Line 5	10%	✓	4.42	✓	30
			50%	✓	3.76	✓	30
			90%	✓	2.93	✓	30
		Line 4	90%	✗	TP	✓	—
		Line 6	10%	✗	TP	✓	—
	SLG-1Ω	Line 5	10%	✓	2.71	✓	30
			50%	✓	2.44	✓	30
			90%	✓	1.73	✓	30
	SLG-10Ω	Line 5	10%	✓	1.71	✓	30
			50%	✓	1.46	✓	30
			90%	✓	0.75	✓	30
	SLG-50Ω	Line 5	10%	✓	1.02	✓	30
			50%	✓	0.76	✓	30
			90%	✓	0.08	✓	40

TP, temporarily positive.

fault resistance was considered 0.01–50 Ω. The results show, if a fault occurs at Line 5 (inside the protection zone), FDI_i is positive continually. So, after six sequential positive sample trips, a command will be generated for Brk6. In addition, if a fault occurs at the adjacent lines (outside the protection zone), FDI_i holds the negative value (similar to normal conditions) or becomes temporarily positive, so the trip command will not be created. This indicates the stability of the proposed scheme during the faults on the adjacent lines and load changes. Nevertheless, the performance of the proposed scheme was evaluated for connecting a load of 40 kV A with a power factor of 0.9 lag to buses E and F at t = 10 s in grid-connected and islanded modes, and the results confirmed the correct performance of the proposed scheme.

Moreover, these evaluations were repeated for this network with constant impedance loads, and similar results were obtained. In the same way, this protection scheme is implemented for Brk7 at the end of Line 5. Hence, Brk6 and Brk7 will protect Line 5.

The performance of this scheme was also evaluated for all fault types on overhead Line 4, and the results show the correct performance of the proposed scheme.

In contrast to the transmission system, in distribution lines, due to their short length, noise pollution of the data during the transmission is infrequent, and usually, it is not considered. In

TABLE 5 Performance of the proposed scheme for pre-fault condition variation and high-impedance faults.

Condition	Mode of operation	Fault type	Location of the fault		Inside the prot. zone	FDI_i	Correct perf.	Resp. time (msec)
Pre-fault conditions variation with $R_f = 50\Omega$	Grid-connected	3P	Line 5	90%	✓	0.050	✓	50
		DLG			✓	0.050	✓	45
		LL			✓	0.050	✓	45
		SLG			✓	0.050	✓	50
	Islanded	3P			✓	0.053	✓	50
		DLG			✓	0.051	✓	50
		LL			✓	0.053	✓	50
		SLG			✓	0.058	✓	50
High-impedance faults	Grid-connected	SLG	Line 5	10%	✓	1.07	✓	30
				50%	✓	0.83	✓	35
				90%	✓	0.26	✓	45
			Line 4	90%	✗	Negative	✓	—
			Line 6	10%	✗	Negative	✓	—
		LL	Line 5	10%	✓	1.25	✓	30
				50%	✓	0.99	✓	30
				90%	✓	0.32	✓	35
			Line 4	90%	✗	Negative	✓	—
			Line 6	10%	✗	Negative	✓	—
	Islanded	SLG	Line 5	10%	✓	1.06	✓	30
				50%	✓	0.82	✓	30
				90%	✓	0.22	✓	30
			Line 4	90%	✗	Negative	✓	—
			Line 6	10%	✗	TP	✓	—
		LL	Line 5	10%	✓	1.24	✓	35
				50%	✓	0.99	✓	35
				90%	✓	0.30	✓	50
			Line 4	90%	✗	Negative	✓	—
			Line 6	10%	✗	Negative	✓	—

TP, temporarily positive.

addition, because of the short length of distribution lines, determination of fault location does not work.

Generally, in the short circuit fault studies, because the fault current is high, the pre-fault currents of the lines and fault inception time are not so important. However, in high-resistance fault studies, the fault current is not high in comparison to the currents of loads of the network. So, load currents and fault inception time may affect the operation of the protection system. To study the effect of pre-fault conditions on the high-resistance fault detection of the proposed scheme, new pre-fault conditions were discussed. In this case, DG3 was turned off, load 1 to load 6 were doubled, and the fault was initiated at 10.005 s (voltage angle was $\frac{\pi}{2}$). Based on the simulation results, the proposed scheme had correct performance under the new pre-fault conditions. These results confirmed the robustness of the proposed scheme against uncertainties of loads, generations, and variations of fault inception time.

So far, for simplicity, the faults have been modeled by net resistance, and the non-linear properties of the high-impedance faults have been ignored. However, to evaluate the performance of the proposed scheme in the high-impedance faults with non-linear properties (Figure 14), V_p was considered to be varied between 150 V and 170 V and V_n between 145 and 155 V

TABLE 6 proposed scheme for line-to-line faults in the MV line.

Mode of operation	Fault type-fault res.	Location of the fault		Inside the prot. zone	FDI_{LL}	Correct perf.	Resp. time (msec)
Grid-connected	LL-0.01Ω	Line 8	10%	✓	3.20	✓	30
			50%	✓	2.31	✓	30
			90%	✓	1.22	✓	40
		Line 7	90%	✗	TP	✓	—
	LL-1Ω	Line 8	10%	✓	2.6	✓	30
			50%	✓	2.12	✓	30
			90%	✓	1.15	✓	40
	LL-10Ω	Line 8	10%	✓	1.68	✓	30
			50%	✓	1.41	✓	30
			90%	✓	0.68	✓	50
	LL-50Ω	Line 8	10%	✓	0.98	✓	30
			50%	✓	0.72	✓	40
			90%	✓	0.09	✓	80
Islanded	LL-0.01Ω	Line 8	10%	✓	5.63	✓	30
			50%	✓	5.76	✓	30
			90%	✓	3.88	✓	35
		Line 7	90%	✗	TP	✓	—
	LL-1Ω	Line 8	10%	✓	2.68	✓	30
			50%	✓	2.47	✓	35
			90%	✓	1.75	✓	35
	LL-10Ω	Line 8	10%	✓	1.67	✓	30
			50%	✓	1.46	✓	35
			90%	✓	0.74	✓	35
	LL-50Ω	Line 8	10%	✓	1.00	✓	35
			50%	✓	0.74	✓	35
			90%	✓	0.05	✓	45

TP, temporarily positive.

randomly and independently every 0.1 ms. In addition, R_p and R_n were considered to take different values between 15 and 25 Ω and change randomly and independently every 0.1 ms. Based on the simulation results, the proposed scheme operated correctly in the high-impedance SLG and LL faults at different points of the line in both operation modes. Accordingly, the non-linear properties of high-impedance faults did not affect the performance of the proposed scheme. The performance of the proposed scheme for pre-fault condition variation and high-impedance faults is shown in Table 5.

Considering that the proposed scheme can detect high-impedance faults, the accuracy of the line parameter value affects its performance significantly. To evaluate this effect, the presence of −5% to +5% error in the considered values for line parameters was studied. The results showed that the proposed scheme does not perform correctly for errors of −5% to −1.5% in the line parameters. In addition, for −1.5% to 0% errors, the proposed scheme can detect faults along the line without any effect, up to 50 Ω fault resistance. For the positive errors, the fault detection capability is limited to the maximum fault resistance shown in Figure 16.

So, the proposed scheme detects all fault types in both operation modes of the microgrid. In addition, according to the results of the investigations, this scheme detects faults in a timeline between 30 and 50 ms, and its average response time is 32.8 ms, which is approximately 34% faster than that of the conventional schemes with a response time of approximately 50 ms.

Furthermore, in order to assess the performance of the proposed scheme in the MV lines, all fault types with different resistances are

TABLE 7 proposed scheme for single-line-to-ground faults in the MV line.

Mode of operation	Fault type–fault res.	Location of the fault		Inside the prot. zone	FDI_{SLG}	Correct perf.	Resp. time (msec)
Grid-connected	DLG-0.01Ω	Line 8	10%	✓	3.40	✓	30
			50%	✓	2.49	✓	35
			90%	✓	1.41	✓	35
		Line 7	90%	✗	TP	✓	—
	DLG-1Ω	Line 8	10%	✓	2.63	✓	30
			50%	✓	2.21	✓	35
			90%	✓	1.34	✓	35
	DLG-10Ω	Line 8	10%	✓	1.68	✓	30
			50%	✓	1.42	✓	35
			90%	✓	0.69	✓	45
	DLG-50Ω	Line 8	10%	✓	0.98	✓	35
			50%	✓	0.71	✓	35
			90%	✓	0.09	✓	75
Islanded	DLG-0.01Ω	Line 8	10%	✓	4.56	✓	30
			50%	✓	4.22	✓	30
			90%	✓	3.58	✓	40
		Line 7	90%	✗	TP	✓	—
	DLG-1Ω	Line 8	10%	✓	2.67	✓	30
			50%	✓	2.42	✓	30
			90%	✓	1.75	✓	40
	DLG-10Ω	Line 8	10%	✓	1.68	✓	30
			50%	✓	1.42	✓	30
			90%	✓	0.75	✓	40
	DLG-50Ω	Line 8	10%	✓	0.99	✓	30
			50%	✓	0.74	✓	30
			90%	✓	0.05	✓	40

TP, temporarily positive.

TABLE 8 Comparison of the proposed scheme and the introduced scheme in Huang et al. (2014).

	Proposed scheme	Scheme in Huang et al. (2014)
Number of quantities sent by the communication system	1	2
Sampling frequency	200	1,200
Threshold value determination	Simple	Complex
Implementation	1 routine	3 subroutines
Studied lines	Cable and overhead	Overhead
Studied network	LV and MV	LV

studied at Line 8. The results for line-to-line and single-line-to-ground faults are illustrated in Tables 6, 7. Evaluations for two other fault types also yielded similar results. Considering the results for all fault types, this scheme detects faults correctly in MV lines too. However, in MV lines, response time is between 30 and 80 ms, and the average response time is 35.9 ms.

So, the proposed scheme has advantages compared to the one in Huang et al. (2014). Three subroutines were introduced for detecting solid and low-, medium-, and high-impedance faults in Huang et al. (2014); so, its implementation was complex. However, the proposed scheme detects all faults by the same routine.

In addition, in Huang et al. (2014), the impedance calculated at the end of the line including the absolute value and angle (two quantities) should be sent to the beginning of the line. However, in the proposed scheme, only the absolute value of the positive sequence voltage (one quantity) is sent. This means at least a 50% reduction in data exchange. In addition, the low sampling frequency (200 Hz) is one of the advantages of this scheme compared to that of Huang et al. (2014), with a sampling frequency of 1,200 Hz. So, the lower data exchange leads to more free-up of the communication system for other applications in the microgrid.

Furthermore, one of the properties of the proposed protection scheme is the drastic reduction of $Z_{\alpha,i}$ during the faults compared to under normal conditions. This significantly simplifies the determination of the threshold value of FDIi and is an advantage of the proposed scheme compared to that of Huang et al. (2014). The threshold value in Huang et al. (2014) should have been taken close to the line impedance, which was a small value in short distribution lines, and it could challenge the threshold determination.

In addition, in the evaluation of the proposed scheme, overhead and cable lines were studied in LV and MV networks, while evaluations of the main protection scheme in Huang et al. (2014) were conducted only on the LV overhead lines. Table 8 shows these differences.

6 Conclusion

In this article, in order to model short-circuit faults in active distribution networks, new equivalent circuits, including SPS, SNS, and SZS, were proposed by reforming conventional sequence equivalent circuits. Then, equivalent delta circuits of these proposed circuits were achieved using star to delta transformation. A significant change in one of the impedances in these delta circuits was the foundation of the proposed protection scheme for microgrids.

In this scheme, the FDI_n index was introduced, which can detect the faults in both grid-connected and islanded modes at LV and MV distribution lines. In addition, the proposed scheme was capable of operating correctly in both overhead and cable lines. Considering its average response time, its performance was relatively fast. Releasing at least 50% of the communications system and the low sampling rate of the measurement were advantages of this scheme. In addition, the possibility of high-impedance fault detection, robustness against network reconfigurations, and load and generation uncertainties were capabilities of the proposed scheme. Additionally, infeed and transient situations did not affect the correct performance of the proposed scheme. It was evaluated by simulating in PSCAD and MATLAB software, and the results confirmed its precision.

Data availability statement

The original contributions presented in the study are included in the article/Supplementary Material; further inquiries can be directed to the corresponding author.

Author contributions

SN: conceptualization; formal analysis; investigation; methodology; project administration; software; supervision; validation; writing—original draft; writing—review and editing. AK: conceptualization; investigation; methodology; project administration; supervision; validation; writing—review and editing.

Conflict of interest

The authors declare that the research was conducted in the absence of any commercial or financial relationships that could be construed as a potential conflict of interest.

Publisher's note

References

Adly, A. R., El Sehiemy, R. A., and Abdelaziz, A. Y. (2017). "Optimal reclosing time to improve transient stability in distribution system," in *Cired - open access proc* (Journal), 2017, 1359–1362.1

Aghdam, T. S., Kazemi Karegar, H., and Zeineldin, H. H. (2019). Variable tripping time differential protection for microgrids considering DG stability. *IEEE Trans. Smart Grid* 10 (3), 2407–2415. doi:10.1109/tsg.2018.2797367

Aminifar, F., Fotuhi-Firuzabad, M., Safdarian, A., Davoudi, A., and Shahidehpour, M. (2014). Synchrophasor measurement technology in power systems: Panorama and state-of-the-art. *IEEE Access* 2, 1607–1628. doi:10.1109/access.2015.2389659

Best, R. J., Morrow, D. J., and Crossley, P. A. (2009). "Communication assisted protection selectivity for reconfigurable and islanded power networks," in *Proc. of the 44th int. universities power engineering Conf. (UPEC)* (Glasgow, Scotland, 1–4.

Biller, M., and Jaeger, J. (2018). "Voltage-free distance protection method for closed loop structures," in *IEEE PES innovative smart grid technologies conf. Europe (ISGT-Europe)* (Sarajevo: Bosnia-Herzegovina).

Blaabjerg, F., Yang, Y., Yang, D., and Wang, X. (2017). Distributed power-generation systems and protection. *Proc. IEEE* 105 (7), 1311–1331. doi:10.1109/jproc.2017.2696878

Bottrell, N., and Green, T. C. (2013). "An impedance-based method for the detection of over-load and network faults in inverter interfaced distributed generation," in *2013 15th European conf. On power electronics and applications (EPE)* (Lille, 1–10.

Darabi, A., Bagheri, M., and Gharehpetian, G. B. (2020). Highly sensitive microgrid protection using overcurrent relays with a novel relay characteristic. *IET Renew. Power Gener.* 14 (7), 1201–1209. doi:10.1049/iet-rpg.2019.0793

Esmaeili Dahej, A., Esmaeili, S., and Hojabri, H. (2018). Co-optimization of protection coordination and power quality in microgrids using unidirectional fault current limiters. *IEEE Trans. Smart Grid* 9 (5), 5080–5091. doi:10.1109/tsg.2017.2679281

Sortomme, E., Venkata, S. S., and Mitra, J. (2010). Microgrid protection using communication-assisted digital relays. *IEEE Trans. Power Del.* 25, 2789–2796. doi:10.1109/tpwrd.2009.2035810

FangJia, Y. K., Yang, Zh., Li, Y., and Bi, T. (2019). Impact of inverter-interfaced renewable energy generators on distance protection and an improved scheme. *IEEE Trans. Industrial Electron.* 66 (9), 7078–7088. doi:10.1109/tie.2018.2873521

Furlan, R. H., Beuter, C. H., Bataglioli, R. P., Faria, I. d. M., and Oleskovicz, M. (2018). "Improvement of overcurrent protection considering distribution systems with distributed generation," in *18th int. Conf. On harmonics and quality of power* (Ljubljana, Slovenia: ICHQP).

Garcia, V. T., Guillen, D., Olveres, J., Ramirez, B. E., and Rodriguez, J. R. R. (2020). Modelling of high impedance faults in distribution systems and validation based on multiresolution techniques. *Comput. Electr. Eng.* 83, 106576. doi:10.1016/j.compeleceng.2020.106576

Ghanbari, T., and Farjah, E. (2013). Unidirectional Fault current limiter: An efficient interface between the microgrid and main network. *IEEE Trans. Power Syst.* 28 (2), 1591–1598. doi:10.1109/tpwrs.2012.2212728

Hooshyar, A., and Iravani, R. (2017). Microgrid protection. *Proc. IEEE* 105 (7), 1332–1353. doi:10.1109/jproc.2017.2669342

Huang, W., Nengling, T., Zheng, X., Fan, Ch., Yang, X., and Kirby, B. J. (2014). An impedance protection scheme for feeders of active distribution networks. *IEEE Trans. Power Del.* 29 (4), 1591–1602. doi:10.1109/tpwrd.2014.2322866

Jiao, Z., Jin, J., Liu, L., Wang, Y., Wang, Q., and Wang, Z. (2015). A practical setting method for over-current relay and automatic recloser in distribution network with photovoltaic station. *Int. J. Electr. Energy* 3, 225–229. doi:10.18178/ijoee.3.4.225-229

Kar, S., Samantaray, S. R., and Dadashzadeh, M. (2017). Data mining model based intelligent differential microgrid protection scheme. *IEEE Syst. J.* 11 (2), 1161–1169. doi:10.1109/jsyst.2014.2380432

Khederzadeh, M. (2012). "Preservation of over current relays coordination in microgrids by application of static series compensators," in *Proc. of the 11th Int. conf. on developments in power systems protection* (Birmingham,UK: DPSP), 1–6.

Laaksonen, H., Ishchenko, D., and Oudalov, A. (2014). Adaptive protection and microgrid control design for Hailuoto island. *IEEE Trans. Smart Grid* 5 (3), 1486–1493. doi:10.1109/tsg.2013.2287672

Loix, T., Wijnhoven, T., and Deconinck, G. (2009). "Protection of microgrids with a high penetration of inverter-coupled energy sources," in *CIGRE/IEEE PES joint symposium integration of wide-scale renewable resources into the power del. System* (Canada: Calgary, AB), 1–8.

Mirsaeidi, S., Said, D. M., Mustafa, M. W., Habibuddin, M. H., and Ghaffari, K. (2016). "Modeling and simulation of a communication-assisted digital protection scheme for microgrid," in *Elsevier. Renewable and sustainable Energy reviews*, 57, 867–878.

Nikolaidis, V. C., Tsimtsios, A. M., and Safigianni, A. S. (2018). Investigating particularities of infeed and fault resistance effect on distance relays protecting radial distribution feeders with DG. *IEEE Access* 6, 11301–11312. doi:10.1109/access.2018.2804046

Nobakhti, S. M., Ketabi, A., and Shafie-khah, M. (2021). A new impedance-based main and backup protection scheme for active distribution lines in AC microgrids. *Energies* 14 (2), 274. doi:10.3390/en14020274

Orji, U., Schantz, C., Leeb, S. B., Kirtley, J. L., Sievenpiper, B., Gerhard, K., et al. (2017). Adaptive zonal protection for ring microgrids. *IEEE Trans. Smart Grid* 8 (4), 1843–1851. doi:10.1109/tsg.2015.2509018

Oureilidis, K. O., and Demoulias, Ch. S. (2016). A Fault clearing method in converter-dominated microgrids with conventional protection means. *IEEE Trans. Power Electron.* 31 (6), 4628–4640. doi:10.1109/tpel.2015.2476702

Pandakov, K., and Hoidalen, H. K. (2017). "Distance protection with fault impedance compensation for distribution network with DG," in *IEEE PES innovative smart grid technologies conf. Europe (ISGT-Europe)* (Torino, Italy.

Shabani, A., and Mazlumi, K. (2020). Evaluation of a communication-assisted overcurrent protection scheme for photovoltaic-based DC microgrid. *IEEE Trans. Smart Grid* 11 (1), 429–439. doi:10.1109/tsg.2019.2923769

Sharma, N. K., and Samantaray, S. R. (2019). Assessment of PMU-based wide-area angle criterion for fault detection in microgrid. *IET Gener. Transm. &amp. Distrib.* 13 (19), 4301–4310. doi:10.1049/iet-gtd.2019.0027

Sharma, N. K., and Samantaray, S. R. (2020). PMU assisted integrated impedance angle-based microgrid protection scheme. *IEEE Trans. Power Deliv.* 35 (1), 183–193. doi:10.1109/tpwrd.2019.2925887

Teimourzadeh, S., Aminifar, F., Davarpanah, M., and Guerrero, J. M. (2016). Macroprotections for microgrigs: Toward a new protection paradigm subsequent to distributed energy resource integration. *IEEE Ind. Electron. Mag.* 10 (3), 6–18.

Wang, X., Gao, J., Wei, X., Song, G., Wu, L., Liu, J., et al. (2019). High impedance Fault Detection method based on variational mode decomposition and teager–kaiser energy operators for distribution network. *IEEE Trans. Smart Grid* 10 (6), 6041–6054. doi:10.1109/tsg.2019.2895634

Zamani, M. A., Sidhu, T. S., and Yazdani, A. (2011). A protection strategy and microprocessor-based relay for low-voltage microgrids. *IEEE Trans. Power Del.* 26 (3), 1873–1883. doi:10.1109/tpwrd.2011.2120628

Zeineldin, H. H., El-saadany, E. F., and Salama, M. M. A. (2006). "Distributed generation microgrid operation: Control and protection," in *Power systems conf. Advanced metering, protection, control, communication, and distributed resources* (Clemson, SC, USA, 105–111.

frontiers | Frontiers in Energy Research

TYPE Original Research
PUBLISHED 14 June 2023
DOI 10.3389/fenrg.2023.1211269

OPEN ACCESS

EDITED BY
Srete Nikolovski,
Josip Juraj Strossmayer University of Osijek, Croatia

REVIEWED BY
Dehao Qin,
Clemson University, United States
Adel Oubelaid,
Université de Bejaia, Algeria

*CORRESPONDENCE
Weijie Wen,
weijie.wen@tju.edu.cn

RECEIVED 24 April 2023
ACCEPTED 31 May 2023
PUBLISHED 14 June 2023

CITATION
Li A, Li B, Wen W, Li B and Chen X (2023), Research on circuit breaker failure protection and the secondary accelerated fault isolation scheme of VSC-HVDC grids.
Front. Energy Res. 11:1211269.
doi: 10.3389/fenrg.2023.1211269

Research on circuit breaker failure protection and the secondary accelerated fault isolation scheme of VSC-HVDC grids

Andi Li, Botong Li, Weijie Wen*, Bin Li and Xiaolong Chen

Key Laboratory of Smart Grid of Ministry of Education, Tianjin University, Tianjin, China

When the direct current circuit breaker (DCCB) fails to operate, the fault range will further expand, endangering the safe operation of the power gird. Therefore, this study proposes a DCCB failure protection method and a secondary accelerated fault isolation scheme of voltage source converter-based high-voltage direct current (VSC-HVDC) grids. On the basis of considering the influence of DCCB disconnection, characteristics of fault current after the failure of the DCCB are analyzed, and a circuit breaker failure protection method based on "increase current" discrimination is proposed. By analyzing the logical relationship among failed breaker re-tripping, adjacent DCCB action, blocking of the converter station, and AC circuit breaker action, a secondary accelerated fault isolation scheme is proposed to minimize the fault isolation area. The scheme achieves the accelerated isolation of DC faults after the failure of the DCCB and avoids the trip of the AC circuit breaker effectively. Simulation results verify the effectiveness of the proposed scheme.

KEYWORDS

VSC-HVDC grids, direct current circuit breaker, circuit breaker failure protection, failure discrimination, secondary accelerated fault isolation

1 Introduction

The high voltage direct current grid based on the modular multilevel converter (MMC-HVDC), with the advantages of large transmission capacity, low loss, and high reliability, has broad development prospects in the fields of distributed power access, new energy delivery through isolated islands, and the interconnection of asynchronous AC grids (Wang et al., 2021; Khosravi et al., 2021; Zhu et al., 2021; Oubelaid et al., 2022a). In MMC-HVDC grids, the most ideal fault isolation method is to use a direct current circuit breaker (DCCB) to cut the fault line, which isolates only the fault area and ensures that the rest of the system can continue to operate normally (Franck, 2011; Xu et al., 2018; Oubelaid et al., 2022b). However, the circuit breaker operation has the possibility of failure. When the circuit breaker fails to operate, the rapid fault isolation will fail, and the fault range of the grid will be further expanded. Therefore, to quickly remove the fault line to ensure the safe operation of the system, it is of important practical value to study the secondary accelerated fault isolation scheme, which minimizes the extended area after the rapid isolation failure caused by the circuit breaker failure.

When components such as lines or transformers fail and the relay protection device sends a trip signal but the circuit breaker refuses to act, the circuit breaker failure protection acts. It utilizes the fault information of the failed circuit breaker and the protection action information of the faulty components to distinguish the fault state of the circuit breaker and cut off the relevant circuit breakers as soon as possible to achieve fault isolation within the

minimum range. Experts and scholars in related fields have conducted extensive research on circuit breaker failure protection in AC systems. Ding. (2006) and Zhang and Chang. (2003) introduce the basic composition of circuit breaker failure protection, elaborate on the feasibility and universality of using the "present current" discrimination method and protection action information to form "AND" logic to release voltage blocking, and analyze the problems of circuit breaker failure protection in high-voltage power grids. Song. (2008) analyze the setting method of phase current in the circuit breaker failure protection current discrimination element and propose a scheme for the phase current setting value to vary with normal load current to ensure that the current discrimination element has sufficient sensitivity after a fault occurs at the end of the line. He and Li. (2010) analyze the position of the current transformer where the current discrimination element is located in the startup failure circuit of the circuit breaker failure protection and pointed out the only correct installation position. At present, research on circuit breaker failure protection in AC systems has been relatively mature and widely applied in practical engineering.

With the continuous expansion of the construction scale of MMC-HVDC projects in recent years, the demand for the development and application of high-voltage DCCB has become prominent, and research on DCCB failure protection has also received industry attention. Qin et al. (2022) propose a three-level hierarchical microgrid protection scheme based on the different response times among the solid-state circuit breaker, the hybrid circuit breaker, and the traditional mechanical breaker. A hybrid DC circuit breaker combines the advantages of a solid circuit breaker and a mechanical circuit breaker and is widely used in flexible DC power grids at present. Wang et al. (2021) propose a failure backup protection algorithm for DCCBs, which utilizes the reverse voltage generated in the energy-absorbing circuit to construct fault identification criteria, achieving accurate identification of partial and overall faults caused by various component faults of the circuit breaker. This protection algorithm fully considers the influence of measurement errors and aging of energy-absorbing components, but insufficient consideration is given to the fault isolation scheme after circuit breaker failure. Azad et al. (2016) use linear discriminant analysis to divide the voltage current plane into two regions by detecting the voltage and current at the end of the line and producing a large number of training samples for learning. By utilizing the characteristics of low current and high voltage when the fault has been cleared, and high current and low voltage when the fault has not been cleared, accurate detection of circuit breaker failure state is achieved. This method has a complex protection criterion setting and high requirements for a protection action delay setting. Perez-Molina et al. (2021) determines the failure state of the circuit breaker by detecting the voltage change rate at both ends of the upper limit current reactor of the DC line. When the circuit breaker fails and refuses to operate, the backup DC circuit breaker is tripped to isolate the fault. However, in this method, the setting of the protection criterion depends on simulation values and the ability to resist transition resistance is weak.

Through a summary of the research status, it has been shown that, at present, the industry has carried out a preliminary discussion on DCCB failure protection, but in the identification process of the DCCB failure state, the influence of other factors, such as breaker breaking delay and the opposite circuit breaker breaking process, has been considered less. Therefore, it is necessary to conduct in-depth research on the electrical characteristics and secondary isolation methods after DCCB failure in the MMC-HVDC grid to understand the secondary accelerated fault isolation after the rapid fault isolation failure caused by the circuit breaker failure and provide a guarantee for the safe and stable operation of the system.

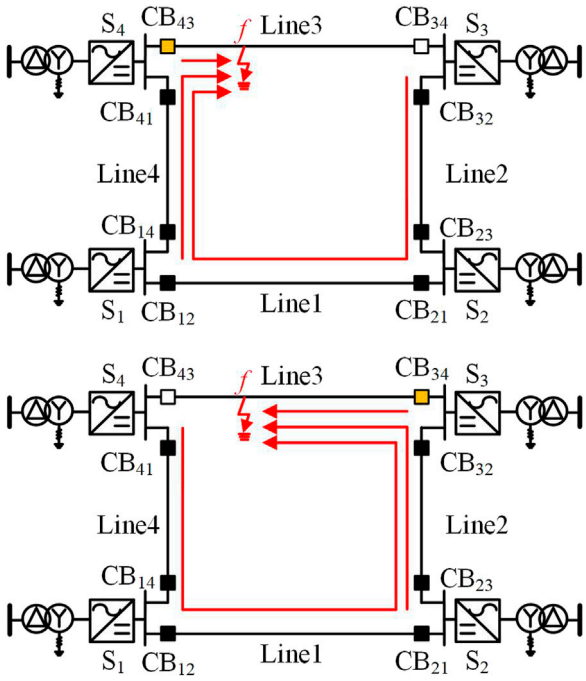

FIGURE 1
The fault isolation process after the failure of the circuit breaker.

This study proposes a protection scheme in case of rapid fault isolation failure caused by circuit breaker failure. By identifying whether the fault is eliminated by the changing trend of the fault current flowing through the circuit breaker, the failure protection of DCCB is constructed. On this basis, a secondary accelerated fault isolation scheme including DCCB re-tripping, blocking of the converter station, and AC circuit breaker operation is proposed to minimize the expansion of the isolation area. The article is organized as follows. In the next section, the fault current characteristics after the failure of the DCCB are analyzed on the basis of considering the influence of the disconnection process of the opposite circuit breaker. Following this, the method of circuit breaker failure discrimination using "increase current" judgment is studied, and the secondary accelerated fault isolation scheme of minimizing the isolation area is proposed. Then, the effectiveness of the proposed scheme is verified by simulation. The final section provides conclusions.

2 Characteristics of fault current after the failure of the DCCB

This section analyzes the fault current characteristics of the DCCB at the transmitting end and the receiving end of the fault line,

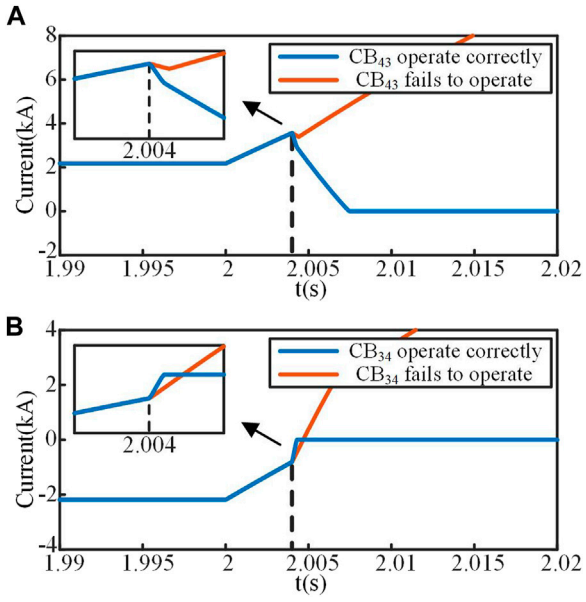

FIGURE 2
Comparison of fault currents when the circuit breaker operates correctly or fails to operate. **(A)** Fault current of the transmitting terminal I_CB_{43}. **(B)** Fault current of the receiving terminal I_CB_{34}.

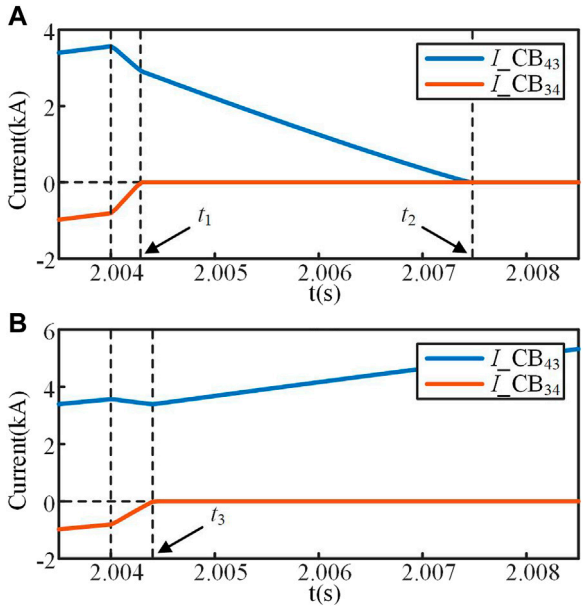

FIGURE 3
Comparison of the fault currents of the failed circuit breaker at the transmitting end and the opposite circuit breaker. **(A)** Circuit breakers operate correctly. **(B)** CB_{43} fails to operate.

which serves as the theoretical basis for the construction of DCCB failure protection.

For the Zhangbei 4-terminal grid shown in Figure 1, it is assumed that a positive grounding fault occurs at *f* on Line3. The fault isolation process of the DC side when circuit breakers CB_{43} and CB_{34} fail to operate is shown in Figure 1.

Figure 1 shows that when CB_{43} or CB_{34} fails to operate, although one side of the fault line is successfully cut off, each inverter will continue to inject fault current into the fault point through the failed circuit breaker.

2.1 Characteristics of fault current

Assuming that a positive grounding fault occurs at the midpoint of Line3 at 2s, the fault current characteristics of CB_{43} at the transmitting end and CB_{34} at the receiving end are analyzed.

CB_{43} and CB_{34} both receive trip signals at 1 ms after the fault. Considering that the circuit breaker breaking delay t_{cb} is 3 ms, if the circuit breaker operates normally, the current breaking process should start at 4 ms after the fault.

Converter station S_4 is the rectifier station and converter station S_3 is the inverter station. During the normal operation of the system, station S_4 transmits current to station S_3. The comparison of I_CB_{43} when CB_{43} operates correctly or fails to operate is shown in Figure 2A. The comparison of I_CB_{34} when CB_{34} operates correctly or fails to operate is shown in Figure 2B.

It can be seen from Figure 2A that when CB_{43} operates correctly, I_CB_{43} begins to drop at 2.004 s and finally reaches zero, and the fault line is successfully removed. When CB_{43} fails to operate, I_CB_{43} begins to experience a short decline at 2.004 s due to the disconnection of CB_{34} on the opposite side of the fault line. Although the opposite circuit breaker CB_{34} acted correctly to remove the fault line on one side of the fault point, the fault discharge circuit on the other side of the fault point is not removed, so I_CB_{43} rises again after a short fall.

It can be seen from Figure 2B that when CB_{34} operates correctly, the rise speed of I_CB_{34} increases at 2.004 s and finally reaches zero, and the fault line is successfully removed. When CB_{34} fails to operate, I_CB_{34} begins to experience acceleration at 2.004 s due to the disconnection of CB_{43} on the opposite side of the fault line. Although the opposite circuit breaker $CB4_3$ acted correctly to remove the fault line on one side of the fault point, the fault discharge circuit on the other side of the fault point is not removed, so I_CB_{34} continues to rise after rising to zero.

2.2 Influence of the opposite circuit breaker disconnection on the fault current at the transmitting end

The comparison between I_CB_{43} and I_CB_{34} when circuit breaker CB_{43} operates correctly or fails to operate is shown in Figure 3. Figure 3A shows that after the fault occurs, CB_{34} and CB_{43} operate correctly. At 2.004 s, CB_{34} and CB_{43} begin to operate simultaneously. At time t_1, CB_{34} is cut off, and I_CB_{34} drops to zero, and the rate of change of $I\_$ CB_{43} changes. At time t_2, CB_{43} is cut off, I_CB_{43} drops to zero and the fault line is completely cut off.

Figure 3B shows that after the fault occurs, CB_{43} fails to operate, while CB_{34} operates correctly. At 2.004 s, CB_{34} begins to operate, and owing to its disconnection, $I\_$ CB_{43} begins to experience a brief decline process. At time t_3, CB_{34} is cut off, and $I\_$ CB_{34} drops to zero.

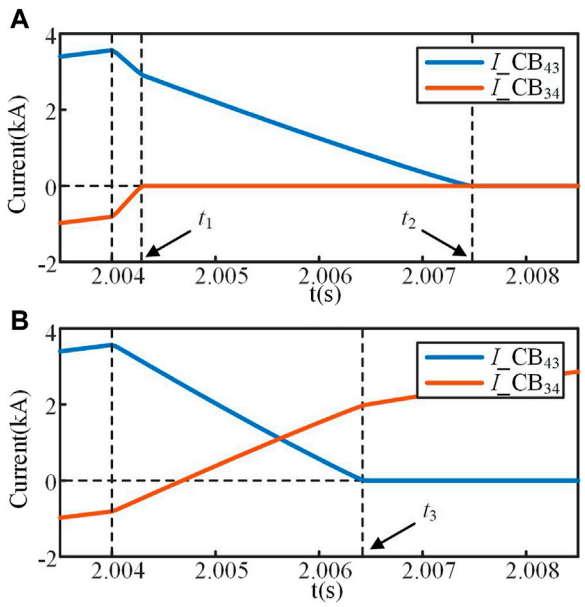

FIGURE 4
Comparison of the fault currents of the failed circuit breaker at the receiving end and the opposite circuit breaker. **(A)** Circuit breakers operate correctly. **(B)** CB_{34} fails to operate.

As the fault discharge circuit through the failed circuit breaker CB_{43} has not been cut off, the inverters in the network will continue to inject current into the fault point. Therefore, I_CB_{43} rises again after a brief decline process. According to the above analysis, when the circuit breaker at the transmitting end fails to operate, owing to the influence of the opposite circuit breaker disconnection, the rising speed of the fault current flowing through the circuit breaker at the transmitting end slows and may even decrease for a short time.

2.3 Influence of the opposite circuit breaker disconnection on the fault current at the receiving end

The comparison between I_CB_{43} and I_CB_{34} when circuit breaker CB_{34} operates correctly or fails to operate is shown in Figure 4. Figure 4A shows that after the fault occurs, CB_{34} and CB_{43} operate correctly. At 2.004 s, CB_{34} and CB_{43} begin to operate simultaneously. At time t_1, CB_{34} is cut off, I_CB_{34} drops to zero, and the rate of change of I_CB_{43} changes. At time t_2, CB_{43} is cut off, I_CB_{43} drops to zero and the fault line is completely cut off.

Figure 4B shows that after the fault occurs, CB_{34} fails to operate, while CB_{43} operates correctly. At 2.004 s, CB_{43} begins to operate, and owing to its disconnection, I_CB_{34} begins to experience an accelerated rising process and cross zero. At time t_3, CB_{43} is cut off and I_CB_{43} drops to zero. As the fault discharge circuit through the failed circuit breaker CB_{34} has not been cut off, the inverters in the network will continue to inject current into the fault point. Therefore, the rate of change of I_CB_{34} resumes and continues to rise.

According to the above analysis, when the circuit breaker at the receiving end fails to operate, owing to the influence of the opposite circuit breaker disconnection, the rising speed of the fault current flowing through the circuit breaker at the receiving end increases.

2.4 Analysis of the influence of circuit breaker disconnection

For the Zhangbei 4-terminal grid shown in Figure 1, it is assumed that a fault occurs at f on Line3; the fault current path and composition are shown in Figure 5. Converter station S_4 is a rectifier station that is at the transmitting end, and converter station S_3 is an inverter station that is at the receiving end. Only Line3 and its converter stations on both sides are considered here, while other lines and converter stations are omitted in the figure.

Figure 5 shows that the fault currents I_CB_{43} and I_CB_{34} are composed of load current I_{load}, fault additional current I_f_4, and fault additional current I_f_3:

$$\begin{cases} I\_CB_{43} = I\_f_4 + I_{load} \\ I\_CB_{34} = I\_f_3 - I_{load} \end{cases} \quad (1)$$

According to 1), the fault current at transmitting end I_CB_{43} is composed of load current I_{load} and fault additional current at transmitting end I_f_4. When the circuit breaker at receiving end CB_{34} begins to operate, the load current I_{load} passing through the fault line decreases accordingly. The total current at transmitting end I_CB_{43} has the same direction as the load current I_{load}, so the rising speed of I_CB_{43} decreases.

According to 1), the fault current at receiving end I_CB_{34} is composed of load current I_{load} and fault additional current at receiving end I_f_3. When the circuit breaker at transmitting end CB_{43} begins to operate, the load current I_{load} passing through the fault line decreases accordingly. The total current at receiving end I_CB_{34} is in the opposite direction to the load current I_{load}, so the rising speed of I_CB_{34} increases.

The disconnection process of the opposite circuit breaker will lead to a decrease in the rise rate of the fault current at the transmitting end. The disconnection process of the opposite circuit breaker will lead to an increase in the rising rate of the fault current at the receiving end.

3 DCCB failure protection

In traditional AC circuit breaker failure protection, the discriminant element determines whether the fault is eliminated by detecting whether there is still current in the system after the protection action, and then, together with the starting element that reflects the protection action, forms the operating condition of AC circuit breaker failure protection. In MMC-HVDC grids, the development of the fault is very fast, and the traditional "present current" discrimination method used in AC systems has a long discrimination process, which cannot meet the rapid demand of circuit breaker failure protection action in the MMC-HVDC grid.

According to the analysis of fault current characteristics after the failure of DCCB in Section 2.1, in MMC-HVDC grids, when a circuit breaker fails to operate, the fault current flowing through the failed circuit breaker will continue to rise after the cut-off time. Based on

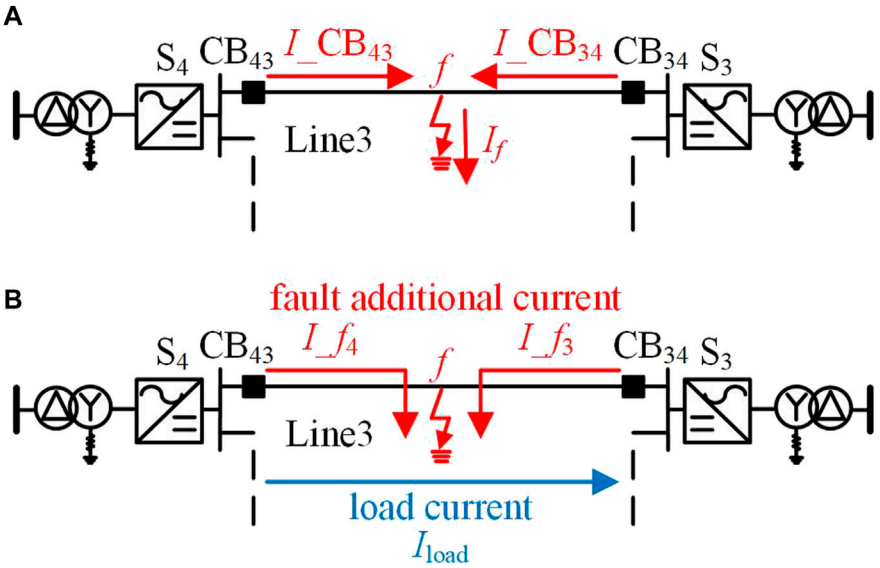

FIGURE 5
Fault current path and composition on the fault line. **(A)** Fault current path. **(B)** Fault current composition.

the above characteristics, an "increase current" discrimination method for DCCBs is studied, which identifies whether the fault has been eliminated by the changing trend of the fault current flowing through the circuit breaker, and then the failure protection of DCCB is constructed. Compared with the traditional "present current" judgment method, the "increase current" judgment method can rapidly determine the failure state of circuit breakers in MMC-HVDC grids, which is conducive to the fast action of circuit breaker failure protection.

3.1 Discrimination method of circuit breaker failure

The hybrid DCCB has a circuit breaker opening delay when cutting off the current When the circuit breaker opening delay is set to its maximum value, the circuit breaker is disconnected at the latest possible moment. For the circuit breaker failure state discrimination process, to ensure that the fault current has begun to decrease at the cut-off time, the cut-off time in this chapter refers to the situation when the breaker's opening delay reaches the maximum value The first "increase current" discrimination is carried out at the cut-off time.

In view of the different influences caused by the disconnection process of circuit breakers at the transmitting end and receiving end, the circuit breaker failure protection is set to two different modes: the transmitting end and the receiving end. In practical engineering, the mode is switched according to the running state to ensure the correct action of circuit breaker failure protection.

3.1.1 Discrimination of circuit breaker failure at the transmitting end

For circuit breakers at the transmitting end, when a fault occurs on the line where the circuit breaker is located, the direction of the fault current change is the same as that of the current in normal operation. Fault current is always in the rising stage from the time the circuit breaker receives the tripping command to the start of the cut-off, so the fault current is always positive before the cut-off time. When the circuit breaker operates correctly or the opposite circuit breaker begins to operate, the rising speed of the fault current will decrease. Therefore, after the cut-off time, once the current flowing through the circuit breaker rises, it can be determined that the circuit breaker fails to operate.

The first "increase current" judgment is made at the cut-off time. If the fault current rises, it is determined that the circuit breaker fails to operate. If the fault current drops, it cannot be determined whether the circuit breaker operates correctly. It is necessary to continuously conduct "increase current" judgment considering the influence of opposite circuit breaker disconnection and the blocking of converter stations. Before the fault current drops to zero, once the trend of the fault current changes and starts to rise, it is determined that the circuit breaker fails to operate. If the fault current continues to decrease and eventually reaches zero, it is determined that the circuit breaker operates correctly. The failure discrimination flow chart of the circuit breaker at the transmitting end is shown in Figure 6.

3.1.2 Discrimination of circuit breaker failure at the receiving end

For circuit breakers at the receiving end, when a fault occurs on the line where the circuit breaker is located, the direction of the fault current change is opposite to the direction of the current in normal operation, so the fault current may cross zero. According to the zero-crossing situation of the fault current at the cut-off time, the failure discrimination of circuit breakers at the receiving end can be divided into the following two cases:

When the fault current at the receiving end has passed zero at the cut-off time, the failure discrimination process of circuit breakers at the receiving end is the same as that at the transmitting end.

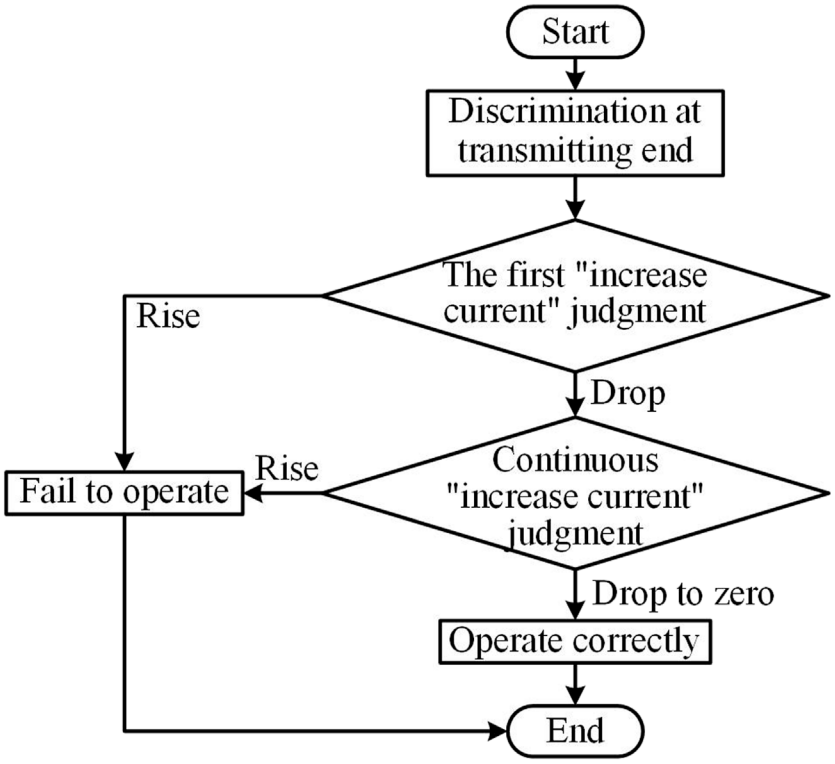

FIGURE 6
The failure discrimination of circuit breakers at the transmitting end.

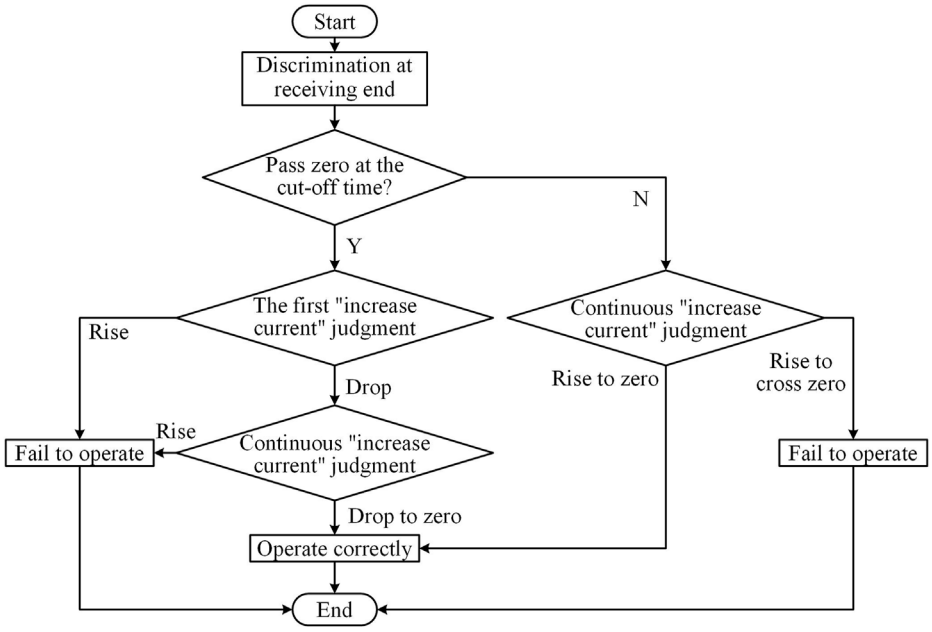

FIGURE 7
The failure discrimination of circuit breakers at the receiving end.

When the fault current at the receiving end remains negative and does not cross zero before the cut-off time, the direction of the fault current change is positive. When the circuit breaker operates correctly or the opposite circuit breaker begins to operate, the rising speed of the fault current will increase. Therefore, the fault current must be a rising trend during the first "increase current" judgment. If the fault current continues to rise to zero and no longer increases, it is determined that the circuit breaker operates correctly. If the fault current continues to rise above zero and continues to rise, it is determined that the circuit breaker fails to operate. The failure discrimination flow chart of the circuit breaker at the receiving end is shown in Figure 7.

3.2 Failure criterion of the DCCB

In the process of circuit breaker failure discrimination, it is necessary to distinguish the trend of fault current change. Considering the influence of measurement errors, the following "increase current" judgment criteria are proposed for the DCCB.

$$\begin{cases} \dfrac{\mathrm{d}i_{\mathrm{cb}}}{\mathrm{d}t} > 0 \ \& \ t_{\mathrm{inc}} > t_{\mathrm{pb}}, \text{fault current rises} \\ \dfrac{\mathrm{d}i_{\mathrm{cb}}}{\mathrm{d}t} < 0 \ \& \ t_{\mathrm{inc}} > t_{\mathrm{pb}}, \text{fault current drops} \end{cases} \tag{2}$$

where i_{cb} is the fault current flowing through the circuit breaker and t_{inc} is the time when the change rate of the fault current continues to be greater than or less than 0. t_{pb} is the set time of discrimination, which depends on the accuracy of current detection and was set to 0.2 ms in this study. To ensure the reliability of the criterion, the fault current can only be determined to rise or fall when t_{inc} reaches the set time of discrimination.

In the process of circuit breaker failure discrimination, it is necessary to distinguish the return to zero state of the fault current. Considering the influence of measurement errors, the following "return to zero" judgment criteria are proposed for the DCCB.

$$|i_{\mathrm{cb}}| < i_{\mathrm{set}} \ \& \ t_{\mathrm{rz}} > t_{\mathrm{pb}}, \text{fault current returns to zero} \tag{3}$$

where i_{cb} is the fault current flowing through the circuit breaker. i_{set} is the set value of zero discrimination, t_{rz} is the time when the absolute value of the fault current continues to be less than the set value of zero discrimination, and t_{pb} is the set time of discrimination. To ensure the reliability of the criterion, the fault current can only be determined to return to zero when t_{inc} reaches the set time of discrimination.

3.3 Analysis of discrimination of DCCB failure protection

For circuit breakers at the transmitting end, according to the completion time of the circuit breaker failure discrimination, the discrimination results can be divided into three cases: 1) The fault current rises when the first judgment is made, indicating that the circuit breaker fails to operate. 2) The fault current first drops and then rises, indicating that the circuit breaker fails to operate. 3) The fault current drops to zero, indicating that the circuit breaker operates correctly.

For circuit breakers at the receiving end, according to the zero crossing of the fault current at the cut-off time and the completion time of the circuit breaker failure discrimination, the discrimination results can be divided into four cases: 1) the fault current has passed zero at the cut-off time, and then the fault current rises, indicating that the circuit breaker fails to operate; 2) the fault current has passed zero at the cut-off time, and then the fault current drops to zero, indicating that the circuit breaker operates correctly; 3) the fault current has not passed zero at the cut-off time, and then the fault current rises to cross zero, indicating that the circuit breaker fails to operate; and 4) the fault current has not passed zero at the cut-off time, and then the fault current rises to zero and will no longer rise, indicating that the circuit breaker operates correctly.

3.4 Secondary accelerated fault isolation scheme

When a fault occurs in the MMC-HVDC grid and the circuit breaker fails to operate, it can lead to rapid isolation failure. In this case, targeted isolation measures need to be taken to minimize the fault isolation scope and complete fault isolation as soon as possible.

When the failure of DCCB is caused by non-serious faults, such as internal control or driving mechanism errors, sending a tripping signal again can make the failed circuit breaker trip successfully. Therefore, when the circuit breaker failure protection acts, the first step is to send a re-tripping command to the failed circuit breaker. In addition, during the circuit breaker failure discrimination, the converter connected to the circuit breaker may be blocked. After the converter is blocked, the non-fault line on the other side cannot exchange energy normally. Therefore, when the converter is blocked, a trip signal should be immediately sent to the circuit breaker on the non-fault line on the other side of the converter station to accelerate the removal of the fault line.

Based on the above analysis, a secondary accelerated fault isolation scheme is proposed, which includes failed breaker re-tripping, adjacent DCCB action, the blocking of the converter station, and AC circuit breaker action, so as to achieve the secondary accelerated fault isolation after the failure of the DCCB in the MMC-HVDC grids. Below is a detailed explanation of two aspects: DC side fault isolation and AC side fault isolation.

For DC side fault isolation: after the circuit breaker failure protection action, if the failed circuit breaker successfully re-trips before the converter is blocked, the adjacent DCCB does not need to operate and other parts of the system can continue to operate except for the successful removal of the fault line. If the converter is blocked before the failed circuit breaker successfully re-trips, a trip signal should be immediately sent to the circuit breaker on the non-fault line on the other side of the converter station. If the circuit breaker fails to re-trip and the converter is not blocked, the converter should be blocked immediately, and a trip signal should be sent to the circuit breaker on the non-fault line on the other side of the converter station. After the circuit breaker failure protection action, it can quickly send a trip signal to the adjacent circuit breaker to achieve secondary accelerated isolation of DC faults.

For AC side fault isolation: after the circuit breaker failure protection action, regardless of whether the converter connected to the failed circuit breaker is blocked or not, as long as the failed circuit breaker does not trip successfully, the AC side can continuously inject fault current into the fault point through the

TABLE 1 The circuit breaker failure discrimination process.

Fault case		Time to receive trip signal	First judgment time (ms)	First judgment result	Continuous judgment time	Continuous judgment result	Judgment result
Transmitting end	Case 1	1.000 ms	4.000	Rise	\	\	Fails to operate
	Case 2	1.000 ms	4.000	Drop	4.575 ms	Rise	Fails to operate
	Case 3	1.000 ms	4.000	Drop	7.650 ms	Return to zero	Operates correctly
Receiving end	Case 1	4.000 ms	7.000	Rise	\	\	Fails to operate
	Case 2	4.00 0ms	7.000	Drop	9.850 ms	Return to zero	Operates correctly
	Case 3	1.000 ms	4.000	Rise	5.600 ms	Cross zero	Fails to operate
	Case 4	1.000 ms	4.000	Rise	4.600 ms	Return to zero	Operates correctly

failed circuit breaker. At this point, it is necessary to disconnect the AC circuit breaker connected to the converter station to achieve the removal of the fault path. However, the operation time and re-input time of the AC circuit breaker are relatively long. Considering the requirements of rapid DC fault isolation and rapid recovery after fault isolation, the tripping of the AC circuit breaker can be avoided as much as possible by re-tripping the failed circuit breaker. If the failed circuit breaker re-trips successfully, there is no need to cut off the AC circuit breaker connected to the converter station where the failed circuit breaker is located. If the failed circuit breaker fails to re-trip, a trip signal should be immediately sent to the AC circuit breaker connected to the converter station where the failed circuit breaker is located to remove the fault path between the AC side and the fault point.

4 Simulation verification

For the Zhangbei 4-terminal grid shown in Figure 1, the effectiveness of the circuit breaker failure state discrimination method and secondary accelerated fault isolation scheme is verified by a simulation on PSCAD.

The maximum breaking delay t_{cb} of the circuit breaker is set as 3 ms, and the sampling frequency is 40 kHz. To avoid data errors caused by interference, the set time for "increase current" discrimination t_{pb} is set as 0.2 ms, and the set value of zero discrimination i_{set} is set as 0.01 kA.

4.1 Verification of circuit breaker failure discrimination

In view of the possible discriminant process of circuit breaker failure, the failure state of the circuit breaker at the transmitting end and the circuit breaker at the receiving end are verified. The specific circuit breaker failure discrimination process is shown in Table 1.

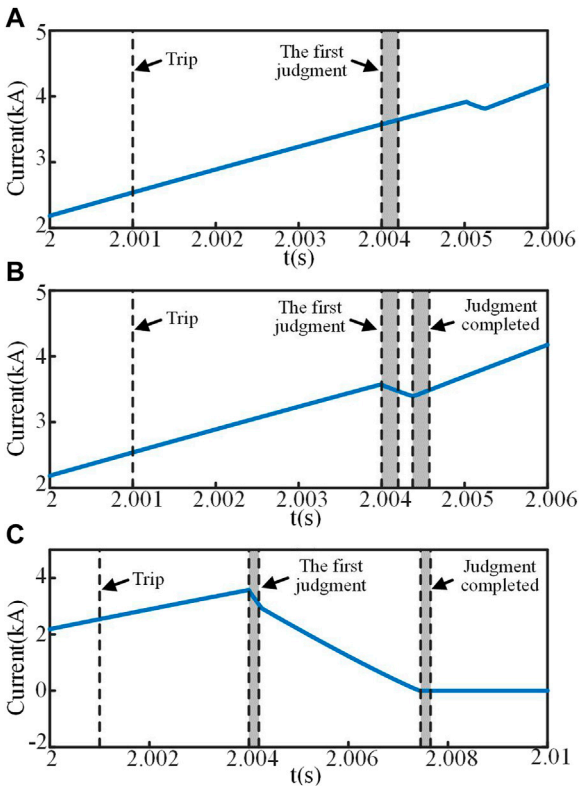

FIGURE 8
Failure discrimination for circuit breakers at the transmitting end. **(A)** Case 1. **(B)** Case 2. **(C)** Case 3.

4.1.1 Verification of failure discrimination for circuit breakers at the transmitting end

Assume that a positive grounding fault occurs at the midpoint of Line3 at 2 s. For circuit breakers at the transmitting end, according

to the time when the circuit breakers receive trip signals, the change of fault current can be divided into three cases.

Case 1: CB_{43} fails to operate, and the fault current rises during the first discrimination.

Assuming that CB_{43} at the transmitting end receives a trip signal at 2.001 s and CB_{34} at the receiving end receives a trip signal at 2.002 s, the fault current I_CB_{43} is shown in Figure 8A. The circuit breaker failure protection starts to conduct failure discrimination at 2.004 s. After 0.2 ms, the first "increase current" judgment is completed and I_CB_{43} is detected as a rising trend, indicating that CB_{43} fails to operate. Therefore, the circuit breaker failure protection will act immediately.

Case 2: CB_{43} fails to operate, and the fault current first drops and then rises.

Assuming that both CB_{43} at the transmitting end and CB_{34} at the receiving end receive trip signals at 2.001 s, the fault current I_CB_{43} is shown in Figure 8B. The circuit breaker failure protection starts to conduct failure discrimination at 2.004 s. After 0.2 ms, the first "increase current" judgment is completed, and I_CB_{43} is detected as a dropping trend. At this time, the circuit breaker failure state cannot be determined, and it is necessary to continuously conduct "increase current" judgment. At 4.575 ms after the fault, I_CB_{43} is detected to be on the rise, and the failure discrimination is completed, indicating that CB_{43} fails to operate. Therefore, the circuit breaker failure protection will act immediately.

Case 3: CB_{43} operates correctly, and the fault current drops to zero.

Assuming that both CB_{43} at the transmitting end and CB_{34} at the receiving end receive trip signals at 2.001 s, the fault current I_CB_{43} is shown in Figure 8C. The circuit breaker failure protection starts to conduct failure discrimination at 2.004 s. After 0.2 ms, the first "increase current" judgment is completed, and I_CB_{43} is detected as a dropping trend. At this time, the circuit breaker failure state cannot be determined, and it is necessary to continuously conduct "increase current" judgment. At 7.650 ms after the fault, I_CB_{43} is detected to be zero and will no longer rise, and the failure discrimination is completed, indicating that CB_{43} operates correctly. Therefore, the circuit breaker failure protection will no longer act.

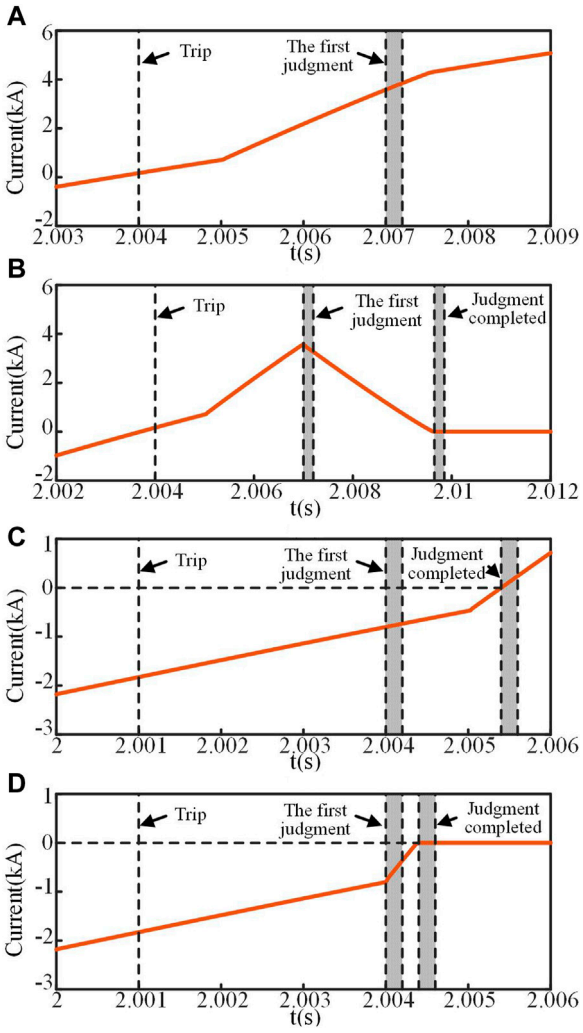

FIGURE 9
Failure discrimination for circuit breakers at the receiving end. **(A)** Case 1. **(B)** Case 2. **(C)** Case 3. **(D)** Case 4.

4.1.2 Verification of failure discrimination for circuit breakers at the receiving end

For circuit breakers at the receiving end, according to the zero-crossing situation of fault current at the cut-off time and the time when the circuit breakers receive trip signals, the change of fault current can be divided into four cases.

It is assumed that a positive grounding fault occurs at the end of Line3 at 2 s, corresponding to the change of fault current in case 1 and case 2. It is assumed that a positive grounding fault occurs at the midpoint of Line3 at 2 s, corresponding to the changes in fault current in case 3 and case 4.

Case 1: CB_{34} fails to operate. The fault current has passed zero and rises during the first discrimination.

Assuming that CB_{43} at the transmitting end receives a trip signal at 2.002 s and CB_{34} at the receiving end receives a trip signal at 2.004 s, the fault current I_CB_{34} is shown in Figure 9A. The circuit breaker failure protection starts to conduct failure state discrimination at 2.007 s. After 0.2 ms, the first "increase current" judgment is completed and I_CB_{34} is detected as a rising trend, indicating that CB_{34} fails to operate. Therefore, the circuit breaker failure protection will act immediately.

Case 2: CB_{34} operates correctly. The fault current has passed zero and drops to zero.

Assuming that CB_{43} at the transmitting end receives a trip signal at 2.002 s and CB_{34} at the receiving end receives a trip signal at 2.004 s, the fault current I_CB_{34} is shown in Figure 9B. The circuit breaker failure protection starts to conduct failure discrimination at 2.007cs. After 0.2cms, the first "increase current" judgment is completed, and I_CB_{34} is detected as a dropping trend. At this time, the circuit breaker failure state cannot be determined, and it is necessary to continuously conduct "increase current" judgment. At 9.850cms after the fault, I_CB_{34} is detected to be zero and will no longer rise, and the failure discrimination is completed, indicating that CB_{34} operates correctly. Therefore, the circuit breaker failure protection will no longer act.

Case 3: CB_{34} fails to operate. The fault current has not passed zero and rises to cross zero.

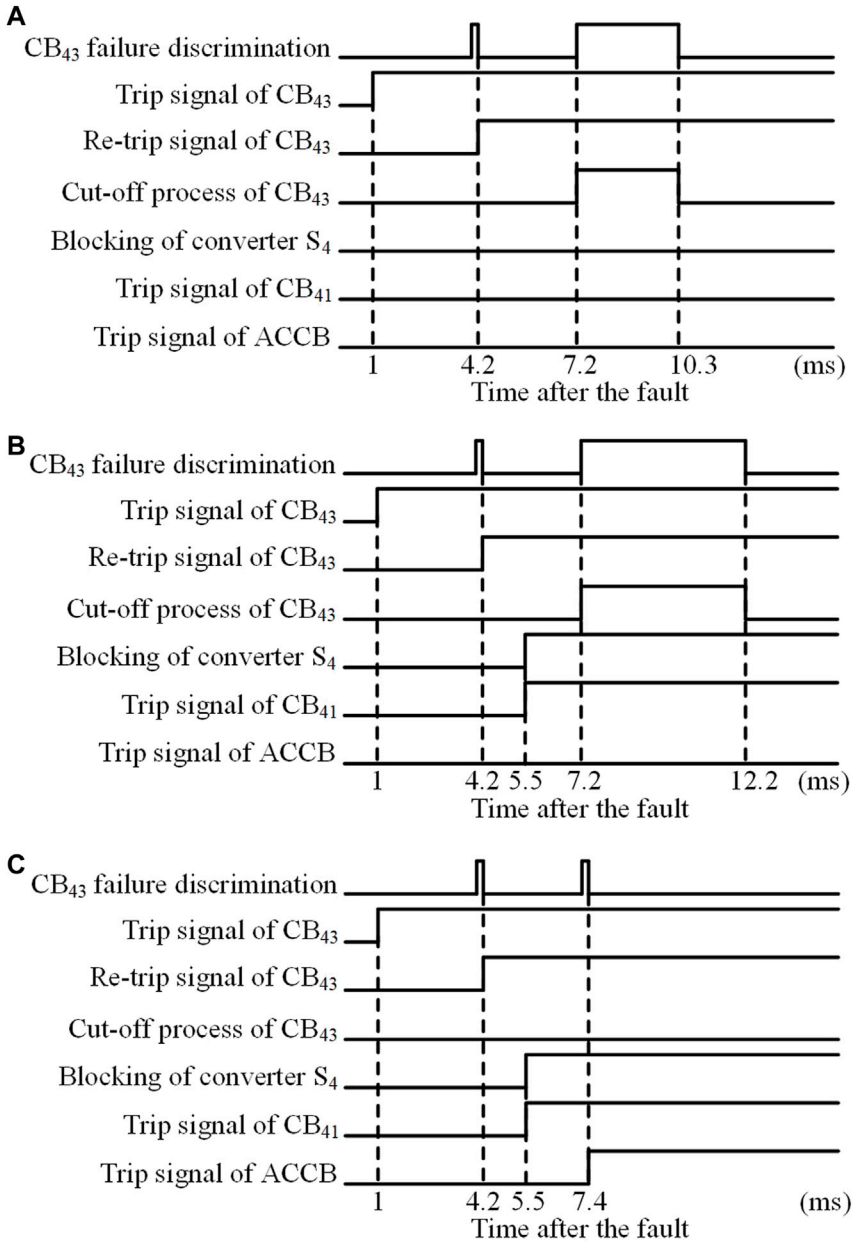

FIGURE 10
The sequence of the fault isolation process. **(A)** Case 1. **(B)** Case 2. **(C)** Case 3.

Assuming that CB_{43} at the transmitting end receives a trip signal at 2.002 s and CB_{34} at the receiving end receives a trip signal at 2.001 s, the fault current I_CB_{34} is shown in Figure 9C. The circuit breaker failure protection starts to conduct failure discrimination at 2.004 s. After 0.2 ms, the first "increase current" judgment is completed, and I_CB_{34} is detected as a rising trend. At this time, the circuit breaker failure state cannot be determined, and it is necessary to continuously conduct "increase current" judgment. At 5.600 ms after the fault, I_CB_{34} is detected to cross zero and continue to rise, and the failure discrimination is completed, indicating that CB_{34} fails to operate. Therefore, the circuit breaker failure protection will act immediately.

Case 4: CB_{34} operates correctly. The fault current has not passed zero and rises to zero and will no longer rise.

Assuming that CB_{43} at the transmitting end receives a trip signal at 2.002 s and CB_{34} at the receiving end receives a trip signal at 2.001 s, the fault current I_CB_{34} is shown in Figure 9D. The circuit breaker failure protection starts to conduct failure discrimination at 2.004 s. After 0.2 ms, the first "increase current" judgment is completed, and I_CB_{34} is detected as a rising trend. At this time, the circuit breaker failure state cannot be determined, and it is necessary to continuously conduct "increase current" judgment. At 4.600 ms after the fault, I_CB_{34} is detected to be zero and will no longer rise, and the failure discrimination is completed, indicating

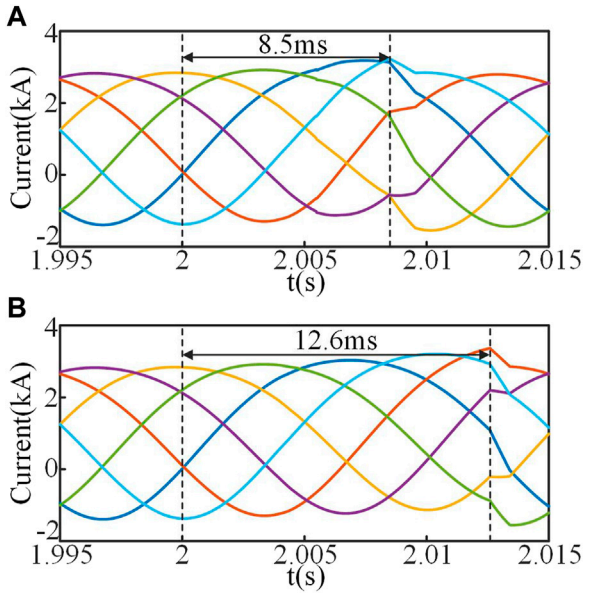

FIGURE 11
Comparison of the bridge arm current changes of S_1. **(A)** The failure protection trips CB_{41} after the failure of CB_{43}. **(B)** The main protection of S_1 trips CB_{14} after the failure of CB_{43}.

that CB_{34} operates correctly. Therefore, the circuit breaker failure protection will no longer act.

4.2 Verification of a secondary accelerated fault isolation scheme

Assuming that a fault occurs on Line3 and CB_{43} fails and refuses to operate, the fault isolation scheme, including the re-tripping of the failed circuit breaker CB_{43}, adjacent DCCB action, the blocking of converter station S_4, and AC circuit breaker action, is verified. The fault isolation can be divided into three cases.

Case 1: the failed circuit breaker re-trips successfully before the converter is blocked.

A positive ground fault with a transition resistance of 100 Ω occurs at the midpoint of Line3 at 2s.

It is assumed that CB_{43} receives a trip signal at 1 ms after the fault, and CB_{43} is judged to fail to operate, and a re-tripping signal is sent at 4.2 ms after the fault. The re-tripping failure discrimination is conducted at 7.2 ms after the fault, and CB_{43} is judged to re-trip successfully at 10.3 ms after the fault. At this time, the converter station S_4 is still not blocked, so the adjacent circuit breaker CB_{41} and the AC circuit breaker do not need to trip. In this case, the fault isolation process is shown in Figure 10A.

Case 2: the converter has been blocked before the re-tripping failure discrimination is completed, and the failed circuit breaker re-trips successfully.

A positive ground fault occurs at the midpoint of Line3 at 2 s.

It is assumed that CB_{43} receives a trip signal at 1 ms after the fault, and CB_{43} is judged to fail to operate, and a re-tripping signal is sent at 4.2 ms after the fault. The converter station S_4 is blocked, and a trip signal is immediately sent to the adjacent circuit breaker CB_{41} at 5.5 ms after the fault. The re-tripping failure discrimination is conducted at 7.2 ms after the fault, and CB_{43} is judged to have re-tripped successfully at 12.2 ms after the fault. At this time, the AC circuit breaker does not need to trip. In this case, the fault isolation process is shown in Figure 10B.

Case 3: the converter has been blocked before the re-tripping failure discrimination is completed, and the failed circuit breaker fails to re-trip.

A positive ground fault occurs at the midpoint of Line3 at 2 s.

It is assumed that CB_{43} receives a trip signal at 1 ms after the fault, and CB_{43} is judged to have failed to operate, and a re-tripping signal is sent at 4.2 ms after the fault. The converter station S_4 is blocked, and a trip signal is immediately sent to the adjacent circuit breaker CB_{41} at 5.5 ms after the fault. The re-tripping failure discrimination is conducted at 7.2 ms after the fault, and CB_{43} is judged to have failed to re-trip at 7.4 ms after the fault. At this time, a trip signal is immediately sent to the AC circuit breaker connected to converter station S_4. In this case, the fault isolation process is shown in Figure 10C.

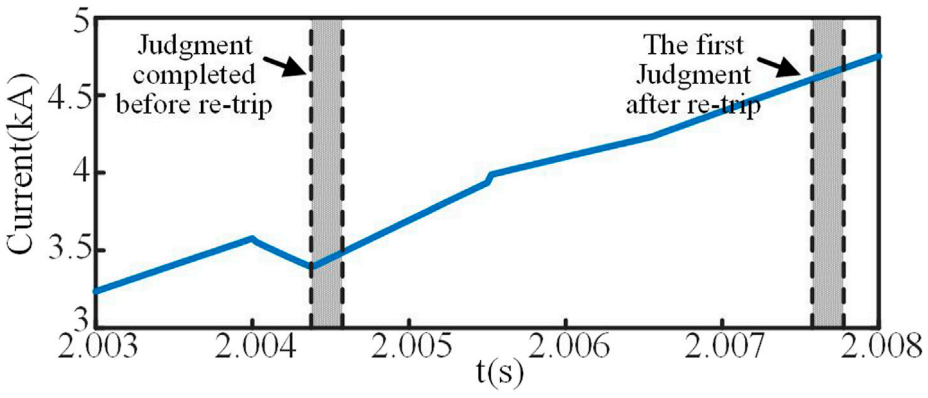

FIGURE 12
The re-tripping failure discrimination when CB_{43} fails to re-trip.

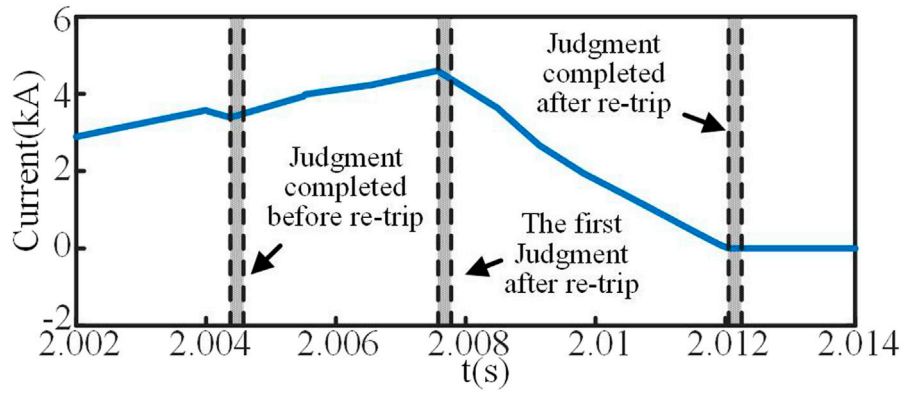

FIGURE 13
The re-tripping failure discrimination when CB_{43} re-trips successfully.

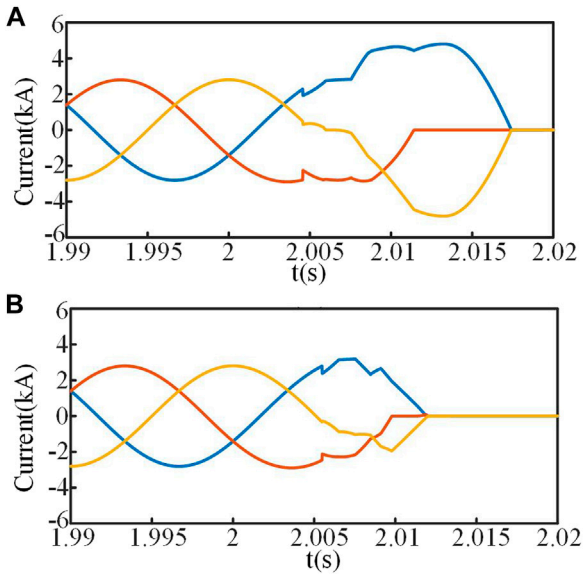

FIGURE 14
Comparison of the AC current changes of S_4. **(A)** The failed circuit breaker CB_{43} fails to re-trip. **(B)** The failed circuit breaker CB_{43} re-trips successfully.

4.3 Verification of the secondary accelerated isolation effect

After the DCCB failure protection action, the accelerated isolation of DC faults is achieved by tripping the adjacent DCCB. Assuming that a positive grounding fault occurs at the midpoint of Line3 at 2 s and CB_{43} fails to operate, the acceleration isolation effect of DC faults is simulated and analyzed.

When the circuit breaker failure protection is configured in the system, during the circuit breaker failure discrimination, the converter station S_4 is blocked, and the circuit breaker failure protection acts immediately at 5.5 ms after the fault. A trip signal is sent to CB_{41} located on the non-fault line on the other side of the converter station to isolate the fault, and the main protection set in converter station S_1 no longer acts.

When the circuit breaker failure protection is not configured in the system, CB_{41} will no longer operate. The main protection set in converter station S_1 predicts the blocking time of the converter station according to the real-time fault current data and selects CB_{14} as the pre-trip circuit breaker based on the fault current direction criterion. When the protection acts, a tripping signal will be sent to CB_{14} to remove the fault.

With or without circuit breaker failure protection configured in the system, the comparison of the bridge arm current changes of the converter station S_1 is shown in Figure 11. Figure 11A shows that the DC fault is cleared at 8.5 ms after the fault when the failure protection trips CB_{41}. Figure 11B shows that the DC fault is cleared at 12.6 ms after the fault when the main protection of converter station S_1 trips CB_{14}. From this, when a fault occurs in the DC grid and the circuit breaker fails to operate, the circuit breaker failure protection action can remove the fault faster, achieving the accelerated isolation of DC faults.

4.4 Verification of the Re-tripping of the failed circuit breaker

The re-tripping of the failed circuit breaker can effectively avoid the problem of long tripping time caused by isolating faults through the action of AC circuit breakers. It is assumed that when a positive ground fault occurs at the midpoint of Line3 at 2 s and CB_{43} fails to operate, the re-tripping process of the failed circuit breaker after the failure of the DCCB is verified.

Assuming that both CB_{43} and CB_{34} receive trip signals at 2.001 s, the circuit breaker failure protection starts to conduct failure discrimination at 2.004 s. The first "increase current" judgment is completed at 4.200 ms after the fault, but the circuit breaker failure state cannot be determined. At 4.575 ms after the fault, I_CB_{43} is detected to be on the rise, and the failure discrimination is completed, indicating that CB_{43} fails to operate. Therefore, the trip signal is immediately sent to CB_{43} again, and the re-tripping failure discrimination is conducted at 7.575 ms after the fault.

When CB_{43} fails to re-trip, the fault current I_CB_{43} is shown in Figure 12. The first judgment after re-tripping is completed at 7.775 ms after the fault, and I_CB_{34} is detected as a rising trend, indicating that CB_{43} fails to re-trip. Therefore, a trip signal is immediately sent to the relevant AC circuit breaker.

When CB_{43} re-trips successfully, the fault current I_CB_{43} is shown in Figure 13. The first judgment after re-tripping is completed at 7.775 ms after the fault, and I_CB_{34} is detected as a dropping trend. At this time, the circuit breaker failure state cannot be determined. At 12.250 ms after the fault, I_CB_{43} is detected to be zero and will no longer rise, and the re-tripping failure discrimination is completed, indicating that CB_{43} re-trips successfully. Therefore, the AC circuit breaker does not need to trip.

The comparison of AC current flowing into converter station S_4 between successful and failed re-tripping of the failed circuit breaker CB_{43} is shown in Figure 14. Figure 14 shows that when the failed circuit breaker re-trips successfully, there is no need to disconnect the AC circuit breaker to isolate the fault, and the AC fault current injected into the converter station where the failed circuit breaker is located will be cleared faster.

5 Conclusion

This paper proposes a secondary accelerated fault isolation scheme for MMC-HVDC grids after rapid fault isolation failure. Considering the influence caused by the disconnection process of the opposite circuit breaker, the fault current characteristics after the failure of the DCCB are analyzed. The method of circuit breaker failure discrimination using "increase current" judgment is studied. By analyzing the logical relationship among failed breaker re-tripping, adjacent DCCB action, the blocking of the converter station, and AC circuit breaker action, a secondary accelerated fault isolation scheme is proposed to minimize the fault isolation area. The main conclusions and innovations are as follows:

1) The fault current characteristics after the failure of the DCCB are analyzed. In MMC-HVDC grids, when a circuit breaker fails to operate, the overall trend of the fault current flowing through the failed circuit breaker continues to rise when the influence of the opposite circuit breaker disconnection is not considered. The disconnection process of the opposite circuit breaker will lead to a decrease in the rise rate of the fault current at the transmitting end, and will lead to an increase in the rise rate of the fault current at receiving end.
2) A method of circuit breaker failure discrimination using "increase current" judgement is proposed. The method fully considers the influence of the opposite circuit breaker disconnection. Compared with the traditional "present current" judgement method, the "increase current" judgement method can rapidly determine the failure state of the DCCB, which is conducive to the fast action of circuit breaker failure protection.
3) A secondary accelerated fault isolation scheme after rapid isolation failure in the MMC-HVDC grid is proposed. The scheme achieves the accelerated isolation of DC faults by tripping the adjacent DCCB, which is beneficial for the safe operation of the non-fault parts of the system. Additionally, by re-tripping the failed circuit breaker, the fault point is successfully isolated from the AC side line, which can effectively avoid the trip of the AC circuit breaker.

Data availability statement

The original contributions presented in the study are included in the article/supplementary material, further inquiries can be directed to the corresponding author.

Author contributions

AL: Software, methodology, data Curation, writing—original draft; BoL: Conceptualization, software, investigation; WW: Supervision, Writing—review and editing, visualization; BiL and XC: Supervision; writing—review and editing. All authors contributed to the article and approved the submitted version.

Funding

This work was supported by the Joint Funds of the National Natural Science Foundation of China (U2166205).

Conflict of interest

The authors declare that the research was conducted in the absence of any commercial or financial relationships that could be construed as a potential conflict of interest.

Publisher's note

All claims expressed in this article are solely those of the authors and do not necessarily represent those of their affiliated organizations, or those of the publisher, the editors and the reviewers. Any product that may be evaluated in this article, or claim that may be made by its manufacturer, is not guaranteed or endorsed by the publisher.

References

Azad, S. P., Leterme, W., and Hertem, D. V. (2016). Fast breaker failure backup protection for HVDC grids. *Electr. Power Syst. Res.* 138, 99–105. doi:10.1016/j.epsr.2016.03.003

Ding, S. (2006). Analysis on some problems of breaker failure protection. *Automation Electr. Power Syst.* 30 (3), 89–91. doi:10.3321/j.issn:1000-1026.2006.03.017

Franck, C. M. (2011). HVDC circuit breakers: A review identifying future research needs. *IEEE Trans. Power Deliv.* 26 (2), 998–1007. doi:10.1109/TPWRD.2010.2095889

He, C., and Li, X. (2010). Analysis of some problems on 220 kV circuit breaker failure protection of main transformer high-voltage side. *Power Syst. Prot. Control* 38 (1), 102–106. doi:10.3969/j.issn.1674-3415.2010.01.024

Khosravi, N., Abdolvand, A., Oubelaid, A., Khan, Y., Bajaj, M., and Govender, S. (2021). Improvement of power quality parameters using modulated-unified power quality conditioner and switched-inductor boost converter by the optimization techniques for a hybrid AC/DC microgrid. *Sci. Rep.* 12 (1), 21675. doi:10.1038/s41598-022-26001-8

Oubelaid, A., Albalawi, F., Rekioua, T., Ghoneim, S., Taib, N., and Abdelwahab, S. (2022a). Intelligent torque allocation based coordinated switching strategy for comfort enhancement of hybrid electric vehicles. *IEEE ACCESS* 10, 58097–58115. doi:10.1109/ACCESS.2022.3178956

Oubelaid, A., Taib, N., Nikolovski, S., Alharbi, T., Rekioua, T., Flah, A., et al. (2022b). Intelligent speed control and performance investigation of a vector controlled electric vehicle considering driving cycles. *Electronics* 11 (13), 1925. doi:10.3390/electronics11131925

Perez-Molina, M., Larruskain, D., Eguia, P., and Abarrategi, O. (2021). Circuit breaker failure protection strategy for HVDC grids. *Energies* 14 (14), 4326. doi:10.3390/en14144326

Qin, D., Chen, Y., Zhang, Z., and Enslin, J. (2022). "A hierarchical microgrid protection scheme using hybrid breakers," in IEEE International Symposium on Power Electronics for Distributed Generation Systems, Chicago, IL, USA. 28 June 2021 - 01 July 2021 (IEEE), doi:10.1109/PEDG51384.2021.9494192

Song, Y. (2008). Research on several questions of line circuit breaker failure protection. *Power Syst. Prot. Control* 36 (23), 88–91. doi:10.3969/j.issn.1674-3415.2008.23.021

Wang, M., Zaja, M., Beerten, J., Jovcic, D., and Van, H. D. (2021). Backup protection algorithm for failures in modular DC circuit breakers. *IEEE Trans. Power Deliv.* 36 (6), 3580–3589. doi:10.1109/TPWRD.2020.3045262

Xu, Z., Xiao, H., and Xu, Y. (2018). Study on basic principle and its realization methods for DC circuit breakers. *High. Volt. Eng.* 44 (2), 347–357. doi:10.13336/j.1003-6520.hve.20180131002

Zhang, H., and Chang, F. (2003). Breaker failure protection of high voltage power system. *Electr. Power Autom. Equip.* 23 (5), 79–81. doi:10.3969/j.issn.1006-6047.2003.05.023

Zhu, B., Li, H., Xu, P., Jiao, S., Zhang, L., and Xin, Y. (2021). Coordinated control strategy of DC fault ride-through for the WF connected to the grid through the MMC-HVDC. *Front. Energy Res.* 9, 465. doi:10.3389/fenrg.2021.743465

frontiers | Frontiers in Energy Research

TYPE Original Research
PUBLISHED 04 August 2023
DOI 10.3389/fenrg.2023.1235467

OPEN ACCESS

EDITED BY
Srete Nikolovski,
Josip Juraj Strossmayer University of Osijek, Croatia

REVIEWED BY
Yushuai Li,
University of Oslo, Norway
Adel Oubelaid,
Université de Bejaia, Algeria

*CORRESPONDENCE
Xinxin Lv,
xinxinlvhhuc@163.com

RECEIVED 06 June 2023
ACCEPTED 19 July 2023
PUBLISHED 04 August 2023

CITATION
Huang T and Lv X (2023), Load frequency control of power system based on improved AFSA-PSO event-triggering scheme.
Front. Energy Res. 11:1235467.
doi: 10.3389/fenrg.2023.1235467

Load frequency control of power system based on improved AFSA-PSO event-triggering scheme

Tenghao Huang and Xinxin Lv*

School of Information Science and Engineering, Zhejiang Sci-Tech University, Hangzhou, China

Aiming at the impact of redundant information transmission on network resource utilization in current power systems, an improved event-triggered scheme based on particle swarm optimization and artificial fish swarm algorithm for power system load frequency control (LFC) with renewable energy is proposed. First of all, to keep the stability and security of power systems with renewable energy, the load frequency control scheme is investigated in this paper. Then, to relieve the communication burden and increase network utilization, an improved event-triggered scheme based on the particle swarm algorithm and artificial fish swarm algorithm is explored for the power system load frequency control. Then, by utilizing improved Lyapunov functional and the linear matrix inequality method, sufficient condition for the H_∞ stability of the load frequency control system is established. Finally, a two-area load frequency control system and IEEE-39 node simulation models are constructed to verify the effectiveness and applicability of the proposed method.

KEYWORDS

event-triggered scheme, LFC systems, particle swarm optimization, artificial fish swarm algorithm, IEEE-39 node simulation models

1 Introduction

In the context of global clean energy and low-carbon development, environmental protection issues have gained increasing attention from numerous countries in recent years. Conventional power generation technologies' defects in the economy and environmental protection have become more prominent (Liu et al., 2021). Meanwhile, several new problems affecting the stable operation of power systems have arisen due to the rapid development of clean energy generation technology. For instance, new energy power systems are often subject to interruptions or fluctuations in power supply (Gholamrezaie et al., 2018; Oubelaid et al., 2022a). Energy storage technology is then applied to solve the technical deficiencies of the system power supply and ease the instability of the new energy power system (Oubelaid et al., 2022b). Therefore, the power system combines with a growing number of renewable energy sources and battery storage (Choi et al., 2016; Mi et al., 2017; Pulazza et al., 2021; Oubelaid et al., 2022c). However, environmental variations can have a significant impact on the output of renewable energy sources, leading to fluctuations in the power system's output power after the integration of renewable energy. Therefore, ensuring the maintenance of the load frequency within a safe range becomes particularly crucial after the integration of renewable energy sources into the power grid (Yan et al., 2022). Hence, the system needs a control strategy for regulation. As the core application of automatic power generation

control in power systems, load frequency control (LFC) is also an essential tool for dealing with grid frequency matters resulting from load changes (Zhao et al., 2022; Sun et al., 2023). LFC mainly adjusts the grid frequency deviation and the exchange power value of the contact line to make the system frequency reach the rated value, while maintaining the tie-lines exchanged power at the normal value (Yang et al., 2020).

It is worth mentioning that traditional LFC technology usually uses a dedicated line communication method to transmit data (Wang et al., 2022), with the drawbacks of high maintenance costs and poor flexibility. The last few decades have witnessed a spurt of progress in communication, computer, and control technology. Thus, this traditional method of communication is gradually being replaced by open networks (Aluko et al., 2021). However, the application of open communication networks in power systems has brought new problems such as communication delays and limited network bandwidth constraints (Yuan et al., 2021). Therefore, how to improve the utilization of network resources has been the focus of investigation on the power system in the modern communication network environment. It is worth noting that event-trigger scheme can effectively relieve bandwidth pressure (Li M. et al., 2019; Zhang et al., 2020).

In an event-trigger scheme, the event generator will only release the data packet signal while the preset event-trigger conditions are satisfied. Therefore, the event-triggered scheme is adopted in modern power systems to achieve the expected goal of saving the occupancy of communication channels (Wen et al., 2016). Based on the event-triggered scheme, LFC has received considerable attention in the power system. In (Bu et al., 2022), an event-triggered data-driven LFC scheme via model-free adaptive control is proposed, which achieves better data-driven linear frequency regulation based on an event-triggered scheme and dynamic linearization technique. In (Hossain et al., 2022), a distributed event-trigger scheme has been applied, whose triggering conditions depend on output information for specific regions. It is noteworthy that the performance of the event-trigger scheme is related to the trigger threshold, however, In the design of the event-trigger scheme in the above research results, the performance of the trigger scheme has been limited since the trigger threshold is required to be preset in advance (Wu et al., 2018). In consideration of the above situation, various research scholars have applied adaptive event-trigger schemes (Chen et al., 2022) to the study of power systems. For example, an adaptive event-trigger scheme for multi-area power systems with communication bandwidth constraints is designed (Peng et al., 2018). Consequently, the system can adaptively adjust the threshold parameters based on current and past data; the dynamic event-trigger scheme and adaptive event-trigger scheme for networked power systems are investigated (Wu et al., 2020). The trigger parameters of the dynamic scheme are the upper limit of the trigger parameters of the adaptive scheme, both of which work together to balance the system control performance and the number of transmitted signals (Shangguan et al., 2022). Even though there have been many research results on the LFC event-triggered scheme, little research has been conducted on the optimal design of the event-trigger scheme.

Artificial fish swarm algorithm (AFSA) is a class of swarm intelligence optimization algorithms based on fish activity behavior (Tang et al., 2021). The algorithm has the ability of distributed processing as well as strong robustness of parameters and initial values (Lin et al., 2020; Yang et al., 2022). Particle swam optimization (PSO) is an algorithm inspired by the predatory behavior of birds and used to solve optimization problems (Tang et al., 2021; Belaid et al., 2022). The velocity of a particle is dynamically adjusted by its own and its companion's flight experience, thus enabling the individual to search in the solvable space. It is rather remarkable that AFSA has a strong global search capability, but the algorithm converges slowly at a later stage (Zhu and Gao, 2020). In contrast, PSO has the capability of local fast convergence but tends to fall into the local optimum (Dashtdar et al., 2022). This paper presents a hybrid AFSA-PSO algorithm, to make the merits and demerits of the two algorithms complementary, thereby addressing the optimization problem better. AFSA uses an adaptive vision and step size which can dynamically regulate the operating speed of the algorithm. Additionally, the introduction of the compression factor and adaptive inertia weight to PSO ensures the convergence of the algorithm and removes the boundary restriction on the velocity, resulting in a more satisfactory solution.

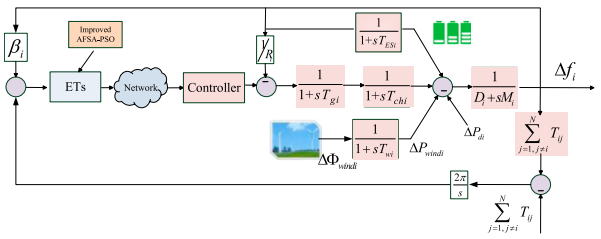

FIGURE 1
The structure of *i*-th area LFC.

Accordingly, to enhance the network bandwidth utilization, and reduce the transmission of redundant information for power system, this paper offers an improved event-triggered LFC based on a hybrid AFSA-PSO algorithm.

In consideration of the above discussions, this paper investigates a multi-area power system LFC based on the AFSA-PSO event-triggered scheme. The main contributions of this work are displayed below:

1) Since network communication is constrained by limited network bandwidth, this paper introduces an event-trigger scheme. The specific form of performance is to improve the utilization of network resources and ease the pressure on communication bandwidth by screening the measured output signal of the LFC power system. In the meantime, a hybrid AFSA-PSO algorithm is proposed to optimize the parameters that determine the threshold conditions in this paper, leading to the improved performance of the event-trigger scheme. AFSA is employed early in the method, and PSO has applied afterward, which makes the algorithm have high solution accuracy and convergence speed. In addition, this paper also optimizes and improves the AFSA and PSO respectively, to enable the algorithm to attain better performance.
2) The conservatism of the stability criterion design process is reduced under improved Lyapunov function. On the one hand, an improved Lyapunov function is constructed in the stability-proof process. On the other hand, the utilization of the double B-L inequality in the inequality scaling process decreases the conservatism of the resulting criterion.

TABLE 1 LFC symbol description of the multi-area power system.

Symbol	Description
ΔP_{di}	Load deviation
ΔP_{mi}	Generator mechanical output deviation
ΔP_{vi}	Valve position deviation
Δf_i	Frequency deviation
M_i	Moment of inertia
D_i	Generator damping coefficient
T_{gi}	Time constant of the governor
T_{chi}	Time constant of the turbine
R_i	Speed drop
β_i	Frequency bias factor
T_{ij}	Tie-line synchronizing coefficient

2 Problem statement

2.1 Describe of LFC model

For multi-area power systems, the LFC system structure of the i-th area can be shown in Figure 1. The parameters of i-th control area are listed in Table 1.

The multi-area power system dynamics LFC model studied in this paper can be described as:

$$\begin{cases} \dot{x}(t) = Ax(t) + Bu(t) + F\omega(t) \\ y(t) = Cx(t) \end{cases} \tag{1}$$

where:

$$x_i(t) = \left[\Delta f_i \;\; \Delta P_{mi} \;\; \Delta P_{vi} \;\; \Delta P_{windi} \;\; \Delta P_{Bi} \;\; \int ACE_i \;\; \Delta P_{tie-i}\right]^T$$
$$x(t) = \left[x_1{}^T(t) \;\; x_2{}^T(t) \;\; x_3{}^T(t) \;\; \ldots \;\; x_n{}^T(t)\right]^T$$
$$\omega_i(t) = \left[\Delta P_{di} \;\; \Delta\Phi_{windi}\right]^T, A_{ij} = \left[(7,1) = -2\pi T_{ij}\right]$$
$$u(t) = \left[u_1{}^T(t) \;\; u_2{}^T(t) \;\; u_3{}^T(t) \;\; \ldots \;\; u_n{}^T(t)\right]^T$$
$$y_i(t) = \left[ACE_i \;\; \int ACE_i\right]^T, B = diag\{B_1, .., B_n\}$$
$$\omega(t) = \left[\omega_1{}^T(t) \;\; \omega_2{}^T(t) \;\; \omega_3{}^T(t) \;\; \ldots \;\; \omega_n{}^T(t)\right]^T$$
$$y(t) = \left[y_1{}^T(t) \;\; y_2{}^T(t) \;\; y_3{}^T(t) \;\; \ldots \;\; y_n{}^T(t)\right]^T$$

$$A_{ii} = \begin{bmatrix} (1,1) = \dfrac{-D}{M_i}, (1,2) = \dfrac{1}{M_i}, (1,4) = \dfrac{1}{M_i}, \\ (1,5) = \dfrac{1}{M_i}, (1,7) = \dfrac{-1}{M_i}, (2,2) = \dfrac{-1}{T_{chi}}, \\ (2,3) = \dfrac{1}{T_{chi}}, (3,1) = \dfrac{-1}{RT_{gi}}, (3,3) = \dfrac{-1}{T_{gi}}, \\ (4,4) = \dfrac{-1}{T_{wi}}, (5,1) = \dfrac{1}{T_{ESi}}, \\ (5,5) = -\dfrac{1}{T_{ESi}}, (6,1) = \beta_i, \\ (6,6) = 1, (7,1) = 2\pi \sum_{j=1, j\neq i}^{n} T_{ij} \end{bmatrix}$$

$$A = \begin{bmatrix} A_{11} & \ldots & A_{1n} \\ \vdots & \ddots & \vdots \\ A_{n1} & \ldots & A_{nn} \end{bmatrix}$$
$$B_i = \begin{bmatrix} 0 & 0 & \left(\frac{1}{T_{gi}}\right)^T & 0 & 0 & 0 & 0 \end{bmatrix}^T$$
$$C_i = \begin{bmatrix} \beta_i & 0 & 0 & 0 & 0 & 0 & 1 \\ 0 & 0 & 0 & 0 & 0 & 1 & 0 \end{bmatrix}$$
$$F_i = \begin{bmatrix} \frac{-1}{M_i{}^T} & 0 & 0 & 0 & 0 & 0 & 0 \\ 0 & 0 & 0 & \frac{1}{T_{wi}} & 0 & 0 & 0 \end{bmatrix}^T$$
$$C = diag\{C_1, .., C_n\}, F = diag\{F_1, .., F_n\}$$

The Area Control Error (ACE) for each control area can be expressed by:

$$ACE_i = \beta_i \Delta f_i + \Delta P_{tie-i} \tag{2}$$

2.2 Design of improved event-triggered scheme

To save network bandwidth resources, and improve information transmission efficiency, an event-triggered scheme based on the improved AFSA-PSO algorithm is proposed to increase the utilization of network resources in this study. When the transmitted signal meets the trigger scheme, it may be transmitted; otherwise, the sampling signal will not be transmitted, and the event-triggered conditions are designed as follows (Yue et al., 2013):

$$\left[x(t_l h + jh) - x(t_l h)\right]^T \Phi \left[x(t_l h + jh) - x(t_l h)\right] > \beta x(t_l h)^T \Phi x(t_l h) \tag{3}$$

where, Φ is the positive definite weighting matrix; β is the event-triggered threshold in the range of $[0, 1)$; $t_l h$ denotes the most recent data transmission moment and $t_l h + jh$ is the current sampling moment.

The event trigger determines the transmission of the system state. Assuming that the data has been successfully transferred at time $t_l h$, the next trigger moment $t_{l+1} h$ is:

$$t_{l+1} h = t_l h + \min\Big\{jh \Big| \left[x(t_l h + jh) - x(t_l h)\right]^T \Phi \left[x(t_l h + jh) - x(t_l h)\right] > \beta x(t_l h)^T \Phi x(t_l h)\Big\} \tag{4}$$

Transmission delays are unavoidable due to the presence of communication networks. It is reflected in the trigger scheme as whether $x(t_l h)$ or $x(t_{l+1} h)$ is received first. Define $\tau(t)$ as the transmission delay between the event trigger and the zero-order device at moment $t_l h$, and the maximum value of $\tau(t)$ is $\tau_{\max}$. Define the error between the most recently transmitted data and the currently sampled data as $e_l(t)$. The event-trigger scheme is treated in two cases as follows:

(1) When $t_l h + h + \tau_{\max} \geq t_{l+1} h + \tau_{l+1}$, define $\tau(t) = t - t_l h$, $\tau(t) \in [\tau_l, (t_{l+1} - t_l)h + \tau_{l+1}]$, and $e_l(t) = 0$。
(2) When $t_l h + h + \tau_{\max} < t_{l+1} h + \tau_{l+1}$, the subintervals are discussed as follows:

$$\tau(t) = \begin{cases} t - t_l h, k \in \Omega_0 \\ t - t_l h - nh, k \in \Omega_n \\ t - t_l h - jh, k \in \Omega_j \end{cases} \quad (5)$$

where,

$$\Omega_0 = [t_l h + \tau_l, t_l h + \tau_{\max})$$
$$\Omega_n = [t_l h + nh + \tau_{\max}, t_l h + nh + h + \tau_{\max})(n = 1, 2, .., j-1)$$
$$\Omega_j = [t_l h + jh + \tau_{\max}, t_{l+1} h + \tau_{l+1})$$

Thus, $e_l(t)$ can be written as:

$$e_l(t) = \begin{cases} 0, k \in \Omega_0 \\ x(t_l h) - x(t_l h + nh), k \in \Omega_n \\ x(t_l h) - x(t_l h + jh), k \in \Omega_j \end{cases} \quad (6)$$

where, $x(t_l h)$ is the most recent moment transmission data; $x(t_l h + nh)$ and $x(t_l h + jh)$ are the current moment sampling data, respectively.

Therefore, $y(t)$ can be rewritten as follows

$$y(t_l h) = Ce_l(t) + Cx(t - \tau_l(t)) \quad (7)$$

Remark 1: In this paper, a PSO with adaptive inertia weights (Li et al., 2019b) and compression factors (Zhou et al., 2019) are designed. This improved algorithm balances the local search and global search capability of PSO. Meanwhile, the boundary restriction on the conventional particle velocity is removed to ensure the convergence and accuracy of PSO. PSO can utilize the mechanism of sharing information among individuals in a group to make the whole solution process orderly. The core formula of the algorithm is given below:

$$v_i^d = \omega v_i^{d-1} + c_1 r_1 \left(pbest_i^d - x_i^d\right) + c_2 r_2 \left(gbest^d - x_i^d\right) \quad (8)$$

$$x_i^d = x_i^{d-1} + v_i^{d-1} t \quad (9)$$

Eq. 8 is the speed of the individual's step d, which consists of the speed inertia of the previous step itself ωv_i^{d-1}, the self-cognition part $c_1 r_1 (pbest_i^d - x_i^d)$, and the social cognition part $c_2 r_2 (gbest^d - x_i^d)$. Eq. 9 is the position of the individual at step d, which is determined by the position x_i^{d-1} at step $d-1$ and the velocity of step $d-1 \times$ time of motion, with the time of each step generally taken as 1. ω denotes the velocity inertia weight, c_1 denotes the individual acceleration factor, c_2 denotes the social acceleration factor, and r_1, r_2 are the random numbers on $[0, 1]$.

Where, $pbest_i^d$ represents the best position that the particle i has passed through by the end of the d iteration, and $gbest^d$ represents the best position that all particles have passed through. ω, c_1 and c_2 are important factors to be considered in optimizing the PSO. However, the traditional PSO usually sets these parameters to fixed values, making the algorithm unable to be dynamically adjusted according to the operation results. On the other hand, due to the fast information exchange between particles, the particles all move in the optimal direction and tend to be homogeneous, which tends to cause local convergence. This work proposes an improved PSO with the following formulations to address these defects.

$$v_i^d = \alpha\left[\omega_i^d v_i^{d-1} + c_1 r_1 \left(pbest_i^d - x_i^d\right) + c_2 r_2 \left(gbest^d - x_i^d\right)\right] \quad (10)$$

The algorithm is designed with adaptive inertia weights ω_i^d, whose value can change with the change of the fitness value. Take the problem of minimizing the degree of adaptation as an example: the smaller the current degree of adaptation, the closer to the optimal solution, the more local search is needed, and accordingly, the inertia weights become smaller; the larger the degree of adaptation, the farther away from the optimal solution, the more global search is needed, which requires a larger value of inertia weights. The details are shown in the following formula:

$$\omega_i^d = \begin{cases} \omega_{\min} + (\omega_{\max} - \omega_{\min}) \dfrac{f(x_i^d) - f_{\min}^d}{f_{average}^d - f_{\min}^d}, f\left(x_i^d\right) \le f_{average}^d \\ \omega_{\max}, f(x_i^d) > f_{average}^d \end{cases} \quad (11)$$

Individual learning factor c_1 and social (group) learning factor c_2 indicate information exchange among the particle swarm. A bigger value of c_1 causes the particles to seek too much within their local range, whereas a larger value of c_2 causes the particles to converge on the local optimum too soon. The flight speed of the particles is also hard to select. To effectively control the flight speed of particles and achieve an effective balance between global search and local search, this algorithm introduces a compression factor. The convergence of the PSO algorithm can be guaranteed by selecting the appropriate parameters. Taking $c_1 = c_2 = 2.05$, $C = c_1 + c_2 = 4.1$. The specific expression of the compression factor is listed as follows:

$$\alpha = \frac{2}{\left|\left(2 - C - \sqrt{C^2 - 4C}\right)\right|} \quad (12)$$

In conclusion, the simultaneous introduction of adaptive inertia weights and compression factors can effectively improve the search capability and convergence accuracy of PSO, thus enhancing PSO performance.

Remark 2: In addition, an AFSA with an adaptive field of view and step size (Yuan and Yang, 2019) is designed in this paper. The algorithm can adaptively adjust the field of view and step length of the fish, which can enhance the global search ability in the early stage of the algorithm and accelerate the convergence speed in the late stage of the algorithm. The AFSA is a swarm intelligence stochastic optimization algorithm, in which the artificial fish self-renew by behavior such as prey, swarm, and follow, thus achieving the optimal search. However, the traditional AFSA involves the concept of the field of view in which the selection of viewpoints is random and the step length of movement is also random, which not only causes a lot of wasted computation time but also affects the search speed and accuracy. Given this, this paper presents the adaptive field of view factor γ, and step size adjustment factor m_1. Through γ, the algorithm can purposefully adjust the field of view each time. In the initial stage of the algorithm, a large field of view is given to the prey behavior, and the field of view is gradually reduced as the iteration of the algorithm proceeds. On the other hand, a too small field of view in the later stages of the algorithm may lead to a smaller probability of searching for the global optimal solution. Therefore, when the number of iterations of the algorithm exceeds half, the reduction of the field of view is stopped so that it remains half of the initial value (the lower limit of the parameter field of view value can be set according to the specific problem). The expression is shown below:

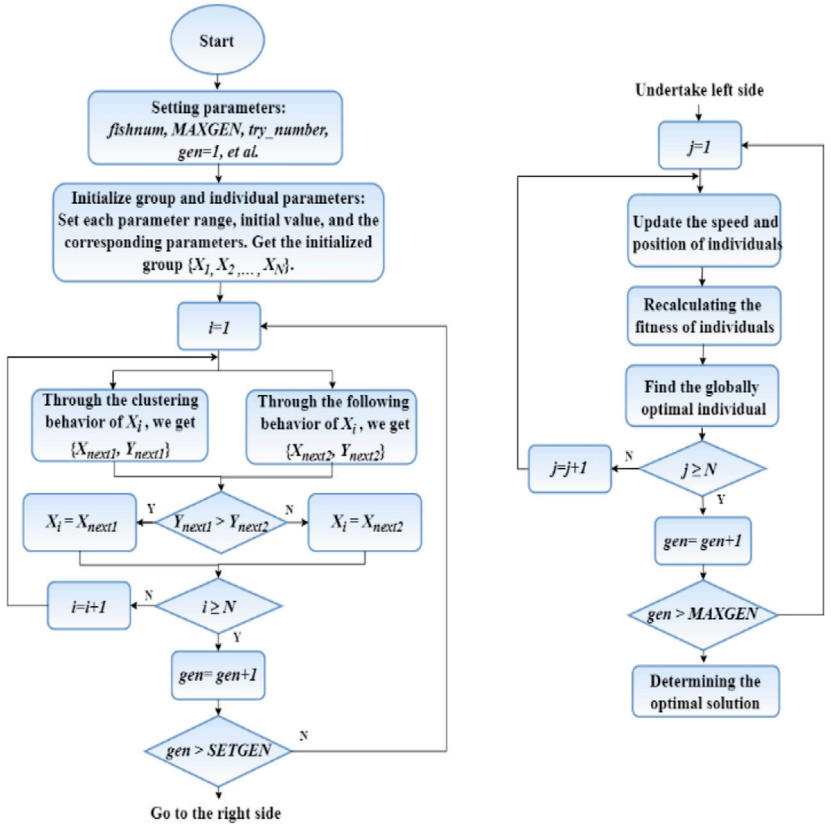

FIGURE 2
Flowchart of AFSA-PSO in optimizing event-triggered scheme.

$$\gamma_i^d = \begin{cases} \gamma_{\min} + (\gamma_{\max} - \gamma_{\min}) \dfrac{f(x_i^d) - f^d_{\min}}{f^d_{average} - f^d_{\min}}, f(x_i^d) \le f^d_{average} \\ \gamma_{\max}, f(x_i^d) > f^d_{average} \end{cases} \tag{13}$$

$$\begin{cases} vision_i^d = \gamma_i^d vision_0, d \le \dfrac{N}{2} \\ vision_i^d = \lambda vision_0, d > \dfrac{N}{2} \end{cases} \tag{14}$$

where, d is the current number of iterations of the algorithm, γ_i^d is the adaptive field of view factor, λ is the lower limit of the field of view factor, whose value is set according to the actual situation, N is the maximum number of iterations of the algorithm, $vision_0$ is the initially selected field of view value, and $vision_i^d$ is the field of view value obtained in this iteration.

The step size is similar to the selection of the field of view, which needs to be selected adaptively according to the fish population and concentration distribution. Therefore, as shown in (15), this paper introduces the step size adjustment factor, which enables the step size to be adjusted depending on the change in the field of view. Meanwhile, the step of redefining the step size is eliminated, and the algorithm becomes more concise.

$$step_i^d = m_1 vision_i^d \tag{15}$$

Remark 3: It is worth noting that AFSA has a strong global search capability, but the algorithm converges slowly at a later stage; PSO has a local fast convergence capability and can obtain a more accurate solution by adjusting the parameters, but it is easy to fall into a local optimum. Even though the two algorithms have been optimized separately, the above mentioned defects are still difficult to eliminate, which allows the introduction of hybrid optimization algorithms (Veerasamy et al., 2020). The algorithm proposed in this paper combines AFSA and PSO, which can combine the good characteristics of the two basic algorithms (Tsai and Lin, 2011). AFSA is applied in the early stage of the algorithm to expand the search range of individual best position and group best position, and PSO is utilized in the later stage of the algorithm to achieve a fine step-by-step search. It is proved that the algorithm can improve the convergence speed and solution accuracy to a certain extent.

Remark 4: Using disturbance attenuation level γ as the objective function, we obtain the optimal event-trigger threshold λ. The steps of the AFSA-PSO are shown below:

Step 1: Set parameters: such as fishnum(number of artificial fish),MAXGEN(maximum number of iterations), try_number(maximum number of tries), gen = 1(current number of iterations), etc.,; Initialize the population and individual parameters: set the range of each parameter, assign initial values to variables,

TABLE 2 Simulation parameters of the numerical example.

	T_p/s	T_T/s	T_G/s	T_{ES}/s
Area 1	10	0.3	0.1	0.038 2
Area 2	8	0.4	0.17	0.038 2
	K_p	R/(Hz/Mw)	K	β
Area 1	1	0.05	1	24
Area 2	0.667	0.05	1	24

form the population from the random array generated in the given range, set inertia weights, compression factors, control coefficients, etc.,;

Step 2: Start iteration, when the number of iterations is less than the preset value, the AFSA is used, otherwise the PSO is used;

Step 3: When the AFSA is used, the following operations are performed for each individual: set the adaptive field of view and step size, compare the fitness after performing following and swarming behaviors respectively, and keep the better fitness, then compare it with the individual optimum and population optimum, and update the fitness value;

Step 4: When the PSO is used, the following operations are performed for each individual: update the adaptive inertia weights, calculate the speed and position of the individual combined with the compression factor, recalculate the fitness value of the individual, find the global optimal individual, and update the optimal position of the individual and the group;

Step 5: Stop iteration when the maximum number of iterations is reached, and the obtained is the optimal solution.

Figure 2 can show the implementation of the code.

3 Stability analysis of multi-area LFC

In this section, an improved Lyapunov function and the B-L inequality are applied to study the stability criteria for the multi-area LFC with the improved event-triggered scheme (Lv et al., 2020).

Lemma 1: (Peng and Zhang, 2016): For a given positive matrix $R>0$, and differentiable function $\{\varphi(u)|u\in[a,b]\}$, the following inequality holds:

$$\int_a^b\int_\beta^b \dot{\varphi}^T(\alpha)R\dot{\varphi}(\alpha)\mathrm{d}\alpha\mathrm{d}\beta \geq 2\Omega_1^T R\Omega_1 + 4\Omega_2^T R\Omega_2 \tag{16}$$

$$\int_a^b\int_a^\beta \dot{\varphi}^T(\alpha)R\dot{\varphi}(\alpha)\mathrm{d}\alpha\mathrm{d}\beta \geq 2\Omega_3^T R\Omega_3 + 4\Omega_4^T R\Omega_4 \tag{17}$$

where:

$$\Omega_1 = \varphi(b) - \frac{1}{b-a}\int_a^b \varphi(\alpha)\mathrm{d}\alpha$$

$$\Omega_2 = \varphi(b) + \frac{2}{b-a}\int_a^b \varphi(\alpha)\mathrm{d}\alpha - \frac{6}{(b-a)^2}\int_a^b\int_\beta^b \varphi(\alpha)\mathrm{d}\alpha\mathrm{d}\beta$$

$$\Omega_3 = \varphi(a) - \frac{1}{b-a}\int_a^b \varphi(\alpha)\mathrm{d}\alpha$$

$$\Omega_4 = \varphi(a) - \frac{4}{b-a}\int_a^b \varphi(\alpha)\mathrm{d}\alpha + \frac{6}{(b-a)^2}\int_a^b\int_\beta^b \varphi(\alpha)\mathrm{d}\alpha\mathrm{d}\beta$$

The stability of the system (1) without disturbances will then be presented. The system (1) can be described as follows:

$$\dot{x}(t) = Ax(t) - BKCe(t) - BKCx(t-\tau(t)) \tag{18}$$

Theorem 1: For given positive d, τ_M, σ_m, the system (18) is asymptotically stable, if there exist positive definite matrices P, Q, R, S, Φ and appropriate dimensions X_1, X_2, X_3, X_4, such the following matrix inequalities hold:

$$\Pi_2 = \Pi_1 + \hat{H}_2\tilde{\varphi}_1\hat{H}_2^T + \varphi_3 + \varphi_4 + 2P\chi_1 + \chi_1\upsilon_2\chi_1^T < 0 \tag{19}$$

$$\tilde{\varphi}_1 = \begin{bmatrix} \varphi_1 & * \\ T_1 & \varphi_1 \end{bmatrix} > 0 \tag{20}$$

where:

$$\Pi_1 = e_1\upsilon_{1r}e_1^T - e_2\Phi e_2^T - e_3Q_2e_3^T - e_4\upsilon_3e_4^T$$

$$\upsilon_{1r} = Q_2 + \tau_M R_2,\ \upsilon_{2r} = d_M^2R_1 + \frac{d_M^2}{2}S_1 + \frac{d_M^2}{2}S_2$$

$$\upsilon_3 = (1-\dot{\tau}(t))Q_3 - \lambda(t_k h)\Phi$$

$$\tilde{\varphi}_2 = \begin{bmatrix} \varphi_{1r}+\tilde{S}_1 & * \\ T_1 & \varphi_{1r}+\tilde{S}_2 \end{bmatrix} > 0, \tilde{\varphi}_1 = \begin{bmatrix} \varphi_1 & * \\ T_1 & \varphi_1 \end{bmatrix},$$

$$H_1 = [e_1 - e_4 | e_1 + e_4 - 2e_5 e_1 - e_4 - 6e_6]$$

$$H_2 = [e_4 - e_3 | e_3 + e_4 - 2e_7 e_4 - e_3 - 6e_8], \hat{H}_2 = [H_1 H_2],$$

$$\varphi_1 = diag\{R_1, 3R_1, 5R_1\}, \tilde{S}_1 = diag\{S_1, 3S_1, 5S_1\}$$

$$\tilde{S}_2 = diag\{S_2, 3S_2, 5S_2\}, T_1 = \begin{bmatrix} T_{11} & T_{12} & T_{13} \\ T_{21} & T_{22} & T_{23} \\ T_{31} & T_{32} & T_{33} \end{bmatrix}$$

$$H_3 = \begin{bmatrix} e_1 - e_5 & e_1 - e_5 - 3e_6 & e_4 - e_7 & e_4 - e_7 - 3e_8 \end{bmatrix}$$

$$\varphi_3 = diag\{-2S_1, -4S_1, -2S_1, -4S_1\}$$

$$H_4 = \begin{bmatrix} e_5 - e_4 & e_4 - e_5 + 3e_6 & e_7 - e_3 & e_3 - e_7 + 3e_8 \end{bmatrix}$$

$$\varphi_4 = diag\{2S_2, 4S_2, 2S_2, 4S_2\}$$

$$\chi_1 = Ae_1 + BKCe_2 + BKCe_4$$

Proof: Defining the Lyapunov function as:

$$V(t) = V_1(t) + V_2(t) + V_3(t) + V_4(t)$$

$$V_1(t) = x^T(t)Px(t)$$

$$V_2(t) = \int_{t-\tau_M}^t x^T(s)Q_2x(s)ds + \int_{t-d(t)}^t x^T(s)Q_3x(s)ds$$

$$V_3(t) = d_M\int_{-d_M}^0\int_{t+\alpha}^t \dot{x}^T(s)R_1\dot{x}(s)ds\mathrm{d}\alpha + \int_{-d_M}^0\int_{t+\alpha}^t x^T(s)R_2x(s)ds\mathrm{d}\alpha$$

$$V_4(t) = \int_{-d_M}^0\int_\beta^0\int_{t+\alpha}^t \dot{x}^T(s)S_1\dot{x}(s)ds\mathrm{d}\alpha\mathrm{d}\beta + \int_{-d_M}^0\int_{-d_M}^\beta\int_{t+\alpha}^t \dot{x}^T(s)S_2\dot{x}(s)ds\mathrm{d}\alpha\mathrm{d}\beta$$

where: $P>0$, $Q>0$, $R>0$, $S>0$ are positive-definite matrices.

Calculating the derivate along the trajectory (18) yields the following inequality:

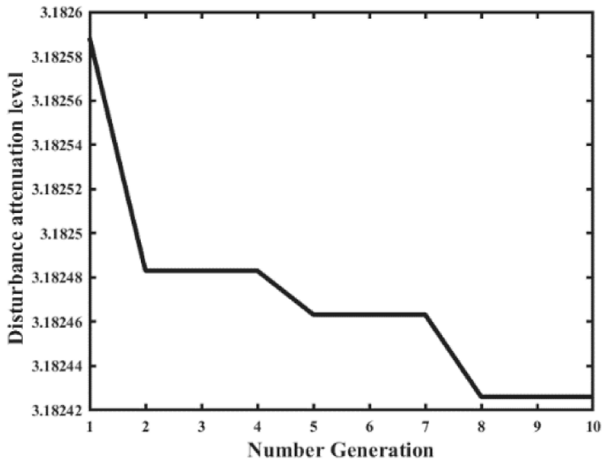

FIGURE 3
Optimizing algorithm performance.

$$\Delta V(t) = \Delta V(t)_1 + \Delta V(t)_2 + \Delta V(t)_3 + \Delta V(t)_4 \tag{21}$$

where:

$$\Delta V_1(t) = 2\dot{x}^T(t)Px(t)$$

$$\Delta V_2(t) = x^T(t)Q_2x(t) - x^T(t-d_M)Q_2x(t-d_M) + x^T(t)Q_3x(t) - \left(1-\dot{d}(t)\right)x^T(t-d(t))Q_3x(t-d(t))$$

$$\Delta V_3(t) = d_M^2\dot{x}^T(t)R_1\dot{x}(t) - d_M\int_{t-d_M}^{t}\dot{x}^T(\alpha)R_1\dot{x}(\alpha)d\alpha + d_Mx^T(t)R_2x(t) - \int_{t-d(t)}^{t}x^T(\alpha)R_2x(\alpha)d\alpha$$

$$\Delta V_4(t) = \frac{d_M^2}{2}\dot{x}^T(t)S_1\dot{x}(t) - \int_{-d(t)}^{0}\int_{t+\alpha}^{t}\dot{x}^T(s)S_1\dot{x}(s)dsd\alpha - \int_{-d_M}^{-d(t)}\int_{t+\alpha}^{t-d(t)}\dot{x}^T(s)S_1\dot{x}(s)dsd\alpha - (d_M-d(t))\int_{t-d(t)}^{t}\dot{x}^T(\alpha)S_1\dot{x}(\alpha)d\alpha + \frac{d_M^2}{2}\dot{x}^T(t)S_2\dot{x}(t) - \int_{-d(t)}^{0}\int_{t-d(t)}^{t+\alpha}\dot{x}^T(s)S_2\dot{x}(s)dsd\alpha - \int_{-d_M}^{-d(t)}\int_{t-d_M}^{t+\alpha}\dot{x}^T(s)S_2\dot{x}(s)dsd\alpha - d(t)\int_{t-d_M}^{t-d(t)}\dot{x}^T(s)S_2\dot{x}(s)ds$$

Defining the following augmenting state variable:

$$\xi(t) = [x(t) \quad e(t) \quad x(t-d_M) \quad x(t-d(t)) \quad \frac{1}{d(t)}\int_{-d(t)}^{0}x(t+\alpha)d\alpha \quad \frac{1}{d(t)}\int_{-d(t)}^{0}\lambda_{-\tau(t)}(\alpha)x(t+\alpha)d\alpha \quad \frac{1}{d_M-d(t)}\int_{-d_M}^{-d(t)}x(t+\alpha)d\alpha \quad \frac{1}{d_M-d(t)}\int_{-d_M}^{-d(t)}\lambda_{-\tau(t)}(\alpha)x(t+\alpha)d\alpha]$$

Thus, the next inequality can be obtained:

$$\Delta V(t) \le \xi(t)\Pi_1\xi^T(t) + 2\dot{x}(t)Px^T(t) + \dot{x}(t)v_2\dot{x}^T(t) + \Delta\tilde{V}_1(t) + \Delta\tilde{V}_2(t) + \Delta\tilde{V}_3(t)$$

where:

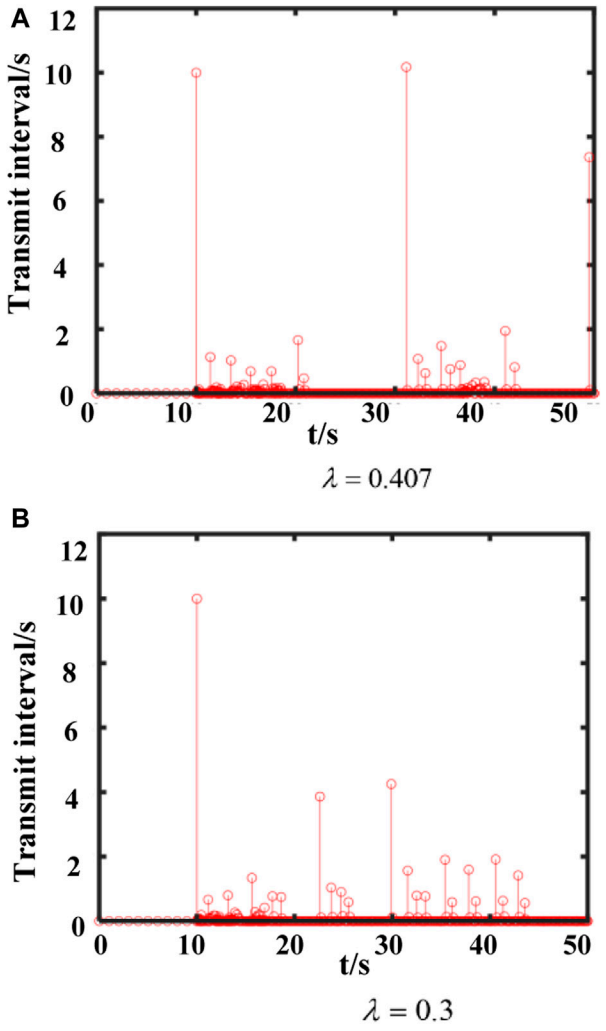

FIGURE 4
Release instant and release intervals.

$$\Delta\tilde{V}_1(t) = -d_M\int_{t-d_M}^{t}\dot{x}(s)R_1\dot{x}^T(s)ds - \left(d_M-\dot{d}(t)\right)\int_{t-d(t)}^{t}\dot{x}(s)S_1\dot{x}^T(s)ds - \dot{d}(t)\int_{t-d_M}^{t-d(t)}\dot{x}(s)S_2\dot{x}^T(s)ds$$

$$\Delta\tilde{V}_2(t) = -\int_{-d(t)}^{0}\int_{t+\alpha}^{t}\dot{x}(s)S_1\dot{x}^T(s)dsd\alpha - \int_{-d_M}^{-d(t)}\int_{t+\alpha}^{t-d(t)}\dot{x}(s)S_1\dot{x}^T(s)dsd\alpha$$

$$\Delta\tilde{V}_3(t) = -\int_{-d(t)}^{0}\int_{t-d(t)}^{t+\alpha}\dot{x}(s)S_2\dot{x}^T(s)dsd\alpha - \int_{-d_M}^{-d(t)}\int_{t-d_M}^{t+\alpha}\dot{x}^T(s)S_2\dot{x}(s)dsd\alpha$$

Applying the B-L inequality, $\Delta\tilde{V}_1(t)$ can be rewritten as:

$$\Delta\tilde{V}_1(t) \le -\frac{1}{\iota}\xi(t)H_1\left(\varphi_1+\tilde{S}_1\right)H_1^T\xi^T(t) - \frac{1}{\kappa}\xi(t)H_2\left(\varphi_1+\tilde{S}_2\right)H_2^T\xi^T(t) + \xi(t)H_1\tilde{S}_1H_1^T\xi^T(t) + \xi(t)H_2\tilde{S}_2H_2^T\xi^T(t) \le -\xi(t)\hat{H}_2\tilde{\varphi}_1\hat{H}_2{}^T\xi^T(t)$$

Applying Lemma 1, we obtain:

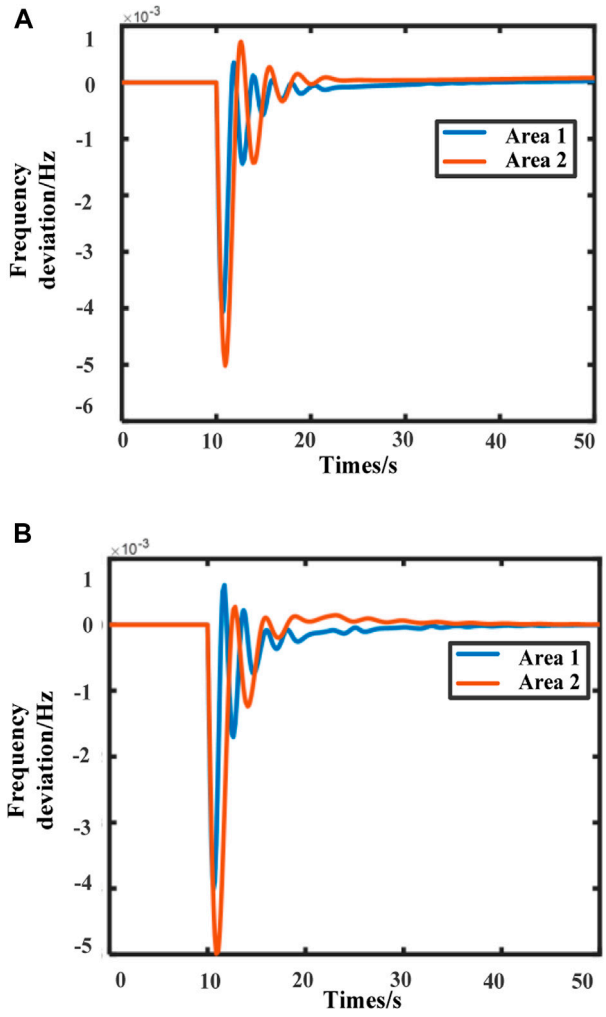

FIGURE 5
Frequency deviations of LFC power system.

$$\Delta\tilde{V}_2(t) \le H_3\varphi_{3r}H_3^T$$
$$\Delta\tilde{V}_3(t) \le -H_4\varphi_4H_4^T$$

Therefore, if $\tilde{\varphi}_2 = \begin{bmatrix} \varphi_1 + \tilde{S}_1 & * \\ T_1 & \varphi_1 + \tilde{S}_2 \end{bmatrix} > 0$ can be satisfied, the following result can be obtained:

$$\begin{aligned}\Delta V(t) &\le \xi(t)\Pi_1\xi^T(t) + 2\dot{x}(t)Px^T(t) + \dot{x}(t)\upsilon_2\dot{x}^T(t) \\ &+\Delta\tilde{V}_1(t) + \Delta\tilde{V}_2(t) + \Delta\tilde{V}_3(t) \\ &\le \xi(t)\Pi_2\xi^T(t)\end{aligned}$$

LMI (17) can be verified if $\Pi_2 < 0$ is satisfied and Lemma 1 is applied. Considering a sufficiently small scalar $c \in (0, 1]$, it is possible to verify that $\Delta V(t) < \xi(t)\Pi_2\xi^T(t) < -c\|\xi(t)\|^2 < 0$. Therefore, according to Theorem 1, the system (18) is stochastically stable. Theorem 1 provides the criterion of asymptotic stability. Next, the H_∞ stability criterion for the system (18) will be designed.

Theorem 2: For given positive constant γ, d, τ_M and σ_m, if there exist positive definite matrices P, Q, R, S, W, Φ and appropriate dimensions X_1, X_2, X_3, X_4, such the following matrix inequalities hold, the system (18) is asymptotically stable with H_∞ prescribed attenuation level γ.

$$\begin{aligned}\Pi_2' = \Pi_1 + \hat{H}_2\tilde{\varphi}_1\hat{H}_2^T + \varphi_3 + \varphi_4 + 2P\chi_1' + \chi_1'\upsilon_2\chi_1'^T \\ -\gamma^2 e_{10}^T e_{10} + e_1^T C^T C e_1 < 0\end{aligned} \tag{22}$$

where:

$$\chi_1' = Ae_1 + BKCe_2 + BKCe_4 + Fe_9$$
$$e_j = \left[\underset{j-1}{0\ldots0}, 1, \underset{9-j}{0\ldots0}\right], \ (j = 1, \ldots, 9)$$

Proof: The proof of this theorem is based on Theorem 1. For the prescribed attenuation level $\gamma > 0$, the cost function J can be defined as:

$$J = \int_0^\infty y^T(t)y(t) - \gamma^2\omega^T(t)\omega(t)\mathrm{d}t \tag{23}$$

For $\omega(t) \in l_2[0, \infty]$, and $t > 0$, the next inequality we have:

$$J \le \int_0^\infty y^T(t)y(t) - \gamma^2\omega^T(t)\omega(t) + \Delta V(t)\mathrm{d}t \tag{24}$$

Considering the improved event-triggered scheme, if the following inequality hold, $J < 0$ can be satisfied,

$$\begin{aligned}&y^T(t)y(t) - \gamma^2\omega^T(t)\omega(t) + \Delta V(t) \\ &-e^T(t)\Phi e(t) + \lambda x^T(t - \tau(t))\Phi x(t - \tau(t)) < 0\end{aligned} \tag{25}$$

Defining the augmenting state variable:

$$\xi'(t) = [\,\xi(t) \ \ \omega(t)\,]$$

For

$$\begin{aligned}\Omega^1 = &y^T(t)y(t) - \gamma^2\omega^T(t)\omega(t) + \Delta V(t) \\ &-e^T(t)\Phi e(t) + \lambda x^T(t - \tau(t))\Phi x(t - \tau(t))\end{aligned}$$

it yields:

$$\Omega^1 = \xi^T(t)\Pi_2'\xi'(t) \tag{26}$$

Thus, Theorem 2 is proved. The stability with H_∞ prescribed attenuation level γ of the system (18) is obtained.

From the above discussion, it is clear that to maintain a better stable performance and obtain a better event-triggered scheme, the attenuation level γ is necessary to minimize. By optimizing with AFSA-PSO, we can get the desired event-triggered threshold.

4 Case studies and discussion

In this section, two simulation examples are carried out to verify the performance of the proposed event-triggered LFC based on an improved AFSA-PSO. In this section, the two-area LFC system model as well as the IEEE-39 node system model are built using Simulink. Among them, the parameters of the two-area system model are shown in Table 2.

4.1 Two-area LFC system simulation experiment

Since the thresholds of different event-triggered schemes in LFC systems can have an impact on the system's performance. Therefore, this simulation experiment uses the hybrid AFSA-PSO to optimize the event-triggered scheme threshold with the system performance as the optimization objective. The process between the number of algorithm iterations and the optimized performance is shown in

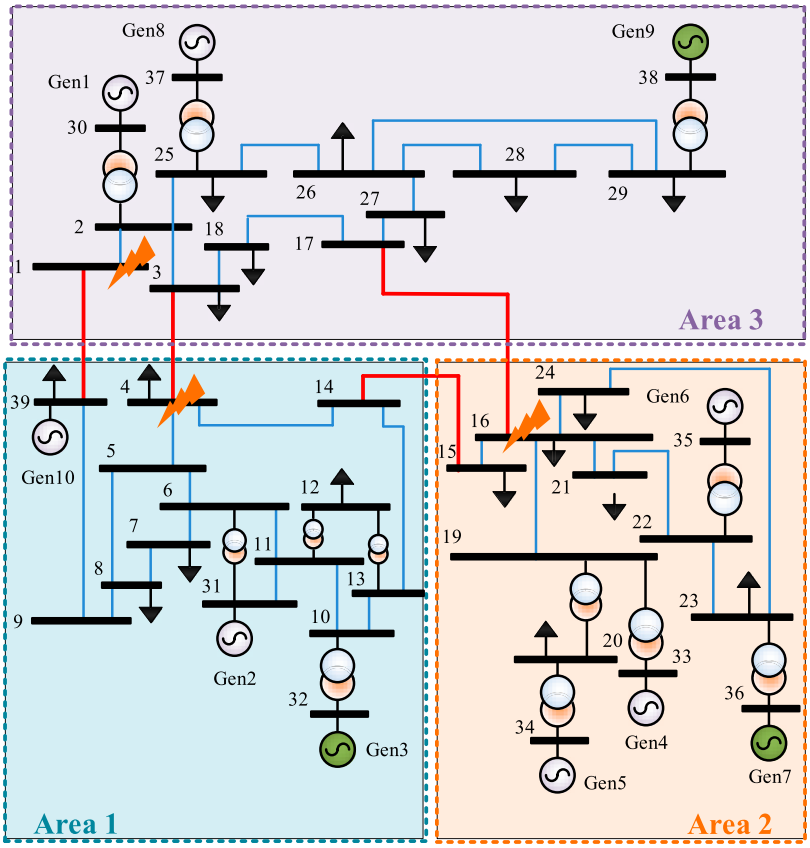

FIGURE 6
IEEE-39 bus test system.

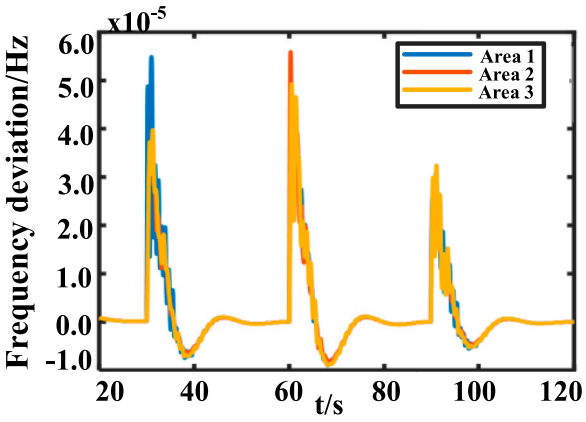

FIGURE 7
Frequency deviations of IEEE-39 bus test system.

Figure 3. Meanwhile, this experiment takes the two-area LFC system as the object and adds $\Delta P_d = 2Hz$ perturbations to Area 1 and Area 2 respectively when the system runs to 10s, to verify the LFC performance under the designed event-triggered scheme.

Based on the data presented in Figure 3, it is evident that the system's target value converges to a constant value of 3.18243 after eight iterations of the algorithm. Consequently, selecting the trigger threshold λ as 0.407 results in the minimization of the optimal attenuation level γ to 3.18243. Figure 4A displays the data release time and the interval of the two-area LFC system under the optimal attenuation level $\gamma = 3.18243$ and the triggered threshold $\lambda = 0.407$.

To assess the performance of the proposed event-triggered scheme, Figure 4B presents the release time and interval of data for the LFC system in two areas with the trigger threshold $\lambda = 0.3$. The figure indicates that the system functions normally and releases a relatively small amount of data between 0 and 10 s. However, when the system experiences disturbances, its performance is adversely affected, leading to the release of a significant amount of data. From the comparison of Figure 4A and Figure 4B, it can be seen that when the threshold value of the event-triggered scheme is 0.407, the amount of data released is less, which reduces the system performance loss as well as increases the network resource utilization.

To verify the performance of the LFC under the designed event-triggered scheme, the frequency deviation response plots of the system under the two event-triggered schemes are given separately, as shown in Figure 5. Figures 5A, B show the system frequency deviation Δf response curves when the system suffers a load deviation perturbation at $\lambda = 0.407$ as well as $\lambda = 0.3$, respectively. As can be seen from Figure 5, the Δf response can converge to zero in a short period when the system suffers a load

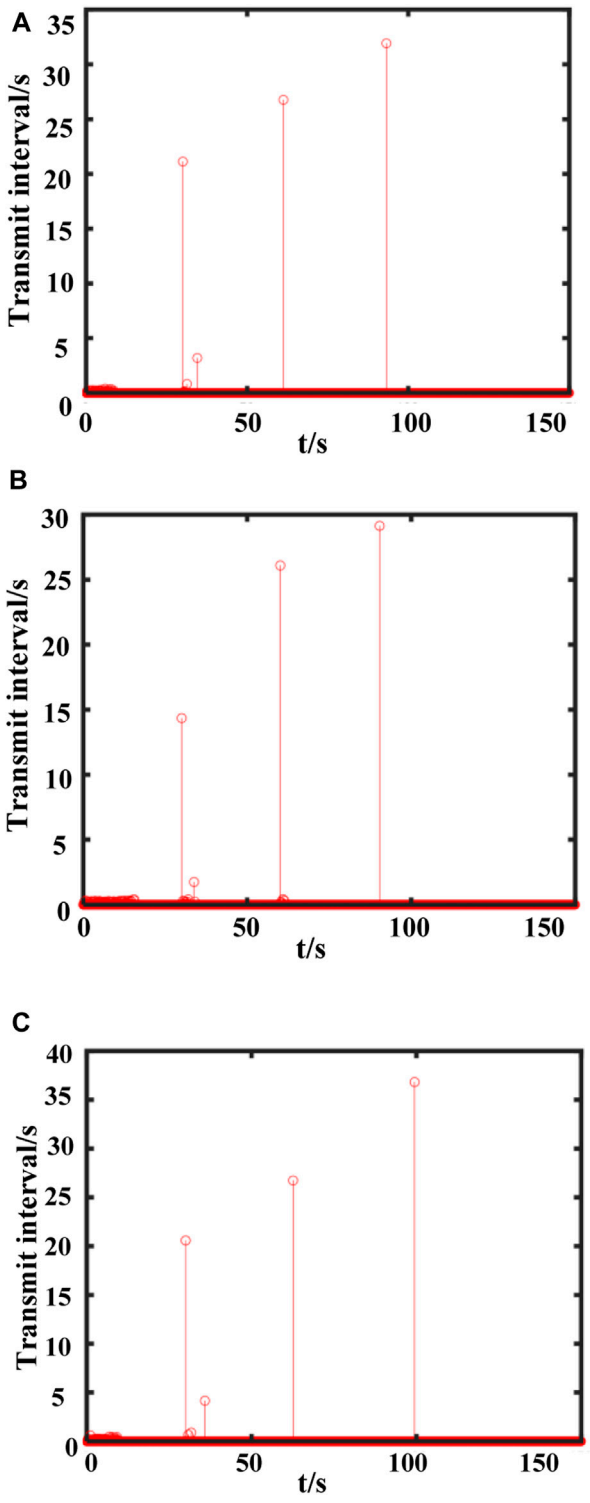

FIGURE 8
Release instant and release intervals of IEEE-39 bus test system.

disturbance at 10s. In addition, when $\lambda = 0.407$, the Δf response has a small overshoot and a short stabilization time. Therefore, the hybrid AFSA-PSO based event-triggered scheme designed in this paper has a better performance in reducing the amount of redundant information transmission. At the same time, the LFC system has better robustness to external disturbances under this event-triggered scheme.

4.2 IEEE-39 node system

In this simulation experiment, an IEEE-39 node model is built using MATLAB/Simulink. The model contains 10 diesel generators along with 19 loads and 34 transmission lines (Shangguan et al., 2022). Also, to verify the performance of the proposed LFC based on the improved event-triggered scheme, the system is divided into three control areas, with Gen3 as the selected generator in Area 1, Gen7 as the selected generator in Area 2, and Gen9 as the selected generator in Area 3. Figure 6 shows the schematic diagram of the IEEE-39 bus test system and the division of the control area.

At $t = 30s$, a 0.038p.u. Perturbation is added to node 8; at $t = 60s$, a 0.064p.u. Perturbation is added to node 16; at $t = 90s$, a 0.038p.u. Perturbation is added to node 3. At this time, the Δf response in the three areas and the trigger interval and trigger time in the event-triggered scheme are shown in Figure 7 as well as Figure 8.

From Figure 7 and Figure 8, it can be seen that the frequency deviation Δf in the three areas converges to a steady state within a short period when load perturbations are added to the three areas at $t = 30s$, $t = 60s$ and $t = 90s$, respectively. Figures 8A–C show the release instant and release intervals of the three areas, respectively. Meanwhile, at the moment of the perturbation, the system performance needs a large amount of data for improvement, and it can be seen from Figure 7 that the event-triggered scheme transmits a large amount of data at this time. And, as can be seen from Figure 8, the overshoot of the Δf response in the three areas is different at the three different moments of perturbation. At the moment of different disturbances, the generators responsible in the three areas respond to the load disturbance, and at the same time, the control errors between the areas deviate due to the interconnection between the areas, and the generating units in the remaining areas respond to the deviation of the exchange power between the areas. Therefore, the LFC with an improved event-triggered scheme designed in this paper has superior performance in the IEEE-39 node system.

5 Conclusion

To save network communication resources and reduce the information transmission frequency of multi-area power systems, this paper proposes an improved event-triggered scheme based on a hybrid AFSA-PSO and investigates LFC based on this scheme. In this paper, an LFC model with wind power and battery storage is established based on Markov theory. Based on this model, the stability of this system is studied by an improved Lyapunov function. Moreover, the conservatism of the resulting stability criterion is reduced by utilizing the double B-L inequality in the inequality scaling process. Compared with the traditional event-triggered scheme, the hybrid AFSA-PSO can optimize the threshold value rapidly and efficiently. The algorithm adopts the improved AFSA in the first stage and applies the improved PSO in the later stage, which can take into account the global and

local aspects of the search so that the algorithm has high solution accuracy and convergence speed. High performance event-triggered schemes obtained by optimizing event-triggered thresholds enable better frequency control while transmitting less information. In conclusion, this paper verifies the effectiveness of the improved event-triggered scheme in the two-area LFC system model as well as the IEEE-39 node system model.

Data availability statement

The original contributions presented in the study are included in the article/supplementary material, further inquiries can be directed to the corresponding author.

Author contributions

TH contributed to the conception of the study. The corresponding author XL is responsible for ensuring that the descriptions are accurate and agreed upon by all authors. All authors contributed to the article and approved the submitted version.

Conflict of interest

The authors declare that the research was conducted in the absence of any commercial or financial relationships that could be construed as a potential conflict of interest.

Publisher's note

All claims expressed in this article are solely those of the authors and do not necessarily represent those of their affiliated organizations, or those of the publisher, the editors and the reviewers. Any product that may be evaluated in this article, or claim that may be made by its manufacturer, is not guaranteed or endorsed by the publisher.

References

Aluko, A. O., (2021). Robust State Estimation Method for Adaptive Load Frequency Control of Interconnected Power System in a Restructured Environment. *IEEE Syst. J.* 15 (4), 5046–5056. doi:10.1109/jsyst.2020.3005979

Belaid, S., (2022). Proposed Hybrid Power Optimization for Wind Turbine/Battery System. *Periodica Polytech. Electr. Eng. Comput. Sci.* 66 (1), 60–71. doi:10.3311/ppee.18758

Bu, X., (2022). Event-Triggered Data-Driven Load Frequency Control for Multiarea Power Systems. *IEEE Trans. Ind. Inf.* 18 (9), 5982–5991. doi:10.1109/tii.2021.3130415

Chen, P., (2022). Dynamic Event-Triggered Output Feedback Control for Load Frequency Control in Power Systems With Multiple Cyber Attacks. *IEEE Trans. Syst. Man. Cybern. Syst.* 52 (10), 6246–6258. doi:10.1109/tsmc.2022.3143903

Choi, J. W., Heo, S. Y., and Kim, M. K. (2016). Hybrid Operation Strategy of Wind Energy Storage System for Power Grid Frequency Regulation. *IET Gener. Transm. Distrib.* 10 (3), 736–749. doi:10.1049/iet-gtd.2015.0149

Dashtdar, M., (2022). Improving the Power Quality of Island Microgrid With Voltage and Frequency Control Based on a Hybrid Genetic Algorithm and PSO. *IEEE Access* 10, 105352–105365. doi:10.1109/access.2022.3201819

Gholamrezaie, V., (2018). An Optimal Frequency Control Method Through a Dynamic Load Frequency Control (LFC) Model Incorporating Wind Farm. *IEEE Syst. J.* 12 (1), 392–401. doi:10.1109/jsyst.2016.2563979

Hossain, M. M., (2022). Bandwidth Allocation-Based Distributed Event-Triggered LFC for Smart Grids Under Hybrid Attacks. *IEEE Trans. Smart Grid* 13 (1), 820–830. doi:10.1109/tsg.2021.3118801

Li, M., (2019a). An Improved Particle Swarm Optimization Algorithm With Adaptive Inertia Weights. *Int. J. Inf. Technol. Decis. Mak.* 18 (03), 833–866. doi:10.1142/s0219622019500147

Li, Y., (2019b). Event-Triggered-Based Distributed Cooperative Energy Management for Multienergy Systems. *IEEE Trans. Ind. Inf.* 15 (4), 2008–2022. doi:10.1109/tii.2018.2862436

Lin, L., (2020). Deep Reinforcement Learning for Economic Dispatch of Virtual Power Plant in Internet of Energy. *IEEE Internet Things* 7 (7), 6288–6301. doi:10.1109/jiot.2020.2966232

Liu, Y., (2021). Automatic Generation Control for Distributed Multi-Region Interconnected Power System With Function Approximation. *Front. Energy Res.* 9. doi:10.3389/fenrg.2021.700069

Lv, X., (2020). Event-Triggered Load Frequency Control for Multi-area Power Systems Based on Markov Model: A Global Sliding Mode Control Approach. *IET Gener. Transm. Distrib.* 14 (21), 4878–4887. doi:10.1049/iet-gtd.2020.0186

Mi, Y., (2017). Sliding Mode Load Frequency Control for Multi-area Time-delay Power System With Wind Power Integration. *IET Gener. Transm. Distrib.* 11 (18), 4644–4653. doi:10.1049/iet-gtd.2017.0600

Oubelaid, A., (2022a). Fuzzy-Energy-management-based Intelligent Direct Torque Control for A Battery—Supercapacitor Electric Vehicle. *Sustainability* 14 (14), 8407. doi:10.3390/su14148407

Oubelaid, A., (2022b). Secure Power Management Strategy for Direct Torque Controlled Fuel Cell/Supercapacitor Electric Vehicles. *Front. Energy Res.* 10. doi:10.3389/fenrg.2022.971357

Oubelaid, A., Taib, N., and Rekioua, T. (2022c). Novel Coordinated Power Sources Switching Strategy for Transient Performance Enhancement of Hybrid Electric Vehicles. *COMPEL - Int. J. Comput. Math. Electr. Electron. Eng.* 41 (5), 1880–1919. doi:10.1108/compel-10-2021-0399

Peng, C., and Zhang, J. (2016). Delay-Distribution-Dependent Load Frequency Control of Power Systems With Probabilistic Interval Delays. *IEEE Trans. Power Syst.* 31 (4), 3309–3317. doi:10.1109/tpwrs.2015.2485272

Peng, C., Zhang, J., and Yan, H. (2018). Adaptive Event-Triggering ${H}_{\infty }$ Load Frequency Control for Network-Based Power SystemsH∞Load Frequency Control for Network-Based Power Systems. *IEEE Trans. Ind. Electron* 65 (2), 1685–1694. doi:10.1109/tie.2017.2726965

Pulazza, G., (2021). Transmission Planning With Battery-Based Energy Storage Transportation For Power Systems With High Penetration of Renewable Energy. *IEEE Trans. Power Syst.* 36 (6), 4928–4940. doi:10.1109/tpwrs.2021.3069649

Shangguan, X.-C., (2022). Control Performance Standards-Oriented Event-Triggered Load Frequency Control for Power Systems Under Limited Communication Bandwidth. *IEEE Trans. Control Syst. Technol.* 30 (2), 860–868. doi:10.1109/tcst.2021.3070861

Sun, Y., (2023). Stability Analysis of Load Frequency Control for Power Systems With Interval Time-varying Delays. *Front. Energy Res.* 10. doi:10.3389/fenrg.2022.1008860

Tang, J., Liu, G., and Pan, Q. (2021). A Review on Representative Swarm Intelligence Algorithms for Solving Optimization Problems: Applications and Trends. *IEEE/CAA J. Autom. Sinica* 8 (10), 1627–1643. doi:10.1109/jas.2021.1004129

Tsai, H.-C., and Lin, Y.-H. (2011). Modification of the Fish Swarm Algorithm With Particle Swarm Optimization Formulation and Communication Behavior. *Appl. Soft Comput.* 11 (8), 5367–5374. doi:10.1016/j.asoc.2011.05.022

Veerasamy, V., (2020). A Hankel Matrix Based Reduced Order Model for Stability Analysis of Hybrid Power System Using PSO-GSA Optimized Cascade PI-PD Controller for Automatic Load Frequency Control. *IEEE Access* 8, 71422–71446. doi:10.1109/access.2020.2987387

Wang, X., (2022). A Data-Driven Uncertainty Quantification Method for Stochastic Economic Dispatch. *IEEE Trans. Power Syst.* 37 (1), 812–815. doi:10.1109/tpwrs.2021.3114083

Wen, S., (2016). Event-Triggering Load Frequency Control for Multiarea Power Systems With Communication Delays. *IEEE Trans. Ind. Electron.* 63 (2), 1308–1317. doi:10.1109/tie.2015.2399394

Wu, Z.-G., (2018). Event-Triggered Control for Consensus Problem in Multi-Agent Systems With Quantized Relative State Measurements and External

Disturbance. *IEEE Trans. Circuits Syst. I Regul. Pap.* 65 (7), 2232–2242. doi:10.1109/tcsi.2017.2777504

Wu, Z., (2020). Adaptive Event-Triggered Observer-Based Output Feedback $\mathcal L_{\infty }$ Load Frequency Control for Networked Power SystemsL∞Load Frequency Control for Networked Power Systems. *IEEE Trans. Ind. Inf.* 16 (6), 3952–3962. doi:10.1109/tii.2019.2942637

Yan, C.-H., (2022). Stabilization of Load Frequency Control System via Event-Triggered Intermittent Control. *IEEE Trans. Circuits Syst. II Express Briefs* 69 (12), 4934–4938. doi:10.1109/tcsii.2022.3197460

Yang, D., (2020). Inertia - Adaptive Model Predictive Control-based Load Frequency Control for Interconnected Power Systems With Wind Power. *IET Gener. Transm. Distrib.* 14 (22), 5029–5036. doi:10.1049/iet-gtd.2020.0018

Yang, L., (2022). Indirect Multi-Energy Transactions of Energy Internet with Deep Reinforcement Learning Approach. *IEEE Trans. Power Syst.* 37 (5), 4067–4077. doi:10.1109/tpwrs.2022.3142969

Yuan, G., and Yang, W. (2019). Study on Optimization of Economic Dispatching of Electric Power System Based on Hybrid Intelligent Algorithms (PSO and AFSA). *Energy* 183, 926–935. doi:10.1016/j.energy.2019.07.008

Yuan, Z.-L., (2021). Delay-dependent Stability Analysis of Load Frequency Control for Power System With EV Aggregator. *Front. Energy Res.* 9. doi:10.3389/fenrg.2021.771465

Yue, D., Tian, E., and Han, Q.-L. (2013). A Delay System Method for Designing Event-Triggered Controllers of Networked Control Systems. *IEEE Trans. Autom. Contr.* 58 (2), 475–481. doi:10.1109/tac.2012.2206694

Zhang, H., Liu, J., and Xu, S. (2020). H-Infinity Load Frequency Control of Networked Power Systems via an Event-Triggered Scheme. *IEEE Trans. Ind. Electron.* 67 (8), 7104–7113. doi:10.1109/tie.2019.2939994

Zhao, X., (2022). Robust LFC of Power Systems With Wind Power Under Packet Losses and Communication Delays. *IEEE J. Emerg. Sel. Top. Power Electron.* 12 (1), 135–148. doi:10.1109/jetcas.2022.3141108

Zhou, Z., (2019). Application of Kriging Algorithm based on ACFPSO In Geomagnetic Data Interpolation. *Math. Probl. Eng.* 2019, 1–14. doi:10.1155/2019/1574918

Zhu, Y., and Gao, H. (2020). Improved Binary Artificial Fish Swarm Algorithm and Fast Constraint Processing for Large Scale Unit Commitment. *IEEE Access* 8, 152081–152092. doi:10.1109/access.2020.3015585

frontiers | Frontiers in Energy Research

TYPE Original Research
PUBLISHED 01 September 2023
DOI 10.3389/fenrg.2023.1208296

OPEN ACCESS

EDITED BY
George Tsekouras,
University of West Attica, Greece

REVIEWED BY
Vassiliki T. Kontargyri,
National Technical University of Athens, Greece
Omar Abdel-Rahim,
Aswan University, Egypt

*CORRESPONDENCE
Adel El-Shahat,
asayedah@purdue.edu

RECEIVED 18 April 2023
ACCEPTED 11 August 2023
PUBLISHED 01 September 2023

CITATION
Esmail EM, Alsaif F, Abdel Aleem SHE, Abdelaziz AY, Yadav A and El-Shahat A (2023), Simultaneous series and shunt earth fault detection and classification using the Clarke transform for power transmission systems under different fault scenarios.
Front. Energy Res. 11:1208296.
doi: 10.3389/fenrg.2023.1208296

Simultaneous series and shunt earth fault detection and classification using the Clarke transform for power transmission systems under different fault scenarios

Ehab M. Esmail[1], Faisal Alsaif[2], Shady H. E. Abdel Aleem[3], Almoataz Y. Abdelaziz[4], Anamika Yadav[5] and Adel El-Shahat[6]*

[1]Department of Electrical Engineering, Valley High Institute of Engineering and Technology, Science Valley Academy, Qalyubia, Egypt, [2]Department of Electrical Engineering, College of Engineering, King Saud University, Riyadh, Saudi Arabia, [3]Department of Electrical Engineering, Institute of Aviation Engineering and Technology, Giza, Egypt, [4]Faculty of Engineering & Technology, Future University in Egypt, Cairo, Egypt, [5]Department of Electrical Engineering, National Institute of Technology, Raipur, India, [6]Energy Technology Program, School of Engineering Technology, Purdue University, West Lafayette, IN, United States

For high-voltage (symmetric and non-symmetric) transmission networks, detecting simultaneous faults utilizing a single-end-based scheme is complex. In this regard, this paper suggests novel schemes for detecting simultaneous faults. The proposed schemes comprise two different stages: fault detection and identification and fault classification. The first proposed scheme needs communication links among both ends (sending and receiving) to detect and identify the fault. This communication link between both ends is used to send and receive three-phase current magnitudes for sending and receiving ends in the proposed fault detection (PFD) unit at both ends. The second proposed scheme starts with proposed fault classification (PFC) units at both ends. The proposed classification technique applies the Clarke transform on local current signals to classify the open conductor and simultaneous faults. The sign of all current Clarke components is the primary key for distinguishing between all types of simultaneous low-impedance and high-impedance faults. The fault detection time of the proposed schemes reaches 20 ms. The alternative transient program (ATP) package simulates a 500 kV–150-mile transmission line. The simulation studies are carried out to assess the suggested fault detection and identification and fault classification scheme performance under various OCFs and simultaneous earth faults in un-transposed and transposed TLs. The behavior of the proposed schemes is tested and validated by considering different fault scenarios with varying locations of fault, inception angles, fault resistance, and noise. A comparative study of the proposed schemes and other techniques is

Abbreviations: ATP/EMTP, alternative transient program/electromagnetic transient program; ATP, alternative transient program; TLs, transmission lines; OC, open conductor; OCFs, open conductor faults; OCRE/EFSE, OCFs at the receiving end followed by earth fault in the sending end; OCSE/EFRE, OC at the sending end followed by earth fault in the receiving end; LIFs, low-impedance faults; HIFs, high-impedance faults; DFT, discrete Fourier transform; PFD, proposed fault detection; PFC, proposed fault classification; DWT, discrete wavelet transform.

presented. Furthermore, the proposed schemes are extended to another transmission line, such as the 400 kV–144 km line. The obtained results demonstrated the effectiveness and reliability of the proposed scheme in correctly detecting simultaneous faults, low-impedance faults, and high-impedance faults.

KEYWORDS

Clarke transform, simultaneous faults, open conductor, down conductor, earth faults, high-voltage transmission lines

1 Introduction

1.1 Background and motivation

The most challenging task in protecting transmission lines is detecting faults the power system faces at a reliable performance level. Transmission line faults based on nature in terms of resistance are divided into low-impedance faults (LIFs) and high-impedance faults (HIFs). The main distinction between them is that the increased impedance is within the path of the fault current, limiting the arc current. LIFs comprise single line-to-ground faults, phase-to-phase faults, etc. HIFs result from unwanted contact with power conductors that are poorly connected to surfaces, making it difficult to detect these faults using traditional protection relays (Ghaderi et al., 2017). Like the open conductor (OC), a pathway toward the ground is not always included in HIFs. The open conductor faults (OCFs), like the series HIFs, cause the circuit breaker to not open due to the direct opening bridle. This is followed by the descent of the conductor to the ground (Jeerings and Linders, 1991). In addition, the OC in the transmission lines (TLs) is a challenging problem in power system operation. As a result, the system's stability suffers as the power transmitted over the line is lowered and healthy phases may be subjected to overloading. Furthermore, if the system is non-earthed, the voltage in the healthy phases may increase (Velez, 2014). Electric shocks and fire hazards generated by open conductor faults (OCFs) are also significant concerns regarding community safety, property failure, and losses. So, first and foremost, fast detection of OCFs is essential to transmission utilities (Abdel-Aziz et al., 2017). Because OCFs do not considerably increase current or voltage drop, distance protective relays, considered the TLs' principal protection mechanism, cannot detect them. As a result, the distance relay does not trip, and the fault will continue to occur in the open connector until the connector falls to the ground and is detected by another protection relay. In some cases, an earth fault relay can identify this fault-based high value of current when the conductor falls on a surface with meager resistance; however, since it is considered a standby protective for TLs, it will suffer from a delay time.

1.2 Literature overview

According to the literature, there are two proposals for identifying OCFs in transmission systems. The negative sequence was the suggested technique for identifying open and down conductor faults, where the negative sequence to the positive sequence current portion is introduced (ALSTOM, 2017). Different artificial intelligence schemes, such as neural networks (Koley et al., 2014) and In (Shukla et al., 2017), utilized the wavelet and naïve Bayes classifier to detect the OCF in six-phase TLs. Most previous schemes, such as thresholds in ALSTOM (2017), do not fully define the OCF problem and offer specific practical implementation challenges. Furthermore, the robustness of the artificial neural network protection scheme proposed by Gilany et al. (2010) has several practical constraints to be fabricated, as the reliability of these systems is highly determined by the nature of the design and the level of changes made to it, such as higher increased loads. In Elmitwally and Ghanem (2021), detecting the fault, selecting the faulty phase, and identifying the fault point depended on measuring the three-phase current at the protective relay in superimposed components of compensated TLs. In Khoshbouy et al. (2022), the ratio for the phase voltage at the sending end to the sum of the ratio for the phase current for two ends in TLs, called pilot superimposed impedance, was used to detect interior and exterior faults competed to a predetermined value, which was estimated based on Thevenin impedance.

Furthermore, many algorithms have been introduced in the literature over the past 20 years to detect OCFs in electric distribution utilities. For instance, voltage unbalance over the feeder was measured to identify the OCFs using sensors (Vieira et al., 2019); however, these sensors need sophisticated communication between these devices. In addition, the proportion of the SC current was inspected in Jayamaha et al. (2017); this requires the installation of current sensors over the line to protect it and deal with numerous challenges that may be difficult to overcome. Other proposed approaches, such as that introduced in Silva et al. (2018), relied on installing a device that measures the second or third harmonics of the current and follows the changes that may occur due to faults. Other schemes of detecting OCFs relied on the data measured from phase-measuring units (Zanjani et al., 2012). However, this necessitated precise management between these units and the control center. The detection strategy presented in Adewole et al. (2020) to identify an open phase was based on the current imbalance prevalent during the occurrence of OCFs; however, it was only suitable for earthed distribution utilities. Additionally, the current arc value changes rapidly over time during HIFs, which presents another challenge for schemes that rely on measuring the variance in frequency components (FCs) of the current due to arcing. The concept behind this is extracting the transient change in the fault (Shukla et al., 2017). In addition, many research works have been published to identify the fault in TLs based on wavelet transform applications,

such as discrete wavelet transform, wavelet packet transform, and single-wave entropy schemes. Numerous works used the discrete wavelet transform scheme because time–frequency localization can assess the transients during HIFs (Saravanababu et al., 2013). However, the schemes that rely on high-frequency components, as described in Ashok et al. (2019), result in weak discrimination between LIFs and HIFs. Conversely, algorithms such as those used in Rathore and Shaik (2015) relied on low-frequency components that failed to distinguish HIFs. It should be mentioned that incorporating between low and high frequencies was discussed using predetermined values in Shaik and Pulipaka (2015). However, the fault was not detected when switching a large load case because the value of the low-frequency component primarily relies on the value of the load current. Furthermore, research works (Usama et al., 2014) based on wavelet analysis focused on detecting earth faults, not OCFs. Accordingly, the difficulty in detecting and locating OCFs remarkably affects the state of OCFs on both sides of TL systems. In Asuhaimi Mohd Zin et al. (2015), fault detection and classification utilized discrete wavelet transform and back-propagation neural networks based on Clarke's parallel-transmission transformation. The fault detection and classification of fault types that are triggered in three-phase TLs using the artificial neural network is described in Assadi et al. (2023). The proposed scheme can detect and classify several faults, including line-to-ground, line-to-line, double-line-to-ground, triple-line, and triple-line-to-ground faults. In Mahanty and Gupta (2007), the methodology for fault analysis uses current samples with the help of fuzzy logic. In this technique, only one end of the three-phase current samples was considered to achieve fault classification. The neural network was utilized for training, and a fuzzy view point was applied to gain an insight into the system and to reduce the complexity of the system (Dash et al., 2000). Jayabharata Reddy and Mohanta (2007) presents a real-time wavelet–Fuzzy combined scheme for digital relaying. The algorithm for fault classification utilizes wavelet multi-resolution analysis to overcome the complications combined with conventional voltage and current-based measurements due to the effect of fault inception angle, fault impedance, and fault distance. No scheme has proven its superiority and effectiveness in all fault scenarios. Thus, new effective solutions are therefore needed.

1.3 Contributions and novelty

This work discusses a detection scheme that relies on the Clarke transform conversion for the current signals in TLs, such as the OCF on both sides and the OCF on a single side, followed by an earthed fault on another side through LIFs and HIFs. The sign of all current Clarke components is the primary key for distinguishing between all types of simultaneous LIFs and HIFs. The alternative transient program (ATP) package simulates a 500 kV–150-mile transmission line. The behavior of the proposed schemes is tested and validated considering different fault scenarios with different fault locations, inception angles, fault resistance, and noise.

Furthermore, the proposed schemes are extended to another transmission line, such as the 400 kV–144 km line. The obtained results demonstrated the effectiveness and reliability of the proposed scheme in detecting simultaneous faults, LIFs, and HIFs correctly in 20 mS.

The novelty in the proposed scheme and the essential features that verify the accomplishment achievement of its purpose effectively compared to the preceding approaches are as follows:

- Functionality: It can correctly discriminate between OCFs (series faults), two types of broken conductors together with earth faults (shunt fault) occurring after a short period (simultaneous earth faults), HIFs, and LIFs. These faults are correctly detected at both ends compared to other existing schemes that see these faults at a single end.
- Cost: It does not require the installation of new current transformers because it relies on the measurements at both ends and does not use the high sampling frequency compared to other existing schemes.
- Flexibility and independency: It utilizes powerful threshold values at both ends and relies on a detailed description study in this manuscript. Consequently, the proposed threshold values are appropriate for all fault scenarios and do not need adaptive values under variations of network configuration (independent of the system topology) or variations in load current.
- Speed: It has advantages in terms of speed and visibility in its application compared with other existing schemes because it corrects discrimination using communication links between both ends already installed.

1.4 Organization

The rest of the manuscript is organized as follows: Section 2 clarifies the fundamental problem investigated in this work. The proposed fault detection strategy is introduced in Section 3. In Section 4, the behavior assessment for the proposed scheme is conducted using ATP to examine the ability to identify the fault. In Section 5, a comparison is made between the proposed scheme and other schemes presented in the literature. Finally, Section 6 is dedicated to the conclusion drawn and future work directions. A schematic overview of the proposed scheme's assessment steps and the work's organization is given in Figure 1.

2 Problem description

Figure 2 shows both types of OCFs (series faults) and broken conductors together with earth faults (shunt faults) occurring after a short period (simultaneous earth faults). Figure 2A illustrates an OC from two sides. The OCF can occur if the bridle wire is open and banned at two sides, as seen in Figure 2B. An OC (broken conductor) happens on one end, followed by a down conductor appearing on the opposite end (simultaneous faults). As a result of opening the same conductor, the down conductor takes time to touch the soil, depending on the height of the conductor above the ground and the acceleration due to gravity. The surface/soil resistance value significantly affects the fault current's value. The OC in the receiving end side at 0.08 s is followed by a shunt fault

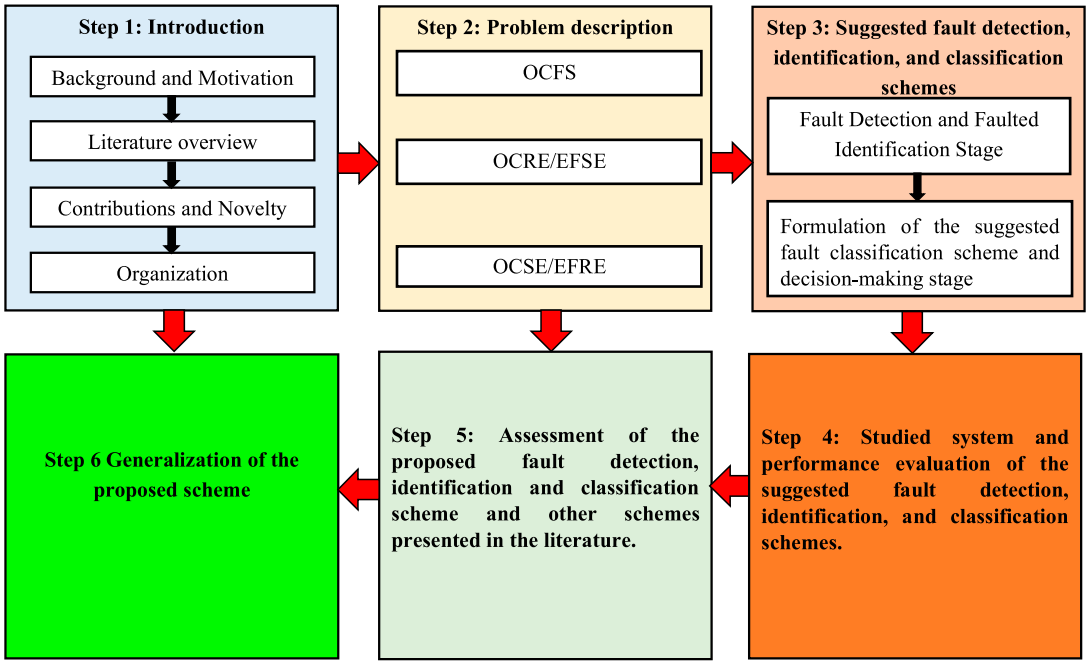

FIGURE 1
Schematic overview of the proposed scheme's assessment steps and work organization.

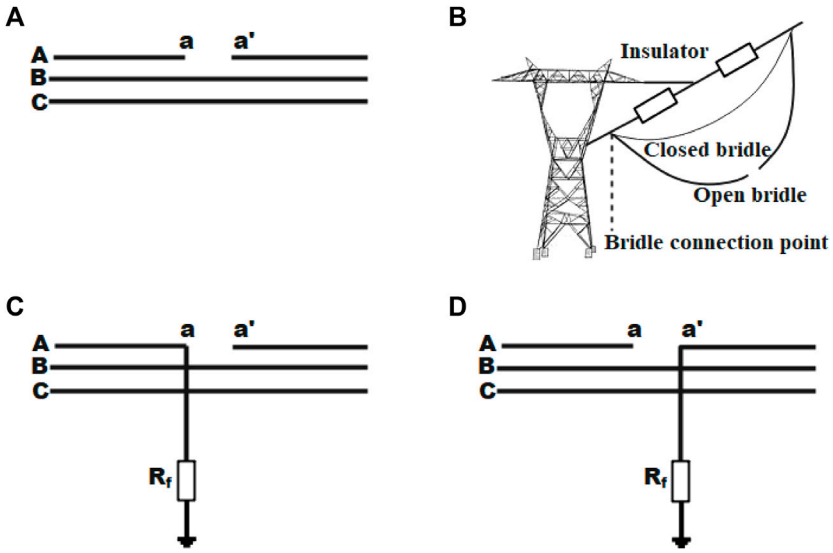

FIGURE 2
Presentation of an open conductor and simultaneous faults for phase A: **(A)** open circuit fault; **(B)** exhibition of OCF; **(C)** OC at the receiving end followed by a shunt fault at the sending end (denoted OCRE/EFSE); **(D)** OC at the sending end followed by a shunt fault at the receiving end (denoted OCSE/EFRE).

across LIFs and HIFs at the sending end side, as illustrated in Figure 2C. The OC at the sending end side, after 0.08 s, is followed by a shunt fault across LIFs and HIFs at the receiving end side, as illustrated in Figure 2D. Consequently, HIFs can be termed as shunt faults disregarding the OC case (Banner and Don Russell, 1997). HIFs usually occur beside the OC near the receiving end and touch a surface of the ground or by other elements at the sending end side of the transmission system.

HIFs are affected by several factors, including the material of the ground surface, moisture of the surface, levels of voltage, and weather circumstances. One factor that significantly impacts the characteristics of HIFs is surface humidity, where surfaces with high

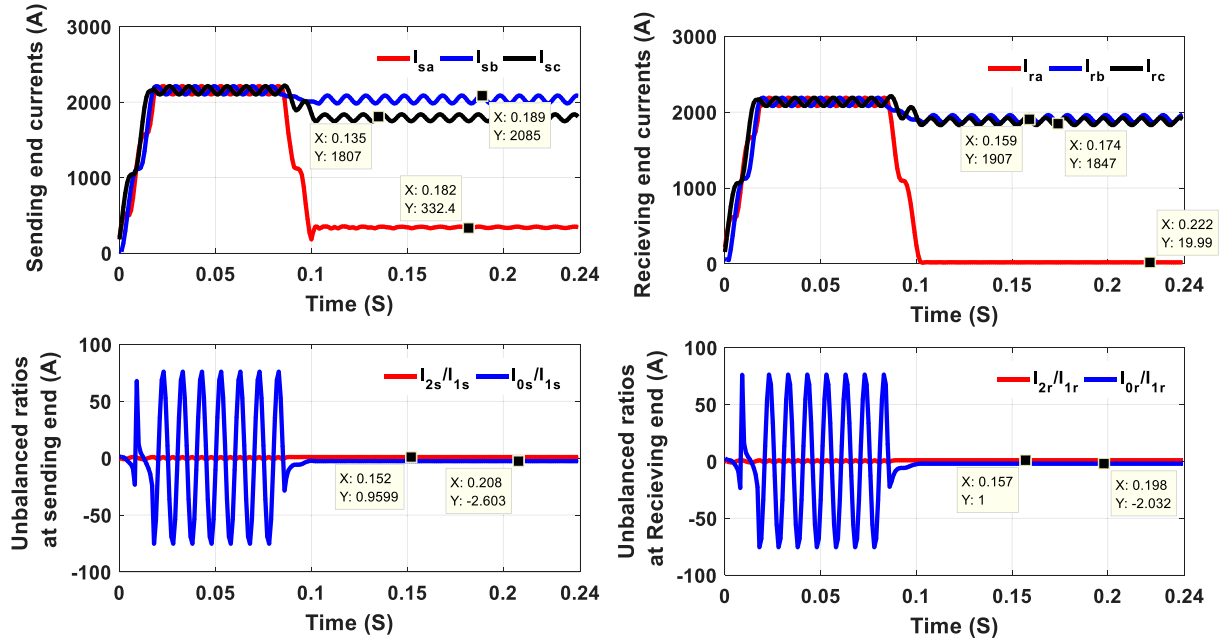

FIGURE 3
DFT-based amplitudes for three-phase currents and imbalance ratios considering OCFs at both ends.

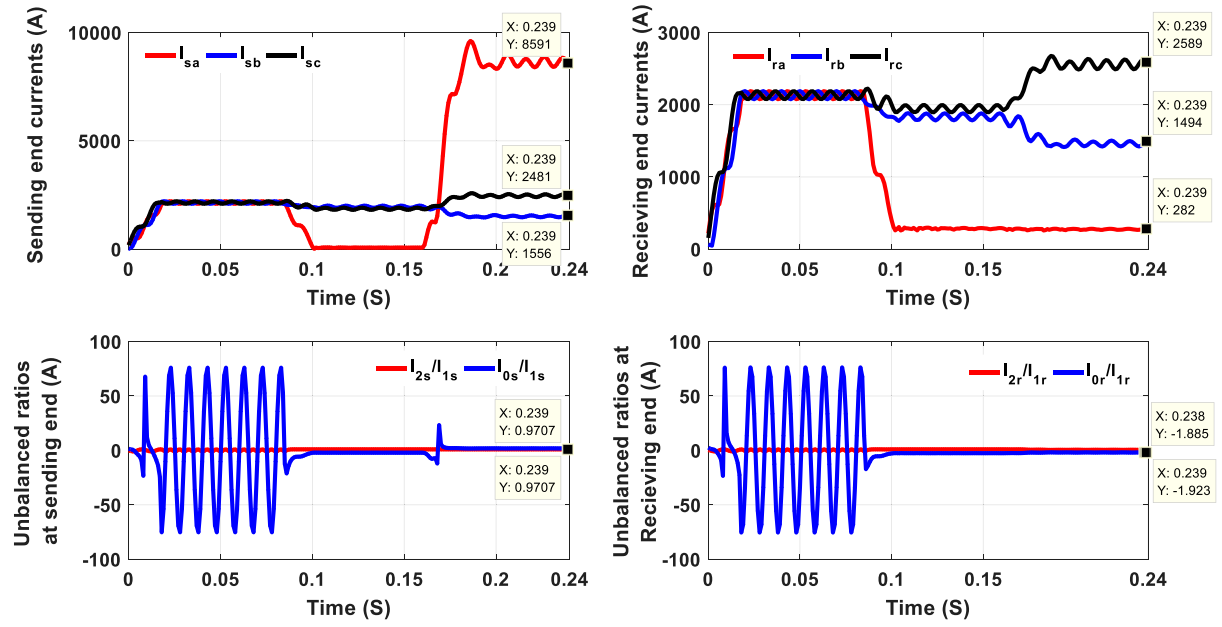

FIGURE 4
DFT-based amplitudes for three-phase currents and unbalanced ratios considering OCFs at the receiving end followed by earth fault at the sending end (OCRE/EFSE) at both ends.

humidity lead to increased fault current magnitude (Kavaskar and Kant, 2019). In addition, HIFs occurring through different materials could lead to other voltage–current characteristics. Materials that touch down-conductors from the tower may include tree branches, lawns, gravel, deep gravel, thin gravel, asphalt, concrete, sand, crushed stone, board blocks, and cement. Recently, the down conductor problem in distribution networks has been solved, as explored by Esmail et al. (2022). This motivated the authors to investigate solving the same problem in transmission line systems.

This work investigates the problem of detecting simultaneous series and shunt earth faults in conventional protection relays in the

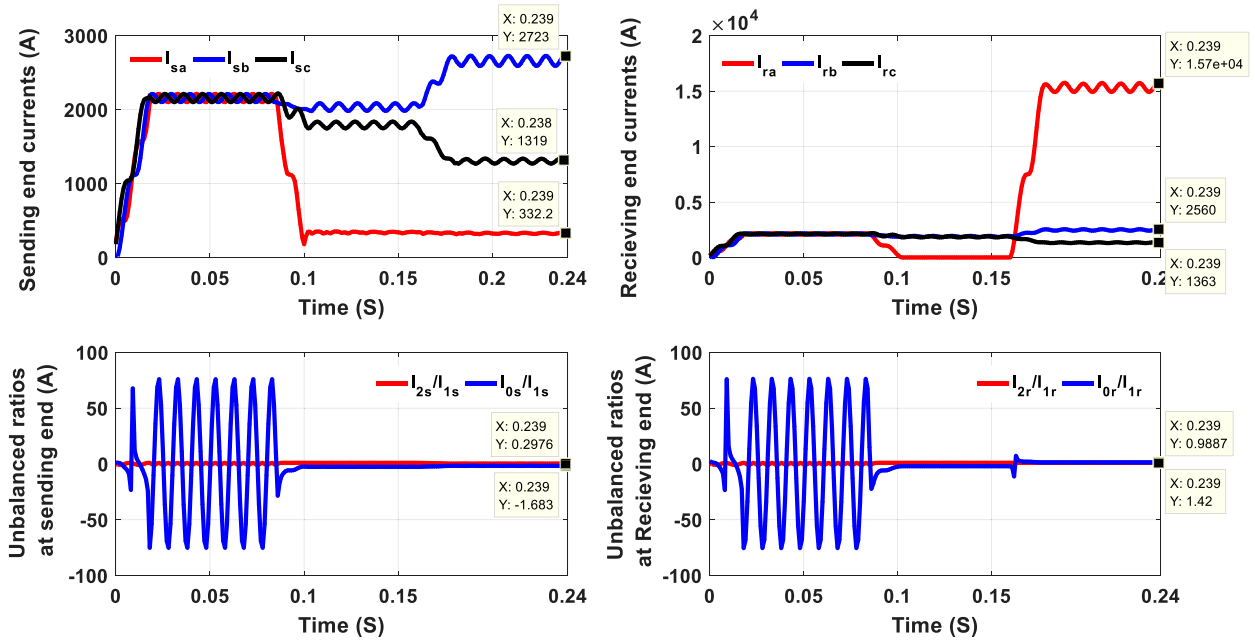

FIGURE 5
DFT-based amplitudes for three-phase current and unbalanced ratios considering OC at the sending end followed by earth fault at the receiving end (OCSE/EFRE) at both ends.

TL by applying different simulation cases in power systems. All simulated cases were taken at 130 miles from the sending end, which emphasized the actual performance of the protection relay, which is not seen in these types of faults owing to the small fault current value. At the same location, various faults were implemented, with OCFs and an OC at the receiving end side, followed by an earth fault on the sending end side, and an OC at the sending end side, followed by an earth fault on the receiving end side.

The traditional protection performance under these simulated faults was examined, as shown in Figure 3, by computing the discrete Fourier transform (DFT)-based amplitude for three-phase currents and imbalance ratios (I_2/I_1, I_0/I_1), considering OCFs at both ends. Conventional protection cannot detect the broken conductor fault by investigating the results. The value for the current amplitude of phase A and I_2/I_1, I_0/I_1 ratios at the sending end provide a maloperation for the device. Furthermore, the current amplitude of phase A gives (10–15) % of its values at normal operation.

In addition, the behavior of the traditional protective relay under these simulated faults was examined, as shown in Figure 4, by computing the DFT-based amplitude for three-phase currents and ratios (I_2/I_1, I_0/I_1) at both ends. The value of the current amplitude of phase A gives (140–160) % from its value at normal operation at the sending end, which is considered a shunt fault, but the value of the same phase A gives (10–15) % from its values at normal operation at the receiving end, which is considered a series fault. Moreover, the values of both ratios (I_2/I_1, I_0/I_1) at both ends resulted in a malfunction for both protection devices. Figure 5 shows the DFT-based amplitudes for three-phase currents and unbalanced ratios under an OC at the protective relay aspect, followed by earth fault in the reverse protection relay aspect at both ends. The recorded amplitude for phase A at the sending end gives (10–15) % of its values at normal operation, demonstrating that its devices cannot detect this fault condition. However, at the receiving end, the recorded amplitude for the same phase gives (140–160) % of its value at normal operation, which is considered a shunt fault. Furthermore, the unbalanced ratios at both ends cannot provide any detection for this type of fault condition. These results highlighted the incapability of traditional protection strategies in detecting these types of faults.

3 Suggested fault detection, fault identification, and classification schemes

3.1 Fault detection, identification, and classification

The proposed schemes comprise different stages: fault detection, identification, and classification, as declared in Figure 6. As illustrated in Figure 6, the introduced scheme relies on the existing phasor measurement unit at the high-voltage side. Each phasor measurement monitors the three-phase currents' magnitudes. Phasors are considered the primary tool for analyzing the power system in its steady state or transient situations, so phasor estimation is quite essential for protection applications. Estimating the voltage and current phasor is performed concerning one frequency, which is usually the fundamental power frequency. A phasor measurement unit, or synchrophasor, is a device that measures a power system's synchronized current

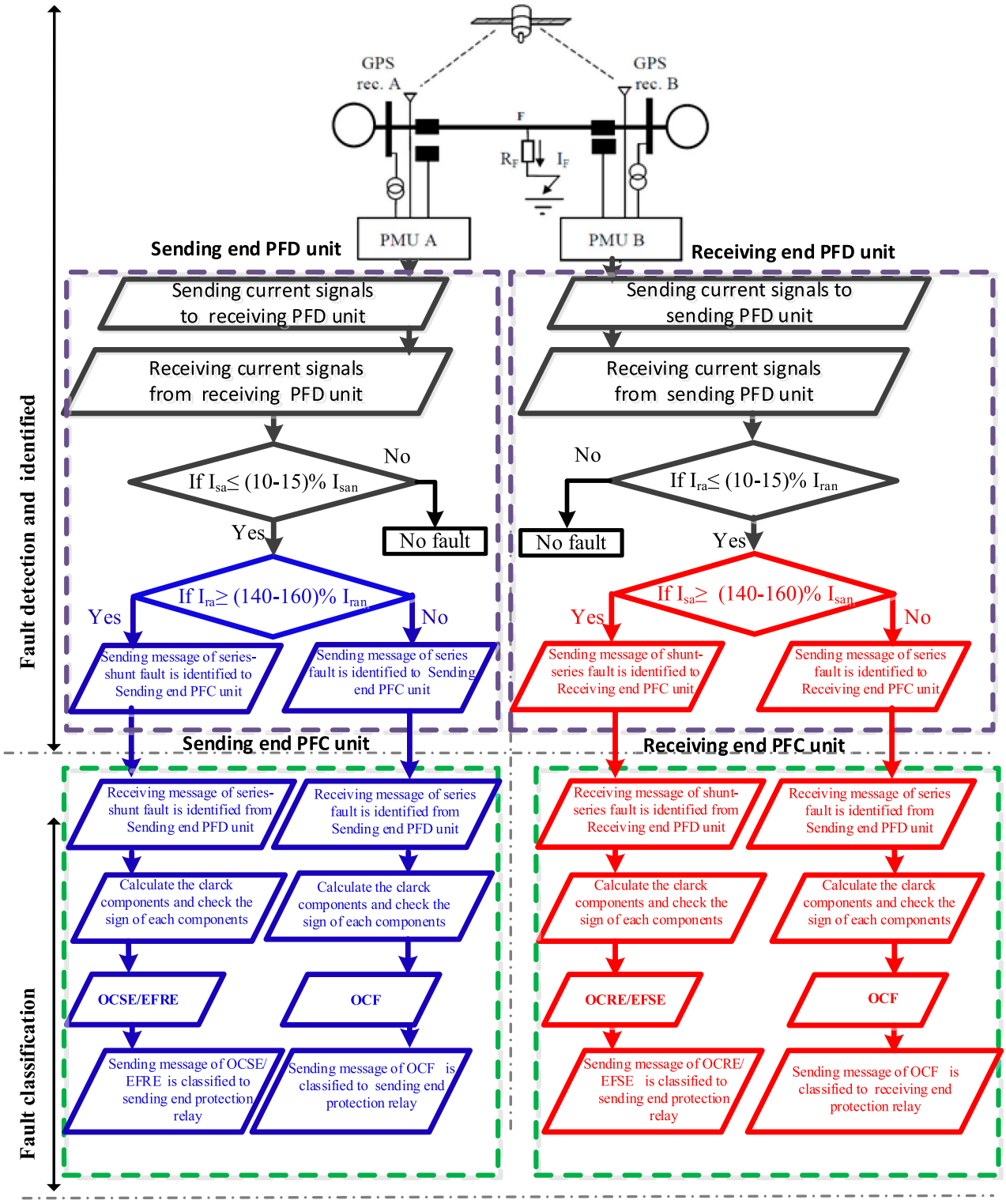

FIGURE 6
Flow chart of the proposed fault detection, identification, and fault classification schemes.

phasor. Synchronization among phasor measurement units is achieved by same-time sampling of voltage and current waveforms using a famous synchronizing signal. The ability to calculate synchronized phasors makes the phasor measurement unit one of the most important measuring devices in the future of power system monitoring and control. Precise synchronization of sampling clocks throughout the power system became possible with the advent of the global positioning system (GPS) satellite system.

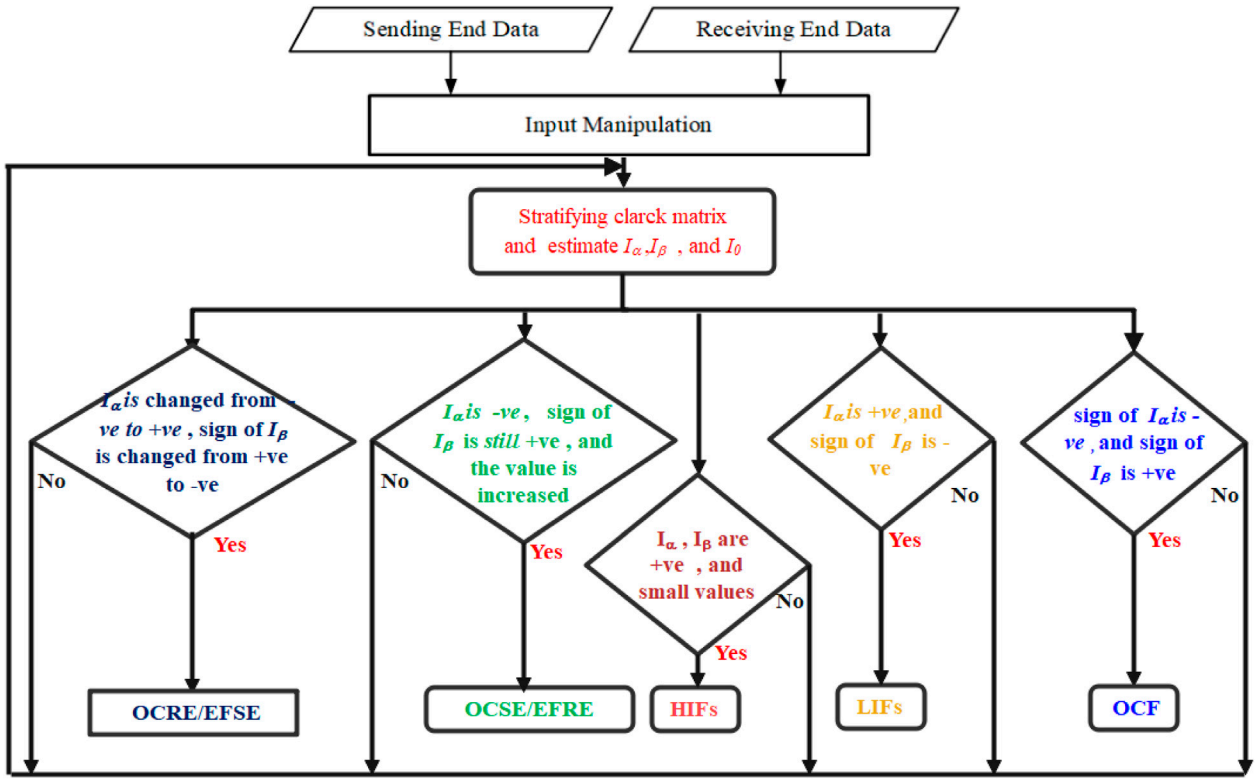

FIGURE 7
Flow chart of the proposed fault classification scheme in PFC units at both ends.

Although the precision of synchronization was not very good in the early years of the system, at present, it is possible to achieve synchronization accuracies of 1 μs or better.

The applicability and feasibility of the proposed schemes are clear. Nevertheless, the proposed scheme needs communication links between both ends (sending and receiving end) to detect, identify, and classify the fault. This communication link between both ends is used to send and receive three-phase currents' magnitudes for sending and receiving ends in the proposed fault detection (PFD) unit at both ends. The presented scheme is embedded in the PFD unit on both ends to detect and identify these faults when one or two conditions are verified. In the sending end PFD unit, the first condition is proving if the obtained sending end current for phase a at fault is equal to or less than (10–15) % of the sending end current for phase A at normal operation. The second condition is verifying if the obtained receiving end current for phase A at fault is equal to or more than (140–160) % of the receiving end current for phase A at normal operation. Furthermore, in the receiving end PFD unit, the first condition is verifying if the obtained receiving end current for phase A at fault is equal to or less than (10–15) % of the receiving end current for phase A at normal operation. The second condition is verifying if the obtained sending end current for phase A at fault is equal to or more than (140–160) % of the sending end current for phase A at normal operation. The security attribute for the presented algorithm is achieved under unbalanced load conditions. Thus, the obtained sending end or receiving end current for phase A at fault is more than (140–160) % of the sending end or receiving end for phase A at normal operation. According to the proposed detection scheme, this is the second condition monitoring if the first condition is verified.

Consequently, the proposed scheme is not affected by unbalanced load conditions. On the other hand, the presented algorithm is susceptible to consideration because the computed current signal significantly increases to specific high ratios according to the fault type. The threshold values ((10–15) % and (140–160) %) are selected based on the detail analysis under all possible fault conditions in Section 2. The expected threshold values under these faults are as follows:

3.1.1 Series fault

Under series faults, the obtained sending end current for phase a at fault is equal to (10–15) % of the sending end current for phase a at normal operation in the sending end PFD unit, and the obtained receiving end current for phase a at fault is less than (10–15) % of the receiving end current for phase a at normal operation in the receiving end PFD unit, which means that only the first condition is verified, and then sending a message of series fault being identified to the sending end PFC unit. Accordingly, the process of the fault classification PFC unit starts after receiving a message that the series fault is identified from the sending end PFD unit.

3.1.2 Series–shunt fault

Under the series–shunt fault, in the receiving end PFD unit, similarly, the first condition is verified. The second condition is checked (if the obtained sending end current for phase a at

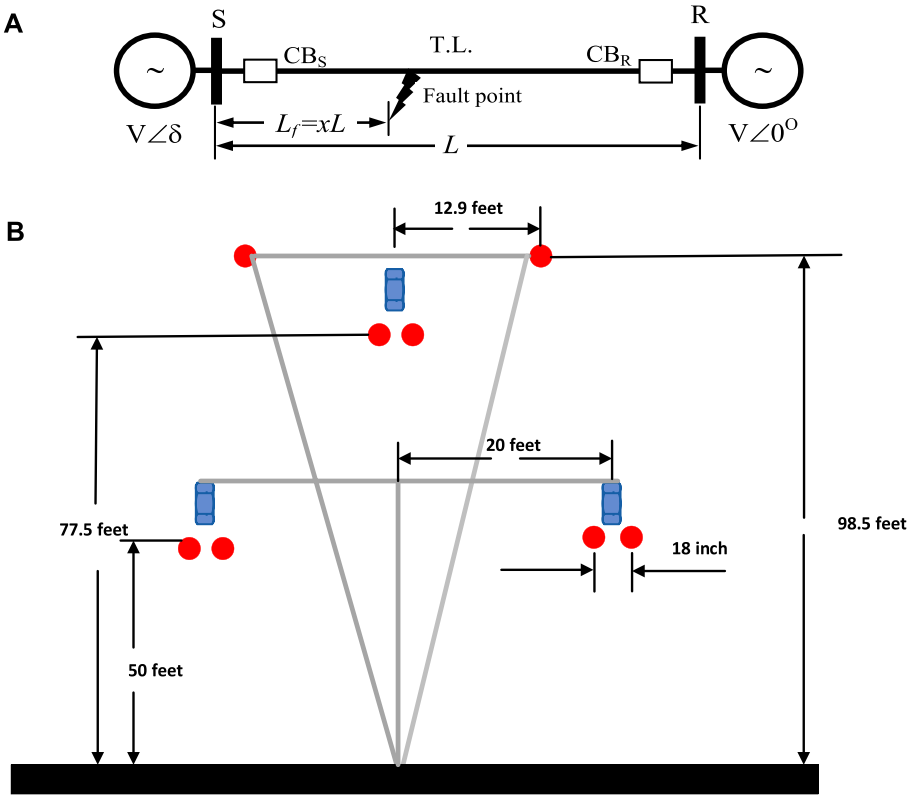

FIGURE 8
Single-line diagram (SLD) of the simulated TL system and the selected tower: **(A)** SLD; **(B)** tower configuration.

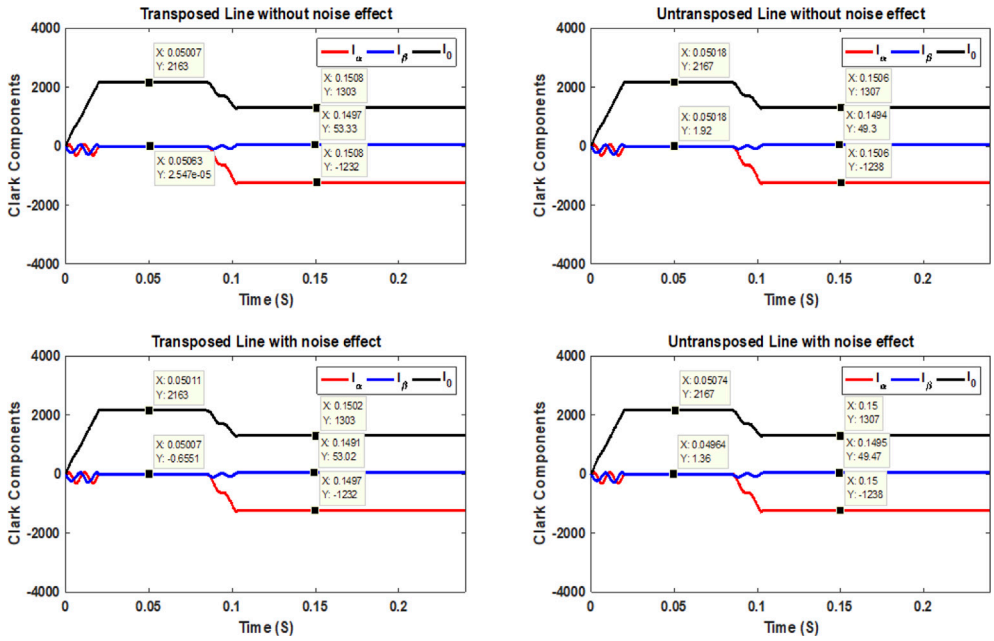

FIGURE 9
Clarke comments on the sending end currents at OCFs.

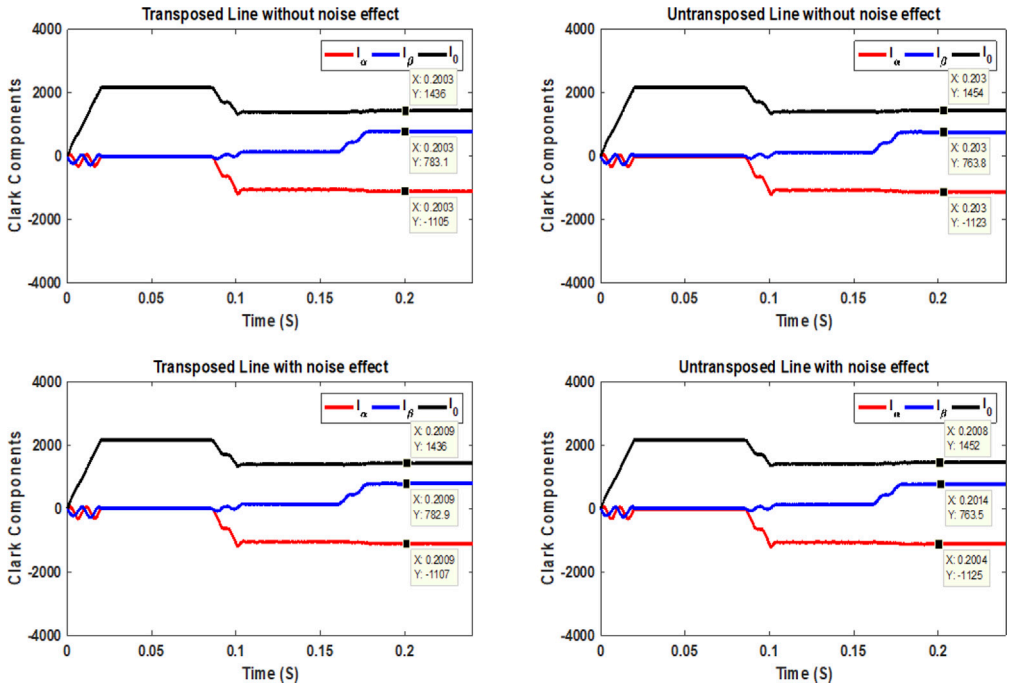

FIGURE 10
Clarke comments on the sending end currents at OCSE/EFRE.

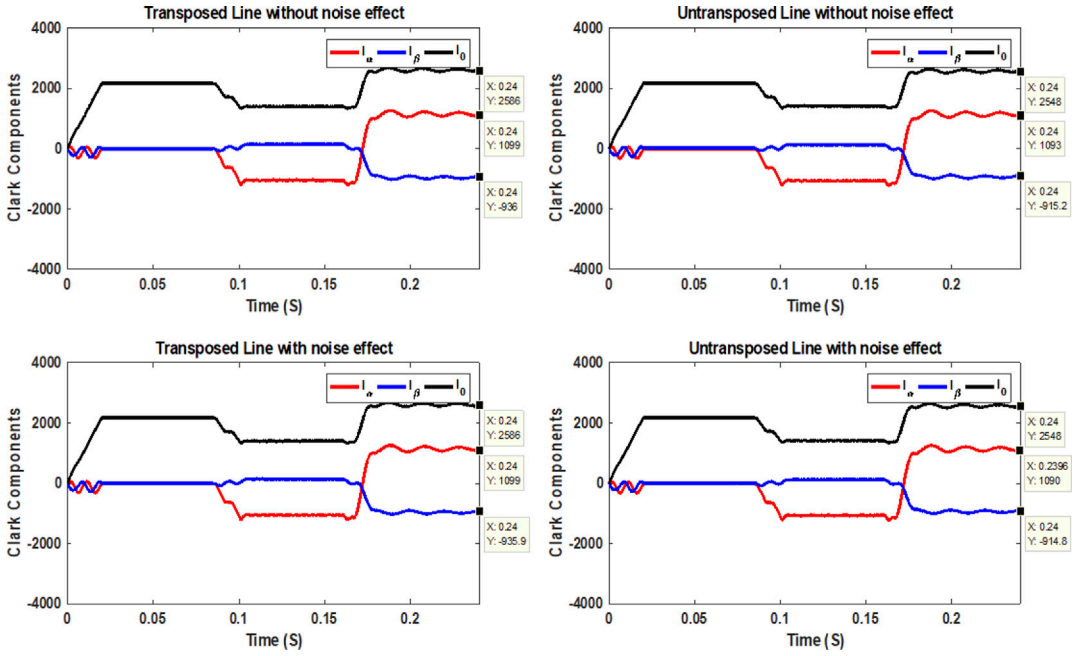

FIGURE 11
Clarke comments on the sending end currents at an OCRE/EFSE.

fault is equal to or more than (140–160) % of the sending end current for phase a at normal operation) and verified. If two conditions are verified, the PFD unit sending a message of series–shunt fault is identified to the sending end PFC unit, and the flow of fault classification starts after receiving this message in its unit.

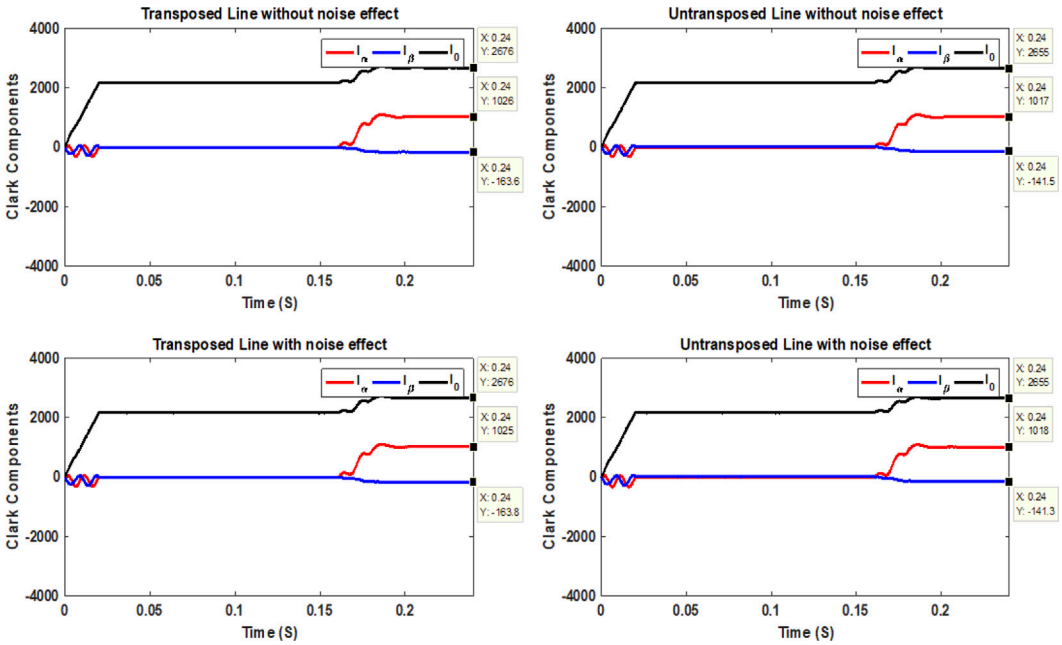

FIGURE 12
Clarke comments on sending end currents at the LIF.

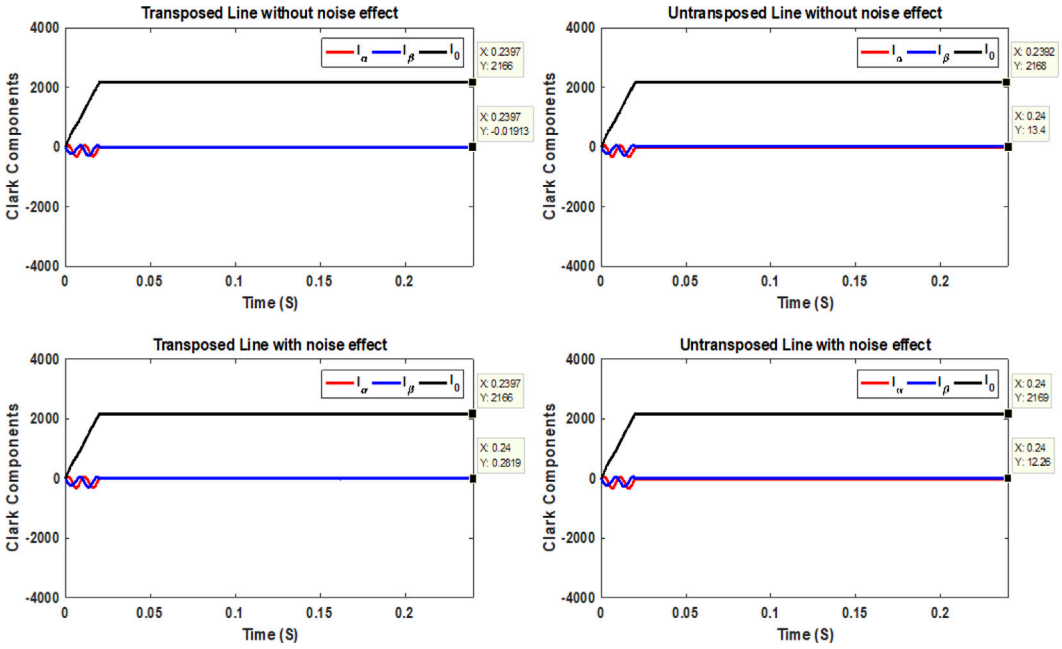

FIGURE 13
Clarke comments on sending end currents at the HIF.

3.1.3 Shunt–series fault

Under shunt–series fault, the first condition is verified in the sending end PFD unit. The second condition is detected (if the obtained receiving end current for phase a at fault is equal to or more than (140–160) % of the receiving end current for phase a at normal operation) and verified. If two conditions are verified, and then receiving a message of shunt–series fault is identified from the receiving end PFD

TABLE 1 Results of OCF fault detection, identification, and fault classification using the proposed schemes for the considered transposed and un-transposed lines with and without noise effect.

System transposed	Noise effect	Fault		R_f (Ω)	ϕ (degree)	I_α (A)	I_β (A)	I_0 (A)	Classification	Response time (mS)	Security
		Type	*Location*								
Y	*N*	OCFs	13.8	-	0	−1257.4	40.983	1292.4	OCF	20	Secured
		OCFs	27.6	-	30	−1231.8	53.407	1302.9	OCF	20	Secured
	Y	OCFs	13.8	-	0	−1257.5	41.233	1292.5	OCF	20	Secured
		OCFs	27.6	-	30	−1231.7	53.149	1302.9	OCF	20	Secured
N	*N*	OCFs	13.8	-	0	−1269.1	24.785	1303.8	OCF	20	Secured
		OCFs	27.6	-	30	−1248.4	34.519	1317.6	OCF	20	Secured
	Y	OCFs	13.8	-	0	−1269.3	25.048	1304.0	OCF	20	Secured
		OCFs	27.6	-	30	−1248.4	34.307	1317.8	OCF	20	Secured

Note: Y: yes; N: no.

TABLE 2 Results of OCF fault detection, identification, and fault classification using the DWT-based algorithm for the considered transposed and un-transposed lines with and without noise effect.

System transposed	Noise effect	Fault type	$M_a < M_{th}$, and $M_b < M_{th}$, and $M_c < M_{th}$	$H_a > H_{th}$, or $H_b > H_{th}$, or $H_c > H_{th}$	$R_a > >1$, or $R_b > 1$, or $R_c > 1$	Event classification	Fault detection time (mS)	Security
Y	*N*	OCFs	49.74< M_{th}, and 2770.9< M_{th}, and 2670.5< M_{th}	2717.5> H_{th}	1.0376 > 1	OCF	21.46	Secured
		OCFs	100.64< M_{th}, and 2783.7< M_{th}, and 2652.9< M_{th}	2678.6> H_{th}	1.0493 > 1	OCF	21.63	Secured
	Y	OCFs	62.536< M_{th}, and 2805.7< M_{th}, and 2702.4< M_{th}	15211> H_{th}	1.0382 > 1	OCF	21.46	Secured
		OCFs	116.48< M_{th}, and 2822.4< M_{th}, and 2680< M_{th}	13295> H_{th}	1.0532 > 1	OCF	21.63	Secured
N	*N*	OCFs	48.965< M_{th}, and 2775.9< M_{th}, and 2714.1< M_{th}	2722.7> H_{th}	1.0228 > 1	OCF	21.46	Secured
		OCFs	97.888< M_{th}, and 2789.9< M_{th}, and 2709.6< M_{th}	2690.9> H_{th}	1.0296 > 1	OCF	21.63	Secured
	Y	OCFs	61.843< M_{th}, and 2805.2< M_{th}, and 2757.9< M_{th}	15523> H_{th}	1.0172 > 1	OCF	21.46	Secured
		OCFs	114.42< M_{th}, and 2813.7< M_{th}, and 2731.5< M_{th}	13754> H_{th}	1.0301 > 1	OCF	21.63	Secured

unit, the flow of fault classification starts in the receiving end PFC unit.

According to the previous subsection, fault detection, identification, and fault classification are performed in both PFD units at both ends. Furthermore, the first step of fault classification is checked in both PFC units using PFC units on both ends, as seen in Figure 6. The fault classification procedure further takes place after calculating the Clarke components and checking the sign of each component using the chart seen in Figure 7. Then, all PFC units in both sending and receiving ends send the message of fault classification to the sending and receiving end protection relay, respectively.

TABLE 3 Results of OCRE/EFSE fault detection, identification, and fault classification using proposed schemes for the considered transposed and un-transposed lines with and without noise effect.

System transposed	Noise effect	Fault type	Fault locations	R_f (Ω)	ϕ (degree)	I_α (A)	I_β (A)	I_0 (A)	Classification	Response time (mS)	Security
Y	N	OCRE/EFSE	41.4	5	60	3473.4	−669.13	3733.7	OCRE/EFSE	20	Secured
			55.2	5	90	2722.3	−709.78	3354.5	OCRE/EFSE	20	Secured
			69.0	10	120	2177.6	−725.91	3114.9	OCRE/EFSE	20	Secured
			82.8	10	150	1827.1	−764.66	2942.7	OCRE/EFSE	20	Secured
	Y	OCRE/EFSE	41.4	5	60	3474.0	−669.44	3734.1	OCRE/EFSE	20	Secured
			55.2	5	90	2721.5	−709.93	3354.2	OCRE/EFSE	20	Secured
			69.0	10	120	2177.2	−725.85	3114.7	OCRE/EFSE	20	Secured
			82.8	10	150	1826.8	−764.36	2942.1	OCRE/EFSE	20	Secured
N	*N*	OCRE/EFSE	41.4	5	60	3474.5	−663.45	3713.3	OCRE/EFSE	20	Secured
			55.2	5	90	2736.6	−709.34	3346.3	OCRE/EFSE	20	Secured
			69.0	10	120	2182.8	−721.06	3093.4	OCRE/EFSE	20	Secured
			82.8	10	150	1819.5	−759.25	2915.6	OCRE/EFSE	20	Secured
	Y	OCRE/EFSE	41.4	5	60	3475.2	−663.01	3713.6	OCRE/EFSE	20	Secured
			55.2	5	90	2737.2	−709.27	3346.5	OCRE/EFSE	20	Secured
			69.0	10	120	2182.4	−721.38	3093.4	OCRE/EFSE	20	Secured
			82.8	10	150	1819.6	−758.99	2915.7	OCRE/EFSE	20	Secured

3.2 Formulation of the suggested fault classification scheme and decision-making stage

In the PFC units, the formula of the suggested fault classification is examined under some critical insights into un-transposed and transposed TLs. In this regard, the impedance matrix is symmetrical in the un-transposed case (symmetrical space between the conductors). In a symmetrical space between the conductors, the self or diagonal terms are generally unequal, and neither is the mutual or off-diagonal term in the impedance matrix. The current flowing in any one conductor will induce voltage drops in the other two conductors, which may be unequal even if the currents are balanced. Asymmetric voltage drops caused by the mutual impedances are unequal. This issue can be solved by making the TLs a perfectly transposed line in which the three sections have equal lengths. The perfect transposition results in the same total voltage drop for each phase conductor and equal average series self-impedance of each phase conductor. This effect applies to the average series phase mutual impedance and the average shunt phase mutual susceptance. Consequently, the phase impedance for a perfectly transposed single circuit is symmetric. Applying an entire transpose scheme suffers from expensive costs and inconvenience. Accordingly, the line may be transposed at one or two locations along the line route. This configuration provides a symmetrical impedance matrix.

In the proposed fault classification procedure, the output of the Clarke matrix is reflected in signals of the phase currents to detect various OCFs in un-transposed and transposed TLs precisely. The time-domain transformation is used with Clarke components, denoted as α, β, and 0, which are extracted as follows:

$$\begin{bmatrix} I_\alpha \\ I_\beta \\ I_0 \end{bmatrix} = \begin{bmatrix} 2/3 & -1/3 & -1/3 \\ 0 & 1/\sqrt{3} & -1/\sqrt{3} \\ 1/3 & 1/3 & 1/3 \end{bmatrix} \begin{bmatrix} I_a \\ I_b \\ I_C \end{bmatrix}. \quad (1)$$

The Clarke components are represented by Eq. 1, considering phase *a* as a reference, and two other Clarke components concerning phases *b* and *c*. In general, the same zero "0" component exists for any reference, whereas phases *a*, *b*, and *c* have three "*β*" components. These components are called aerial modes 1, 2, and 3 when OCFs or simultaneous earth faults occur. First, when conductor *a* opens, as shown in Figure 2B, one can note the following for Clarke's components:

$$I_\alpha = \frac{2}{3}I_a - \frac{1}{3}I_b - \frac{1}{3}I_c, \quad (2)$$

$$I_\beta = \frac{1}{\sqrt{3}}(I_b - I_c), \quad (3)$$

$$I_0 = \frac{1}{3}(I_a + I_b + I_c). \quad (4)$$

Second, when the simultaneous earth fault at phase *a* happens, as shown in Figure 2C or Figure 2D, one can find that Clarke's matrix components change as follows:

$$I_\alpha = \frac{2}{3}I_a - \frac{1}{3}I_b - \frac{1}{3}I_c, \quad (5)$$

$$I_\beta = \frac{1}{\sqrt{3}}(I_b - I_c), \quad (6)$$

$$I_0 = \frac{1}{3}(I_a + I_b + I_c). \quad (7)$$

TABLE 4 Results of OCRE/EFSE fault detection, identification, and fault classification using the DWT-based algorithm for the considered transposed and un-transposed lines with and without noise effect.

System transposed	Noise effect	Fault type	$M_a < M_{th}$, and $M_b < M_{th}$, and $M_c < M_{th}$	$H_a > H_{th}$, or $H_b > H_{th}$, or $H_c > H_{th}$	$R_a > >1$, or $R_b > 1$, or $R_c > 1$	Event classification	Fault detection time (mS)	Security
Y	*N*	OCRE/EFSE	10322> M_{th}, and 2044.8< M_{th}, and 3683.9> M_{th}	8200.8 > H_{th}	5.0477 > 1	Failed	-	Unsecured
			8773.6 > M_{th}, and 1968.8 < M_{th}, and 3705.7 > M_{th}	6663.4> H_{th}	4.4564 > 1	Failed	-	Unsecured
			7511.5 > M_{th}, and 2020.3 < M_{th}, and 3798.1 > M_{th}	5510.7 > H_{th}	3.718 >1	Failed	-	Unsecured
			6751.7 > M_{th}, and 1934.5 < M_{th}, and 3807.4 > M_{th}	4811.3 > H_{th}	3.4902 > 1	Failed	-	Unsecured
	Y	OCRE/EFSE	10414 > M_{th}, and 2078.4 < M_{th}, and 3737.3 > M_{th}	47334 > H_{th}	5.010 > 1	Failed	-	Unsecured
			8848.1 > M_{th}, and 1989.8 < M_{th}, and 3738.5 > M_{th}	36679 > H_{th}	4.446 > 1	Failed	-	Unsecured
			7545.7> M_{th}, and 2050< M_{th}, and 3829.2> M_{th}	29736> H_{th}	3.6808 > 1	Failed	-	Unsecured
			6798.6 < M_{th}, and 1966.6 < M_{th}, and 3841.2 > M_{th}	21584 > H_{th}	3.457 > 1	Failed	-	Unsecured
N	*N*	OCRE/EFSE	10318> M_{th}, and 2019.5 < M_{th}, and 3619.9< M_{th}	8197.3> H_{th}	5.1091 > 1	Failed	-	Unsecured
			8793.6 > M_{th}, and 1970.2 < M_{th} and 3667.6 < M_{th}	6687.7 > H_{th}	4.4632 > 1	Failed	-	Unsecured
			7488.2> M_{th}, and 1996.2< M_{th}, and 3756.5> M_{th}	5518.4> H_{th}	3.7513 > 1	Failed	-	Unsecured
			6703.6 > M_{th}, and 1906.9 < M_{th}, and 3764.3 > M_{th}	4790.4 > H_{th}	1. 351 > 1	Failed	-	Unsecured
	Y	OCRE/EFSE	10384 > M_{th}, and 2042.9 < M_{th}, and 3647.3 < M_{th}	2717.5> H_{th}	5.082 > 1	Failed	-	Unsecured
			8859 > M_{th}, and 1990.5 < M_{th}, and 3711.3 > M_{th}	35706 > H_{th}	4.450 >1	Failed	-	Unsecured
			7552.6> M_{th}, and 2020.4< M_{th}, and 3785.3> M_{th}	30206> H_{th}	3.7381 > 1	Failed	-	Unsecured
			6761 > M_{th} and 1928.4 < M_{th}, and 3799.1 < M_{th}	20733 > H_{th}	3.506 > 1	Failed	-	Unsecured

10.3389/fenrg.2023.1208296

TABLE 5 Results of OCSE/EFRE fault detection, identification, and fault classification using the proposed schemes for the considered transposed and un-transposed lines with and without noise effect.

System transposed	Noise effect	Fault type	Fault locations	R_f (Ω)	ϕ (degree)	I_α (A)	I_β (A)	I_0 (A)	Classification	Response time (mS)	Security
Y	N	OCSE/EFRE	96.6	5	180	−1180.3	920.37	1421.4	OCSE/EFRE	20	Secured
			110.4	5	30	−1139.3	885.87	1416	OCSE/EFRE	20	Secured
			124.2	50	120	−1047	465.72	1365.6	OCSE/EFRE	20	Secured
			130	50	90	−1036.5	394.14	1372.4	OCSE/EFRE	20	Secured
	Y	OCSE/EFRE	96.6	5	180	−1180.4	920.06	1421.3	OCSE/EFRE	20	Secured
			110.4	5	30	−1139.3	885.68	1416.2	OCSE/EFRE	20	Secured
			124.2	50	120	−1046.7	465.8	1365.3	OCSE/EFRE	20	Secured
			130	50	90	−1036.6	394.05	1372.3	OCSE/EFRE	20	Secured
N	*N*	OCSE/EFRE	96.6	5	180	−1213.5	895.86	1452.9	OCSE/EFRE	20	Secured
			110.4	5	30	−1172.8	870.35	1447.8	OCSE/EFRE	20	Secured
			124.2	50	120	−1069.4	442.87	1385.2	OCSE/EFRE	20	Secured
			130	50	90	−1055.7	372.93	1388.7	OCSE/EFRE	20	Secured
	Y	OCSE/EFRE	96.6	5	180	−1213.6	895.66	1452.8	OCSE/EFRE	20	Secured
			110.4	5	30	−1173	870.61	1448.3	OCSE/EFRE	20	Secured
			124.2	50	120	−1069.3	442.59	1385.3	OCSE/EFRE	20	Secured
			130	50	90	−1055.9	372.87	1388.7	OCSE/EFRE	20	Secured

Evaluating the three components of the Clarke matrix shows that aerial modes 1 and 2 best identify OCFs and simultaneous earth faults. The values of aerial modes 1 and 2 are 0 under healthy conditions. If OCFs occur, analysis of Clarke's matrix components reveals that the value of aerial mode 1 is negative and the value of aerial mode 2 is positive, as shown in Figure 7.

The same components are examined when LIFs are involved in the investigation. Aerial mode 1 is found to have a positive sign, while aerial mode 2 has a negative sign. This means that OCFs and LIFs are entirely different when compared to each other. Moreover, the sign of aerial modes 1 and 2 is positive, and their values are low if HIFs occur. In addition, if an OCRE/EFSE fault occurs, it will be found that the sign of aerial mode 1 changes from negative to positive, and the sign of aerial mode 2 changes from positive to negative. Furthermore, the sign of aerial mode 1 is negative, and its value increases, while the sign of aerial mode 2 is positive, and its value increases when an OCSE/EFRE fault occurs.

4 Studied system and performance evaluation of the suggested fault detection, identification, and fault classification schemes

Figure 8A shows the single-line diagram of the 500 kV, 138-mile TL simulated in the ATP/EMTP program. The ATPDraw software is an interface to implement the system (Prikler and Høidalen, 2009). This TL model is a benchmark in ATPDraw software, and it is represented using the three-phase JMARTI frequency dependence model in the ATPDraw field using the line/cable module (Prikler and Høidalen, 2009). The JMARTI representation is a frequency-fitted model in a specific frequency range. The JMARTI model is utilized to apply the simulated line and therefore take waveforms for the fault case in evaluating the proposed schemes. The results taken in this study are the same as the results taken on the same system in Elkalashy, 2014; Elkalashy et al., 2016. For simultaneous series and shunt earth fault detection and classification using the Clarke transform for TLs under different fault scenarios, the line parameters have been extracted, and results show that the self-impedance of this line, for a length of 138 miles, is 0.1431 + j1.2999 Ω, while that of the mutually linked one is 0.1052 + j 0.6249 Ω, according to the retrieved line parameters. Using a mutually linked RL circuit, Thevenin's equivalent impedance at buses S and R is expressed as R_1 = 1.0185 Ω, L_1 = 50.929 mH and zero sequences are R_0 = 2.037 Ω, L_0 = 101.85 mH at bus S and R_1 = 1.0185 Ω, L_1 = 42.85 mH, R_0 = 1.735 Ω, L_0 = 101.85 mH at bus R. The TL configuration is illustrated in Figure 8B, where the DC resistance is 0.05215 Ω/mile, the outer diameter of the conductor is 1.602 inch, and the inner radius of the tube is 0.2178 inch. The sky wires are solid; their dc resistance is 2.61 Ω/mile, and the outer diameter is 0.386 inch. The resistivity of the soil is equal to 100 Ω.

The JMARTI model is fundamentally depicted by the rational approximation of the characteristic impedance (*Zc*) and by the elements of the propagation matrix (H). The JMARTI model's fitting technique is based on the theory of asymptotic approximations of magnitude functions. This rational approximation technique starts with only real poles and zeros and, therefore, real state variables. A small error in simulation

TABLE 6 Results of OCSE/EFRE fault detection, identification, and fault classification using the DWT-based algorithm for the considered transposed and un-transposed lines with and without noise effect.

System transposed	Noise effect	Fault type	$M_a < M_{th}$, and $M_b < M_{th}$, and $M_c < M_{th}$	$H_a > H_{th}$, or $H_b > H_{th}$, or $H_c > H_{th}$	$R_a > >1$, or $R_b > 1$, or $R_c > 1$	Event classification	Fault detection time (mS)	Security
Y	*N*	OCSE/EFRE	341.51< M_{th}, and 3973> M_{th}, and 1718.9< M_{th}	3630.4> H_{th}	2.3114 > 1	Failed	-	Unsecured
			391.58< M_{th}, and 3904.7> M_{th}, and 1734.4< M_{th}	3502> H_{th}	2.2513 > 1	Failed	-	Unsecured
			450.76< M_{th}, and 3246.5< M_{th}, and 2106.1< M_{th}	2791.2> H_{th}	1.5415 > 1	OCF	24.37	Secured
			474.91< M_{th}, and 3160.5< M_{th}, and 2195.1< M_{th}	2682.1> H_{th}	1.4398 > 1	OCF	21.06	Secured
	Y	OCSE/EFRE	354.32< M_{th}, and 4027.6> M_{th}, and 1742.2< M_{th}	17978> H_{th}	2.3118 > 1	Failed	-	Unsecured
			404.03< M_{th}, and 3943.4> M_{th}, and 1766.6< M_{th}	19598> H_{th}	2.2321 > 1	Failed	-	Unsecured
			462.51< M_{th}, and 3281.4< M_{th}, and 2124< M_{th}	16917> H_{th}	1.5449 > 1	OCF	24.37	Secured
			492.99< M_{th}, and 3184.8< M_{th}, and 2225.4< M_{th}	14794> H_{th}	1.4311 > 1	OCF	21.06	Secured
N	*N*	OCSE/EFRE	338.98< M_{th}, and 4010.6> M_{th}, and 1817.1< M_{th}	3669> H_{th}	2.2072 > 1	Failed	-	Unsecured
			389.8< M_{th}, and 3955.1> M_{th}, and 1829< M_{th}	3553.8> H_{th}	2.1625 > 1	Failed	-	Unsecured
			447< M_{th}, and 3262.6< M_{th}, and 2177.2< M_{th}	2810.7> H_{th}	1.4986 > 1	OCF	24.37	Secured
			471.57< M_{th}, and 3171.6< M_{th}, and 2257.2< M_{th}	2696.5> H_{th}	1.4051 > 1	OCF	21.06	Secured
	Y	OCSE/EFRE	351.04< M_{th}, and 4054> M_{th}, and 1847< M_{th}	19989> H_{th}	2.195 > 1	Failed	-	Unsecured
			404.75< M_{th}, and 3999.2> M_{th}, and 1850.6< M_{th}	20356> H_{th}	2.161 > 1	Failed	-	Unsecured
			458.19< M_{th}, and 3302.5< M_{th}, and 2201.1< M_{th}	17334> H_{th}	1.5004 > 1	OCF	24.37	Secured
			490.86 < M_{th}, and 3197.8 <M_{th}, and 2275.1 < M_{th}	14976 > H_{th}	1.405 > 1	OCF	21.06	Secured

10.3389/fenrg.2023.1208296

TABLE 7 LIF and HIF fault detection, identification, and fault classification results using the proposed schemes for the considered transposed and un-transposed lines with and without noise effect.

System transposed	Noise effect	Fault		R_f (Ω)	ϕ (degree)	I_α (A)	I_β (A)	I_0 (A)	Classification	Response time (mS)	Security
		Type	*Location*								
Y	*N*	LIF	69	10	120	1995.6	−55.112	3161.9	LIF	20	Secured
		HIF	110.4	100000	150	0.71441	0.010888	2163.1	HIF	20	Secured
	Y	LIF	69	10	120	1994.7	−55.41	3161.8	LIF	20	Secured
		HIF	110.4	100000	150	0.45203	0.34165	2163.1	HIF	20	Secured
N	*N*	LIF	69	10	120	1987.4	−68.214	3158.7	LIF	20	Secured
		HIF	110.4	100000	150	17.184	13.58	2170.1	HIF	20	Secured
	Y	LIF	69	10	120	1987.7	−68.119	3158.6	LIF	20	Secured
		HIF	110.4	100000	150	17.364	13.347	2170.3	HIF	20	Secured

TABLE 8 LIF and HIF fault detection, identification, and fault classification results using the DWT-based algorithm for the considered transposed and un-transposed lines with and without noise effect.

System transposed	Noise effect	Fault type	$M_a < M_{th}$, and $M_b < M_{th}$, and $M_c < M_{th}$	$H_a > H_{th}$, or $H_b > H_{th}$, or $H_c > H_{th}$	$R_a > >1$, or $R_b > 1$, or $R_c > 1$	Event classification	Fault detection time (mS)	Security
Y	*N*	LIF	7294.1> M_{th}	-	LIF	23.08	Secured	LIF
		HIF	-	0.99999 < 1	HIF	24.01	Secured	HIF
	Y	LIF	7389.8> M_{th}	-	LIF	23.08	Secured	LIF
		HIF	-	0.99925 < 1	HIF	24.01	Secured	HIF
N	*N*	LIF	7278.4> M_{th}	-	LIF	23.08	Secured	LIF
		HIF	-	0.98289 < 1	HIF	24.01	Secured	HIF
	Y	LIF	7360> M_{th}	-	LIF	23.08	Secured	LIF
		HIF	-	0.98254 < 1	HIF	24.01	Secured	HIF

for 500 kV TL is found using system verification in the ATPDraw software program. In Bañuelos-Cabral et al. (2019), the model's accuracy was increased by using only real poles through vector fitting.

The simulation studies are carried out to assess the suggested fault detection, identification, and fault classification scheme performance under various OCFs and simultaneous earth faults (OCSE/EFRE, OCSE/EFRE) in un-transposed and transposed TLs while sampling the current signal at 200 kHz, such that a conductor opens on both sides (OCFs): an OC on the relay aspect at 0.08 s, followed by a shunt fault on the opposite aspect due to low resistance of 3 Ω (OCSE/EFRE), and an OC on the relay's opposite aspect at 0.08 s, followed by a shunt fault caused by 3 Ω low resistance (OCRE/EFSE). The two kinds are repeated with HIFs and LIFs.

Furthermore, the proposed fault detection, identification, and fault classification schemes were verified during the recorded signals considering noise impacts as in practical TLs. Therefore, the recorded error signals captured in the proposed schemes are contaminated with white Gaussian noise, with a 30–60 dB signal-to-noise ratio. The proposed schemes are unaffected by any signal-to-noise ratio; however, a signal-to-noise ratio equal to 40 dB is used in this work.

First, we suppose an OCF occurs at 130 miles from the sending end. In that case, the values of Clarke components are shown in Figure 9 considering four scenarios (transposed line without noise effect, transposed line with noise effect, un-transposed line without noise effect, and un-transposed line with noise effect. When the conductor opens, one can find that phase a's current value decreases to the lowest value compared to its value before opening the conductor. For phase current *b*, a decrease in the current value up to 1,983 A occurs. Then, an increase in the current value up to 2,040 A occurs, followed by a reduction in its value up to 1,887 A and then an increase in its value up to 1965 A. For phase current c, an increase in the current value up to 2,193 occurs, followed by its decrease to 1995 A, then increases to 2,044 A, followed by a reduction in its value to 1873 A, taking into account that the value of phase current *b* is higher than that of phase current c, after steadying their values after a series of fluctuations. This, in turn, resulted in the sign of aerial modes 1 and 2 being negative and the sign of the grounding mode being positive. Based on the successive

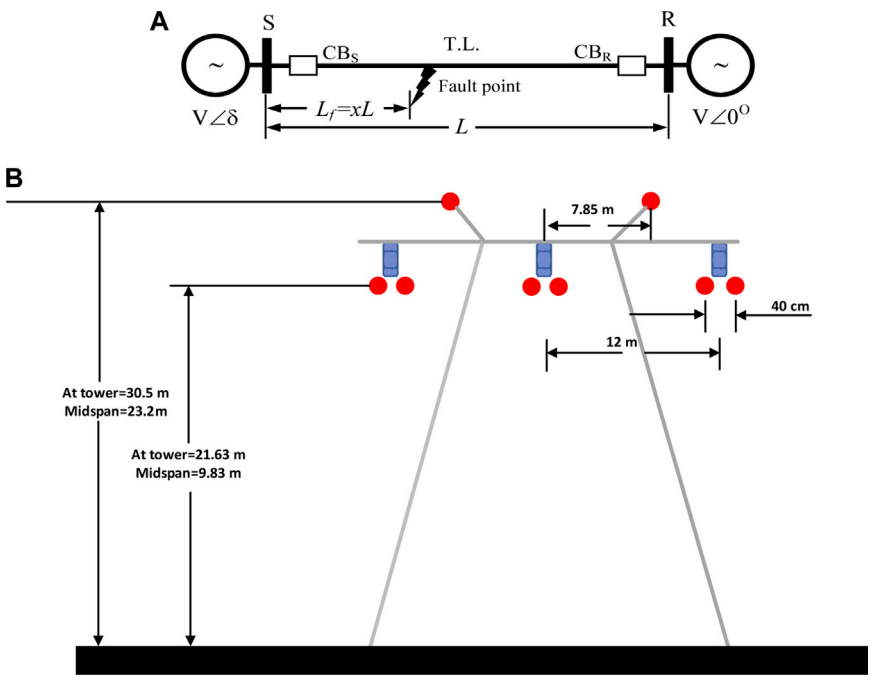

FIGURE 14
Single-line diagram of the second simulated TL system and the selected tower: **(A)** SLD; **(B)** tower configuration.

change in the values of phase currents *b* and *c*, it is possible to determine when the opening occurs (0.08 s) as the instant before the change.

Second, the values of the Clarke components in Figure 10 are shown when the OCSE/EFRE occurs at 130 miles from the sending end. In this figure, aerial mode 1 has a negative sign at the opening instant of the conductor (0.08 s), and its sign is still negative at the instant of a down conductor (0.16 s). When phase a touches the ground, one can notice that the current value of phase a remains at its minimum value, which reaches 331.3 A after opening the same phase a. In addition to the high value of phase current b (2667 A), compared to its exact value after opening phase a, as in the OCF case, phase c also causes a decrease in its current value to 1,310 A compared to its exact value after opening phase a. The high value of phase current b makes aerial mode 2 have a positive sign at the open conductor instant (0.08 s). Its value increases at the down conductor instant (0.16 s). The grounding mode has a positive sign, and its value slightly increases at the down conductor instant. Furthermore, based on the change in the values of phase currents b and c, it is possible to determine when the conductor was down (i.e., before this change). Third, the values of the Clarke components for OCRE/EFSE occurring at 130 miles from the sending end are shown in Figure 11 based on the values of the three-phase currents. As seen in this figure, the sign change from negative to positive for aerial mode 1 is caused by increasing the value of phase current a at the contact with the ground instant, which reaches 3,678 A, decreasing the value of phase current b (reaches 1,226 A) and increasing the value of phase current c, which reaches 2,844 A. Furthermore, aerial mode 2 has a positive sign at the open conductor instant (0.08 s) and changes to a negative sign at the down conductor instant (0.16 s). In comparison, the grounding mode has a positive sign, instantly increasing its value at the down conductor. On the other hand, the LIF was examined as a simulated case to state that the case is considered simple from the point of view of protection systems, giving a high fault current value.

Fourth, the values of the Clarke components are shown in Figure 12 for a condition of LIF happening at 130 miles away from the sending end. Aerial mode 1 has a positive sign at the LIF instant, and aerial mode 2 has a negative sign at the same instant. The grounding mode, however, has a positive sign, and its value increases at the LIF instant. The signs of Clarke components are caused by increasing the phase current reaches 3,703 A for phase a, 2,021 A for phase b, and 2,325 A for phase c after the LIF instant.

Fifth, for a HIF occurring at 130 miles away from the sending end, the Clarke components values are given in Figure 13.

In most cases, aerial modes 1 and 2 have a positive sign at the HIF. The value of the grounding mode increases at the moment of a HIF and has a positive sign at 0.16 s. These signs are caused by increasing the three-phase currents after the HIF instant (reaches 2,166 A).

5 Assessment of the proposed fault detection, identification, and fault classification schemes and other schemes presented in the literature

The suggested fault detection, identification, and fault classification scheme's behavior was verified distinctly by comparing it with the discrete wavelet transform (DWT)-based algorithm (Abd-Elhamed Rashad et al., 2020) through simulation

results. First approximation A_1 and first detail D_1 coefficients are extracted from three-phase current signals and are examined to detect various OCFs and simultaneous earth faults.

The following are the stages followed for the detection and classification of faults:

For the three-phase current signals (i_a, i_b, and i_c), apply single-level decomposition using db1 to obtain high-frequency components (D_1: 50–100 kHz) and low-frequency components (A_1: 0–50 kHz). Parameters are estimated at this stage using Eq. 8 expressions.

$$\begin{aligned} M_a(k) &= max\left|i_{a(n)}\right|_{n-k-N+1^k}, \\ M_b(k) &= max\left|i_{b(n)}\right|_{n-k-N+1^k}, \\ M_c(k) &= max\left|i_{c(n)}\right|_{n-k-N+1^k}. \end{aligned} \tag{8}$$

Here, n represents a sample demand in a sliding window covering a complete cycle, and N is the total number of samples in a process. Furthermore, one should calculate the highest absolute values of A_1 for the three-phase current signals (M_a, M_b, and M_c) at sample k.

Using the mathematical formulas in Eq. 9, determine the absolute decomposed currents' detail coefficients (S_a, S_b, and S_c) as follows:

$$\begin{aligned} S_a(k) &= \sum_{n=k-N+1}^{k} \left|D1i_{a(n)}\right|, \\ S_b(k) &= \sum_{n=k-N+1}^{k} \left|D1i_{b(n)}\right|, \\ S_c(k) &= \sum_{n=k-N+1}^{k} \left|D1i_{c(n)}\right|. \end{aligned} \tag{9}$$

Then, determine the differences in the absolute sum value for the three-phase current signals (H_a, H_b, and H_C) as follows:

$$\begin{aligned} H_a &= |S_a - S_b|, \\ H_b &= |S_b - S_c|, \\ H_c &= |S_c - S_a|. \end{aligned} \tag{10}$$

Next, determine the approximation coefficient ratios (R_a, R_b, and R_c) to detect OCFs.

$$\begin{aligned} R_a &= \left|M_a/M_b\right|, \\ R_b &= \left|M_b/M_c\right|, \\ R_c &= \left|M_c/M_a\right|. \end{aligned} \tag{11}$$

Finally, if the following criteria are met, the OCF is declared confirmed.

None of the M values exceed the predetermined M_{th} value, as expressed in Eq. 12.

$$M_a < M_{th}\ and\ M_b < M_{th}\ and\ M_c < M_{th}. \tag{12}$$

One of the H values is higher than the threshold value H_{th} and remains there for more than 20 ms, as expressed in Eq. 13.

$$H_a > H_{th}\ or\ H_b > H_{th}\ or\ H_c > H_{th}. \tag{13}$$

One or more of the R ratios exceeds 1.

$$R_a > 1\ or R_b > 1\ or R_c > 1. \tag{14}$$

It must be emphasized that the predetermined values in this platform (M_{th} and H_{th}) are determined based on the pre-fault (M_a, M_b, and M_c) with no operator interference (Abd-Elhamed Rashad et al., 2020).

5.1 Cases studied

Distinctive fault types across the TL length were evaluated through various fault situations (locations, inception angles, and fault resistance values) to explain the efficacy of the suggested schemes in detecting simultaneous OCSE/EFRE and OCSE/EFRE. The cases can be organized as follows to detect and classify faults successively:

Case 1: OCFs at different locations and fault time occurrence (inception angle ϕ in degrees).

Case 2: OCRE/EFSE at different locations and fault time occurrence considering fault resistance effects.

Case 3: OCSE/EFRE at different locations and fault time occurrence considering fault resistance effects.

Case 4: LIF and HIF at a specific location and specific fault time occurrence considering fault resistance effects.

5.2 Response of fault detection, identification, and fault classification schemes

5.2.1 Simulation results: case 1

Two test scenarios in case 1 are studied to determine the proposed scheme's ability to detect and classify faults correctly. First, we suppose an OCF occurring 13.8 miles from the sending end at a fault inception angle set to 0°. In this case, the values of Clarke components are presented in Table 1 for the transposed TL without the noise effect in the first row, the transposed line with noise effect in the first shadow row, the un-transposed line without noise effect in the third row, and the un-transposed line with noise effect in the second shadow row.

As shown in all previous tables, changing the fault location and ϕ has no effect on the results of the proposed scheme. Moreover, the suggested fault detection, identification, and classification schemes have identified all of them correctly.

The results of the DWT-based algorithm (Abd-Elhamed Rashad et al., 2020) in the same cases are also where the values of (M_a, M_b, and M_c), (H_a, H_b, and H_c), and (R_a, R_b, and R_c) are calculated in the four scenarios considered (the transposed line without noise in Table 2 in the first row, the transposed line with noise effect in the first shadow row, the un-transposed line without noise effect in the third row, and the un-transposed line with noise effect in the second shadow row.

As shown in the previous results, fault detection time in the DWT-based algorithm is greater than that in the suggested proposed schemes.

5.2.2 Simulation results: case 2

The security of the proposed schemes was verified by changing the fault resistance values and fault locations; different fault inception angles were examined with OCRE/EFSE. In this case, the values of the Clarke components are presented in Table 3 for the transposed line with no noise in the

TABLE 9 Fault detection, identification, and fault classification results using the proposed schemes for the transposed and un-transposed lines with and without noise effect.

System transposed	Noise effect	Fault		R_f (Ω)	I_α (A)	I_β (A)	I_0 (A)	Classification	Response time (mS)	Security
		Type	*Location*							
Y	*N*	OCFs	104	-	−1252.3	62.346	1374.3	OCF	20	Secured
		OCRE/EFSE	104	10	1560.2	−810.96	2936.5	OCRE/EFSE	20	Secured
		OCSE/EFRE	104	10	−1275.9	869.98	1391.9	OCSE/EFRE	20	Secured
		LIF	104	10	1484.3	−37.923	2991.4	LIF	20	Secured
		HIF	104	100000	0.64859	0.00001	2243.5	HIF	20	Secured
	Y	OCFs	104	-	−1252.3	62.778	1374.3	OCF	20	Secured
		OCRE/EFSE	104	10	1559.8	−810.81	2936.3	OCRE/EFSE	20	Secured
		OCSE/EFRE	104	10	−1275.5	869.95	1391.8	OCSE/EFRE	20	Secured
		LIF	104	10	1483.8	−37.957	2991.3	LIF	20	Secured
		HIF	104	100000	0.49608	0.46507	2243.5	HIF	20	Secured
N	*N*	OCFs	104	-	−1291.6	44	1411.8	OCF	20	Secured
		OCRE/EFSE	104	10	1507.2	−734.19	2841.9	OCRE/EFSE	20	Secured
		OCSE/EFRE	104	10	−1380.5	836.52	1494.9	OCSE/EFRE	20	Secured
		LIF	104	10	1388.9	−38.121	2963.8	LIF	20	Secured
		HIF	104	100000	55.258	71.208	2253.8	HIF	20	Secured
	Y	OCFs	104	-	−1291.8	44.222	1411.6	OCF	20	Secured
		OCRE/EFSE	104	10	1507.4	−733.34	2841.9	OCRE/EFSE	20	Secured
		OCSE/EFRE	104	10	−1380.5	836.29	1494.7	OCSE/EFRE	20	Secured
		LIF	104	10	1388.9	−38.144	2963.9	LIF	20	Secured
		HIF	104	100000	55.241	71.272	2253.7	HIF	20	Secured

first row, the transposed line with noise effect in the first shadow row, the un-transposed line without noise effect in the third row, and the un-transposed line with noise effect in the second shadow row.

This table shows that changing fault locations, fault resistances, and fault inception angles does not affect the effectiveness of the proposed fault detection, identification, and fault classification scheme.

Similarly, the results of the DWT-based algorithm (Abd-Elhamed Rashad et al., 2020) in the same cases are presented. The values of (M_a, M_b, and M_c), (H_a, H_b, and H_c), and (R_a, R_b, and R_c) are calculated considering the four scenarios, as shown in Table 4, respectively. As shown in this table, $M_a > M_{th}$ and $M_c > M_{th}$ are unsatisfied, which was caused by small fault resistance values. In such cases, the DWT-based algorithm failed to detect this type of fault and can be considered insecure against small values of fault resistances.

5.2.3 Simulation results: case 3

The proposed fault detection, identification, and fault classification schemes were examined considering OCSE/EFRE at different locations, inception angles, and fault resistance values. In this case, the values of Clarke components are shown in Tables 5 for the investigated scenarios, respectively. This table shows that changing fault locations, fault resistances, and fault inception angles does not affect the proposed fault detection, identification, and classification schemes.

Furthermore, as seen in Table 5, the signs of aerial modes 1 and 2 and ground mode are−ve, +ve, and +ve, respectively, at different fault locations, inception angle, and fault resistance values. Furthermore, the configuration of TL and noise impact does not affect the proposed fault detection, identification, and fault classification schemes. The DWT-based algorithm (Abd-Elhamed Rashad et al., 2020) was also examined as in the previous cases. The values of (M_a, M_b, and M_c), (H_a, H_b, and H), and (R_a, R_b, and R_c) are calculated for the four scenarios, as shown in Table 6.

TABLE 10 Fault detection, identification, and fault classification results using the DWT-based algorithm for transposed and un-transposed lines with and without noise effect.

System transposed	Noise effect	Fault type	OCF:$M_a < M_{th}$, and $M_b < M_{th}$, and $M_c < M_{th}$ and LIF: $M_a > M_{th}$ or $M_b > M_{th}$, or $M_c > M_{th}$	$H_a > H_{th}$, or $H_b > H_{th}$, or $H_c > H_{th}$	$R_a > >1$, or $R_b > 1$, or $R_c > 1$ HIF: $R_a < <1$, or $R_b < 1$, or $R_c < 1$	Event classification	Fault detection time (mS)	Security
Y	N	OCFs	172.54 < 3675.34, and 2910.3 < 3675.34, and 2757.8 < 3675.35	2732.6 > 367.534	1.0553 > 1	OCF	21.46	OCFs
		OCRE/EFSE	6451.9 > 3675.34, and 2085 < 3675.34, and 4070.7 > 3675.34	4324.1 > 367.535	3.0944 > 1	Failed	-	OCRE/EFSE
		OCSE/EFRE	165.89 < 3675.34, and 3939.8 > 3675.34, and 1809.2 < 3675.36	3771.2 > 367.537	2.1776 > 1	Failed	-	OCSE/EFRE
		LIF	6333.1 > M_{th}	-	-	LIF	23.08	LIF
		HIF	-	-	0.93995 < 1	HIF	24.01	HIF
	Y	OCFs	195.29 < 3675.34, and 2957.8 < 3675.34, and 2793.7 < 3675.35	8872.6 > 367.534	1.0587 > 1	OCF	21.46	Secured
		OCRE/EFSE	6476.4 > 3675.34, and 2118.9 < 3675.34, and 4101.2 > 3675.34	11633 > 367.535	3.0564 > 1	Failed	-	Unsecured
		OCSE/EFRE	191.9 < 3675.34, and 3969.4 > 3675.34, and 1836.2 < 3675.36	12223 > 367.537	2.1618 > 1	Failed	-	Unsecured
		LIF	6374.3 > M_{th}	-	-	LIF	23.08	Secured
		HIF	-	-	0.96703 < 1	HIF	24.01	Secured
N	N	OCFs	169.97 < 3675.34, and 2969.1 < 3675.34, and 2859.4 < 3675.35	2793.2 > 367.534	1.0384 > 1	OCF	21.46	Secured
		OCRE/EFSE	6245.7 < 3675.34, and 2089.4 < 3675.34, and 3876 > 3675.34	4117.7 > 367.535	2.9892 > 1	Failed	-	Unsecured
		OCSE/EFRE	161.14 < 3675.34, and 4121.3 > 675.34, and 2068.5 < 3675.36	3956.4 > 367.537	1.9924 > 1	Failed	-	Unsecured
		LIF	6158 > M_{th}	-	-	LIF	23.08	Secured
		HIF	-	-	0.93835 < 1	HIF	24.01	Secured
	Y	OCFs	194.72 < 3675.34, and 3001.1 < 3675.34, and 2884.8 < 3675.35	9911.6 > 367.534	1.0403 > 1	OCF	21.46	Secured
		OCRE/EFSE	6289.1 > 3675.34, and 2123 < 3675.34, and 3902 > 3675.34	9041.8 > 367.535	2.9624 > 1	Failed	-	Unsecured
		OCSE/EFRE	187.37 < 3675.34, and 4155.5 > 3675.34, and 2097.1 < 3675.36	13154 > 367.537	1.9816 > 1	Failed	-	Unsecured
		LIF	6205.6 > M_{th}	-	-	LIF	23.08	Secured
		HIF	-	-	0.93878 < 1	HIF	24.01	Secured

The first two cases failed to detect the fault caused by small fault resistance values. Furthermore, the DWT-based algorithm takes more time to detect the fault than the proposed fault detection, identification, and classification schemes.

5.2.4 Simulation results: case 4

The proposed fault detection, identification, and classification schemes also examined faults, such as LIFs and HIFs, considering various locations, inception angles, and fault resistance values. In

this case, the values of Clarke components for the investigated scenarios are shown in Table 7. As presented in this table, the proposed fault detection, identification, and fault classification schemes are accurately distinguished between LIFs and HIFs. The DWT-based algorithm was also examined for the same scenarios in this case. The values of (M_a, M_b, and M_c), (H_a, H_b, and H_c), and (R_a, R_b, and R_c) are calculated and presented in Table 8.

The tables show that the DWT-based algorithm provided good discrimination between LIFs and HIFs. However, the DWT-based algorithm took considerable time for fault detection compared to the proposed fault detection, identification, and classification schemes.

5.3 Generalization of the proposed schemes

The proposed fault detection, identification, and fault classification schemes can also be generalized for any transmission system. Figure 14A shows the single-line diagram of 400 kV, 144 km TL simulated in the ATP/EMTP program. The ATPDraw software is an interface to implement the system (Prikler and Høidalen, 2009). This TL model is a benchmark in the ATPDraw software, and it is represented using the three-phase JMARTI frequency dependence model in the ATPDraw field using the line/cable module (Prikler and Høidalen, 2009). The JMARTI representation is a frequency-fitted model in a specific frequency range. The JMARTI model is utilized to apply the simulated line and, therefore, take waveforms for the fault case in evaluating the proposed schemes. For simultaneous series and shunt earth fault detection and classification using Clarke transform for TLs under different fault scenarios, the line parameters have been extracted, and results show that the self-impedance of this line, for a length of 144 km, is 0.3382 + j1.6009 Ω, while that of the mutually linked one is 0.3282 + j 0.8493 Ω, according to the retrieved line parameters. Using a mutually linked RL circuit, Thevenin's equivalent impedance at buses S and R are expressed as R_1 = 1.0185 Ω and L_1 = 50.929 mH, and zero sequences are R_0 = 2.037 Ω, L_0= 101.85 mH at bus S and R_1 = 0.6366 Ω, L_1 = 31.83 mH, R_0= 1.2732 Ω, L_0= 63.66 mH at bus R. The TL configuration is illustrated in Figure 14B, where the dc resistance is 0.0522 Ω/km, and the outer diameter of the conductor is 3.18 cm. The sky wires are solid, their dc resistance is 0.36 Ω/mile, and the outer diameter is 1.46 cm. The resistivity of the soil is equal to 200 Ω. Similarly, a small error in simulation for 400 kV TL is found using system verification in the ATPDraw software program.

The proposed fault detection, identification, and classification schemes are also examined using another TL data, considering several fault types. In this case, the values of Clarke components for the investigated scenarios are shown in Table 9. In addition, the DWT-based algorithm was examined in the same scenarios, as shown in Table 10, where the values of (M_a, M_b, and M_c), (H_a, H_b, and H_c), and (R_a, R_b, R_c) were calculated. As presented in these tables, considering the OCRE/EFSE occurred, the values of $M_a > M_{th}$ and $M_c > M_{th}$ caused by small fault resistances were unmet. In addition, the values are $H_a > H_{th}$ and R_a>1. Furthermore, the proposed fault detection, identification, and fault classification schemes provided precise fault detection, identification, and fault classification for the investigated types of faults.

The proposed schemes' challenge is their performance if the current transformers' saturation occurs. The current transformers must correctly provide the protection relays with the stepped-down fault current level. Proper means to detect current transformer saturation are essential for digital signal processing. Esmail et al. (2015) suggested an effective method for detecting current transformer saturation with a universal distinction index without a necessity for setting a definition. For this point, the instantaneous sample-based multiplication of the secondary current by its derivative is individually employed to distinguish between saturated and unsaturated wave portions.

Reconstructing the detected saturated secondary current is accomplished using Kalman filtering to obtain the phasor quantities of the unsaturated current portion professionally.

6 Conclusion

This study solves the challenge of detecting simultaneous earth faults in high-voltage transmission systems as traditional distance relays, for example, the inability to find or detect OCFs and simultaneous earth faults. The proposed schemes comprise two different stages: fault detection and identification and fault classification. The first proposed scheme needs communication links among both ends (sending and receiving) to detect and identify the fault. This communication link between both ends is used to send and receive three-phase currents' magnitudes for sending and receiving ends in the proposed fault detection (PFD) unit at both ends. The second proposed scheme starts with proposed fault classification (PFC) units at both ends. The proposed classification technique applies the Clarke transform on local current signals to classify the open conductor and simultaneous faults. The sign of all current Clarke components is the primary key for distinguishing between all types of simultaneous LIFs and HIFs. Numerous simulation tests were investigated to analyze the performance of the suggested fault detection, identification, and classification schemes. In all scenarios, the fault type was accurately detected, identified, and classified within 20 mS after fault occurrence.

The security of the proposed schemes was also verified with different fault resistance values, and the suggested scheme provided precise fault detection, identification, and classification. The results demonstrated that fault detection, identification, and classification schemes are immune to fault types, locations, and inception angles. Furthermore, the suggested schemes detected both instants of the open conductor and down conductor. The developed scheme's superiority was also validated through a comparison study with another published procedure based on discrete wavelet transform. No sophisticated artificial intelligence techniques were required to detect, identify, and classify the faults accurately. Also, the proposed fault detection, identification, and fault classification schemes have low mathematical requirements. It should be mentioned that the Clarke transform was used with a low sampling frequency in this work; hence, the suggested fault detection, identification, and classification approaches are guaranteed to be promising schemes

that can be implemented in practice. Finally, other applications of the proposed schemes in series compensated transmission lines will be investigated in future works.

Data availability statement

The original contributions presented in the study are included in the article/Supplementary Material; further inquiries can be directed to the corresponding author.

Author contributions

Conceptualization: EE and FA; software: MC, EE, FA, and SA; validation: AA, AY, and AE-S; formal analysis: EE and FA; investigation: EE and AA; resources: SA; writing—original draft preparation: EE and SA; writing—review and editing: FA and SA; visualization: EE and AE-S. All authors contributed to the article and approved the submitted version.

Acknowledgments

This work was supported by the Researchers Supporting Project (RSPD 2023R646), King Saud University, Riyadh, Saudi Arabia.

Conflict of interest

The authors declare that the research was conducted in the absence of any commercial or financial relationships that could be construed as a potential conflict of interest.

Publisher's note

All claims expressed in this article are solely those of the authors and do not necessarily represent those of their affiliated organizations, or those of the publisher, the editors, and the reviewers. Any product that may be evaluated in this article, or claim that may be made by its manufacturer, is not guaranteed or endorsed by the publisher.

References

Abd-Elhamed Rashad, B., Ibrahim, D. K., Gilany, M. I., and El'Gharably, A. F. (2020). Adaptive single-end transient-based scheme for detection and location of open conductor faults in HV transmission lines. *Electr. Power Syst. Res.* 182, 106252. doi:10.1016/j.epsr.2020.106252

Abdel-Aziz, A., Hasaneen, B. M., and Dawood, A. A. (2017). Detection and classification of one conductor open faults in parallel transmission line using artificial neural network. *Int. J. Sci. Res. Eng. Trends*. https://api.semanticscholar.org/CorpusID:28122028.

Adewole, A. C., Rajapakse, A., Ouellette, D., and Forsyth, P. (2020). Residual current-based method for open phase detection in radial and multi-source power systems. *Int. J. Electr. Power Energy Syst.* 117, 105610. doi:10.1016/j.ijepes.2019.105610

Alstom, G. (2017). "Network protection and automation guide: protective relays," in *Meas. Control*. Retrieved 9th Febr.

Ashok, V., Yadav, A., and Abdelaziz, A. Y. (2019). MODWT-based fault detection and classification scheme for cross-country and evolving faults. *Electr. Power Syst. Res.* 175, 105897. doi:10.1016/j.epsr.2019.105897

Assadi, K., Slimane, J. B., Chalandi, H., and Salhi, S. (2023). Shunt faults detection and classification in electrical power transmission line systems based on artificial neural networks. *COMPEL - Int. J. Comput. Math. Electr. Electron. Eng.* ahead-of-print. doi:10.1108/COMPEL-10-2022-0371

Asuhaimi Mohd Zin, A., Saini, M., Mustafa, M. W., Sultan, A. R., and Rahimuddin, (2015). New algorithm for detection and fault classification on parallel transmission line using DWT and BPNN based on Clarke's transformation. *Neurocomputing* 168, 983–993. doi:10.1016/j.neucom.2015.05.026

Banner, C. L., and Don Russell, B. (1997). Practical high-impedance fault detection on distribution feeders. *IEEE Trans. Ind. Appl.* 33, 635–640. doi:10.1109/28.585852

Bañuelos-Cabral, E. S., Gutiérrez-Robles, J. A., García-Sánchez, J. L., Sotelo-Castañón, J., and Galván-Sánchez, V. A. (2019). Accuracy enhancement of the JMarti model by using real poles through vector fitting. *Electr. Eng.* 101, 635–646. doi:10.1007/s00202-019-00807-8

Dash, P. K., Pradhan, A. K., and Panda, G. (2000). A novel fuzzy neural network based distance relaying scheme. *IEEE Trans. Power Deliv.* 15, 902–907. doi:10.1109/61.871350

Elkalashy, N. I., Kawady, T. A., Khater, W. M., and Taalab, A.-M. I. (2016). Unsynchronized Fault-location technique for double-circuit transmission systems independent of line parameters. *IEEE Trans. Power Deliv.* 31, 1591–1600. doi:10.1109/TPWRD.2015.2472638

Elkalashy, N. I. (2014). Simplified parameter-less fault locator using double-end synchronized data for overhead transmission lines. *Int. Trans. Electr. Energy Syst.* 24, 808–818. doi:10.1002/etep.1736

Elmitwally, A., and Ghanem, A. (2021). Local current-based method for fault identification and location on series capacitor-compensated transmission line with different configurations. *Int. J. Electr. Power Energy Syst.* 133, 107283. doi:10.1016/j.ijepes.2021.107283

Esmail, E. M., Elkalashy, N. I., Kawady, T. A., Taalab, A.-M. I., and Lehtonen, M. (2015). Detection of partial saturation and waveform compensation of current transformers. *IEEE Trans. Power Deliv.* 30, 1620–1622. doi:10.1109/TPWRD.2014.2361032

Esmail, E. M., Elgamasy, M. M., Kawady, T. A., Taalab, A.-M. I., Elkalashy, N. I., and Elsadd, M. A. (2022). Detection and experimental investigation of open conductor and single-phase earth return faults in distribution systems. *Int. J. Electr. Power Energy Syst.* 140, 108089. doi:10.1016/j.ijepes.2022.108089

Ghaderi, A., Ginn, H. L., and Mohammadpour, H. A. (2017). High impedance fault detection: A review. *Electr. Power Syst. Res.* 143, 376–388. doi:10.1016/j.epsr.2016.10.021

Gilany, M., Al-Kandari, A., and Hassan, B. (2010). "ANN based technique for enhancement of distance relay performance against open-conductor in HV transmission lines," in 2010 The 2nd International Conference on Computer and Automation Engineering, Singapore, 26-28 February 2010 (ICCAE), 50–54.

Jayabharata Reddy, M., and Mohanta, D. K. (2007). A wavelet-fuzzy combined approach for classification and location of transmission line faults. *Int. J. Electr. Power Energy Syst.* 29, 669–678. doi:10.1016/j.ijepes.2007.05.001

Jayamaha, D. K. J. S., Madhushani, I. H. N., Gamage, R. S. S. J., Tennakoon, P. P. B., Lucas, J. R., and Jayatunga, U. (2017). "Open conductor fault detection," in 2017 Moratuwa Engineering Research Conference, Moratuwa, Sri Lanka, 29-31 May 2017 (MERCon), 363–367.

Jeerings, D. I., and Linders, J. R. (1991). A practical protective relay for down-conductor faults. *IEEE Power Eng. Rev.* 11, 59. doi:10.1109/MPER.1991.88840

Kavaskar, S., and Kant, N. (2019). Detection of high impedance fault in distribution networks. *Ain Shams Eng. J.* 10, 5–13. doi:10.1016/j.asej.2018.04.006

Khoshbouy, M., Yazdaninejadi, A., and Bolandi, T. G. (2022). Transmission line adaptive protection scheme: A new fault detection approach based on pilot superimposed impedance. *Int. J. Electr. Power Energy Syst.* 137, 107826. doi:10.1016/j.ijepes.2021.107826

Koley, E., Yadav, A., and Thoke, S. A., (2014). Artificial neural network based protection scheme for one conductor open faults in six phase transmission line. *Int. J. Comput. Appl.* 101, 42–46. doi:10.5120/17678-8522

Mahanty, R. N., and Gupta, P. B. D. (2007). A fuzzy logic based fault classification approach using current samples only. *Electr. Power Syst. Res.* 77, 501–507. doi:10.1016/j.epsr.2006.04.009

Prikler, L., and Høidalen, H. K. (2009). *For windows 9x/NT/2000/XP/vista users ' manual.*

Rathore, B., and Shaik, A. G. (2015). "Fault detection and classification on transmission line using wavelet based alienation algorithm," in 2015 IEEE Innovative Smart Grid Technologies - Asia (ISGT ASIA), Bangkok, Thailand, 03-06 November 2015, 1–6.

Saravanababu, K., Balakrishnan, P., and Sathiyasekar, K. (2013). "Transmission line faults detection, classification, and location using Discrete Wavelet Transform," in 2013 International Conference on Power, Energy and Control, Dindigul, India, 6-8 February 2013 (ICPEC), 233–238.

Shaik, A. G., and Pulipaka, R. R. V. (2015). A new wavelet based fault detection, classification and location in transmission lines. *Int. J. Electr. Power Energy Syst.* 64, 35–40. doi:10.1016/j.ijepes.2014.06.065

Shukla, S. K., Koley, E., and Ghosh, S. (2017). "Detection and classification of open conductor faults in six-phase transmission line using wavelet transform and naive Bayes classifier," in 2017 IEEE International Conference on Computational Intelligence and Computing Research, Coimbatore, India, 14-16 December 2017 (ICCIC), 1–6.

Silva, S., Costa, P., Gouvea, M., Lacerda, A., Alves, F., and Leite, D. (2018). High impedance fault detection in power distribution systems using wavelet transform and evolving neural network. *Electr. Power Syst. Res.* 154, 474–483. doi:10.1016/j.epsr.2017.08.039

Usama, Y., Lu, X., Imam, H., Sen, C., and Kar, N. C. (2014). Design and implementation of a wavelet analysisbased shunt fault detection and identification module for transmission lines application. *IET Gener. Transm. Distrib.* 8, 431–441. doi:10.1049/iet-gtd.2013.0200

Velez, F. (2014). "Open conductor analysis and detection," in 2014 IEEE PES General Meeting | Conference and Exposition, Dallas, Texas, United States, July 2014, 1–7.

Vieira, F. L., Santos, P. H. M., Carvalho Filho, J. M., Leborgne, R. C., and Leite, M. P. (2019). A voltage-based approach for series high impedance Fault Detection and location in distribution systems using Smart meters. *Energies* 12, 3022. doi:10.3390/en12153022

Zanjani, M. G. M., Kargar, H. K., and Zanjani, M. G. M. (2012). "High impedance fault detection of distribution network by phasor measurement units," in 2012 Proceedings of 17th Conference on Electrical Power Distribution, Tehran, Iran, 2-3 May 2012, 1–5.

Frontiers in
Energy Research

Advances and innovation in sustainable, reliable and affordable energy

Explores sustainable and environmental developments in energy. It focuses on technological advances supporting Sustainable Development Goal 7: access to affordable, reliable, sustainable and modern energy for all.

Discover the latest Research Topics

See more →

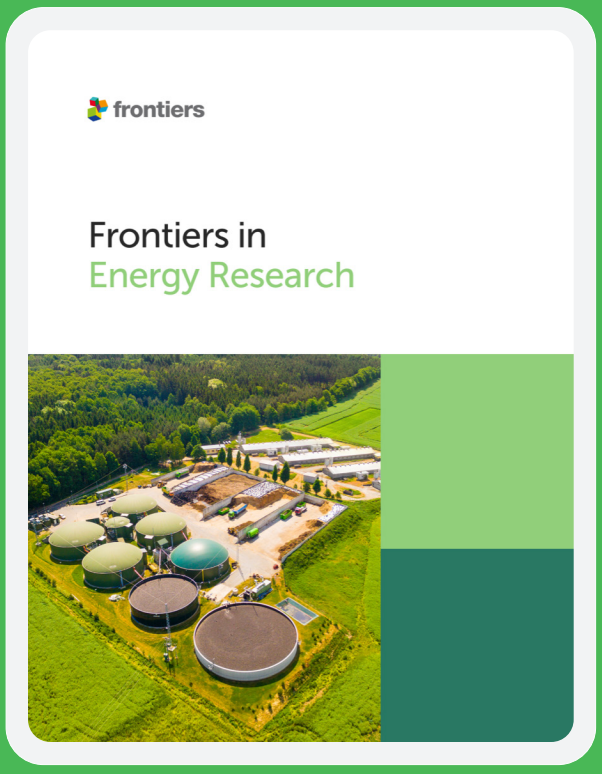

Frontiers

Avenue du Tribunal-Fédéral 34
1005 Lausanne, Switzerland
frontiersin.org

Contact us

+41 (0)21 510 17 00
frontiersin.org/about/contact